CORA Cork Open Research Archive
Cartlann Taighde Oscailte Chorcaí

Title	Macro to micro-scale insights into granite petrogenesis; a case study from the Caledonian Ross of Mull granite (ROMG), Argyllshire, Northwest Scotland
Authors	Zaniewski, Adam
Publication date	2018
Original Citation	Zaniewski, A. 2018. Macro to micro-scale insights into granite petrogenesis; a case study from the Caledonian Ross of Mull granite (ROMG), Argyllshire, Northwest Scotland. PhD Thesis, University College Cork.
Type of publication	Doctoral thesis
Rights	© 2018, Adam Zaniewski. - http://creativecommons.org/licenses/by-nc-nd/3.0/
Download date	2026-11-06 12:32:35
Item downloaded from	https://hdl.handle.net/10468/6704



Macro to Micro-scale insights into granite petrogenesis; a case study from the Caledonian Ross of Mull Granite (ROMG), Argyllshire, Northwest Scotland

Adam Zaniewski

Submitted in fulfilment for the degree of Doctor of Philosophy,

March 2018

Supervisors: R.J. Reavy, A.A. Finch & J.A. Gamble



School of Biological, Earth & Environmental Sciences,
National University of Ireland,
Cork

Head of School: Prof. S. Culloty

ABSTRACT

The Ross of Mull Granite (ROMG) occupies the largest part of the Pre-Paleogene inlier of the Ross of Mull peninsula, Isle of Mull, Argyllshire, Scotland and is the most south-westerly of the Northwest Highland Caledonian granitoid complexes.

Re-mapping of the entire intrusion (Zaniewski *et al.* 2006) has revealed a reverse zonation of facies resulting from mafic-felsic magma interaction prior to ascent at the proposed intersection of the Sound of Iona Fault and Great Glen Fault with north-eastward emplacement of flattish sheets into high-grade lithologies of the Moine Supergroup. Subsequent to mapping, Quantitative X-Ray Diffractometry (QXRD) has re-enforced modal classifications of Zaniewski *et al.* (2006).

To further examine if this phenomenon is also encoded at the micro-scale (crystal), and if a correlation exists with macro-scale (field) studies, *in-situ* elemental and Pb-Pb isotopic zoning in magmatic feldspars from all ROMG components were analysed. The following micro-scale studies have been undertaken: (a) detailed textural study of feldspars using cold Cathodo-Luminescence (CL) and Back-Scatter Electron (BSE) imaging; (b) acquisition of feldspar major and minor element abundances by Electron Probe Micro Analysis (EPMA) and Pb-Pb isotopes by Laser Ablation Multicollector Inductively Coupled Plasma Mass Spectrometry (LA-MC-ICP-MS).

Feldspars throughout the components display a three-fold CL magmatic zonation associated with dissolution at the core followed by elemental spike zones of Ba, Sr (0.00 - 1.00 wt. %) and Ab [mol. %] with elemental re-equilibration back towards the rims. Such resorption surfaces correspond to rim-ward increase of $^{206}Pb/^{204}Pb$ and $^{208}Pb/^{204}Pb$ in alkali feldspars in host granitoid and andesine in early phase MME advocate dissolution attributed to punctuated mafic magmatic recharge from a mantle-derived component interacting with a crustal component. Bulk Pb-Pb isotope data also highlight the importance of magma mixing and mingling in the petrogenesis of the complex and define a simple binary mixing array reflecting quasi-contemporaneous hybridisation between such components.

A temporal sequence of macro-scale and micro-scale events is proposed and it is evident that the process of mafic-felsic magma interaction seen at the outcrop-scale is encoded at the crystal-scale.

TABLE OF CONTENTS

Abstract *i*

Table of Contents *iii*

List of Figures *xiii*

List of Tables *xv*

Declaration *xvi*

Acknowledgements and Dedication *xvii*

CHAPTER ONE: INTRODUCTION **1**

Chapter One: INTRODUCTION TO THIS THESIS

1.1 Introduction **2**

1.2 Why Study the Ross of Mull Granite (ROMG) **7**

1.3 Thesis Structure (Chapters and Objectives) **8**

CHAPTER TWO: FIELD RELATIONSHIPS AND PETROGRAPHY **12**

Chapter Two: THE CRYSTALLISATION HISTORY OF THE ROSS OF MULL GRANITE

2.1 Introduction **13**

Refer to Attachments to Appendix A8.1 - Field Map (1): ROMG (found in back-sleeve)

2.2 Nature and Distribution of the Granites **14**

2.2.1 **RM1**: The 'Red Bay' type facies 15

2.2.2 **RM1a**: The 'White' granite - *Refer to Appendix A8.2/3 - Field Maps (2) & (3)* 18

2.2.3 **RM2**: The 'Knockvologan' type facies - *Refer to Appendix A8.4 - Field Map (4)* 20

2.2.4 Summary of the granitoids 21

2.3 Aplitic micro-granites, Pegmatites and Syenite 22
2.3.1 Aplitic micro-granites 23
2.3.2 Pegmatites 26
2.3.3 Syenite 27
2.3.4 Zones of alteration 28
2.3.5 Summary of aplitic micro-granites, pegmatites and syenite 29

2.4 Diorite Masses 30

Refer to Attachments to Appendix A8.4 - Field Map (4)

2.4.1 Type 1 diorite component: 'Knockvologan' suite 30
2.4.2 Type 2 diorite component: 'Aird Mór' suite 35

2.5 MME of the ROMG 35
2.5.1 Enclave types and distribution; the Knockvologan mixing and mingling zone 37
2.5.2 Hornblende phyric enclaves from the Knockvologan mixing and mingling zone 38

2.6 Caledonian Minor Intrusions; Nature, distribution and structure 39
2.6.1 Type 1 lamprophyres 39
2.6.2 Type 2 lamprophyres 43

2.7 Interpretation of textural heterogeneity within the ROMG and Caledonian Minor Intrusions 46

2.8 Inferences from Structural Observations/Data: Diorites, MME & *Sub-Solidus* Features 50

2.9 Discussion and Conclusions 53
2.9.1 Interpretation of the crysallisation history of the ROMG 54
2.9.2 Overview: field to crystal scale heterogeneity across the ROMG 58
2.9.3 ROMG Emplacement Model 61

CHAPTER THREE: MODAL ANALYSIS 64

Chapter Three: MODAL ANALYSIS

3.1 Introduction 65

3.2 Materials and Methods 66
3.2.1 Field Modes 67
3.2.2 Point Count Modes 68
3.2.3 QXRD Modes 69

3.3 Results **71**
3.3.1 Field Mode Data 71
3.3.2 Point Count Data 73
3.3.3 QXRD/SIROQUANT Refined Data 74
3.3.4 Precision of all Modal Methods 77

3.4 Discussion and Conclusions **80**

CHAPTER FOUR: FINGERPRINTING PETROLOGICAL PROCESSES IN THE ROMG VIA MICRO SCALE STUDIES ON FELDSPARS **86**

Chapter Four: COLD CATHODOLUMINESCENCE (CL) WITH INTEGRATED *IN SITU* ELEMENTAL & ISOTOPIC GEOCHEMISTRY ON ROMG FELDSPARS

4.1 Introduction **87**

4.2 Materials & Methods **89**
4.2.1 Cold Cathodoluminescence (CL) 90
4.2.2 Electron Probe Micro Analysis (EPMA) 90
4.2.3 Laser Ablation Multiple Collector-Inductively Coupled Plasma Mass Spectrometry (LA MC-ICP-MS) 91

4.3 Results; CL Petrography and *In Situ* analysis of ROMG feldspars **94**
4.3.1 RM1 95
4.3.2 RM1a 104
4.3.3 RM2 110
4.3.4 Mafic components; MME Phase 1 & MME Phase 2 116

4.4 Discussion and Conclusions **127**

CHAPTER FIVE: SUMMARY & CONCLUSIONS **140**

Chapter Five: SUMMARY & CONCLUSIONS

5.1 Macro to Micro-scale study of the ROMG **141**

5.2 Macro to Micro-sequence **143**

APPENDICES AND REFERENCES **146**

APPENDICES

A1 Field Data **147**

A1.1 MME 2D data tables for rose diagrams in **Fig. 2.24** (refer to **Fig. 2.24** for codes depicting place names**)**. Two tables depict unordered and ordered data. 148

A1.2 MME 3D data tables for stereogram in **Fig 2.24**. 151

A1.3 Major joint plane data for stereogram in **Fig. 2.25**. 152

A1.4 'Aplitic' microgranite-sheet data for stereogram in **Fig. 2.25**. 154

A2 Petrography **156**

A2.1 Petrographic descriptions with accompanying sketches from mafic to felsic components of the ROMG**.** 157

A2.2 Thin section magma mixing/mingling textures in ROMG components. 195

A3 Modal Analysis **214**

A3.1 Field mode data. 215

A3.2 Point count data. 216

A3.3 QXRD/SIROQUANT refined data. 217

A3.4 XRF - Summary of procedural blank and standards data (**A3.5 - A3.7**). 219

A3.5 Quartz procedural blank trace element data with calibration ranges used for all samples in this study. 222

A3.6 RM1 sample AZ005 trace element heterogeneity test. 223

A3.7 Major element and trace element data for RM1 sample DLC1/AF0207. 224

A3.8 Preparation of analyses for QXRD. 225

A3.9 SIROQUANT procedure. 234

A3.10 Weighed standards used for SIROQUANT QXRD. 238

A3.11 Precision. 238

A3.12 Precision around averages. 239

A4 CL & Mineral Geochemistry 240

A4.1 CL Manual (University of St. Andrews). 241

A4.2 Tabulated bulk EPMA feldspar data. 248

A4.3 Bulk NIST 610 glass data only. 252

A4.4 Tabulated bulk Pb-Pb feldspar data. 253

A4.5 Tabulated bulk Pb-Pb feldspar average data. 256

A5 ROMG Sample Stations 257

A5.1 Sample reference list. 258

A5.2 Sample stations map. 262

A5.3 Lamprophyre sample sations map. 263

A6 Published Material 264

A6.1 ZANIEWSKI, A., REAVY, R.J. & HARRIS A.L. 2006. Field relationships and emplacement of the Ross of Mull Granite (ROMG), Argyllshire. *Scottish Journal of Geology* **42,** 179-189. 265

REFERENCES 276

ATTACHMENTS TO APPENDIX (on memory stick labelled AZ ROMG 2017)

A7 DLC Electronic Raw Data

A7.1 Raw EPMA hardcopy generated data sheets.

A7.2 EPMA converted/tabulated data per mineral sample only.

A7.3 Raw Pb-Pb AXIOM hardcopy generated data sheets.

A7.4 AXIOM Pb-Pb fractionation corrections for data per mineral sample only.

A8 Original Field Sheets

A8.1 Map (1) ROMG 1:25 000 – Also found folded and placed in thesis back sleeve.

A8.2 Map (2) Bendoran 1:10 000.

A8.3 Map (3) Ardalanish Bay 1:5 000.

A8.4 Map (4) Knockvologan 1:10 000.

LIST OF FIGURES

Chapter One: INTRODUCTION TO THIS THESIS

Fig. 1.1	Location and extent of study area considered on the Ross of Mull, Isle of Mull, Argyllshire, Scotland.	3
Fig. 1.2	Geological map of Mull and Iona (modified from Potts *et al.* 1995).	4
Fig. 1.3	Map depicting extent of ROMG outcrop, localities on the Ross of Mull and series of offshore islands (Zaniewski *et al.* 2006).	4
Fig. 1.4	Outcrops of Caledonian granitoids including major faults and thrusts north of the Iapetus Suture (modified after Atherton & Ghani 2002).	5
Fig. 1.5	Tectonic map around Mull, north of the Great Glen Fault (modified from Potts *et al.* 1995; Pharoah *et al.* 1996).	6
Fig. 1.6	Flow diagram depicting techniques used in this study to assist in assessment of objectives and ROMG petrogenesis.	8

Chapter Two: FIELD RELATIONSHIPS AND PETROGRAPHY

Fig. 2.1	Solid geological map of the western end of the Ross of Mull (revised from Sheet 43 S and modified from Zaniewski *et al.* 2006).	14
Fig. 2.2	Petrographic image of RM1 (sample No. RR0104 (NM [2990 2318])) (XPL) highlighting equal distributions of quartz (**qtz.**), alkali (**kf.**) and plagioclase feldspar (**pf.**).	15
Fig. 2.3	Example of joint plane system in structural continuity within RM1 gently dipping WNW. Photograph depicting cross section is taken North of Fionnphort where this feature is easier to	17

observe (looking northeast from (NM [3017 2383])). Iona is in the background.

Fig. 2.4 (a-c) **(a)** Petrographic contact of RM1a with Moine meta-sediments (RM1a to left of white arrows) highlighting quartz rich equigranular nature of RM1a at Ardalanish Bay (sample No. JR43 (NM [3670 1790])) (XPL). **(b)** Slightly coarser variant of RM1a with rare micas (none depicted here) and more microcline at Whitish, Ardalanish (sample No. JR2 (NM [3680 1790])) (XPL). **(c)** Medium grained equigranular RM1a with even distributions of quartz, alkali feldspar and plagioclase from Bendoran (sample No. JR7 (NM [3640 2180])) (XPL). Symbols for all images are as follows; quartz (**qtz.**), alkali feldspar (**kf.**), plagioclase feldspar (**pf.**), muscovite (**mu**.) and biotite (**bi**.). 19

Fig. 2.5 Geological map of Eilean Srianach also showing lateral extent of a Type 1 Caledonian sheet considered in this study. 20

Fig. 2.6 Petrographic image of RM2 (sample No. RR107 (NM [3005 2238])) (XPL). White arrow denotes Carlsbad twin in orthoclase perthite megacryst and two plagioclases with different zonation occur at the centre of the image. Black arrow shows a thin tenth of a mm sericitised zone characteristic of some of the plagioclases in RM2. Symbols for image are as follows; quartz (**qtz.**), alkali (**kf.**) and plagioclase feldspar (**pf.**). 21

Fig. 2.7 Aplitic micro-granite in RM1 occurring sub-parallel in terms of orientation to the major joint planes observed at Fionnphort. This example pinches out and is orientated at 184/28^{o}W displaying a cm scale sacharoidal upper margin made up of quartz (NM [3064 2494]). 23

Fig. 2.8 Solid geological map of Eilean nam Bo. 24

Fig. 2.9 Porphyritic aplitic micro-granite (sample No. AZ025 (NM [2958 2157])) (XPL) displaying corroded poly-crystalline quartz (**qtz.**), anhedral to subhedral plagioclase feldspars (**pf.**) and isolated hornblende (**hbld.**) mantled by small felsic minerals. Groundmass is mainly made up of felsic minerals and minor hornblende. 25

Fig. 2.10 Syenite phase from Tormore Cottage (sample No. AZ007 (NM [3016 2420])) (PPL). Symbols for image are as follows; quartz (**qtz.**), plagioclase feldspar (**pf.**), biotite (**bi.**) and titanite (**ti.**). 27

Fig. 2.11 Petrographic image of sample No. AZ024 (NM [2952 2166]) (XPL) highlighting a very fine-grained purple-green mottled 28

and granular appearance of all plagioclases throughout the rock. An example of a whole plagioclase feldspar is depicted in the top left area of the image that has anhedral interstitial quartz at the top of the crystal.

Fig. 2.12 (a-d) **(a)** A 2 km north to south panoramic across the Erraid Sound Looking east from Erraid (NM [3014 1888]) highlighting locations presented in **(b)**, **(c)** & **(d)**. **(b)** Appearance of Knockvologan Type 1 diorite at Knockvologan Beach (NM [3089 1925]). **(c)** Exposure of the contact between host RM2 granitoid and Type 1 diorite with cm to m scale MME having lobate contacts at the southwest portion of Eilean nan Griogag (NM [3066 1908]). **(d)** Example of a disrupted diorite body with cuspate xenocrystic MME west- southwest of Torr Mór a' Chonairst (NM [3094 1902]). The bulk distribution dip 20-30 east-southeast (main elongation direction in the photo) and a vague internal fabric is defined by an orientation of xenocrysts running in the same direction. 31

Fig. 2.13 A cut and polished slab of Type 1 diorite taken from Knockvologan Beach (NM [3089 1925]). 33

Fig. 2.14 (a-d) Petrographic features for Type 1 diorites depicting a range of textural heterogeneity (symbols for all images are as follows; quartz (**qtz.**), plagioclase feldspar (**pf.**), biotite (**bi.**), hornblende (**hbld.**) and titanite (**ti.**)): **(a)** Equigranular medium grained diorite (sample No. RR131 (NM [3093 2076]) composed of acicular biotite, hornblende and small glomerophyric clots of hornblende. Groundmass is predominantly laths of plagioclase and minor quartz (PPL). **(b)** A much coarser grained variant with abundant subhedral zoned plagioclase feldspar and minor hornblende in sample No. JR35 (NM [3080 1480]) (XPL). **(c)** Isolated subhedral plagioclase feldspar micro-phenocryst with a three-fold zonation. White arrows highlight a patchy beige sericitised zone that is characteristic in some plagioclase feldspar micro-phenocrysts observed throughout a spectrum of diorite masses (sample No. JR 27 (NM [2780 1400]) (PPL). **(d)** Glomerophyric amphibole clots mantled by biotite, titanite or opaque oxides (sample No. JR 30 (NM [3009 1890]) (XPL). 34

Fig. 2.15 Thin section displaying between MME and RM2 host granitoid (black arrows denote a small area of alkali feldspars nestling at the contact) in sample No. AZ040 (NM [2922 1921]). Note glomerophyric amphibole clots (green areas), rounded quartz (transparent areas) and alkali feldspar (light pink areas) commonly mantled by amphibole making up the characteristic heterogeneous crystal assemblage throughout the MME. 36

Fig. 2.16 (a-c) **(a)** Contact between MME and host RM2 in sample No. AZ040 (NM [2922 1921]) highlighted by black arrows and high concentration of biotite/opaque oxides. Highly corroded large quartz in top left area marks the limit of RM2 (PPL). **(b)** Contact between MME and host RM2 in sample No. JR27 (NM [2780 1400]) again highlighted by black arrows. Subhedral plagioclase feldspar defines limit of RM2 whilst the smaller aligned area consisting of biotite, minor euhedral titanite with zoned and un-zoned plagioclase defines the boundary of the MME (XPL). **(c)** Petrographic image of the central area of the MME considered in **(b)** illustrating a homogeneous equigranular texture (PPL). Symbols for images are as follows; quartz (**qtz.**), plagioclase feldspar (**pf.**), biotite (**bi.**), hornblende (**hbdl.**) and titanite (**ti.**). 36

Fig. 2.17 (a-d) **(a)** Bifurcating Type 1 Caledonian minor intrusion with planar And irregular contacts against RM1 at Fionnphort Pier orientated 012/23^{o} NW (NM [2985 2336]). Island in the background is Iona. **(b)** Perpendicular section through the sheet depicted in **(a)** displaying highly irregular contacts against host RM1 granitoid. **(c)** Continuation of the sheet in **(a)** at Eilean Eion (NM [3007 2415]) highlighting a considerably more mafic chilled upper margin (above dashed line) and subhedral to euhedral alkali feldspar xenocrysts derived from RM1 within the centre of the sheet. **(d)** Rapakivi feldspar glomeroxenocryst within the sheet in **(a)** (length of rapakivi glomeroxenocryst is 15 mm)). 40

Fig. 2.18 Petrographic image of the Type 1 Caledonian sheet considered in **Fig. 2.17 (c)** at Eilean Eion (sample No. ZSLS02 (NM [3007 2412])) (XPL). Fine-grained groundmass is chiefly made up of acicular to elongate hornblende and biotite, zoned subhedral plagioclase (often with sericitised cores) and minor interstitial quartz and calcite. The large subhedral plagioclase feldspar in the top left area of the image is individually mantled by smaller varieties of zoned and un-zoned plagioclase feldspar. 41

Fig. 2.19 (a-d) Caledonian Type 1 minor intrusion at Eilean Srianach (NM [3475 1685]): **(a)** Near perpendicular section through the complex hybridised Sheet illustrating the composite nature (most mafic area is in the top left area of the image) of such intrusions and consistent linear trails of dextrally sheared MME set within a more felsic hybridised medium. Orientation of the sheet is 028/44^{o}NW. **(b)** Ovoid cm scale MME commonly containing glomerocrystic amphibole clots and corroded anhedral quartz displaying dextrally sheared tails in a more hybridised felsic medium considered in **(c)** (British ten pence piece coin is in for scale). White arrow highlights a micro-granite globule. **(c)** Hybridised felsic medium absent of MME displaying a 42

highly porphyritic texture made up of variable crystal assemblages as amphibole clots, subhedral to euhedral alkali feldspar phenocrysts and xenocrysts. Largest pink crystal observed is a euhedral alkali feldspar monocryst.
(d) Base of the sheet (top left area) in contact with a Moine xenolith (indicated by black arrows) where an overall leopard skin texture dominates above the contact (British two pence piece coin is in for scale).

Fig. 2.20 (a-c) **(a)** A view of a bifurcating Type 2 Caledonian minor intrusion roughly along strike of the contact with RM2 host granitoid (NM [3224 1851]). 44
(b) Sheared margin of a Type 2 sheet at NM [3093 1866] in contact with RM2. Black arrow defines the orientation of elongate glomerophyric anhedral amphibole clots.
(c) Rare example of an upper margin of a Type 2 Caledonian sheet dominated by cm and mm scale anhedral alkali feldspar xenocrysts and glomerocrystic amphibole mantled by alkali feldspar (NM [3243 1700]).

Fig. 2.21 (a-b) **(a)** Petrographic image of Type 2 Caledonian minor intrusion (sample No. JR23 (NM [3090 1680])) (XPL) displaying an agglomerated amphibole clot made up of several glomerocrysts at the top of the image and an overall fine-grained equigranular groundmass composed of plagioclase, biotite, amphibole and little to no quartz. 45
(b) Presence of large areas of interstitial calcite (top and central area of image) is also a common feature in Type 2 minor intrusions (same sample as in **(a)** (XPL)).

Fig. 2.22 Simplified thin section textures in the ROMG and associated Caledonian minor intrusions related to mafic-felsic magma interaction (scale bars are 1mm for each sketch unless stated otherwise, and refer to **Table 2.1** for description and interpretation of textures in **A-I**). 47

Fig. 2.23 Summary of field to crystal scale heterogeneity across the ROMG (west to east traverse). Block diagram of mixing/ mingling features in syn-plutonic diorite (white text), all MME and directly adjacent granodioritic RM2; black text refers to features in RM2 only; black text set within a black border refers to features prevalent in all ROMG components and black text set in white borders refers to features observed in RM1 only. 49

Fig. 2.24 Equal area weighted rose diagrams showing principal long axes measurements in MME and *c*-axes of alkali feldspar xenocrysts within MME on a 2D plane in Type 1 syn-plutonic diorite intrusions and predominantly host RM2. Data reflects a traverse from the Erraid Sound to Rubh' Ardalanish. Letters in rose diagrams correspond to the areas in the map where measurements 51

were made. Stereogram depicts gross orientation data for all MME measured in Type 1 syn-plutonic diorite sheets and host RM2 from the Erraid Sound to Rubh' Ardalanish (stereographic data plotted as poles to planes, and all data calculated in GeoorientV9.2 (Holcombe 2005)).

Fig. 2.25 Stereographic plot depicting all measurements of acid sheet and joint plane orientations within the ROMG (all data plotted as planes and calculated in GeoorientV9.2 (Holcombe 2005). 53

Fig. 2.26 Diagram (modified from Fernandez & Barbarin 1991; Barbarin 2005) displaying hybridisation stages for the ROMG are shown in photographs **(1)** to **(4)**:
(1) RM1 from Red Bay Quarry (NM [3115 2541]);
(2) MME at Knockvologan beach (NM [3088 1924]) (taken from Zaniewski *et al.* 2006);
(3a) Refer to **Fig. 2.12 (d)**;
(3b) MME 'flow channel' near Na Maoil Mhóra (NM[33690 16730]); **(4)** Refer to **Fig. 2.17 (a)**. 57

Fig. 2.27 Regional diagrammatic cross-section across the Sound of Iona Fault (SIF) zone (extensional model) (adapted from Potts *et al.* 1995). 61

Fig. 2.28 Block diagram across the Sound of Iona Fault (SIF) zone depicting the emplacement geometry of the flattish batches of melt within and extensional regime created by the combined movements of the SIF and eastward-directed collapse within Caledonia thrust nappes. An accompanying simplified cross-section through the sheeted ROMG is also depicted highlighting key areas and processes (adapted from Zaniewski *et al.* 2006). 62

Chapter Three: MODAL ANALYSIS

Fig. 3.1 Location and facies map of the ROMG (adapted from Zaniewski *et al.* 2006); place names are given for ease to use as when cited in the text. 66

Fig. 3.2 (a) ROMG Field mode sample stations. 67

(b) ROMG Point Count mode sample stations. 68

(c) ROMG QXRD mode sample stations. 70

Fig. 3.3 **(a.)** to **(c.)** Streckiesen (1976) QAP (quartz-alkali feldspar-Plagioclase feldspar) plots for ROMG components from all modal techniques. Streckiesen (1976) QAP fields as follows; (2) Alkali feldspar granite; (3) Granite; (4) Granodiorite; (5) Tonalite; (6) Alkali feldspar syenite; (6*) Alkali fedspar quartz syenite; (7*) Syenite; (8) Monzonite; (8*) Quartz 72

monzonite; (9) Monzodiorite; (9*) Quartz monzodiorite; (10) Diorite; (10*) Quartz Diorite.
(d.) to **(g.)** Bottom right four diagrams are Streckiesen (1976) QAP plots comparing fields for individual components as per respective modal technique (Mi in **(g)** refers to QXRD calibration for microcline).
(h.) Repeat of sample runs AZ005 for all types of modal analysis (n=5).
(i.) RM1 averages and data spread for all types of modal analyses (Field n =7; Point Counting n=36; QXRD n=88).

Chapter Four: COLD CL & FELDSPAR CHEMOSTRATIGRAPHY

Fig. 4.1	Map depicting the location of samples used for CL and *in-situ* geochemical analysis (adapted from Zaniewski *et al.* 2006).	88
Fig. 4.2 (a-c)	Cold CL petrographic textures of feldspars within RM1 (**DLC1A/AF0207** (**RM1**) **(a), (b) & (c)**).	96
Fig. 4.3 (part 1&2)	EP backscatter, cold CL image of RM1 alkali feldspar (DLC1A/AF0207) with line drawing of zonation profile and respective *in-situ* elemental and Pb-Pb isotopic traverses (A-B).	99/100
Fig. 4.4 (part 1&2)	EP backscatter, cold CL image of RM1 alkali feldspar (DLC1D/AF0207) with line drawing of zonation profile and respective *in-situ* elemental and Pb-Pb isotopic traverses (C-D).	101/102
Fig. 4.5 (a-c)	Cold CL petrographic textures of feldspars within RM1a (**DLC3A/AF/02/01** (**RM1a**) **(a), (b) & (c)**).	105
Fig. 4.6 (part 1&2)	EP backscatter image of RM1a alkali feldspar (DLC3A/AF/02/01) from Bendoran with line drawing of zonation profile and respective *in-situ* elemental and Pb-Pb isotopic traverses (E-F).	107/108
Fig. 4.7 (a-b)	Cold CL petrographic textures of feldspars within RM2 (**DLC7A/RR120** (**RM2**) **(a)** & **(b)**).	110
Fig. 4.8 (part 1&2)	EP backscatter, cold CL image of RM2 (adjacent to disrupted diorite in terms on m's) alkali feldspar (DLC7A/RR120) from Knockvologan with line drawing of zonation profile and respective *in-situ* elemental and Pb-Pb isotopic traverses (G-H).	113/114
Fig. 4.9	Double MME at Knockvologan beach (NM [3084 1967]) depicting locality where Phase 1 MME and 2 MME feldspar crystal samples are directly obtained from (modified from Zaniewski *et al*. 2006)	117

Fig. 4.10	Cold CL petrographic textures of feldspars within Phase 1 Type MME/Type 1 Diorite (**DLC10-11/RR019 Phase 1 Type MME/Type 1 Diorite (a), (b), (c)** & **(d)**).	118
Fig. 4.11 (part 1&2)	EP backscatter, cold CL image (an analogue is used for CL) of Phase 1 MME (DLC10-11/RR019) from Knockvologan with line drawing of zonation profile and respective *in-situ* elemental and Pb-Pb isotopic traverses (J-K).	121/122
Fig. 4.12 (part 1&2)	EP backscatter and photographic image (an analogue is used for CL) of Phase 2 MME (DLC8-9F/JR37) from 'Knockvologan' with line drawing of zonation profile and respective *in-situ* elemental and Pb-Pb isotopic traverses (L-M).	125/126
Fig. 4.13	Ternary feldspar plots depicting all in-situ elemental traverses for all feldspar crystal samples considered in this chapter.	129
Fig. 4.14	Cartoon depicting petrogenesis of feldspars within mafic and felsic components of the ROMG.	132
Fig. 4.15	Individual in-situ Pb-Pb isotopic traverses (Pb-Pb isotopic ratio vs. mineral zone/distance) for all feldspar crystals considered in this Chapter.	135
Fig. 4.16	Bulk *in-situ* Pb-Pb isotopic bivariate graphs for the ROMG.	136
Fig. 4.17	Sub-solidus textures in RM1.	138

LIST OF TABLES

Chapter Two: FIELD RELATIONSHIPS AND PETROGRAPHY

Table 2.1	Summary of textures **A-I** as observed in **Figure 2.22**.	48

Chapter Four: COLD CL AND FELDSPAR CHEMOSTRATIGRAPHY

Table 4.1 (a)	DLC1A:AF0207 (RM1) - Raw data ranges for BaO, SrO, Or % and Pb-Pb isotopic systems.	98
Table 4.1 (b)	DLC1A:AF0209 (RM1) - Raw data ranges for BaO, SrO, Or % and Pb-Pb isotopic systems.	98
Table 4.2	DLC3A:AF/02/01 (RM1a) - Raw data ranges for BaO, SrO, Or % and Pb-Pb isotopic systems.	109

Table 4.3	DLC7A:RR120 (RM2) - Raw data ranges for BaO, SrO, Or % and Pb-Pb isotopic systems.	115
Table 4.4	DLC10-11B:RR019 (MME1) - Raw data ranges for BaO, SrO, Or % and Pb-Pb isotopic systems.	120
Table 4.5	DLC8-9F/JR37 (MME2) - Raw data ranges for BaO, SrO, Or % and Pb-Pb isotopic systems.	124
Table 4.6	Pb-Pb rim with respect to core data for all crystals considered in this study.	130

DECLARATION

This is to certify that the work I am submitting is my own and has not been submitted for another degree, either at University College Cork or elsewhere. All external references and sources are clearly acknowledged and identified within the contents. I have read and understood the regulations of University College Cork concerning plagiarism.

Adam Zaniewski

December 2017

ACKNOWLEDGEMENTS & DEDICATION

Where does one begin with a study that has taken in excess of ten years to simply sit down and write-up? The science part of this thesis was never in doubt and completed within three-years from the beginning of enrolling as a student at University College Cork, however the writing up…..well, after I ran out of many excuses, grew up after life taught me a few harsh lessons (with a great deal of trial and error of course), I can only stress that this journey could not have been completed without having the right people on board constantly supporting me, both academic and otherwise.

This study was conceived and instigated by my supervisor, John Reavy, who I can picture right now sitting at a table in John and Eleanor Wagstaff's house overlooking a sunset over Red Bay Quarry saying *'this is my favourite place in the world'*. I'm glad both of us have this connection in common and would like to thank him the most for his continued support, help in the field, correcting of manuscripts, and most of all, never giving up on me.

Whilst I collected the bulk of the samples in this study, the late Robert Hunter is thanked for introducing John Reavy to the complexity of mafic-felsic magma interaction on Knockvologan beach and for use of his collected ROMG samples I utilised in this study.

Special thanks also goes to my other supervisor, Adrian Finch, for help in the field and correction of manuscripts regarding absolutely anything to do with feldspars. Without his insight and use of laboratory at the University of St. Andrews, the micro-scale aspect of this study would never have been possible. His patience and gentle way of helping me through difficult patches were really appreciated. Angus Calder is also thanked for teaching me absolutely everything I need to know in a practical sense about X-ray powder diffractometry. Ruth Robinson is also thanked for helping me with accommodation during my stays in St Andrews, even after I accidentally put a hole in one of her walls.

Financial and logistical support, with which this thesis would not have been possible, was provided by a number of people and organisations. I acknowledge financial support from University College Cork and thank John Gamble for assisting in helping me to obtain a successful E.U. Marie Curie Fellowship to exploit the micro-geochemical facet of this study at the now extinct Danish Lithosphere Centre, Copenhagen. This really made me open up my

eyes in terms of networking in the world of igneous petrology. It was here where I fortuitously bumped into Tod Earl Waight, where after pestering him, he allowed me valuable probe time at the University of Copenhagen which was next door. I am grateful for his input regarding Chapter Four. Joel Baker and Martin Bizzaro are also thanked for AXIOM time and respective guidance.

Throughout this study, Malcolm Hole and Jeremy Preston, who were my undergraduate supervisors at the University of Aberdeen, always kept in touch and assisted me where appropriate. They are also thanked for introducing me to Caledonian magmatism.

Everyone of the Ross of Mull who assisted in terms of the logistical support during field seasons such as Nigel and Rosie Burgess, John and Eleanor Wagstaff and John Faithfull are also thanked.

My family and friends have given me 'plenty of stick' over these many years for not finishing of this piece of work. I can't stress how important my Mom Dee Chapman and Step-Dad Ian Chapman have been in encouraging me to write up and finish this thesis once and for all. Without their love, guidance and strong-will, I don't think I'd probably even be where I am now.

When I wake up every morning and know I've got Shelly Seddon by my side, I can accomplish anything. Her love and support has been a breath of fresh air and I can only thank her for accepting me for who I am.

Finally, this thesis is dedicated to both my grandfathers, Adam Zaniewski and Jan Wilkowski, who are sadly no longer with us. Clearly without their sacrifices, I wouldn't have had this opportunity.

Chapter One

INTRODUCTION

An introduction to the location and geology of the Ross of Mull, its granitoid complex, and to the main objectives of this study.

Chapter One

THE ROSS OF MULL GRANITE

Chapter One – Introduction

This chapter highlights the common igneous geological phenomenon of magma mingling/mixing and its importance in the context of granitoid petrogenesis. In using the Ross of Mull Granite (ROMG), Argyllshire, Scotland as a case study, which typifies a mid crustal putonic Caledonian igneous complex, it introduces the setting, location, relevant literature and highlights why this intrusion is a candidate to characterise and interpret this phenomenon from the field to crystal scale (hence the title of this thesis). This approach has been taken to improve our scientific understanding of ROMG petrogenesis post Zaniewski *et al.* (2006) (the most in-depth field study of the ROMG) literature, as it aims; to (i) document ROMG pluton-scale petrogenesis and to (ii) propose a detailed mixing history/series of events based on comparing macro-scale (field) to micro-scale (crystal) observations. Integrating classical geological mapping with modern-day micro-analytical techniques has meant the thesis structure is broken down into macro to micro-scale objectives.

1.1 Introduction

This thesis is concerned with understanding the role and significance of the process of mafic-felsic magma interaction in plutonic igneous systems. The Ross of Mull Granite belongs to a series of Caledonian granitoids (Dewey *et al*. 2015) that display abundant field to thin section scale textural evidence for this process playing a key role during their genesis. Such textures are associated with diorite, mafic magmatic enclaves (MME) (Barbarin 2005) and host granitoid. The ROMG thus provides a natural laboratory to study this process. To address the role and dominance of mafic-felsic magma interaction in the ROMG the techniques incorporated in this study are introduced in this chapter.

In recognition of this well-defined geological process, this study focuses on observations from the field and uses mineral and geochemical investigations on the ROMG and its MME to interpret the petrological evolution of this Caledonian granitoid complex.

The location of the ROMG and area of study is depicted in **Fig. 1.1**. The ROMG (414 ± 6 Ma, K-Ar age of Beckinsale & Obradovich 1973; 414 ± 3 Ma, Rb-Sr age of Halliday *et al.* 1979; 418 ± 5 Ma, U-Pb age of Oliver *et al.* 2008 via sensitive high-resolution ion micro-

probe (SHRIMP); 425 ± 6 Ma, U-Pb age of McAteer 2009 (ion micro-probe concordia age determination from a zircon separate)) occupies the western end of the pre-Palaeogene inlier on the Ross of Mull (**Fig. 1.2** & **Fig 1.3**) and is the most south-westerly of the Northwest Highland Caledonian granitoids (see Soper 1986; Potts *et al.* 1995; Atherton & Ghani 2002; Oliver *et al.* 2008 and Dewey *et al.* 2015 for the geochronological, structural and geochemical context of Caledonian granitoids). The intrusion belongs to a suite of 'Newer' (Read 1961) now termed 'Late' Caledonian granites (**Fig. 1.4**) that were emplaced in Scotland and Ireland during the Caledonian Orogeny between 447 and 383 Ma (Atherton & Ghani 2002; Oliver *et al.* 2008; Dewey *et al.* 2015).

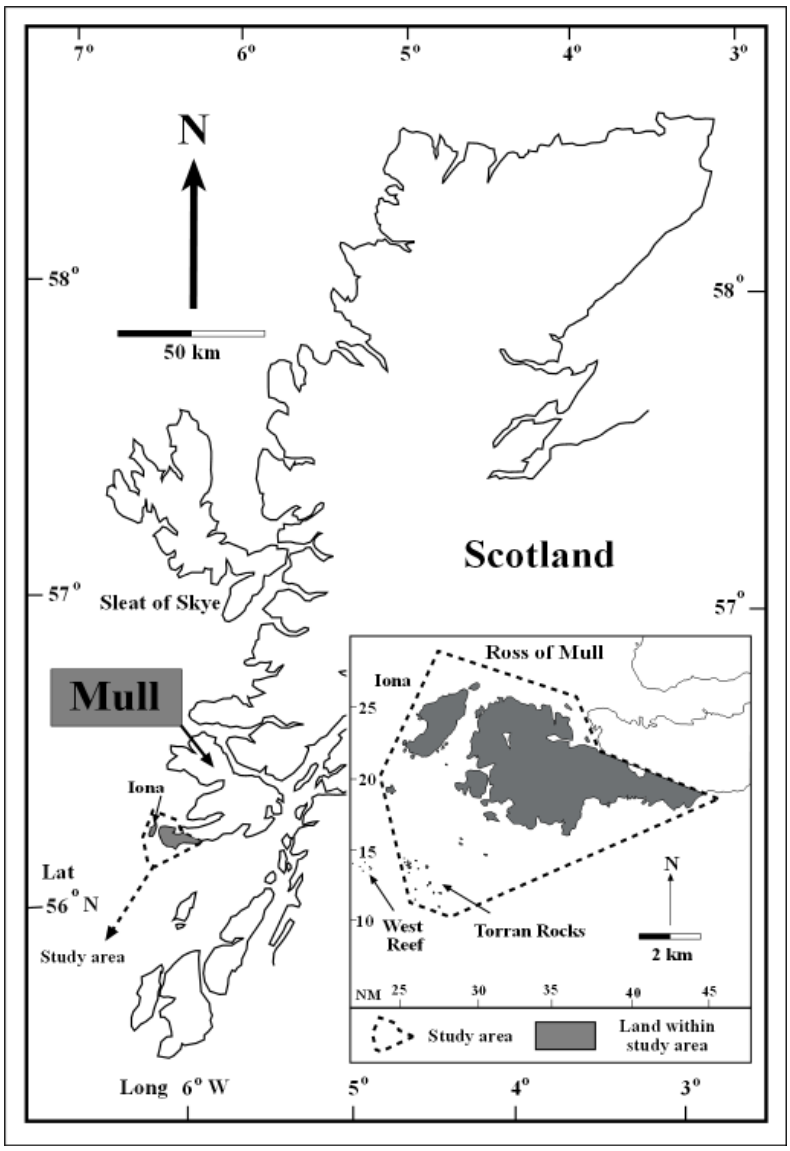


Fig. 1.1 Location and extent of study area considered on the Ross of Mull, Isle of Mull, Argyllshire, Scotland.

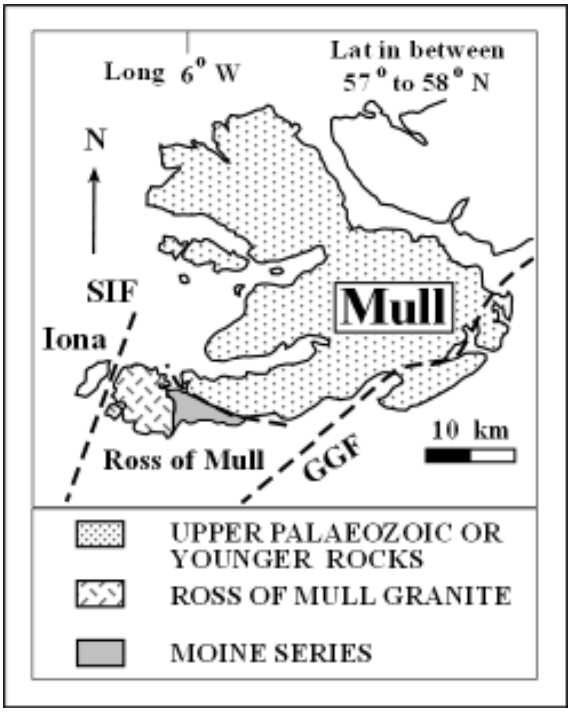


Fig. 1.2 Geological map of Mull and Iona (modified from Potts *et al.* 1995).

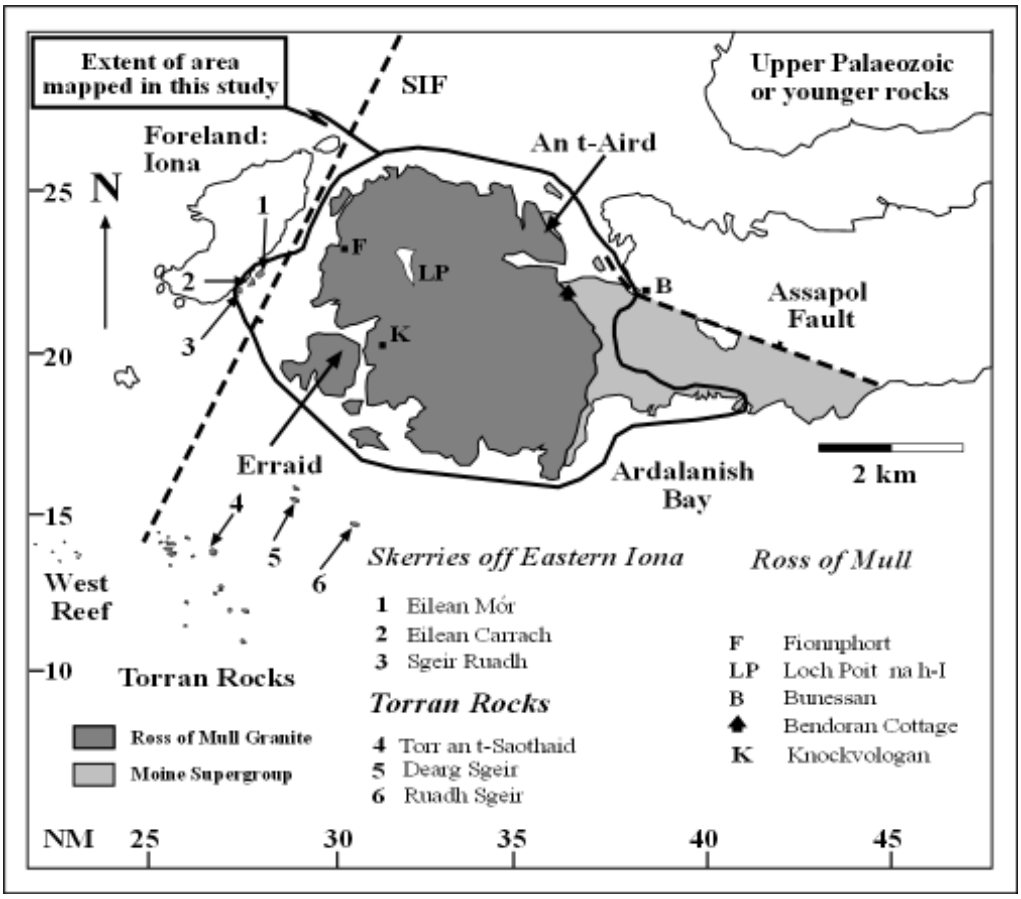


Fig. 1.3 Map depicting extent of ROMG outcrop, localities on the Ross of Mull and series of offshore islands (Zaniewski *et al.* 2006).

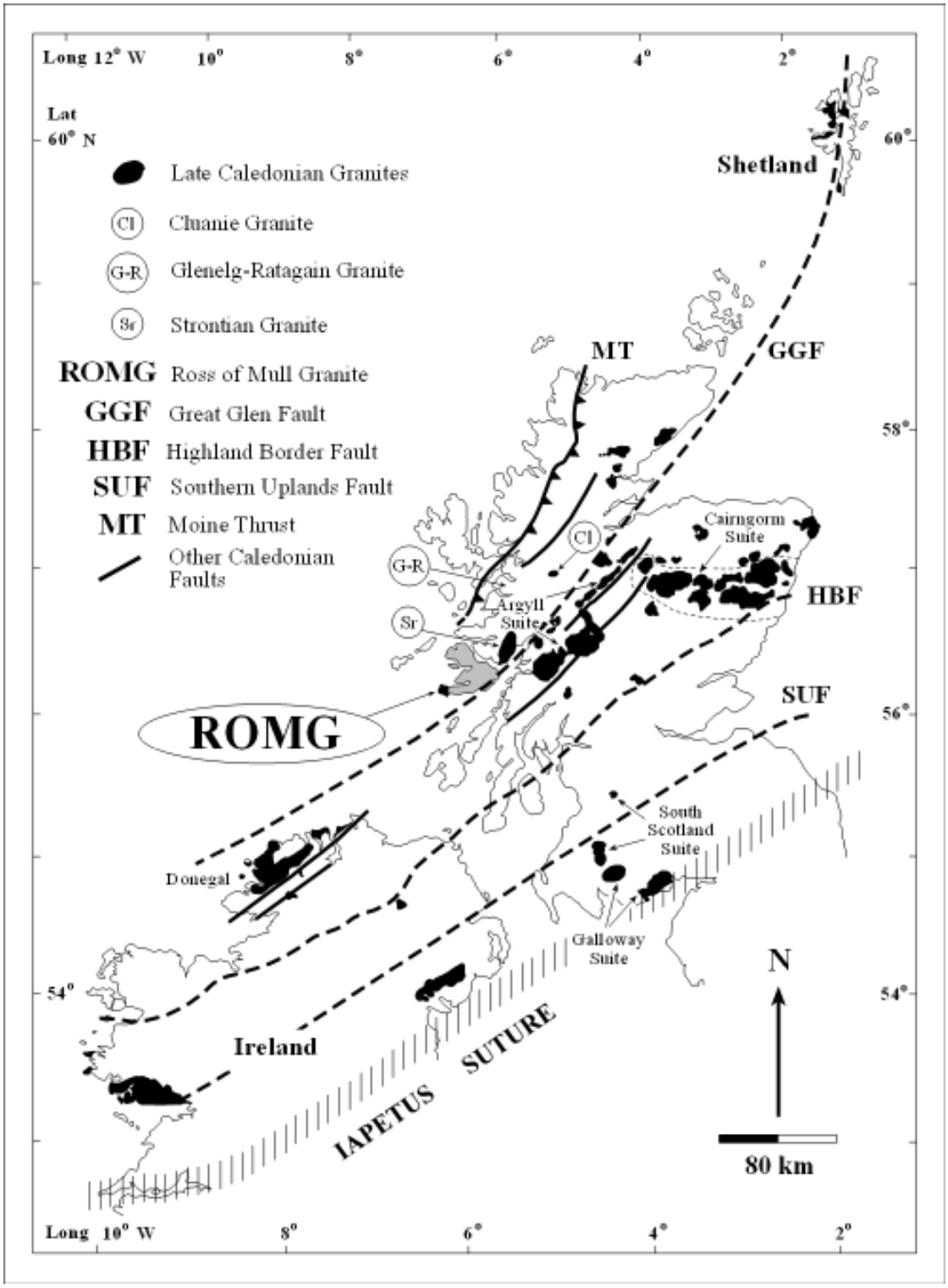


Fig. 1.4 Outcrops of Caledonian granitoids including major faults and thrusts north of the Iapetus Suture (modified after Atherton & Ghani 2002).

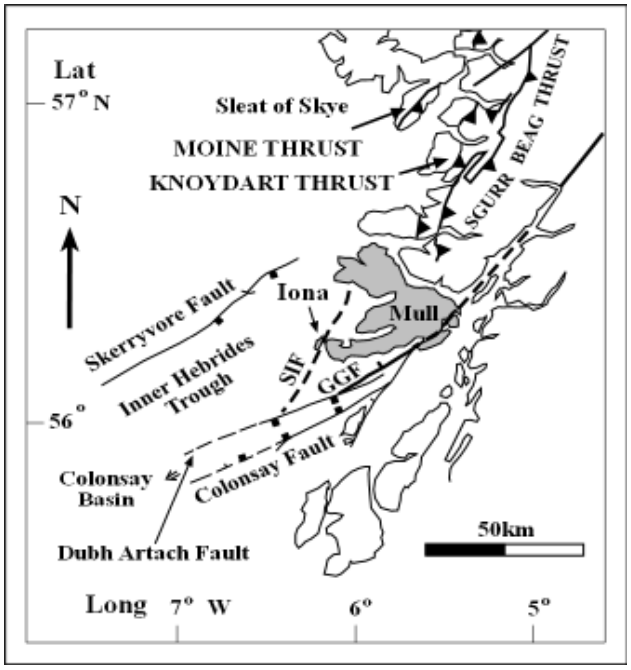


Fig. 1.5 Tectonic map around Mull, north of the Great Glen Fault (modified from Potts *et al.* 1995; Pharoah *et al.* 1996).

The most up-to date model for the genesis of these granitoids (including the ROMG) is presented by Atherton & Ghani (2002) to which the implications (pros and cons) of their model with respect to Caledonian magmatism are philosophically re-summarised in Dewey *et al.* (2015). Atherton & Ghani (2002) demonstrated a complex model depicting a sequence of events on slab breakoff resultant from collision of Baltica, Laurentia and Avalonia in relation to Caledonian plutonsism. In their model they demonstrate the syn-collisional nature of the timing of 'Late' Caledonian granitoids. They explain in relation to the process of slab rupture, post-Scandian imbrication (435 Ma), the significance of underplating of sub continental lithosphere by appintic/lamprophyric magmas of mantle origin to form granitic magmas at a peak maxima at 410 - 400 Ma; to which a geochemical/field distinction in relation to these granitoids occurring geographically/tectonically either side of the trench are accounted for in Stephens & Halliday (1984).

Jacques & Reavy (1994) highlighted the importance of lithospheric structures in facilitating siting, ascent and emplacement of Caledonian granitoids. Zaniewski *et al.* (2006) provided detailed re-mapping of the ROMG recognising the importance of the intersection of the Sound of Iona Fault (SIF) and Great Glen Fault (GGF) (the ROMG lies between these structures (**Fig. 1.5**)) in siting and magma ascent of the ROMG. Emplacement of the ROMG was interpreted by Zaniewski *et al.* (2006) as being facilitated by an overall post-orogenic

extensional collapse within stacked Moine nappes post-Scandian orogenic thrusting (Potts *et al.* 1995) by a mechanism in which batches of magma were emplaced northwards and eastwards to form flattish sheets that now make up the reversely zoned complex.

Micro-analytical work presented in McLeod *et al.* (2011) utilised carefully selected magmatic titanite micro-samples from mafic-felsic components to define titanite chemo-stratigraphy to make inferences on ROMG petrogenesis and define magma mixing events. McLeod *et al.* (2011) highlighted punctuated mafic magmatic recharge in specific growth zones as being evident and dominant within such components. Their model highlights that although some fractional crystallisation may be apparent in ROMG diorite, mingling and mixing are chiefly the dominant processes in ROMG petrogenesis. This is typified in their study using opposite trends of LREE/HREE (Light/Heavy Rare Earth Elements) for diorite-host granitoid titanites; whereby LREE rim-growth enrichment of titanites in host-granitoid is inferred to have captured mixing resultant from parental mafic magmatic replenishment.

Petronis *et al.* (2012) utilised Anisotropy of Magnetic Susceptibility (AMS) on the ROMG to interpret and propose a slightly alternative model of emplacement for the ROMG occurring either prior to orogenic collapse or during a period of compressional reactivation.

1.2 Why Study the Ross of Mull Granite (ROMG)?

The present erosion level within the ROMG provides a southwest to northeast section through a reversely zoned sheeted granitoid complex. In the southwest it displays abundant diorite and associated flattened MME (Zaniewski *et al.* 2006) and as one progresses northeast such mafic components within host granitoid diminish. It has been chosen for this study simply because of its unique field relationships; its reverse zonation coupled with extensive coastal exposures and natural wave cut sections allow direct access to all components.

As previous research regarding the petrogenesis of the ROMG (Zaniewski *et al.* 2006; McLeod *et al.* 2011) highlights extensive evidence for mafic-felsic magma interaction, the ROMG serves as a case-study granitoid to utilise field mapping integrated with whole rock to crystal scale geological techniques to identify, test, and quantify the extent and role of this process in granitoid petrogenesis. In the case of the ROMG, that is adjacent to the Argyll Suite, but the most south-westerly occurring of the Northwest Highland Caledonian granitoids (refer back to **Fig. 1.4**), a study of mixing and mingling from this igneous complex also has

implications on understanding current models of Caledonian magmatism. However, it is stressed that this is a pluton-scale study, where the aims of this thesis are to thus compare macro to micro-scale observations to (i) unravel the petrogenesis of the ROMG at the pluton scale and to provide (ii) a review of granitoid petrogenesis expanding on relevant literature (e.g. McLeod *et al*. 2011).

1.3 Thesis Structure (Chapters and Objectives)

This thesis has five chapters. In order to test the role and dominance of mafic-felsic magma interaction in the ROMG, Chapters Two to Four utilise various geological techniques to make inferences on petrogenesis. Chapter Five forms a synopsis.

The flow diagram in **Fig. 1.6** depicts all techniques used in this study to analyse the

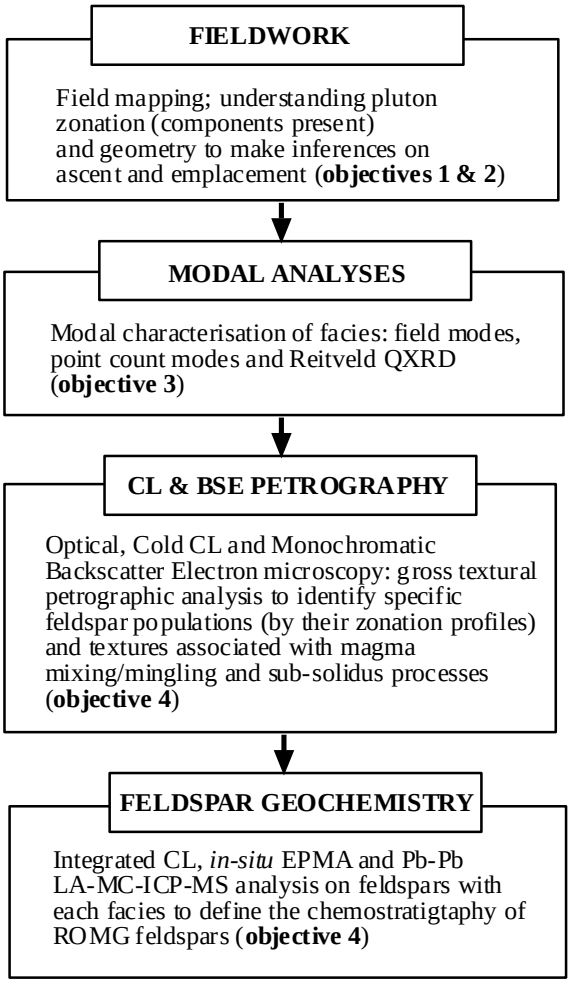


Fig. 1.6 Flow diagram depicting techniques used in this study to assist in assessment of objectives and ROMG petrogenesis.

ROMG in order to make inferences on petrogenesis so that all objectives presented are achieved.

The chapters with respective objectives are as follows:

Chapter One. Overview and background

Chapter One is an introduction to this study, presenting study area location and its geology, the geological setting, and why the ROMG has been chosen for research. It outlines the main structure and objectives presented with relevant themes of Caledonian granitoid research.

Chapter Two. Fieldwork and petrography

The fieldwork aspect of Chapter Two has been addressed in Zaniewski *et al.* (2006) (this publication is included in **Appendix A6.1**):

Zaniewski, A., Reavy, R.J. & Harris, A.L. 2006. Field relationships and emplacement of the Caledonian Ross of Mull Granite, Argyllshire. *Scottish Journal of Geology* **42**, 179 - 189.

The following two objectives have already been achieved:

Objective (1)

A solid geological 1: 25 000 scale map has been constructed from re-mapping the entire ROMG complex on a 1: 10 000 scale (completed in order to produce the maps published in Zaniewski *et al.* 2006). The extent of the area mapped is shown in **Fig 1.3**.

Objective (2)

An emplacement model depicting the geometry and structure has been proposed based on field observations and interpretation of regional tectonic structure (published in Zaniewski *et al.* 2006).

Despite the work compiled and presented in Zaniewski *et al.* (2006), the detailed field sheets (provided in the appendices) utilised to produce the maps in Zaniewski *et al.* (2006) have never been published. Chapter Two forms a field and petrographic study summarising ROMG components in greater detail and provides additional field relationships and petrography not covered in Zaniewski *et al.* (2006). The aim of this descriptive chapter is to

detail ‘field to thin’ section scale heterogeneity across the ROMG so that the internal zonation with respect to crystallisation history is understood.

Chapter Three. Modal Analysis

Chapter Three utilises modal analytical techniques (field modes, point counting and semi-quantitative Rietveld X-ray diffractometry (QXRD)) to characterise the heterogeneity of the ROMG. The methods, precision, accuracy and error of these techniques are critically assessed and patterns are presented.

Objective (3)

Such modal techniques are thus chiefly utilised to define ‘true’ pluton-scale mineralogical zonation and to also test the validity of field classifications of ROMG components proposed in Zaniewski *et al.* (2006).

Chapter Four. Characterisation of feldspars for fingerprinting mafic-felsic magma interaction

Chapter Four describes and details the micro-analytical approach utilised on ROMG feldspars. As feldspars are sensitive to changes in composition, temperature and pressure in open magmatic systems (Vance 1962 & 1965; Lofgren 1974; Hibbard 1981), analysis of their populations, disequilibrium textures, zonation and related geochemical stratigraphy is undertaken to address petrogenesis.

Cold Cathodoluminescence (CL) combined with detailed optical microscopy has led to select magmatic feldspars in Chapter Four that have a common type of mineral zonation within each ROMG component. The feldspars presented are considered as reflecting within facies representative micro-samples in terms of the type of feldspar found across the reverse zonation of the ROMG. Only *in-situ* mineral elemental and Pb-Pb isotopic analysis was applied for each facies independent representative feldspar via Electron Probe Micro Analysis (EPMA) coupled with Laser Ablation Multiple Collector Inductively Coupled Plasma Spectrometry (LA-MC-ICP-MS). Data are presented as (i) independently for each crystal and (ii) in bulk for all crystals so that inferences from signatures can be identified in capturing localised and whole ROMG scale petrogenetic processes.

Objective (4)

All integrated techniques on feldspars above allow detailed re-construction of the petrogenesis of the ROMG by mapping a textural understanding of mineral zonation/crystal isotope stratigraphy (chemostratigraphy) in order to 'fingerprint' the mixing history of the ROMG; i.e.to define an overall magma mixing model for the ROMG.

Chapter Five. Summary and Conclusions

Chapter Five presents a brief summary of the salient (macro to micro-scale) points of this study. It compares and contrasts a macro-scale (field) sequence with a micro-scale (crystal) sequence to see if a correlation exists in order to draw conclusions on ROMG petrogenesis.

Chapter Two

FIELD RELATIONSHIPS & PETROGRAPHY

Detailed field relationships, classification and textural assessment of all defined ROMG components.

Chapter Two

THE ROSS OF MULL GRANITE

Chapter Two – Field relationships and Petrography

Field relationships, petrography and classification of all ROMG components have essentially been addressed in Zaniewski *et al.* (2006) (see **Appendix A6.1**). Objectives (1) and (2) have thus been defined and (3) can essentially begin to be assessed, i.e. an understanding of field scale heterogeneity is desired prior to choosing appropriate samples for geochemical analysis (as per Chapter Three and Four).

The purpose of this chapter is to further describe and provide a very detailed field and textural petrographic framework for all plutonic igneous rocks that comprise the ROMG. In building on the work from Zaniewski *et al.* (2006), this chapter uses field petrology/petrography to define a simple field scale interpretation of the crystallisation history of the ROMG. A detailed emplacement model is also proposed.

2.1 Introduction

The regional geological setting, location and study area has already been outlined in Chapter One, and is summarised in Zaniewski *et al.* (2006), McLeod *et al.* (2011) and Petronis *et al.* (2012). Where place names and field data are presented, they are referenced to the detailed 1:25 000 Solid Geological Map of the ROMG found in the sleeve at the back of this thesis (also found in **Attachments to Appendix A8.1** on the memory stick labelled **AZ ROMG 2017**).

For the purposes of this chapter, plutonic rocks are documented first in order of emplacement followed by rocks associated with late stage processes. Full petrographic descriptions with sketches of each ROMG component are also provided in **Appendix A2.1**.

The aims of this chapter are to:

- Summarise the nature and distribution of all ROMG components in greater petrographic detail.
- Summarise areas of petrological significance not included in Zaniewski *et al.* (2006).
- Provide additional field to thin section scale textures associated with mafic-felsic magma interaction and structural data (not included in Zaniewski *et al.* 2006) to further characterise internal heterogeneity and propose a model highlighting crystallisation phases.

- Describe textures associated within late stage phases never documented before in any study on the ROMG.

2.2 The Nature and Distribution of the Granites

As per Zaniewski *et al.* (2006), the facies of granite identified within the ROMG (**Fig. 2.1**) are as follows:

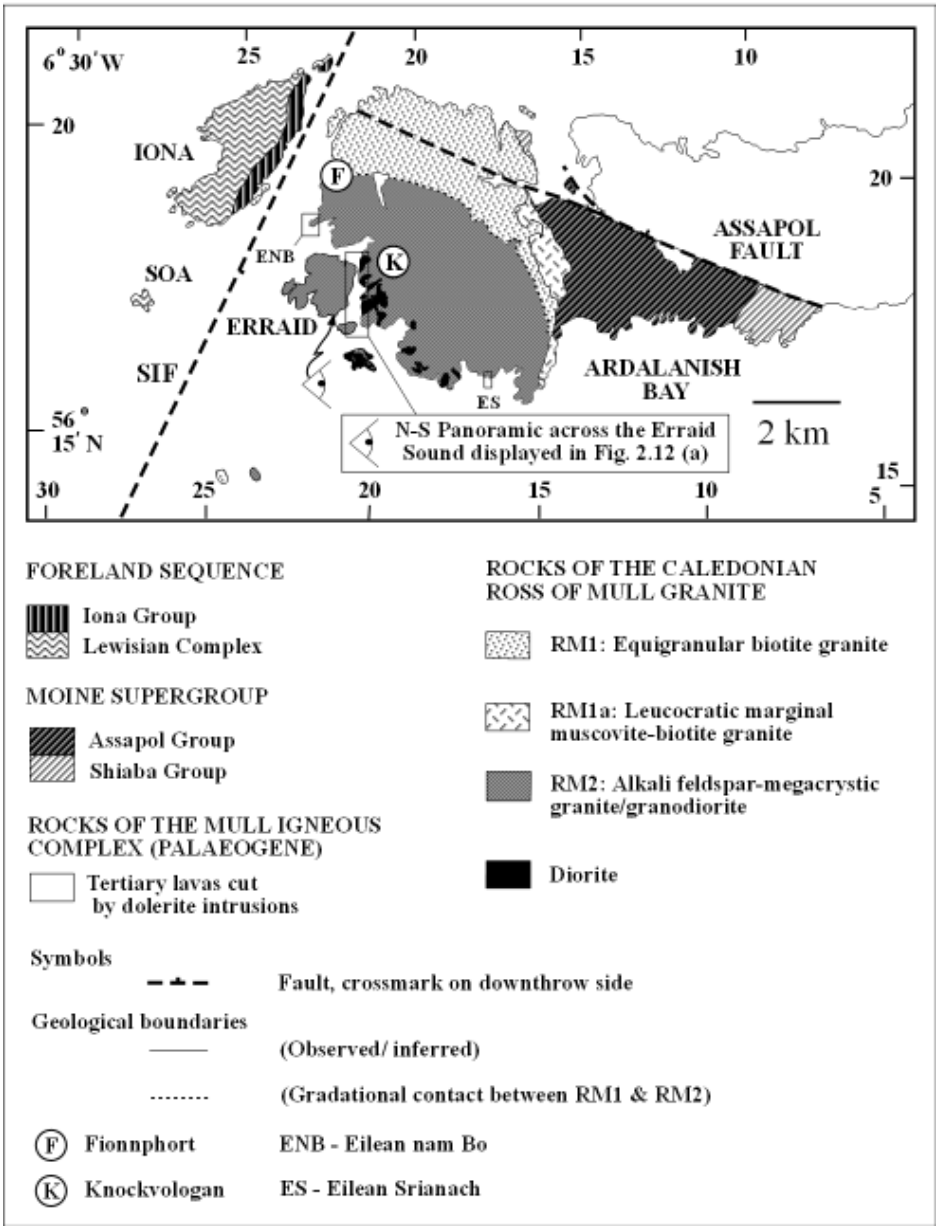


Fig. 2.1 Solid geological map of the western end of the Ross of Mull (revised from Sheet 43 S and modified from Zaniewski *et al.* 2006).

'1. An equigranular biotite granite, here termed RM1 (=G_{RM1} on the British Geological Society (BGS), Ross of Mull (43 S) Sheet (Harris & Highton 1999).

2. A leucocratic, marginal muscovite-biotite granite, RM1a, (=G_{RM1} on the BGS, Ross of Mull (43 S) Sheet) which forms a white contact facies up to c.800m wide along the eastern contact and locally adjacent to pelitic Moine xenoliths.

3. An alkali feldspar-megacrystic biotite granite/granodiorite RM2 (=to both G_{RM2} and G_{RM3} on the BGS, Ross of Mull (43 S) Sheet). G_{RM3} is not now recognised as an independent facies; contacts between RM1 and RM2 are gradational over about a km and hence the intrusion is here described as 'zoned' rather than 'composite''.

2.2.1 RM1: The 'Red Bay' type facies

RM1 makes up the outer facies and is a coarse-grained equigranular, quartz-rich, biotite granite. Generally, all the grains are anhedral to subhedral with red/pink alkali feldspar being the dominant and larger mineral phase present (13 mm average length). The type locality for this granitoid is at Red Bay Quarry (NM [3115 2541]) and a petrographic image for this granite is shown in **Fig. 2.2**.

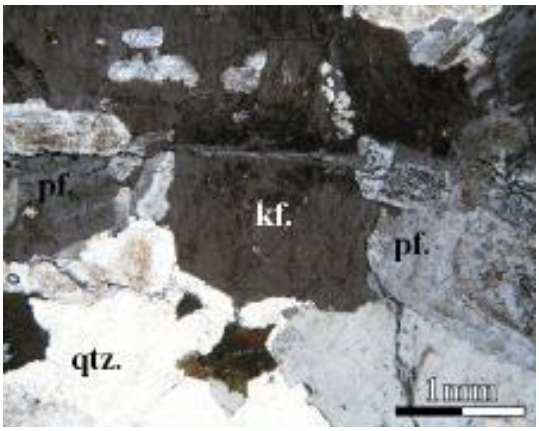


Fig. 2.2 RM1 (sample No. RR0104 (NM [2990 2318])) (XPL) highlighting equal distributions of quartz (**qtz.**), alkali (**kf.**) and plagioclase feldspar (**pf.**).

Classification of this facies is difficult, as field petrography suggests that RM1 is modally an alkali feldspar granite; '*thin-section petrography reveals plagioclase constitutes 20-25% of the felsic minerals, by mode* (**Fig. 2.2**), *but is frequently reddened'* (Zaniewski *et*

al. 2006). Quartz is relatively inclusion free, and alkali feldspar (around 13 mm on average length) is also fresh commonly containing smaller poikilitic subhedral crystals of zoned and unzoned plagioclase feldspar (**Fig. 2.2**). Plagioclase feldspar predominantly exists as unzoned turbid subhedral crystals, but some heterogeneously distributed varieties that generally display simple concordant zonation profiles (right side in **Fig. 2.2**) are less common. A key feature with RM1 is that it tends to be hornblende free, except in discrete hornblende rich patches that may be related to MME or xenolithic patches. Intensely brown anhedral to subhedral biotite is a well defined feature in this facies and is commonly altered to chlorite; it is associated with Fe-Ti opaque oxides and in rarer cases, inclusions of colourless zircon. Additional accessories are titanite, which is visible in hand specimen where present as euhedral bronze rhombuses (up to 0.5mm to 1mm in length), apatite, zircon (both less than 0.15 mm) and zoned euhdral to subhedral allanite (0.3 mm in length).

Although highly homogeneous looking in the field with an absence of MME at the current erosion level, RM1 contains numerous petrographic textural heterogeneities that could be inferred as being related to mafic-felsic magma mixing interaction. These heterogeneities range from:

a.) Isolated crystals or scarce patchy areas of variably zoned plagioclase feldspars (clusters can occur up to 1.5 mm by 1.5mm patches) with or without sericitised cores juxtaposed.

b.) Glomerocrystic plagioclase domains.

c.) Variable intensities of boxy cellular structures in plagioclase feldspar (Grogan & Reavy 2002).

d.) Mantling relationships on alkali feldspar by smaller subhedral crystals of plagiolcase feldspar that may or not be alligned at the crystal edges.

e.) Euhedral titanite showing oscillatory zoning and disequilibrium features in the form of embayed areas that could be associated with fluctuations of contrasting magma composition as a result of mixing (McLeod *et al.* 2011).

Fabrics are absent and whilst MME or other igneous enclaves are rare, an example of an igneous enclave in this facies of the ROMG is observed directly on the coastline at Tormore Cottage (NM [3014 2422]), west of Torr Mór Quarry (NM [3090 2340]). The 40-60 cm enclave concerned is granodiorite which displays irregular contacts with host RM1. Rare

isolated monogenic MME within RM1 can also be observed at Port na Mona (NM [3005 2367]).

One of the characteristic macroscopic features observed in the northwest areas of the ROMG in RM1, is a northwest gentle to moderately dipping joint plane system (**Fig. 2.3**). This is well developed at Fionnphort (NM [3020 2325]) and along the whole area of An-t-Aird (NM [3570 2370]) in the northeast. This feature is less obvious at the coastline particularly in RM2 as one moves southwards through the complex from Fionnphort and all the way around the Ross to Rubh' Ardalanish (NM [3592 1645]).



Fig. 2.3 Example of joint plane system in structural continuity within RM1 gently dipping WNW. Photograph depicting cross section is taken north of Fionnphort where this feature is easier to observe (looking northeast from (NM [3017 2383])). Iona is in the background.

Throughout the ROMG, numerous cm to m and even km scale xenoliths of Moine country rock exist. Within RM1, one of the most accessible places to observe m scale tabular Moine rafts close to the current erosion level is in the northeast part of the complex, at the disused Camas Tuath Quarry (NM [3524 2424]). Most of the country rock xenoliths within RM1 are from the adjacent Shiaba Group, readily identified due to the nature of their quartzo-feldspathic lithologies and pronounced cross-bedding. Other Shiaba Group xenoliths of various scales exist along the northern coastline but the Moine rafts at Camas Tuath are some of the largest examples observed throughout the whole of RM1.

This granitoid is in contact with country rocks at the western and eastern margins of the complex with widespread development of RM1a along much of the eastern contact (**Fig. 2.1**).

2.2.2 RM1a: The 'White' granite

RM1a occurs as a contact related facies essentially present in two main areas at the eastern margin of the ROMG. The areas that RM1a is confined to are Bendoran (where it is adjacent to RM1 in the northeast) and Ardalanish Bay (where it is predominantly adjacent to RM2 in the southeast) (see **Fig. 2.1**). Its mapped presence on the British Geological Survey (BGS), Ross of Mull (43 S) Sheet north of An t-Aird at Beinn Liathanach (NM [3552 2425]), West of Loch na Lathaich (NM [3650 2350]) is incorrect as Zaniewski *et al.* (2006) depict the presence of RM1 here.

The ROMG envelope has been described in detail by Zaniewski *et al.* (2006) and field relationships are not covered here. RM1a is a generally equigranular, leucocratic, medium-grained, two mica granite. Biotite is anhedral and 3 mm on average with 4 mm maximum length. Pale pink (where in close proximity to RM1) to predominantly white alkali feldspars are subhedral, being 3 mm on average. Plagioclase is 'frosty' white, subhedral to euhedral, forming tabular crystals that are 2.5 to 3 mm on average. Anhedral quartz is transparent, interstitial, and is 2.5 to 3 mm on average. Thin section *'petrography reveals an equigranular quartz-rich rock (30% on average),* (**Fig. 2.4 (a)** to **(c)**) *with generally equal proportions of plagioclase and perthitic microcline'* (Zaniewski *et al*. 2006) at Bendoran and Ardalanish. Intensely brown biotite is a feature of this granite, and muscovite is not common. Accessory minerals range from subhedral zircon occurring in biotite or as clusters, apatite and Fe-Ti opaque oxides. This is the only granite facies lacking titanite.

Textural heterogeneity in RM1a occurs throughout the outcrops at Bendoran and Ardalanish Bay, and is intimately related to plagioclase feldspars. These heterogeneities in plagioclase feldspars range from:

a.) Variable sericitic alteration highlighting simple two to threefold zonation profiles.
b.) Glomerocryst domains.
c.) Skeletal to dendritic cores or rims.
d.) Multiple zonation profiles defined by uneven sericite within these zones.
e.) Isolated outer zones of sericitic alteration.

RM1a is not just confined to the eastern limits of the ROMG, but also occurs in direct primary association with pelitic Moine xenoliths throughout the complex. In some cases, pelitic Moine xenoliths display a cm to m scale single margin of 'white' granitoid, which may

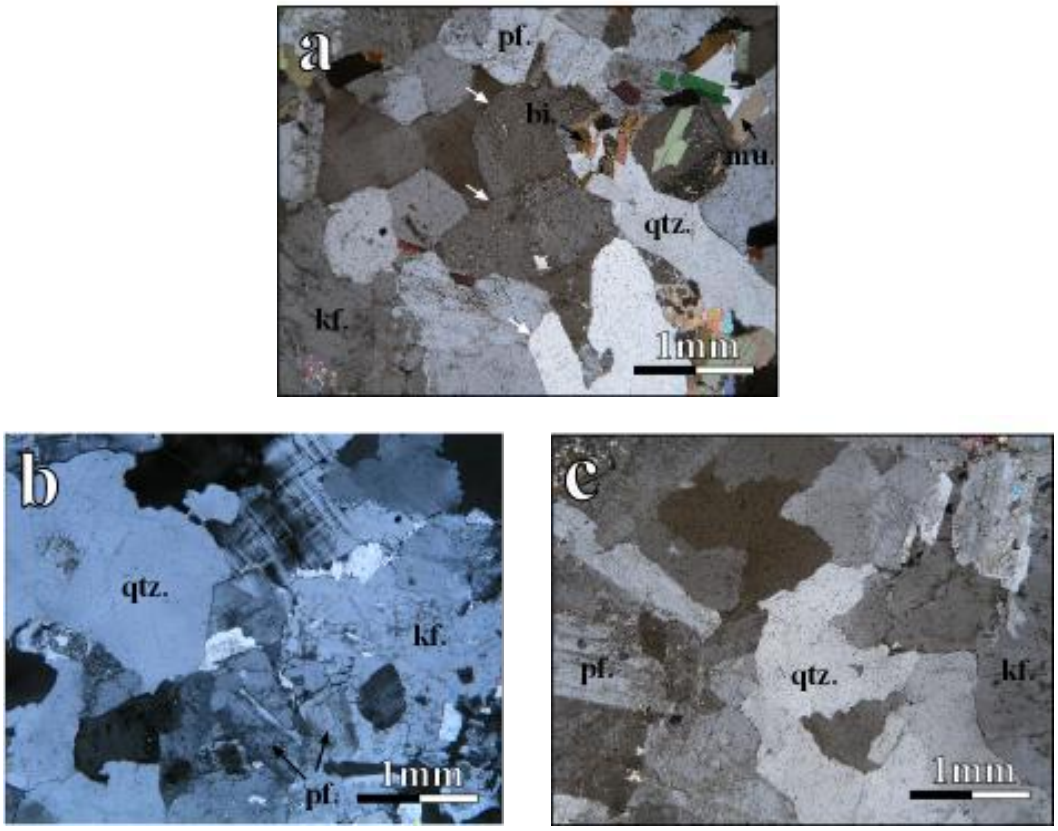


Fig. 2.4 (a-c) **(a)** contact of RM1a with Moine meta-sediments (RM1a to left of white arrows) highlighting quartz rich equigranular nature of RM1a at Ardalanish Bay (sample No. JR43 (NM [3670 1790])) (XPL). **(b)** Slightly coarser variant of RM1a with rare micas (none depicted here) and more microcline at Whitish, Ardalanish (sample No. JR2 (NM [3680 1790])) (XPL). **(c)** Medium grained equigranular RM1a with even distributions of quartz, alkali feldspar and plagioclase from Bendoran (sample No. JR7 (NM [3640 2180])) (XPL). Symbols for all images are as follows; quartz (**qtz.**), alkali feldspar (**kf.**), plagioclase feldspar (**pf.**), muscovite (**mu**.) and biotite (**bi**.).

have internal vertical grain size variation. RM1a is generally absent where there are isolated psammitic xenoliths in the ROMG (from the Assapol Formation) but in some cases a sacharoidal fine to medium-grained pink biotite leucogranite of non-uniform distribution may be in direct association (e.g. Eilean Srianach (NM [3476 1685]) (See **Fig. 2.1** and areas labelled 2 in **Fig. 2.5**). As a whole this leucogranite is not always entirely white and can commonly appear pink in places (paler than main RM1) where adjacent to such isolated psammitic xenoliths.

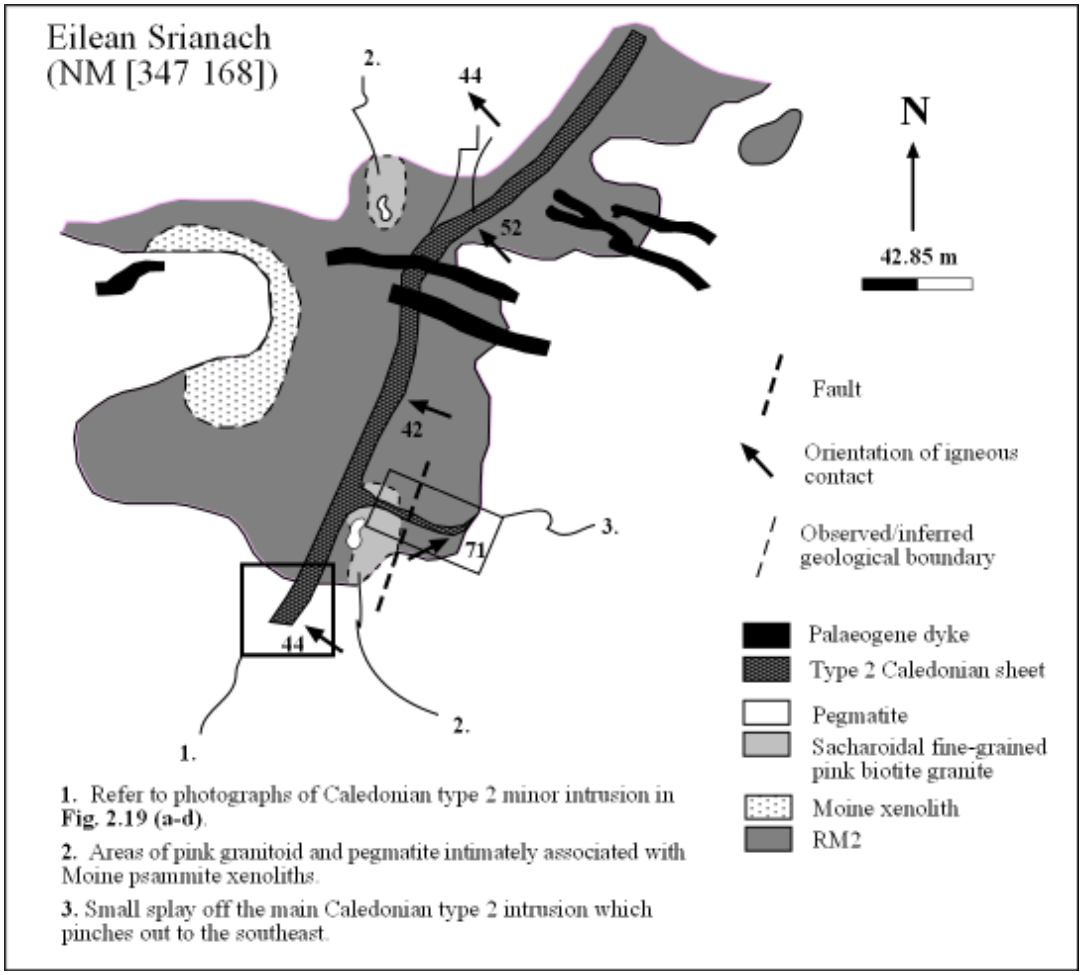


Fig. 2.5 Geological map of Eilean Srianach depicting location of sacharoidal pink biotie leucogranites.

2.2.3 RM2: 'The Knockvologan' type facies

RM1 has a gradational contact with RM2. The RM2 granitoid contains more plagioclase and biotite and less quartz than RM1 and has greater amounts of hornblende. RM2 stands out because of its megacrystic alkali feldspars, ranging in size, from 8-15 mm (**Fig. 2.6**) and has an increase in ovoid cm scale MME as one moves south towards Knockvologan.

RM2 is an alkali feldspar-phyric, coarse-grained granite to granodiorite. Biotite is anhedral to subhedral, ranging from 0.05 to 4mm in length. Alkali feldspar megacrysts approximately make up 30% of the rock over 49cm^2 with the groundmass comprising chiefly of plagioclase feldspar (around 60% or 70%) and quartz making up the rest, with microcline and biotite comprising the last 10%. The alkali feldspar megacrysts tend to be more increasingly common as one moves south from the RM1/RM2 contact towards Knockvologan, however this field petrographic feature is difficult to quantify in relation to

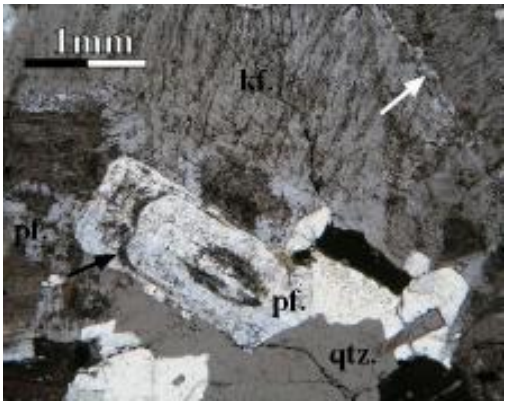


Fig. 2.6 Petrographic image of RM2 (sample No. RR107 (NM [3005 2238])) (XPL). White arrow denotes Carlsbad twin in orthoclase perthite megacryst and two plagioclases with different zonation occur at the centre of the image. Black arrow shows a thin tenth of a mm sericitised zone characteristic of some of the plagioclases in RM2. Symbols for image are as follows; quartz (**qtz.**), alkali (**kf.**) and plagioclase feldspar (**pf.**).

where RM2 is adjacent to diorite due to modal heterogeneity present. Hornblende is quite common and chlorite, calcite and muscovite are minor constituents. Accessories comprise zircon, lozenge shaped titanite, apatite, zoned allanite and Fe-Ti opaque oxides.

RM2 is the most heterogeneous facies of granitoid within the ROMG having the greatest concentration of MME and diorite. It also has the most complex and greater range of crystal scale textural heterogeneity. Such textural hetorerogeneity in thin section can be found as:

a.) Plagioclase feldspars with variable boxy cellular structures.

b.) Isolated zoned plagioclase glomero-xenocrysts with highly sericitised cores.

c.) Variably zoned plagioclase feldspars with or without sericitised cores.

d.) Isolated multiply zoned plagioclase glomero-xenocrysts with or without highly sericitised cores juxtaposed to each other.

e.) Isolated multiply zoned plagioclases.

f.) Evenly distributed acicular apatite occuring throughout RM2.

g.) Corroded allanite displaying oscillatory zoning with embayed areas.

2.2.4 Summary of the granitoids

Within the ROMG, two types of granite facies have been described that contain MME, one facies being equigranular grading into a megacrystic facies. The contact separating RM1 and

RM2 (**Fig 2.1**) is gradational. Heterogeneity in the ROMG (as one does a southward coastal transect from RM1/Fionnphort to RM2/Knockvologan (**Fig 2.1**)) is not only apparent by the change in gross mineralogy and nature of the contact relationship between the RM1/RM2, but by an overall increase in the distribution of mafic inclusions (as MME and diorites). One of the main westward coastal areas where there is a cryptic break or a marked boundary in MME abundance occurs between Cnoc an Laailt (NM [2975 2263]) and eastwards of Eilean an Aba (NM [2974 2250]). MME with crenulated margins south of this area are not uniformly distributed in RM2 and occur in isolation or confined around diorite intrusions. Based on the north south field transect alone, heterogeneity increases as one moves to the centre of the complex and RM2 is more mineralogically variable.

Gross petrographic features also highlight that within RM2, there is a greater variety of zonation types in plagioclase feldspars juxtaposed to unzoned varieties that could relate to batch mixing from different sources (Grogan 2004). In contrast, as RM1 has minimal MME and a homogenous nature in the field, it is feasible that this could be the most mixed component. It is worth noting that petrographic textures in RM1 such as heterogeneous titanite populations, some with ilmenite zones, rare patchy hornblende clots, granodiorite xenoliths and rare MME advocate magma mixing to have occurred.

RM1a does not contain MME, has no titanite and is always associated with Moine lithologies (forming cm to m scale margins on isolated Moine xenoliths in the southwest of the intrusion). At Bendoran, the nature of the contact between RM1 and RM1a is important as cm scale fingers of RM1 'feed' into pelitic lithologies, and in some cases these fingers are partly composed of RM1a that correspond to the bulk RM1a granitoid. On such field relationships alone, it is feasible to interpret RM1a as representing an anatectic melt of a Moine pelitic country rock. Variability in terms of RM1a coarseness at the contact could also relate to localised anatectic melt of heterogeneous Moine lithologies. It is worth however noting, given the abundance of muscovite in adjacent country rocks and aureole pegmatites, muscovite is present in scarce amounts in RM1a; the nature of which is not fully understood.

2.3 Aplitic micro-granites, Pegmatites and Syenite

The ROMG contains a network of aplitic micro-granites, variable pegmatites associated with Moine xenoliths and a very rare syenite outcrop. As with most granitoids, such rock types are generally associated with residual fluids. Any understanding of such components might

therefore be an important factor when trying to understand how dominant these residual fluids have been during granitoid petrogenesis; something to consider in terms of the overall reddened appearance of the ROMG and to what degree have original primary magmatic textures been overprinted?

2.3.1 Aplitic micro-granites

The ROMG has a complicated array of aplitic micro-granite sheets, pods and veins that generally range from 1 cm to 0.8 m thick (**Fig. 2.7**). These rocks are highly heterogeneous



Fig. 2.7 Aplitic micro-granite in RM1 occurring sub-parallel in terms of orientation to the major joint planes observed at Fionnphort. This example pinches out and is orientated at 184/28^{o}W displaying a cm scale sacharoidal upper margin made up of quartz (NM [3064 2494]).

internally/laterally and have been documented as:

(i) Porphyritic micro-granites (phenocrysts of alkali feldspar and quartz and sometimes rare hornblende covering an area of >25% per 49 cm^2 density) that can be gradational to (ii) non-porphyritic micro-granites where hornblende is absent.

(iii) Pink fine-grained leucocratic aplitic micro-granite veins, pods and sheets which are widespread across the ROMG joints where hornblende is absent. These also may contain graphic texture, have pegmatitic or quartz pods and a few have traces of white mica. Biotite where present in such varieties is always less than in the host granite.

ROMG aplitic micro-granites are readily identified in the field as they cross-cut the intrusion and have planar contacts. They are abundant on the peninsula of Eilean nam Bo

(NM [2955 2155]) (see **Fig. 2.1** and **Fig. 2.8** for locality). They are also sometimes associated with druzy quartz infills forming separate mono-mineralic margins or entire pegmatitic margins.

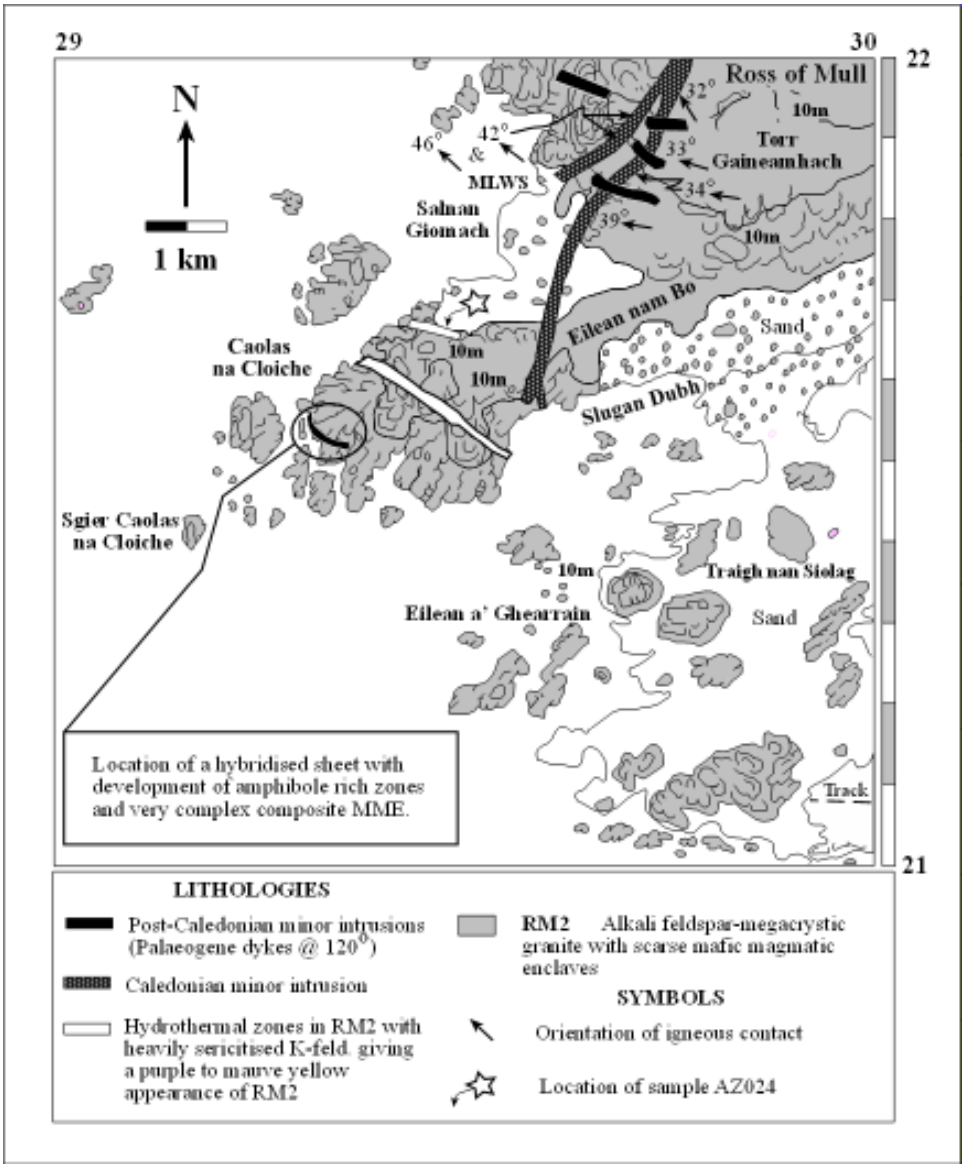


Figure 2.8 Solid geological map of Eilean nam Bo.

Porpyhritic types (i) are the most readily identifiable in the field due to their texture (**Fig. 2.9**) characterised by isolated and highly corroded large anhedral crystals of quartz. Thin section petrography reveals a highly heterogeneous porphyritic and groundmass assemblage (**Fig. 2.9**) in places. Quartz is commonly poly-crystalline, deeply embayed and is un-mantled. Plagioclase phenocrysts when present are commonly subhedral to anhedral and strongly zoned varieties have simple concordant profiles that are often juxtaposed to unzoned

varieties (**Fig. 2.9**). Similarly, the groundmass assemblage is comprised of crystals having a highly non-uniform grain size. Hornblende where present, occurs as acicular varieties in porphyritic types; however some rare isolated subhedral crystals are mantled by alkali feldspar.

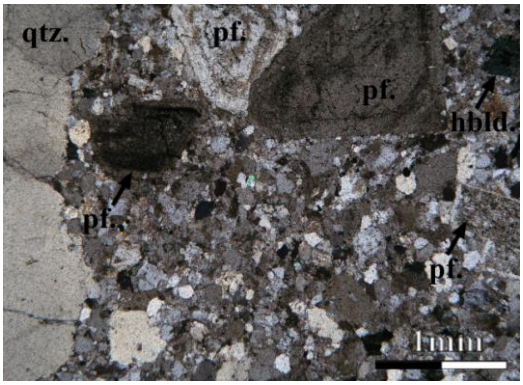


Fig. 2.9 Porphyritic aplitic micro-granite (sample No. AZ025 (NM [2958 2157])) (XPL) displaying corroded poly-crystalline quartz (**qtz.**), anhedral to subhedral plagioclase feldspars (**pf.**) and isolated hornblende (**hbld.**) mantled by small felsic minerals. Groundmass is mainly made up of felsic minerals and minor hornblende.

Where (ii) non-porphyritic lithologies are present, they tend to be considerably more micro-granular. Laterally or vertically they can sometimes grade into a micro-porphyritic texture, which is difficult to notice in the field. One marked difference observed between porphyritic and non porphyritic areas internally is the nature of the quartz and rare hornblende where present in thin section. Within these 'intermediate' micro-porphyritic types, quartz is commonly embayed and sometimes mantled by smaller aggregates of granular hornblende. Hornblende is also considerably more granular (often as isolated glomerocrystic aggregations) that may be mantled by alkali feldspar.

Aplitic micro-granites ((i) & (ii)) possess heterogeneous xenocrystic assemblages such as:

a.) Corroded, multiply zoned and embayed plagioclase feldspar xenocrysts.

b.) Skeletal zones in plagioclase feldspar.

c.) Multiply zoned altered plagioclases juxtaposed to unzoned fresh varieties.

d.) Alkali feldspar xenocrysts.

e.) Highly corroded quartz xenocrysts.

f.) Variably embayed rare hornblende with a plagioclase mantling phase.

2.3.2 Pegmatites

The pegmatites that occur within the ROMG are predominantly confined to forming margins of variable thickness (cm to m scale) on pelitic Moine xenoliths. Pegmatites that occur in RM2/RM1 host granitoids are chiefly comprised of quartz, orthoclase perthite, plagioclase feldspar, where orthoclase crystals tend to be larger than 3 cm and in some cases may reach up to 8-10 cm in size. The largest pegmatite mass of this type observed in the ROMG occurs as a sheet adjacent to a 250 m Moine xenolith (forming a margin conforming to the dip of the xenolith) at Eilean Srianach (NM [3480 1686]) (See **Fig 2.1** and **Fig. 2.5**).

Other very rare pegmatitic associations that have been found to exist in RM1 only (which may relate to the current level of erosion) are isolated drusy cavities filled with hexagonal quartz and can be observed northeast of Ardfenaig Farm, at Cnoc Glas (NM [3484 2334]). It is interpreted that the cavities are intimately associated with unroofing processes. Rare small (often rather purplish) graphic textured pegmatitic veins, up to a couple of cm thick, with gradational boundaries within host RM1 also exist.

Pegmatites that occur within RM1a mirror the mineralogy of host RM1a. These pegmatites comprise an equigranular medium-grained 'white' variant with well-developed muscovite books (3 cm on average size) and alkali feldspar (1 to 3 cm). Such pegmatites are always in close proximity to, and associated with pelitic Moine lithologies commonly forming as patches in xenoliths. In some cases, the geometry of such RM1a pegmatites gives the impression of conforming to and stringing in from biotite/amphibole rich layers in semi-pelitic Moine xenoliths. Other rare examples can contain muscovite, pyrite, garnet, plus locally (e.g. at Bendoran Cottage) green flourapatite crystals (up to a few mm), and in rare cases at the west side of Ardalanish Bay, small turbid beryl crystals (up to a few mm across).

Other pegmatite masses that occur in the RM1a zone are associated with Moine amphibolite xenoliths (occurring as margins or in beds of directly adjacent pelitic lithologies in xenoliths) within the zone at Ardalanish Bay (e.g. (NM [3622 1661]). These pegmatites display similar features in the RM1/RM2 pegmatites in terms of grain size, but also have graphic quartz in orthoclase, bladed biotite (5 cm on average), muscovite rosettes (4-5 cm) and display both perthitic and anti-perthitic textures that can be seen with the naked eye in orthoclase. Such pegmatites are not entirely restricted to the RM1a zone at Ardalanish Bay, and have also been found to occur in the RM1a/Moine pelitic contact zone Glac a' Bhodaich, Bendoran (NM [3726 2073]).

2.3.3 Syenite

The only occurrence of a syenite phase observed within the ROMG exists in RM1 adjacent to the pier directly at Tormore Cottage (NM [3016 2420]), which is only accessible at low tide. The petrographic image in **Fig. 2.10** is from this locality and was obtained from a m scale uneven patch that has a gradational contact in RM1 directly connected to an aplitic micro-granite sheet. Field modes for this specimen are estimated as 5% quartz, 90% alkali feldspar and 5% plagioclase feldspar. Minor quartz is evident and all plagioclase is reddened (**Fig. 2.10**).

One of the main features obvious in hand specimen is the presence of pitted mm scale lozenge shaped areas. Thin section work confirms that these areas are in fact heavily altered titanite and such varieties often display skeletal morphologies (**Fig. 2.10**). In some cases, planar and continuous mm zones having intense alteration of felsic minerals associated with skeletal titanite and aggregations of biotite occur (**Fig. 2.10**). Alkali feldspars that are not present in such zones, but are adjacent, often retain textural similarities to alkali feldspars in RM1, however plagioclase feldspars often have deep brown to mauve granular cores. Fresher plagioclase feldspars varieties retain similar features to RM1 in terms of zonation, however cores are mauve brown in zoned varieties throughout the sample in **Fig. 2.10**. White arrows in **Fig. 2.10** define an example of one of many mm lateral zones, which commonly display a textural assemblage of heavily altered plagioclase, highly corroded and pitted titanite, biotite and opaque oxides which in some cases may show vague alignment.

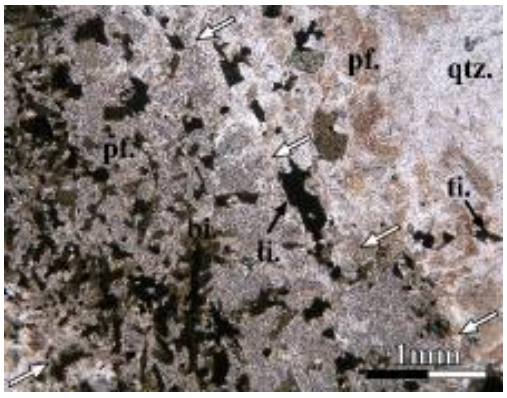


Fig. 2.10 Syenite phase from Tormore Cottage (sample No. AZ007 (NM [3016 2420])) (PPL). Symbols for image are as follows; quartz (**qtz.**), plagioclase feldspar (**pf.**), biotite (**bi.**) and titanite (**ti.**).

Thin section *sub-solidus* textures in ROMG syenite are essentially defined by networks of planar zones having intense alteration, with selective alteration of titanite (removal of Ca) to give anatase pseudomorphs. Plagioclases appear granular including the highly variable nature of polysynthetic albite twins; late stage fluidisation has meant an internal gradation with a reduction of quartz, new plagioclase to be formed (albitic?) with alkali feldspar, chloritised biotite and titanite being pseudomorphed.

2.3.4 Zones of alteration

Other rare zones of interest within the ROMG not present on the BGS, Ross of Mull Sheet (43S) are confined to m scale linear areas of intense alteration that can be observed at Eilean nam Bo (NM [2952 2166]) (see **Fig. 2.1** & **Fig. 2.8** for location of sample AZ024 displayed in **Fig. 2.11**). Such zones of heavy alteration are rare as they have only been found to exist here in RM2 displaying similar orientations (120^{o}) to Palaeogene dykes (refer back to **Fig. 2.8**).

In the field, these zones have an uneven gradational contact with RM2 and display a characteristic purple to mauve yellow colouration. As a whole, these zones which are highly weathered are not well indurated and crumble apart when hammered.

Thin section work highlights that feldspars have a frosted looking appearance and are heavily altered (**Fig. 2.11**). Further textural analysis reveals the most intensely altered form of granitoid observed throughout the whole of the ROMG. Plagioclase feldspar maintains a wholly uniform granular appearance (highly broken down to clay minerals), and as a result, crystal boundaries are not very discernible (**Fig. 2.11**). Biotite is commonly chloritised, and a

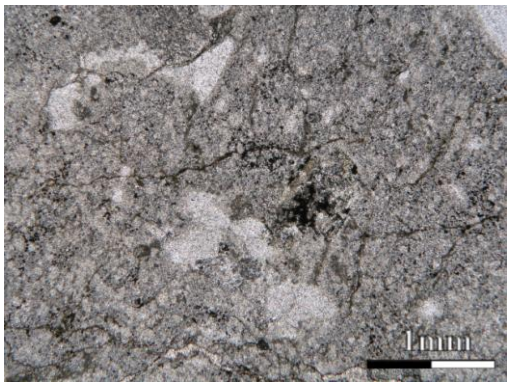


Fig. 2.11 Petrographic image of sample No. AZ024 (NM [2952 2166]) (XPL) highlighting a very fine-grained purple-green mottled and granular appearance of all plagioclases throughout the rock. An example of a whole plagioclase feldspar is depicted in the top left area of the image that has anhedral interstitial quartz at the top of the crystal.

network of small brown tenth of a mm scale stringlets (more clay) is pervasive throughout the rock either pronounced in between crystal boundaries or cutting across plagioclase feldspars. Quartz appears to be secondary as it is isolated, having a hackly shape conformed and confined to edges of anhedral plagioclases (forming a drusy mosaic).

2.3.5 Summary of Aplitic Micro-granites, Pegmatites and Syenite

ROMG aplitic micro-granites, pegmatites, syenite and zones of intense alteration clearly display complex field scale relationships and textural characteristics. Due to their range of heterogeneity, no attempt has been made to form an outright classification scheme.

Within the Mid-Silurian to early Devonian, Caledonian granitoid magmatism was contemporaneous with, or closely preceded rapid post orogenic uplift (Watson 1984) where un-roofing of granitoids would be associated with late stage cooling. The rock type association presented here is commonly associated with such processes, where residual fluids utilise joint and fracture systems in granitoid complexes. The main facts that support this for the ROMG are:

(i) Stereographic data of aplitic micro-granites and joint planes overlap together within the northwest part of RM1; field observations in this part of the ROMG shows both commonly dip northwest (refer later on to structural section **2.9**).

(ii) A rare syenite forming gradational patches in RM1 (that has corroded titanite within internal mm scale sericitised zones) is connected to an aplitic micro-granite network; this could imply that aplitic micro-granites form a feeder-type system for late-stage residual fluids which may relate to the overall reddening of the ROMG?

(iii) Rare drusy pegmatite cavities occurring in a higher topographic level in RM1.

Whether the aplitic micro-granites in this study are defined by a uniform late stage process or directly related to a longer sequence involving several processes including overlap with mafic-felsic/felsic-felsic magma interaction is unknown. The intensely altered gross textural assemblages including the nature of feldspars (some maintaining RM1/RM2 zonation which is overprinted by a discolouration or granular sericitisation) in the syenite component could advocate late stage fluidisation to have occurred during unroofing processes.

The significance of the zones of intense alteration that occur at Eilean nam Bo with respect to the ROMG is also not known, however data was presented just in case any future work involves this area of interest.

2.4 Diorite Masses

Although there is a complex spectrum of petrological and textural features present, two main facies of diorite and their associated MME were recognised by Zaniewski *et al.* (2006). The first type of diorite discussed makes up the vast proportion of diorite outcrop in the ROMG and is termed by Zaniewski *et al.* (2006) as follows:

'Type 1 diorite; Plagioclase- hornblende-phyric biotite diorites (Knockvologan type)'.

The second type of diorite that exists within the ROMG occurs south of Port nan Ron (NM [3250 1850]) and at Aird Mór (NM [3230 1770]) and is classified by Zaniewski *et al.* (2006) as follows:

'Type 2 diorite; Equigranular diorites/quartz diorites (Aird Mór type)'.

2.4.1 Type 1 diorite component: the Knockvologan mixing and mingling zone

Type 1 diorites are largely confined to the southwest/central area of the ROMG, which is characterised by the presence of a high concentration of syn-plutonic diorite and related MME. They form sheeted bodies displaying abundant pillow-like MME, generally dipping east or west in RM2 mainly on the eastern side of the tidal inlet of the Erraid Sound (NM [3070 2020]), or present on wave cut exposures on Eilean nan Griogag (NM [3070 1910]) and other unnamed skerries to the south and north of Eilean Duibh (NM [3050 1850]). Such diorites and MME define a mixing and mingling zone at Knockvologan (refer to **Fig 2.1**, **Fig. 2.12 (a)** to **(d)**) and map presented in **Fig. 6** in Zaniewski *et al.* (2006). Other offshore skerries southwest from this study area, such as the Torran Rocks (refer back to Chapter One and see **Fig. 1.3** for location), effectively lie within the limits of the Knockvologan mixing and mingling zone (Zaniewski *et al.* 2006).

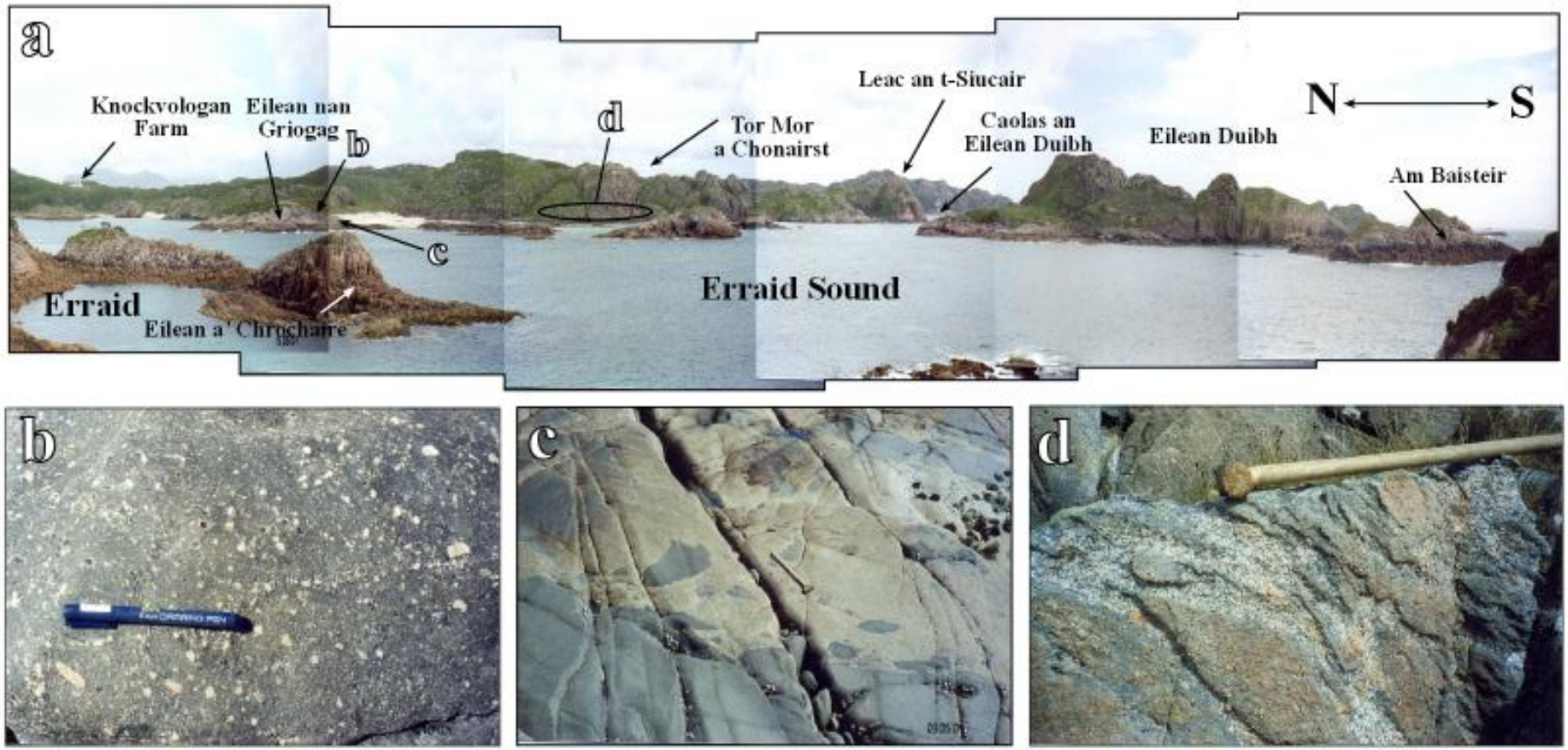


Fig. 2.12 (a - d): (a) A 2 km north to south panoramic across the Erraid Sound looking east from Erraid (NM [3014 1888]) highlighting locations presented in **(b), (c)** & **(d)**. **(b)** Appearance of Knockvologan Type 1 diorite at Knockvologan Beach (NM [3089 1925]). **(c)** Exposure of the contact between host RM2 granitoid and Type 1 diorite with cm to m scale MME having lobate contacts at the southwest portion of Eilean nan Griogag (NM [3066 1908]). **(d)** Example of a disrupted diorite body with cuspate xenocrystic MME west- southwest of Torr Mor a' Chonairst (NM [3094 1902]). The bulk distribution dip 20-30° east-southeast (main elongation direction in the photo) and a vague internal fabric is defined by an orientation of xenocrysts running in the same direction.

All diorite intrusions within the Knockvologan mixing and mingling zone are not strictly 100% diorite, but were mapped where there is >60-70% diorite/MME with respect to host RM2 granitoid. The field relationships of Type 1 diorites are described from three localities within this mixing and mingling zone (**Fig. 2.12 (a)** to **(d)**). Type 1 diorites are massive, highly heterogeneous (**Fig. 2.12 (a)** & **(b)**) and usually fragmented and broken into MME that can range from a few cm to m typified by their highly crenulate and sharp margins with host RM2 granitoid (**Fig. 2.12 (c)** & **(d)**). Mapping of the structural orientation of the Knockvologan diorite bodies and their associated MME swarms (refer to section **2.8** where MME swarms adjacent to diorite sheets strike roughly north-south in east to west dipping planes/sheets) show that in many cases gently inclined tabular sheets were emplaced syn-plutonically into the granitoid and subsequently became disrupted producing swarms of extremely flattened and intensely sheared enclaves (**Fig. 2.12 (a)** & **(d)**).

Some of the diorites display radial to dendritic fine-grained interconnected monzogranitic melt channels (Petford *et al.* 1996). An example is seen within the diorite at the southwest portion of Eilean nan Griogag (NM [3070 1910]). Within such diorites, rare east-west trending porphyritc monzogranite dykes are present that have linear and crenulated mono-mineralic margins composed of amphibole. Such linear zones entirely composed of amphiboles are referred to as amphibole rich zones in this study.

The Knockvologan type diorite rocks are petrographically highly heterogeneous (see **Fig. 2.12 (a)** to **(b)** with **Fig. 2.13**). Textures consist of subhedral glomerophyric amphibole (clots) mantled by alkali feldspar (occurs *vice-versa*), cuspate orientated swirls of predominantly resorbed subhedral plagioclase and embayed alkali feldspar xenocrysts (some rapakivi feldspar megacrysts/xenocrysts). A fine-grained, isolated micro-granite 'globule' of the ROMG with characteristic acicular biotite is also present at the lower part of the slab in **Fig 2.13**.

Such textural characteristics in Type 1 diorite rocks, including the presence of fine-grained granitoid enclaves (**Fig. 2.13**) imply that material from host RM2 granitoid has been mechanically incorporated into the diorites to form hybrid mixtures (xenocrystic crystal assemblages in diorites have similar dimensions to the crystals in host RM2 granitoid).

The spectrum of textural heterogeneity in terms of grain size, xenocrystic crystal assemblages and specific characteristic textures is highlighted in **Fig. 2.14 (a)** to **(d)**). Where xenocrystic assemblages are absent, some areas within a Type 1 diorite may appear to chiefly be composed of an equigranular micro-diorite (**Fig. 2.14 (a)**) or diorite (**Fig. 2.14 (b)**). Such grain size variations can exist within the space of a few m internally within Type 1 diorites.

Thin section petrography also shows that the alkali feldspar xenocrysts have perthitic cores and a highly sericitised plagioclase rim (10mm core with 1mm rim on average; rapakivi feldspars). Resorbtion surfaces within plagioclase feldspar xenocryst crystals are common



Fig. 2.13 A cut and polished slab of Type 1 diorite taken from Knockvologan Beach (NM [3089 1925]).

(**Fig. 2.14 (c)**). In Type 1 diorites, the groundmass is a mosaic of zoned plagioclase, hornblende, alkali feldspar and quartz. Titanite is a common accessory phase and acicular apatite, indicative of quenching, occurs throughout. One of the most common types of texture prevalent in all Type 1 diorites is mm scale mono-mineralic clots of amphibole (**Fig. 2.14 (d)**) that can vary in grain size, shape and mantling structures.

The following consistent thin section scale textures, indicative of mixing, documented in Type 1 diorite are:

a.) Alkali feldspar with threefold zonation with embayed core region.

b.) Complex simple concordant plagioclase zonation with intense mantling phases.

c.) Plagioclase feldspar xenocrysts.

d.) Corroded rapakivi feldspars.

e.) Glomerocrystic amphibole clots.

f.) Poly-crystalline quartz ocelli.

Petrographic textural heterogeneity chiefly consists of variable mantling phases of subhedral amphibole on alkali feldspar (or *vice-versa*), cuspate orientated swirls of subhedral-

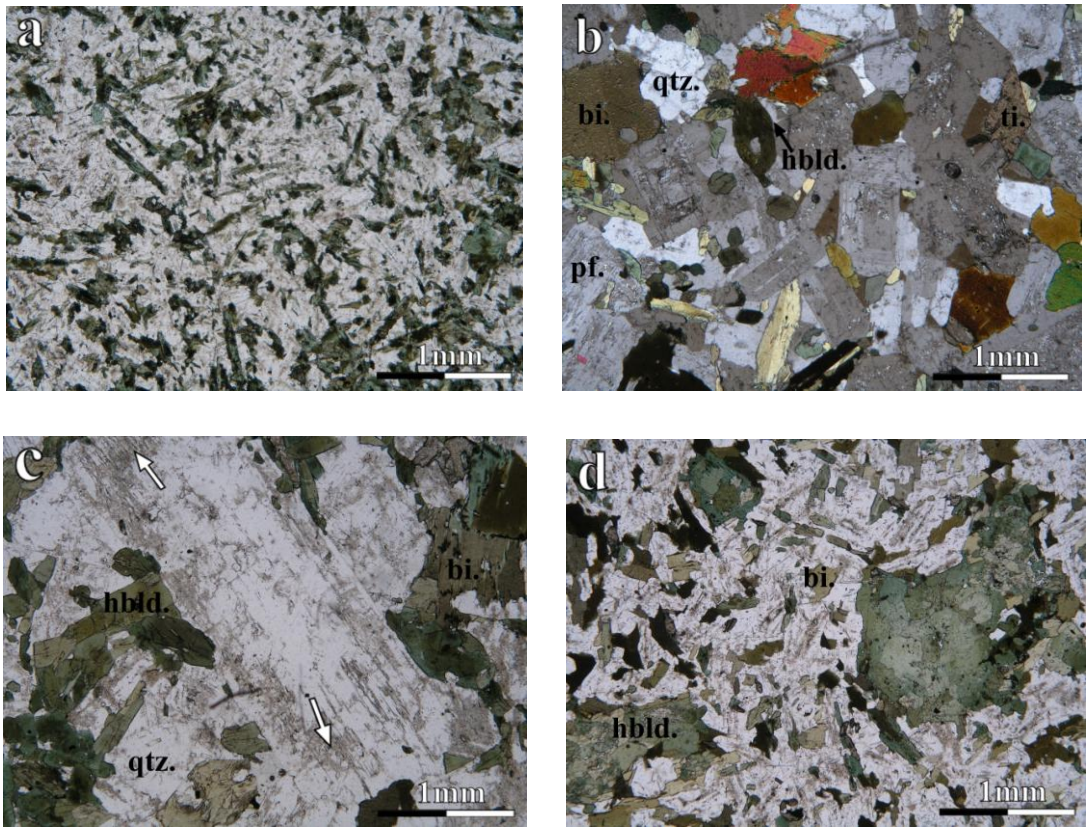


Fig. 2.14 (a-d) Petrographic features for Type 1 diorites depicting a range of textural heterogeneity (symbols for all images are as follows; quartz (**qtz.**), plagioclase feldspar (**pf.**), biotite (**bi.**), hornblende (**hbld.**) and titanite (**ti.**)); **(a)** Equigranular medium grained diorite (sample No. RR131 (NM [3093 2076]) composed of acicular biotite, hornblende and small glomerophyric clots of hornblende. Groundmass is predominantly laths of plagioclase and minor quartz (PPL). **(b)** A much coarser grained variant with abundant subhedral zoned plagioclase feldspar and minor hornblende in sample No. JR35 (NM [3080 1480]) (XPL). **(c)** Isolated subhedral plagioclase feldspar micro-phenocryst with a threefold zonation. White arrows highlight a patchy beige sericitised zone that is characteristic in some plagioclase feldspar micro-phenocrysts observed throughout a spectrum of diorite masses (sample No. JR 27 (NM [2780 1400]) (PPL). **(d)** Glomerophyric amphibole clots mantled by biotite, titanite or opaque oxides (sample No. JR 30 (NM [3009 1890]) (XPL).

euhedral resorbed plagioclase, embayed alkali feldspar, xenocrysts (some rapakivi-type megacrysts/glomeroxenocrysts having corroded uneven internal contacts with each other), ocelli type mantling phases on quartz xenocrysts, clots of glomerophyric hornblende (Castro & Stephens 1992; Sial *et al.* 1998; Janoušek *et al.* 2000; Ubide *et al.* 2014), and evenlydistributed acicular apatite. Xenocrystic alkali feldspars from adjacent RM2 (some having amphibole inclusion trails restricted to individual zones) are commonly present within diorite and also cross-cut RM2/diorite crenulate interfaces.

2.4.2 Type 2 diorite component: the 'Aird Mór' suite

Type 2 diorites are aphanitic, more homogeneous and finer grained than the Knockvologan Type 1 diorites. In thin section there is a marked textural and grain size contrast compared to Type 1 diorites and xenocrysts are scarcer, however, there are some examples of isolated xenocrystic anhedral to subhedral quartz. One of the main features observed in these diorites is the complex breakdown of clino-pyroxene (augite) to hornblende and quartz within the cores of subhedral crystals giving a skeletal outer rim. Hornblende can occur as unevenly distributed glomerocrystic clusters (clots) comprising of individual anhedral to subhedral crystals. These clots are associated with enclosed biotite that is also anhedral to subhedral, generally being elongate and hackly edged. Within the matrix, larger hornblende occurs as anhedral to subhedral grains that are commonly altered and associated with biotite.

Plagioclase crystals are all normally zoned and in most cases, highly sericitised. In severe cases, calcite has occurred as a breakdown product of plagioclase but this is minor. Plagioclase crystals are anhedral to subhedral, and most certainly interstitial. In more complex varieties, whilst poly-synthetic albite twins are visible, there is a high degree of sericitisation present within the cores, and interestingly, rims are often uneven and in some cases almost 'vermicular' looking.

Calcite is very minor, occurring as anhedral to subhedral rare patches. Apatite occurs as euhedral crystals restricted to being poikilitically included entirely within plagioclase feldspar**.** Poikilitic inclusions of hornblende in biotite can often be associated with a corona of titanite which itself is composed of anhedral grains; elsewhere titanite can be found within the matrix abs subhedral to anhedral crystals.

No inferences can be made on the structural nature of Type 2 diorites at Aird Mór due to dense vegetation and the only accessible fresh outcrop is arduously found directly at the summit (NM [3227 1777]).

2.5 MME of the ROMG

Most MME within the ROMG are highly ovoid, and have variable proportions of xenocrystic crystal assemblages adjacent to a more granodioritic variant of RM2 (**Fig. 2.15** & **Fig. 2.16 (a) to (c)**). In particular, there is a multitude of crystal-scale disequilibrium textures (**Fig. 2.16 (a) to (c)**).

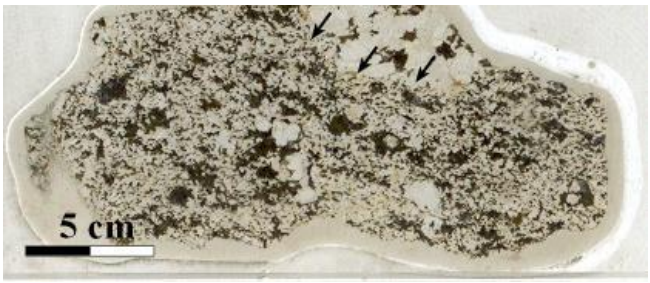


Fig. 2.15 Thin section displaying contact between MME and RM2 host granitoid (black arrows denote a small area of alkali feldspars nestling at the contact) in sample No. AZ040 (NM [2922 1921]). Note glomerophyric amphibole clots (green areas), rounded quartz (transparent areas) and alkali feldspar (light pink areas) commonly mantled by amphibole making up the characteristic heterogeneous crystal assemblage throughout the MME.

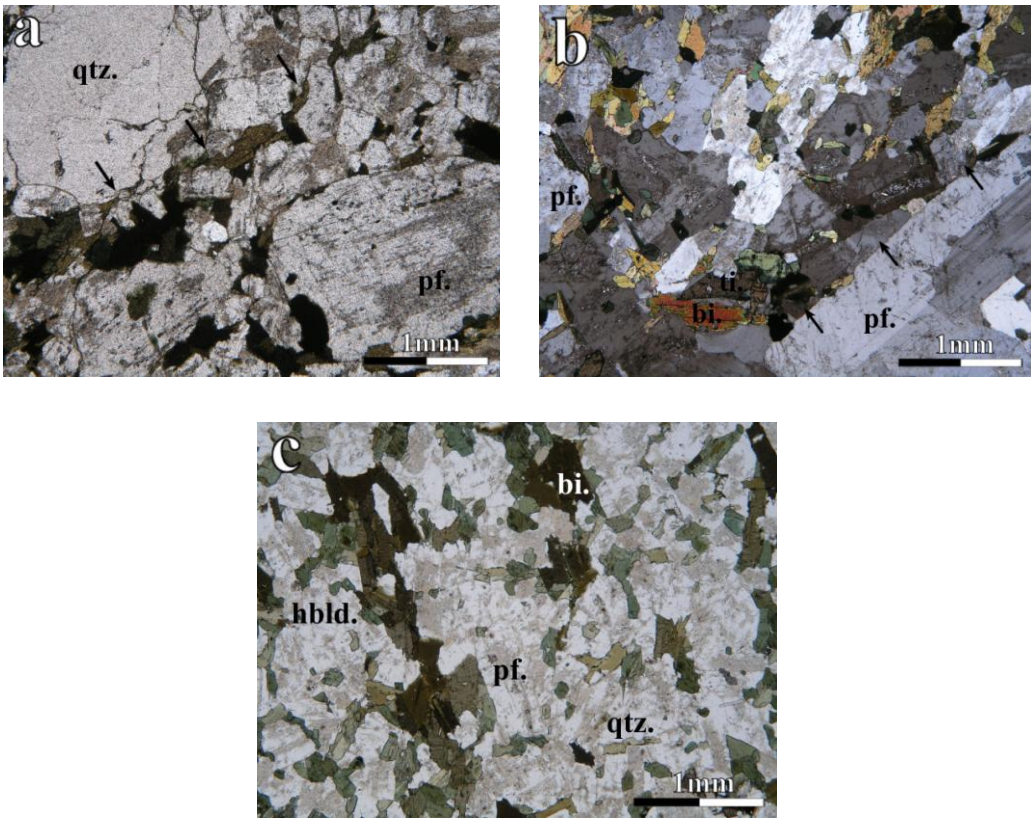


Fig. 2.16 (a-c) **(a)** Contact between MME and host RM2 in sample No. AZ040 (NM [2922 1921]) highlighted by black arrows and high concentration of biotite/opaque oxides. Highly corroded large quartz in top left area marks the limit of RM2 (PPL). **(b)** Contact between MME and host RM2 in sample No. JR27 (NM [2780 1400]) again highlighted by black arrows. Subhedral plagioclase feldspar defines limit of RM2 whilst the smaller aligned area consisting of biotite, minor euhedral titanite with zoned and un-zoned plagioclase defines the boundary of the MME (XPL). **(c)** Petrographic image of the central area of the MME considered in **(b)** illustrating a homogeneous equigranular texture (PPL). Symbols for images are as follows; quartz (**qtz.**), plagioclase feldspar (**pf.**), biotite (**bi.**), hornblende (**hbdl.**) and titanite (**ti.**).

As the bulk of MME lie within the Knockvologan mixing and mingling zone (the limits as defined in **Fig 2.1** and **Fig. 2.12 (a)**), their distribution and textures are covered in greater detail in the next section.

2.5.1 Enclave types and distribution: the Knockvologan Mixing and Mingling Zone

Previous research by Pugliese & Petford (2001) classified four different types of MME populations to occur within the Knockvologan mixing and mingling zone (based on textural criteria). Boundaries for micro-diorite bodies of similar lithologies were constructed to form a map for this zone in their study. In this study, MME and diorites are not rigorously characterised into specific textural types. It is also highly unlikely that the proposed boundaries and MME types of Pugliese & Petford (2001) are tenable due to the internal heterogeneity that exists in close proximity internally within these mafic components.

The tidal island of Eilean nan Griogag (NM [3067 1915]) provides wave cut exposure displaying a mingled contact between syn-plutonic diorite and host RM2 with examples of elongated/flattened MME confined to a specific structural level within RM2. MME here are ovoid displaying clear crenulate contacts and range up to a few m in diameter. MME at the southern-eastern portion of Eilean nan Griogag (see **Fig. 2.12 (c)** for field appearance and locality) do not tend to be as flattened and orientated as those in the southwest within diorite sheets southwest of Tor Mór a' Chonairst (see **Fig. 2.12 (d)** that depicts flattened MME at respective locality).

Thin section contacts between MME and host RM2 granitoid are provided (**Fig. 2.15** & **Fig. 2.16 (a)** to **(c)**) highlighting an irregular contact where quartz, or plagioclase feldspar in host granitoid may be corroded or mantled by smaller plagioclase crystals or biotite aggregates. The sharp contact between the two lithologies is shown by the abrupt contrast in grain size, and textural heterogeneities are defined by corroded quartz (with or without an ocellus phase) and glomerocrystic plagioclase domains composed of different zonation profiles (**Fig. 2.16 (a)** & **(b)**). Textural heterogeneities including variable grain sizes (**Fig. 2.16 (c)**) that are present in the Type 1 diorites are essentially mirrored in the related MME that are adjacent to their crenulate contacts.

Although limited in the field, composite MME within the Knockvologan mixing and mingling zone occur where a cuspate interface between a double MME is characterised by variable proportions of xenocrystic crystal assemblages, predominantly in the form of alkali feldspar xenocrysts (as previously highlighted in Zaniewski *et al.* 2006).

The only other textures presented here that are not particularly abundant to MME associated with Type 1 diorites are:

a.) Glomerocrystic biotite clots.

b.) Poly-crystalline quartz with biotite/titanite ocellus phase.

c.) Glomerocrystic titanite.

2.5.2 Hornblende-phyric enclaves from the Knockvologan mixing and mingling zone

Rare 'relict pyroxene'-phyric MME occur at the north-west side of Eilean nan Griogag (NM [3072 1911] that either tend to form flat elongated sheets or ovoid MME (up to 5-40 cm). MME comprise of 5-10% subhedral-euhedral phenocrysts of primary (early magmatic) pyroxene sometimes showing selective replacement by glomerophyric amphibole clots. Augites are common anhedral phenocryst phases generally mantled by various phases. The groundmass in these enclaves is typically micro-diorite preserving in some cases flow foliation of plagioclases comprising the matrix around xenocrysts. Pugliese & Petford (2001) classified them as hornblende-phyric micro-diorites in their study. Occasionally, pegmatitic clots and monzogranitic globules once entrained from RM2 and 'frozen in' the enclave are present in some varieties. Textural heterogeneity is characterised by a non uniform distribution of glomerocrystic clots that display variable mantling phases, and much rarer highly corroded isolated quartz xenocrysts and zoned plagioclase feldspar xenocrysts that display high degrees of *'incipient melting and the development of plumose orthoclase mantles'* (Pugliese & Petford 2001).

Textures interpreted as resulting from mafic-felsic magma interaction are:

a.) Highly corroded and embayed plagioclase feldspar xenocrysts having plumose resorbtion surfaces and a threefold type zonation.

b.) Quartz ocelli.

c.) Complex selective poly-phase mantling of amphibole on relict augite (at least two fibrous phases have been documented).

d.) Clots of glomerophyric hornblende with various mantling phases.

2.6 Caledonian Minor Intrusions: Nature, distribution and structure

As per Zaniewski *et al.* (2006) two types have been classified:

'1. Type 1 Lamprophyre; Composite porphyritic micro-granodiorites/diorites'.

'2. Type 2 Lamprophyre; Non-composite, porphyritic micro-diorites'.

Refer to Zaniewski *et al.* (2006) for an accurate map showing their distribution.

2.6.1 Type 1 lamprophyres

Type 1 lamprophyres occur throughout the ROMG and are commonly in the order of a few m in terms of thickness and may thin or pinch out laterally. The most accessible area to observe an example is just tens of m southwest of Fionnphort pier (NM [2985 2336]). Here, the Type 1 lamprophyre is moderate to gently dipping to the northwest (**Fig. 2.17 (a)**) and on perpendicular sections the sheet displays highly crenulate and bifurcating contacts with host RM1 granitoid (**Fig. 2.17 (b)**). Laterally, the contact can vary from irregular to planar in the order of a few m. The sheet has a melanocratic appearance at Fionnphort, having an angular fracture and a megacrystic mineral assemblage similar to what is observed in Type 1 diorites. The megacrysts that occur within the sheet at Fionnphort chiefly consist of highly corroded quartz (which is mantled by small acicular amphibole or biotite), highly corroded and embayed alkali feldspar (some having a rapakivi texture), biotite and glomerocrystic amphibole clots (**Fig.2.17 (c)**).

This sheet is one of the largest Caledonian minor intrusions within the ROMG, and can be traced from this locality southwards to Eilean nam Bo (refer back to **Fig. 2.1** and **Fig. 2.8** for location). One of the important features that exist within such sheets is that they are laterally heterogeneous in terms of their xenocrystic crystal assemblages that make up their porphyritic texture, groundmass assemblage and contact relationships with RM1/RM2 granitoid. At Fionnphort, the groundmass is uniform micro-diorite, however a km north directly via the Bull Hole at Eilean Eoin (NM [3007 2415]), the appearance of the sheet is markedly different. Here the contact with RM1 is planar (a more mafic fine-grained chilled upper margin is present that is gradational with the core of the sheet) and the groundmass comprising the core of the sheet is granodiorite (**Fig. 2.17 (c)**). A greater density of

xenocrystic crystal assemblages is also much more apparent here compared to Fionnphort; roughly 0-60% megacrysts per 49 cm^2 with respect to groundmass can be observed in hand specimen compared to 0-10% at Fionnphort. One of the key features present in all Type 1 sheets is the variable distribution of alkali feldspars. These have similar characteristics of RM1/RM2 alkali feldspars in terms of shape and colour, can straddle lobate contacts between the two different mediums, and often have embayments or the development of a rapakivi

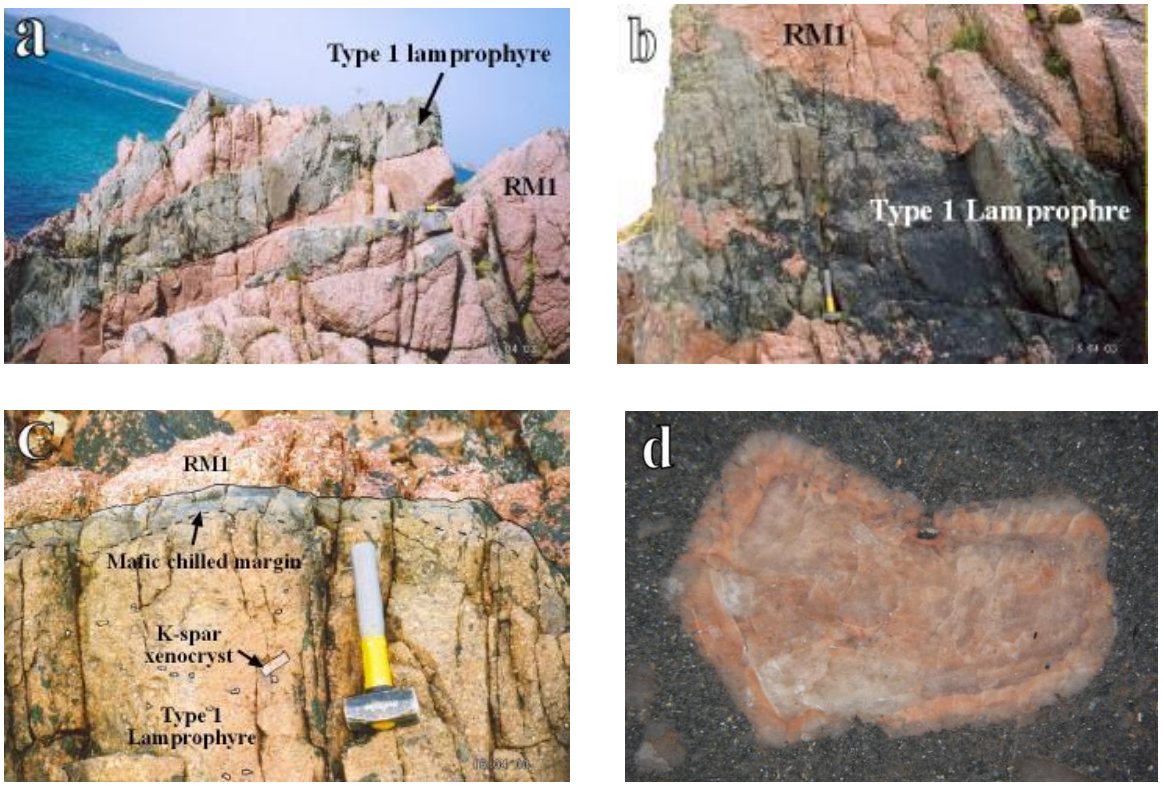


Fig. 2.17 (a-d) **(a)** Bifurcating Type 1 Caledonian minor intrusion with planar and irregular contacts against RM1 at Fionnphort Pier orientated 012/23^o NW (NM [2985 2336]). Island in the background is Iona. **(b)** Perpendicular section through the sheet depicted in **(a)** displaying highly irregular contacts against host RM1 granitoid. **(c)** Continuation of the sheet in **(a)** at Eilean Eion (NM [3007 2415]) highlighting a considerably more mafic chilled upper margin (above dashed line) and subhedral to euhedral alkali feldspar xenocrysts derived from RM1 within the centre of the sheet. **(d)** Rapakivi feldspar glomeroxenocryst within the sheet in **(a)** (length of rapakivi glomeroxenocryst is 15 mm)).

mantle. Closer inspection reveals that in some cases such alkali feldspar megacrystic phases are in fact glomerocrysts that have internal corroded contacts with each other, and may have several separate rapakivi phase growths. Due to these features, these are inferred as xenocrysts or rapakivi glomero-xenocrysts (in the case of **Fig. 2.17 (d)**) that have been entrained in mafic magma during the petrogenesis of the lamprophyric magmas.

A thin section with corresponding gross petrographic image of the core of the Type 1 sheet at Eilean Eion is provided in **Fig. 2.18**. Thin section petrography reveals an intimate array of textural heterogeneity again similar to that observed in Type 1 diorites. Micro-globular structures are prevalent in the form of unevenly distributed corroded quartz, glomerocrystic amphibole clots and embayed alkali feldspars that all have variable types of mantling structures (**Fig. 2.18**). The groundmass is granodiorite, but anhedral to subhedral amphibole and biotite are unevenly distributed throughout the rock.

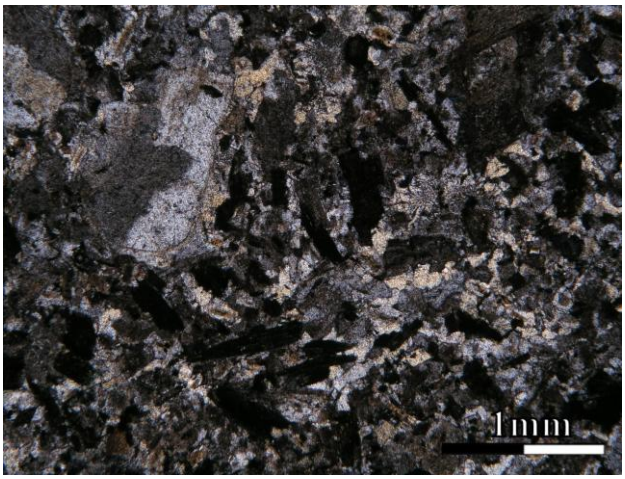


Fig. 2.18 Petrographic image of the Type 1 Caledonian sheet considered in **Fig. 2.17 (c)** at Eilean Eion (sample No. ZCLS02 (NM [3007 2412])) (XPL). Fine-grained groundmass is chiefly made up of acicular to elongate hornblende and biotite, zoned subhedral plagioclase (often with sericitised cores) and minor interstitial quartz and calcite. The large subhedral plagioclase feldspar in the top left area of the image is individually mantled by smaller varieties of zoned and un-zoned plagioclase feldspar.

Additional mixing textures comprise of:

a.) Intense boxy cellular structure in plagioclase xenocrysts.

b.) Plagioclase feldspar glomero-xenocrysts and groundmass feldspars in close proximity having contrasting zonation profiles.

c.) Quartz ocelli.

The Type 1 sheet at Fionnphort provides an example of a composite sheet displaying a wealth of lateral heterogeneity in the orders of a few m to km; however vertical heterogeneity is less apparent, apart from the presence of chilled margins or variations in xenocrystic mineral assemblages. Some Type 1 sheets are truly composite with respect to their vertical

heterogeneity by displaying evidence for multiple intrusions composed of magmas of contrasting composition. The most complex composite and hybridised Caledonian Type 1 sheet observed in the ROMG occurs in the south of the granitoid complex at Eilean Srianach (NM [3475 1685]) (**Fig 2.1**, **Fig. 2.5 area 1** & **Fig. 2.19 (a)** to **(d)**). Here, the sheet has the same orientation of the Type 1 sheet at Fionnphort (026/31^{o} WNW), and is cut by numerous aphyric Palaeogene dykes trending roughly 120^{o}. In some areas the sheet bifurcates in a perpendicular fashion forming separate sheets that are often adjacent to or cross cut Moine xenoliths (see **area 3** in **Fig 2.5**) that are intimately associated with a pink sacharoidal isolated facies of granitoid and pegmatite (see **area 2** in **Fig. 2.5**).

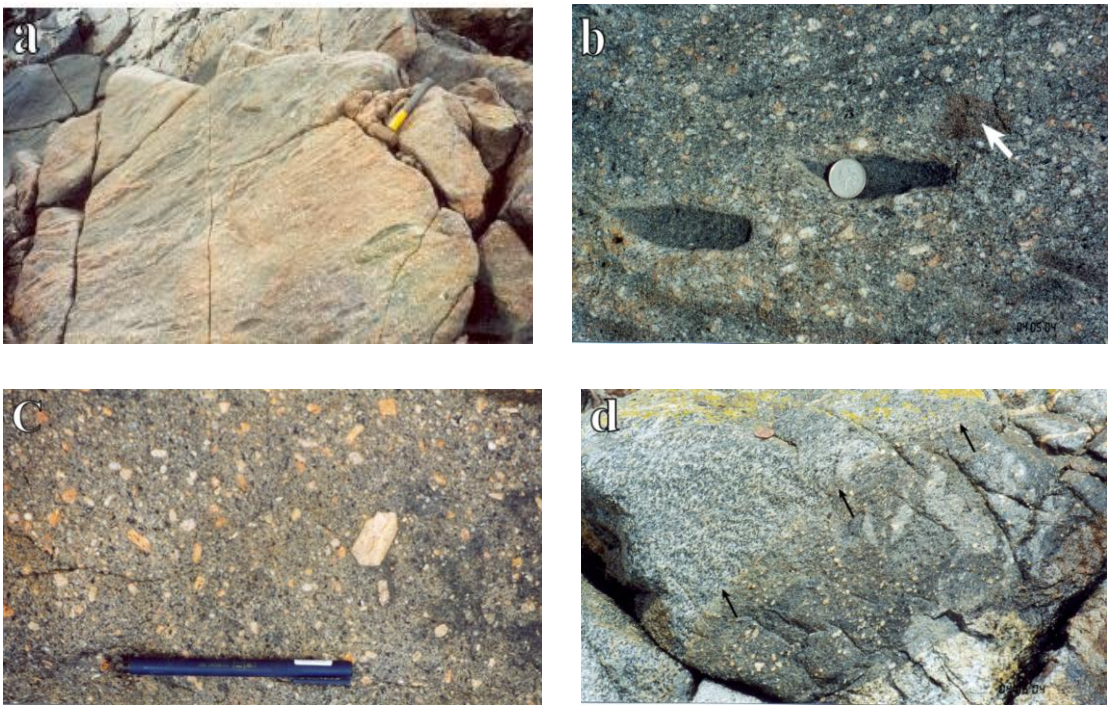


Fig. 2.19 (a-d) Caledonian Type 1 minor intrusion at Eilean Srianach (NM [3475 1685]): **(a)** Near perpendicular section through the complex hybridised sheet illustrating the composite nature (most mafic area is in the top left area of the image) of such intrusions and consistent linear trails of MME set within a more felsic hybridised medium. Orientation of the sheet is 028/44^{o}NW. **(b)** Ovoid cm scale MME commonly containing glomerocrystic amphibole clots and corroded anhedral quartz in a more hybridised felsic medium considered in **(c)** (British ten pence piece coin is in for scale). White arrow highlights a micro-granite globule. **(c)** Hybridised felsic medium absent of MME displaying a highly porphyritic texture made up of variable crystal assemblages as amphibole clots, subhedral to euhedral alkali feldspar phenocrysts and xenocrysts. Largest pink crystal observed is a euhedral alkali feldspar monocryst. **(d)** Base of the sheet (top left area) in contact with a Moine xenolith (indicated by black arrows) where an overall leopard skin texture dominates above the contact (British two pence piece coin is in for scale).

Fig. 2.19 (a) represents a photographic cross-section through the sheet with associated internal MME in **Fig. 2.19 (b)** (note white arrow in **Fig. 2.19 (b)** denotes micro-granitoid globule). The Type 1 sheet at Eilean Srianach is highly heterogeneous, having three different internal lithologies that have irregular contacts with each other, various xenocrystic crystal assemblages (**Fig. 2.19 (c)**) and variable syn-magmatic fabrics expressed by orientated trails of alkali feldspar xenocrysts mirroring elongate directions of MME.

The most mafic components are MME observed in **Fig. 2.19 (b)** and are the most homogeneous components in terms of equigranular nature and modal mineralogy. However, the elongated trails of oriented alkali feldspar xenocrysts (from host RM2 granitoid) incorporated MME within this area suggests that lamprophyric magmas have formed in a dynamic turbulent magmatic environment.

A final and separate contact related lithology is also present and unique (**Fig. 2.19 (d)**) to this sheet (the nature of which is presented but not discussed in this study) which cross cuts an adjacent Moine psammite-amphibolite xenolith at its base.

2.6.2 Type 2 lamprophyres

Type 2 lamprophyres occur in the southwest part of the ROMG within RM2 host granitoid, and are found directly on the coastline within the east and west limits of the Erraid Sound to the southeast of Aird Mór (NM [3360 1680]). Within the Knockvologan mixing and mingling zone, there are numerous Type 2 sheets cross-cutting RM2, Moine psammitic xenoliths (NM [3094 1875]) and Type 1 diorite masses (NM [3091 1893]) east of Erraid. These sheets are also in the order of a few m in terms of thickness and lateral extent. The type locality for classification of these sheets occurs within the Knockvologan mixing and mingling zone just before Caolas an Eilean Duibh (NM [3093 1866]). Here the sheet is arcuate (in the space of a few m), dips in the opposite sense to Type 1 lamprophyres to the northeast and displays highly crenulate and bifurcating contacts with host RM2 granitoid. An exact analogue of this sheet can be found in a series of sheeted Type 2 lamprophyres east of Port nan Ron (NM [3200 1870]) and northeast of Bágh Tir Chille (NM [3249 1835]), at NM [3224 1851] (**Fig. 2.20 (a)**). Type 2 lamprophyres comprise a fine-grained melanocratic rock that is highly homogeneous with respect to Type 1 sheets, and lacks the characteristic xenocrystic mineral assemblages.

All Type 2 lamprophyres have highly irregular contacts with RM2 granitoid (**Fig. 2.20 (a)**), a lack of xenocrysts discernable to the naked eye, and a homogeneous and high

distribution of mm scale glomerocrystic amphibole clots (that can be up to or over 50% with respect to groundmass). In some cases, amphibole glomerocrysts are aligned at the margins in contact with host granitoid. Where this is prevalent, the fabric is inclined and is homogeneous within the core region, however the lower and upper contacts (where the sheet is in contact with RM2 host granitoid) display opposite sense of shear with respect to each other (**Fig. 2.20 (b)**).

Type 2 lamprophyres do not mirror the mixing textures observed in Type 1 lamprophyres in terms of xenocrystic crystal assemblages or groundmass assemblages, as they are homogeneous. However, the main characteristic textural feature already documented

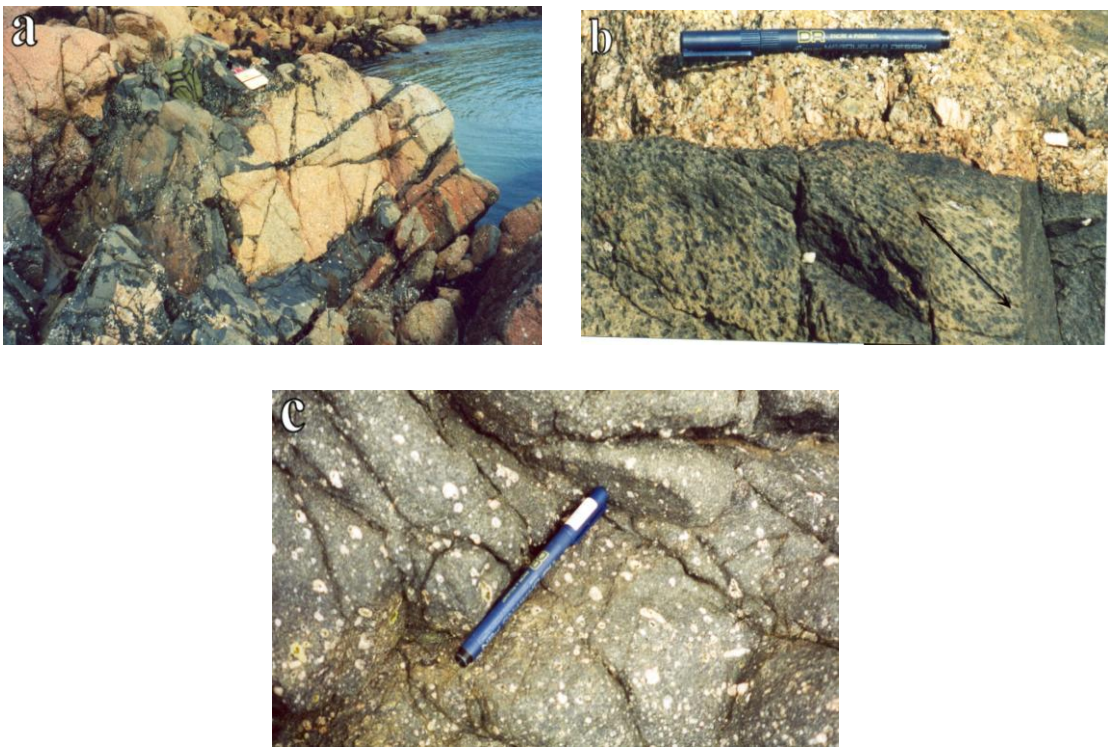


Fig. 2.20 (a-c) **(a)** A view of a bifurcating Type 2 Caledonian minor intrusion roughly along strike of the contact with RM2 host granitoid (NM [3224 1851]). **(b)** Sheared margin of a Type 2 sheet at NM [3093 1866] in contact with RM2. Black arrow defines the orientation of elongate glomerophyric anhedral amphibole clots. **(c)** Rare example of an upper margin of a Type 2 Caledonian sheet dominated by cm and mm scale anhedral alkali feldspar xenocrysts and glomerocrystic amphibole mantled by alkali feldspar (NM [3243 1700]).

to be prevalent throughout such sheets is glomerocrystic hornblende, which in some cases can be mantled by biotite, titanite or Fe-Ti opaque oxides.

Another variant of Type 2 lamprophyre is similar in terms of grain size and texture. These types of sheets are rare within the ROMG and are confined to the coastline south of

Aird Mór (NM [3243 1700]). The most distinguishing feature present in such sheets that is not observed in any other type of lamprophyre sheet is a cryptic 30-40 cm upper zone chiefly comprising heterogeneously distributed anhedral to subhedral mm scale alkali feldspar xenocrysts (**Fig. 2.20 (c)**). Alkali feldspar xenocrysts often display highly corroded crystal margins, embayments, rapakivi texture, and in some cases concentric amphibole inclusion trails. Examples of glassy green amphibole glomerocrysts mantled by alkali feldspar are also another mantling type relationship observed in this zone.

Thin section petrography reveals that the groundmass is comprised of equigranular subhedral to anhedral plagioclase feldspar (some varieties are zoned and juxtaposed to fresh unzoned plagioclases), subhedral amphibole and biotite, with minor quartz (**Fig. 2.21 (a)**).

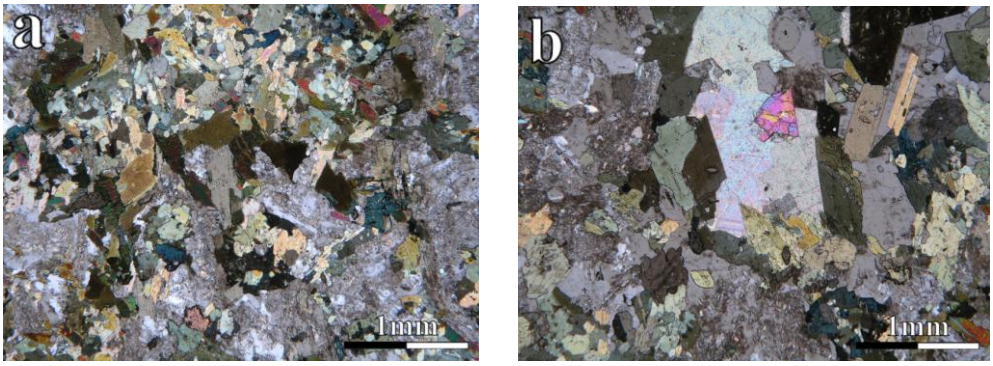


Fig. 2.21 (a-b) (a) Type 2 Caledonian minor intrusion (sample No. JR23 (NM [3090 1680])) (XPL) displaying an agglomerated amphibole clot made up of several glomerocrysts at the top of the image and an overall fine-grained equigranular groundmass composed of plagioclase, biotite, amphibole and little to no quartz. **(b)** Presence of large areas of interstitial calcite (top and central area of image) is also a common feature in Type 2 minor intrusions (same sample as in **(a)** (XPL)).

The characteristic glomerocrystic amphibole phase is in fact made of subhedral amphibole with minor plagioclase feldspar and quartz, and in some cases such clots may be co-joined forming composite clots (**Fig. 2.21 (a)**). Calcite appears to be more obvious in Type 2 lamprophyres as opposed to Type 1 lamprophyres, and can often be found in 1-2 mm interstitial patches within the groundmass (**Fig. 2.21 (b)**).

2.7 Interpretation of textural heterogeneity within the ROMG and Caledonian Minor Intrusions

The mafic and felsic components that make up the ROMG all contain numerous thin section scale textural heterogeneity. Thin section scale textural heterogeneity (including plagioclase zonation) associated with mafic-felsic magma interaction becomes petrographically more difficult to observe as one moves northeast from the Knockvologan mixing and mingling zone towards the eastern contact. It also mirrors field scale heterogeneity whereby there is a decrease in diorite, MME and a cryptic gradational contact with RM2/RM1 (with RM1 being the most homogeneous facies) as one moves north-eastwards. Textures primarily associated with mixing throughout the ROMG depicting this trend are summarised in **Fig. 2.22** with corresponding descriptions and interpretations shown in **Table 2.1**.

The volume of textural heterogeneity presented in **Fig. 2.22** and **Fig. 2.23** shows that mixing textures are abundantly present throughout the ROMG. The heterogeneous nature of mixing in the ROMG is indicated by the varying distribution of textures between and within lithologies. Regarding mixing and mingling textures, as one moves from the Knockvologan mixing and mingling zone through to the eastern contact the following observations have been noted:

i.) Distribution, intensity and density of boxy cellular feldspar structures decreases.

ii.) Rapakivi feldspars (resulting from alkali feldspar xenocrysts either from host RM1/RM2 granitoid being entrained in mafic components generally decreases indicating more mingling in the south-west portion of the ROMG.

iii.) Plagioclase feldspar zonation profiles (simple concordant types) generally have less mineral zones in host granitoid (i.e. generally less complexity arises in mineral zonation in RM1/RM2 feldspars as one moves towards the eastern contact) advocating more mixing as one moves towards the eastern contact.

iv.) Embayments, plumose structures and corroded margins indicative of disequilibrium (that are more enhanced in xenocrysts phases in mafic components) decrease.

v.) Juxtaposition of plagioclases with contrasting zonation profiles and smaller plagioclase mantling larger plagioclase decreases and is harder to observe.

Fig. 2.22: Simplified thin section scale textures in the ROMG and Caledonian minor intrusions associated with mafic-felsic magma interaction (scale bars are all 1mm for each sketch unless stated otherwise, and refer to **Table 2.1** for description of textures in **A-I**).

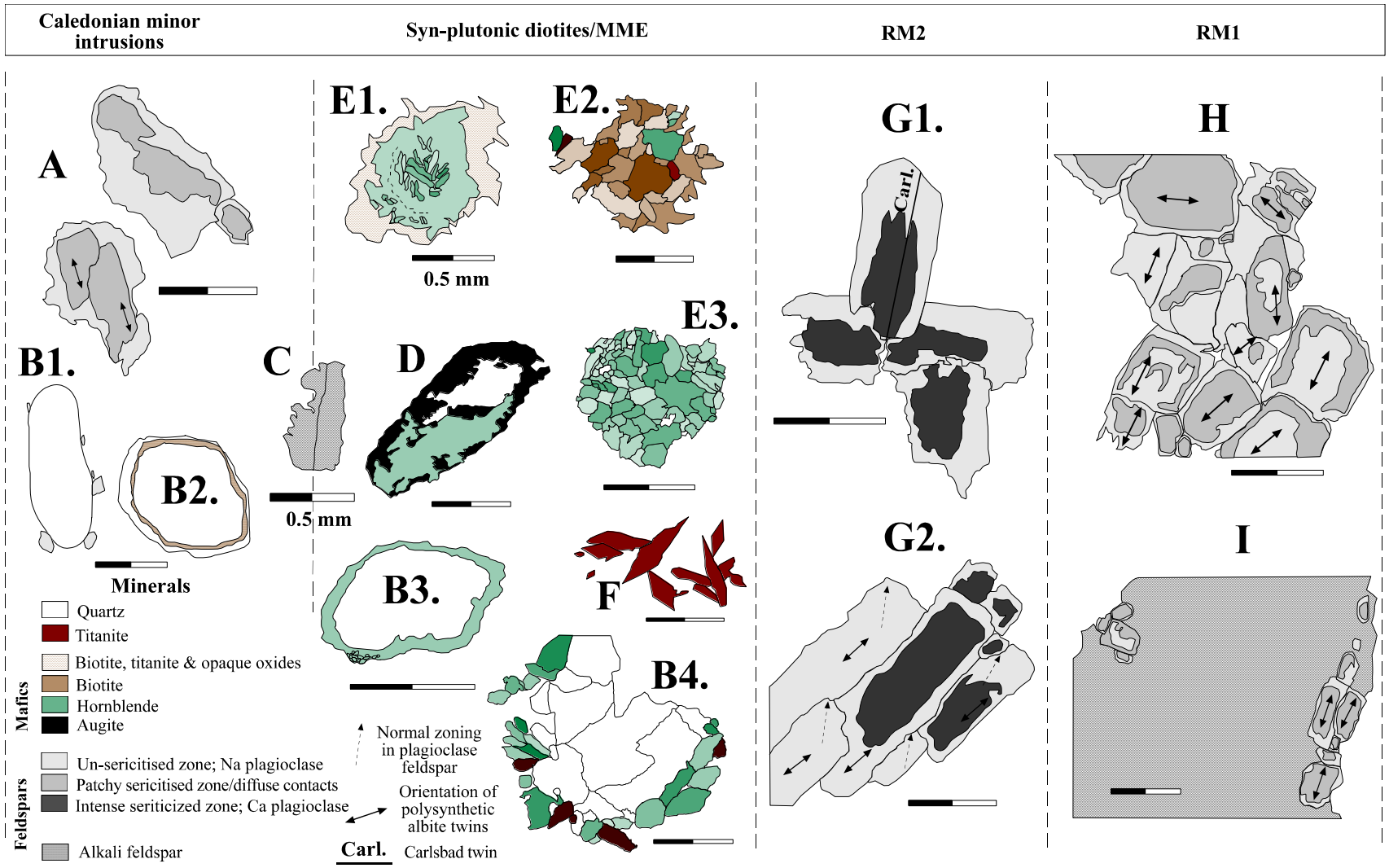


Table 2.1 Summary of feldspar textures **A-I** as observed in **Fig. 2.22**

	Description/Interpretation
A - Isolated mantled plagioclase xenocryts	Isolated highly anhedral to subhedral crystals where the core regions show variable degrees of sericitisation and may appear to be lobate. In some cases the core regions are mutually attatched (and appear to have a more uniform sericitic concordant alteration confined to more subhedral looking varieties) in glomeroxenoccrysts. Whole glomeroxenocrysts are mantled by a phase of smaller plagioclase feldspar crystals. The isolated nature, similar zonation profiles observed in RM1/RM2 plagioclases making up these glomerocrysts in ROMG lamprophyres, indicates these xenocrysts result from mafic-felsic magmatic exchange between alamprophyric melts and granitic crystal mushes of felsic RM1/RM2.
B1.-B4. - Quartz Occelli	A spectrum exists in ROMG mafic components that include: (**B1.**) Isolated higly ovoid quartz with a cryptic mantle of small plagioclase crystals; (**B2.**) Corroded rare varieties with an ocellus of biotite, titanite and opaques locked in by a zone of inclusion free fresh quartz; (**B3.**) Highly corroded varieties with internal embayments with a mono-minerallic ocellus phase entirely composed of hornblende; (**B4.**) Poly-crystalline interlocking anhedral quartz mantled by subhedral hornblende and titanite. Quartz ocelli are not common in Aird Mór Type 2 diorites. They have formed as a result of magma mixing whereby quartz from felsic ROMG facies is incorporated into mafic components giving mafic hybrids, where quartz is unstable allowing partial melt of quartz xenocrysts with diffusion into the melt corona (resorption of quartz gives rounded morphology), stimulating growth of mafic minerals or plagioclase on the retreating surface. Subsequent precipitation of quartz may lock in a mafic ocellus phase (see **B2.**) giving an inclusion free outer rim that preserves the texture (refer to Baxter & Feely 2002).
C - Alkali feldspar xenocrysts	Totally isolated mm scale alkali feldspars within mafic components that have a multitude of disequilibrium textures in the form of highly resorbed crystal interfaces that frequently contain embayments (particularly characterisitc in hornblede phyric MME), and in porhyritic varieties of MME have skeletal to tabular morphologies (some rare examples occur with resorbed irregular cores separated by an internal re-grown rim of small biotite/ amphibole crystals). Resultant from mechanical mass transfer of RM2/RM1 alkali feldspars that sometimes overlap/straddle contacts of mafic-felsic mediums (essentially capturing this process) into mafic components of the ROMG.
D - Replacement of augite by quartz & hornblende	Euhedral to subhedral augite is replaced primarily within the core region by hornblende and quartz leaving a skeletal looking shell (in ROMG diorites and MME only). This could be related to the way amphibole clots form but must include hydration reactions within an open magmatic system. Without EPMA analysis, an interperetation on textures alone is limited.
E1.-E3. - Mafic clots	Various examples exist that are confined to ROMG mafic components only. Examples include: (**E1.**) Monomineralic clots of possibly zoned subhedral hornblende in the core, followed by smaller more fibrous varieties at the edge (transition marked by dashed line) of the clot and a mantle composed of a micro-granular aggregate of biotite, titanite and opaque oxides; (**E2.**) Anhedral to subhedral biotie dominant clots that have minor hornblende and quartz with no mantling phase present; (**E3.**) Equigranular mono-mineralicclots entirely composed of anhedral hornblende with no mantle present. Observations from complex amphibole mantling phases in hornblende-phyric MME has shown these to form by replacement of early-magmatic clinopyroxene phenocrysts that could be related to a consequence of re-eqilibriation following magma mixing (Castro & Stephens (1992) and references therein).
F - Titanite agglomerations	Very rare texture only observed in Type 1 diorite related porphyritic MME that could relate to magmatic mixing simply due to the heterogeneous distribution of isolated high concentrations of titanite.
G1.-G2. - Plagioclase glomerocrysts	Different types of glomerocrysts in RM2 that could be xenocrystic due to their isolated nature with respect to a homogeneous groundmass (not drawn). Glomerocrysts in (**G1.**) represent a stellate isolated nestling of either RM1/RM2 plagioclase feldspars that all have sericitised concordant core zones, and all have corrosion zones that go through the *Z*-axis of crystals that define the contacts with each other. Example in (**G2.**) depicts an isolated glomerocrystic patch in RM2, where normaly zoned subhedral crystals (with variable zonation profiles juxtaposed) are amalgamated together with a vague orientation relative to the length axis of the largest crystal. Such features typify batch mixing processes.
H - Plagioclase domains	Hetrogeneous cryptic agglomeration of subhedral plagioclase feldspars containing variable zonation profiles that have been observed in a spectrum of RM1/RM2 samples juxtaposed to fresher varieties in the grounmass (not drawn here) supporting more textural information towards batch mixing processes as being dominant in RM1.
I - Other mantling	Subhedral zoned plagioclase feldspar forming a mantling phase have been re-orientaded parallel to the advancing crystal surface of larger alkali feldspar. They have similar zonation to plagiocases which form the equigranular graoundmass. This texture can occur via a dynamic magmatic flow during mafic-felsic magma interaction (Vance 1969).

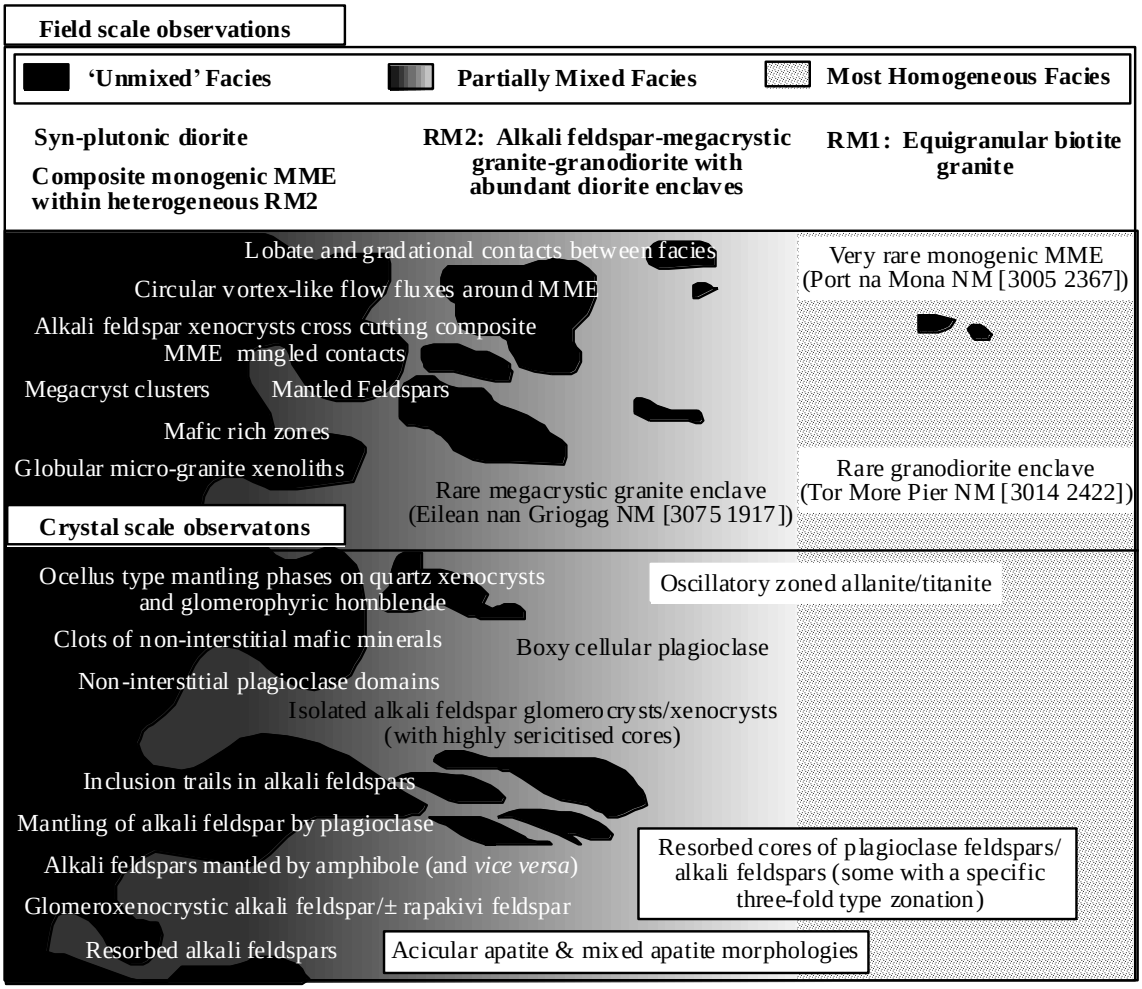


Fig. 2.23 Summary of field to crystal scale heterogeneity across the ROMG (west to east traverse). Block diagram of mixing/mingling features in syn-plutonic diorite (white text), all MME and directly adjacent granodioritic RM2; black text refers to features in RM2 only; black text set within a black border refers to features prevalent in all ROMG components and black text set in white borders refers to features observed in RM1 only.

vi.) Amphibole clots (with various mantling phases), quartz ocelli (with various ocellus phases), altered augite and plagioclase xenocrysts (with corroded cores or margins) are confined within mafic components (aplitic micro-granites are not included here).

vii.) Plagioclase xenocrysts/glomerocrysts (isolated crystals or domains with contrasting zonation profile juxtaposed) and mantling structures on plagioclase decrease.

Due to the complex array of micro-textures observed combined with recorded occurrences of MME throughout the ROMG, it is inferred that mafic-felsic magma interaction has occurred throughout the whole of the ROMG.

2.8 Inferences from Structural Observations/Data: Diorites, MME and *Sub-Solidus* Features

Diorites: Orientation of syn-plutonic diorite intrusions and MME swarms (striking north-south and dipping east/west) are confined to gently inclined tabular sheets that show abundant evidence for disruption, flattening and shearing (**Fig. 2.12 (a)** to **(c)**). The sheeted diorite locality (**Fig. 2.12 (d)**) within the mingling and mixing zone at Knockvologan represents part of a structural traverse comprising of aligned/pillowed MME and incorporated, sheared Moine xenoliths that dip in a southeasterly plane. The plane is identifiable as the proportions of MME within the sheeted intrusion are completely absent above the sheet/within the upper limits of the cliff face. The top of this sheet is identified at (NM [3110 1902]). A coastal traverse from this diorite sheet locality to Traigh a' Mhill (NM [3127 1859]) via Caolas an Eilean Duibh (NM [3081 1857]) highlights a consistent orientation of elongate MME confined to such structural limits.

Abundant Moine pelitic xenoliths are present such as the semi-pelitic/pelitic one at Eilean nan Griogag (NM [3067 1912]) (Zaniewski *et al.* 2006). They are adjacent to syn-plutonic diorite as a result of being incorporated in the ROMG during emplacement from the south-west, some of which display mechanical shearing where caught up in sheeted-tabular diorite intrusions.

The Knockvologan mixing and mingling zone contains numerous xenolithic inclusions and blocks of Moine metasediment, completely surrounded at outcrop by granite or diorite, which are a conspicuous feature of many parts of the complex. The orientation of tectonic structures and fabrics (D1-D3 features as described by Holdsworth *et al.* 1987) in the larger bodies is sufficiently coherent to suggest that they are essentially *in situ* (an example of this can be found within the xenoliths on Erraid at (NM [2965 1989]) and (NM [3030 1970]). This conclusion is supported by the ghost preservation of the Morar (=Shiaba)/Glenfinnan (=Assapol) lithostratigraphic boundary by xenoliths in the granite (Holdsworth *et al*. 1987). A gravity survey by Tucson (see Beckinsale & Obradovich 1973) highlighted that the

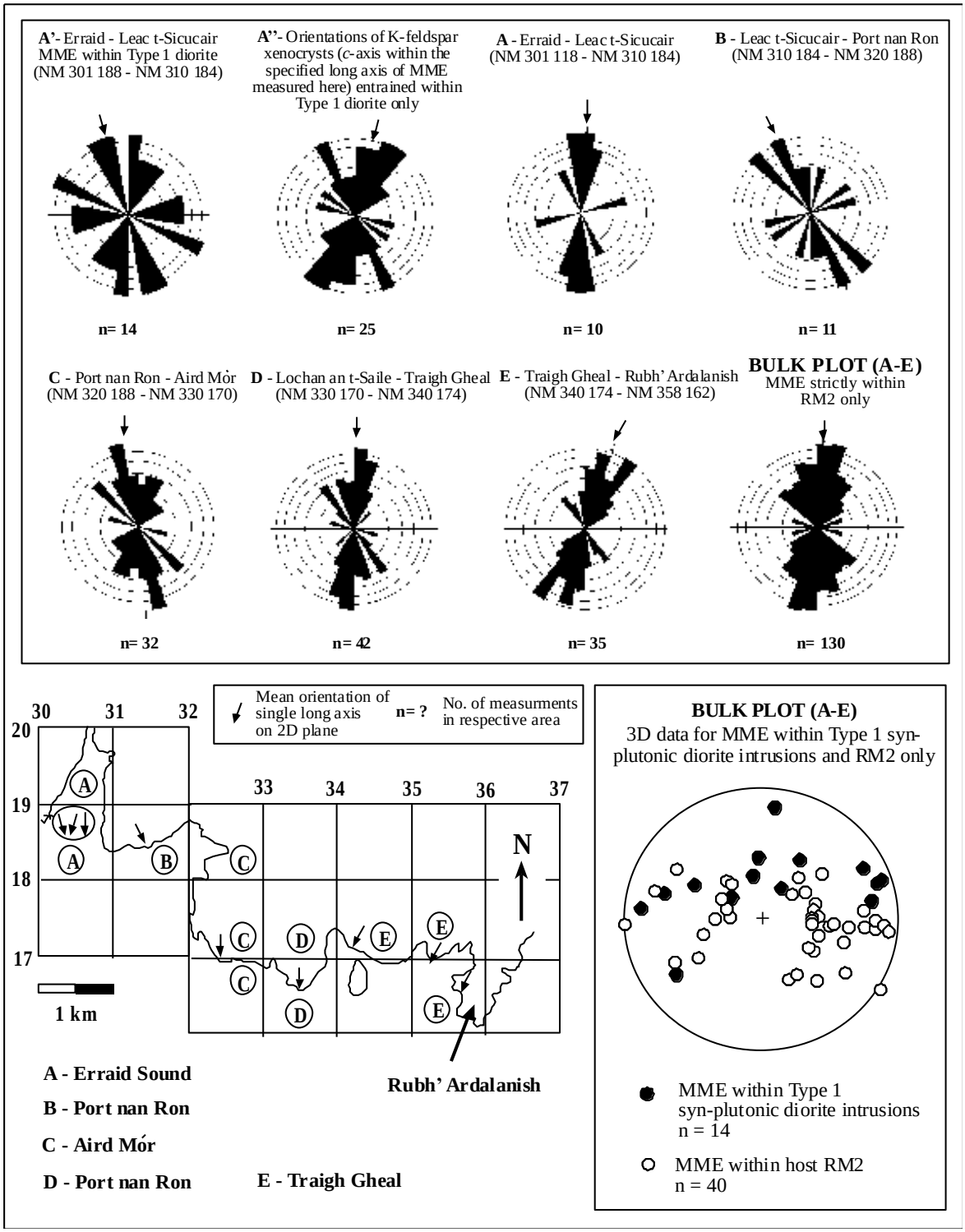


Fig. 2.24 Equal area weighted rose diagrams showing principal long axes measurements in MME and *c*-axes of alkali feldspar xenocrysts within MME on a 2D plane in Type 1 syn-plutonic diorite intrusions and predominantly host RM2. Data reflects a traverse from the Erraid Sound to Rubh' Ardalanish. Letters in rose diagrams correspond to the areas in the map where measurements were made. Stereogram depicts gross orientation data for all MME measured in Type 1 syn- plutonic diorite sheets and host RM2 from the Erraid Sound to Rubh' Ardalanish (stereographic data plotted as poles to planes, and all data calculated in GeoorientV9.2 (Holcombe 2005)).

interpretation for the ROMG was a sheet in the order of 3.5 km thick with a wedge angle 30^{o} dipping to the east. Due to presence of known Moine xenoliths, diorites constrained to sheets where MME in such sheets are vertically absent above them (at above approximately 40 m MME are absent), inferred gravity thickness and basic field evidence coupled with the south-to-north AMS presented data in Petronis *et al.* (2012), it is inferred that the diorites mirror the sheeted emplacement of the whole the ROMG as per Zaniewski *et al.* (2006).

MME: Structural measurements of elongate axes of MME on 2D planes and 3D planes (where 3D geometry of MME are exposed allowing strike and dip measurements to be taken) were collected on a coastal traverse from the Knockvologan mixing and mingling zone towards Rubh' Ardalanish and are presented in **Fig. 2.24**. The 2D data (refer to **Appendix A1** - from **A1.1** to **A1.2**) shows that MME swarms throughout the granitoid complex are generally confined to having a dominant north-south trend and 3D data depicts that MME in host RM2 granitoid generally dip to the east or west.

Aplitic micro-granites & Joint Planes: A key feature associated with ROMG aplitic micro-granites is their structural continuity with respect to the joint plane system within the ROMG. This is particularly well developed in the northwest part of the complex in RM1, where they often dip and conform to the joint plane system developed in RM1; an example of this can be readily found at Fionnphort in a traverse from NM [3013 2387] to NM [3028 2373]. They can often be found within tens of m apart within this system. To highlight this relationship, data collected for every joint plane and aplitic micro-granite sheet measured in this study (refer to **Appendix A1 - A1.3** & **A1.4** for data presented) is plotted together in the stereogram in **Fig. 2.25**. Similarities are evident from the spatial clustering of both data sets and a northwest dipping joint plane system in RM1 has already been highlighted. As both data sets for aplitic micro-granites and joint planes overlap, with field observations showing aplitic micro-granites conforming to within joint planes, it is inferred that the petrogenesis of the aplitic micro-granites is related to the unroofing and cooling of the ROMG; where late stage fluids and volatiles have fed and utilised these cooling joints and fracture planes to form planar sheets of cm to m scale aplitic micro-granites.

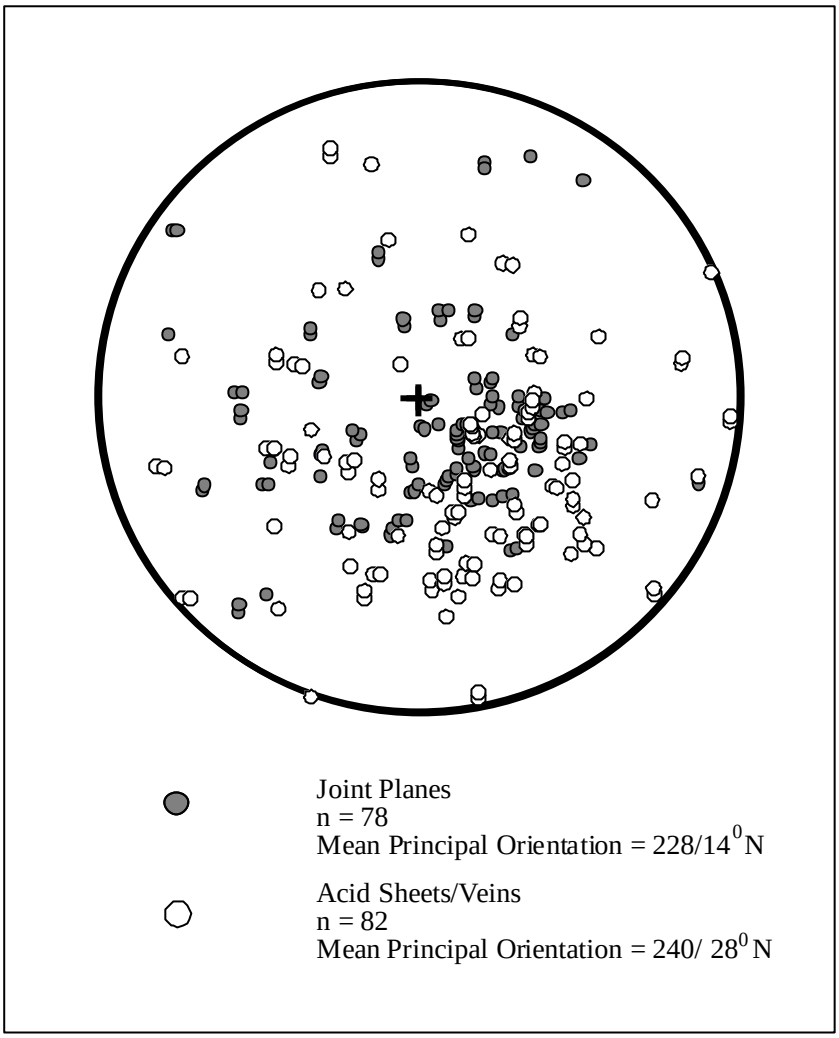


Fig. 2.25 Stereographic plot depicting all measurements of acid sheet and joint plane orientations within the ROMG (all data plotted as planes and calculated in GeoorientV9.2 (Holcombe 2005).

2.9 Discussion and Conclusions

Field to thin section petrographic observations throughout all mafic to felsic components that make up the ROMG have been already documented. In this section, it is necessary to critically examine these observations (2.9.1) so that an accurate summary of the crystallisation history of the ROMG can be provided, with an understanding of overall magmatic heterogeneity at the field scale (2.9.2). A detailed emplacement model is then provided in 2.9.3.

2.9.1 Interpretation of the Crystallisation History of the ROMG

ROMG MME commonly preserve evidence for mechanical incorporation of host ROMG into enclave magmas to form hybrid mixtures (Petford *et al.* 1996; Pugliese & Petford 2001; Zaniewski *et al.* 2006; McLeod *et al.* 2011). Although there is evidence of *in-situ* mixing at the present level, the mafic-felsic mixing in the diorites is interpreted to have occurred at deeper levels prior to their emplacement within host granitoid Zaniewski *et al.* (2006). This is inferred by presence of highly heterogeneous xenocryst assemblages (such as rapakivi feldspars, embayed alkali feldspar xenocrysts/glomeroxenocrysts, zoned plagioclase feldspars with resorbed cores and various ocelli mantling relationships (Angus 1962; Palivcowá *et al.* 1995) present in MME phases (which may be composite).

Textures constituting evidence for magma mixing in heterogeneous variants of RM2 are primarily variable degrees of boxy-cellular plagioclase populations (their formation is covered in Hibbard 1981 & 1991; Grogan & Reavy 2002; Grogan 2004). The presence of evenly distributed acicular apatite juxtaposed to mixed morphologies also confirms a quench-induced environment (Wyllie *et al.* 1962). Feldspars with different growth zones from different magma batches in close proximity to each other in terms of mm to ones that display little to no zoning in homogeneous varieties of RM2 are also consistent with a genetic model of mixing of mafic and felsic magmas.

All Knockvologan mixing and mingling zone localities presented in this study display evidence of *in-situ* mixing pre and syn-ROMG emplacement; hybrid diorite melts have been emplaced into partially crystallised, cooler, host megacrystic RM2 granitoid, producing highly heterogeneous lithologies. The eastern limits of Erraid Sound provides a natural laboratory to envisage the mechanical injection of discrete diorite pulses pillowing off globular MME that have subsequently been partially disrupted, dispersed and sheared prior to complete crystallisation of host RM2 granitoid.

Outside the limits of the Knockvologan mixing and mingling zone, but still within RM2 host granitoid, lies the most complex association of composite MME observed within the ROMG at Eilean nam Bo (NM [2931 2155]) (refer back to **Fig. 2.8** for location). Composite MME and associated abundant alkali feldspar megacrysts at Eilean nam Bo additionally offer an outcrop to access mechanical mass transfer processes of xenocrystic assemblages during mafic-felsic interaction within the ROMG. Most ROMG MME are highly ovoid with irregular margins indicative of once undergoing poly-phase liquid-liquid interaction. Xenocrysts commonly straddle single and composite MME phases highlighting

mass transfer and dynamic phenocryst exchange during formation of hybrid mixtures throughout the continuum of hybridised MME observed. Elongate orientations of heterogeneous MME, (sometimes straddling each other) again with differing proportions of xenocrystic assemblages adjacently superimposed and related xenocrysts in asymmetrical flame structures reflects synchronous magmatic swirling between mafic enclave and felsic magmas; thus giving differing degrees of local scale hybridisation. In some cases, the presence of linear trails of feldspar xenocrysts in syn-plutonic diorite/MME could also represent a mechanical interplay relating to flow channels within advection domains (Petford *et al.* 1996; Pugliese & Petford 2001) or other complex magmatic transport in a buoyant turbulent environment. Similarly, amphibole rich zones can form by deformation and smearing out of a MME that is not fully crystallised and host RM2 crystal mushes relating to a plastic rheology, resulting in sub-horizontal mafic rich zones finer-grained than host RM2 granitoid. This is interpreted by the presence of MME with highly strung out cm scale mafic fingers (that are sub parallel to amphibole rich zones) occurring within a hybridised sheet at Eilean nam Bo (NM [2931 2155]).

Evidence for co-existence of differing mechanical flow regimes within the ROMG during mafic-felsic magma interaction is highlighted by the observations made within the most complex composite MME phase at Eilean nam Bo. Here, it is important to understand the nature of alkali feldspar xenocrysts. Observations are as follows:

(i) Patchy distributions of skeletal looking and highly resorbed varieties (some rare examples occur with resorbed irregular cores separated by an internal re-grown rim of small biotite/amphibole crystals) in the largest MME phase.

(ii) Circular vortex-like flow fluxes (Poli & Perugini 2002) around internal MME relative to the main enclave phase occurring adjacently to the necks of flame structures.

(iii) Cryptic asymmetrical flame structures.

(iv) Agglomerated net captured (synneuesis related (Vance 1969; Stull 1979) distributions in the necks of flame structures (which could clog up the overall ‘pore throat’ of host granitoid injection in MME, plausibly restricting further localised hybridisation in MME).

Such observations allow one to infer that even at a local scale hybridisation of magmas occurs as a dynamic process within a chaotic turbulent environment sometimes forming cryptic laminar and rotational xenocryst distributions.

Theoretical and experimental considerations highlight the nature of mafic-felsic magma interaction is primarily dominated by the function of relative physical properties between co-existing contrasting magmas (Sparks & Marshall 1986). As relative rheology of the felsic component is intimately related to temperature, composition and crystallisation rate, sequential interactions may occur yielding stages of characteristic hybridism from same parental magmas; as such physical variables do not generally differ simultaneously during the petrogenesis of an open magmatic system (Barbarin 1988 & 2005; Fernandez & Barbarin 1995). Similarities drawn from these studies regarding stages of hybridism relative to crystallisation stages of felsic magma (also refer to Pitcher 1991 for a review) can also be applied to the ROMG. Although the model discussed has been adapted for other calc-alkaline granitoids such as those within the Sierra Nevada Batholith, U.S.A., similar demonstrable field relationships are evident.

In the case of the ROMG, at least four characteristic hybridisation episodes/crystallisation phases are envisaged to have occurred during a continuum of close spatially and temporally related mafic and felsic magmatism (refer to **Fig. 2.26** and corresponding numbers where appropriate):

(1) RM1 granitoid: Mixing at depth of at least two or more components whereby the mafic magma is introduced into a partly crystallised felsic magma (rheological field I of Sparks & Marshall 1986). Thus thorough mixing proceeds to give the most homogeneous looking facies with scarce MME, equigranular nature, oscillatory zoned allanite, mixed apatite morphologies and a cryptic threefold growth zonation is retained in some alkali-feldspar varieties.

(2) RM2 granitoid: Some degree of mixing at depth of at least two or more components, however when the mafic magma is introduced slightly later into the felsic magma, the felsic magma has a lower viscosity (rheological field II of Sparks & Marshall 1986) permitting a viscosity contrast large enough to advocate mingling as the main process. MME are pillowed, scattered and concentrated as swarms confined to diorite sheets that have been considerably modified/flattened during mass emplacement of the ROMG.

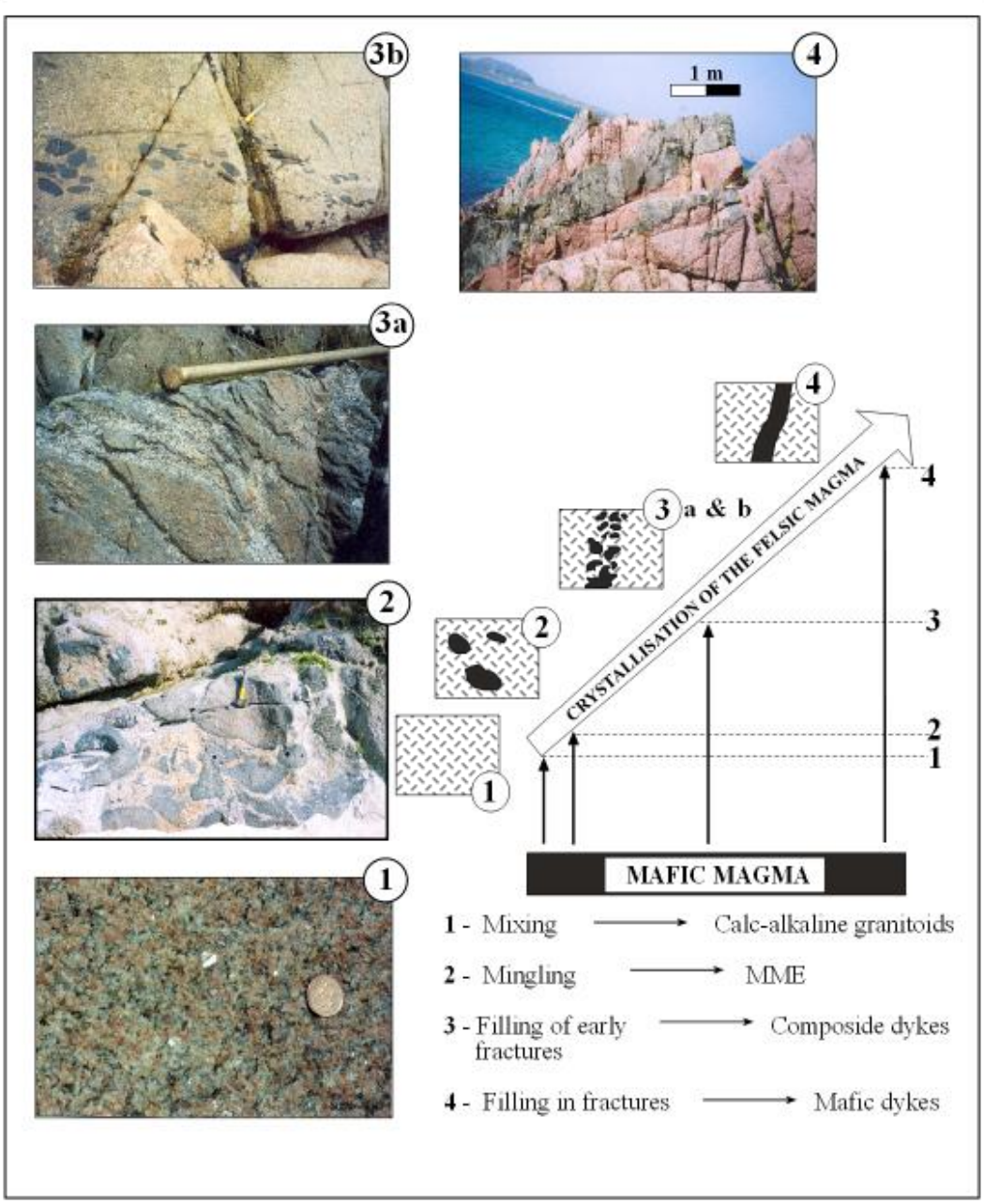


Fig. 2.26 Diagram (modified from Fernandez & Barbarin 1991; Barbarin 2005) displaying hybridisation stages for the ROMG are shown in photographs **(1)** to **(4)**: **(1)** RM1 from Red Bay Quarry (NM [3115 2541]); **(2)** MME at Knockvologan Beach (NM [3088 1924]) (taken from Zaniewski *et al.* 2006); **(3a)** Refer to **Fig. 2.12 (d)**; **(3b)** MME 'flow channel' near Na Maoil Mhóra (NM [33690 16730]); **(4)** Refer to **Fig. 2.17 (a)**.

(3a) & **(3b)** **Syn-plutonic diorite dykes with linear trails of MME**: Mafic magma is incorporated into the felsic magma during advancement of the felsic magma to the second rheological threshold. Mafic magma is subsequently channelled in to early fractures giving localised hybridisation with the felsic component (in the form of crenulate contacts and variable xenocryst assemblages). Frozen in, 'late stage' dismemberment of syn-plutonic

diorite dykes into linear trails of angular or amoeboid MME (flow stream) occurs with the latter having irregular margins with host ROMG. An example of this relationship with development of amphibole rich zones at the edges of the dyke is observed at Na Maoil Mhóra (NM [33690 16730]).

(4) Caledonian minor intrusions (lamprophyric sheets): Rheological contrasts (rheological field III of Sparks & Marshall 1986) between mafic and felsic magmas give sheets without amoeboid MME, planar contacts with host ROMG and very little degree of internal hybridisation in non-composite Type 2 varieties. However, there are composite lamprophyric sheets (Type 1; Zaniewski *et al.* 2006) with irregular contacts, internal associated MME and have variable proportions of xenocrystic crystal assemblages. Such composite varieties represent a pre-cursor stage to the non-composite varieties that reflect a slightly more advanced stage in terms of a viscosity contrast and limited hybridisation even in the waning stages of lamprophyric magmatism. From field observations only, one would concur that the active processes of mixing mafic and felsic magmas (i.e. lamprophyric and granitoid magmas) could certainly produce the hybridised spectrum evident in the vertical variation of the composite sheets. As 3D lateral dimensions of these units are not fully known it is more sensible to interpret that the composite nature of Type 1 sheets is a result of closely intimate contemporaneous pulses of mafic-felsic magmas that have interacted within an incompletely mixed open magmatic system as the bulk of the components are highly heterogeneous.

Un-roofing synchronous with late stage development of proto-fractures/joint planes during depressurisation and volatile loss has enabled pooling and fluidisation of a network of late stage fractionates of aplitic micro-granitoid rocks to be channelled in veins, pods and sheets to form throughout the complex. In rare cases, a syenite phase has been observed to be formed as a product in RM1 that has fed off such a network (post-dating the hybridised granitoids) that must be considered when evaluating ROMG petrogenesis.

ROMG pegmatites are on the other hand mostly not considered as late fractionates due to their intimate association with Moine xenoliths (dehydration reactions giving local H_20 enrichment and lower viscosity when forming in surrounding magmas).

One feature of the ROMG is the potassium rich nature of RM1 (as gleaned from XRF data to assist in running XRD fractions not presented here; see Chapter Three). Low modal concentrations of plagioclase in the outer pink equigranular facies is related to this problem since cold CL petrography has shown that the plagioclase present in RM1 is extensively

replaced by alkali feldspar which are often found to have purple luminescent cores (as presented in Chapter Four). Features of plagioclase replacement by alkali feldspar, the presence of calcite and the marginal reddening of feldspar could be interpreted as resulting from widespread potassium metasomatism by a pervasive CO_2 rich fluid. An induced temperature gradient resulting from interaction of the more felsic magmas into the 'centre' of the intrusion could favour potassium migration to the outer coolest portions of the granite.

2.9.2 Overview: Field to crystal scale heterogeneity across the Ross of Mull Granite

The ROMG and its plutonic components at Knockvologan offer coastally exposed field scale examples of mafic-felsic magma interaction expressed by the presence of syn-plutonic diorite and related MME. Field and petrographic features in a variety of assemblages from components of the ROMG at Knockvologan display a spectrum of disequilibrium/re-equilibrium textures such as resorbed alkali feldspar xenocrysts, resorbed plagioclase feldspars, rapakivi feldspars, various ocelli mantling phases on quartz xenocrysts and amphibole clots. Within heterogeneous varieties of host RM2 granitoid, variable proportions of isolated plagioclase feldspar glomerocrysts/xenocrysts, alkali feldspars with quartz/plagioclase and amphibole inclusion trails, boxy-cellular plagioclase feldspars and oscillatory-zoned titanite and allanite are present. However, textures associated with mafic-felsic magma interaction are considerably more cryptic in more homogeneous varieties of RM2, where MME are rare or absent. Evenly distributed acicular apatite and variable apatite morphologies are common throughout all ROMG components.

Such thin section scale textures have been documented in other open magmatic mixed igneous systems (e.g. Baxter & Feely 2002) and experimental petrological simulations of disequilibria particularly in plagioclase (e.g. Lofgren 1974; Loomis 1982). Thus, the presence of such textures and assemblages advocate mafic-felsic magma interaction in the overall petrogenesis of the ROMG.

The most homogeneous facies of the ROMG is RM1 and has limited field-scale evidence for mafic-felsic magma interaction by having a consistent equigranular nature with a gradational contact with RM2 (based on alkali feldspar megacryst size and density), extremely rare MME and lack of feldspar zonation in thin section. RM1 is considered the most mixed facies of the ROMG, retaining a threefold zonation in some alkali feldspars, which is prevalent in all components of the ROMG and related lamprophyric minor intrusions (mainly discernible via cold CL and Electron Probe Monochromatic backscatter imaging (this

is expanded upon in Chapter Four)). RM1a is a product of localised anatexis of adjacent Moine country rock.

As a whole textures previously documented within host RM1/RM2 advocate models involving a magma mixed origin (e.g. Hibbard 1981 & 1991; Anderson 1984; Andersson & Eklund 1994; Pembroke 1997; Grogan & Reavy 2002; Grogan 2004). The prevalence of such mixing-compatible textures in all the plutonic components of the ROMG from the Knockvologan mixing and mingling zone to the eastern contact suggest that mafic-felsic interaction was a major process in the overall petrogenesis of the ROMG; that is not just related to localised incidental mixing. A west-east transect through the reversely zoned sheet thus highlights increasingly gradational contacts between facies (in the case of RM1 and RM2), a decrease in MME, a decrease in megacryst clustering, increasingly intimate textural heterogeneity and homogeneous disequilibrium. This is summarised in **Fig. 2.23**.

Field scale textures advocating an origin associated with mafic-felsic magma interaction clearly depict 'frozen in'/captured textures of a central sheeted diorite complex pillowing/spalling off globular Mafic Magmatic Enclaves (MME) during ROMG petrogenesis. Textures in diorites, MME and less evolved hybridised granitic components document various ocellar mantling relationships in quartz and amphibole, rapakivi feldspars, cellular structures in feldspars, dissolution zones in feldspars and feldspar xenocrysts which are more cryptic in more evolved components or absent. Such textures decrease as one completes a southwest to northeast transect through the reverse zonation; implying more advocated mixing and less mingling across the ROMG as one progresses towards more evolved components. This indicates that mafic-felsic magma interaction played an important role throughout ROMG petrogenesis. A wealth of late stage felsic components associated with late stage fluidisation processes have also been introduced for the first time in any study of the ROMG. Field relationships depict ROMG pegmatites are mostly not late fractionates due to their intimate association with country rock xenoliths whilst a network of aplitic micro-granite veins, pods and sheets with a rare syenite are interpreted as late fractionates and fluidisation phases formed during cooling and un-roofing processes.

The ROMG shows open magmatic stirring and periodic injection is commonplace with forming disequilibrium textures and disaggregated mafic rich zones such as amphibole rich zones (Pembroke 1997). Cryptic rotational and laminar xenocryst distributions within composite MME phases in RM2 at Eilean nam Bo could advocate turbulent magmatic stirring as a dominant mechanical process in aiding an efficient means of hybridisation in host RM2 granitoid. However, such relationships discussed within Eilean nam Bo are unique in the

ROMG and it is therefore difficult to qualitatively access how dominant such a magmatic stirring process was throughout the whole of the ROMG. Periodic injection and field scale hybridisation for the ROMG in turn can be sequentially summarised by a multiple hybridisation process model (Barbarin 1988 & 2005; Fernandez & Barbarin 1991) as presented in **Fig. 2.26**.

2.9.3 ROMG Emplacement Model

Studies of the tectonics of granitoids in the area (e.g. Jacques & Reavy 1994; Reavy 2001) have emphasized the distinction between siting, ascent and emplacement. Ascent is the transport of batches of melt through the crust from the site of melt generation to the level of emplacement. This phenomenon will usually be closely controlled by the lithospheric-scale structures responsible for the siting of the initial magmatism. Work in the SW Grampian area by Jacques & Reavy (1994) showed that concentric zoned or composite plutons are sited above the intersections of major crustal lineaments and fault/shear zones.

Emplacement involves the construction of so-called "plutons" from the batches or pulses of ascended magma. In many cases this is probably by lateral spreading whereby flattish sheets were emplaced to form thin tabular and often discoid laccolithic bodies. As the ROMG is reversely zoned and centred offshore to the SW and assuming that it has similar controls on its siting as other adjacent plutons in SW Argyllshire, the most likely site of magma ascent must be at the intersection of the SIF and the GGF which occurs SW of the Torran Rocks (Pharaoh *et al.* 1996). The SIF has been proposed as a steep extensional, post-thrusting fault throwing down several km to the ESE (Potts *et al.* 1995) and initially bringing Ross of Mull amphibolite-facies Moine rocks into contact with Iona Group rocks and Lewisian gneisses (**Fig. 2.27**).

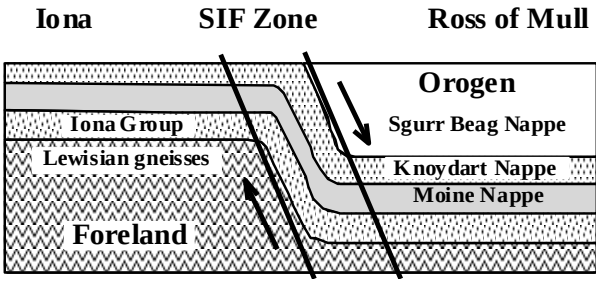


Fig. 2.27 Regional diagrammatic cross-section across the Sound of Iona Fault (SIF) zone (extensional model) (adapted from Potts *et al.* 1995).

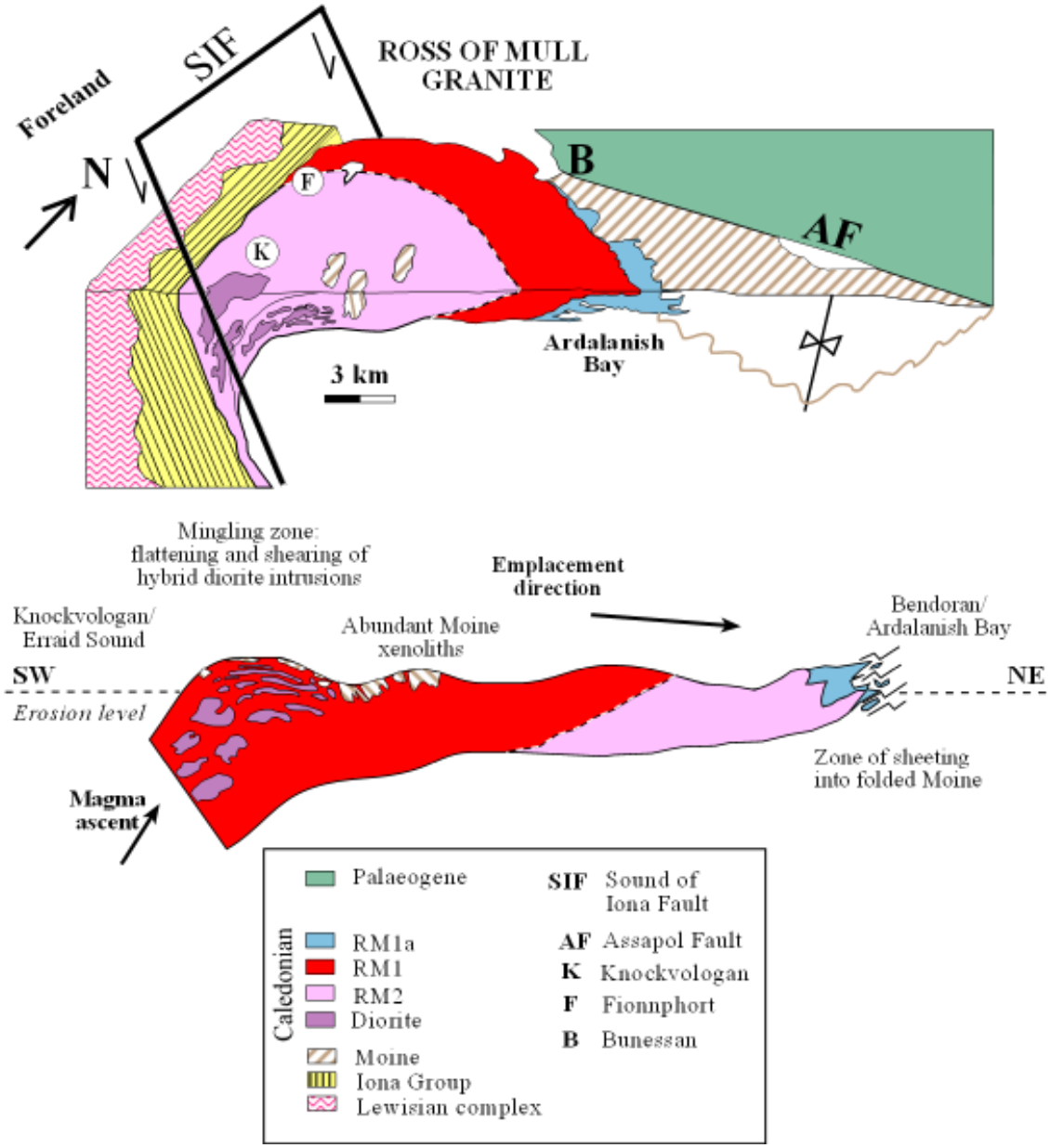


Fig. 2.28 Block diagram across the Sound of Iona Fault (SIF) zone depicting the emplacement geometry of the flattish batches of melt within and extensional regime created by the combined movements of the SIF and eastward-directed collapse within Caledonia thrust nappes. An accompanying simplified cross-section through the sheeted ROMG is also depicted highlighting key areas and processes (adapted from Zaniewski *et al.* 2006).

Direct evidence for the thrust relationship is no longer seen because the initial thrust contact has been displaced by the SIF and the ROMG. It is tenable that steep extensional movements on the SIF may have been linked to more general extensional collapse within the Caledonian orogen, as is consistent with the interpretation of Dewey & Strachan (2003). It is envisaged that the ROMG was constructed from pulses of magma rising in the conduit provided by the fault intersection described above. Magma passing up this ascent zone was

then emplaced northeastward as flattish sheets (**Fig. 2.28**) in the late-orogenic extensional environment produced by the collapse of Scandian nappes.

Further evidence to support this emplacement style comes from xenolith studies of a Permian dyke just north of Fionnphort (Faithfull & Upton 2006). The varied suite of crustal xenoliths contained in this dyke strongly suggests that the ROMG is underlain by a variety of crustal lithologies at no great depth below its base (Faithfull & Upton 2006). As the horizontal distance across the onshore outcrop (from Knockvologan to Ardalanish) is approximately 6 km it is difficult to envisage that the ROMG can be more than several km thick (Zaniewski *et al.* 2006).

Chapter Three

MODAL ANALYSIS

Modal analysis of ROMG components by field modes, point counting and Reitveld Quantitative X-ray Diffractometry (QXRD) via Siroquant.

Chapter Three
THE ROSS OF MULL GRANITE

Chapter Three – Modal Analysis

Chapter Three, defines, utilises, compares and contrasts the results obtained from three different types of modal techniques. These are field modes, point counting and Quantitative (Rietveld) X-Ray Diffractometry (QXRD). The first two methods of modal analysis are often used to rapidly classify components within granitoid complexes in order to characterise pluton scale heterogeneity as they are easy techniques and cost effective; the latter laboratory technique is rarely used to address modal mineralogy in granitoids in part due to nature of research topics today and related cost. When one of the first two mentioned methods is used in isolation, the results yielded may not always reflect a true picture of what actually comprises the granitoid complex in question. Whilst this chapter aids in further characterising ROMG heterogeneity (also allowing evaluation of the field classification scheme of Zaniewski *et al.* 2006), it aims to address the comparative precision and accuracy of all these methods.

3.1 Introduction

Modal analysis refers to obtaining the proportion of minerals that make up the bulk constituents of a rock, and it is one of the fundamental routes to rock classification. It is done in the field by estimation with the naked eye, and then corroborated with thin section studies by point counting by an optical microscope. However the precision and accuracy of such methods are difficult to quantify.

Another way of characterising modal proportions is using QXRD (Reitveld 1967 & 1969; Lovas & Buda 2004 gives a summary of XRD quantification of mineral abundance in granitic rocks). The QXRD study highlighted in this chapter uses a computer-modelling package called SIROQUANT to quantify the modes for the suite of plutonic igneous rocks comprising the ROMG. The trends for the complex via visual estimation, point counting in thin section and QXRD are compared and contrasted to explore the precision of each method and accuracy for QXRD is also quantified.

The location, area of study, geological setting and geological map of the ROMG showing relevant components has already been covered (Chapter Two and Zaniewski *et al.* 2006). All place names where cited in this chapter can be directly found in **Fig. 3.1**, which recaps the location and facies making up the complex. All samples and data presented for

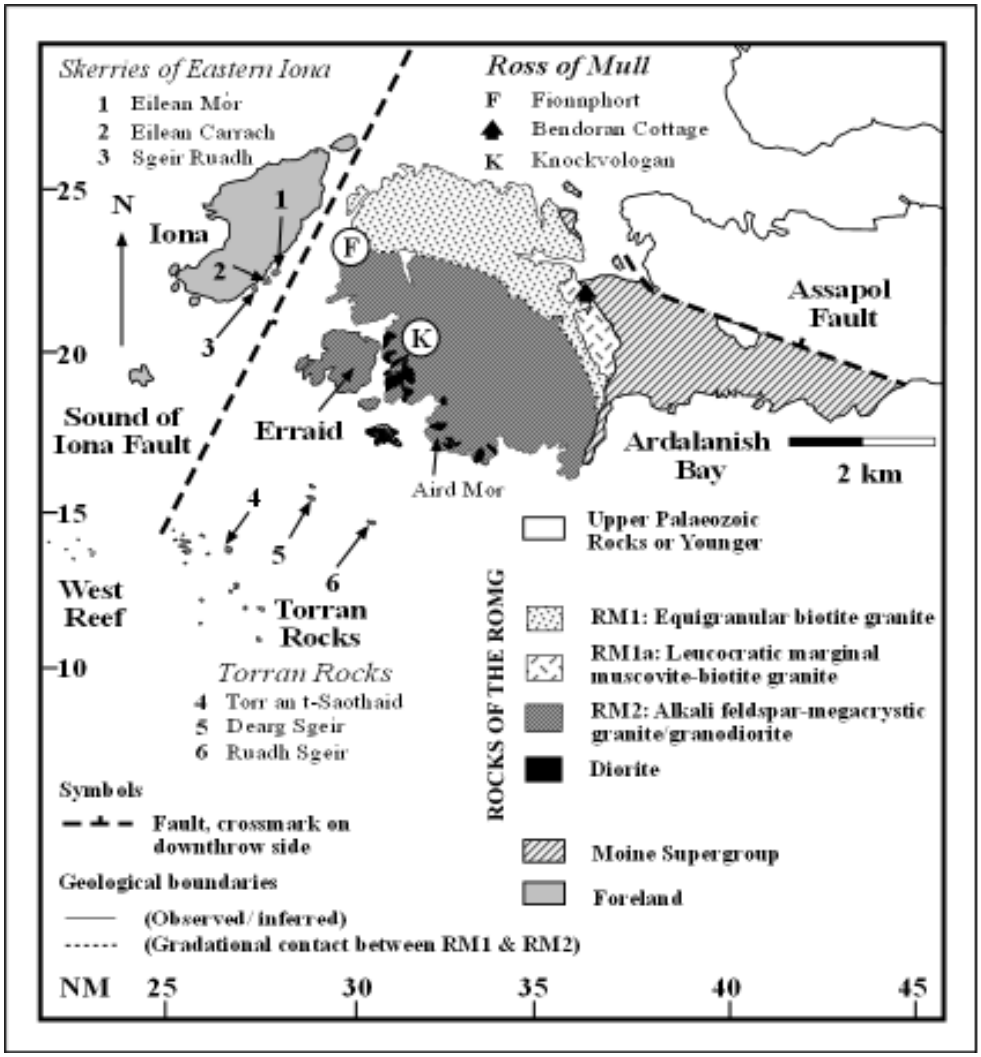


Fig. 3.1 Location and facies map of the ROMG (adapted from Zaniewski *et al.* 2006); place names are given for ease to use as when cited in the text.

each individual modal technique including the methods and procedures used (including procedural blanks and standards) can be found within tables and appendices (**Appendix A3 - Modal Analysis**) that are cited in order throughout the main text.

3.2 Materials and Methods

From outcrop to thin section, to representative rock powder, the adopted materials and methods utilised to obtain mineralogical modes for the ROMG are briefly depicted within this section.

3.2.1 Field Modes

In coarse-grained zoned granitoid complexes, modal field classifications using the QAP system of Streckeisen (1976) is often the first rapid step in trying to establish gross field scale heterogeneity. Thus at every few hundreds of m, particularly in a north-south coastal traverse along the western coast of the Ross of Mull (from Fionnphort to Aird Mór (**Fig. 3.1**)) samples were collected. Samples collected (see **Fig. 3.2 (a)** for sample locality map) encompass all components of the ROMG and a total of fifty-nine samples were used in this part of the field

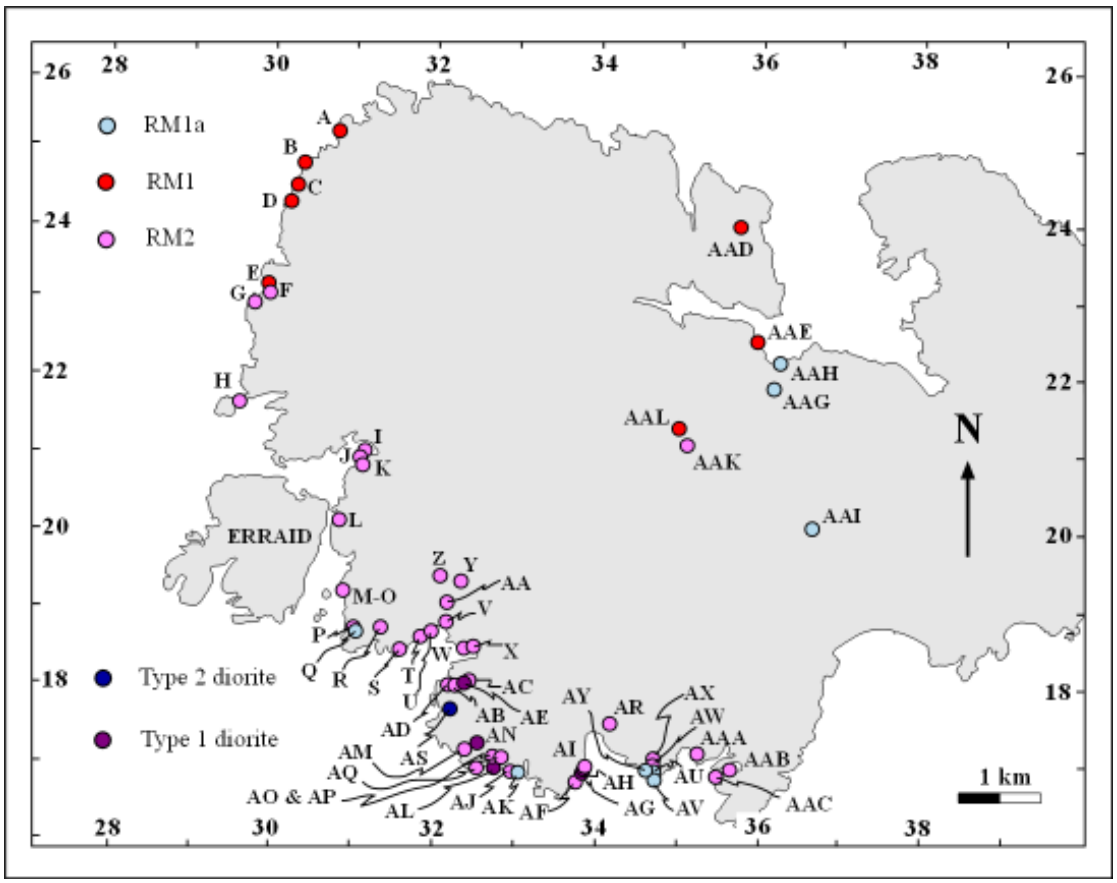


Fig. 3.2 (a) ROMG Field mode sample stations.

study (from A to AAL; refer to **Appendix A3.1** for grid references and raw data). For all samples, the modes of quartz, alkali feldspar and plagioclase feldspar were estimated using the naked eye over a seven by seven cm grid.

3.2.2 Point Count Modes

In this study, a SWIFT point counter was used with a stage interval of three and the sampling target used for each thin section was five hundred. A total of thirty-six samples were used (from JR1 to JR41; refer to **Fig. 3.2 (b)** for sample locality map and **Appendix A3.2** for grid references and raw data) and the sum of all mineral phases present is calculated as gross percentages.

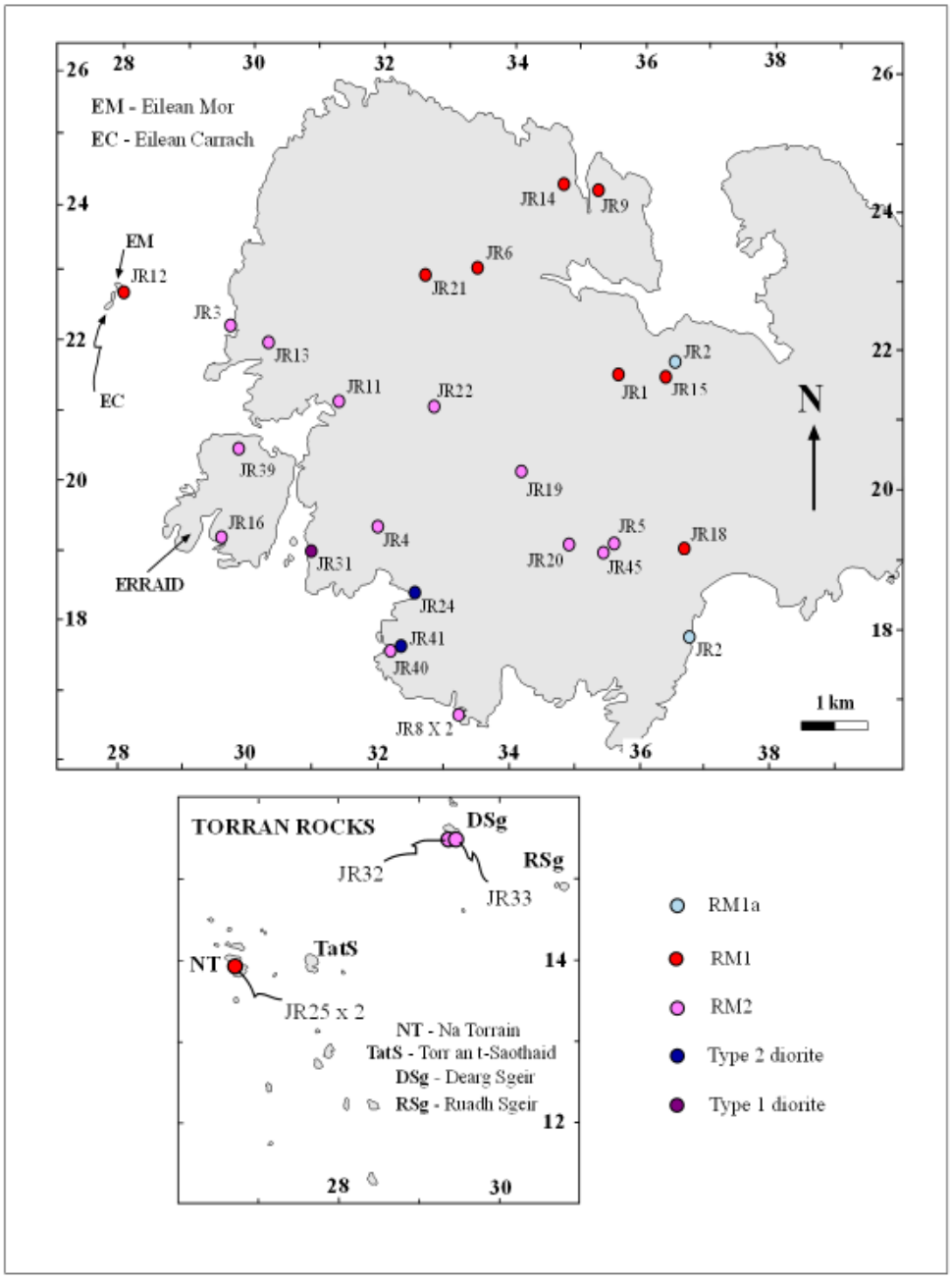


Fig. 3.2 (b) ROMG Point Count mode sample stations.

3.2.3 QXRD Modes

XRD is a technique used for qualitative identification of mineral phases present in samples with concentrations >0.5% (Hagni 2002). Quantitative analysis of the peak integrals of XRD data in polyphase mixtures can be used to determine phase concentrations. The method used involves a computer-modelling package that models the whole spectrum using a method known as Rietveld refinement. The advantage of using QXRD in this study in order to characterise the ratio of mineral phases is that it has a typical detection limit of ≤1%, precision of ~2% and accuracy of ±≤10% relative (Hagni 2002). All QXRD data generated in this study for the ROMG were carried out within the X-Ray laboratory at the University of St. Andrews, U.K; refer to **Appendix A3.3**.

Prior to QXRD, samples run must be of an extremely fine grained fraction and prepared in a manner whereby this fraction is homogeneous to reflect a coarse grained granitoid sample of at least 5-10 kg. In order to address issue of sample homogeneity so that a representative amount of known sample could be used for XRD analysis, procedural quartz blanks and various powdered mixtures of RM1 sample AZ005 with repeated runs of RM1 sample DLC1/AF207 were run via X-Ray Fluorescence (XRF) for major and trace element analysis. This provided adequate whole rock standards for the ROMG. For in-depth laboratory procedures used in this chapter to generate quartz blanks and standards for QXRD refer to **Appendix A3.4** (with respective tables in **Appendix A3.5** to **A3.7**) and **Appendix A3.8** for sample preparation. All XRD fractions were initially obtained from representative XRF pulp fractions for the ROMG.

There are various QXRD packages widely used for Rietveld refinements that can be used to obtain quantitative modes from rock powder. The computer software package chosen was SIROQUANT version 2 as it was easy to use, as there are less parameters to modify when one is refining XRD spectra. However it required a licence and hardware. For the SIROQUANT procedure used in this chapter, refer to **Appendix A3.9**.

SIROQUANT refines a large number of variables such as: phase scales, line asymmetry, phase preferred orientation, phaseline widths (U, V, and W), instrument zero, the lineshape parameter for each phase, and the phase unit cell dimensions. There are many more correction factors in the program, but importantly, the software contained a crystal structure databank, which covered all minerals associated with calk-alkaline granitoids and can be used to obtain credible starting parameters. In this study, all mixtures had refinement of plagioclases corresponding to International Centre for Diffraction Data database card entry

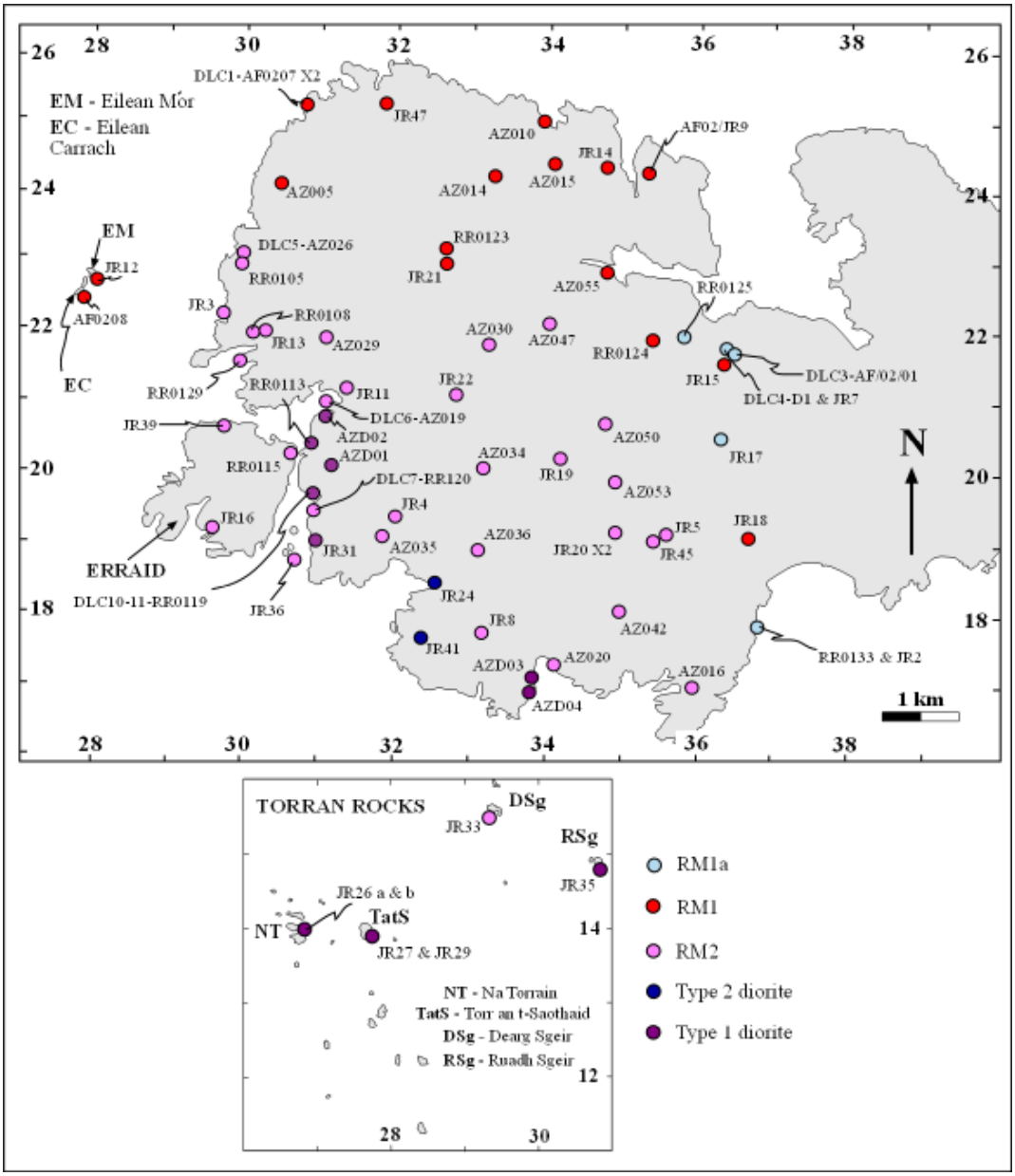


Figure 3.2 (c) ROMG QXRD mode sample stations.

00-041-1480. Alkali feldspar on the other hand was ran separately from a hand-picked crystal from a pegmatite (NM [3473 1684]) and mixtures refined to Orthoclase (Or1).

Key factors that must be questioned within any study involving powder diffractometry must completely address whether collected samples are co-genetic, or is the quantity and type of samples used for different components representative to the overall heterogeneity within the studied granitoid. Procedural blanks should also be utilised so that stray data can be questioned and were run in this study to note any feasible contamination. To solely determine accuracy of QXRD in this study to perform Streckeisen (1976) QAP classifications, known weighed out standards were prepared and consistently run for QXRD. These were

subsequently analysed by SIROQUANT, and the accuracies determined are shown in **Appendix A3.10**. The detection limit of the technique is again within 1% and the data in this study have an accuracy of <2.1% for mixtures of quartz, alkali feldspar and plagioclase.

All samples used for QXRD analysis in this study come from a large sample population that represents all components of the intrusion**.** The sample population concerned was constructed from collection of the whole mainland of the ROMG including offshore islands. A total of eighty-eight samples were analysed using QXRD (from AF0207(1) to JR41 (see **Fig. 3.2 (c)** for sample locality map with corresponding table in **Appendix A3.3** which gives grid references and raw data for each sample)).

3.3 Results

Within this section, for all modal methods concerned, data gleaned from all samples provided in **Figs. 3.2 (a)** to **(c)** are essentially plotted in the series of Streckeisen (1976) diagrams in **Fig. 3.3** so that patterns in terms of ROMG mineralogical zonation can be highlighted; the advantage being comparisons/contrasts per method can be critically evaluated, mineralogical heterogeneity can begin to be understood and the field classification of Zaniewski *et al.* (2006) can later be tested.

3.3.1 Field Mode Data

Data for all field petrological estimates of samples A to AAL representing all ROMG components collected are plotted in **Fig. 3.3 (a)**. Although a small sample population set is used, basic trends that define the ROMG can be observed. Firstly, a distinction between mafic and felsic components is apparent, and reverse zonation (a coastal north-south traverse) is broadly reflected in **Fig. 3.3 (a)** as one moves from the left side of the QAP diagram from RM1 (alkali feldspar granite field) through to Type 1 and Type 2 diorite that plots in the diorite field or lower right area of the diagram. As a whole, field petrology shows that the ROMG plots mainly in the granite field of Streckeisen (1976) (**Fig. 3.3 (a)**).

Although there is a limited sample population obtained for RM1, there is minimal overlap with RM2, with it consistently plotting in the alkali feldspar granite field. Field data in QAP **Fig. 3.3 (a)** give rise to a felsic end member for the ROMG in the form of sample AAL (near the central area of the complex in terms of RM1) and an overall bi-modal

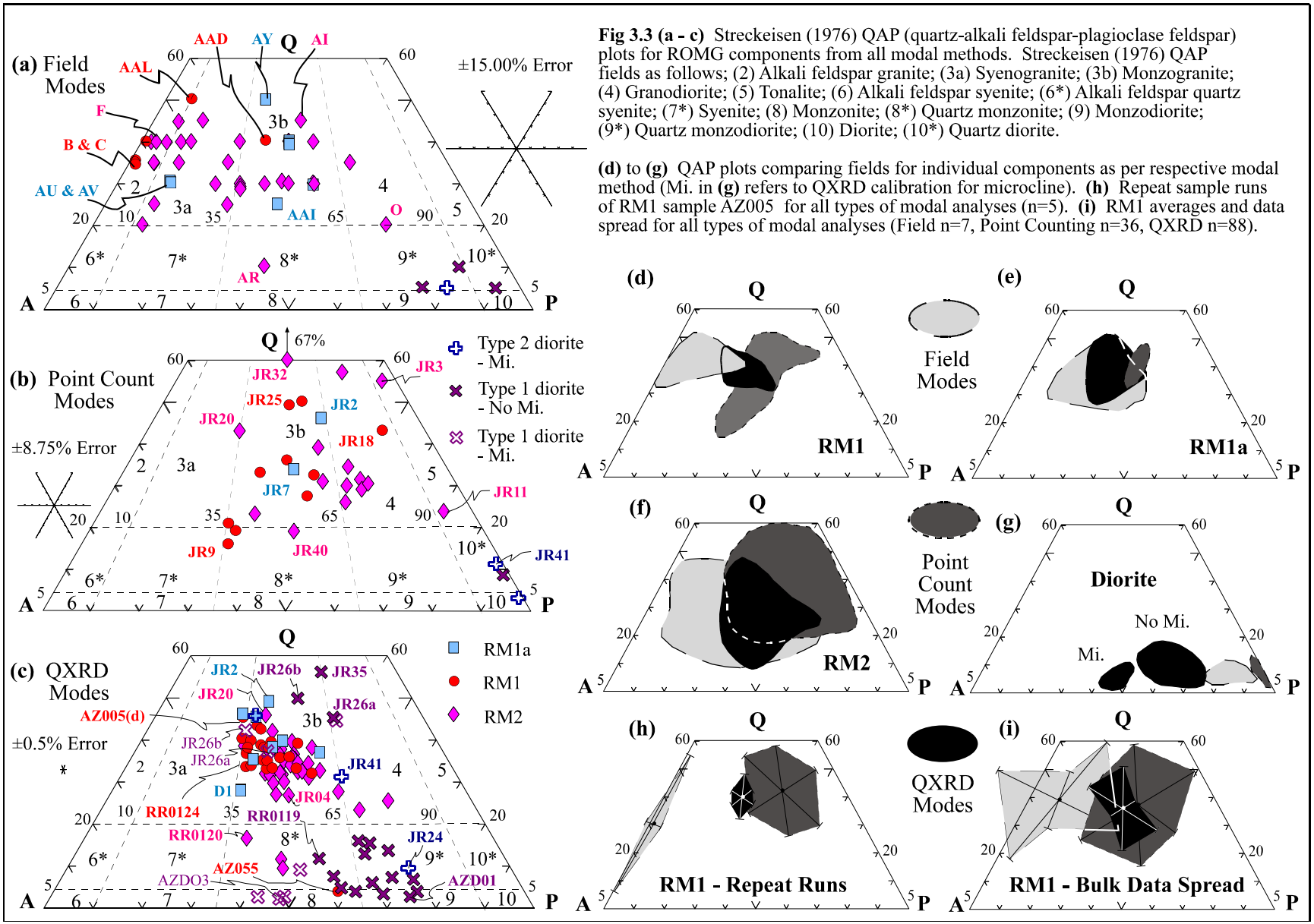


Fig 3.3 (a - c) Streckeisen (1976) QAP (quartz-alkali feldspar-plagioclase feldspar) plots for ROMG components from all modal methods. Streckeisen (1976) QAP fields as follows; (2) Alkali feldspar granite; (3a) Syenogranite; (3b) Monzogranite; (4) Granodiorite; (5) Tonalite; (6) Alkali feldspar syenite; (6*) Alkali feldspar quartz syenite; (7*) Syenite; (8) Monzonite; (8*) Quartz monzonite; (9) Monzodiorite; (9*) Quartz monzodiorite; (10) Diorite; (10*) Quartz diorite.

(d) to **(g)** QAP plots comparing fields for individual components as per respective modal method (Mi. in **(g)** refers to QXRD calibration for microcline). **(h)** Repeat sample runs of RM1 sample AZ005 for all types of modal analyses (n=5). **(i)** RM1 averages and data spread for all types of modal analyses (Field n=7, Point Counting n=36, QXRD n=88).

distribution of minimal data are constrained to the alkali feldspar field (samples B, C, F; samples from the northwest part of the complex) and granite field (samples AAD and AAE; samples from the northeast part of the complex).

A substantial amount of RM2 samples (particularly where it occurs at the RM1/RM2 boundary south of Fionnphort Pier; sample E to F) also overlap with RM1 in **Fig. 3.3 (a)**. In the case of RM2, which has the largest amount of samples collected for field petrological estimates, as one moves from the RM1/RM2 gradational contact towards the centre of the complex, a greater range of rock types is apparent particularly where RM2 is adjacent to hybrid diorite. This heterogeneity is reflected in **Fig. 3.3 (a)**, where this facies has the greatest spread of data (constrained in between sample points F, AI, O and AR), mainly being confined to the granite field (where it is not in direct contact with diorite), with rare isolated samples plotting in the granodiorite field (e.g. point O) and the monzonite field (where RM2 is directly adjacent to Type 1 diorite; point AR). A bi-modal looking distribution with a break of in-between 20% plagioclase is apparent for RM2 that has some vague overlap with the spread of RM1.

A small sample set for relatively equigranular varieties of the contact related facies RM1a is also constructed (**Fig. 3.3 (a)**). Sample AY (in the uppermost area of the granite field) has the highest amount of quartz (approximately 50%) and comes directly from a margin formed on a semi-pelitic/psammitic Moine xenolith in host RM2. Samples AU and AV (lower left area of the granite field) have a lower amount of quartz (ranging from 20-35%) and come from margins on more pelitic rich Moine xenoliths. Samples taken directly from the RM1/Moine contact are samples AAG, AAH (Bendoran) and AAI (Southern Bendoran/Ardalanish) and where RM1 occurs adjacent to more politic varieties of Moine, it tends to be less quartz rich. As a whole, RM1a dominantly plots in the granite field having little variation with exception of samples AU and AV. Diorites on the other hand are confined within the limits of monzodiorite or diorite field (lower right areas in **Fig. 3.3 (a)**).

3.3.2 Point Count Data

At least half the sample population size is used here for the modal point count technique compared to that used for the field mode method. However, the distribution of gross samples collected for this method could be considered to be more representative in considering reverse zonation of the ROMG. In comparison to the sample spread for the field modal method, samples collected are not solely restricted to the coastline and encompass a greater average

spread across the whole of the ROMG; ranging from the western offshore skerries of Eilean Mór and Eilean Carrach right through to the offshore southwest skerries that form the Torran Rocks (see **Fig. 3.1** for location).

Sample population and spread of sampling stations across the ROMG used for field and modal analysis are limited in this study as a larger population data set are used for QXRD. The data and patterns shown in **Fig. 3.3 (b)** should thus be used as a rough guide for characterising all facies present. What is noticeable with respect to data obtained from field estimates are that the data set for the ROMG via this method shows less variability. With exception of the RM2 sample JR32, plotting at 67% quartz, the spread of ROMG data ranges between the granite-quartz monzonite (defined by RM2 sample JR20 and RM1 sample JR9) to diorite (e.g. Type 2 diorite sample JR41). One can observe that the greatest difference is that none of the RM1 or RM2 samples lie within the alkali feldspar granite field. The bulk of RM1 data are confined within the plagioclase-rich side of the granite field with exception of the isolated JR18 sample plotting as granodiorite. However the bulk of the RM2 data are constrained within the plagioclase-poor side of the granodiorite field, with exception of outer most points such as JR20, and JR3 to JR11 that plot as tonalite. Although the RM1 and RM2 data can be distinguished into two separate adjacent fields, there is overlap between the two facies, but this is minimal in comparison to modal data obtained for fieldwork estimates.

RM1a samples JR2 and JR7 are in accordance with field mode estimates and also plot in the granite field with the more evolved variant coming from the southern contact as opposed to the northern contact (**Fig. 3.3 (b)**). However, thin section work reveals that pink plagioclase could be commonly misidentified in RM1a field modal estimates as alkali feldspar, which could shift the body of modal data to the alkali feldspar corner if caution were not applied.

3.3.3 QXRD/SIROQUANT Refined Data

QXRD data for all samples are depicted in **Fig. 3.3 (c)**. The data produced for all components were constructed and calculated in terms of fitting and calibrating other component profiles to a standard Reitveld profile using RM1 sample AF0207 as a constant standard. To highlight precision and accuracy of Reitveld fitted data with respect to the RM1 standard profile, a global chi-squared value is calculated by SIROQUANT. Chi-squared is an inferential statistical test used to analyse frequencies of nominal data allowing comparisons between observed frequencies of data and frequencies that would be expected by chance. All global

chi-squared data are predominantly below 10.00 and range from 5.53 to 13.55 indicating that satisfactory statistical fits to the XRD profiles were obtained.

All mineral phase data calculated by SIROQUANT were initially calculated as a corrected weight percent, and the calculated total of quartz, alkali feldspar and plagioclase feldspar are expressed within **Fig. 3.3 (c)** as a ratio between the three mineral phases. Also, all data generated for each mineral phase within all components are generally within the limits of <1% precision; although there are minimal exceptions in this case, such as albite in RM1 sample AZ055 that has the largest of all precision at 1.9 (refer to **Appendix A3.3**), precision is within suitable constant limits throughout all samples per component. Excluding RM1 sample AZ055, this trend is reflected by the range of precision for the following mineral phases present in all RM1 samples; quartz (0.4 to 0.8), orthoclase (0.4 to 0.8), microcline (0.4 to 0.9), albite (0.5 to 1.3) and biotite (0.2 to 0.6). Muscovite was run only for RM1a samples as sufficient amount was identified in thin section with respect to other components having precision ranging from 0.8 to 1.3. Although no microprobe data are presented for determining the precise composition of amphiboles in this study, actinolite and tremolite were used for QXRD analysis; as these are simplest and readily understood when using SIROQUANT in all ROMG mafic components. Precision for actinolite within all mafic components range from 0.5 to 0.9 with data focussed around two modes of 0.7 and 0.7, whilst the range for precision is slightly higher for tremolite at 0.9 to 1.4.

Microcline is sometimes visible and present in variable amounts in xenoliths within Type 1 diorites. Thus, although minimal in thin section, a data set and related precision were constructed for microcline from a small sample run of Type 1 diorite (explanation of the facies of diorite is given later on in this section). This was partly done to highlight the dangers for future XRD studies, so that implications of calibrating for an extra mineral phase (that could be misinterpreted as being present in abundance) could be qualitatively understood. As a whole, as thin section work reveals microcline is a minimal constituent within such diorites, the bulk of the diorite data has not been calibrated for microcline as a major mineral phase present.

Trends depicted in **Fig. 3.3 (c)** for QXRD are commented on from now on in this section as they characterise each component of the ROMG. For RM1, twenty-four samples were run and all but one (sample AZ055) form a tight distribution around the centre of the granite field. Upper limits of RM1 are defined by the most evolved sample AZ005(d) (44.6% quartz), whilst lower limits are defined by sample RR0124 (32.5% quartz). Although different mixtures of RM1 sample AZ005 were used as a within sample heterogeneity tester

(AZ005(a) to AZ005(d)), the total range difference for quartz is 12.1%. The isolated sample AZ055 is an example of an erroneous point for RM1 as it has some of the largest precision for mineral phases (e.g. the largest precision of 1.3 for orthoclase) and a large chi-squared value of 8.27. This is most likely due to the fact that the fraction produced was not within the necessary limits of grain size needed for XRD analysis, or not enough total sample was ran.

Thirty-four samples were run for RM2, which lie between samples JR20 (45.8% quartz) and JR04 (26.8% quartz). RM2 shows a greater range difference for quartz than RM1 having almost double the difference of 18.9% quartz when just considering samples ranging from JR20 to JR04. The bulk of RM2 data plots within the limits of the granite field overlapping the right hand side distribution of RM1 data; thus confined within plagioclase-rich limits of the monzogranite field. Sample JR20 comes from the southeast near the Ardalanish contact zone where diorite is absent, whilst sample JR04 verges within the limits of the Knockvologan mixing and mingling zone. The other three isolated samples, RR120 to JR36, that plot in the quartz monzonite field, depict a greater heterogeneity for RM2. They contain considerably lower amounts of quartz and come from samples directly within the Knockvologan mixing and mingling zone that are adjacent within m to Type 1 diorite.

The seven samples for RM1a essentially overlap the distribution of data for the RM1 facies of the ROMG, and range from the most evolved sample of JR2 (47.3% quartz) to the least evolved sample D1 (24.9% quartz). RM1a plots within the granite field and there are two different populations forming a break between around 40.0% quartz.

Regarding ROMG mafic components, QXRD analysis is mainly focussed on more samples concerning Type 1 diorite (‘*Plagioclase- hornblende-phyric biotite diorites’* (Zaniewski *et al.* 2006)). This is due to them having greater field scale heterogeneity and inaccessibility of being able to obtain more samples of homogeneous looking Type 2 diorite (‘*Equigranular diorites/quartz diorites’* (Zaniewski *et al.* 2006)) in and around Aird Mór (refer to **Fig. 3.1**). Two sets of data runs using same sample fractions for Type 1 diorites are depicted in this study. Fourteen samples were run having refinement for microcline as a main mineral phase not occurring, whilst half the sample size was used for refinement of microcline occurring. In the case of Type 2 diorite, only two samples were run via QXRD methods without microcline. Firstly, the whole data set for all diorites forms two populations. The first data set are represented by the bulk distribution of diorite data congregating within the limits below 20.0% quartz and extends from the monzonite (sample AZD03) and quartz monzonite fields (sample RR0119) to the monzodiorite (sample AZD01) and quartz-monzodiorite field (sample JR24). The second data set are characterised by a greater spread

of points occurring above 30.0% quartz, defined by samples JR41 (31.0% quartz), JR26a (without microcline) and both JR35 samples (55.7% to 56.0% quartz) that fall on the granite to granodiorite boundary, right through to sample JR26b (with microcline) that plots roughly within the central area of the granite field.

In considering Type 1 diorite data for samples with or without Reitveld refinements for microcline (samples JR26a, JR26b and JR35) there is a general difference. Those samples refined for microcline occur toward the plagioclase poor side, making the diorite in question appear to be more felsic and within the limits of RM1 and RM2. Thus, using this example only, addition of a mineral phase or multiple mineral phases that do not exist in sufficient quantities can yield an overall impression of refined data that are actually misleading. Hence importance of thin section petrography, which shows microcline as a minimal constituent within such diorites; sometimes occurring as variable megacrystic xenocrysts.

Further observation of the representative Type 1 diorite data highlight an arcuate array of data from sample RR0119 to the most mafic sample of AZD01 with a small cluster of three samples in the top left hand corner of the quartz-monzodiorite field. Isolated sample JR35 and samples JR26a and JR26b, which are runs from the same sample, plot way out of the limits with respect to the bulk data set.

Type 2 diorite samples JR24 and JR41 were run without microcline and sample JR41 plots on the granodiorite-granite boundary, whilst sample JR24 plots near Type 1 diorite sample AZD01, and lies in the monzodiorite field.

In evaluating bulk spatial distribution of all QXRD data, the main observation is that a bi-modal distribution is apparent. Excluding all felsic samples that occur below the dashed 20.0% line for quartz, including all mafic samples plotting above this line, there is roughly a 10.0% transition in quartz between mafic and felsic components; the difference between RM2 sample JR04 and Type 1 diorite sample JR27 is 11.1% quartz. Felsic-rich rocks plot within the middle of the QAP diagram within the granite field and there is overlap between all felsic facies particularly between RM1 and RM2. Mafic components on the other hand are more widespread defining greater heterogeneity mainly plotting within the monzonite to monzodiorite fields, with eight samples plotting above the 20.0% dashed line for quartz.

3.3.4 Precision of all Modal Techniques

In order to understand the implications of such data generated by all three methods, one must characterise precision of methods used. Accuracy has already been addressed earlier on only

for QXRD. Precision for felsic components was adressed in three ways; firstly, (i) looking at re-runs of one sample of RM1 granitoid only, (ii) then addressing the precision of all felsic components around an average for the components and finally, (iii) the precision around all the data excluding looking at precision around averages for felsic components. Essentially in (i) to (iii) we compare and contrast the data ranges produced per respective modal technique to make inferences on precision.

To assess (i) within sample precision of one granitoid sample only, an easily accessible, fresh sample of RM1 (sample AZ005) was analysed five times by all three techniques. The results are plotted in **Fig. 3.3 (h)** and data are found in **Appendix A3.11**. Modal data generated from field and point counting were constructed from repeated analysis (from the same hand specimen or thin section), whereas modal data from QXRD arisen from hand specimens being broken off (and prepared as QXRD fractions) from one large 5 to 10 kg specimen. From looking at data in **Appendix A3.11**, the following observations with respect to within sample precision of RM1 sample AZ005 only (expressed to two standard deviations (2σ)) can be made:

Quartz - 2σ data decrease roughly by half per method as one scales down in technique from 27.3 (field) to 16.3 (point count) to 8.7 (QXRD).

Alkali feldspar - 2σ shows a similar pattern with respect to quartz in terms of scaling down by half per method from 28.5 (field) to 14.7 (point count) to 5.3 (QXRD).

Plagioclase feldspar - As plagioclase is pink in RM1, which makes it seem that it is near absent in RM1 field estimations, it is unsurprising 2σ is expressed as 3.6 for field modes (see discussion and conclusions section). Again as one scales down in technique (19.9 (point count) to 4.8 (QXRD)), 2σ decreases.

In terms of considering (ii) precision of all techniques concerned for felsic components around averages, data within columns for RM1/RM2 granite in **Appendix A3.12**, can be used to make appropriate inferences on bulk precision. This is due each having the largest sample sets per technique in comparison to other ROMG components. Respective data are plotted in **Fig. 3.3 (i)**.

From analysis of largest data ranges per respective technique for RM1:

Quartz - 35.6 (QXRD) to 38.6 (field) gives a 2.9 range between methods, meaning similar results are obtained by all methods.

Alkali feldspar - 27.9 (point count) to 52.3 (field) gives a range of 24.4 between methods.

Plagioclase feldspar - 9.1 (field) to 35.4 (point count) gives a range of 26.3 between methods. These form the largest data range observed for a mineral phase with respect to RM1 and RM2.

From analysis of largest data ranges per respective technique for RM2:

Quartz - 32.4 (field) to 35.0 (point count) gives a range of 2.6 between methods, meaning similar results are obtained by all methods.

Alkali feldspar - 22.9 (point count) to 43.8 (field) gives a range of 20.9 between methods.

Plagioclase feldspar - 23.6 (field petrology) to 42.1 (point count) gives a range of 18.5.

Here we address (iii) precision of all felsic components but not around the averages. From analysis of all precision for felsic components ((data in **Appendix A3.1** to **A3.3** as expressed to two standard deviations (2σ)) per respective technique for RM1:

Quartz - Highest value of 21.6 (point count) is followed by 15.3 (QXRD) and 11.3 (field).

Alkali feldspar - 27.2 (field) followed by 25.5 (point count) to 5.8 (QXRD) giving a large drop of about 20.0 when considering QXRD.

Plagioclase feldspar - There is a difference of around 10.0 between field and other techniques. Largest value is 25.4 (field) compared to 16.7 (point count) and 15.9 (QXRD).

From analysis of all precision for felsic components (expressed to two standard deviations (2σ)) per technique for RM2:

Quartz - Highest value of 27.8 (point count) which is a difference of 10.0 compared to 16.0 (field) and 15.0 (QXRD).

Alkali feldspar - There is a decrease in precision as one scales down from 27.2 (Field), to 29.8 (point count) and 10.7 (QXRD).

Plagioclase feldspar - Similar to above whereby there is a decrease in precision as one scales down from 30.3 (field), to 29.3 (point count) and 9.8 (QXRD).

Data from RM1 and RM2 show that for all mineral phases, as one scales down there is an increase in precision (with a small exception for quartz) and QXRD has the greatest precision (in terms of smallest error bars/distorted hexagon for QXRD compared to other modal techniques in **Fig. 3.3 (i)**) in considering such components. Whilst there is a smaller difference for quartz between field modes and QXRD of 0.9, point counting gives higher precision. The feldspar data for RM1/RM2 show that the precision differences considered with QXRD compared to other methods are at least 20.0% lower. In the case of RM1a similar data patterns are observed. For mafic components, little inferences can be made due to the limited number of samples used (due to known petrographic mineralogical heterogeneity) for field and point counting. It is worth noting that QXRD precision for felsic minerals in diorite is considered is high reflecting petrological heterogeneity; 26.1 to 45.4 for quartz, 3.7 to 26.7 for alkali feldspar and 16.2 to 34.4 for plagioclase feldspar.

3.4 Discussion & Conclusions

In the case of the ROMG, (1) using different modal techniques show a systematic shift in data per component in relation to precision with a shift towards 'tighter' data arrays plotting in the granite field for felsic components as one scales down per technique; (2) the field petrology based classification scheme of Zaniewski *et al.* (2006) is reasonable; (3) QXRD data are the most precise with accuracy within 2.1% for QAP, where the data depict a bi-modal mafic-

felsic distribution reflecting reverse zonation for the complex being a true reflection of overall facies heterogeneity.

These points are expressed in (1) to (3) as follows:

(1) Multiple types of modal techniques employed in any study concerning a granitoid complex may often yield several different types of data spreads for the same spectrum of samples respectively. This occurs within the ROMG. In analysing QAP plots in **Fig. 3.3 (d)** to **(g)** that show fields for each component for the complex per respective modal technique (lower right hand side of the diagram), one can observe systematic shifts as follows:

RM1 (**Fig 3.3 (d)**): Field mode data plot within the alkali-feldspar granite field due to bias in overestimating plagioclase feldspar as alkali-feldspar in hand specimen and not taking into account selective replacement of plagioclase feldspar by alkali feldspar. As previously highlighted in Zaniewski *et al.* (2006), RM1 appears as alkali feldspar granite in the field due to its homogeneous reddened appearance.

Point counting modes generally range from lower right to upper right hand side of the granite field reflecting heterogeneity and issues involved when point counting coarse grained plutonic rocks. These issues relate to textural heterogeneity in open magmatic systems, and in the case of the ROMG, there are some problems associated with this method. In coarse-grained rocks that display textural heterogeneity associated with mixing and mingling, there may be a bias to where the set stage falls on and the nature of mineral phases counted in close proximity may not be fully understood. The RM1 facies in the field appears to be reddened equigranular alkali-feldspar granite, but cold Cathodoluminescence (CL) petrography (as depicted in the next chapter) highlights a greater distribution of plagioclase and in turn the RM1 facies is actually an equigranular biotite-granite. More problems arise as CL has also highlighted selective replacement of plagioclase feldspar with alkali feldspar and presence of interstitial calcite that might give skewed data when point counting this facies.

QXRD modal data form a smaller neat cluster within the middle right hand side of the monzogranite field which ‘sits’ in between both field and point count modal data depicting a true monzogranite composition for RM1.

RM1a (**Fig 3.3 (e)**): Compositions for all modal techniques fall in the granite field. The data for all techniques is similar to RM1 in that field mode data are to the left reflecting overestimation of alkali feldspar and point counting modes are to the right with QXRD data

plotting in the middle of the other techniques. Data for point counting form a tight cluster as only two samples were analysed.

RM2 (**Fig 3.3 (f)**): Similar to RM1/RM1a in QXRD data plotting in the middle of the other techniques essentially within the monzogranite field. Data for all techniques form larger clusters than the other felsic components reflecting the gross mineralogical variability of RM2 particularly where adjacent to diorite.

Diorite (**Fig 3.3 (g)**): Point count data form a strict cluster within the quartz diorite field for three samples. Field data move towards the left of point count data and plot within a slightly larger cluster for four samples in the quartz monzodiorite field. QXRD data on the other hand for a larger sample set, form a larger cluster and are to the left of the data for both other modal techniques lying in between quartz monzonite/monzonite and quartz monzodiorite/monzodiorite where there is no refinement for microcline. Where there is a refinement for microcline via QXRD, data are erroneously shifted towards the middle of the quartz monzonite/monzonite field. The non microcline QXRD refined data accurately reflect the heterogeneous nature of diorites in relation to their porphyritic texture and gross mineralogical heterogeneity. Whilst point counting has expressed the heterogeneous equigranular nature of Type 2 diorite, for Type 1 diorites it cannot really be used to reflect the true textural nature of this type of diorite. Many problems arise when point counting Type 1 diorites due to their textural heterogeneity defined by abundant xenocrystic mineral assemblages as opposed to the equigranular Type 2 quartz diorites. Field data on the other hand show some variability for Type 1 diorites.

(2) The field classification scheme for the ROMG in Zaniewski *et al.* (2006) correlates to some extent with QXRD data (in terms of a QAP plot) as follows.

- *'RM1 - Equigranular biotite granite'*; QXRD analysis shows twenty-four samples form a tight distribution around the left hand side of the monzogranite field.

- *'RM1a - Leucocratic, marginal muscovite-biotite granite'*; QXRD analysis shows seven samples for RM1a essentially overlap the distribution of data for RM1.

- *'RM2 - Alkali feldspar-megacrystic biotite granite/granodiorite'*; QXRD analysis shows thirty-four samples plot within the limits of the granite field overlapping the

right hand side distribution of RM1 data and thus confined within plagioclase-rich limits of the monzogranite field.

- *'Type 1 diorite - Plagioclase hornblende-phyric biotite diorites'*; QXRD analysis shows fourteen samples run without microcline congregate within the limits below 20.0% quartz extending from the monzonite, to quartz monzonite, to monzodiorite and quartz-monzodiorite fields; thus these are essentially monzodiorites.

- *'Type 2 diorite - Equigranular diorites/quartz diorites';* QXRD analysis of two samples without microcline plot in the granodiorite-granite boundary or monzodiorite.

(3) In the case of the ROMG, QXRD data show RM1 and Type 1 diorites occur as end members defined by a major 10.0% quartz break (**Fig. 3.3 (c)**) (from roughly 15.0% to 25.0%). As a whole, the reverse field zonation is reflected by the overlap in felsic components with a marked gap for diorites. There is symmetry between mafic and felsic components on the QXRD QAP diagram (see **Fig. 3.3 (c)**). Such distributions are also not so discernible within field and point count modal data. In utilising RM1 as a 'standard ROMG facies', QXRD data has also been highlighted to have the greatest numerical precision as follows:

Precision for a repeated RM1 sample: As a general rule of thumb in terms of precision, if there were limited precision on repeat analyses, then this would produce small to no area for precision expressed to +/-2σ on sample points forming a 'small distorted' hexagon for QAP (in relation to **Fig. 3.3 (h)**); thus the larger the area of precision then the larger the area of the 'distorted hexagon' will be. If one observes **Appendix A3.11** data plotted in **Fig. 3.3 (h)**, the QXRD data of all mineral phases form the smallest 'distorted hexagon' whereby values of precision are less than 10.0 compared to other techniques. As one scales down in terms of technique, precision roughly drops down a third per technique from field to point counting to QXRD and it is evident that the QXRD method is more precise. QXRD data also plot in between field and point count data for all mineral phases, and just about overlaps the left hand side of the point count data. The clear contrast/erroneous shift are the isolated average plot for field data having largest area of precision for alkali feldspar and quartz,

forming a sharp rhombus **Fig. 3.1 (h)** where there is no overlap with the other two modal methods.

Precision around averages for RM1 and RM2 data: Data from RM1 and RM2 show that for quartz (**Appendix A3.12**), point counting has the largest area of precision whilst the other two modal methods display similar results but with smaller area for precision. This is expressed in diagram in **Fig. 3.3 (i)**. Quartz can be accurately picked up per technique because of its crystalline interstitial morphology, no reddening and its easily characterised via XRD and also field petrology; the problems of coarseness granites means when point counting, one can sometimes cause bias as previously addressed, and point counting in this case does not do justice in providing a true picture of quartz in RM1. However, when dealing with plagioclase feldspars, data per method for RM1 ranges roughly from 15.0% to 25.0%; it is evident in QXRD that this method has the smallest area of precision (**Appendix A3.12** and **Fig. 3.3 (i)**) for plagioclase feldspar. What is clear is that as per **Fig. 3.3 (i)**, for alkali feldspar, the QXRD method has the greatest precision (smallest error bars occur for the QXRD distorted hexagon compared to other modal techniques). Similar to **Figs 3.3 (d)** to **(h)** QXRD area of precision data again plot in the middle of the other two modal methods, forming the smallest 'distorted hexagon' with field modal data having the least overlap. As such, it is tenable that as a result of these consistent patterns, the QXRD method has the greatest precision essentially showing a more accurate picture of modal heterogeneity for RM1 when compared to other modal methods.

Precision around bulk data for all components: As a whole as one scales down in terms of technique, it has been shown precision genarally increases (particulary evident in the feldspars for RM1/RM2 as QXRD always has the smallest area of precision values). In considering all modal data generated by all methods **Fig 3.1 (a)** to **(c)**, with representative gross area of precision depicted per data set as per respective technique, the QXRD data array is most likely to reflect the true nature of bulk heterogeneity for the ROMG. This is not primarily because it is the most precise method used with accuracy of 2.1% for QAP, but there is an overall consistency in between data sets in terms of the considerable narrowing of data for the mafic-felsic end members per data set. The QXRD bulk data are also collected from an unbiased sample distribution set ranging across the whole of the ROMG that has average XRD

compositions utilised in respect to the powders used. In addition, the data are less precise within the observational techniques, which make it more difficult to envisage qualitatively average compositions and realistic end members for each facies of the ROMG.

This study demonstrates that trends depicted by QXRD in granitoids can represent a quantitative distribution of heterogeneity providing sample collection and laboratory procedure guidelines provided are followed. In using three different types of modal analysis, the heterogeneity of a granitoid complex can be expressed (and compared) by methods that involve an overall scaling down technique of mineral quantification. It has also provided an opportunity to test classifications previously proposed for a zoned igneous complex and to actually define the precision, and accuracy of precision for methods used where viable.

In any study integrating modal analysis with field mapping, using field scale modal estimations as a starting point allows rapid characterisation of facies as an important factor when constructing facies classification schemes, or identifying their distributions and related igneous contacts. The most facies representative field samples can then be used for thin-section modal point count analysis in order to test the validity or framework that is used to construct an accurate field map. Finally, the more robust technique of QXRD offers a quantitative way (as standards can be used) to obtain modal data that can be compared to the other qualitative observational methods. This approach could be usefully applied to any granitoid complex where detailed facies characterisation is required.

Chapter Four

COLD CATHODOLUMINESCENCE (CL) WITH INTEGRATED *IN SITU* ELEMENTAL & ISOTOPIC ANALYSIS OF ROMG FELDSPARS

Micro-analysis of individual ROMG feldspar samples within each facies via cold CL, EPMA, and Pb-Pb LA MC-ICP-MS techniques; fingerprinting the chemo-stratigraphy of ROMG feldspars to understand granite petrogenesis.

Chapter Four

THE ROSS OF MULL GRANITE

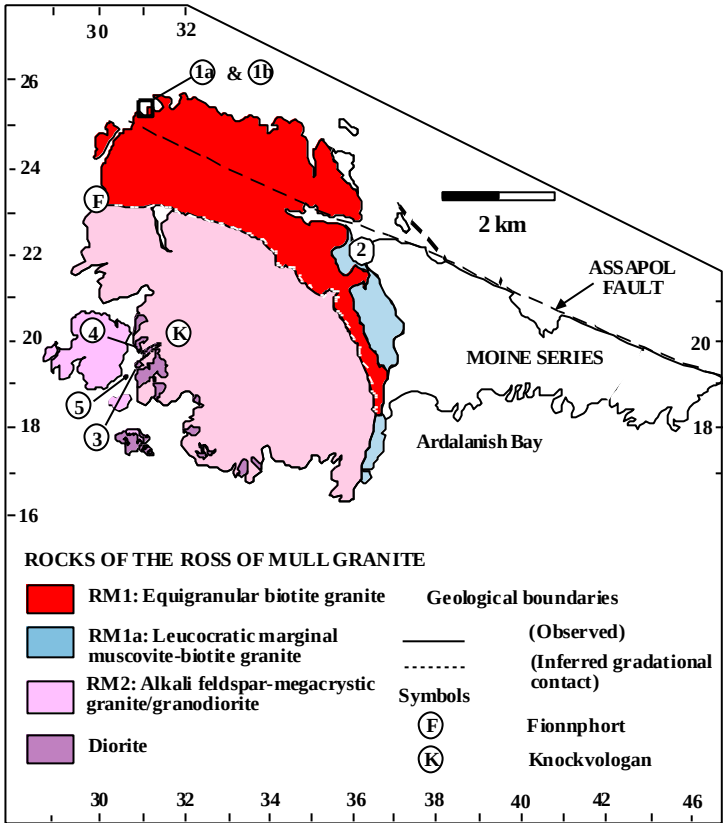
Chapter Four – Cold Cathodoluminescence (CL) with integrated *in-situ* elemental and Pb-Pb isotopic geochemistry on ROMG feldspars

Chapter Four describes detailed micro-analytical investigations of ROMG feldspars. This chapter presents the cold Cathodoluminescence (CL) characteristics of ROMG feldspars per component in conjunction with *in-situ* elemental and Pb-Pb isotopic zoning in magmatic feldspar megacrysts. Analyses of alkali feldspars are presented for all felsic components; for mafic components, where a rare relationship of a double Mafic Microgranular Enclave (MME) phase is presented, plagioclases have been analysed for each MME phase. This approach was taken to characterise a spectrum of feldspars reflecting the mapped reverse zonation of the granitoid complex. As a result, the studied crystals provide ample opportunity to use CL together with *in-situ* elemental and isotopic techniques to assess the role and dominance of open-system processes in granite petrogenesis and to characterise the components involved during interaction between contrasting magmas (see Davidson *et al.* 2007; Ginibre *et al.* 2004 & 2007; Blundy & Cashman 2008).

Where ROMG feldspar data is presented in this chapter, relevant table(s) can be found within **Appendix A4 - CL & Mineral Geochemistry**; associated raw data with mathematical conversions/tabulated data per respective mineral sample can be found within folders in **Attachments to Appendix A7 - DLC Electronic Raw Data** on the memory stick labelled **AZ ROMG 2017**. Where elemental data for Ba and Sr are cited in the text, or on graphs, they represent weight percent oxide [wt. %] analyses of BaO and SrO. In the case of a plagioclase solid-solution end member e.g. Or [mol. %], this refers to the percentage of molar orthoclase with respect to sum of albite, anorthite and orthoclase. Presentation of Pb-Pb data on the other-hand is self explanatory (refer to section 4.2.3) as the systems utilised are labelled on graphs and cited accordingly in the text.

4.1 Introduction

This chapter combines cold CL with detailed optical microscopy to map mineral zonation of inferred magmatic feldspars within mixed and mingled plutonic components. In understanding the distribution of mapped feldspar populations and respective zonation in relation to this phenomenon, specific plagioclases have been picked to represent micro-samples from representative zoned components taken from field scale type localities



Sample No	Reference	Facies and feldspar	Location/GR
1(a) & 1(b)	DLC1A & 1D (AF0207)	RM1 - x2 K-feldspar megacrysts	Red Bay Quarry NM [3115 2541]
2	DLC3A (AF/02/01)	RM1a - K-feldspar	Bendoran, Tor na Tor na h'Annaid NM [3641 2171]
3	DLC7A (RR120)	RM2 - K-feldspar megacryst	Knockvologan, WSW of Torr Mór a' Chonairst NM [3096 1941]
4	DLC10-11B (RR019)	Phase 1 MME - Plagioclase micro-phenocryst	Knockvologan Beach NM [30888 19248]
5	DLC8-9F (JR37)	Phase 2 MME - Plagoiclase mega-xenocryst	Knockvologan, Eilan nan Griogag NM [3060 1890]

Fig. 4.1 Map depicting location of samples used for CL and *in-situ* geochemical analysis (adapted from Zaniewski *et al.* 2006).

(**Fig.4.1**). To therefore achieve objective (4) (refer to page eight regarding thesis objectives), *in-situ* mineral elemental and Pb-Pb isotopic analysis were applied to representative feldspars from each facies via Electron Probe Micro-Analysis (EPMA) coupled with Laser Ablation Multiple Collector Inductively Coupled Plasma Mass Spectrometry (LA-MC-ICP-MS). The EPMA mineral traverse data are presented independently for each crystal as individual spot analyses making up a traverse. Pb-Pb linear traverses (as whole line scans incorporating exsolution blebs in feldspar) are also presented for the same crystals, and then all traverses are

plotted as a whole for the ROMG in terms of respective Pb-Pb systems, so that inferences from signatures can be identified to characterise localised and pluton scale petrogenetic processes.

The same methods, laboratory procedures and facilities used in this study are documented in Gagnevin *et al.* (2005) and Willigers *et al.* (2002). This chapter aims to present an elemental and Pb isotopic investigation of feldspars from the ROMG. This direction was chosen following field mapping and thin section studies firstly due to the abundant evidence of field scale mixing/mingling, and secondly, due the assumption of low U and Th contents, with generally high Pb contents, *in-situ* isotopic studies of alkali feldspar naturally provide robust isotopic tracers of magmas and petrogenetic processes due to preservation of initial isotopic ratios that are unchanged from crystallisation (Tyrell *et al.* 2006 and references therein).

On this basis, as isotopic variations in magmatic feldspars provide useful tools for understanding the processes evident from field observations (e.g. Gagnevin *et al.* 2005) this chapter presents a study documenting the chemical heterogeneity and mixing history of the crystal cargo in carefully selected samples (see samples in **Fig. 4.1**), searching for measurable heterogeneity within samples to enable reconstruction of the mixing history for the complex.

The importance of using CL not only as a mapping tool in this study but also combining it with *in- situ* chemical and isotopic analyses also means that CL can also be utilised to address how both magmatic and *sub-solidus* processes can be recognised and highlighted as volumetrically significant in granitoid rocks. The luminescent characteristics of each feldspar (growth zones from core to rim) chosen to reflect each plutonic component are thus compared/contrasted in relation to *in- situ* elemental and isotopic mineral stratigraphy where appropriate to try to understand and define an overall model of mineral stratigraphy per crystal; so inferences can be made on how each mafic to felsic component(s) have evolved throughout ROMG petrogenesis.

4.2 Materials, Sample Selection, Justification & Methods

As the reverse zonation of the complex is mapped and understood (Zaniewski *et al.* 2006), thin section studies coupled with CL were completed after field mapping prior to generating data for mineral stratigraphy. This was completed to define fresh looking inferred magmatic

feldspars within each component and so that the most representative crystal samples based on populations/mineral zonation could be focused on for *in-situ* elemental and isotopic analysis.

CL has highlighted (see **Fig. 4.1**) a characteristic threefold zonation in all magmatic alkali feldspar megacrysts. In some crystals a rounded irregular purple/blue core is succeeded and punctuated by a near concentric bright blue luminescent zone, with a gradation of similar CL characteristics back towards the mantle that exist in the core (see **Fig. 4.2**(**a**) in section **4.3.1 RM1** for a representation of this which occurs throughout all felsic components). Where a threefold zonation occurs within in Mafic Microgranular Enclaves (MME), a contrasting luminescence can exist in varying proportions per component whereby some plagioclases exhibit a red luminescent corroded core, succeeded by a concentric punctuated blue rim with a diffuse gradation back towards a red mantle.

Whilst the different types of generation of feldspar in terms of their CL petrographic characteristics per component are documented within this chapter, this chapter does not attempt to define the actual causes of specific types of CL emission spectra in feldspar. Feldspar micro-samples presented here are inferred as natural candidates to provide perspectives on mineral stratigraphy from components reflecting the mapped reverse zonation purely to understand ROMG petrogenesis. To achieve this, samples were collected (see **Fig. 4.1**) and analysed by cold CL, EPMA and LA-MC-ICP-MS methods respectively.

4.2.1 Cold Cathodoluminescence (CL) Methods

The Cold CL apparatus used at the University of St. Andrews (see **Appendix A4.1**) was a Technocyn 8200 MK V CL cold luminoscope was fitted with an Alcatel Vacuum pump. The chamber is mounted on a Nikon Optiphot microscope which had the normal stage replaced by the CL chamber. A digiman camera is mounted on the third ocular of the microscope. Working conditions were maintained at 14kV and 600 microA. For appropriate more detailed working methodologies/conditions regarding set up of CL lab apparatus used here, refer to Finch & Klein (1999), Götze *et al.* (2000), Krbetseck *et al.* (2002), Brooks *et al.* (2002) and Finch *et al.* (2003).

4.2.2 Electron Probe Micro Analysis (EPMA) Methods

Mineral analyses were performed at the Department of Geology and Geography at Copenhagen University using a JEOL JXA-8200 WD/ED combined micro-analyser

(Superprobe) fitted with five wave-length dispersive (WDS) Spectrometers and one energy dispersive (ED) spectrometer. Analyses were carried out using a 15 kV accelerating voltage, a beam current of 15 nA and a spot size of 5µm. Count times were 10 seconds on peaks and in backgrounds for Na and K and 20 seconds on peak and on backgrounds for all other elements. Matrix corrections were carried out using the phi-rho-z-method.

The instrument was standardised using in house silicates, oxides and metals as listed here: Albite (Na where Na_2O = 11,90%), Orthoclase (K where K_2O = 14,90%), Wollastonite (Ca + Si where SiO_2 = 51,35% and CaO = 48,03%), Rutile (Ti where TiO_2 = 99,4%), Corrundum (Al where Al_2O_3 = 100,00%), Hematite (Fe where FeO = 89,89%), Marjalathi Olivine (Mg where MgO = 48,08%), MnTi-oxide (Mn = 47,0%), Cr-oxide (Cr_2O_3 = 100%) and Ni metal (Ni where Ni = 100%). Further details of methods and instrument settings can be found in Sandrin *et al.* (2009) as operating conditions used in this study followed those guidelines.

Ba was standardised using barite and Sr using celestine. 20 second counting times (10 for Na and K) for most elements were assumed. Raw EPMA data that can be found in **Attachments to Appendix A7.1** on the memory stck labelled **AZ ROMG 2017** depict; Element – which element is being looked at; Peak – the position the spectrometer sits to analyse that element; Net CPS – Total CPS minus backgrounds; Bg- & Bg+ – CPS on the backgrounds; SD% – percentage error; DL – detection limit which is based on a detectable signal where this is larger than three times the noise of the background signal. Detection limits are around 100 to 600 ppm roughly equating to SrO and BaO of 0.01 to 0.06 [wt. %] and Mikson corrections were applied when calculating data (Waight *pers comm.* 2017). Individual EPMA mineral traverse data where presented here is tabulated in bulk in **Appendix A4.2** for all samples from traverse corrections in **Attachments to Appendix A7.2** that can be found on the memory stick labelled **AZ ROMG 2017**.

4.2.3 Pb isotopes by Laser Ablation Multiple Collector-Inductively Coupled Plasma Mass Spectrometry (LA MC-ICP-MS) Methods

Pb isotope ratios were determined at the Danish lithosphere Centre (DLC) in Copenhagen. A CETAC LSX-200 Nd-YAG 266 nm laser ablation system attached to an AXIOM MC-ICPMS was utilised. National Institute of Standards and Technology (NIST) 610 standard (500 ppm Pb) was repeatedly measured between unknowns to estimate precision and accuracy of the laser ablation analyses. Instrumentally induced mass fractionation was corrected using the

measured thallium isotope ratio in interspersed NIST 610 analyses. An in-depth explanation of methods, laboratory conditions and procedures utilised here are found in Gagnevin *et al.* (2005) and Willigers *et al.* (2002). Analyses comprised 50 s (i.e., 100 measurements of 0.5 s duration) of data collection whereby alkali feldspar was rastered at a speed of 10 µm/s using a spot size of 100 µm (total analysis area being approximately 0.06 mm^2) where the laser operated at a pulse rate of 20 Hz and a power of 5 mJ. Due care was given to make sure consistent operating conditions were maintained per interspersed samples and NIST 610 standards, and the gas flow rate was monitored as this can have bearings on instrumental mass fractionation.

At the start of the day, the AXIOM takes time to warm up so initial analyses of NIST 610 were gathered and carefully monitored so that the instrument was within appropriate calibration ranges, and a consistent reproducibility was obtained prior to running laser traverses on crystal samples.

The NIST 610 data utilised and presented in this study comprise thirty-one analyses in total and can be found within **Appendix A4.3 (**raw un-tabulated NIST 610 glass data per sample traverse can be found in **Attachments to Appendix A7.3** with fractionation corrected data in **Attachments to Appendix A7.4** on the memory stick labelled **AZ ROMG 2017**). **Appendix A4.3** also depicts pre and post-traverse measured NIST 610 data for each crystal laser traverse (completed as a line scan). As defined in **Appendix A4.3**, mean values for each isotope system are presented with absolute values to two standard deviation in a manner so that direct comparison with similar relevant studies/literature can be made (in this case Willigers *et al.* 2002; Mathez & Waight 2003; Baker *et al.* 2004; Gagnevin *et al.* 2005). The data produced coincide with Willigers *et al.* (2002) and Baker *et al.* (2004) double spike solution numbers so once can be confident in understanding that the laboratory methods and reproducibility of the NIST 610 data set utilised in this study are well within the limits of accepted literature on this field.

In generating the Pb-Pb isotope data, it is important to summarise the mathematics utilised on the AXIOM generated raw data using NIST 610 glass to apply a correction for mass fractionation by reference to the measured thallium isotope ratio (Willigers *et al.* 2002 and Waight. *pers comm.* 2017). An example from within the spreadsheet found within the memory stick labelled **AZ ROMG 2017** in **Attachments to Appendix A7.4 → Fig. 4.3 → Pb MC-ICPMS DLC1A FC Calcs** (as used to generate **Fig. 4.3 part 2**; see section **4.3.1 RM1** granite) is used to highlight this.

In Tl-doped mass fractionation of Pb (assuming exponential mass fractionation), the assumption is that Tl behaves in the same way as Pb and thus the following equation is applied:

$$\frac{206_{Pb}}{204_{Pb_{frac.corr.}}} = \frac{\frac{206_{Pb}}{204_{Pb_{measured}}}}{\left(\frac{\frac{205_{Tl}}{203_{Tl_{measured}}}}{\frac{205_{Tl}}{203_{Tl_{natural}}}}\right)^{\left(\frac{ln\left(\frac{mass\,206_{Pb}}{mass\,204_{Pb}}\right)}{ln\left(\frac{mass\,205_{Tl}}{mass\,203_{Tl}}\right)}\right)}}$$

The natural $^{205}Tl/^{203}Tl$ ratio = 0.238765 is utilised and the same formula above is used for $^{207}Pb/^{204}Pb$ and $^{208}Pb/^{204}Pb$ changing the appropriate atomic masses accordingly as per the periodic table. When running the NIST 610 glass one can use the Tl present in the glass to fractionation correct the Pb analysis. When running interspersed feldspars (contain Pb but not Tl), the mass fractionation factor ($^{205}Tl/^{203}Tl_{measured}/^{205}Tl/^{203}Tl_{natural}$) is then used to correct the measured Pb isotopic compositions.

If one looks at one of the Pb isotope traverse data files as previously highlighted on the memory stick (e.g. Pb MC-ICPMS DLC1A FC Calcs) the following is presented in the spreadsheet:

Column B: The numbers straight of the machine - fractionation corrected to a manually input $^{205}Tl/^{203}Tl$ measured/real (this is just labeled $^{205}Tl/^{203}Tl$ - e.g. cell A69 = 1.019182).

Column D: Depicts a correction for a small interference from ^{204}Hg on ^{204}Pb.

Column E: Removes the mass fractionation correction (using a re-arrangement of the equation on the previous page) so one obtains raw un-fractionated data.

Column G: Re-fractionates the data to a new 205/203 m/r (a linear interpolation of the 205/203 m/r based on the NIST 610 run immediately previously and immediately afterwards, where a protocol of NIST 610, then four unknowns, followed by NIST 610 again was ran). The signals on the plagioclase data are quite low which can potentially cause larger errors on especially all the Pb isotope data normalised to ^{204}Pb (as it is by far the lightest isotope) and it

is affected by possible interferences from Hg, however the $^{207}Pb/^{206}Pb$ and $^{208}Pb/^{206}Pb$ data is not affected by this so should be more robust (see Mathez & Waight 2003).

All re-fractionated data presented in this study (**Attachments to Appendix A7.4**) were carefully checked and all errors on re-fractionated Pb-Pb plots in this chapter are in run errors expressed to two standard deviations. All such tabulated bulk data can be found in **Appendix A4.4** with averages per mineral zones in **Appendix A4.5**.

4.3 Results; CL Petrography and *In-Situ* analysis of ROMG feldspars

This section presents and describes the common CL petrographic characteristics observed in each of the facies. It then draws attention to the detail of the CL features of each feldspar micro-scale sample chosen for analysis from each ROMG component (see **Fig. 4.1**). Crystal samples are thus individually fingerprinted in terms of their cold CL characteristics, and similarly, the *in-situ* elemental and Pb-Pb isotopic data ranges are presented per mineral zone.

Within the next sub-sections from **4.3.1 RM1** to **4.3.4 Mafic components; MME Phase 1 & MME Phase 2**, where figures are appropriately presented for each respective individual feldspar analysed per component (e.g. see **Fig. 4.3 part 1** & **part 2**), they are split into two parts. Part 1 is a photograph of the crystal in CL or BSE imaging, and part 2 comprises *in-situ* elemental and Pb-Pb traverse data. A summary of all observations that make data comparison relatively easy, and where these areas are referenced in the text, these diagrams are all compartmentalised into the following **areas**:

part 1

A – BSE Image.

B – Where appropriate to express zonation profile/petrographic characteristics of crystal in question; CL Image; Cartoon; Photograph.

part 2

C – EPMA traverses comprising single spot analyses (e.g. **1a2** as one single spot analysis) each making up a traverse avoiding albite-rich exsolutions where possible.

D – $^{206}Pb/^{204}Pb$, $^{207}Pb/^{206}Pb$, $^{208}Pb/^{204}Pb$ and $^{208}Pb/^{206}Pb$ LA MC-ICP-MS laser traverses completed as line scans with a starting and ending point that encompass albite-rich exsolutions.

4.3.1 RM1

Zaniewski *et al.* (2006) classified RM1 in the field as a characteristic reddened coarse grained equigranular biotite granite and according to powder X-ray diffractometry (see Chapter Three) is a monzogranite.

Within this facies, most alkali feldspars (generally 15-20 mm in length) show irregular and rounded purple/blue luminescent cores verging on red (zone 1), followed by a punctuated bright blue luminescent mantle (zone 2), which then grades back toward the rim which exhibits similar characteristics to the cores (zone 3). Where this threefold zonation is apparent (see **Fig. 4.2(a)**, **Fig. 4.3 part 1 area A** & **B** & **Fig. 4.4 part 1 area A** & **B** which all display this luminescent zonation pattern), the contacts between the first two zones are generally sharp however the contact between zones 2 and 3 are gradational; zoning in such varieties is generally concentric, however not always restricted to these three zones and sometimes a twofold zonation where zone 3 is absent can occur (see **Fig. 4.2(b)**).

Plagioclases on the other hand are altered in varying degrees, particularly in the cores and within oscillatory zones that show dark brown luminescence, depicting turbidity, there is sericitic alteration (**Fig. 4.2(b)** and **Fig. 4.2(c)**). Some rarer varieties do not display such alteration, but have rather bright blue luminescent remnant cores, whilst the rims have a characteristic brick red.

Whilst CL petrography has aided in distinguishing between the two different sets of plagioclase populations accordingly (i.e. alkali feldspar and plagioclase), it has also separately highlighted extensive replacement of plagioclase feldspar by alkali feldspar where corroded patches of remaining plagioclase remain in approximately less than 5-10% of the modal plagioclase content for this facies.

Two representative alkali feldspar samples were chosen to represent this facies in **Fig. 4.1** and both were carefully selected from a homogeneous large slab (10-15kg) from Red Bay Quarry primarily because this is the type locality for this facies (the name Red Bay comes from the reddened nature of this granitoid) and due to its accessibility. DLC1A/AF0207 is stored at the School of Earth and Environmental Sciences, University of St Andrews (refer to **Appendix A5 - ROMG Sample Stations**). This approach was done only for this facies merely to assess within sample heterogeneity in alkali feldspars, and as these were the first samples utilised for *in-situ* elemental analyses, the two resultant data sets can be checked to

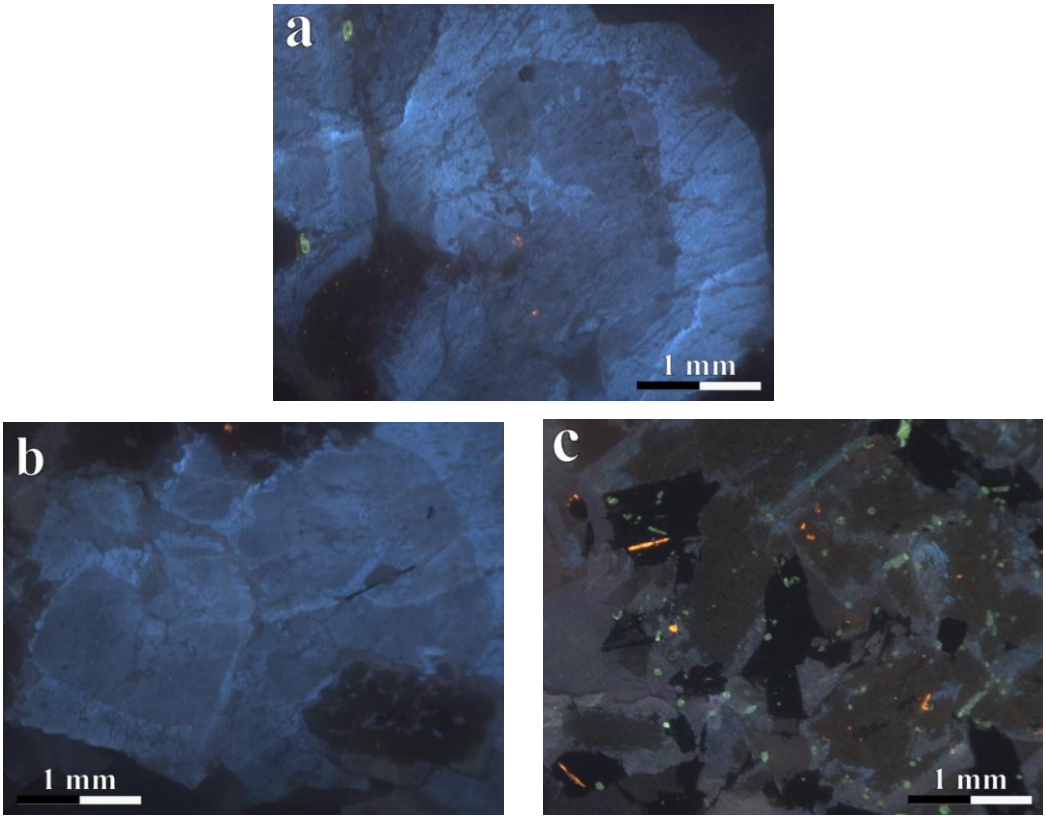


Fig. 4.2 (a-c) Cold CL petrographic textures of feldspars within RM1 (**DLC1A/AF0207**). **(a)** Common example of anhedral to subhedral equigranular alkali feldspar crystal depicting threefold zonation profile as described within the text with highly embayed core. **(b)** Glomerocrytstic cluster of alkali feldspars with similar luminescence profiles as observed in **(a)** with subhedral plagioclase feldspar (bottom right) superimposed displaying another different pattern for plagioclases observed in RM1. This plagioclase has a turbid brown/dark red luminescent core (boxy cellular structure) followed by a dark blue luminescent rim. **(c)** Plagioclase rich area (possible glomerocrysts) depicting crystals with a turbid brown/dark red luminescent core followed by a dark blue luminescent rim. Calcite stringlets occur across biotite cleavage and there is high abundance of anhedral to subhedral elongate apatite.

assess whether instrumentation and methods used were consistently accurate, reproducible and within adequate calibration.

In assessing the RM1 CL characteristics of the alkali feldspar megacryst micro-samples (refer to **area B -** CL images in both **part 1** for **Fig. 4.3** and **Fig. 4.4**) chosen to represent this facies, both display the CL zonation profiles as previously described and documented in **Fig. 4.2(a)**. In the CL image in **Fig. 4.3 part 1 area B**, strong embayment/dissolution is observed towards the central/lower right-hand edge of the large rounded irregular core region, and zone 2 is concentric forming the smallest zone. If one also observes the EPMA monochromatic images in each of **part 1** for **Fig. 4.3** and **Fig. 4.4**, in **area A**, whilst the threefold zonation is apparent by the different orders of grey (lighter grey shades highlight a greater abundance of back-scattered electrons depicting a heavier average chemical composition where K (heavy) is in greater abundance than Na (light)), it is clearly much more difficult to make out without the joint use of cold CL. Bulk average EPMA analyses (where e.g. n=1 expresses the amount of analyses per zone) for each mineral zone show that for both alkali feldspar crystals considered in RM1:

- DLC1A:AF0207 (RM1) - **Fig. 4.3 part 2 area C** - zone 1 (Ab6.46, Or93.88 n=8); zone 2 (Ab7.64, Or91.94 n=15); zone 3 (Ab5.83, Or93.98 n=4)
- DLC1A:AF0207 (RM1) - **Fig. 4.4 part 2 area C** - zone 1 (Ab8.89, Or90.65 n=19); zone 2 (Ab7.77, Or91.81 n=17); zone 3 (Ab6.63, Or93.21 n=19)

In associating CL patterns to geochemistry, it is necessary to break down the bulk data for *in-situ* elemental analysis for the RM1 feldspar observed in **Fig. 4.3** part 1 and 2 reflected in EPMA traverse **1a2-1a37 Fig. 4.3 part 2 area C** and Pb-Pb MC-ICP-MS traverse A-B **Fig. 4.3 part 2 area D** in terms of data ranges for each mineral zone; this is shown in **Table (4.1a)**. It is apparent as one moves from the purple blue/red embayed core region zone 1 to the punctuated bright blue zone 2, there is a marked spike on the line diagrams in **Fig 4.3 part 2 area C** depicting a characteristic increase in Ba (largest data range point adjacent to point **1a30** of 0.750 obviously stands out) and Sr (where **1a30** is the largest spike), and a general decrease in Or [mol. %] ~ 1-2 (where point **1a30** does the opposite in comparison to Ba and Sr). In moving from zone 2 to towards the rim (zone 3), the CL and elemental characteristics seem to corroborate in affinities to that of the core region with a general decrease in Ba, Sr and increase in Or [mol. %] by again ~ 1-2. In terms of the Pb-Pb characteristics, clearly both

Zone	BaO [wt. %]	SrO [wt. %]	Or [mol. %]
3 - Rim	0.038 - 0.213	0.011 - 0.160	90.12 - 94.90
2	0.160 - 0.750	0.053 - 0.188	85.73 - 96.42
1 - Core	0.013 - 0.028	0.027 - 0.085	92.09 - 95.32

Zone	$^{206}Pb/^{204}Pb$	2σ	$^{207}Pb/^{206}Pb$	2σ	$^{208}Pb/^{204}Pb$	2σ	$^{208}Pb/^{206}Pb$	2σ
3 - Rim	16.998	0.011	0.924	0.00022	35.898	0.023	2.148	0.00022
1 - Core	16.918	0.036	0.929	0.00081	35.770	0.061	2.154	0.00044
Rims w.r.t. Cores	Increase 0.080		Decrease 0.005		Increase 0.128		Decrease 0.006	

Table 4.1(a) - **Fig. 4.3 part 2 area C** & **D** - DLC1A:AF0207 (RM1) - Raw data ranges for BaO, SrO, Or % and Pb-Pb isotopic systems.

$^{206}Pb/^{204}Pb$ and $^{208}Pb/^{204}Pb$ systems are de-coupled to $^{207}Pb/^{206}Pb$ and $^{208}Pb/^{206}Pb$. $^{206}Pb/^{204}Pb$ increases from the core (B) to the rim (A) with a range difference of 0.080 and so does $^{208}Pb/^{204}Pb$ with a range difference of 0.128; whilst $^{207}Pb/^{206}Pb$ decreases from the core (B) to rim (A) with a range difference of 0.005 and $^{208}Pb/^{206}Pb$ also does with a range difference of 0.006.

Similarly, for another alkali-feldspar examined from the same sample in **Fig. 4.4 part 2 (area C** - EPMA traverse **1a143-1a206** and **area D** - Pb-Pb MC-ICP-MS traverse C-D) the similar patterns are apparent in terms of elevated Ba, Sr and general decrease in Or [mol. %] in zone 2, with decoupling in the same Pb-Pb systems with the exception of $^{208}Pb/^{206}Pb$ which are opposite to each other. This is reflected in the data ranges in **Table 4.1(b)**:

Zone	BaO [wt. %]	SrO [wt. %]	Or [mol. %]
3 - Rim	0.010 - 0.130	0.018 - 0.082	87.07 - 93.88
2	0.008 - 0.316	0.070 - 0.125	88.42 - 96.14
1 - Core	0.036 - 0.238	0.008 - 0.073	88.66 - 96.45

Zone	$^{206}Pb/^{204}Pb$	2σ	$^{207}Pb/^{206}Pb$	2σ	$^{208}Pb/^{204}Pb$	2σ	$^{208}Pb/^{206}Pb$	2σ
3 - Rim	16.972	0.021	0.918	0.00051	36.580	0.020	2.154	0.00035
1 - Core	16.940	0.019	0.919	0.00026	36.421	0.039	2.150	0.00034
Rims w.r.t. Cores	Increase 0.032		Decrease 0.001		Increase 0.159		Increase 0.004	

Table 4.1(b) - **Fig. 4.4 part 2 area C** & **D** - DLC1A:AF0209 (RM1) - Raw data ranges for BaO, SrO, Or % and Pb-Pb isotopic systems.

Spikes in Ba and Sr in the line diagrams (**Fig. 4.4 part 2 area C**) are evident, however as more analyses were completed throughout the core region in comparison to that to generate

Fig. 4.3 DLC1A/AF0207 (RM1) part 1

A - EP backscatter and **B** - cold CL image (with interpretive line drawing for crystal zonation profile) for an alkali feldspar from the Red Bay (RM1) granitoid type locality.

Refer to **Fig. 4.3 part 2** for respective traverses depicted for **C** - *in-situ* elemental and **D** - Pb-Pb isotopic analyses.

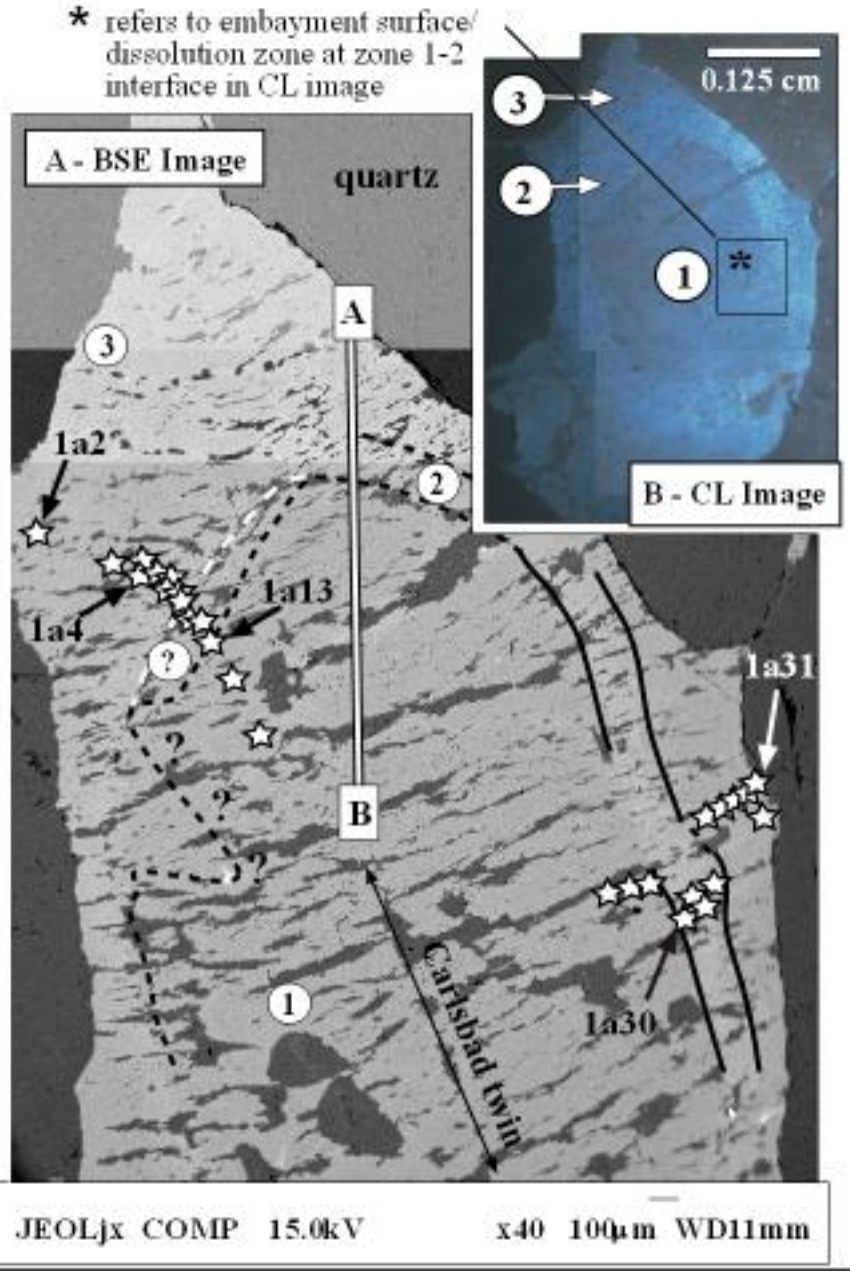
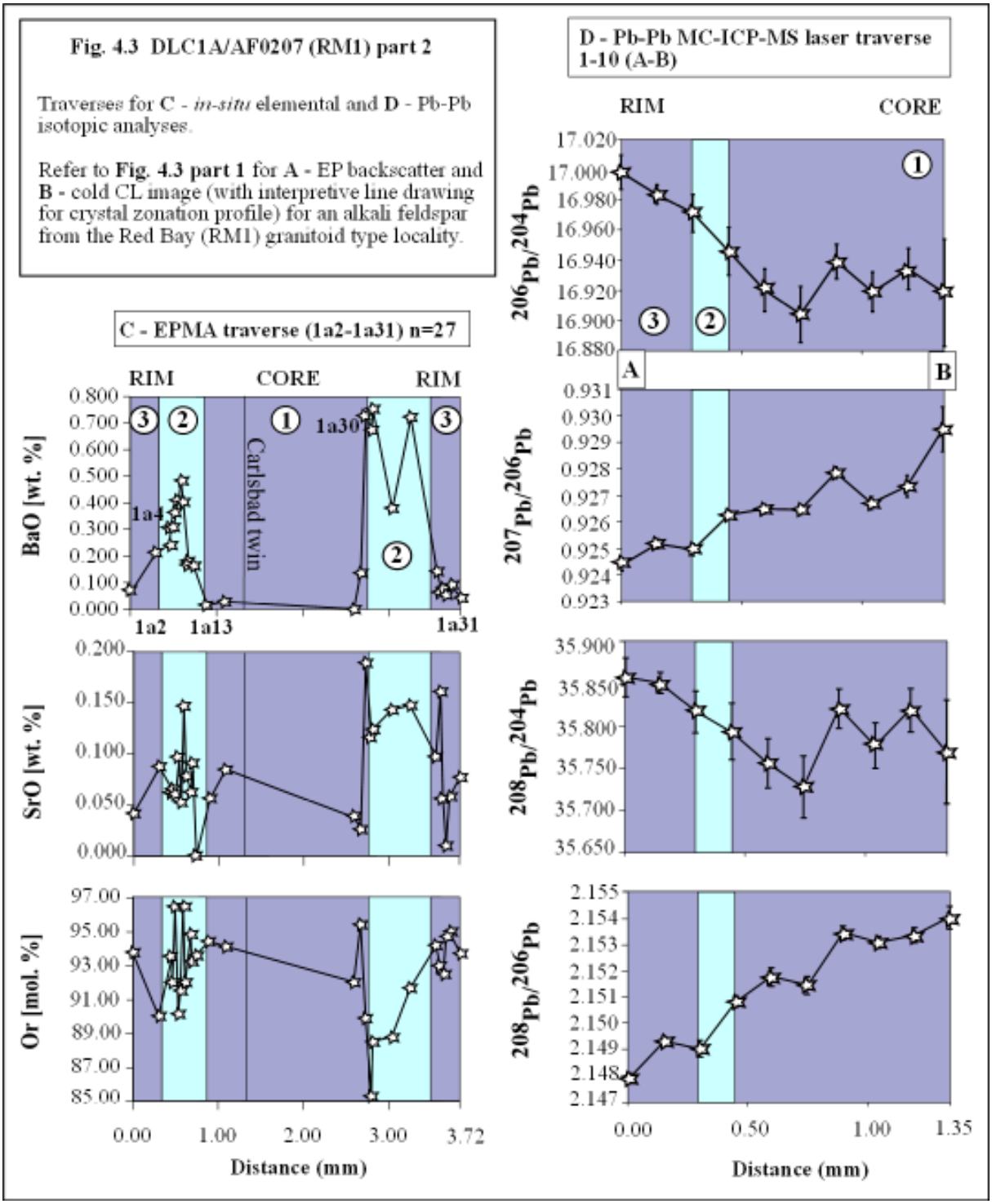


Fig. 4.3 DLC1A/AF0207 (RM1) part 2

Traverses for **C** - *in-situ* elemental and **D** - Pb-Pb isotopic analyses.

Refer to **Fig. 4.3 part 1** for **A** - EP backscatter and **B** - cold CL image (with interpretive line drawing for crystal zonation profile) for an alkali feldspar from the Red Bay (RM1) granitoid type locality.



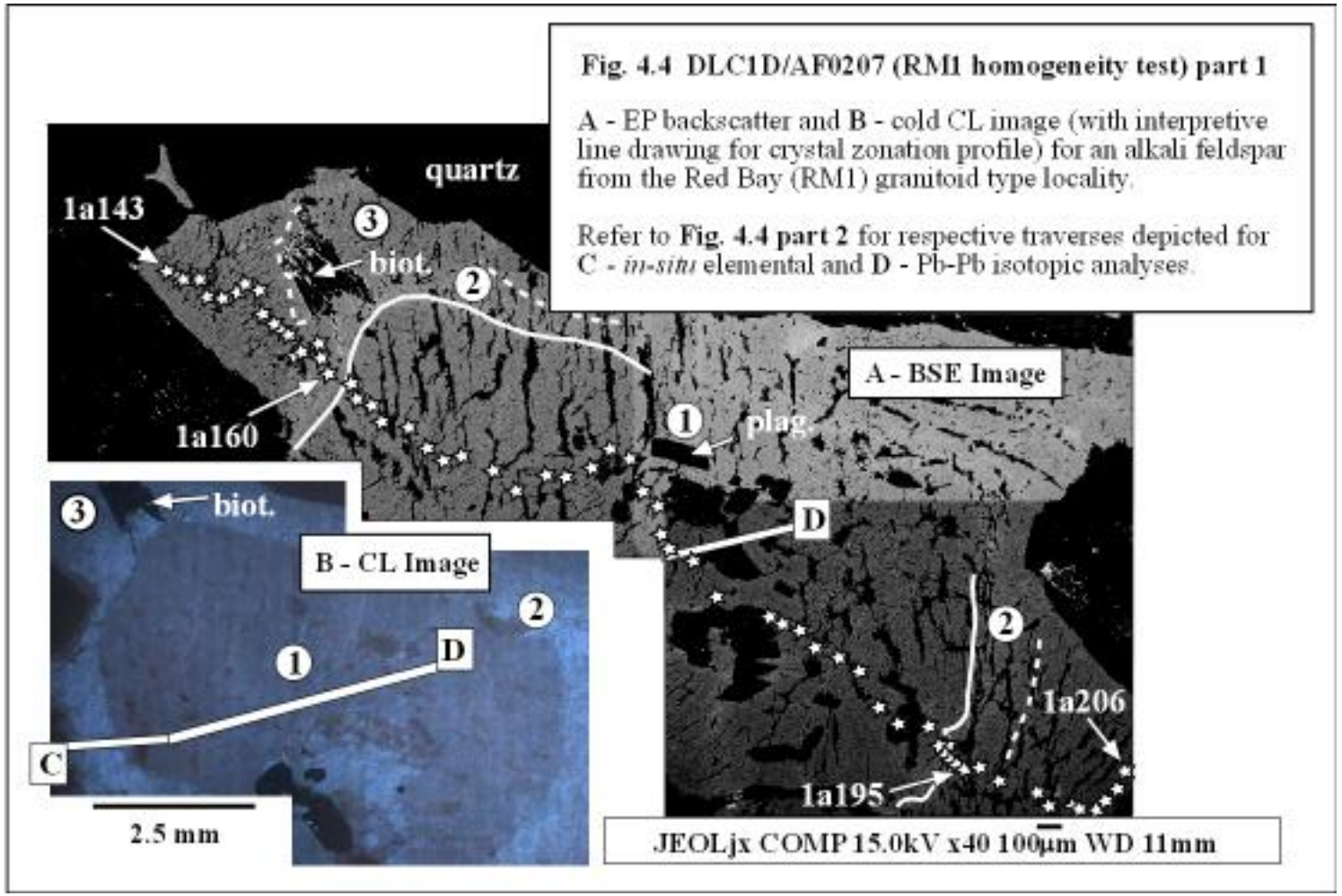


Fig. 4.4 DLC1D/AF0207 (RM1 homogeneity test) part 1

A - EP backscatter and B - cold CL image (with interpretive line drawing for crystal zonation profile) for an alkali feldspar from the Red Bay (RM1) granitoid type locality.

Refer to **Fig. 4.4 part 2** for respective traverses depicted for C - *in-situ* elemental and D - Pb-Pb isotopic analyses.

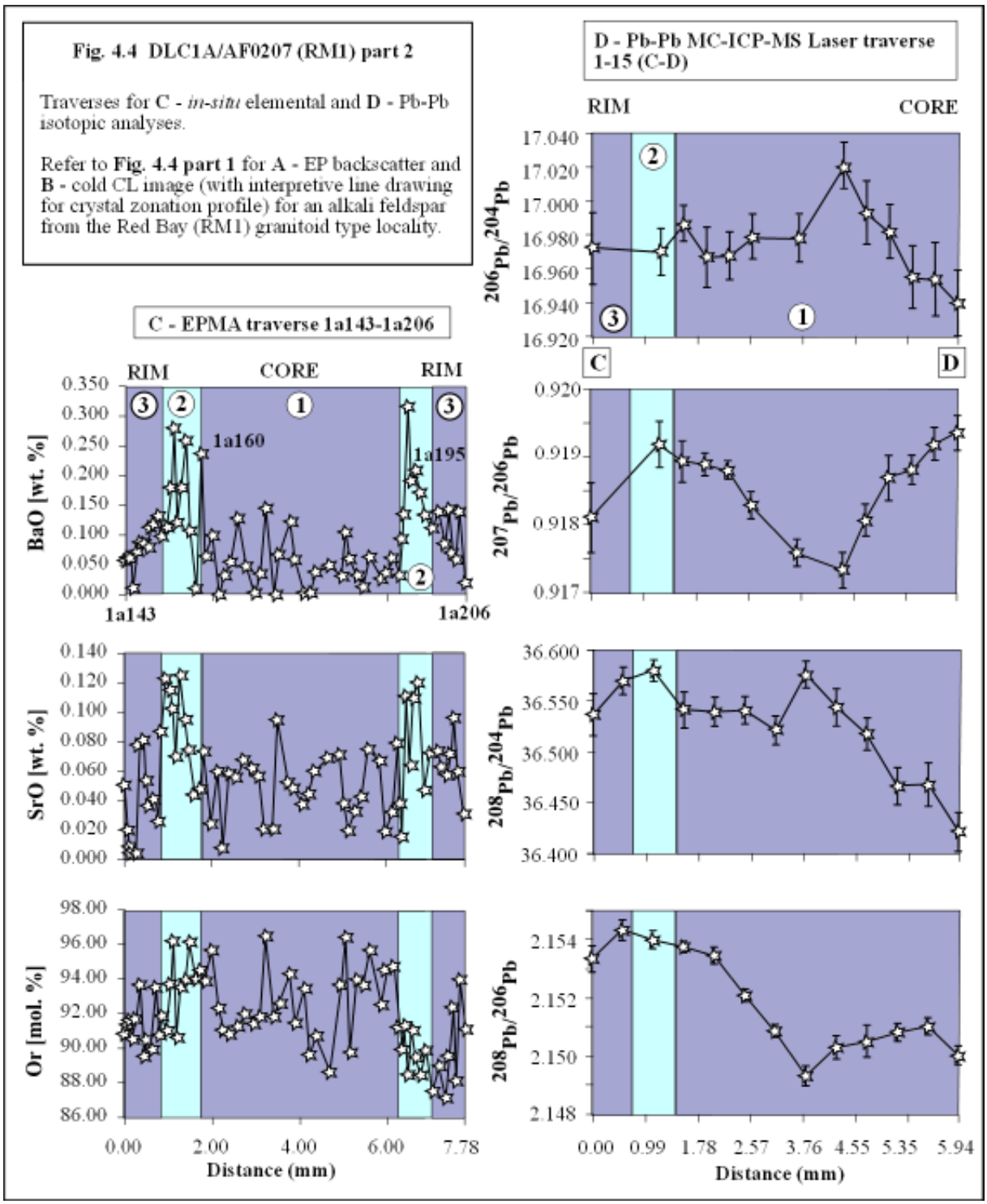

Fig. 4.4 DLC1A/AF0207 (RM1) part 2
Traverses for C - in-situ elemental and D - Pb-Pb isotopic analyses.
Refer to Fig. 4.4 part 1 for A - EP backscatter and B - cold CL image (with interpretive line drawing for crystal zonation profile) for an alkali feldspar from the Red Bay (RM1) granitoid type locality.
D - Pb-Pb MC-ICP-MS Laser traverse 1-15 (C-D)
C - EPMA traverse 1a143-1a206
RIM
CORE
RIM
1a160
1a195
1a143
1a206
BaO [wt. %]
SrO [wt. %]
Or [mol. %]
206Pb/204Pb
207Pb/206Pb
208Pb/204Pb
208Pb/206Pb
C
D
Distance (mm)
Distance (mm)

Fig. 4.3 part 2 area C, the greater variability of data here make it more subtle to pick up existing spike zones. Similarly it is difficult to make out that there is a general decrease for Or [mol. %] in the punctuated bright blue zone 2, although the data ranges above reflect this. Therefore similar elemental trends and respective ranges generally define a consistent pattern between the two alkali feldspars in RM1which contain the same textural and mineral characteristic CL profiles as depicted in both **part 2 B areas**.

In terms of the decoupling in Pb-Pb systems, for the binary diagrams in **Fig. 4.4 part 2 area D**, comparisons between this crystal and the one in **Fig. 4.3 part 2 area D** are difficult to make. The data ranges for **Fig. 4.4 part 2 area D** show from the core (D) to the rim (C) $^{206}Pb/^{204}Pb$ increases with a range difference of 0.032, $^{207}Pb/^{206}Pb$ decreases with a range difference of 0.001 and $^{208}Pb/^{204}Pb$ increases with a range difference of 0.459. $^{208}Pb/^{206}Pb$ trend here is in opposite sense to the alkali feldspar traverse in **Fig. 4.3 part 2 area D** with an increase towards the rim with a range difference of 0.004. The data ranges between each of the two RM1 alkali feldspar crystals for $^{206}Pb/^{204}Pb = 0.786$, $^{207}Pb/^{206}Pb = 0.004$, $^{208}Pb/^{204}Pb = 0.331$ showing dissimilar data spread and for $^{208}Pb/^{206}Pb = 0.002$ however this system appears to be de-coupled in the same petrographic generation of feldspar. The sixth analyses in from the core region in the Pb-Pb diagrams in **Fig. 4.4 part 2 area D** creates the impression that there is an independent separate sharp elevation of $^{206}Pb/^{204}Pb$ and $^{208}Pb/^{204}Pb$ and marked decrease of $^{207}Pb/^{206}Pb$ and $^{208}Pb/^{206}Pb$ in the core region adjacent to the dissolution zone (see the bottom right of the core in **Fig. 4.4 part 1 area B**) making the data in Pb-Pb systems symmetrical. Clearly the Pb-Pb data in **Fig. 4.3 part 2 area D** either show a gradual increase or decrease in gradient for respective Pb-Pb systems in comparison. Pb-Pb data in **part 2 area D** for the core region for the alkali feldspar crystal in **Fig. 4.4 part 1** (in relation to this dissolution zone) could be misleading (i.e. they are not accurate analyses), as the data for the core region may not encompass a true traverse across the core, however in **Fig. 4.3 part 2 area D**, Pb-Pb analyses from the core do in fact depict analyses from fresh areas of the core region (linear traverses also encompass less exsolution blebs in feldspar here).

The main observations within these two alkali feldspar crystals presented from RM1 clearly depict a characteristic resorption surface, indicative of dissolution and interruption of crystal growth (Daly & Poli 1999) between zone 1 and 2 where the bright blue CL zone 2 has elevated spikes in terms of Ba, Sr and decrease in mole% Or. As a whole, RM1 alkali feldspars have mantles/rims that are characterised by high $^{206}Pb/^{204}Pb$, low $^{207}Pb/^{206}Pb$ and

high $^{208}Pb/^{204}Pb$ relative to the cores and the nature of decoupled $^{208}Pb/^{206}Pb$ in RM1 alkali feldspars is not fully understood.

4.3.2 RM1a

Zaniewski *et al.* (2006) classified RM1a in the field as leucocratic muscovite biotite granite and according to powder X-ray diffractometry (see previous chapter) is a monzogranite also overlapping the same modal mineralogy as RM1.

The CL characteristics of feldspars within this facies of white granite are strikingly different compared to those within other ROMG facies. This is particularly in the case of plagioclase feldspars, which are generally less altered and display a bright yellow luminescence (refer to **Fig. 4.5(a) - (c)**). Yellow luminescence is polarised with contrasting luminescence apparent on different sets of twin planes with varieties often displaying fine scale oscillatory zoning in cold CL. Subhedral to anhedral alkali feldspars on the other hand, display the characteristic blue luminescence already described in RM1, where often a twofold zonation exists with embayed dark blue luminescent cores punctuated by a bright blue mantle similar to the composition of alkali feldspar in RM1 (e.g. **Fig. 4.2**). Compositions tend to grade towards more albitic as one moves towards the rim, however the luminescence can appear uniform to the naked eye and the threefold zonation profile already described in RM1 can exist.

The 1.5 cm subhedral alkali feldspar megacryst presented for geochemical analysis in this study comes from the northeast of the granite envelope at Torr na h'Annaid adjacent to Bendoran Cottage (see **Fig 4.1**) in a generally equigranular variant where RM1a is in contact with predominantly Moine pelite (see Zaniewski *et al.* 2006) and in this case, the megacryst is adjacent to a 3cm tabular Moine pelitic xenolith. Whilst this facies of RM1a at Bendoran can appear relatively equigranular, inhomogeneities can occur in the form of sporadic porphyritc patches of alkali feldspar (up to a few metres). The RM1a sample was used here due to its fresh appearance in the field in terms of standing out of in terms of being a more brilliant white looking variant of granite in comparison to the southeast of the envelope where it is in contact with predominantly Moine psammite. The crystal chosen has the most embayed looking core region and most amount of complex mineral zones observed than any other looking RM1a crystal observed in this facies.

This is the only crystal in this study where detailed CL was avoided as the alkali feldspar crystal chosen to represent RM1a in **Fig.4.6** EPMA backscatter comprises twenty

individual images; whilst the bulk of the crystal retains blue CL similar to the cores of RM1 alkali feldspars, it was difficult to produce an accurate depiction of a true CL mosaic/composite image for the whole crystal due to photographic imaging showing different ranges of blue in relation to the photographic bias produced by the digiman camera. As a result of this instrumental bias, the EPMA imaging highlighted a clearer zonation profile as depicted in the cartoon in **Fig. 4.6 part 1 area B** where seven mineral zones are highlighted.

In **Fig 4.6 part 1**, this is an isolated megacryst occurring within a relatively equigranular RM1a variant that displays poikilitic 0.5-1mm subhedral zoned plagioclase in the core region and with some subhedral tabular poikilitic plagioclase with a twofold zonation

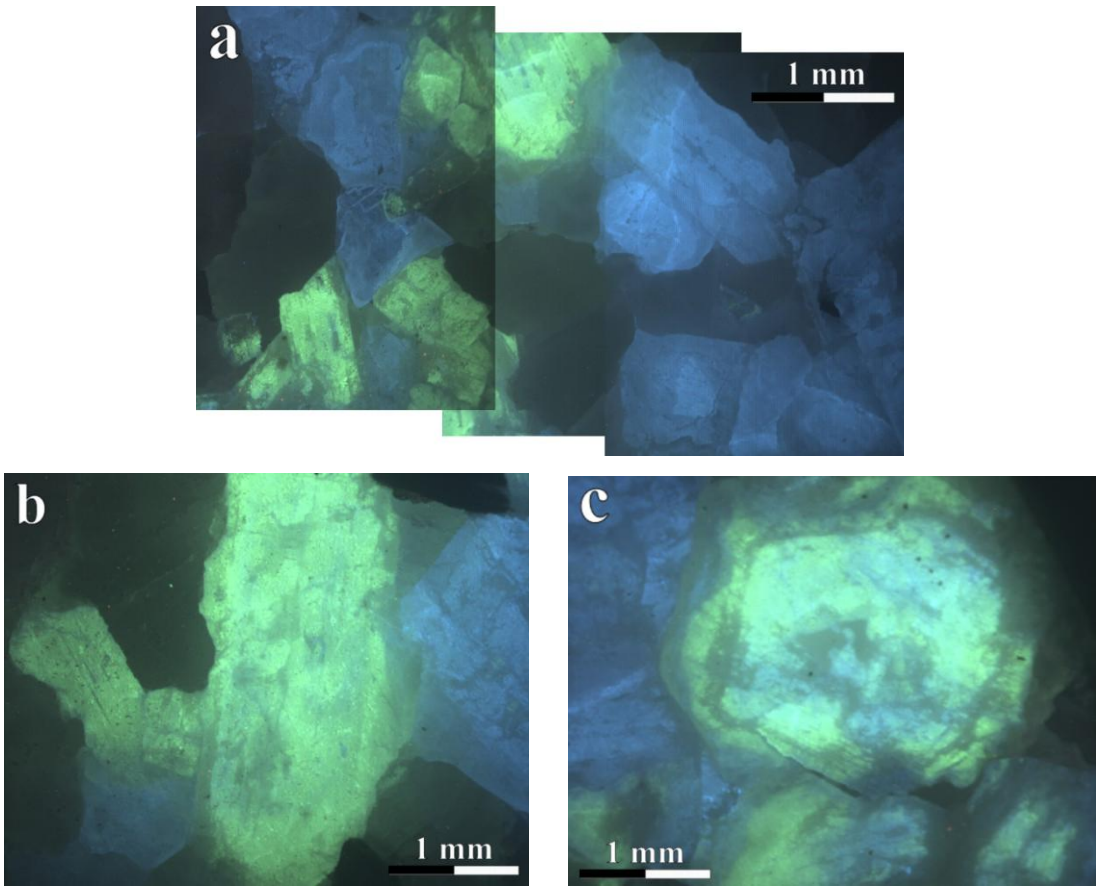


Fig. 4.5 (a-c) Cold CL images of feldspars within **DLC3A/AF/02/01 (RM1a)** as follows: **(a)** Gross textural image of RM1a from Bendoran. Alkali feldspars are anhedral to subhedral with blue luminescence whereas plagioclase feldspars display a bright yellow luminescence which is found to be polarised. **(b)** Subhedral plagioclase feldspar with typical bright yellow luminescence. Darkening of the luminescence at the edge of the crystals occurs, which is turbid and mottled yellow to brown in appearance. **(c)** Anhedral plagioclase with complex zonation. Core region displays blue and yellow luminescence, with a characteristic turbid brown outer zone, which is gradational towards the edge in terms of the yellow luminescence in the core region. Brown mottled areas also run along the twin planes in the crystal.

also occurring conspicuously aligned sub-parallel within zone seven at the edges of the crystal. One of the key characteristics evident in such crystals (including porphyritic areas) is the presence of a distinctive, highly embayed core region (containing the darkest order of grey observed in BSE imaging) which brings to question whether there is the possibility of an inherited Moine core; this feature is dominant where RM1a is juxtaposed to more pelitic lithologies. This alkali-feldspar from RM1a was analysed though to keep consistency in terms of addressing *in-situ* elemental and Pb-Pb characteristics from each plutonic component comprising the intrusion so later comparisons of Pb-Pb isotopic signatures with the rest of the pluton can be utilised to address petrogenesis.

EPMA analyses of the respective mineral zones in **Fig. 4.6 part 1 area B** as seen in **Fig. 4.6 part 2 area C** comprise averages for each mineral zone as follows:

DLC3A: AF/02/01 - Zone 1 (Ab8.65, Or91.27 n=15), Zone 2 (Ab14.24, Or85.62 n=6), Zone 3 (Ab12.48, Or 87.37 n=11), Zone 4 (Ab12.88, Or87.02 n=3), Zone 5 (Ab9.13, Or90.84 n=16), Zone 6 has no analyses completed, and zone 7 (Ab9.01, Or 90.77).

In highlighting geochemical patterns to the zonation profile depicted in **Fig. 4.6 part 1 area A** & **B**, data ranges gleaned from **Fig. 4.6 part 2 area** C are shown in **Table 4.2**. Or [mol. %] across all zones is relatively constant and the lowest data range of 66.80 in the core is likely an error where an analysis may have been completed on an exsolution bleb or more likely a small edge of a poikilitic plagioclase should in theory be discounted, however Or [mol. %] appears to be more elevated within the core zone 1 and zone 5 by 5% or more with respect to other zones. Trends for Ba and Sr are more discernible, and generally mirror each other, whereby the core region zone 1 depicts a low ranges of Ba = 0.136 - 0.716 and Sr = 0.022 - 0.078 with a spike occurring in zone 2, where increases are apparent in zone 2 for Ba = 0.282 - 1.089 and Sr = 0.038 - 0.131. In moving towards zone 3, (**Fig. 4.6 part 2 area C**) both Ba and Sr show a drop (roughly 0.300 for Ba and 0.750 for Sr), with an increase towards 1.00 for Ba and 0.100 for Sr. As one subsequently progresses from zone 3 to the mantle/rim at zone 7, there is a dramatic decrease in gradient particularly for Ba towards point **1a529** at 0.131 and for Sr 0.028.

Pb-Pb isotopic systems as depicted in **Fig 4.6 part 2 area D**, show in comparison to RM1 (with exception of $^{208}Pb/^{206}Pb$ in RM1 where this system is decoupled in two alkali feldspars from the same generation (refer back to **Fig 4.3** & **Fig. 4.4 part 2 area D**)), both $^{206}Pb/^{204}Pb$ and $^{208}Pb/^{204}Pb$ correlate and are decoupled to $^{207}Pb/^{206}Pb$ and $^{208}Pb/^{206}Pb$ systems;

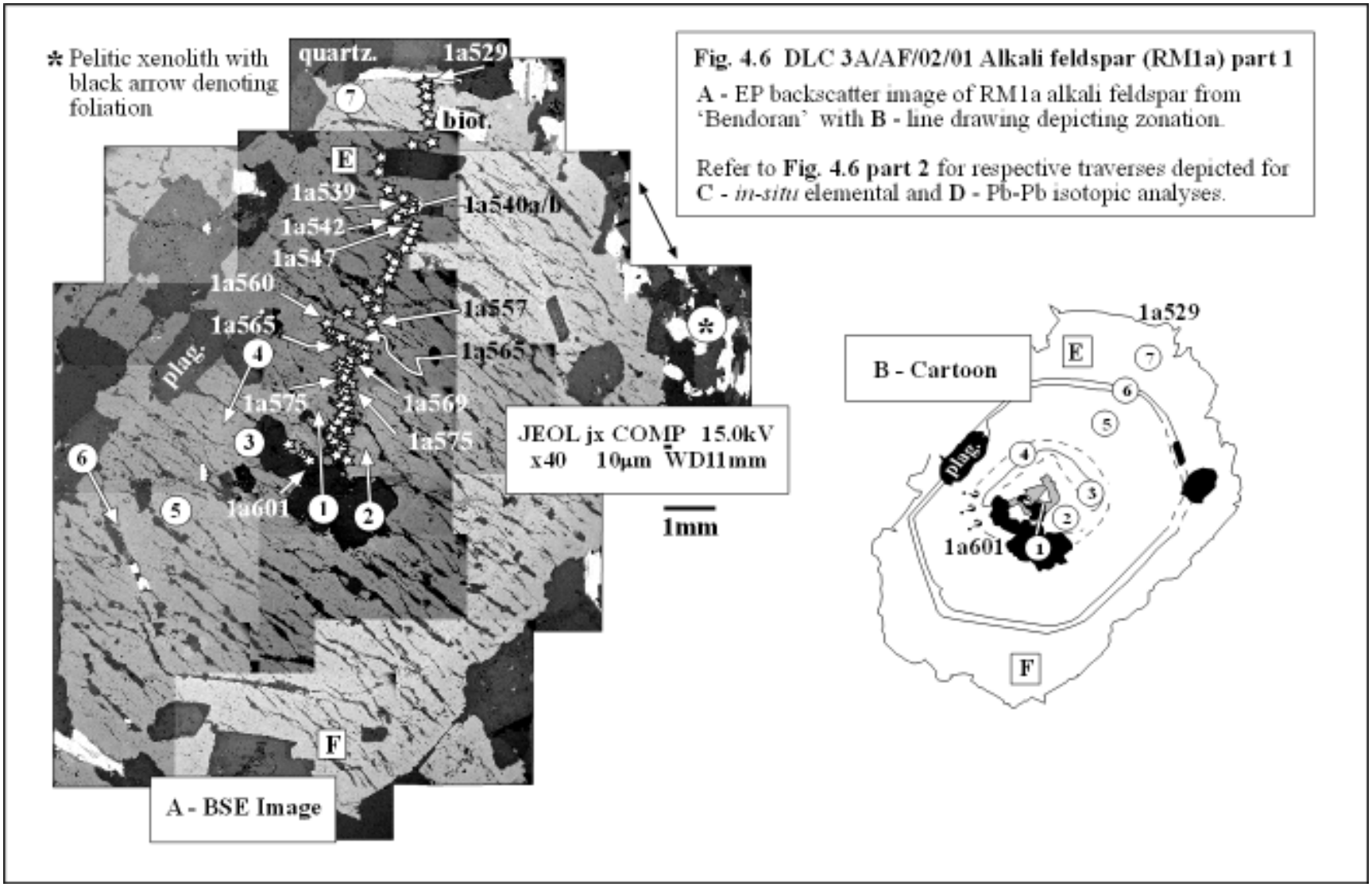
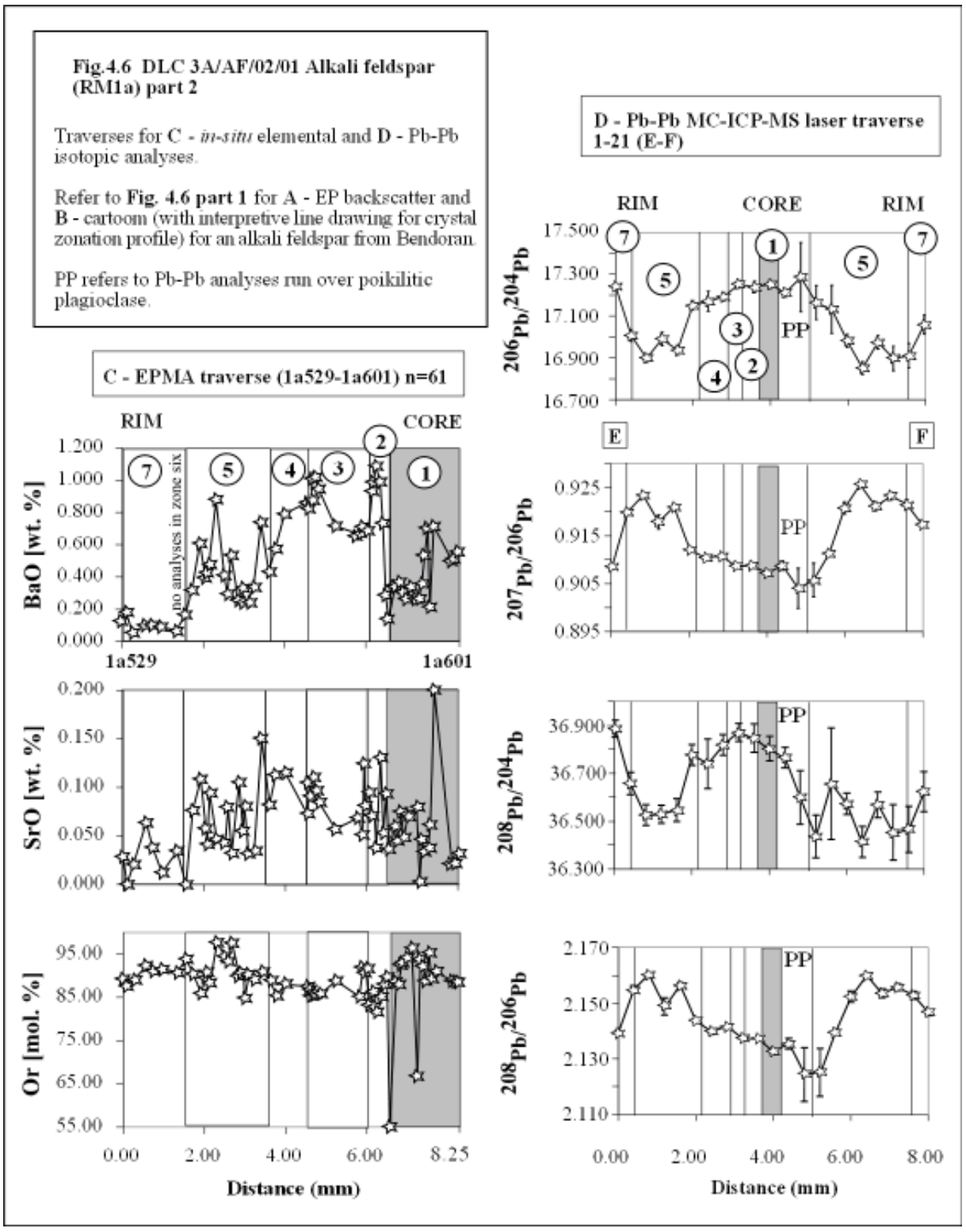

* Pelitic xenolith with black arrow denoting foliation
quartz.
1a529
biot.
E
1a539
1a540g/b
1a542
1a547
1a560
1a557
1a565
1a565 1
plag.
1a575
1a569
1a575
JEOL jx COMP 15.0kV
x40 10µm WD11mm
1mm
1a601
F
A - BSE Image
B - Cartoon
1a529
E
plag.
1a601
F
Fig. 4.6 DLC 3A/AF/02/01 Alkali feldspar (RM1a) part 1
A - EP backscatter image of RM1a alkali feldspar from 'Bendoran' with B - line drawing depicting zonation.
Refer to Fig. 4.6 part 2 for respective traverses depicted for C - in-situ elemental and D - Pb-Pb isotopic analyses.

Fig.4.6 DLC 3A/AF/02/01 Alkali feldspar (RM1a) part 2

Traverses for C - *in-situ* elemental and D - Pb-Pb isotopic analyses.

Refer to **Fig. 4.6 part 1** for A - EP backscatter and B - cartoom (with interpretive line drawing for crystal zonation profile) for an alkali feldspar from Bendoran.

PP refers to Pb-Pb analyses run over poikilitic plagioclase.



Zone	BaO [wt. %]	SrO [wt. %]	Or [mol. %]
7 - Rim	0.052 - 0.179	0.012 - 0.064	87.82 - 93.95
6	-	-	-
5	0.249 - 0.735	0.032 - 0.108	84.88 - 97.63
4	0.574 - 0.863	0.072 - 0.115	85.45 - 88.05
3	0.668 - 1.008	0.051 - 0.125	83.20 - 91.80
2	0.282 - 1.089	0.038 - 0.131	81.80 - 89.72
1 - Core	0.136 - 0.716	0.022 - 0.078	66.80 - 96.91

	$^{206}Pb/^{204}Pb$	2σ	$^{207}Pb/^{206}Pb$	2σ	$^{208}Pb/^{204}Pb$	2σ	$^{208}Pb/^{206}Pb$	2σ
Rim	17.062	0.044	0.926	0.00045	36.623	0.084	2.139	0.00083
Core	17.285	0.163	0.904	0.00412	36.871	0.037	2.133	0.00105
Zone 5 Data	<17.000		>0.920		<36.500		>2.150	
Rims w.r.t.	Decrease		Increase		Decrease		Increase	
Core	0.223		0.021		0.248		0.007	

Table 4.2 - Fig 4.6 part 2 area C & **D** - DLC3A:AF/02/01 (RM1a) - Raw data ranges for BaO, SrO, Or % and Pb-Pb isotopic systems.

whilst this decoupled comparison exists with RM1 and RM1a, overall trends in terms of the rim-ward Pb-Pb data with respect to cores are actually opposite (this is easily explained at the end of this section and by viewing **Table 4.6** later on).

The Pb-Pb systems for this alkali feldspar (see **Fig 4.6 part 2 area D)** including the data ranges in **Table 4.2**, show within the core zone 1 to zone 4 elevated levels of $^{206}Pb/^{204}Pb$ = 17.120 and $^{208}Pb/^{204}Pb$ = 36.800 compared to decoupled and depleted levels of an approximate constant for $^{207}Pb/^{206}Pb$ = 0.910 and $^{208}Pb/^{206}Pb$ = 2.134. Zone 5 depicts in all stated decoupled systems a marked symmetrical change (decrease from the core to this zone for $^{206}Pb/^{204}Pb$ to = 16.900, $^{208}Pb/^{204}Pb$ = 36.500 and increase for $^{207}Pb/^{206}Pb$ = 0.0923, $^{208}Pb/^{206}Pb$ = 2.150) with subsequent re-equilibriation towards the rims in terms of the data presented in the core regions.

As a whole, in contrast to RM1 alkali feldspars, this RM1a alkali feldspar has mantles/rims that are characterised by low $^{206}Pb/^{204}Pb$, high $^{207}Pb/^{206}Pb$, low $^{208}Pb/^{204}Pb$ and high $^{208}Pb/^{206}Pb$ (again this system is decoupled in RM1 feldspars from the same generation) relative to the cores. However, both zones 2 in RM1 and RM1a retain spike zones in elevated Ba and Sr, but a textural dissolution zone at the core in RM1a alkali feldspar as one transgresses into zone 2 is not discernible.

4.3.3 RM2

Zaniewski *et al.* (2006) classified RM2 in the field as a characteristic reddened coarse grained alkali feldspar-megacrystic biotite granite or pink granodiorite (where directly adjacent to diorite) and according to powder X-ray diffractometry (see previous chapter) is classified as being confined within the plagioclase-rich limits of the monzogranite field.

The subhedral to euhedral alkali feldspar in this megacrystic facies range up to 2cm and essentially show similar CL properties as previously described for RM1, with the characteristic threefold zonation profile with different orders of blue (see **Fig. 4.7(a)**) commonly evident in CL. Plagioclase can make up to half of the feldspar content in contrast to RM1 where it is variable and low, sometimes not being apparent in hand specimen [= plagioclase is richer in RM2 than RM1]. Where plagioclase is in contact with alkali feldspars, it can exhibit heavy embayment and an irregular form. Plagioclase crystals in this facies are extensively altered to dark brown luminescent sericite and slight replacement of plagioclase by alkali feldspar is observed, but in smaller quantities than in comparison to RM1.

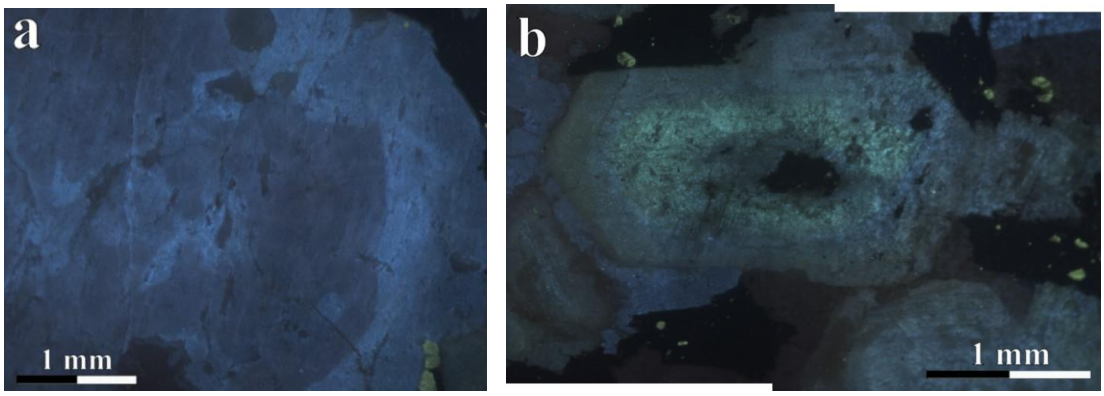


Fig. 4.7 (a-b) Cold CL images of feldspars within **DLC7A/RR120 (RM2)** as follows: **(a)** Subhedral alkali feldspar with luminescence, embayment and zonation profile as seen in RM1 (also seen within **Figure 4.2(a)**). **(b)** Subhedral oscillatory zoned plagioclase feldspar with three zones of interest in terms of CL. Core region comprises of a dark red luminescent core followed by a blue zone and a red luminescent rim (colours described do not appear to be 100% represented in photograph due to poor capture quality; which can be due to many photographic factors when working with a camera mounted on the third ocular of the microscope and a CL chamber).

As a whole plagioclase crystals display generally brick red/purple to even khaki yellow in CL, however, occasionally some unaltered variants can retain a remnant blue luminescence in the core, where the rims can comprise a dark brick red in colour. RM2 seems to have a greater complexity of CL zonation profiles for populations of plagioclases than

RM1 in terms of variants that sometimes can be juxtaposed; in accessing **Fig. 4.7(b)** the 2.5 mm euhedral plagioclase displays a core region comprising of a dark red luminescent core followed by a blue zone and a red luminescent rim which has not been observed occurring in RM1.

Varying concentrations of orange luminescent calcite (which can constitute 3% in mode in and around MME) is apparent and generally found in higher proportion as one migrates from the gradational contact towards the centre of mainland RM2 at Knockvologan. Calcite can occur as large crystals up to 1mm or as small disseminated grains and has also been identified as commonly occurring with what appers to be cleavage planes within titanite. Minor euhedral luminescent apatite is also found and can accur as acicular needles where directly adjacent to MME.

Rather than choosing a feldspar exhibiting the similar threefold varying blue orders of luminescent pattern similarly observed in RM1 to represent this facies (**Fig. 4.7(a)**), the sample chosen for study (see **Fig. 4.8 part 1 area A** & **B**) is a subhedral to euhedral 10 mm alkali feldspar megacryst with four blue CL principal zones of interest taken from a fresh looking granodiorite variant adjacent to a sheeted diorite intrusion at Knockvologan Beach. This sample was purposely chosen because of an extra concentric zone in CL and due to its close proximity to diorite at Knockvologan as opposed to homogeneous looking RM1, so that not only does the sample represent the ROMG components as a whole, inferences in relation to mafic-felsic interaction can be made in the discussion and conclusion section.

In observing the textural CL characteristics of the alkali feldspar in **Fig. 4.8 part 1 area A** & **B**, CL imaging highlights four roughly concentric mineral zones not easily discernible in BSE. The core (zone 1) comprises a dark blue/purple CL luminescent core with strong dissolution/embayment within the right hand bottom area in the core and also at the edge (towards zone 2 where it has a sharp rounded contact). Zone 2 comprises a slightly lighter dark blue/purple CL luminescence than the core and appears to have a gradational contact with zone 3; however the most obvious feature is that zone 3 has a punctuated bright blue luminescence which generally grades back to zone 4 which has similar affinities to zone 2.

EPMA analyses (where e.g. n=1 expresses the amount of analyses per zone) for each mineral zone show that for this alkali feldspar crystal reflecting RM2:

- DLC7A/RR120 (RM2) - **Fig. 4.8 part 2 area C** - zone 1 (Ab7.94, Or91.95 n=16); zone 2 (Ab8.77, Or90.96 n=8); zone 3 (Ab8.66, Or90.60 n=10); zone 4 (Ab10.07, Or89.27 n=15).

In fingerprinting *in-situ* elemental and Pb-Pb isotopic data with respect to CL in order to characterise the mineral zonation profile to this alkali feldspar, data ranges taken from **Fig. 4.8 part 2 area C** & **D** for each mineral zone are presented in **Table 4.3**. Within **Fig. 4.8 part 2 area C** the dark blue/purple CL core region (zone 1), Ba from point **1a103** prior to the elevated spike in zone 2 at point **1a93** remains relatively constant mainly sitting in-between 0.100 - 0.200 and data ranges are from 0.067 - 0.427, where 0.427 occurs adjacent to crossing into zone 2. Data for Ba, Sr and Or [mol. %] from points **1a104 - 1a38** (reflecting the right hand side of the alkali feldspar in **Fig. 4.8 part 1 area A** & **B**) are not commented on as traverses encompass less fresh zones and a clear characteristic dissolution zone whereby embayment within and towards the core is apparent; so not representative to a true data set. Whilst a small spike for Ba occurs at the start of zone 2 (comprising dark blue CL but an offset lighter blue than zone 1) at point **1a93** = 0.498, with higher ranges than zone 1 at 0.141 - 0.498, data drops back to around 0.015 - 0.002 reflecting data in the core zone 1. However as one progresses rim-wards towards zone 3 (bright blue in CL), where data ranges from 0.585 - 1.240, a sharp elevation (spike zone) to point **1a91** = 1.240 stands out with a major sharp decrease in gradient towards the rim at point **1a73** = 0.195 in zone 4 which has similar CL to the core zone 1 and zone 2 and data ranges of 0.058 - 0.852.

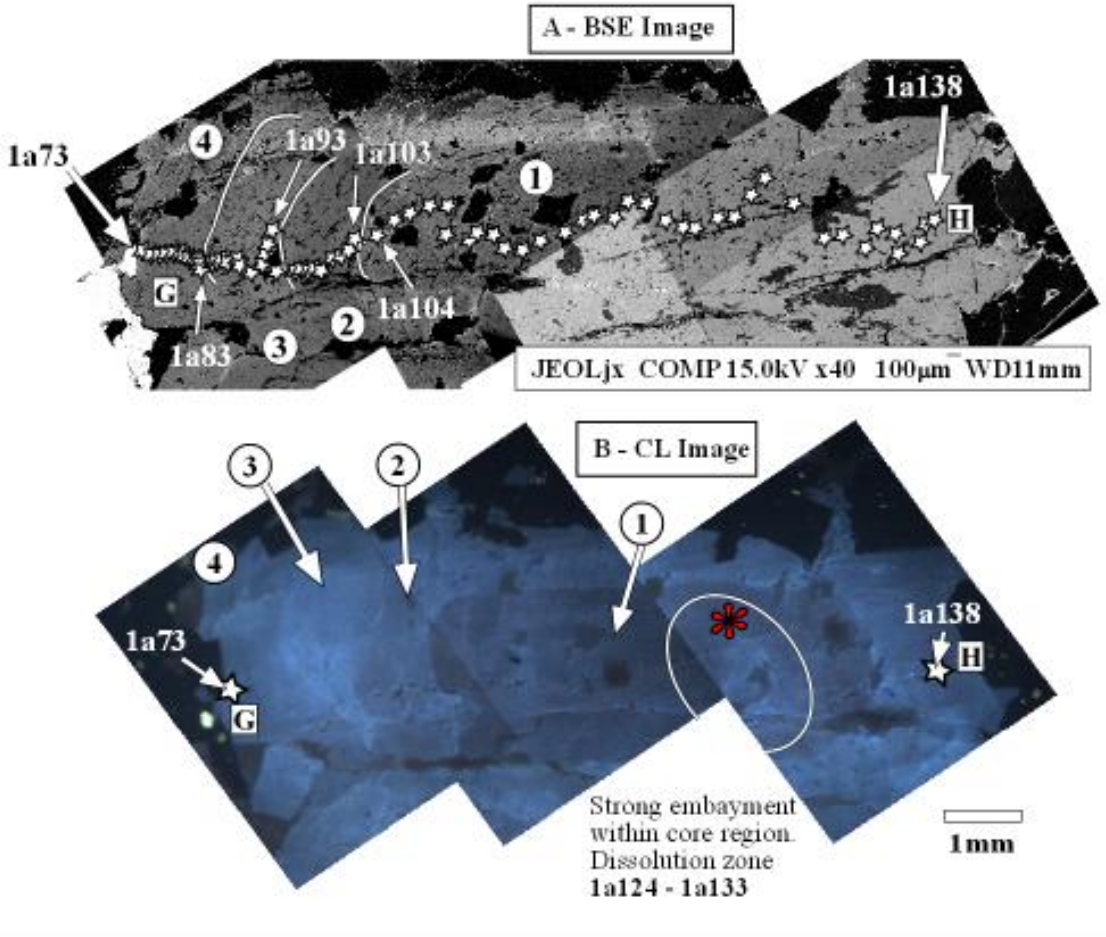
Little inferences on the patterns for the Sr traverse can be made due to its visual sporadic data set as one moves rim-wards from point **1a104** to point **1a73**. However, in line with Ba, the data ranges in **Table 4.3** show as one moves rim-wards an increase of 0.032 - 0.180 in the core zone 1 to 0.081 - 0.221 in zone 3, with a subsequent drop in Sr at the mantle/rim where data ranges reflect the core zone 1 ranging from 0.034 - 0.161.

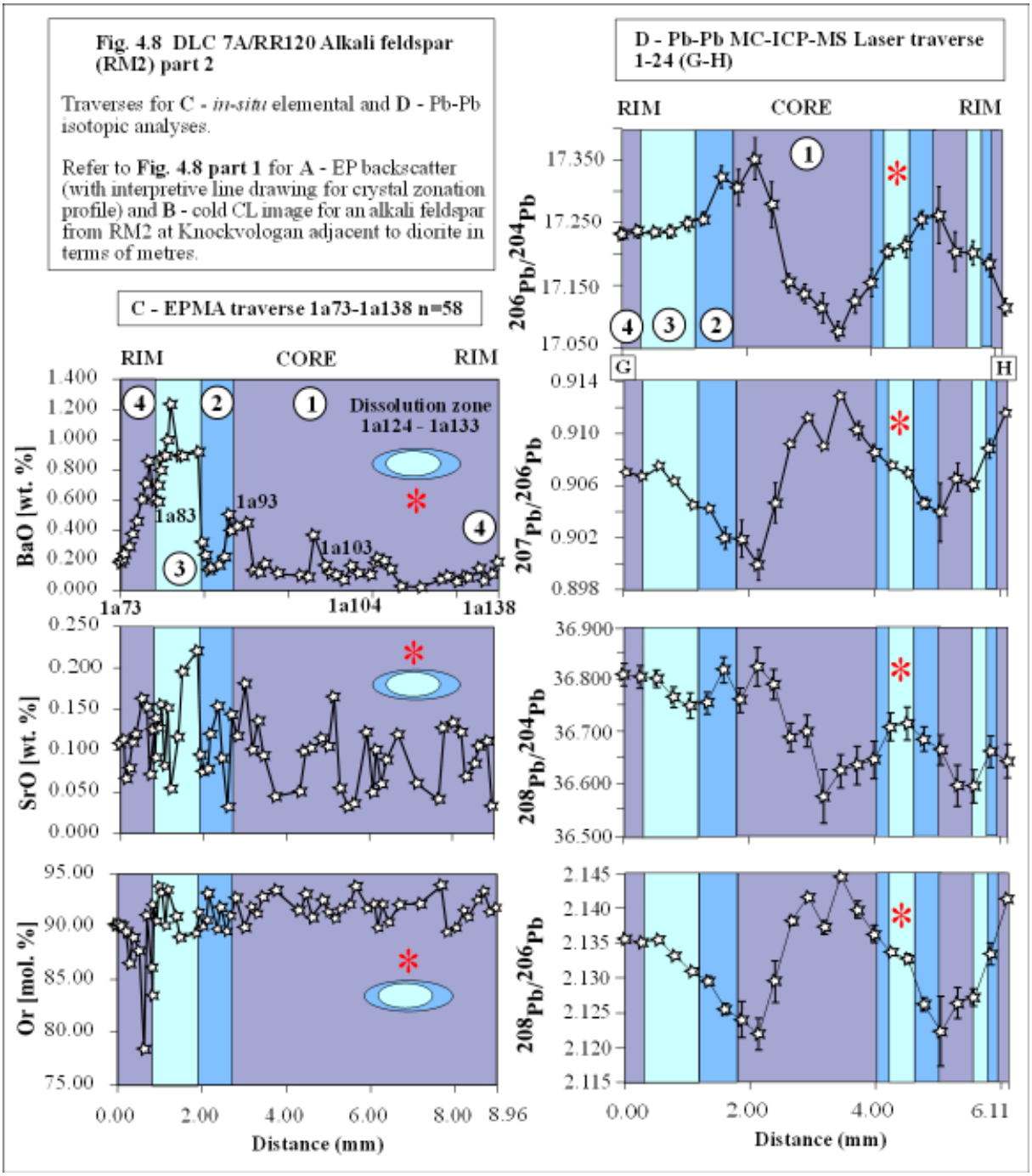
Pb-Pb isotopic traverses in **Fig. 4.8 part 2 area D** and **Table 4.3** depict a visual symmetry between $^{206}Pb/^{204}Pb$ and $^{208}Pb/^{204}Pb$ which have a pronounced increase of these systems in zone 2 whereby there is a general decrease from zone 2 to the rims at zone 4 (this occurs in opposite sense for $^{207}Pb/^{206}Pb$ and $^{208}Pb/^{206}Pb$), and both $^{206}Pb/^{204}Pb$ and $^{208}Pb/^{204}Pb$ systems as per RM1, are also decoupled to $^{207}Pb/^{206}Pb$ and $^{208}Pb/^{206}Pb$. $^{206}Pb/^{204}Pb$ shows overall rim-ward increase of 17.075 to 17.235 with elevation in zone 2 at 17.354 and decrease from this zone towards the mantle/rim zone 4 at 17.231; $^{207}Pb/^{206}Pb$ displays overall rim-ward decrease of 0.913 to 0.907 with a general decrease at the edge of the core towards zone 2 at

Fig. 4.8 DLC 7A/RR120 Alkali feldspar (RM2) part 1

A - EP backscatter (with interpretive line drawing for crystal zonation profile) and B - cold CL image for an alkali feldspar from RM2 at Knockvologan adjacent to diorite in terms of metres.

Refer to **Fig. 4.8 part 2** for respective traverses depicted for C - *in-situ* elemental and D - Pb-Pb isotopic analyses.




Fig. 4.8 DLC 7A/RR120 Alkali feldspar (RM2) part 2
Traverses for C - in-situ elemental and D - Pb-Pb isotopic analyses.
Refer to Fig. 4.8 part 1 for A - EP backscatter (with interpretive line drawing for crystal zonation profile) and B - cold CL image for an alkali feldspar from RM2 at Knockvologan adjacent to diorite in terms of metres.
C - EPMA traverse 1a73-1a138 n=58
D - Pb-Pb MC-ICP-MS Laser traverse 1-24 (G-H)
RIM
CORE
RIM
Dissolution zone 1a124 - 1a133
1a83
1a93
1a103
1a73
1a104
1a138
BaO [wt. %]
SrO [wt. %]
Or [mol. %]
Distance (mm)
206Pb/204Pb
207Pb/206Pb
208Pb/204Pb
208Pb/206Pb
G
H

Zone	BaO [wt. %]	SrO [wt. %]	Ab [mol.%]					
4 - Rim	0.058 - 0.852	0.034 - 0.161	6.32 - 12.98					
3	0.585 - 1.240	0.081- 0.221	6.39 - 15.41					
2	0.141 - 0.498	0.077 - 0.153	6.26 - 10.32					
1 - Core	0.067 - 0.427	0.032 - 0.180	6.16 - 9.73					
	$^{206}Pb/^{204}Pb$	2σ	$^{207}Pb/^{206}Pb$	2σ	$^{208}Pb/^{204}Pb$	2σ	$^{208}Pb/^{206}Pb$	2σ
Rim	17.231	0.009	0.907	0.00016	36.808	0.021	2.136	0.00018
Core	17.075	0.016	0.913	0.00022	36.575	0.051	2.144	0.00027
Rims w.r.t. Core	Increase 0.156		Decrease 0.006		Increase 0.233		Decrease 0.009	

Table 4.3 - **Fig. 4.8 part 2 area C** & **D** - DLC7A:RR120 (RM2) - Raw data ranges for BaO, SrO, Or % and Pb-Pb isotopic systems.

0.900 and increase from this zone towards the mantle/rim zone 4 at 0.907; $^{208}Pb/^{204}Pb$ shows overall rim-ward increase of 36.575 to 36.808 with elevation in zone 2 at 36.817 and decrease from this zone towards the mantle/rim zone 4 at 36.808; $^{208}Pb/^{206}Pb$ displays overall rim-ward decrease of 2.144 to 2.136 with a general decrease at the edge of the core towards zone 2 at 2.122 and increase from this zone towards the mantle/rim zone 4 at 2.136.

Overall, if one observes *in-situ* elemental and Pb-Pb data in **Fig. 4.3 part 2 area C** & **D** (for RM1 alkali feldspar) compared to data in **Fig. 4.8 part 2 area C** & **D** (for RM2 alkali feldspar), similarities of both RM1/RM2 alkali feldspars are apparent across the two facies. Both comprise clear dissolution zones within the core region (zone 1) and essentially a similar CL mineral zonation profile with elevated Ba (increase of approximately 0.700%), Sr spike zones (increase of 0.100%) (with general decrease in Or [mol. %] ~ 5.00-10.00 and increase in Ab [mol. %] ~ 5.00) in zone 3 for RM2 and zone 2 for RM1, which both display the lightest and brightest order of blue in CL; essentially the additional zone 3 for RM2 alkali feldspar here mirrors zone 2 for RM1 alkali feldspar with gradation back to rim that displays similar textural CL, elemental and Pb-Pb trends to that of the core region. Also both RM1/RM2 not only exhibit exactly the same decoupled Pb-Pb isotopic systems, but also show the same trends in terms of the rims with respect to cores (i.e. both RM1/RM2 alkali feldspars have mantles/rims that are characterised by high $^{206}Pb/^{204}Pb$, low $^{207}Pb/^{206}Pb$ and high $^{208}Pb/^{204}Pb$ relative to the cores). Clearly for RM2 alkali feldspar, the elevated and important observation of punctuated increase of high $^{206}Pb/^{204}Pb$ and high $^{208}Pb/^{204}Pb$ as one moves rim-ward in toward zone 2 (marked by a sharp contact with the rounded core region zone 1) is not discernible for the alkali feldspar in **Fig 4.3 part 2 area D**, however there is a small subtle increase in these systems for zone 2 in the alkali feldspar in **Fig 4.4 part 2 area D**.

The nature of the decoupled $^{208}Pb/^{206}Pb$ in RM1 within two alkali feldspar samples from the same generation is unknown; however as all other highlighted RM1/RM2 alkali feldspar Pb-Pb systems generally exhibit the same CL profile and trends between each other in terms of decoupling and core to rim trends, a safe assumption is that (in terms of mantles/rims with respect to cores) as $^{208}Pb/^{206}Pb$ is low for RM2 alkali feldspar, it is highly probable that that $^{208}Pb/^{206}Pb$ is also low for RM1 alkali feldspar if they are indeed sourced from one granitoid parental magma.

4.3.4 Mafic components; MME Phase 1 & MME Phase 2

Zaniewski *et al.* (2006) and Chapter Two highlight all Type 1 diorite intrusions within the *'Knockvologan mixing and mingling zone are not strictly 100% diorite, but were mapped where there is >60-70% diorite/MME with respect to host RM2 granitoid'* and thus MME presented here reflect the petrological heterogeneity in Type 1 diorite and differing modal mineralogy to host RM1/RM2 granitoid as previously documented. Type 1 diorite and their associated MME are classified in the field as plagioclase hornblende-phyric biotite diorites. An exception of a rare pyroxene-phyric appinitic (see Muir *et al.* 1997 for definition) enclave exists on Eilean nan Griogag at Knockvologan (see **Fig. 4.1** and refer back to Chapter Two). According to powder X-ray diffractometry (see previous chapter) mafic components are classified as monzodiorites.

MME are dominantly concentrated in the inner portion of RM2 at Knockvologan in random distribution as swarms generally confined to adjacent sheets comprising Type 1 diorite. MME rarely occur within the evolved outer body of the pluton (RM1), and occur as ovoid (some with cauliflowered margins) to discoid bodies ranging from 0.1 to 1.0 m. To reflect geochemically sampling a representative end-spectrum of mafic components for the intrusion, double MME phases at Knockvologan/Eilean nan Griogag (see **Fig. 4.1** for locations and **Fig. 4.9**) meant that crystals (of andesine composition) from each enclave phase could be analysed.

Texturally MME are fine to medium grained comprising megacrysts of both plagioclase and perthitic orthoclase. Plagioclase megacrysts usually display compositional zoning similar to host granitoid, and alkali feldspars occur as xenocrysts in MME. Biotite and amphibole (as undeformed polygranular aggregates (clots), with some containing rare relict pyroxene that is prevalent in an appinitic MME similar to those described in Castro &

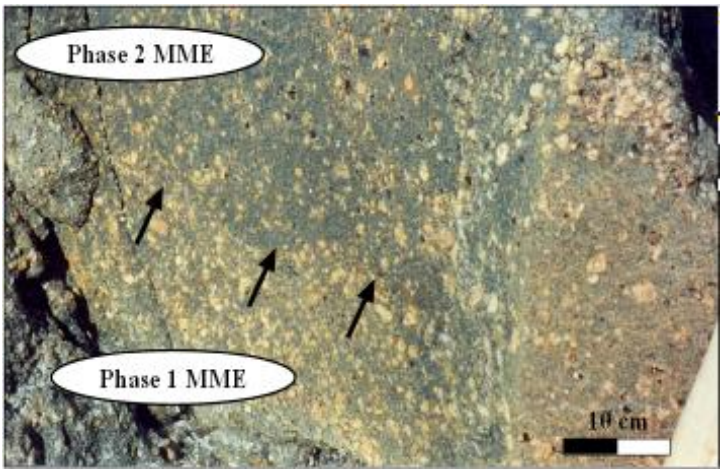


Fig. 4.9 Double MME at Knockvologan beach (NM [3084 1967]) depicting locality where Phase 1 and 2 MME feldspar crystal samples are directly obtained from (modified from Zaniewski *et al*. 2006); refer to text for description of MME phases, and **Fig. 4.1** for location of samples used).

Stephens 1992) are the main mafic phases. Accessories comprise acicular and non-acicular apatite, oscillatory zoned titanite, zircon, calcite and allanite.

In CL, all MME exhibit at least two different types of generations of plagioclase feldspars juxtaposed which is evident in the groundmass (**Fig. 4.10 (a) to (d)**); one group has bright blue unaltered luminescent cores with red luminescence at the rims and the other group has red luminescent cores, punctuated by a bright blue CL concentric zone, whereby this second variety can sometimes display an additional zone in the form of gradation from this bright blue luminescent zone to marginal red luminescence at the mantles/rims (see andesine micro-phenocryst in **Fig. 4.10 (a)**). This feature has also been seen throughout the intrusion but difficult to spot as particularly in MME, plagioclase with blue luminescent cores are dominant, however the ones comprising red cores only constitute a few percent of those found. Alkali feldspars show bright blue CL and are readily distinguished from the red luminescent plagioclases, interstitially comprising 5 - 10% of the mode within monzogranitic variants and also as smaller groups of crystals where the contacts between sub-grains display a dark purple luminescence. Rounded quartz megacrysts with or without an amphibole/biotite occellus phase occur in varying proportions demonstrating the same dark blue CL as observed in the granite and some broad zoning is apparent.

The broad range of CL observations in both alkali and plagioclase feldspar as previously described for all MME, occur heterogeneously within both Phase 1 and 2 MME as observed in **Fig. 4.9**. In simple terms, the difference between the two phases is the

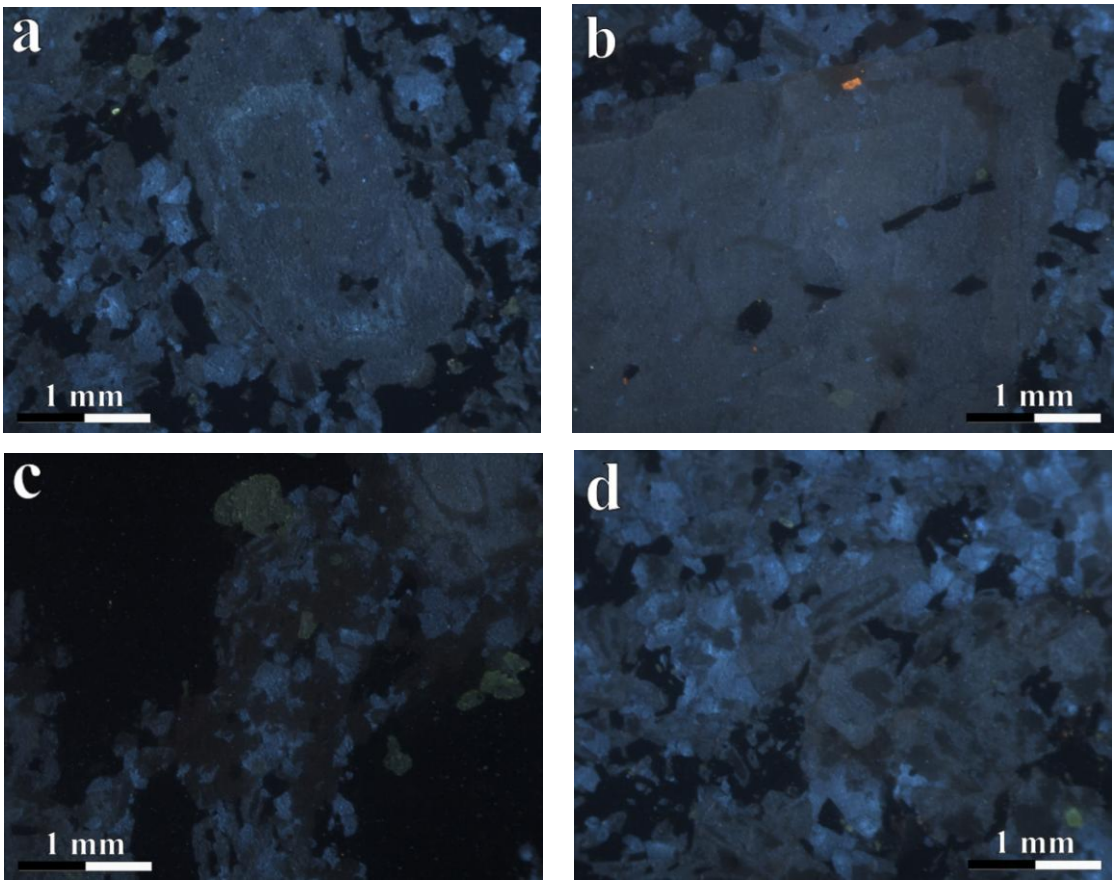


Fig. 4.10 (a-d) Cold CL images of feldspars within **DLC10-11/RR019 Phase 1 Type MME** as follows: **(a)** Subhedral plagioclase feldspar micro-phenocryst with embayed core region comprising threefold luminescent profile as discussed in the text. Surrounding groundmass has feldspars of red and blue luminescence in core regions with different zonation profiles juxtaposed. **(b)** Alkali feldspar xenocryst with rapakivi rim. **(c)** Groundmass with linear areas of anhedral feldspars with blue core region followed by a dark blue rim or feldspars with dark turbid red core (that may be slightly embayed) with a lighter or intermediate red rim juxtaposed. **(d)** Same as in the previous plate however groundmass feldspars form a glomerocrystic patch (with dark red cores and lighter red rims) in the bottom right area of the photo.

heterogeneous porphyritic density of xenocrsts/phenocrysts. The double enclave phase in **Fig. 4.9** essentially depicts Phase 1 characterised by a greater abundance 40 - 70% phenocrysts (chiefly occurring as rusty orange swirls of alkali feldspar xenocrysts, but with unmantled and mantled amphibole clots (with alkali feldspar as a common mantling phase) and quartz occelli) compared to 10 - 20% in Phase 2 MME whereby in **Fig. 4.9**, dark black amphibole clots are more discernible in the field. Phase 2 MME and Phase 1 MME straddle each other however the contact (denoted by black arrows) is defined by alkali feldspars heterogeneously distributed along cuspate interface in-between both enclaves.

Phase 1 MME plagioclase

In accessing the andesine feldspar samples taken to represent the double MME phase, plagioclase from Phase 1 MME, which is taken directly from the outcrop within **Fig. 4.9** at Knockvologan Beach (see **Fig. 4.1** for locality) is firstly assessed. The subhedral plagioclase feldspar micro-phenocryst shown in **Fig 4.11 part 1 area A** & **B** both display three mineral zones in CL, much more difficult to make out in BSE, where **Fig. 4.9** is used for CL as analogous to this feldspar sample; because it is from the same generation, has the same CL profile pattern and the CL image obtained for this feldspar was of poor quality. Mineral zonation is difficult to make out here because of instrumental bias produced in using the digiman camera. However the rounded red luminescent core is sharply terminated by a bright blue luminescent zone; this is succeeded by sharp red luminescence occurring at the mantle/rims, which is similar to that of the core region. Bulk average EPMA analyses (where e.g. n=1 expresses the amount of analyses per zone) for each mineral zone show that for this plagioclase feldspar crystal considered in Phase 1 MME:

- DLC10-11B/RR019 (Phase 1 MME) - **Fig. 4.11 part 2 area C** - zone 1 (Ab63.19, Or1.05 n=12); zone 2 (Ab59.69, Or0.89 n=5); zone 3 (Ab65.47, Or1.05 n=7).

In analysing CL mineral zonation with respect to *in-situ* geochemical data to typify trends in Phase 1 MME, data ranges taken from **Fig. 4.11 part 2 area C** & **D** are presented in **Table 4.4**. The elemental traverses in **Fig. 4.11 part 2 area C**, from point **1a602** to **1a630**, for Ba, Sr and Ab [mol. %] show sporadic data from point to point and visual asymmetry/opposites in terms of either increases/decreases in zone 2 (punctuated light blue CL compared to the red CL in core and mantle/rim); as such it is difficult to identify any subtle trends. Therefore for elemental data, it is probably wise to concentrate on the data ranges presented in **Table 4.4** as the single points for Ba, Sr and Or [mol. %] in zone 2 on either sides of the elemental traverse data for **Fig. 4.11 part 2 area C** skew core to rim interpretations in an opposite manner, and any interpretation should not be made on one point alone. For Ba, elemental ranges show for the core/zone 1 = 0.011 - 0.068, there is an increase to zone 2 = 0.033 - 0.080 and a drop back to similar affinities at the core occurring in zone 3 (mantle/rim) = 0.014 - 0.070, so it is reasonable this bright blue CL zone is associated with higher Ba. However, for Sr and Ab [mol. %], the opposite trend in fact occurs; zone 2 depleted Sr data = 0.240 - 0.298 compared to elevated cores/zone 1 = 0.249 - 0.308 and similar elevated data for zone 3 (mantle/rim data) = 0.254 - 0.309. Similarly Ab [mol. %]

Zone	BaO [wt. %]	SrO [wt. %]	Ab [mol. %]
3 - Rim	0.014 - 0.070	0.254 - 0.309	62.64 - 68.19
2	0.033 - 0.080	0.240 - 0.298	52.32 - 67.75
1 - Core	0.011 - 0.068	0.249 - 0.308	58.08 - 68.65

	$^{206}Pb/^{204}Pb$	2σ	$^{207}Pb/^{206}Pb$	2σ	$^{208}Pb/^{204}Pb$	2σ	$^{208}Pb/^{206}Pb$	2σ
Rim Av. n=2	16.244	0.205	0.931	0.00085	35.315	0.448	2.175	0.00238
Core Av. n=5	16.221	0.116	0.933	0.00161	35.295	0.239	2.175	0.00189
Rims w.r.t.	Increase		Decrease		Increase		N/a	
Core	0.023		0.002		0.021		0.000	

Table 4.4 - **Fig. 4.11 part 2 area C** & **D** - DLC10-11B:RR019 (MME1) - Raw data ranges for BaO, SrO, Or % and Pb-Pb isotopic systems.

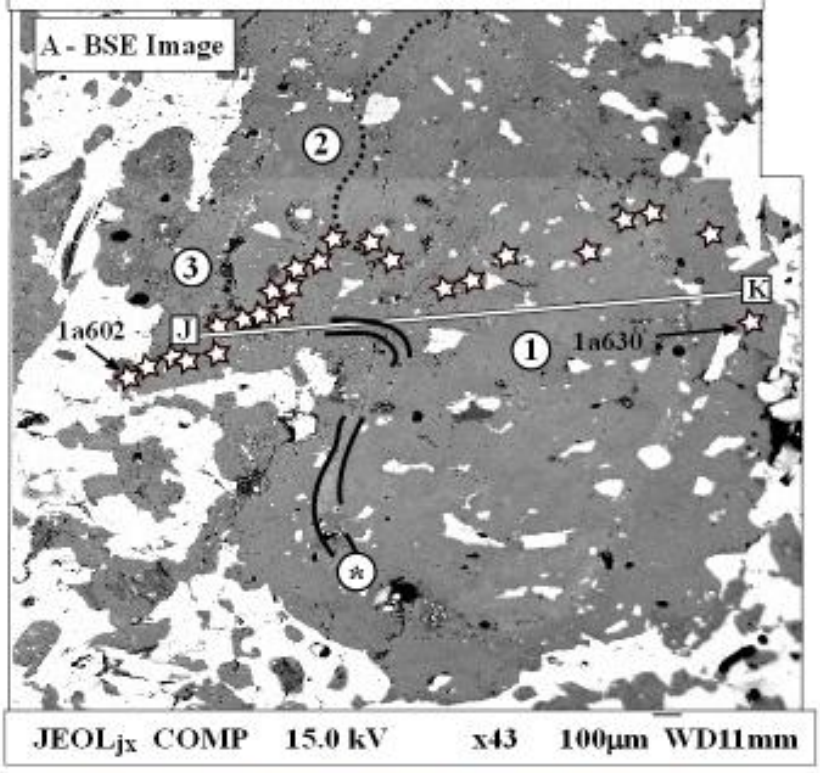
shows zone 2 depleted data = 52.32 - 67.75 compared to elevated cores/zone 1 = 58.08 - 68.65 and similar elevated data for zone 3 (mantle/rim data) = 62.64 - 68.19.

Pb-Pb data in **Fig. 4.11 part 2 area D** highlights for Phase 1 MME, mirrored trends with $^{206}Pb/^{204}Pb$ and $^{208}Pb/^{204}Pb$, which are in comparison to RM1/RM2 alkali feldspars in that these are also decoupled to $^{207}Pb/^{206}Pb$ and $^{208}Pb/^{206}Pb$ isotope systems. In comparison to *in-situ* elemental data, Pb-Pb data all show asymmetry in all systems whereby the data points in zone 2 (bright blue CL) on each side of core region zone 1, either show increases or decreases in each isotopic system, and as such due to a limited data set comprise 5 analyses per traverse, and direct interpretation on trends from core to mantle/rims would be speculative. As such, inferences are made from basic calculated average Pb-Pb data ranges for each mineral zone in **Table 4.4**. $^{206}Pb/^{204}Pb$ shows a rim-ward increase of 0.023 from 16.221 to 16.224; $^{207}Pb/^{206}Pb$ displays a rim-ward decrease of 0.002 from 0.933 to 0.0931; $^{208}Pb/^{204}Pb$ shows rim-ward increase of 0.021 from 35.259 to 35.315; $^{208}Pb/^{206}Pb$ depicts the same averages of 2.175 so little inferences can be made, however as all other Pb-Pb isotope systems in RM1/RM2 show the same core to rim trends for feldspars and decoupling in $^{207}Pb/^{206}Pb$ and $^{208}Pb/^{206}Pb$, it is highly probable $^{208}Pb/^{204}Pb$ in Phase 1 MME mirror these trends and low $^{208}Pb/^{206}Pb$ occurs as one moves rim-ward. Thus, Phase 1 MME is considered as having rims comprising high $^{206}Pb/^{204}Pb$, low $^{207}Pb/^{206}Pb$, high $^{208}Pb/^{204}Pb$ and low $^{208}Pb/^{206}Pb$ with respect to cores which incidentally are the same Pb-Pb trends for alkali feldspars observed in RM1/RM2.

Fig. 4.11 DLC 10-11B/RR019 Plagioclase feldspar (Phase 1 MME) part 1

A - EP backscatter image of an embayed plagioclase micro-phenocryst from within phase one of double MME as seen within **Fig. 4.9**. Note amphibole inclusion trails sub-parralel to a conspicuous zone * indicative of magma mixing. It is envisaged from **B** - CL that 3 definitive zones exist which is demonstrated within a similar representative micro-phenocryst below.

Refer to **Fig. 4.11 part 2** for respective traverses depicted for **C** - *in-situ* elemental and **D** - Pb-Pb isotopic analyses.



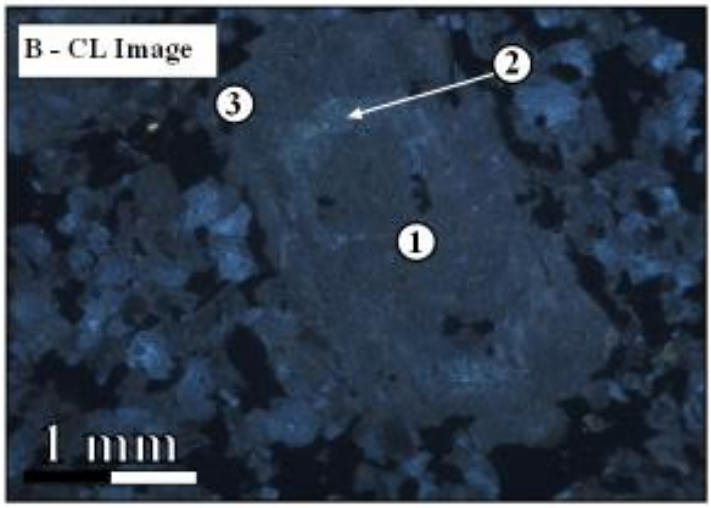
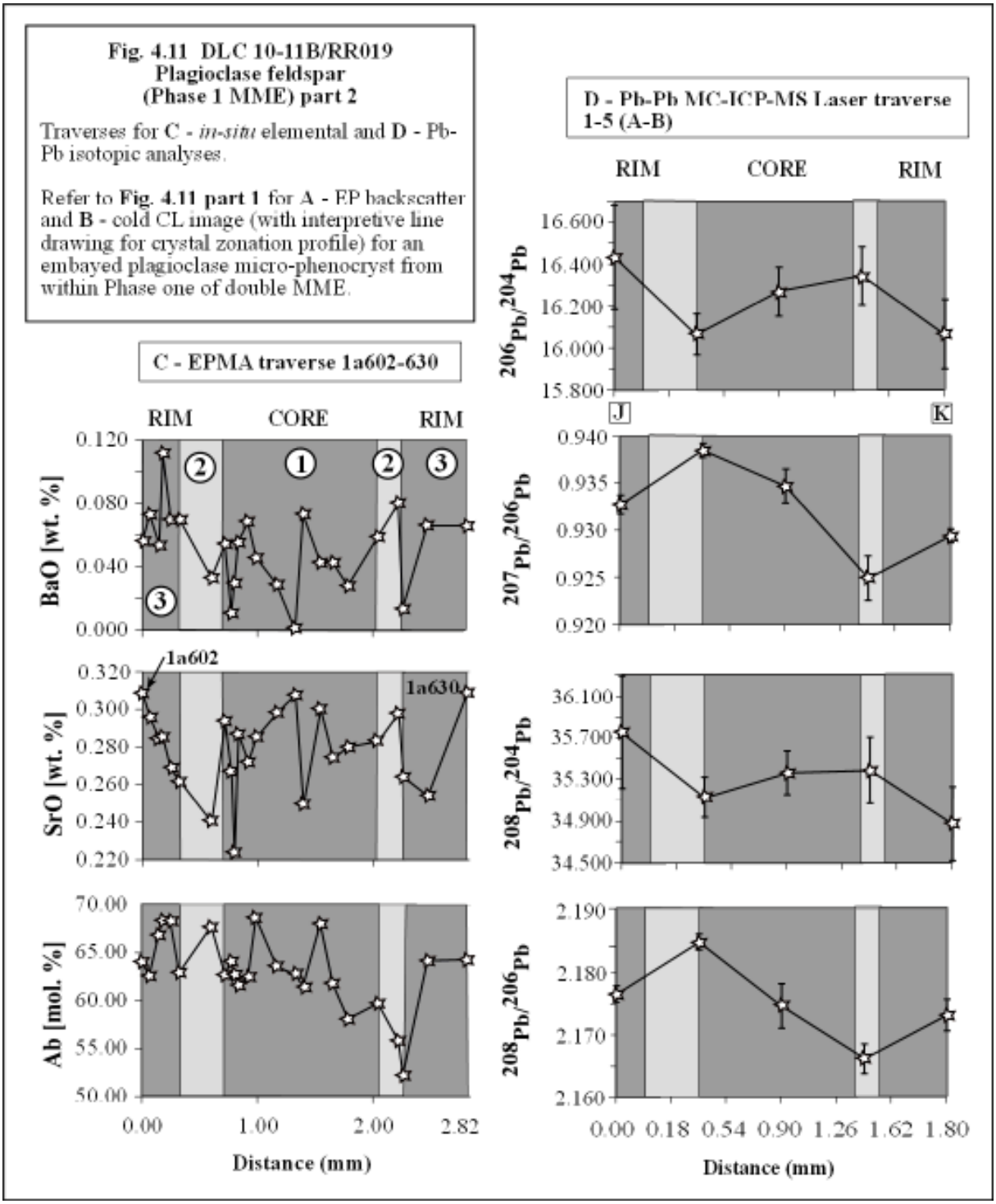


Fig. 4.11 DLC 10-11B/RR019
Plagioclase feldspar
(Phase 1 MME) part 2

Traverses for C - *in-situ* elemental and D - Pb-Pb isotopic analyses.

Refer to **Fig. 4.11 part 1** for A - EP backscatter and B - cold CL image (with interpretive line drawing for crystal zonation profile) for an embayed plagioclase micro-phenocryst from within Phase one of double MME.



Phase 2 MME plagioclase

The plagioclase considered for study taken from Phase 2 MME (as previously characterised in the text and **Fig. 4.9**), is taken from a similar enclave lithology from a double enclave phase occurring at Eilean nan Griogag (see **Fig. 4.1** for locality). **Fig. 4.12 area A part 1** displays a BSE image from at least a third of the milky/glassy white tabular subhedral plagioclase xenocryst (of andesine in composition) that is rounded at the edges set and in a fine to medium grained monzodioritic groundmass (see photo in **Fig. 4.12 area B part 1**). The BSE image in **Fig. 4.12 area A part 1** defines a plagioclase with four principle relatively concentric zones of interest whereby the core zone 1 is rounded and zone 3 is embayed inward towards zone 2. Little inferences were made from CL due to the size and scale of the feldspar in question (as a mosaic would have produced at least 10 overlapping CL photos), however varying orders of dark purple/blue CL are observed across the crystal.

Bulk average EPMA analyses (where e.g. n=1 expresses the amount of analyses per zone) for each mineral zone show that for this plagioclase feldspar crystal considered in Phase 2 MME:

- DLC8-9F/JR37 (Phase 2 MME) - **Fig. 4.12 part 2 area C** - zone 1 (Ab62.46, Or1.01 n=11); zone 2 (Ab57.64, Or1.45 n=6); zone 3 (Ab55.10, Or2.02 n=10); zone 4 = (Ab65.33, Or1.22 n=8).

In analysing CL mineral zonation with respect to *in-situ* geochemical data to typify trends in Phase 2 MME, data ranges taken from **Fig. 4.12 part 2 area C** & **D** are presented in **Table 4.5**.

The core to rim elemental traverses in **Fig. 4.11 part 2 area C**, from point **1a71** to **1a37** highlight for Ba, sporadic data points in between 0.014 - 0.138 for core zone 1 and 0.055 - 0.101 for zone 2, with what appears a small elevation from point **1a61** of 0.076 as one moves within zone 2. A small spike zone for Ba in zone 3 exists with Ba displaying clearly the highest data range in-between 0.070 to 0.173, with subsequent decrease of Ba at the mantle/rim zone 4 of 0.025 - 0.064 reflecting core zone 1/zone 2 data. Sr on the other-hand generally depicts rim-ward elevation from zone 3 = 0.188 - 0.233 and rim zone 4 = 0.158 - 0.272 compared to core zone 1 = 0.121 - 0.233 and zone 2 = 0.181 - 0.233. Or [mol. %] visually generally increases from core zone 1, across zone 2 and towards the spike in zone 3 at 2.400, with decrease from this zone to the mantle/rim zone 4 showing data ranges similar to core zone 1/zone 2; Ab [mol. %] data ranges oppositely mirror this trend, with zone 3

Zone	BaO [wt. %]	SrO [wt. %]	Ab [mol. %]					
4 - Rim	0.025 - 0.064	0.185 - 0.272	57.26 - 64.95					
3	0.070 - 0.173	0.188 - 0.233	49.86 - 59.46					
2	0.055 - 0.101	0.181 - 0.258	49.38 - 63.23					
1 - Core	0.014 - 0.138	0.121 - 0.233	58.04 - 69.90					
	$^{206}Pb/^{204}Pb$	**2σ**	**$^{207}Pb/^{206}Pb$**	**2σ**	**$^{208}Pb/^{204}Pb$**	**2σ**	**$^{208}Pb/^{206}Pb$**	**2σ**
Rim	16.599	0.048	0.932	0.00064	36.163	0.110	2.179	0.00145
Core	16.761	0.096	0.914	0.00095	36.062	0.188	2.151	0.00185
Rims w.r.t. Core	Decrease 0.162		Increase 0.018		Increase 0.101		Increase 0.028	

Table 4.5 - **Fig. 4.12 part 2 area C** & **D** - DLC8-9F/JR37 (MME2) - Raw data ranges for BaO, SrO, Or % and Pb-Pb isotopic systems.

depicting the lowest range of 49.86 - 59.46 with increase at the mantle/rim of 57.26 - 64.95 (**Table 4.5**) reflecting core zone 1 data of 58.04 - 69.90, and zone 2 data of 49.38 - 63.23.

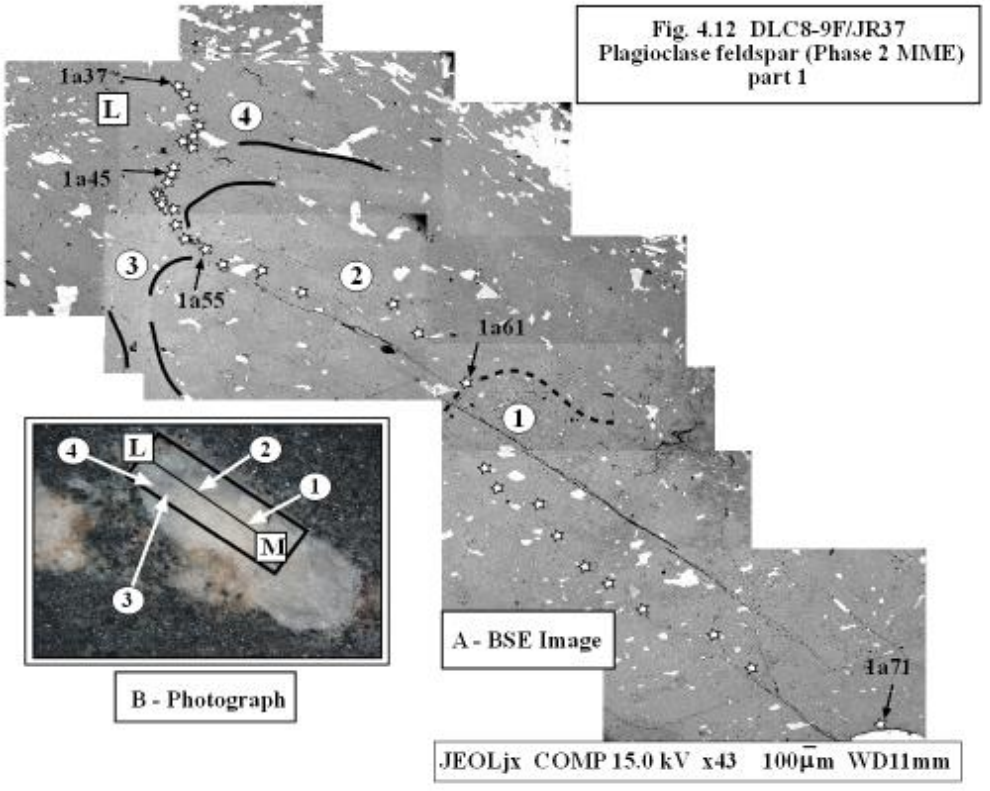
Pb-Pb data in **Fig. 4.12 part 2 area D** highlights for Phase 2 MME, the data trends are easier to make out than elemental data, and this is the only feldspar presented here where $^{206}Pb/^{204}Pb$ appears to be decoupled to all other Pb-Pb isotopic systems. Also, for all Pb-Pb systems in **Fig. 4.12 part 2 area D**, the fourth analyses in from the rim (zone 3) generally has the greatest errors to two standard deviation ($^{206}Pb/^{204}Pb$ = ±0.148; $^{207}Pb/^{206}Pb$ = ±0.00583; $^{208}Pb/^{204}Pb$ = ±0.133; $^{208}Pb/^{204}Pb$ = ±0.01094); so actual spikes created as a result of this data point in all systems may not actually be as pronounced in terms of what they visually appear. Zone 3 (fourth point in from rim), shows in comparison to the fifth point in from the rim (zone 2) pronounced increase for $^{206}Pb/^{204}Pb$ = 16.935 (0.384 increase) and $^{208}Pb/^{204}Pb$ = 36.413 (0.384 increase) with a decrease for $^{207}Pb/^{206}Pb$ = 0.918 (0.010 decrease) and increase for $^{208}Pb/^{204}Pb$ = 2.151 (0.497 increase) as one moves rim-wards.

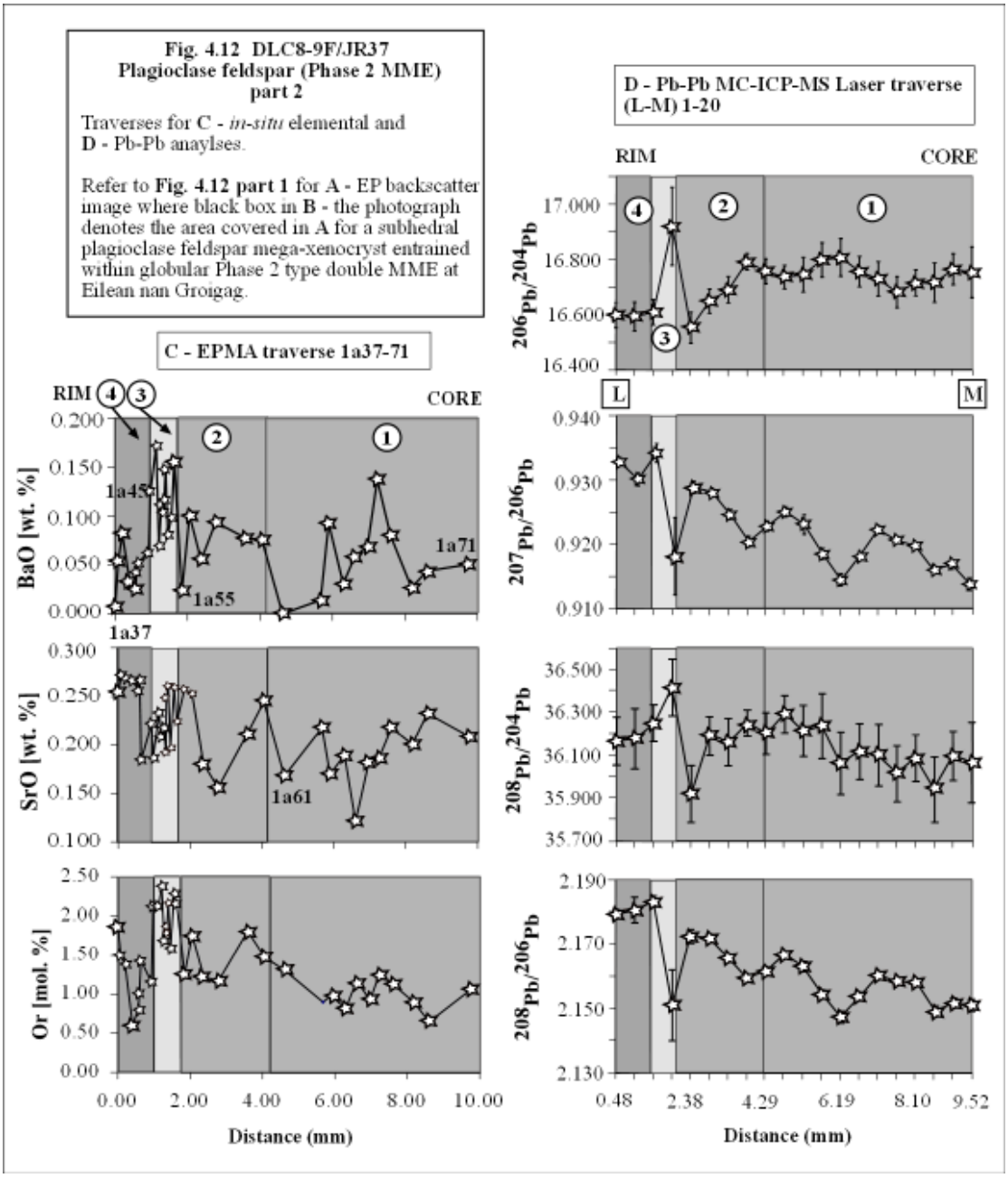
As a whole rim-ward Pb-Pb isotope trends show; $^{206}Pb/^{204}Pb$ has a decrease of 0.162 from 16.761 to 16.599; $^{207}Pb/^{206}Pb$ has an increase of 0.018 from 0.914 to 0.932; $^{208}Pb/^{204}Pb$ has an increase of 0.101 from 36.062 to 36.163; $^{208}Pb/^{206}Pb$ has an increase of 0.028 from 2.151 to 2.179. Thus, Phase 2 MME plagioclase feldspar is considered as having rims comprising low $^{206}Pb/^{204}Pb$, high $^{207}Pb/^{206}Pb$, high $^{208}Pb/^{204}Pb$ and high $^{208}Pb/^{206}Pb$ with respect to cores which incidentally with exception of $^{208}Pb/^{204}Pb$ demonstrate the same Pb-Pb trends for alkali feldspar observed in RM1a.

Subhedral feldspar mega-xenocryst entrained within globular Phase 2 type double MME at Eilean nan Groigag set in similar affinities to the critical locality observed at Knockvologan beach (see **Fig. 4.9**). Note amphibole and biotite inclusion trails within zone four. Zone three is the most characteristic being relatively inclusion free containing embayments towards zone two. Glomerocrystic amphibole and alkali feldspar aggregations occur at the edges of the crystal suggestive of net capture during mixing within a turbulent environment. Diagrams as follows are **A** - EP backscatter image where black box in **B** - the photograph below denotes the area covered in **A** (feldspar is 15 mm long).

Refer to **Fig. 4.12 part 2** for respective traverses depicted for **C** - *in-situ* elemental and **D** - Pb-Pb anaylses.

Fig. 4.12 DLC8-9F/JR37
Plagioclase feldspar (Phase 2 MME)
part 1




Fig. 4.12 DLC8-9F/JR37
Plagioclase feldspar (Phase 2 MME)
part 2
Traverses for C - in-situ elemental and
D - Pb-Pb anaylses.
Refer to Fig. 4.12 part 1 for A - EP backscatter image where black box in B - the photograph denotes the area covered in A for a subhedral plagioclase feldspar mega-xenocryst entrained within globular Phase 2 type double MME at Eilean nan Groigag.
C - EPMA traverse 1a37-71
D - Pb-Pb MC-ICP-MS Laser traverse (L-M) 1-20
RIM
CORE
BaO [wt. %]
SrO [wt. %]
Or [mol. %]
1a37
1a45
1a55
1a61
1a71
Distance (mm)
L
M
206Pb/204Pb
207Pb/206Pb
208Pb/204Pb
208Pb/206Pb
Distance (mm)

4.4 Discussion and Conclusions

As all feldspar micro-samples representing the reverse zonation through each component of the ROMG have now been individually characterised in terms of their CL petrography, *in-situ* elemental and Pb-Pb data trends (including gross CL petrography of the components each feldspar occurs in) interpretive inferences on how each feldspar/component evolved can essentially be made. Also in comparing/contrasting the bulk data gleaned per feldspar per component, a model for the evolution of the igneous complex can also be discussed.

CL zonation, *In-situ* Elemental and Pb-Pb traverses (crystal chemo-stratigraphy)

CL has enabled characterising a specific type of threefold mineral zonation to be prevalent in all feldspars documented in this study that occur throughout all components of the ROMG. Characteristic dissolution zones at the core followed by a punctuated zone 2 associated with general elevations of Ba, Sr ~ 0 - 1 [wt. %] and Ab [mol. %] (or decrease in Or [mol. %], the largest differences occurring in RM1 by around 10.00%) with elemental re-equilibriation back towards the rims is apparent to some degree in all crystal samples presented in this chapter, particularly in alkali feldspars. Such resorption surfaces that have these elemental patterns (as also described by Stimac & Wark 1992; Cox *et al.* 1996) corresponding with rim-ward increase of $^{206}Pb/^{204}Pb$ and $^{208}Pb/^{204}Pb$ in alkali feldspar within ROMG felsic components (except RM1a) and Phase 1 MME andesine having spikes of these systems elevated in bright blue CL zone 2 (and assuming crust has low $^{206}Pb/^{204}Pb$ and $^{208}Pb/^{204}Pb$ i.e. unradiogenic components compared to any mafic/mantle component (see Dickin 1981; Dickin et al. 1984; Peate & Hawkesworth 2005; Peate *et al*. 2008)) indicate dissolution during mixing of magmas (mafic magmatic recharge) with contrasting temperature and composition, with mixing between a crustal and mantle-derived component (as highlighted in phase diagrams of Crabtree & Lange 2011) being highly likely.

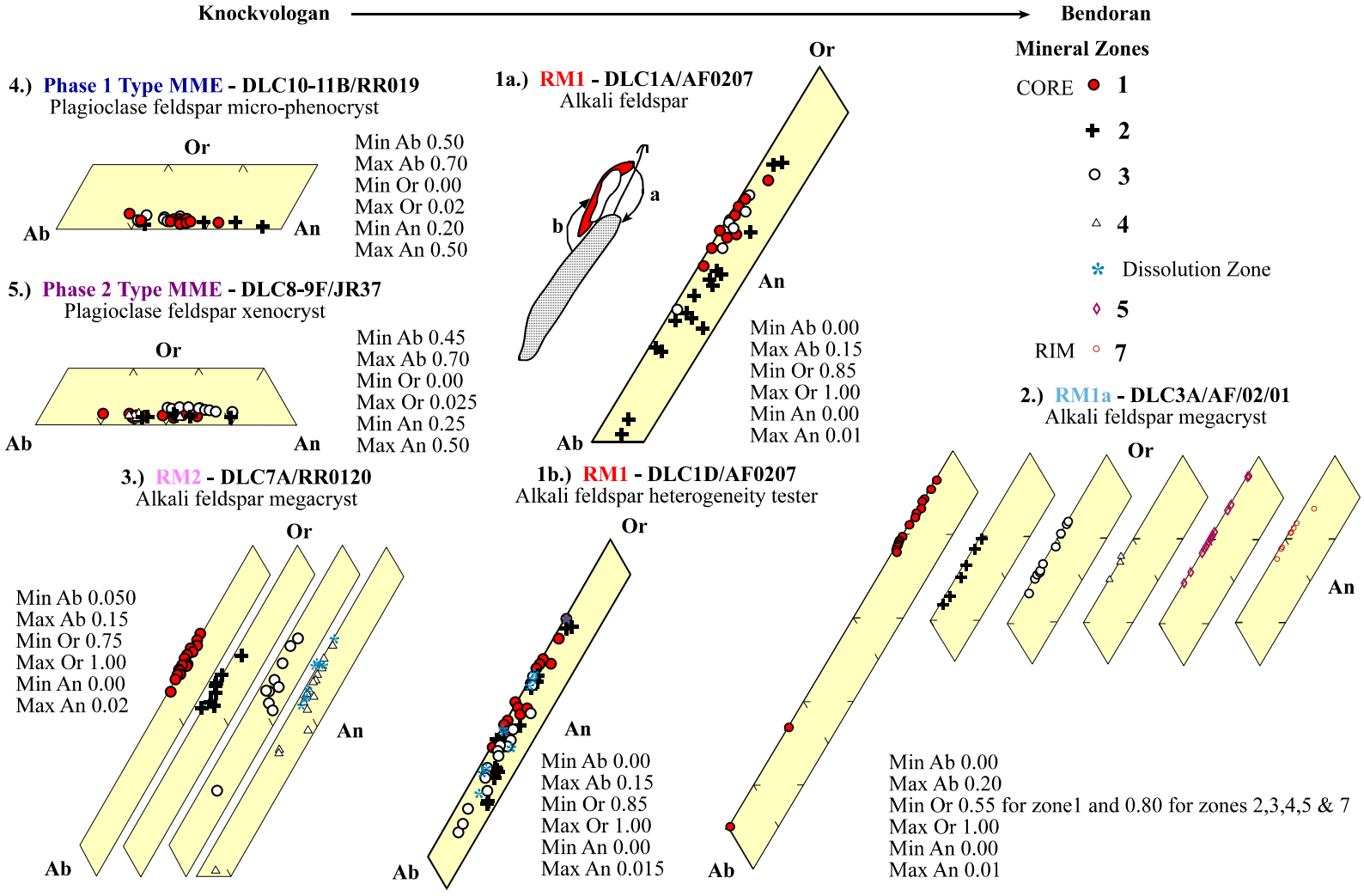
The observation that these textural CL and geochemical patterns occur throughout the intrusion also highlight that magma-mixing has occurred at depth within such components prior to emplacement, leaving a field-scale broad spectrum of diorite and MME and homogeneous looking RM1 granitoid with respect to RM2 (i.e. the reverse zonation). Whilst these trends in relation to dissolution zones are common in alkali feldspars within RM1/RM2 throughout the complex with the use of cold CL, the fact that different MME phases themselves exhibit two different plagioclase feldspar types juxtaposed with contrasting

blue/red CL within core/rim regions locally throughout the rarely occurring Phase 1/2 MME also highlights dynamic phenocryst exchange between diorite/MME themselves and host granitoid. As mingled boundaries of enclaves (Phase 1/2 MME) have not been sealed by quenching, dynamic phenocryst exchange between these mediums (entrained melt) have tried to reached equilibrium with host granitoid magma (Bowen 1922; Stephens *et al.* 1991) to some degree; which is likely to have modified MME textures, making recognition of such process via petrographic techniques difficult. Although the effect of re-equilibration from mafic magmatic recharge on host granitoid could appear to be small given volume relationships, as RM1/RM2 bright blue CL zones (zone 2 in RM1/zone 3 in RM2 alkali feldspar) have a gradation contact towards the rim (displaying similar luminescence to the core) with elemental re-equilibration towards rims and increase in Pb-Pb systems as described above, it is likely the data/CL observations capture reaction and exchange and modification of host granitoid to some degree.

If one observes plagioclase elemental data per mineral zone (for all samples reflecting reverse zonation of the intrusion) represented in ternary plots in **Fig. 4.13**, the same features for feldspars within felsic and mafic components occur. Note that [mol. %] elemental averages for all feldspar samples (per mineral zone) provided have already been presented and not repeated here; with this in mind **Fig. 4.13** simply re-illustrates within RM1/RM2 (ternary plots **1a.)**, **1b.)** and **3.)**), in the cartoon adjacent to ternary plot **1a.)** if one moves from the core regions to zone 2/3 where there is bright blue luminescence, there is a marked decrease in Or [mol. %]/increase in Ab [mol. %] (**arrow a**) reflecting a mafic magmatic recharge influx of hotter magma into host granitoid. This is also corroborated by elevations in Ba and Sr spike zone 2/3 with dissolution/resorbtion surfaces. Subsequent re-equlibration back towards the rims where rim data is similar to the core (**arrow b**) occurs, hence a gradation from bright blue CL in zone 2 back to the rims displaying same purple/dark blue CL of the cores.

These observations are evident for all alkali feldspars within zones 1 to 3 in RM1/RM1a (and including the additional zone 3 for RM2), suggesting the feldspar in RM1a (**Fig. 4.13** ternary plot **2.)**) also has the same core characteristics of RM1 granitoid. As zones 5 and 7 have generally greater Or [mol. %] content it implies modification preceding zone 3, where localised anatexis with Moine pelite (Zaniewski *et al.* 2006) again could account for these elevations. As RM1a alkali feldspar relative to RM1/RM2 Pb-Pb isotopic data also shows opposite rim-ward trends (see **Table 4.6**), i.e. low $^{206}Pb/^{204}Pb$, low $^{208}Pb/^{204}Pb$, and high $^{207}Pb/^{206}Pb$, high $^{208}Pb/^{206}Pb$, localised anatexis of Moine (in relation to the assumptions highlighted in Dickin 1981; Dickin *et al.* 1984; Peate & Hawkesworth 2005; Peate *et al.*

Fig. 4.13 Ternary feldspar plots depicting all *in-situ* elemental traverses for all feldspar crystal samples (based on CL or monochromatic backscatter images of consistent representative mineral zonation within each plutonic facies from Knockvologan to Bendoran) considered in this chapter. Note scales for limits of Ab, Or and An are adjacent to each ternary plot.



RM1 - K-spar	RM1a - K-spar	RM2 - K-spar	MME (1) - Plag. micro-pheno.	MME (2) - plag xeno.
Lo 7/6	Hi 7/6	Lo 7/6	Lo 7/6	Hi 7/6
*Lo 8/6	Hi 8/6	Lo 8/6	Unknown - Speculative Lo 8/6?	Hi 8/6
Hi 6/4	Lo 6/4	Hi 6/4	Hi 6/4	Lo 6/4
Hi 8/4	Lo 8/4	Hi 8/4	Hi 8/4	Hi 8/4

Table 4.6 - Pb-Pb rim with respect to core data for all feldspar crystals considered in this study. * Second crystal analysed for RM1 shows high $^{208}Pb/^{206}Pb$ (opposite trend).

2008) to form RM1a is feasible for zones preceding zone 3. Zone 5 in RM1a alkali feldspar (refer back to also **Fig. 4.6 part 2 area D**) clearly captures enhanced $^{207}Pb/^{206}Pb$, high $^{208}Pb/^{206}Pb$ with respect to the core zone.

Phase 1 MME also show punctuated dissolution zones and spike in Ba, Sr relative to bright blue CL zone 2, where, although all CL zones show sharper contact than zones 2 to 3 in alkali feldspars in host granitoid, zone 2 (**Fig. 4.13** ternary plot **4.)**) depicts an elevated An [mol. %] with rims having similar compositions to that of the core. Pb-Pb systems for rim-ward trends are also in comparison to RM1/RM2 (see **Table 4.6**). Compared to Phase 2 MME andesine, this andesine micro-phenocrytst captures mafic-mafic batch interaction between diorite/MME accounting for the above elemental and Pb-Pb signatures occurring at a localised scale whilst Phase 1 MME are re-equilibrating in host RM2 granitoid. Due to a greater heterogeneous density of phenocrysts comprising phase 1 MME (**Fig. 4.9**), it is inferred that Phase 1 MME reflect more mechanical mingling compared to the mixing that accounts for Phase 2 MME; the transition between these mediums reflects localised hybridism from MME with the same genetic mineralogy.

Phase 2 MME on the other hand reflect dissolution zones, and Ba spikes in zone 3 (**Fig. 4.6 part 2 area C**), however differ from alkali feldspars in RM2/RM1 and Phase 1 MME andesine in that an increase in Sr is observed occurring rim-ward and as in **Fig. 4.13** ternary plot **5.)** An [mol. %] content also increases rim-ward. Data in **Table 4.6** for Phase 2 MME andesine, shows that rim-ward Pb-Pb isotope systematics for this crystal differ and trend in opposite sense to all other components apart from RM1a alkali feldspar; however differences in $^{208}Pb/^{204}Pb$ occur between these crystals. As such, these inferences could reflect greater localised mixing than that compared to Phase 1 MME where a feldspar xenocryst from RM2 has been entrained within diorite/Phase 1 MME mush trying to re-equilibrate within RM2 granitic mush indicating contemporaneous localised rejuvenating injections of silicic magma (felsic recharge) where the Phase 2 MME has been more

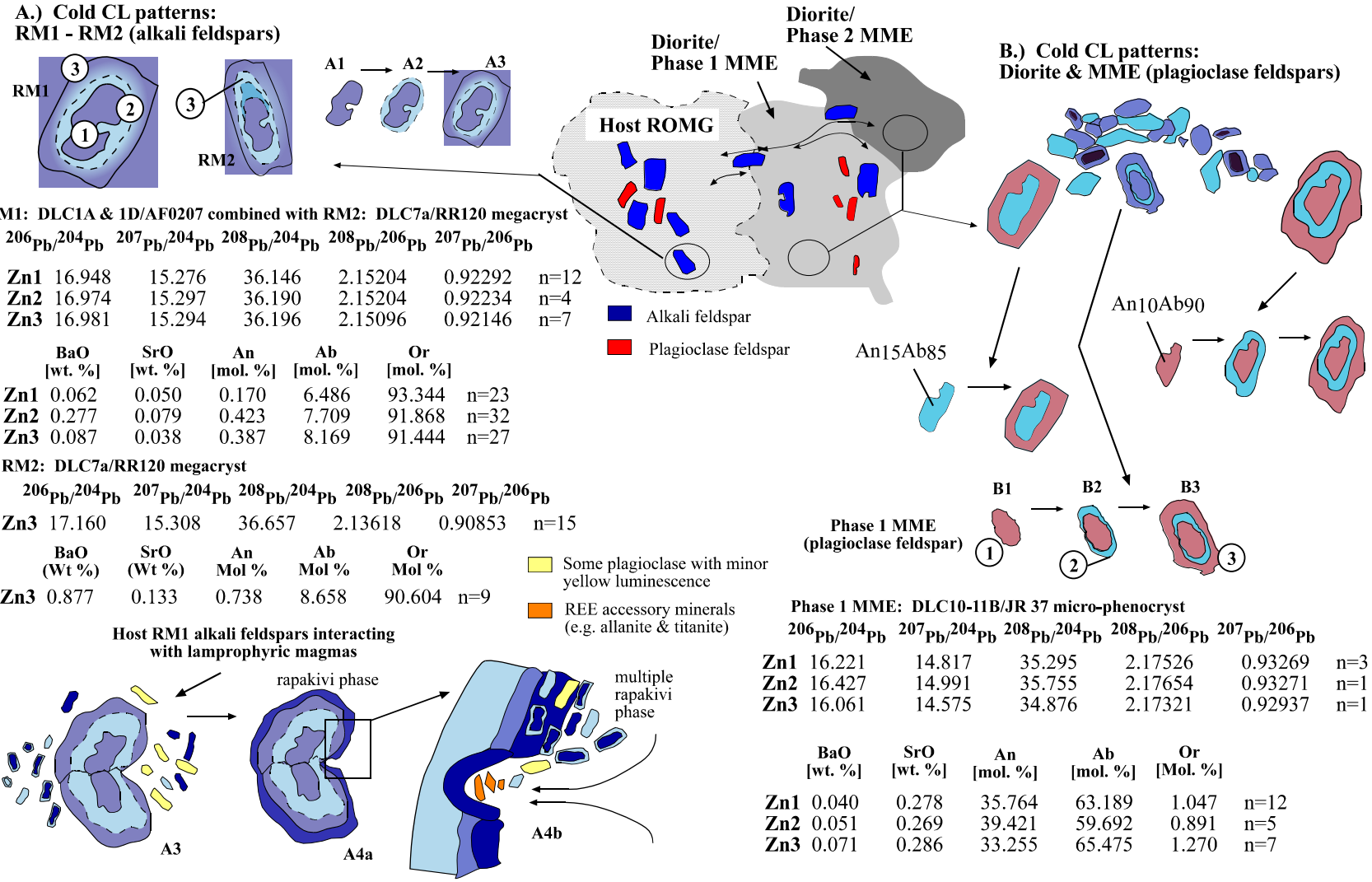
hybridised than its phase 1 counterpart equilibrating in RM2 (hence the rim-ward increase in $^{207}Pb/^{206}Pb$ and $^{208}Pb/^{206}Pb$).

Essentially all the trends documenting the chemical heterogeneity and mixing history of the crystal cargo in carefully selected feldspar samples comprising ROMG components, with the exception of RM1a, are diagrammatically represented in **Fig. 4.14**. **Fig. 4.14** illustrates ovoid globular Phase 1/Phase 2 MME having a mingled interface with alkali-feldspars sometimes straddling the contact, taken to be indicative of dynamic crystal exchange between both mediums which both have contact with homogeneous looking host granitoid. In taking alkali feldspars from host granitoid and andesine from both MME phases, average elemental (Ba, Sr), Or [mol. %] and Pb-Pb data are summarised within mineral zones that have a specific type of luminescence. In the case of blue alkali feldspar from host granitoid **Fig. 4.14 A.)** the threefold CL blue mineral zonation is exhibited from **A1** to **A3**, with **A2** being associated with zone 2 in RM1 or zone 3 in RM2 providing evidence for the bright blue zone in alkali feldspars corresponding to a punctuated mafic magmatic recharge event and subsequent re-equilibration towards the rims in overall pluton-scale host ROMG granitoid development.

Plagioclase in MME, on the other-hand, is less radiogenic in **Fig. 4.14 B.)**, and Phase 1 MME can be incorrectly inferred as having the blue CL pattern of alkali feldspar; CL reveals plagioclase has (**B1** to **B3**) a red core punctuated by bright blue CL zone 2 with sharp contact with red CL at the rims displaying the same CL as the cores. Given the same elemental and Pb-Pb rim-ward trends occur within Phase 1 MME, which has a liquid-liquid interface with Phase 2 MME and in RM1/RM2, including the documented elemental spike zones, both bright blue plagioclases in zone 2 and RM1 zone 2/RM2 zone 3 are attributed to mafic magmatic recharge across all components throughout the intrusion; however the sharp CL contact for plagioclase at the rims for Phase 1 MME could relate to quenching and less time for feldspar re-equilibration than in host granitoid due to more mingling than mixing. Plagioclases with opposite CL zonation (red core/blue rim and *vice-versa*) juxtaposed in groundmass assemblages of variable density provide more textural evidence for mafic-felsic batch mixing.

Lamprophyric waning stages of mafic magmatism (as described in Chapter Two and Zaniewski *et al.* 2006) are important magmatic events associated with the evolution of the ROMG. Alkali-feldspars entrained from RM1 host granitoid within Type 1 lamprophyre (see Chapter Two and Zaniewski *et al.* 2006 for classification and location) were analysed in the same manner, however the data are not presented here; due to CL, and related Pb-Pb data

Figure 4.14 Evolution of alkali feldspars in host ROMG and plagioclase feldspars within diorite/MME. Note figures are mineral zone averages with respect to number of analyses conducted within each mineral zone (as expressed by n = e.g. 1).



RM1: DLC1A & 1D/AF0207 combined with RM2: DLC7a/RR120 megacryst

	$^{206}Pb/^{204}Pb$	$^{207}Pb/^{204}Pb$	$^{208}Pb/^{204}Pb$	$^{208}Pb/^{206}Pb$	$^{207}Pb/^{206}Pb$	
Zn1	16.948	15.276	36.146	2.15204	0.92292	n=12
Zn2	16.974	15.297	36.190	2.15204	0.92234	n=4
Zn3	16.981	15.294	36.196	2.15096	0.92146	n=7

	BaO [wt. %]	SrO [wt. %]	An [mol. %]	Ab [mol. %]	Or [mol. %]	
Zn1	0.062	0.050	0.170	6.486	93.344	n=23
Zn2	0.277	0.079	0.423	7.709	91.868	n=32
Zn3	0.087	0.038	0.387	8.169	91.444	n=27

RM2: DLC7a/RR120 megacryst

	$^{206}Pb/^{204}Pb$	$^{207}Pb/^{204}Pb$	$^{208}Pb/^{204}Pb$	$^{208}Pb/^{206}Pb$	$^{207}Pb/^{206}Pb$	
Zn3	17.160	15.308	36.657	2.13618	0.90853	n=15

	BaO (Wt %)	SrO (Wt %)	An Mol %	Ab Mol %	Or Mol %	
Zn3	0.877	0.133	0.738	8.658	90.604	n=9

Phase 1 MME: DLC10-11B/JR 37 micro-phenocryst

	$^{206}Pb/^{204}Pb$	$^{207}Pb/^{204}Pb$	$^{208}Pb/^{204}Pb$	$^{208}Pb/^{206}Pb$	$^{207}Pb/^{206}Pb$	
Zn1	16.221	14.817	35.295	2.17526	0.93269	n=3
Zn2	16.427	14.991	35.755	2.17654	0.93271	n=1
Zn3	16.061	14.575	34.876	2.17321	0.92937	n=1

	BaO [wt. %]	SrO [wt. %]	An [mol. %]	Ab [mol. %]	Or [Mol. %]	
Zn1	0.040	0.278	35.764	63.189	1.047	n=12
Zn2	0.051	0.269	39.421	59.692	0.891	n=5
Zn3	0.071	0.286	33.255	65.475	1.270	n=7

show the same trends as crystals in RM1 suggesting a xenocrystic origin, consistent with field petrology. The lower left hand side of **Fig. 4.14** depicts alkali feldspar xenocrysts occurring in Type 1 lamprophyre (relative to sample no S71153 of Rock & Hunter 1987), which retain the threefold CL zonation profile observed in RM1, however rims are punctuated by of a 1mm rapakivi rim phase comprised of individual plagioclase laths. Plagioclase laths forming this rim are aligned sub parallel to the megacryst morphology (as are some accessory phases e.g. allanite and titanite) and the rapakivi rim in part is also truncated or embayed, whereby one rapakivi phase has corroded and formed on top of another or in some cases combined with another alkali feldspar xenocryst (hence the term glomero-xenocryst). Rapakivi mantle phases generally envelope entirely the glomero-xenocrysts.

Bulk Pb-Pb data

Fig. 4.15 depicts all average Pb-Pb isotopic ratios for all systems with respect to mineral zones in this study, with exception of $^{207}Pb/^{204}Pb$ depicted here for the first time that essentially mirrors $^{208}Pb/^{204}Pb$ data however this excludes RM1alkali feldspar sitting in between Phase 1 and 2 MME andesine. The figure shows the Pb-Pb rim-ward patterns as previously highlighted in **Table 4.6** for alkali feldspar in felsic components encapsulating mafic magmatic recharge in zone 2 (bright blue CL). However for mafic components, by averaging the mineral zone data, all Pb-Pb isotopic systems for Phase 1 MME andesine display high rim-ward increases and for Phase 2 MME andesine with the exception of $^{206}Pb/^{204}Pb$, all other Pb-Pb systems also exhibit increases. This trend runs counter to those in **Table 4.6** where rim-ward trends are the same for $^{208}Pb/^{204}Pb$ for both MME plagioclase phases but not for other Pb-Pb systems where in Phase 1 MME feldspar $^{206}Pb/^{204}Pb$ and $^{208}Pb/^{204}Pb$ are decoupled to $^{207}Pb/^{206}Pb$, and in Phase 2 MME feldspar $^{206}Pb/^{204}Pb$ is decoupled to all other systems. Averaged mineral zone data for both enclave phase feldspars are higher for $^{206}Pb/^{204}Pb$ and $^{208}Pb/^{204}Pb$ in Phase 1 MME feldspar in zone 2 (bright blue CL) in comparison to depleted levels for this zone in terms of the same isotope systems for Phase 2 MME feldspar; however in assessing **Fig. 4.12 part 2 area D** a marked spike for these isotope systems is observed. Prior to combining such MME phases; Phase 1 MME feldspar thus depicts hybridisation of a host plagioclase micro-phenocryst within an enclave that has undergone localised mafic-mafic magmatic mingling whilst re-equilibrating with host RM2, in contrast the Phase 2 MME feldspar has evolved as a xenocryst from RM2 entrained within a globular mafic enclave that has been rejuvenated by incorporation of felsic recharge whilst equilibrating with RM2 host granitoid.

Bulk Pb-Pb isotope data from all feldspars comprising each component are plotted and presented in **Fig. 4.16** and highlight the importance of mafic-felsic magma mixing in the petrogenesis of the complex. These define a simple binary mixing array between two mafic-felsic end-members, although as especially in ^{207}Pb band and ^{206}Pb band are linked through the decay systems of U, it requires fairly major differences to divert different end-members from a straight line trend (e.g. the Northern Hemisphere Reference Line (Hart 1984)).

In **Fig. 4.16** it is evident that the binary mixing array for the ROMG suggests Phase 1 MME and RM2 as binary mixing end members for the intrusion. RM1 roughly sits in the middle of such Pb-Pb arrays always having some overlap with RM1a in all Pb-Pb isotope systems and significantly has no overlap with RM2. RM1/RM1a has tight intricate overlap in ^{208}Pb/^{206}Pb vs. ^{207}Pb/^{206}Pb with Phase 2 MME also only overlapping these components.

^{207}Pb/^{204}Pb vs. ^{206}Pb/^{204}Pb – Phase 1 MME comprise andesine having the lowest amount of ^{207}Pb/^{204}Pb = 14.575 and ^{206}Pb/^{204}Pb = 16.061 rising to RM2 alkali feldspar having largest values of ^{207}Pb/^{204}Pb = 15.356 and ^{206}Pb/^{204}Pb = 17.324. A marked break increase is characteristic between Phase 1/2 MME for ^{207}Pb/^{204}Pb = 0.088 and ^{206}Pb/^{204}Pb = 0.123. All RM2 data clearly sits to the right of RM1 from the last RM1 point where ^{207}Pb/^{204}Pb = 15.337 and ^{206}Pb/^{204}Pb = 17.062.

^{208}Pb/^{206}Pb vs. ^{207}Pb/^{206}Pb – In comparison to the other Pb-Pb systems, this system reverses the end-members. RM2 comprises alkali feldspar having the lowest amount of ^{208}Pb/^{206}Pb = 2.123 and ^{207}Pb/^{206}Pb = 0.900 rising to Type 1 MME andesine having largest values of ^{208}Pb/^{206}Pb = 2.185 and ^{207}Pb/^{206}Pb = 0.939. In comparison to other Pb-Pb systems, there is no marked break between Phase 1/2 MME sanidine and overlap occurs with Type 2 MME sanidine at where ^{208}Pb/^{206}Pb = 2.183 and ^{207}Pb/^{206}Pb = 0.934. The cause of the off-set but parallel linear data for a RM1alkali feldspar sample is not known.

^{208}Pb/^{204}Pb vs. ^{206}Pb/^{204}Pb – Essentially the same mirrored trend here arises in ^{207}Pb/^{204}Pb vs. ^{206}Pb/^{204}Pb; with Phase 1 MME comprising andesine having the lowest amount of ^{208}Pb/^{204}Pb = 34.876 and ^{206}Pb/^{204}Pb = 16.061 rising to RM2 alkali feldspar having largest values of ^{208}Pb/^{204}Pb = 36.822 and ^{206}Pb/^{204}Pb = 17.356. A marked break is again characteristic between Phase 1/2 MME for ^{208}Pb/^{204}Pb = 0.161 and for ^{206}Pb/^{204}Pb = 0.123. All RM2 data clearly sits to the right of RM1 from the last RM1 point where ^{208}Pb/^{204}Pb = 36.623 and ^{206}Pb/^{204}Pb = 17.062. The cause of the off-set but parallel linear data for a RM1

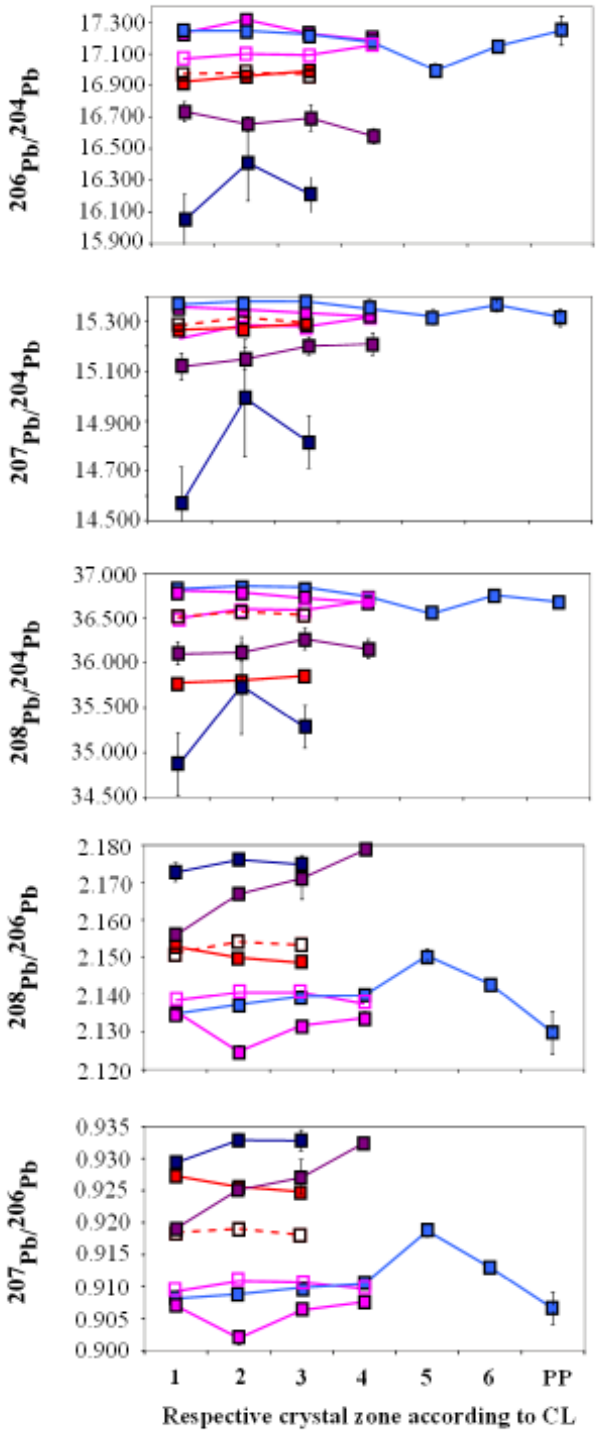
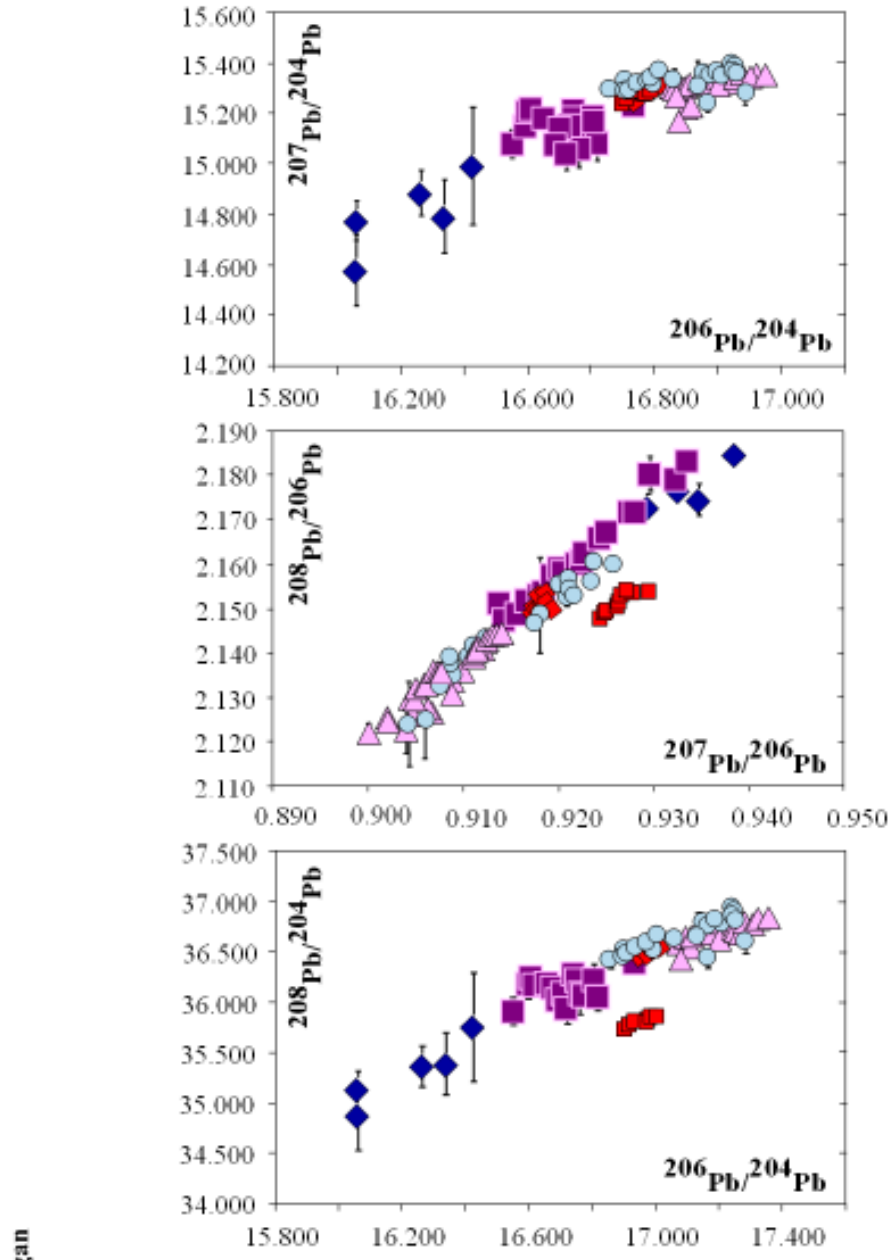


Fig. 4.15

Individual *in-situ* Pb-Pb isotopic traverses (Pb-Pb isotopic ratio vs. mineral zone/ distance) for all ROMG feldspars studied.

Fig. 4.16 Bulk *in-situ* Pb-Pb isotopic bivariate graphs for the ROMG.



alkali feldspar sample is not known.

The Pb-Pb data in **Fig. 4.16** for this granitoid complex are taken to reflect a simple binary mixing array essentially between a crustal/felsic and mantle/mafic component in a series of hybridisation/mixing processes in the formation of the ROMG. The patterns of CL (e.g. initial purple/blue cores punctuated by bright blue CL zone 2 in alkali feldspar) within alkali-feldspars in felsic components and andesine in Phase 1 MME (red-cores punctuated by bright blue CL zone 2) have been shown to represent textural disequilibrium relative to elemental kicks in Ba, Sr while the formation of feldspars representing higher temperature end members, reflect punctuated coeval mafic-magmatic recharge. This is clearly an important driving factor in the overall petrogenesis of the host granitoid including mixing in Phase 2 MME/diorite and mingling in Phase 1 MME/diorite. As previously described, the significance of Phase 2 MME Pb-Pb data mirroring RM1a Pb-Pb data to some degree highlight how felsic rejuvenation of magmas within a spectrum of dioritic MME during emplacement can contribute to signatures indicating a greater crustal input in Phase 2 MME genesis.

Mcleod *et al.* (2011) states regarding the ROMG titanite trends in the diorite and host granitoid, *'Both of these rock types record some evidence of mixing process, although the most evolved sample RM1, is probably not a true end-member of the mixing process. It is likely that fractional crystallization and magma mixing processes at depth have both played a part in formation of the granite prior to emplacement' 'and by comparison, the influence of fractional crystallisation appears to be relatively minor'*. In considering these statements in relation to Pb-Pb systematics in **Fig. 4.16**, taking the middle of the Pb-Pb trend and continually hybridising via 'thorough' mixing Phase 1 MME and RM2 end members, it is possible to generate RM1. Thus RM1 does not represent a true isotopic end member of mafic-felsic magmatic interaction. RM2 on the other-hand which comprises greater field-scale heterogeneity that RM1 with greater abundance of MME relative to host granitoid by volume, sits at the ends of Pb-Pb systems reflecting greater mechanical mingling than mixing of host granitoid to diorite/MME during mafic magmatic recharge. The mixing array in **Fig. 4.16** suggests that there is no stepped/ordered distribution of described components with RM1 reflecting the most isotopically mixed granitoid. It is likely these data have similarities to McLeod *et al.* (2011) in that whilst fractional crystallisation, particularly in the diorite, is not discounted, the Pb-Pb data is likely to reflect the dominant open system processes of mingling and mixing.

A traverse from southwest to northeast across the intrusion from Knockvologan to Bendoran shows an increase in $^{208}Pb/^{204}Pb$ vs. $^{206}Pb/^{204}Pb$ which for the whole intrusion, similar to rim-ward trends in alkali-feldspar in this study, highlights the role and dominance of mafic magmatic recharge in the evolution of the ROMG.

With onset of initial crystallisation of the ROMG, it is clear the blue albitic cores found in RM1a and purple cores of alkali feldspar in host ROMG have been moved out of equilibrium via punctuated mafic magmatic recharge; intrusion of more mafic magmas into the partly crystallised granitoid mush has accounted for contemporaneous hybrisation (including Ba, Sr spike zones attributed to bright-blue CL in dissolution zones and Pb-Pb trends as depicted for feldspar end-members in **Table 4.6**) through time. A case for greater mafic magmatic mingling is observed in Phase 1 type MME in comparison to Phase 2 type MME representing more mechanically induced magma mixing and felsic magmatic

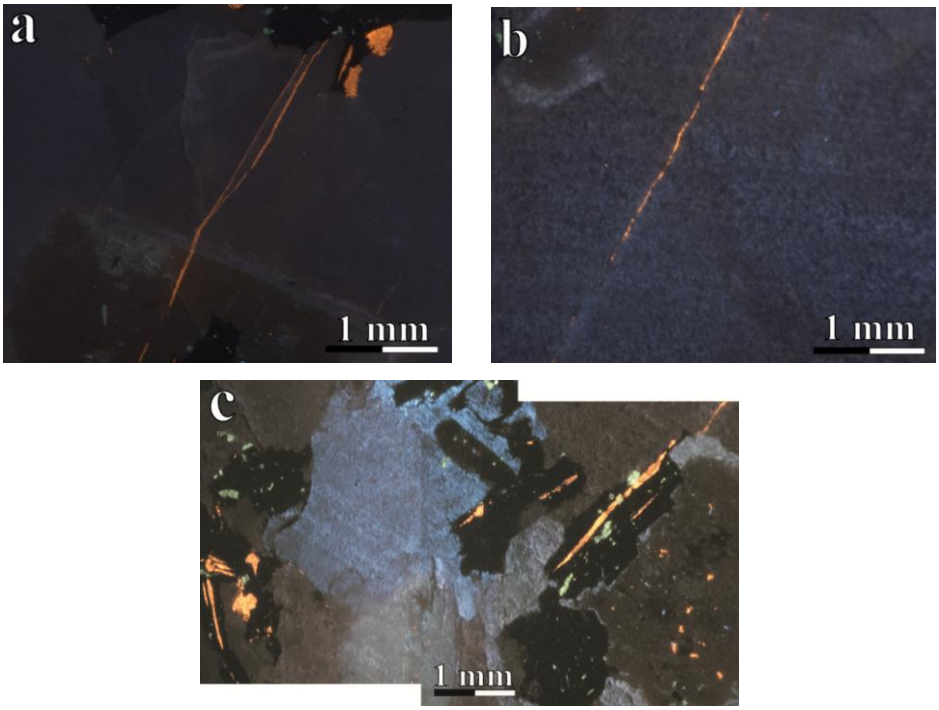


Fig. 4.17 (a-c) Cold CL images of feldspars within **DLC1B/AF0207 (RM1)** depicting sub-solidus textures as follows: **(a)** calcite stringlet pervasive throughout alkali feldspar glomerocrysts. **(b)** Higher magnification reveals calcite stringlets can cross cut polysynthetic albite twins in plagioclase feldspar. Primary plagioclase (as discernible by relict twinning) has been selectively replaced by alkali feldspar (which is indicated by blue CL), which has given turbidity of twinning (that can be dusted with zeolites/artefacts). **(c)** Gross CL petrographic image of RM1 revealing selective replacement of plagioclase feldspar with alkali feldspar, calcite stringlets and calcite that also utilises cleavage planes in biotite (top right of image).

recharge/re-equilibration of enclave with respect to host granitoid.

The final stages of crystallisation in the ROMG were complex involving hybridisation and metasomatism. It is recognised (**Fig. 4.17 (a)** to **(c)**), that textural features such as extensive plagioclase replacement by alkali feldspar with calcite occurring throughout the cracks of some plagioclases could indicate that mafic-felsic magmatism may have produced an induced temperature gradient promoting pervasive metasomatic migration of volatiles, K and CO_2 towards the outer portion of cooler host ROMG.

This chapter detailed LA MC-ICP-MS Pb-Pb isotopic studies of alkali feldspar megacrysts in a host granitoid and plagioclase-feldspar in related MME coupled with use of CL/BSE imaging. The techniques utilised have provided significant insights into understanding the role and extent of disequilibrium caused by magma-mingling and mixing across the ROMG. By selecting different micro-samples to unravel different components involved in petrogenesis, it is demonstrated that the variations presented reflect open system processes/various stages of hybridism; whereby in felsic components and Phase 1 MME, rim-ward increases of $^{208}Pb/^{204}Pb$ vs. $^{206}Pb/^{204}Pb$ (in both systems) as well as field evidence for mafic-felsic mixing, bright-blue zone 2 in CL microscopy coupled to Ba-Sr spike zones, indicate that mafic magmatic recharge has contributed to producing a reversely zoned granitoid.

Chapter Five

SUMMARY & CONCLUSIONS

Summary and conclusions regarding ROMG petrogenesis; inferences on granitoid magma genesis.

Chapter Five
THE ROSS OF MULL GRANITE

Chapter Five – Summary and Conclusions

This chapter breaks down this whole study into two parts. Section **5.1** provides (i) macro to micro-scale conclusions. Section **5.2**, attempts to present a comprehensive temporal sequence of events.

5.1 Macro to Micro-scale Conclusions

As a result of field mapping and utilising QXRD to modally characterise mineralogical heterogeneity, the following macro-scale conclusions are reached:

- Magnificent coastal exposure all around the Ross allowed access to all ROMG components. A 1:25 000 Solid field map was constructed using 1:10 000 scale maps. This work defined a reversely zoned granitoid sheet (Chapter Two and Zaniewski *et al.* 2006). A model has been presented proposing ascent at an intersection of the Sound of Iona Fault and Great Glen Fault, and emplacement of multiple sheets north-eastward into meta-sediments of the Moine Supergroup.

- Field and petrographic textures presented infer mixing and mingling to be the dominant processes in the evolution of this intrusion (with the exception of RM1a being an anatectic migmatitic product of the Moine Supergroup).

- A comparison of modal methods (Chapter Three) show QXRD to be the most precise and accurate technique. QXRD data define a binary trend for mafic and felsic components (with a silica break of around 15.0 to 25.0%) whereby QXRD results corroborate classifications of Zaniewski *et al.* (2006).

In utilising feldspar chemo-stratigraphy with CL to further quantify the mixing and mingling processes in ROMG petrogenesis (Chapter Four), the following micro-scale conclusions are reached:

- Feldspars throughout host granitoid and MME display three-fold zonation associated with dissolution at the core followed by elemental spike zones of Ba, Sr (0.00 - 1.00

wt. %) and Ab [mol. %] (or decrease in Or [mol. %], the largest differences occurring in RM1 by around 10.00%) with elemental re-equilibration back towards the rims. Such resorption surfaces correspond to rim-ward increase of $^{206}Pb/^{204}Pb$ and $^{208}Pb/^{204}Pb$ in alkali feldspars within host granitoid (except RM1a) and andesine in Phase 1 MME indicate dissolution attributable to punctuated mafic magmatic recharge from a mantle-derived component interacting with a crustal component during petrogenesis.

- Rim-ward Pb-Pb trends for RM1, RM2 and Phase 1 MME feldspar micro-samples are in agreement with each other and all comprise high $^{206}Pb/^{204}Pb$, high $^{208}Pb/^{204}Pb$, and low $^{207}Pb/^{206}Pb$, low$^{208}Pb/^{206}Pb$. These components' rim-ward trends are however in the opposite sense to Phase 2 MME and RM1a feldspar micro-samples. Phase 1 MME depict hybridisation of a host plagioclase micro-phenocryst within an enclave that has undergone localised mafic-mafic magmatic mingling whilst trying re-equilibrating with host RM2; Phase 2 MME feldspar has evolved as a xenocryst from RM2 entrained within a globular mafic enclave that has been rejuvenated by incorporation of higher silicic magma whilst this MME phase is also re-equilibrating in RM2 host granitoid. Similarly, Pb-Pb trends in RM1a indicate melting Moine per-aluminous meta-sedimentary crust. RM1a aside, trends depict a hybridisation spectrum of mixing and mingling especially on a localised scale particularly in relation to MME re-equilibrating with host granitoid.

- Bulk Pb-Pb ROMG data highlight a simple binary mixing array between felsic and mafic components. RM2 comprises greater field-scale heterogeneity than RM1 (i.e. greater abundance of MME relative to host granitoid by volume) and is located at the ends of Pb-Pb systems in relation to mafic components reflecting greater mechanical mingling associated with mafic magmatic recharge.

- Moving from south-west to north-east (from Knockvologan to Bendoran), an increase in $^{208}Pb/^{204}Pb$ vs. $^{206}Pb/^{204}Pb$ is seen that is similar to rim-ward trends in alkali-feldspars.

5.2 Macro to Micro-sequence

This study has integrated field mapping with crystal scale studies to determine whether signatures within magmatic feldspars can be correlated with processes inferred from field observations.

Macro-scale studies have highlighted the following sequence of events:

- **RM1**: Thorough mixing of two components (felsic and mafic) prior to emplacement to give the most homogeneous equigranular facies with very rare MME.

- **RM1a**: RM1 intruding into Moine Supergroup has resulted in formation of an eastern envelope comprising heterogeneous white granitoid. In the north side of the peninsula (Bendoran), anatectic migmatite represents partial melting of predominantly pelitic country rock. In the south side of the peninsula (west of Ardalanish Bay), emplacement of granitoid sheets into predominantly psammitic country rock has resulted in minimal *in-situ* anatexis where an intricate stoped zone 0.5 km has developed.

- **RM2**: Punctuated mafic magmatic recharge into cooler partially crystallised felsic magma (RM1) has provided a viscosity contrast large enough to facilitate mingling as the main process in the formation of this facies. MME are pillowed, scattered (where double MME phases have been noted to co-mingle) and concentrated as swarms confined to diorite sheets during synplutonic emplacement into host granitoid. This has resulted in a gradational contact with RM1 and a decrease in MME abundance across the contact in a coastal transect northwards (from RM2 to RM1) between Cnoc an Laailt (NM [2975 2263]) and eastwards of Eilean an Aba (NM [2974 2250]).

- **Ongoing mafic magmatism - syn-plutonic diorite sheets/MME**: Injection of mafic magmas into more crystallised RM2 has meant it has also channelled in to early fractures giving localised mingling within host RM2 granitoid (in the form of crenulate contacts and variable xenocryst assemblages). Dismemberment of syn-plutonic diorite dykes into linear trails of angular or amoeboid MME (flow streams)

occurs (including amphibole rich zones) with MME displaying irregular margins with granitoid.

- **Late stage mafic magmatism - lamprophyric magmas**: During the last stages of mafic magmatism, mafic-felsic magma interaction produces sheets without amoeboid MME, planar contacts with host granitoid and little degree of internal hybridisation (i.e. non-composite Type 2 lamprophyres). The composite Type 1 lamprophyre sheets possess irregular contacts with RM1/RM2, have internal associated MME and represent a pre-cursor stage to the Type 2 lamprophyres.

- **Products associated with un-roofing**: Late stage development of joint planes during uplift enables volatile loss, pooling and fluidisation of a network of late stage fractionates of aplitic micro-granitoid rocks to be channelled in veins, pods and sheets. A rare syenite phase has been observed to be formed as a product in RM1 that has fed off such a network (post-dating the hybridised granitoids). ROMG pegmatites are not considered as late fractionates due to intimate association with Moine xenoliths (dehydration reactions giving local H_20 enrichment and lower viscosity when forming in surrounding magmas).

  Micro-scale studies have highlighted the following sequence of events:

- **Mafic Magmatic recharge - (1) mixing**:
  - Injection of mafic magmas of Phase 1 type MME/diorite composition into granitoid of RM2 composition prior to ascent and emplacement
  - Thorough mixing between such components.
  - Subsequent ascent and emplacement produces RM1 with RM1a forming as a contact related envelope.

- **Punctuated Mafic Magmatic recharge - (2) mingling**: Further magmatic recharge (spatially and temporally related) into more crystallised RM1has produced binary end members with mingling being the dominant process.

Micro-scale studies have shown that mafic-felsic magmatism is contemporaneous. A hybridisation array related to binary batch mixing between crustal and mantle components has been demonstrated. Linear Pb-Pb data arrays highlight RM1/RM2 felsic magmas are from the same parental source that have been modified by stages of hybridism. Mingling is reflected at the opposite ends of all Pb-Pb graphs, and as one moves towards the middle of these arrays, it captures pluton-scale mixing.

In examining if a correlation exists between macro to micro-scale studies, it is evident that the process of mafic-felsic magma interaction seen at the outcrop-scale is encoded at the crystal-scale. This macro to micro-scale approach could be adopted worldwide where the aim(s) are to understand granitoid petrogenesis.

APPENDICES AND REFERENCES

Appendices of field mapping, detailed petrographic descriptions, whole rock modal analyses, feldspar *in-situ* elemental and Pb-Pb isotopic geochemistry, sample localities, electronic raw data and a list of references.

Appendix One
FIELD DATA

Introduction

A full list of structural measurements within the ROMG (Chapter Two) is presented here for MME, aplitic micro-granite sheets and joint planes. This relates to producing diagrams as seen for MME in **Fig. 2.24** and aplitic micro-granite sheets and joint planes in **Fig. 2.25**.

A1.1 MME 2D unordered raw data tables for rose diagrams in **Fig. 2.24** (see **Fig. 2.24** for codes depicting place names). Localities in tables correspond to those within field notebooks.

Loc. No	Locality	n=?	Measurements	Code	Moine xenos.
1	390 (a)	1	13	A	-
2	390 (b)	1	175	A	-
3	390 (c)	1	177	A	-
4	390 (d)	1	10	A	-
5	390 (e)	1	160	A	-
6	390 (f)	1	5	A	-
7	390 (g)	1	71	A	-
8	391	1	11	A	-
9	194	1	174	A	-
10	196	1	9	A	-
11	No Loc. given	1	152	B	-
12	214	2	138 & 136	B	-
13	220	1	134	B	-
14	215.23	1	20	B	-
15	215.10	2	059 & 074	B	-
16	215.12	3	152, 159 & 166	B	-
17	215.45	1	175	B	-
18	228	2	163 & 163	C	-
19	230.4	1	42	C	-
20	245	2	002 & 174	C	-
21	249	4	170, 110, 204 & 208	C	-
22	250	3	020, 016 & 032	C	-
23	252	5	052, 026, 000, 136 & 132	C	132
24	305	6	000, 156, 169, 165, 176 & 174	C	155, 143, 008 & 018
25	302	2	162	C	108, 039, 039 & 034
			160	C	156, 156, 198 & 190
26	298.85	1	164	C	-
27	298.83	6	167, 158, 140, 132, 017 &	C	-
			9		-
28	287.1	7	142, 149, 026, 162, 169, 030	D	-
			& 141		-
29	282.19	3	001, 026 & 015	D	-
30	279 channel	2	in channel-004	D	-
			margin-170		-
			out of channel-026		-
31	278	5	006, 179, 006, 164 & 103	D	-
32	276.1	4	169, 174, 020 & 008	D	-
33	276	13	189, 010, 004, 013, 176, 143	D	-
			168, 020, 012, 006, 047, 011 &		-
			19		-
34	273.1	2	139 & 148	D	-
35	264.23	3	008x3	D	169
36	264.15	5	011, 003, 015, 000 & 177	D	-
37	254	1	5	E	-
38	328.2	1	149	E	-
39	352	3	011, 020 & 152	E	-
40	356	3	24	E	-
41	358	4	000, 010, 010 & 011	E	-

Loc. No	Locality	n=?	Measurements	Code	Moine xenos.
42	368	2	020 & 040	E	-
43	369	2	041 & 034	E	-
44	371	2	017 & 032	E	-
45	375	6	008, 049, 016, 176, 026 & 146	E	048, 160 & 191
46	382	3	058, 028 & 014	E	-
47	381	4	019, 174, 010 & 036	E	-
48	382.1	2	025 & 036	E	-
49	142	4	032x4	E	-
50	**202.1**	**1**	**35**	**A'**	-
51	**287.3**	**1**	**151**	**A'**	-
52	**287.4**	**1**	**161**	**A'**	-
53	**289.6**	**1**	**120**	**A'**	-
54	**389 (b)**	**1**	**154**	**A'**	-
55	**381**	**1**	**174**	**A'**	-
56	**394 (a)**	**1**	**77**	**A'**	-
57	**394 (b)**	**1**	**88**	**A'**	-
58	**394 (c)**	**1**	**28**	**A'**	-
59	**394 (d)**	**1**	**16**	**A'**	-
60	**394 (e)**	**1**	**186**	**A'**	-
61	**394 (g)**	**1**	**169**	**A'**	-
62	**394 (h)**	**1**	**96**	**A'**	-
63	**394 (i)**	**1**	**118**	**A'**	-
64	**389 (a-e)**	**1**	**155**	**A''**	-
65	**389 (a-e)**	**1**	**143**	**A''**	-
66	**389 (a-e)**	**1**	**8**	**A''**	-
67	**389 (a-e)**	**1**	**18**	**A''**	-
68	**389 (a-e)**	**1**	**108**	**A''**	-
69	**389 (a-e)**	**1**	**39**	**A''**	-
70	**389 (a-e)**	**1**	**39**	**A''**	-
71	**389 (a-e)**	**1**	**34**	**A''**	-
72	**389 (a-e)**	**1**	**156**	**A''**	-
73	**389 (a-e)**	**1**	**156**	**A''**	-
74	**389 (a-e)**	**1**	**198**	**A''**	-
75	**389 (a-e)**	**1**	**190**	**A''**	-
76	**389 (a-e)**	**1**	**169**	**A''**	-
77	**389 (a-e)**	**1**	**8**	**A''**	-
78	**389 (a-e)**	**1**	**48**	**A''**	-
79	**389 (a-e)**	**1**	**160**	**A''**	-
80	**389 (a-e)**	**1**	**191**	**A''**	-
81	**389 (a-e)**	**1**	**176**	**A''**	-
82	**389 (a-e)**	**1**	**30**	**A''**	-
83	**389 (a-e)**	**1**	**52**	**A''**	-
84	**389 (a-e)**	**1**	**34**	**A''**	-
85	**389 (a-e)**	**1**	**126**	**A''**	-
86	**389 (a-e)**	**1**	**30**	**A''**	-
87	**389 (a-e)**	**1**	**23**	**A''**	-
88	**389 (a-e)**	**1**	**27**	**A''**	-

A1.1 Data on previous page but ordered.

MME in RM2	←	↔	→	MME in RM2	**MME in Type 1 diorite**	**K-spar xenos. in Type 1 diorite**
A	**B**	**C**	**D**	**E**	**A'**	**A'' M-crysts**
13	152	163	142	5	**35**	**155**
175	138	163	149	149	**151**	**143**
177	136	42	26	11	**161**	**8**
10	134	2	162	20	**120**	**18**
160	20	174	169	152	**154**	**108**
5	59	170	30	24	**174**	**39**
71	74	110	141	0	**77**	**39**
11	152	204	1	10	**88**	**34**
174	159	208	26	10	**28**	**156**
9	166	20	15	11	**16**	**156**
	175	16	6	20	**186**	**198**
n=10		32	179	40	**169**	**190**
	n=11	52	6	41	**96**	**169**
		26	164	34	**118**	**8**
		0	103	17		**48**
		136	169	32	**n=14**	**160**
		132	174	8		**191**
		0	20	49		**176**
		156	8	16		**30**
		169	189	176		**52**
		165	10	26		**34**
		176	4	146		**126**
		174	13	58		**30**
		162	176	28		**23**
		160	143	14		**27**
		164	168	19		
		167	20	174		**n=25**
		158	12	10		
		140	6	36		
		132	47	25		
		17	11	36		
		9	19	32		
			139	32		
		n=32	148	32		
			8	32		
			8			
			8	n=35		
			11			
			3			
			15			
			0			
			177			
			n=42			

A1.2 MME 3D data tables for stereogram in **Fig 2.24**.

Loc. No.	locality	Measurement	MME in RM2			MME in Type 1 diorites		
			Strike	Dip	Orientation	Strike	Dip	Orientation
1	*183*	006/19 E						
2	**202.1**	**035/23 SEE**	6	19	E	**35**	**23**	**S**
3	*203*	140/45 SWW	140	45	S	**151**	**71**	**W**
4	*203*	048/32 SSW	48	32	S	**161**	**79**	**W**
5	*204*	015/70 SSW	15	70	S	**120**	**44**	**S**
6	*199*	021/23 ESE	21	23	E	**154**	**60**	**N**
7	*207*	050/30 SSW	50	30	S	**174**	**62**	**S**
8	*214 (a)*	136/23 SSW	136	23	S	**174**	**62**	**S**
9	*214 (b)*	129/33 SSW	129	33	S	**77**	**28**	**S**
10	*308.1 (a)*	177/32 W	177	32	W	**88**	**39**	**S**
11	*308.1 (b)*	178/29 W	178	29	W	**28**	**47**	**E**
12	*308.1 (a)*	169/30 W	169	30	W	**16**	**64**	**E**
13	*306*	034/61 WNW	34	61	W	**186**	**78**	**E**
14	*305*	006/41 W	6	41	W	**169**	**68**	**W**
15	*303 (a)*	006/42 W	6	42	W	**96**	**75**	**S**
16	*299 (b)*	001/70 W	1	70	W	**118**	**22**	**S**
17	*299 (c)*	001/29 W	1	29	W			
18	*299 (d)*	001/29 W	1	29	W			
19	*298.87 (a)*	005/52 W	5	52	W	**n=15**		
20	*298.87 (b)*	005/80 W	5	80	W			
21	*294.1 (a)*	032/34 WSW	32	34	W			
22	*294.1 (b)*	032/32 NW	32	32	N			
23	*328.2 (a)*	060/40 NWW	60	40	N			
24	*328.2 (b)*	148/45 NWW	148	45	N			
25	**287.3**	**151/71 W**	6	42	W			
26	**287.4**	**161/79 W**	144	30	S			
27	**289.6**	**120/44 SSW**	4	76	W			
28	*303*	006/42 W	163	32	W			
29	*368*	144/30 SWW	32	90	N			
30	*369*	004/76 W	15	50	W			
31	*371 (a)*	163/32 W	50	50	N			
32	*371 (b)*	032/90	166	36	N			
33	*379.4*	015/50 W	28	27	E			
34	*382*	050/50 NW	16	34	W			
35	*381 (a)*	166/36 NEE	178	89	E			
36	*381 (b)*	028/27 ESE	32	62	E			
37	*382.1*	016/34 W	32	62	E			
38	*388*	178/89 E	2	28	E			
39	389 (a)	032/62 ESE	4	70	W			
40	**389 (b)**	**154/60 NEE**	4	62	W			
41	**389 (c)**	**174/62 SWW**	4	29	W			
42	389 (d)	032/62 ESE	65	40	N			
43	**389 (f)**	**174/62 SWW**						
44	**394 (a)**	**077/28 SES**						
45	**394 (b)**	**088/39 S**	**n=41**					
46	**394 (c)**	**028/47 ESE**						
47	**394 (d)**	**016/ 64 ESE**						
48	**394 (e)**	**186/78 ESE**						

Loc. No.	locality	Measurement
49	**394 (g)**	**169//75 S**
50	**394 (h)**	**096/75 S**
51	**394 (i)**	**118/22 S**
52	***333.8 (a)***	*026/79 NWN*
53	***333.8 (b)***	*024/65 WNW*
54	*298.86*	002/28 E
55	*299*	004/70. 62 & 29 W
56	*152*	065/40 NW

n=2	***333.8 (a)& (b)***	Orientation of enclaves in Type 1 lamprophyre sheet Eilean Srianach
n=41	e.g. 299	Orientation of MME in RM2
n=15	**e.g. 389 (a)**	Orientation of MME in Type 1 diorite from the Knockvologan mixing and mingling zone

Locality refers to locality in field notebook

A1.3 Major joint plane data for stereogram in **Fig. 2.25**.

No.	Locality	Measurement	Additional info.	Area
1	4	116	Not (S) plane. Vertical fractures in gr. (same trend as post-cal. dykes)	Deargphort ↓
2	9	104 & 011	Not (S) plane. Vertical fractures in gr.	↓
3	11	144, 154 X 2, 150-160, 084, 096, 107 & 106	Not (S) plane. Vertical fractures in gr. (same trend as post-Cal. dykes)	↓ ↓
4	13	068/	Vertical	↓
5	18	33/33 E & 127/ 66 NE	not (S) joint	↓
6	21	176/45 E & 130/74 NE	not (S) joint	↓
7	23	127/74 SW & 157/60 ENE	not (S) joint	↓
8	24	106/64 SSW	not (S) joint & // to Post-cal. Dykes	↓
9	25	175/45 E	(S) Joint	↓
10	28	*050/20 NW &°017/80 W	(S) joint	↓
11	30	104 & 019	Fractures in gr. Not (S) joint	↓
12	33	142, 035/80 SE & *078/8 NNW	(S) joint	↓
13	39	058/47 N, 115/72 SSW &015/67 E	(S) joints	↓
14	52	070/22 NNW	(S) joint	↓
15	64	062/21 NWN	(S) joint	↓
16	68	040/13 NWW	(S) joint	↓
17	79	036/29 NW	(S) joint	↓
18	82	024/22 NW	(S) joint	↓
19	83	106/22 SW	(S) joint	↓
20	84	030/14 NW	(S) joint	↓
21	87	050/16 NW	(S) joint	↓
22	88	054/32 NW	(S) joint	↓
23	89	048/34 NW	(S) joint	↓
24	90	060/30 NW	(S) joint	Rubh a Chaideimh
25	101	001/31 W	(S) joint	Deargphort
26	120	026/29 WNW	(S) joint	↓
27	125	022/23 NWW	(S) joint	↓
28	131	005/38 W	(S) joint	↓

No.	Locality	Measurement	Additional info.	Area
29	132	015/30 NW & 021/44 W	(S) joints	↓
30	136	012/30 W	(S) joint	↓
31	138	021/33 NW	(S) joint	↓
32	140	006/32 WNW	(S) joint	↓
33	147	006/20 NWW	(S) joint	↓
34	149	091/22 N	Diff. Fracture sets not on field slip.	↓
35	150	168/19 W	(S) joint	↓
36	154	002/26 NNW	(S) joint	↓
37	156	109/23 SSW	(S) joint	↓
38	163	050/22 NNW	(S) joint	↓
39	183	165/15 SSW & 169/19 SSW	(S) joint, 1st & 2nd check	↓
40	184	019/33 W	31018 18669	↓
41	193.19	000/18 W	(S) joint	↓
42	195	013/32 WNW	(S) joint	↓
43	196	018/32 WNW	(S) joint	↓
44	199	018/33WNW	(S) joint	↓
45	216	075/38 SSE	(S) joint	↓
46	243	046/35 NWN	(S) joint	↓
47	244.1	124/26 SW	(S) joint	↓
48	247	039/23NWN	(S) joint	↓
49	248	146/29 SW	(S) joint	Port na luing
50	290	100/36 NNE	(S) joint	Na Maoil Mhora
51	291.1	094/16 N	(S) joint	↓
52	294.5	152/18 NEE & 146/18 NEE	(S) joint	↓
53	295.3	092/24 NNE	(S) joint	↓
54	297.1	040/28 WNW	(S) joint	↓
55	297.2	010/27 WNW	(S) joint	↓
56	297.3	032/35 WNW	(S) joint	↓
57	320.4	080/20 SSE	(S) joint	Aird Mór
58	345	013/25 SEE	(S) joint	↓
59	352	106/23 SSW	(S) joint	↓
60	355	080/39 NWN	(S) joint near fault?	↓
61	361	100/34 NNE	(S) joint near fault?	↓
62	62	097/32 NNE	(S) joint near fault?	↓
63	363.1	122/38 NNE	(S) joint near fault?	↓
64	365	042/14 NW	(S) joint	↓
65	367	141/32 NEE	(S) joint	↓
66	368	150/28 NEE	(S) joint	↓
67	370	015/46 ESE	(S) joint	↓
68	370.1	160/40 NEE & 156/41 NEE	(S) joints	↓
69	370.2	150/45 NEE	(S) joint	↓
70	371	002/46 E	(S) joint	↓
71	373.2	113/36 NNE	(S) joint	Rubh' Ardalanish

Locality refers to locality in field notebook

↓ continuation of coastal traverse that starts from Red Bay Quarry and ends at Rubh' Ardalanish

(S) joint refers to standard most common type of joint plane observed in the ROMG

A1.4 Aplitic micro-granite sheet data for stereogram in **Fig. 2.25**.

No.	Locality	Measurement/s	Type	Additional info.	Area
1	7	035/16 WNW	●	-	Deargphort
2	8	110 vertical	●	-	↓
3	30	028/14 NW, 036/17 NW &060/10 NW	●	Refer to pg 18, bifurcating sheet	↓
4	32	050/37 SE	●	-	↓
5	33	040/82 WNW	●	-	Rubha' Chlaidheimh
6	93	016/16 WNW	●	14 cm wide aplite + sacharoidal Qtz. // to it	Deargphort ↓
7	101	004/28 W	●	-	↓
8	109	026/25 WNW	●	-	↓
9	141	042/57 NW	●	-	↓
10	146a	046/56 NW	●2	Fractures within 0.7m wide sheet @ 034/58 SE	Eilean nam Bo (facies system
11	146b	041/60 NW	●1	-	devised here)
12	148	142/32 SW	●1	-	↓
13	153	161/48 SW	●1	-	↓
14	155	063/24 NNW	●1	-	↓
15	157	046/25 NW	●1	-	↓
16	171	116/24 NE	●	-	Erraid
17	213	126/19 SWW	●	Forming // to lamprophyre contact	Traigh a mhill
18	221	159/31 SWW	●	-	Port nan Ron
19	133	084/24 NNW & 066/27 NWW	●	1st & 2 nd check	↓
20	239	122/41 SW	●	-	↓
21	246	138/25 NNE	●	-	Port na luing
22	255	068/52 NNW	●	-	Aird Dhughail
23	260	079/84 NNW	●	U. margin with discontinuous sacharoidal Qtz.	↓ ↓
24	260.1	104/47 NWN & 113/47 NWN	●	-	↓
25	260.2	076/48 NNW	●	Discontinuous aplitic centres	↓
26	260.3	106/53 NNE & 047/38 SE	●	X 2 sets. Refer to notebook	↓
27	263.7	161/40 NEE	●	Occurring @ planar U. contact with diorite sheet	↓ ↓
28	263.10/	062/40 NWN & 004/85 W	●	Refer to notebook	↓
29	270	084/38 NNW	●	-	↓
30	273	067/52 NWN	●	-	↓
31	273.1	064/54 NWN	●	Coarse gr. U. margin with uneven sacharoidal Qtz. within the core. 5-7cm total width	↓ ↓ ↓
32	281.10/	080/52 NNW	●	Complex bifurcating sheet	↓
33	281.11	036/27 WNW	●	as above	↓
34	284.9	081/34 NWN	●	-	Maol Mhora
35	286.21	023/25 WNW	●	-	↓
36	287.31	137/24 NE	●	Discontinuous pegmatitic U. margin & central coarse gr. pegmatite. 20-25cm width	↓ ↓ ↓
37	287.32	074/45 NWN	●	Coarser U & L gr margin	↓
38	288.19	025/39 WNW	●	40-50cm width. coarse Qtz rich U. margin	↓ ↓
39	290	100/36 NNE?	●	Same as (S) joint plane?	↓
40	290.3	156/37 NEE	●	Coarse gr. U & L margin	↓
41	297.2	008/27 WNW	●	Aplite vein on same plane as (S)	↓

No.	353	Measurement		Additional info.	Area
				joint	↓
42	308	035/47 NW	●	Slightly coarse gr. U & L margin	Port na' Ba' Baine
43	323	017/39 ESE	●	L & U aplitic margin. 5-7 cm wide.	↓
44	325.2	074/30 NWN	●	10 cm wide Moine xenolith x-cut by	↓
				this sheet	↓
45	326.4	019/38 WNW	●	Coarse U & L grained margin. 4cm	↓
				width	↓
46	327.4	164/29 E & 179/28 W	●	Network of aplites	↓
47	330.5	139/50 NE	●2	30-40 cm width	↓
48	333.8	050-056/44 NWN & 106/44 SW	●	Refer to notebook & relevant diagram	↓
				to sheet @ Eilean Srianach	↓
49	340	084/58 NNE	●2	Nice pitted amph.	↓
50	343	079/42 SES & 034/41 WNW	both ●2	-	↓
51	344	024/66 WNW	●	Lovely diorite inclusions	↓
52	346.1	087/48 NWN	●3	micro-phenocrystic- hbld.	↓
				aplite with phenos <5%	↓
53	346.2	010/64 ESE	●2	-	Slochd a Bhodaic
54	347	029/44 WNW & 041/54 W	●2 & ● 1 ●2, ●/● &	Planar & // to Type 1 lamprophyre	↓
55	348	048/44 W, 001/42 W & 139/85 NE	●	Refer to notebook	↓
56	351	042/52 WNW to 032/52 WNW	●2	Strike swings	↓
57	353	156/87 SWW	●1	5cm width	↓
58	359	172/70 W	●2	1cm width	↓
59	360	055/34 SES & 124/68 NNE	●1/●	10cm wide/ 60cm wide	↓
60	364	070/72 S	●2	-	↓
61	368	150/29 NEE	●2	// to (S) joint measurement	↓
62	371.1	165/72 NEE	●1	1cm width	↓
63	373.2	079/31 SEE	●	-	↓
64	373.3	080/25 NNW & 075/30 NNW	●1	-	↓
65	378	083/47 N	●2	30-40cm	↓
66	378.1	118/39 NNE	●2	-	↓
67	381	014/32 ESE	●	-	↓
68	374	100	●1	Planar area in chasm	Rubh' Ardalanish
69	384.7	016/42 WNW	●	2-3 cm aplite sheet with coarse gr.	Erraid
				Pegmatitic U. margin	

- ● Type 0 aplite
- ●1 Type 1 aplite
- ●2 Type 2 aplite
- ● Type 2 aplite with internal MME
- ● Aplite with mingled contacts within a Type 2 lamprophyre

Locality refers to locality in field notebook

↓ continuation of coastal traverse that starts from Red Bay quarry and ends at Rubh' Ardalanish

Appendix Two
PETROGRAPHY

Introduction

This section exhibits petrographic descriptions (**Appendix A2.1**) and thin-section textures inferred to capture evidence of mafic-felsic magma interaction (**Appendix A2.2**) for each ROMG component.

A2.1 Petrographic descriptions with accompanying detailed sketches of the following samples have been made:

Mafic Components

Type 1 diorite; Plagioclase- hornblende-phyric biotite diorites (Knockvologan type)

JR31 (NM [309 189]) Erraid Sound 158

Type 2 diorite; Equigranular diorites/quartz diorites (Aird Mór type)

JR24 (NM [325 185]) Port nan Rón 162
JR41 (NM [323 177]) Aird Mór 168

Type 2 lamprophyre; Non-composite, porphyritic micro-diorite

JR23 (NM [309 186]) Sheared sheet from Erraid Sound 173

Felsic Components

RM2: Alkali feldspar-megacrystic biotite granite/granodiorite (Knockvologan facies)

JR05 (NM [356 192]) West Ardalanish 177
JR32 (NM [295 155]) Dearg Sgier 182

RM1: Equigranular biotite granite (Red Bay facies)

JR15 (NM [364 216]) Bendoran 187

RM1a: Leucocratic, marginal muscovite-biotite granite

JR02 (NM [325 185]) Whitish, Ardalanish 191

In all gross textural petrographic sketches, the left hand side is PPL and the right hand side is in XPL.

Type 1 diorite: Plagioclase- hornblende-phyric biotite diorites (Knockvologan type)
JR31 (NM [309 189]) Erraid Sound

Hand Specimen

The rock is a micro-phyric, generally aphanitic (groundmass), mesocratic to melanocratic, fine-grained plutonic igneous rock. Plagioclase feldspar is just about discernible being lath like and no crystals are greater than 2 mm in terms of length in this section.

The common rock forming minerals are as follows:

Plagioclase feldspar -55%
Hornblende - 25%
Biotite - 20%
Quartz - 1-5%

Accessory minerals are as follows:

Titanite
Apatite

Plagioclase feldspar

Typically anhedral to subhedral, with lath like crystals making up the bulk of the rock. Crystals are 1 mm on average and practically all are vaguely zoned (normal zoning). Cores have highly sericitised areas indicative of a more Ca rich area whilst the rims are not. Single Carlsbad twins are well retained.

Hornblende

Similar affinities to sample JR24 where glomerophyric varieties occur, but only as a less common form associated with a rim of biotite containing Fe-Ti opaque oxides. The

individual crystals that form the glomerophenocrysts are generally subhedral whilst the mantling biotite phase is anhedral-subhedral. Within the rest of the groundmass, hornblende is anhedral to subhedral, occasionally lath shaped and commonly replaced by biotite. There is no evidence here for differentiating what is primary hornblende.

Biotite

Anhedral to subhedral, hackly edged chocolate brown biotite is commonly associated with hornblende. It also occurs in the interlocking groundmass and can be regarded as a secondary mineral.

Quartz

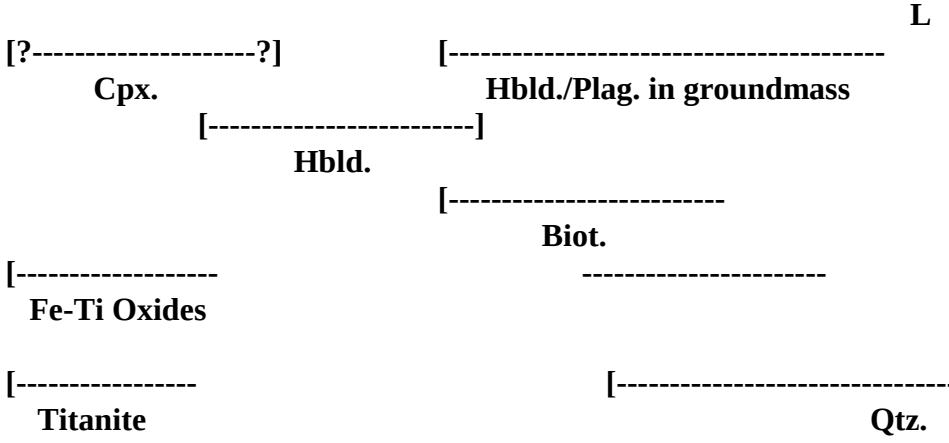
Initially very difficult to observe due to the little abundance of it in thin section. Crystals are anhedral, rounded in terms of habit having undulose extinction.

Textures and other features

Glomerophenocrystic hornblende is again possibly indicative of replacing clino-pyroxene; however there are no relict textures present in this slide (as observed in rare MME containing clino-pyroxene).

Normal zoning is common throughout. Gross texture is allotriomorphic to hypidiomorphic.

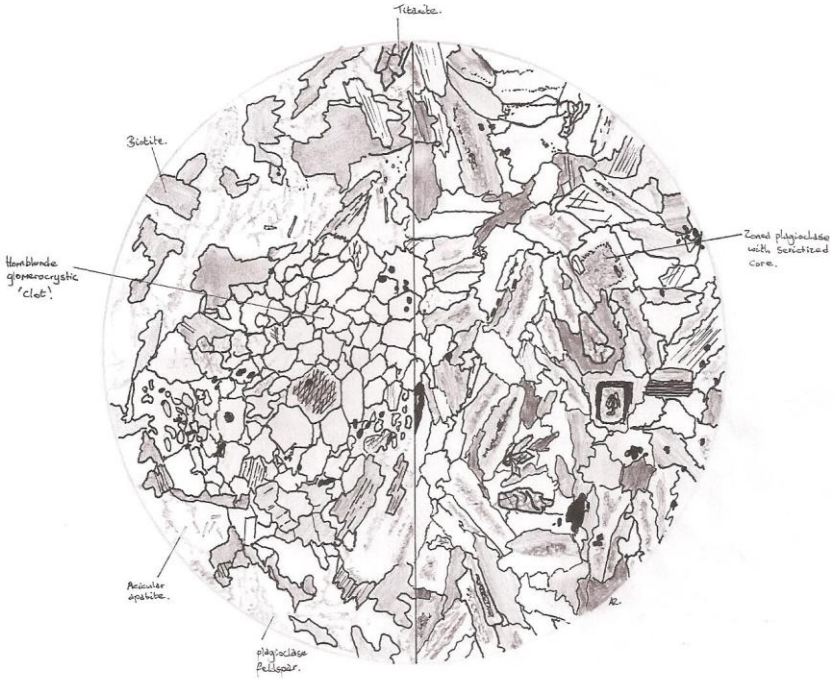
Order of crystallisation



Classification

This is a slightly silica-saturated rock, dominated by plagioclase, hornblende, biotite and no essential alkali feldspar. It is also metaluminous which is evident in all samples relative to the inner diorite sheets at Knockvologan and should be classified as a hornblende-biotite diorite.

(31), GR 309 189, hornblende - biotite diorite from Erraid Sound.



x4/0.10/160.

Type 2 diorite: Plagioclase- hornblende-phyric biotite diorites (Knockvologan type)
JR24 (NM [325 185]) Port nan Rón

Hand Specimen

A phaneritic, aphanitic, hollocrystalline, mesocratic to melanocratic, and medium to coarse grained, highly heterogeneous igneous plutonic rock. This hand specimen does not reflect the heterogeneous porphyritic nature of Type 1 diorite as a whole but the thin section does.

The common rock forming minerals are as follows:

Hornblende (primary?) - poikilitically enclosing biotite
(secondary) - glomerocrystic basal sections in groundmass - 60%
Biotite (secondary)
Plagioclase feldspar (2 phases) - 40%
Calcite - <1%

Minor xenocrysts as follows:

Quartz
Alkali feldspar

Accessory minerals are as follows:

Titanite (commonly observed and as 2 phases)
Apatite
Fe-Ti opaque oxides

Hornblende

Occurring as unevenly distributed glomerocrystic clusters (clots) comprising of individual anhedral to subhedral crystals. These clots are associated with enclosed biotite that

is also anhedral to subhedral, generally being elongate and hackly edged. Biotite replaces hornblende again. There are minor glomerophyric forms present.

The primary hornblende is poikilitically included in biotite and interestingly associated with a corona of titanite which itself is composed of anhedral grains.

Within the matrix, larger hornblende occurs as anhedral to subhedral grains that are commonly altered and associated with biotite. Near basal sections are common but a good example of two cleavages intersecting can be difficult to spot in most. Crystals with first order interference colours commonly show one twin plane.

Biotite

The most distinct mineral in the slide because of its size (4mm in terms of maximum length in prismatic hackly edged subhedral varieties). Cleavage is well maintained in all varieties; however the most interesting feature is the intimate concentrated association of titanite occurring parallel to, within cleavage planes and as rims around piokilitic hornblende within biotite. Kinked cleavages are present in some isolated varieties.

Plagioclase feldspar

Where dominant (because of the highly heterogeneous distribution of minerals in this slide), plagioclase crystals are all normally zoned and in most cases, highly sericitised. In severe cases, calcite has occurred as a breakdown product of plagioclase but this is minor. Plagioclase crystals are anhedral to subhedral, and most certainly interstitial. In more complex varieties, whilst poly-synthetic albite twins are visible, there is a high degree of sericitisation present within the cores, and interestingly, rims are often uneven and in some cases almost ‘vermicular’ looking.

Calcite

Very minor, occurring as anhedral to subhedral rare patches.

Accessories

Apatite occurs as euhedral crystals restricted to being poikilitically included entirely within plagioclase feldspar**.**

Textures and other features

The overall texture is a heterogeneous porphyritic one with an allotriomorphic groundmass, and the mineral replacement series of hornblende to biotite is evident throughout this section.

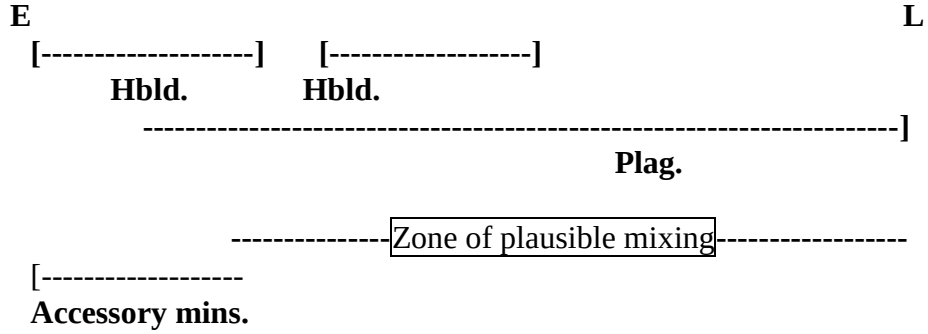
The relationship between titanite and amphibole as shown in the first sketch for this sample is certainly unusual and needs to be revised. A debate on whether this texture is purely magmatic or sub-solidus would be intriguing. However, one would opt for this texture forming in the sub-solidus environment due to the highly anhedral nature of the titanite and its association with secondary hornblende (one would need to think about nucleation/substitution into the amphibole complex lattice so that a stable phase coexists within different environments).

There is evidence for at least two phases of hornblende crystallisation based upon the different nature of the populations present.

Disequilibrium textures are evident in plagioclase whereby there has been a shift(s) in equilibrium with respect to the melt during the late stage development of plagioclase. The cores are not relatively planar (i.e. not conforming to a simple concordant zonation profile) and in some cases the rims are embayed. Closer inspection reveals that in some instances, blebs of the core are retained in the rim, which is relative to exsolution (a feature that can be attributed to magma mixing).

Plagioclases with different zonation profiles juxtaposed, isolated rare embayed (some rapakivi types) alkali feldspar xenocrysts and rare highly corroded quartz (ocelli with or without a mafic mineral ocellus) provide key textural evidence for intimate coexistence of mafic and felsic magmas; that magma mixing to some degree has took place to form a heterogeneous hybrid.

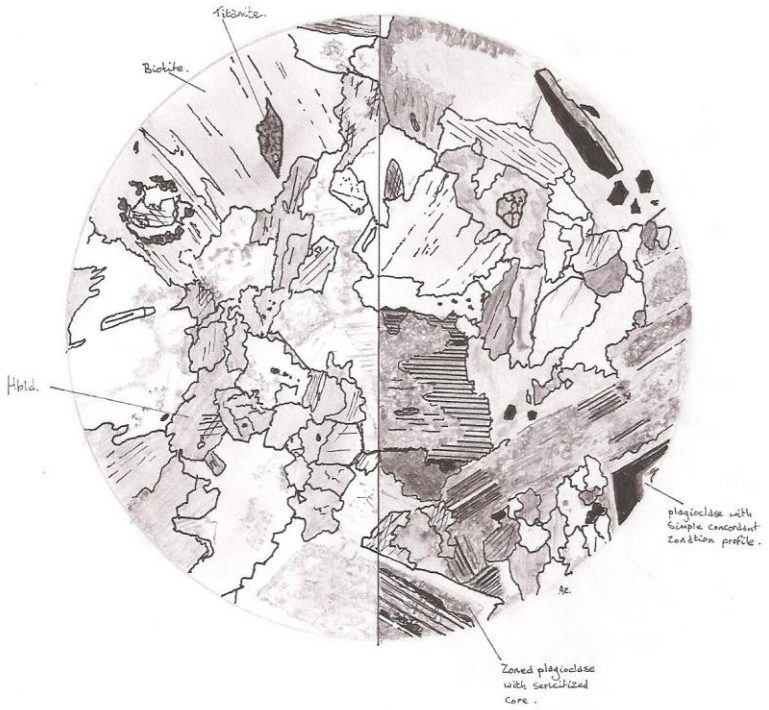
Order of crystallisation



Classification

This is a silica saturated, metaluminous, plutonic igneous rock with no essential alkali feldspar. It has sufficient common hornblende and Na plagioclase to be classified as a hornblende- biotite diorite.

(24), GR 325 185 B, hornblende - biotite diorite from Port nan Ron.



X 4/0.10/160.

(24), G.R. 325 185 B, titanite Coronas on poikilitic hornblende (P.P.L.)



x 0.07mm

Type 2 diorite: Equigranular diorites/quartz diorites (Aird Mór type)
JR41 (NM [323 177]) Aird Mór

Hand Specimen

A phaneritic, only slightly porphyritic in patches, hollocrystalline, mesocratic, and medium-grained plutonic igneous rock.

The common rock forming minerals are as follows:

Plagioclase feldspar - 30-40%

Biotite - 30%
(matrix including rims on Hornblende glomerophenocrysts)

Hornblende - 15%
(matrix and glomerophenocrysts)

Relict Clino-pyroxene - 5-10%
(former primary phenocrysts)

Quartz - 5-10%

Accessory minerals are as follows:

Titanite

Apatite

Zircon

Fe-Ti Opaque oxides

Plagioclase feldspar

Plagioclase feldspar noticeably occurs as two main phases. It occurs as (i) rare anhedral grains poikilitically included in relict clino-pyroxene (composition of plagioclase cannot be determined here by the Levy method as extinction angles of a and a surpass 5^{o} and are therefore rejected).

The bulk of the feldspars (ii) are restricted to the groundmass where they display the common albite law well although heavy sericitic alteration is common. Levy method reveals compositions of $An_{(69)}$ (Labradorite).

Biotite

Anhedral basal sections with enclosing Fe-Ti opaque oxides are common and again associated with hornblende. Prismatic, lath like, bladed subhedral biotite is also evident displaying good cleavage.

Hornblende

Occurring as three different forms. There is evidence for (i) once primary euhedral clino-pyroxene existing but it is replaced by secondary hornblende appearing as an anhedral phase with patchy areas of well developed cleavages (see sketch).

Within the groundmass (ii), hornblende commonly occurs as anhedral to subhedral clusters and is always associated with biotite and Fe-Ti opaque oxides. This is the most dominant form within the slide having uneven distribution.

(iii) The third variety poikilitically includes plagioclase feldspar comprising of anhedral crystals that are 0.2 mm on average.

Relict Clino-pyroxene

Restricted to edges of once former euhedral primary crystals that would have been 4 mm in terms of length (see sketch). A 90^{o} cleavage is present but difficult to find and maximum extinction angle reveals compositions of augite.

Quartz

Minor, anhedral to subhedral interstitially bounded against biotite, hornblende and plagioclase feldspar. Typically having undulose extinction, which is the main feature of the inequant anhedral grains of varying size.

Textures and other features

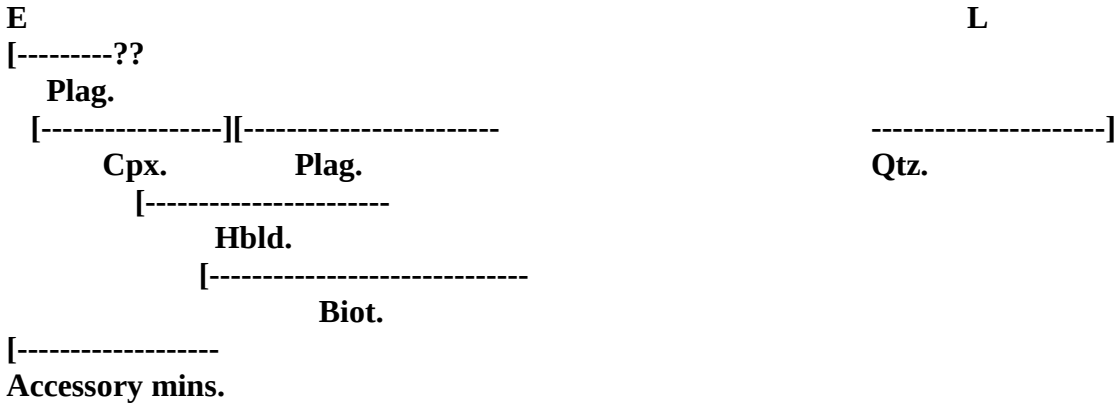
The following breakdown (hydration series) is easily depicted from thin section work;

Clino-pyroxene → Hornblende → Biotite

This breakdown series is very common in these diorites and without being over too interpretive, this could relate to magmatic mixing processes during re-equilibration or to a variety of late stage (sub-solidus) hydration reactions.

It is also difficult to determine what the primary hornblende is within this section. Most of the hornblende is secondary.

Order of crystallisation

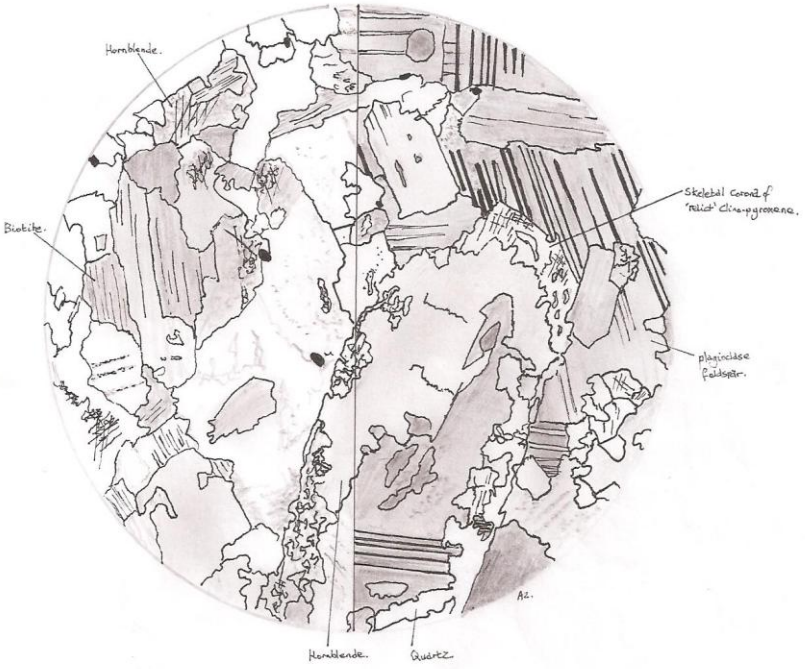


Classification

This is a silica-saturated, metaluminous rock, having no essential alkali feldspar. Due to presence of clino-pyroxene, abundance of amphibole, and a relatively medium to coarse equigranular nature with plagioclase being > $An_{(50)}$ in this section, one could have the grounds to classify this rock as a gabbro. However, grain-size and modal mineralogy can vary in such

Aird Mór type diorites and more homogeneous representative samples have considerably more quartz than Knockvologan diorites that make up the groundmass, and are hence referred to as quartz diorites.

(41), GR 323 177B, hornblende-biotite gabbro from Aird Mor.



X04/012

Type 2 lamprophyre: Non-composite, porphyritic micro-diorite
JR23 (NM [309 186]) Sheared sheet from Erraid Sound

Hand Specimen

There is no hand specimen available, however such varieties of diorite are phaneritic, porphyritic, hollocrystalline, mesocratic, and medium-grained plutonic igneous rock.

The common rock forming minerals are as follows:

Glomerophenocrysts (60%)

Hornblende (with biotite rim) - 60%

Matrix (40%)

Plagioclase feldspar - 50%
Quartz - 25%
Hornblende & biotite - 20%
Calcite (as breakdown product from plagioclase) - <1%

Accessory minerals are as follows:

Titanite - 1-5%
Apatite
Zircon
Fe-Ti Opaque oxides

Hornblende glomerophenocrysts (with biotite rim)

Clearly the most striking feature in this thin section occurring as phenocryst clusters of small hornblende crystals. Individual crystals are anhedral to subhedral, lacking good cleavage and are 0.025 mm on average. These phenocryst clusters (clots) are commonly

associated with an extremely well developed rim of individual anhedral biotite crystals that are themselves associated with Fe-Ti opaque oxides.

Plagioclase feldspar

Poly-synthetic albite twins are difficult to observe and crystals are anhedral to subhedral with 0.45 mm average length. Sericitic alteration is very common. Feldspars commonly display a more Ca rich domain (altered to sericite) and a Na rich domain at the edge (not to be entirely mistaken with pronounced normal zoning).

A more euhedral to even acicular variety occurs and is 1.2 mm on average length displaying a bent morphology and possible fracturing at ends in response to shearing?

Levy method for determination of feldspar composition cannot be used here as equal illumination of albite twins is not apparent.

Quartz

Occurring as anhedral clots within the matrix (heterogeneously distributed), typically having undulose extinction and are 0.9 mm on average. It is commonly associated within enclosed areas within plagioclase and is poikilitically included by biotite, hornblende and titanite.

Hornblende & biotite

Hornblende commonly depicts undulose extinction, some twinning and inclusions of Fe-Ti opaque oxides. It is identified as the principle amphibole in all the diorites observed in thin section so far due to its optical properties. Biotite is generally anhedral to subhedral, hackly edged and 0.2 mm on average length.

Accessory minerals

Titanite is the most abundant accessory mineral displaying a variety of morphologies from anhedral to euhedral (classic lozenge shape) but lacking cleavage.

Apatite is common and pervasive throughout the rock occurring as an acicular form easily observed in quartz rich areas (related as a heterogeneous magma mixing texture).

Zircon is minor, colourless and anhedral.

Textures and other features

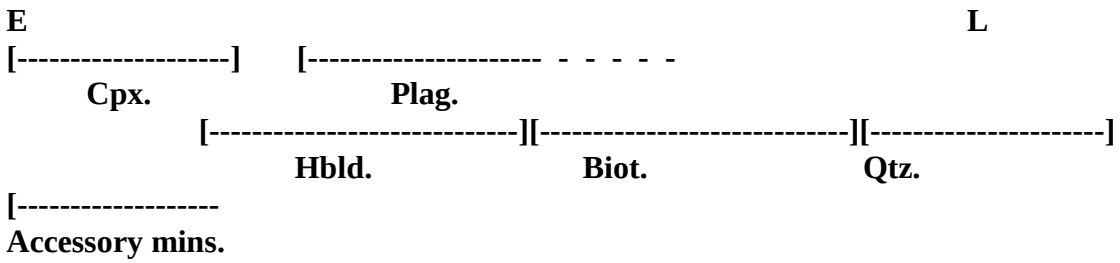
The gross texture is hypidiomorphic. Poikilitic inclusions of biotite, titanite and amphibole in quartz signify an earlier crystallisation history. Quartz is interstitial to all other mineral phases and crystallised much later.

Glomerophyric hornblende is indicative of secondary replacement (a breakdown product) of clino-pyroxene. Evidence for this is best observed in section JR41.

The rim of biotite around the glomerocrysts is also related to alteration, whereby hornblende has broken down to biotite.

Although the sample has been collected from a 'sheared' sheet, there is no evidence for a pervasive shear fabric in thin section (i.e. a dominant mineral alignment in the groundmass). There is a vague orientation of biotite that cannot be interpreted as strong evidence for shearing.

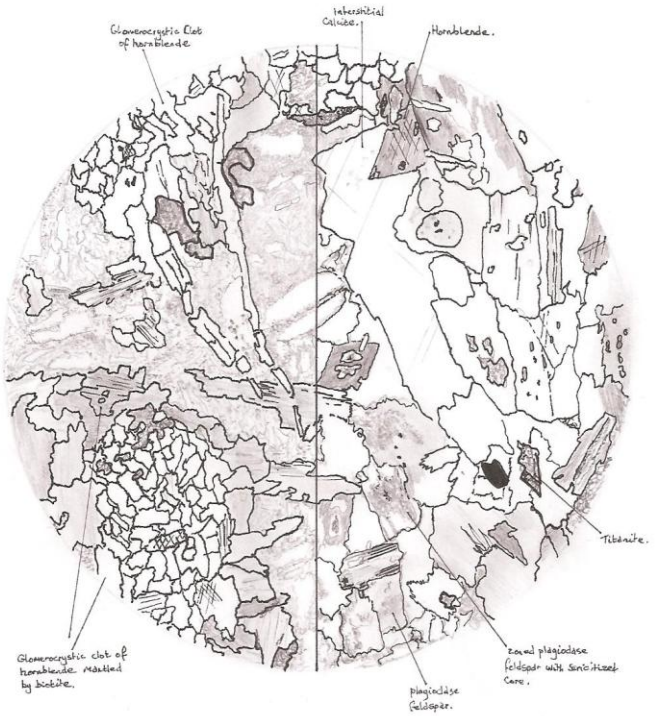
Order of crystallisation



Classification

This is a silica saturated, metaluminous, plutonic igneous rock with no essential alkali feldspar. It has sufficient hornblende and Na plagioclase to be classified as a hornblende-biotite diorite.

(23), GR 309 186 B. Sheared diorite dyke from Erraid Sound.



X4/0.12.

RM2: Alkali feldspar-megacrystic biotite granite/granodiorite (Knockvologan facies)
JR05 (NM [356 192]) West Ardalanish

Hand Specimen

The rock is a porphyritic (alkali feldspar phyric), phaneritic, hollocrystalline, equigranular, and leucocratic to mesocratic, coarse-grained plutonic acid igneous rock. Subhedral, tabular pink alkali feldspar phenocrysts ranging from 1 to 15 mm on average length dominate throughout the hand specimen. The matrix is evidently composed of anhedral quartz (interstitial phase) and biotite. The keen eye can also make out examples of euhedral lozenge shaped titanite that has a golden straw yellow lustre and is 1 to 2 mm average length, restricted to the matrix. From hand specimen alone, one would estimate at the alkali feldspar phenocrysts make up 50 to 60% of the rock in some heterogeneous areas.

The common rock forming minerals are as follows:

Phenocrysts (35%)

Orthoclase micro-perthite - 25-30%
Microcline perthite - 5%

Matrix (65%)

Plagioclase feldspar - 35-40%
Quartz - 20-25%
Biotite (including chloritised biotite) - 10-15%
Relict hornblende - <1%

Accessory minerals are as follows:

Titanite
Apatite
Fe-Ti opaque oxides

Orthoclase micro-perthite phenocrysts

In thin section, most varieties are poikiliticaly included by small subhedral plagioclase, and in some rare zoned cases, these can form aligned restricted zones associated with anhedral blebs of quartz. Exsolution blebs of plagioclase can be deduced, and most varieties are all subhedral megacrysts. Mantling relationships involving small plagioclase (with different zonation profiles and sericitisation) do occur in isolated varieties, where RM2 is heterogeneous.

Microcline perthite phenocrysts

Fresh in thin section commonly displaying classic tartan twinning in subhedral crystals that may or may not be poikilitically included by smaller anhedral to subhedral plagioclase feldspar.

Plagioclase feldspar

The dominant phase within the matrix is primarily subhedral and may also be quite tabular in some varieties. At least three forms can be identified.

The first variety has sericitised cores, which are lobate in places and albite twins are just about visible. Carlsbad twins are also evident in this population.

The other feldspars within the matrix are all normally zoned and there are those with a more complex history. In these more complex varieties, various zones with respect to Ca/Na compositions imply disequilibria has occurred within the system. Their distribution is not entirely ordered and clustering does occur.

Quartz

Typically retaining undulose extinction with anhedral, interstitial crystals. The last crystallising phase in this section.

Biotite

Anhedral to euhedral, interstitial and commonly altered to chlorite. Only the tabular, prismatic hackly edged varieties show good cleavage. Biotite is commonly associated with apatite and Fe-Ti opaque oxides.

Hornblende

Once primary, it is now anhedral, 0.5 mm on average length, and has been broken down and replaced by biotite.

Titanite

Euhedral, classic lozenge shaped titanite is associated with biotite and is solely restricted to the matrix. It is clearly related to an early magmatic phase and crystals are 1 to 2 mm on average length.

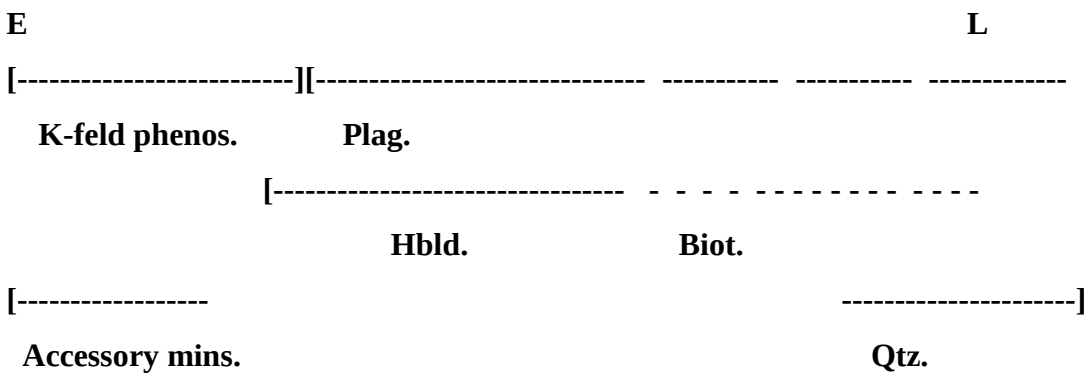
Textures and other features

Breakdown of hornblende to biotite is clearly discernible. The complex disequilibria in plagioclases and the clustering of plagioclase highlight the micro-heterogeneities in terms of adjacent mineral distributions.

In some other varieties of RM2, the following mafic-felsic magma mixing compatible textures have been noted:

- Plagioclase feldspars with variable boxy cellular structures.
- Isolated zoned plagioclase glomeroxenocrysts with highly sericitised cores
- Variably zoned plagioclase feldspars with or without sericitised cores.
- Isolated multiply zoned plagioclase glomeroxenocrysts with or without highly sericitised cores juxtaposed to each other, and isolated multiply zoned plagioclases.

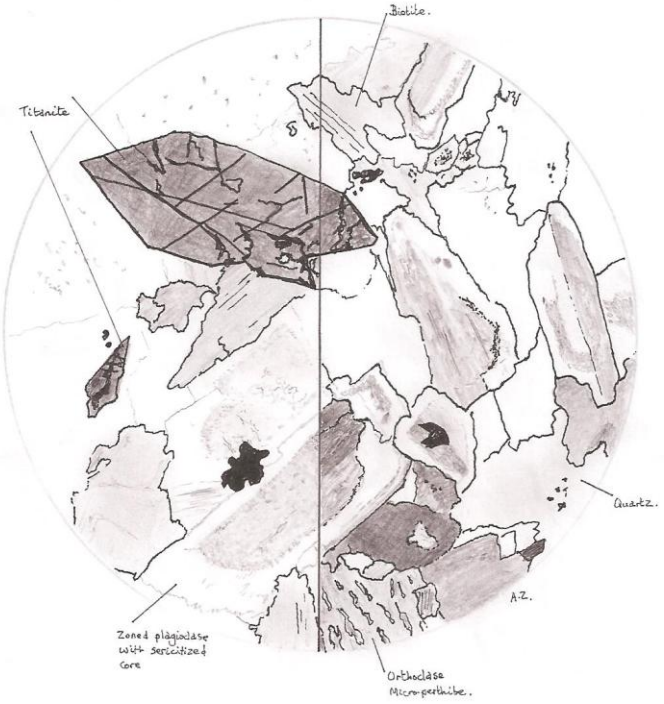
Order of crystallisation



Classification

This is a silica over-saturated igneous rock, dominated by alkali feldspar phenocrysts. During earlier crystallisation, primary magmatic amphibole could have dominated but is now replaced by biotite. The rock is an alkali feldspar megacrystic monzogranite/granite.

(5), 356 192 G, K-feldspar phyric biotite granite relative to RM2 from W. Ardalanish, Ntn traverse.



RM2: Alkali feldspar-megacrystic biotite granite/granodiorite (Knockvologan facies)
JR32 (NM [295 155]) Dearg Sgier

Hand Specimen

Alkali feldspar-phyric in patch areas, phaneritic, hollocrystalline, leucocratic, coarse-grained and clearly a plutonic acid igneous rock. Biotite is anhedral to subhedral, ranging from 0.05 to 4mm in length. Heterogeneous distribution of pearly pink tabular alkali feldspar phenocrysts dominate in a relatively unequigranular rock.

The common rock forming minerals are as follows:

Phenocrysts (30%)

Orthoclase micro-perthite - 30%

Matrix (70%)

Plagioclase feldspar - 60%
Quartz - 30%
Microcline - 1-5%
Biotite - 5%
Minor chlorite - <1%
Minor calcite
Minor muscovite

Accessory minerals are as follows:

Titanite
Apatite
Allanite (zoned)
Fe-Ti Opaque oxides

Orthoclase micro-perthite phenocrysts

Subhedral, ranging up to 10 mm on average length, having exsolution blebs of plagioclase feldspar.

Plagioclase feldspar

Three different forms can be identified in thin section. (i) A very early crystallising phase poikilitically including orthoclase is evident as anhedral to subhedral normally zoned feldspars. This is a relatively common feature. However another, (ii) poikiltic variety of plagioclase within orthoclase exists being larger (1 mm) often exhibiting a single Carlsbad twin plane. The final variety occurs (iii) as glomerocrysts of anhedral to subhedral plagioclase (2 to 3 mm on average size) showing high degrees of sericitic alteration as well as a well-developed Carlsbad twin (Levy method suggests andesine to oligioclase compositions for such feldspars).

Quartz

Typically having undulose extinction, anhedral and interstitial, the last crystallising phase within the slide.

Biotite

Where prismatic and lath like, a good single cleavage is apparent and the common association with Fe-Ti oxides is present. Anhedral varieties are more altered to chlorite.

Allanite

As depicted in the first sketch, allanite is euhedral and 2 mm on average. It is well zoned and associated with titanite and Fe-Ti opaque oxides. It is evidently magmatic, and like that of oscillatory-zoned feldspar, it records changes within a magmatic system (one could look at the distribution and nature of zonation within all components of the ROMG, and analyse core to rim abundances R.E.E. via ion-probe to model and reconstruct magmatic

environmental changes during early crystallisation and sub-solidus processes. Allanites are also useful for dating purposes).

Textures and other features

The gross texture is hypidiomorphic. One should also note the phases of pre orthoclase crystallization of plagioclase feldspar could have formed simultaneously or at separate events. Textures advocated with magma mixed origins in RM2 have been previously mentioned in the sample JR5 description.

Order of crystallisation

E **L**

[----------][----------][----------][----------]

Plag. X2 phases **K-feld.** **Plag.** **Qtz.**

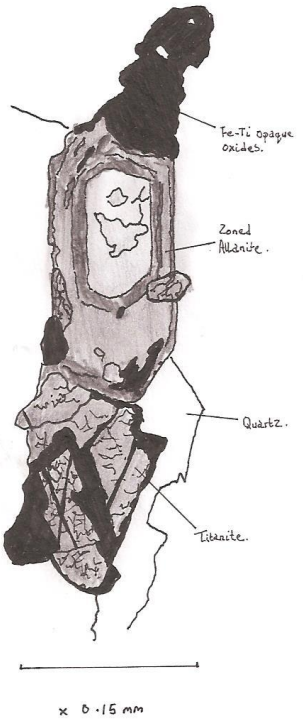
[---------- **[----------**

Accessory mins. **Biot.**

Classification

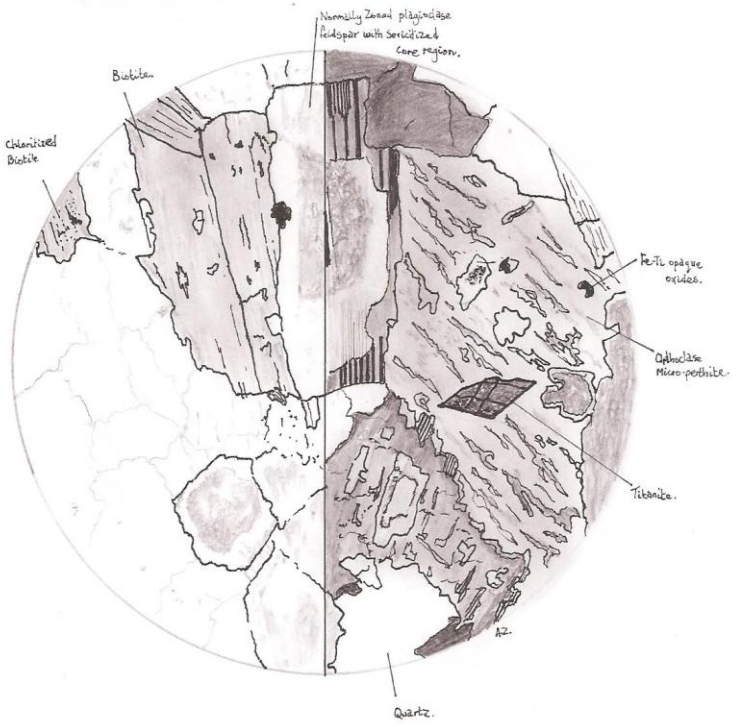
Based upon the estimated mineral content, this is a silica over-saturated rock having relatively equal proportions of alkali feldspar and plagioclase feldspar (monzogranite). Presence of phenocrysts means the rock could be classified as an alkali feldspar megacrystic monzogranite/granite.

(32) 295 155 G 2 Zoned allanite
(P.P.L.)



x 0·15 mm

(32), G.R: 295 155G, Monzogranite relative to RM2.



0 2 4 mm

x2/0.08

RM1: Equigranular biotite granite (Red Bay facies)
JR15 (NM [364 216]) Bendoran

Hand Specimen

The rock is an aphyric, phaneritic, hollocrystalline, equigranular, leucocratic, coarse-grained plutonic acid igneous rock. Generally, all the grains are anhedral to subhedral with pink alkali feldspar being the dominant and larger mineral phase present (13 mm average length).

The common rock forming minerals are as follows:

Plagioclase feldspar -15-20%
Orthoclase micro-perthite &
Microcline (microcline perthite in places) - 40-50%
Quartz - 15-20%
Biotite (some chlorite alteration) - 10%

Accessory minerals are as follows:

Titanite
Apatite (2 forms)
Zircon
Fe-Ti opaque oxides

Plagioclase feldspar

There are two/three forms. The first form (i) is commonly found as clusters of subhedral crystals, 1 to 1.5 mm on average. Twinning of the Carlsbad and albite laws is well displayed. Isolated subhedral crystals (ii) show normal zoning. However, there are (ii) vaguely normally zoned poikilitic varieties in orthoclase micro-perthite that are anhedral and have a highly sericitised core (these are 0.7 mm on average).

Orthoclase micro-perthite

Occurring as anhedral patches having exsolution blebs of plagioclase. An interesting comparison can be seen where it is in contact with microcline. At the sharp contact, completely anhedral crystals of plagioclase exist. The orthoclase is breaking down to microcline, which in turn is directly related to magma thermodynamics.

Microcline

Occurs as anhedral patches and where interstitial with quartz, it has well developed tartan twinning.

Quartz

Typically having undulose extinction, which is the main feature of the equant anhedral grains. Again the last crystallising phase, frequently containing inclusion trails.

Biotite

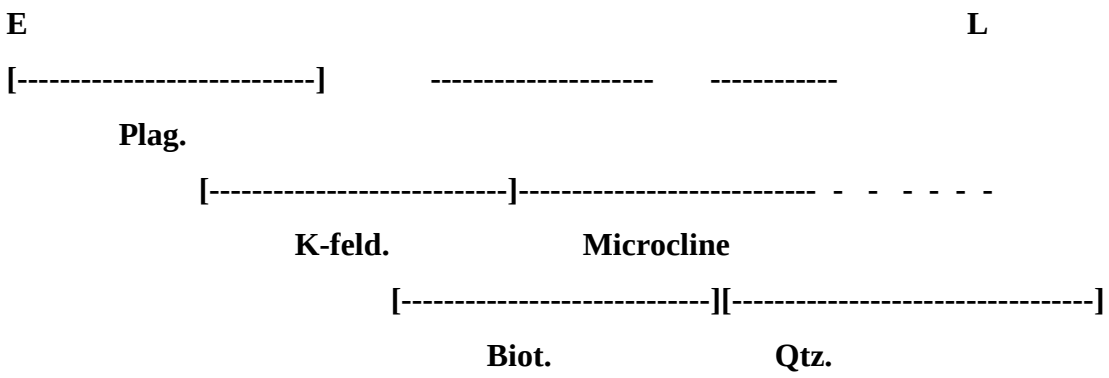
Commonly altered to chlorite and is anhedral to subhedral, displaying relatively good cleavage and is hackly edged. Associated with Fe-Ti opaque oxides and in rare cases, anhedral having inclusions of colourless zircon.

Textures and other features

Genesis of microcline here is directly related to the cooling history of the relevant magmatic facies during space and time. This sample contains more plagioclase than simple field petrology would suggest. Textures associated with mafic-felsic magma interaction are difficult to observe in homogeneous varieties, although the following rare textures have been noted in other RM1 samples:

- Variably zoned plagioclase feldspars with or without sericitised cores.
- Glomerocrystic plagioclase domains.
- Variable intensities of boxy cellular structures in plagioclase feldspar.

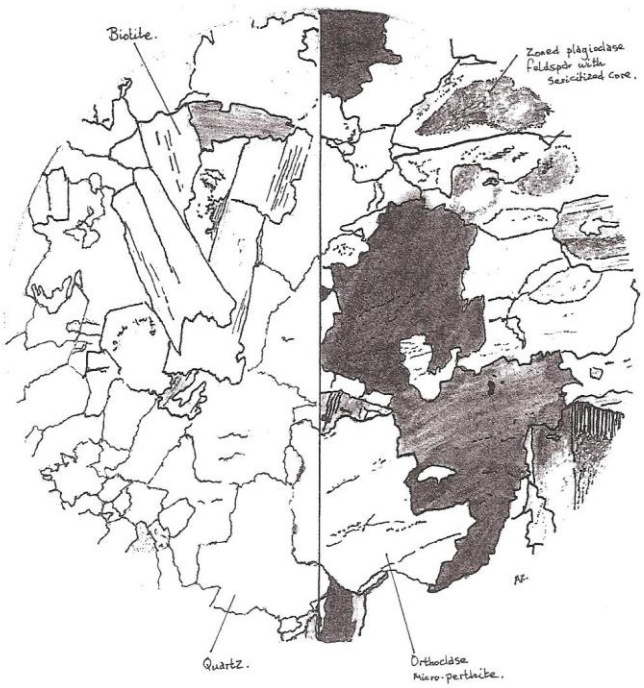
Order of crystallisation



Classification

This is a silica over-saturated igneous rock dominated by alkali feldspar. Although field petrology would suggest RM1 to be alkali feldspar granite, based on estimations of mineral proportions just on petrography alone, one would classify RM1 as equigranular biotite granite.

(15), G.R. 364 216 G. equigranular biotite (Monzo?) granite from Bandoran.



x 2/0.08

RM1a: Leucocratic, marginal muscovite-biotite granite

JR02 (NM [325 185]) Whitish, Ardalanish

Hand Specimen

This is an equigranular, phaneritic, aphyric, hollocrystalline, leucocratic, medium-grained, two mica variant, plutonic acid igneous rock. Biotite is anhedral and 3 mm on average with 4 mm maximum length. Pink alkali feldspars are subhedral, being 3 mm on average. Plagioclase is the 'frosty' white, subhedral to euhedral, tabular looking crystals that are 2.5 to 3 mm on average. Quartz is the transparent, interstitial, anhedral phase and is 2.5 to 3 mm on average. Note the relatively ordered distribution of each mineral phase throughout the rock.

The common rock forming minerals are as follows:

Orthoclase perthite &
Microcline perthite - 30%
Plagioclase feldspar - 35%
Quartz - 30%
Biotite (some chloritic alteration)
Muscovite - 5%

Accessory minerals are as follows:

Apatite
Zircon
Fe-Ti opaque oxides

Orthoclase perthite

Occurring as anhedral to subhedral crystals. Crystals are 3.25 mm on average.

Microcline perthite

Anhedral and showing tartan twinning. Again the relationship between the two feldspars is discussed in the sample JR15 description.

Plagioclase feldspar

Always subhedral and displaying the Carlsbad and albite law well. Three forms are present. Interstitial (i) plagioclase that is 1.5 mm on average is often found in contact with orthoclase perthite where vermicular looking exsolution? blebs occur in plagioclase. A (ii) poikilitic variety again exists within orthoclase perthite. These are subhedral to euhedral, 0.75 to 1 mm on average length, and have a sericitised core region. The final variety (iii) occurs as isolated glomerocrystic patches (crystals are 0.25 to 0.5 mm on average), having undulose extinction and are poikilitically included in alkali feldspar.

Quartz

Anhedral, interstitial, having undulose extinction and therefore the last crystallising phase.

Biotite

Basal sections are typically anhedral and altered to chlorite. Where considerably larger it is subhedral, 4 to 5 mm, having a planar single cleavage. The biotite is a deep rusty red colour often associated with zircon inclusions, apatite and Fe-Ti oxides within cleavage planes. Some minor kinking occurs within cleavage planes.

Muscovite

Minor, not primary and anhedral. It is associated with biotite.

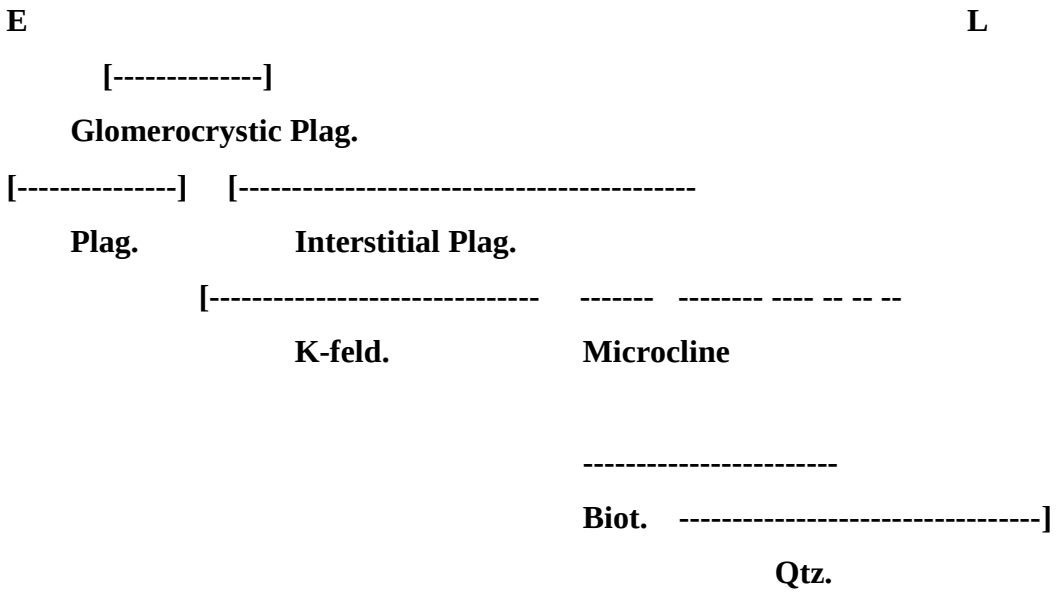
Zircon

Subhedral zircons commonly occur in biotite and also as clusters. The pleiochroic halo within biotite is the indicator that zircon is present.

Textures and other features

Note the absence of titanite in this section and the occurrence of a two mica variant. Evidently the quartz content is considerably higher in this marginal facies that is in contact with Moine meta-sediments.

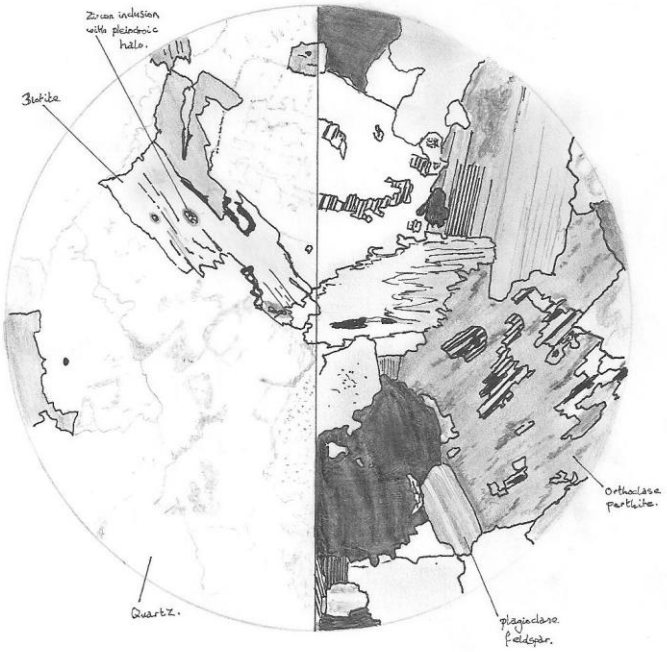
Order of crystallisation



Classification

This is a silica over-saturated rock that is a contaminated variant (with respect to anatexis of Moine meta-sediments), lacking titanite, having the first dominant appearance of muscovite and critical abundance of metamict zircon which would be the only true candidate for an S-Type based upon petrography and field relationships alone. Based upon mineral abundances, it is an equigranular muscovite- biotite monzogranite/granite.

(2), G.R 368 179 GA. Equigranular biotite Monzogranite relative to Ermida, from Whitish, Ardalanish.



0 2 4 mm.

X 2/0 08

A2.2 Magma mixing and *sub-solidus* textures; plagioclase zonation and textural characteristics in all components

This part of the appendix is an accompaniment to Chapter Two. Specific petrographic observations in all ROMG plutonic components are presented and used for interpretation of textures associated with magma mixed origins (based on guidelines in e.g. Baxter & Feely 2002).

The importance of documenting heterogeneous textures within a granitoid complex lies in the fact that if the geometry of the intrusion is known, then the horizontal or vertical prevalence of specific mixing/mingling textures can be used to make qualitative inferences on the nature and degree of this phenomenon within internal components and ultimately, throughout the whole complex.

In the case of the ROMG, feldspar mineral zonation and textures have been characterised in all components and towards the end of Chapter Two, it is shown that a specific mineral zonation is recognised to exist in all facies of the ROMG (that depict textural evidence for magma mixing). The importance of doing this and finding such patterns means that the next step in any similar study is to analyse representative feldspar crystals (with same mineral zonations from different facies) by integrated *in situ* elemental and isotopic studies with CL petrographic analysis to quantitatively assess the degree of magma mixing within a open magmatic system (i.e. crystal isotope stratigraphy).

Note the *sub-solidus* textures presented here are related to the late stage aplitic micro-granites that occur within the ROMG. This study does not intend to solely concentrate on such processes; however critical observations in the late stage components are presented to aid in understanding or interpretation of geochemical data presented in this study. Relevant textures that are ordered in this section are provided on the next page.

Fig. Ap1 (a-e)	Thin section mixing and mingling textures from RM1 (sample No. AF0207/DLC1 (NM [308 252]) (**a-c**) and sample No. RR104 (NM [299 231]) (**d-e**)) (all XPL).	197
Fig. Ap2	EPMA backscatter image of a euhedral oscillatory-zoned titanite from RM1 at Red Bay quarry (sample No. AF0207/DLC-1 (NM [308 252])).	198
Fig. Ap3 (a-f)	Feldspar zonation profiles in RM1a from Bendoran (sample no. JR7 (NM [364 218])) (**a** & **c**), (sample No. RR0125 (NM [357 219])) (**b**) and Whitish, Ardalanish (sample No. JR2 (NM [368 179])) (**d-f**) (all XPL).	199
Fig. Ap4 (a-f)	Thin section disequilibrium/equilibrium textures in host RM2 plagioclase feldspars (sample No. JR5 (NM [356 192]) (**a**, **c, d** & **e**), and sample No. RR107 (NM [300 223]) (**b** & **f**)) where MME are either absent or rare (all XPL).	201
Fig. Ap5	Euhedral oscillatory zoned allanite associated with titanite in RM2 (sample No. JR32 (NM [308 252])) (PPL).	202
Fig. Ap6 (a-f)	Thin section magma mixing textures in Type 2 aplite (sample No. AZ025 (NM [364 218]) (**a-e**)), and Type 1 aplite (sample No. AZ023 (NM [364 218]) (**f**)) (all XPL).	203
Fig. Ap7 (a-b)	Sub-solidus textures in syenite from Tormore Cottage (sample No. AZ007 (NM [301 242])) (both in XPL).	204
Fig. Ap8 (a-c)	Sub-solidus textures in sample No. AZ024 (NM [295 216]) (all XPL).	205
Fig. Ap9 (a-f)	Mafic-felsic magma interaction textures in Knockvologan Type 1 diorite component. Samples used as follows: **a** JR46 (NM [278 140]), **b** RR0114 (NM [307 202]), **c-d** AZD02 (NM [310 208]) and **e** AZD02 (NM [310 208]) (**a-d** XPL and **e-f** PPL).	207
Fig. Ap10	Euhedral clino-pyroxene (augite) replaced by amphibole and quartz in Type 2 Aird Mór diorite (sample No. JR41 (NM [323 177])) (PPL).	208
Fig. Ap11 (a-c)	Mafic-felsic magma interaction textures in MME from Knockvologan (sample No. AZD040 (NM [292 192])) (PPL).	209
Fig. Ap12	Thin section of hornblende phyric MME within host RM2 from Eilean nan Griogag (sample No. AZEN01 (NM [307 191])).	210
Fig. Ap13 (a-d)	Hybridisation textures from a hornblende phyric MME within host RM2 from Eilean nan Griogag (sample No. AZEN01 (NM [307 191])) (**a-b** XPL and **c-d** PPL).	211
Fig. Ap14 (a-c)	Mafic-felsic interaction textures in Type 1 lamprophyres (sample No. ZCLS02 (NM [300 241])) (**a-b** XPL and **c** PPL).	212

A2.2 RM1: The Red Bay type facies

Highly homogeneous looking in the field with an absence of MME, RM1 contains numerous textural heterogeneities related to magma mixing in thin section. These range from (**Fig. Ap1 (a-e)**):

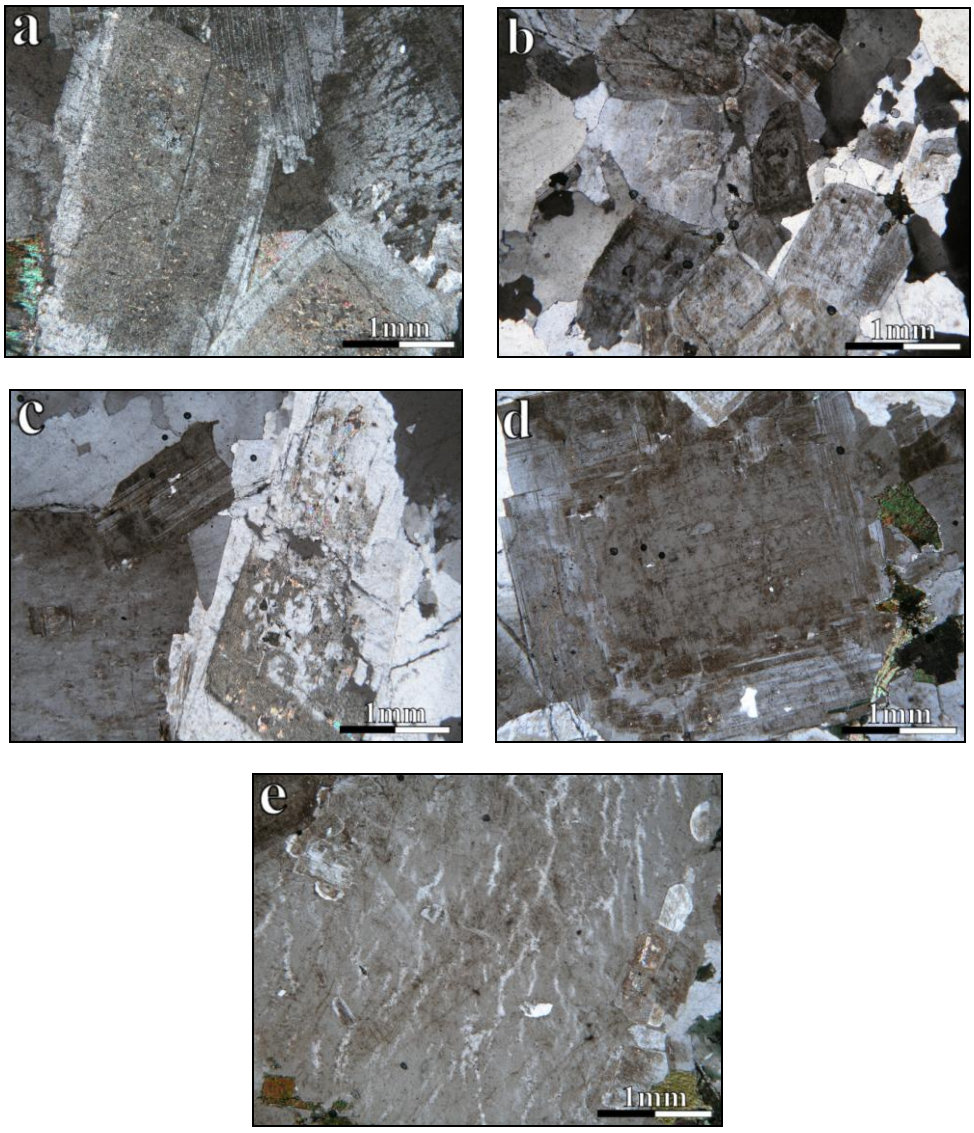


Fig. Ap1 (a-e): Mixing and mingling textures from RM1 (sample No. AF0207/DLC-1 (NM [308 252]) **(a-c)** and sample No. RR104 (NM [299 231]) **(d-e)**) (all XPL): **(a)** Two-fold mineral zonation in isolated plagioclase feldspars with highly sericitised cores. **(b)** Heterogeneous glomerocrystic distribution of subhedral plagioclase feldspars with different zonation profiles juxtaposed. **(c)** Plagioclase feldspar with a dendritic core composed of a cryptic heterogeneous boxy cellular structure. **(d)** Subhedral normally zoned plagioclase feldspar with corroded edges and a boxy cellular texture enhanced at the edges/outer zone. The feldspar is also mantled by smaller subhedral to euhedral plagioclase laths maintaining the same normal zonation to the larger feldspar considered. **(e)** Alkali feldspar mantled by smaller subhedral to euhedral plagioclases that have normal zonation profiles.

a.) Variably zoned plagioclase feldspars with or without sericitised cores

b.) Glomerocrystic plagioclase domains

c-d.) Variable intensities of boxy cellular structures in plagioclase feldspar

e.) Mantling relationships on alkali feldspar

In some cases, euhedral titanite from this facies shows oscillatory zoning and disequilibrium features in the form of embayed areas (Plate Ap2) that could be associated with fluctuations of contrasting magma composition as a result of magma mixing (refer to McLeod *et al.* 2011).

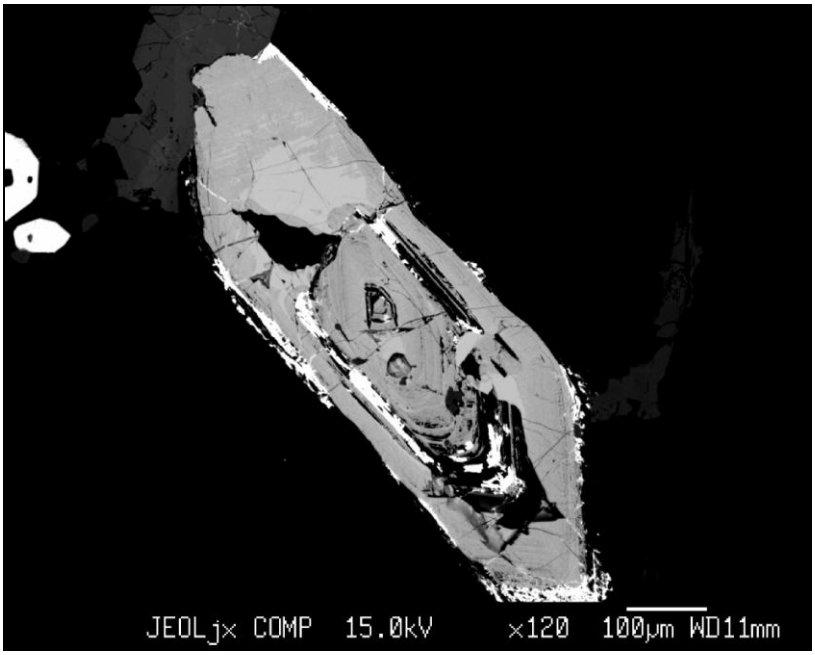


Fig. Ap2: EPMA backscatter image of a euhedral oscillatory-zoned titanite from RM1 at Red Bay Quarry (sample No. AF0207/DLC-1 (NM [308 252])).

A2.2 RM1a: The 'White' granite

Textural heterogeneity in RM1a occurs throughout Bendoran and Ardalanish Bay, and is intimately related to plagioclase feldspars. These heterogeneities in plagioclase feldspars range from (**Fig. Ap3 (a-f)**):

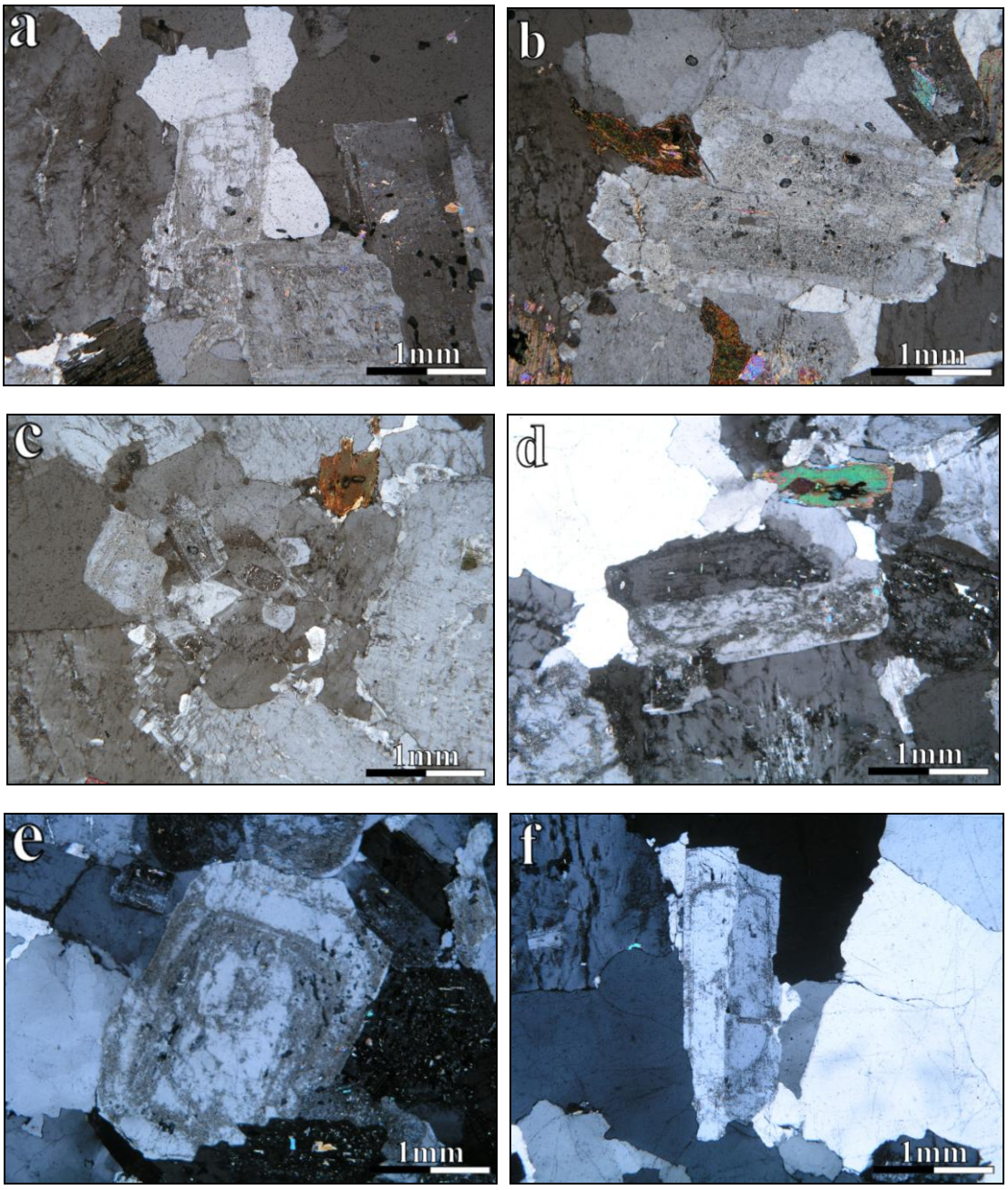


Fig. Ap3 (a-f): Feldspar zonation profiles in RM1a from Bendoran (sample no. JR7 (NM [364 218])) (**a** & **c**), (sample No. RR0125 (NM [357 219])) (**b**) and Whitish, Ardalanish (sample No. JR2 (NM [368 179])) (**d-f**) (all XPL): **(a)** Plagioclase with a patchy sericitised core juxtaposed to a plagioclase with a fresher core and separate thin sericitised outer zone. **(b)** Two subhedral plagioclase feldspars with highly sericitised cores. **(c)** Glomerocrystic patch of plagioclase feldspars with different zonation profiles juxtaposed. **(d)** Intense dendritic sericitised core with a more uniform sericitised outer zone within a plagioclase feldspar. **(e)** Complex multiply zoned plagioclase feldspar displaying at least five different zones characterised by sericitic alteration confined to specific zones. **(f)** Euhedral plagioclase feldspar displaying a thin zone of intense sericitic alteration.

a-b.) Variable sericitic alteration highlighting simple two to three-fold zonation profiles

c.) Glomerocryst domains

d.) Skeletal to dendritic cores or rims

e.) Multiple zonation profiles defined by uneven sericite within these zones

f.) Isolated outer zones of sericitic alteration

A2.2 RM2: The Knockvologan type facies

RM2 is the most heterogeneous facies within the ROMG having the greatest concentration of MME and diorite. It also has the most complex and greater range of crystal scale textural heterogeneity that can be associated with magma mixing. However, elucidation of such textures within more homogeneous varieties of RM2 outside the Knockvologan mixing and mingling zone (and where RM2 has a gradational contact with RM1) is considerably more difficult to observe (see **Fig. Ap4 (a-f)** for an example of such textures):

a-b.) Plagioclase feldspars with variable boxy cellular structures

c.) Isolated zoned plagioclase glomeroxenocrysts with highly sericitised cores

d.) Variably zoned plagioclase feldspars with or without sericitised cores

e.) Isolated multiply zoned plagioclase glomeroxenocrysts with or without highly sericitised cores juxtaposed to each other

f.) Isolated multiply zoned plagioclases

Evenly distributed acicular apatite also occurs throughout RM2 and in some cases, corroded allanite can display oscillatory zoning with embayed areas (**Fig. Ap5**).

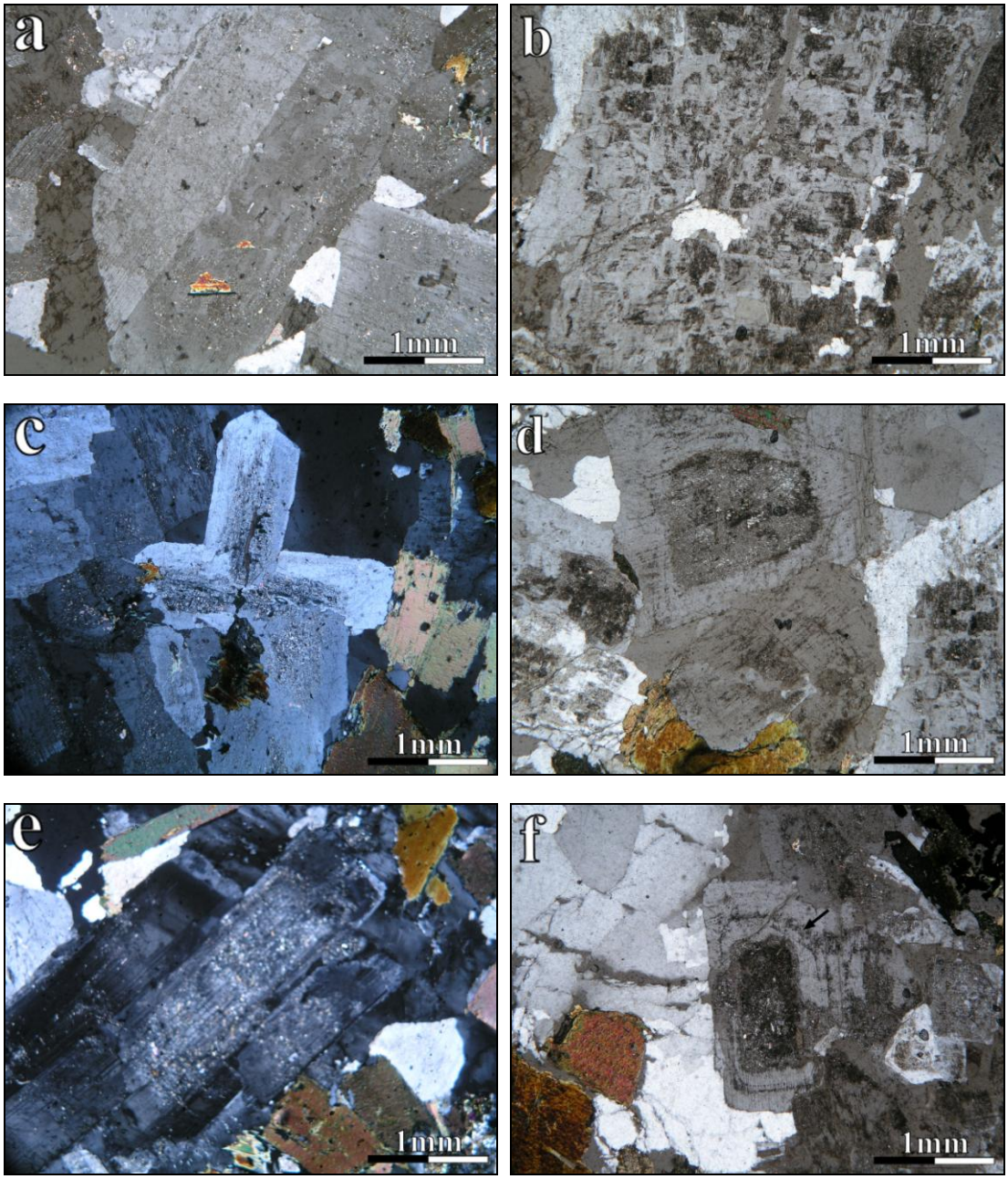


Fig. Ap4 (a-f): Disequilibrium/equilibrium textures in RM2 plagioclase feldspars (sample No. JR5 (NM [356 192]) (**a**, **c, d** & **e**), and sample No. RR107 (NM [300 223]) (**b** & **f**)) (all XPL). Characteristic disequilibrium textures are as follows: **(a)** A normally zoned subhedral boxy-cellular plagioclase feldspar, with development of boxy-cells constrained within the core region of the crystal. **(b)** Most intense example of cellular development observed in RM2 plagioclases with association of graphic quartz. **(c)** Normally zoned subhedral plagioclase feldspars (as glomerocrysts in this case) with highly sericitised cores and corroded core regions. **(d)** Sericitisation of anhedral-subhedral plagioclase cores is generally variable whereby some strongly zoned crystals having such degree of sericitic alteration are adjacent to other fresh crystals. **(e)** Complex subhedral-euhedral oscillatory zoned plagioclase feldspar without a sericitised core region. **(f)** Euhedral plagioclase displaying simple concordant zoning with at least five discernible zones (tenth of a mm outer zone (black arrow) has similar optical properties to the light grey zone that forms the embayment within the core region).

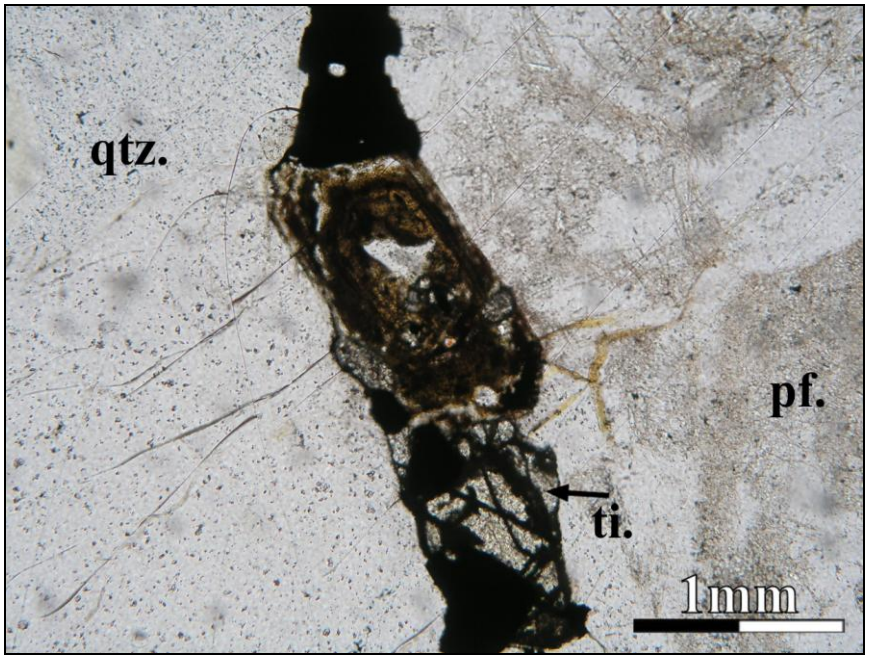


Fig. Ap5: Euhedral oscillatory zoned allanite associated with titanite in RM2 (sample No. JR32 (NM [308 252])) (PPL). Symbols are as follows: (**qtz.)** quartz, (**ti.**) titanite and (**pf.)** plagioclase feldspar.

A2.2 Type 1 and 2 aplites

Aplites display a complex array of textural heterogeneity primarily confined within xenocrystic mineral assemblages (**Fig. Ap6 (a-f)**) that have an inferred magma mixed origin:

a.) Corroded, multiply zoned and embayed plagioclase feldspar xenocrysts

b.) Skeletal zones in plagioclase feldspar

c.) Multiply zoned plagioclases juxtaposed to unzoned fresh varieties

d.) Alkali feldspar xenocrysts with variably zoned plagioclase domains

e.) Highly corroded quartz xenocrysts without an ocellus phase

f.) Variably embayed amphibole with plagioclase mantling phase

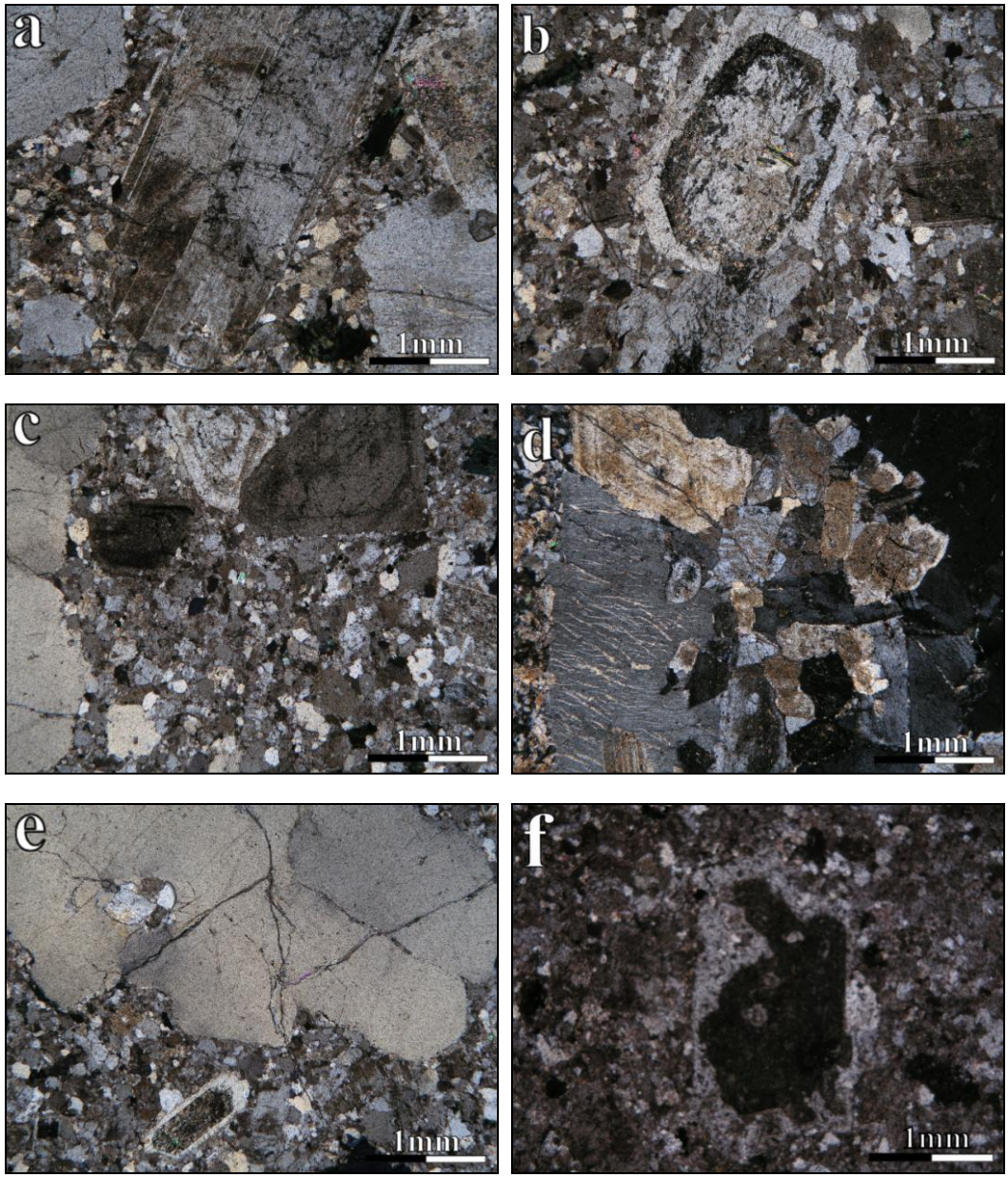


Fig. Ap6 (a-f): Magma mixing textures in Type 2 aplite (sample No. AZ025 (NM [364 218]) (**a**-**e**)), and Type 1 aplite (sample No. AZ023 (NM [364 218]) (**f**)) (all XPL). Textures are as follows: **(a)** Subhedral plagioclase feldspar xenocryst displaying simple concordant zoning with lower edge of crystal corroded through the core region. **(b)** Subhedral plagioclase feldspar with an outer skeletal concordant zone parallel to the crystal edges characterised by intense sericitic alteration. **(c)** Small isolated cluster of euhedral plagioclase feldspars with different simple concordant zoning profiles adjacent to a quartz ocellus. **(d)** Euhedral alkali feldspar adjacent to a glomerocrystic mass of subhedral to euhedral plagioclase feldspars that either display simple two fold or multiple concordant zonation. **(e)** Isolated poly-crystalline quartz with no ocellus phase and highly corroded edges. The isolated euhedral plagioclase feldspar with a highly sericitised core. **(f)** Highly embayed granular looking amphibole mantled by plagioclase.

A2.2 Syenite

Sub-solidus processes in syenites are essentially defined by networks of planar zones having intense alteration, with selective alteration of titanite. Granular and turbid overprinted appearance of fresher plagioclases (that may have relict cellular structures) (**Plate Ap7 (a)**) and the highly variable nature of polysynthetic albite twins in plagioclase feldspar (**Fig. Ap7 (b)**) are other textures associated with late stage processes.

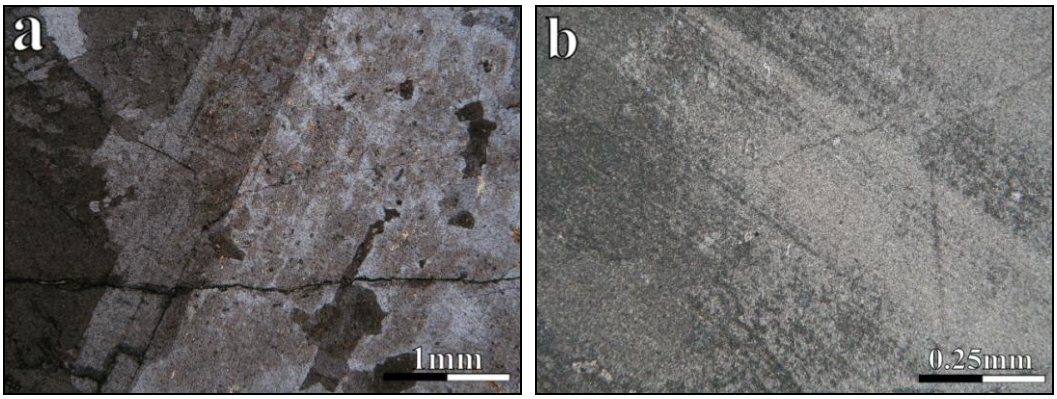


Fig. Ap7 (a-b): Sub-solidus textures in syenite from Tormore cottage (sample No. AZ007 (NM [301 242])) (both in XPL): **(a)** Isolated plagioclase feldspar with dendritic sericitised core (uneven cellular structure in places), graphic quartz intergrowths and a mottled/granular appearance. **(b)** Polysynthetic albite twins displaying selective lateral mottled/granular variation.

A2.2 Other zones of importance

Within the highly altered planar zones at Eilean nam Bo, alkali feldspars show a consistent granular texture (**Plate Ap8 (a)**). Plagioclase feldspar shows similar characteristics but the intensity of this alteration varies where it has overprinted RM2 feldspars having a relict simple two fold concordant zonation profile (**Plate Ap8 (b)**). Many host RM2 plagioclases that have simple two fold concordant zonation profiles often have sericitised cores. The alteration within the core region of the plagioclase feldspar (in **Plate Ap8 (b)**) appears to be more granular and pronounced then that at the outer zone of the crystal (implying a secondary overprint giving a more intense alteration in the core). Also, there are small brown areas (clay minerals) forming selective areas at the crystal margin, which have linear connected 'veins' that emanate towards the centre of the crystal. Subhedral biotite is highly chloritised across

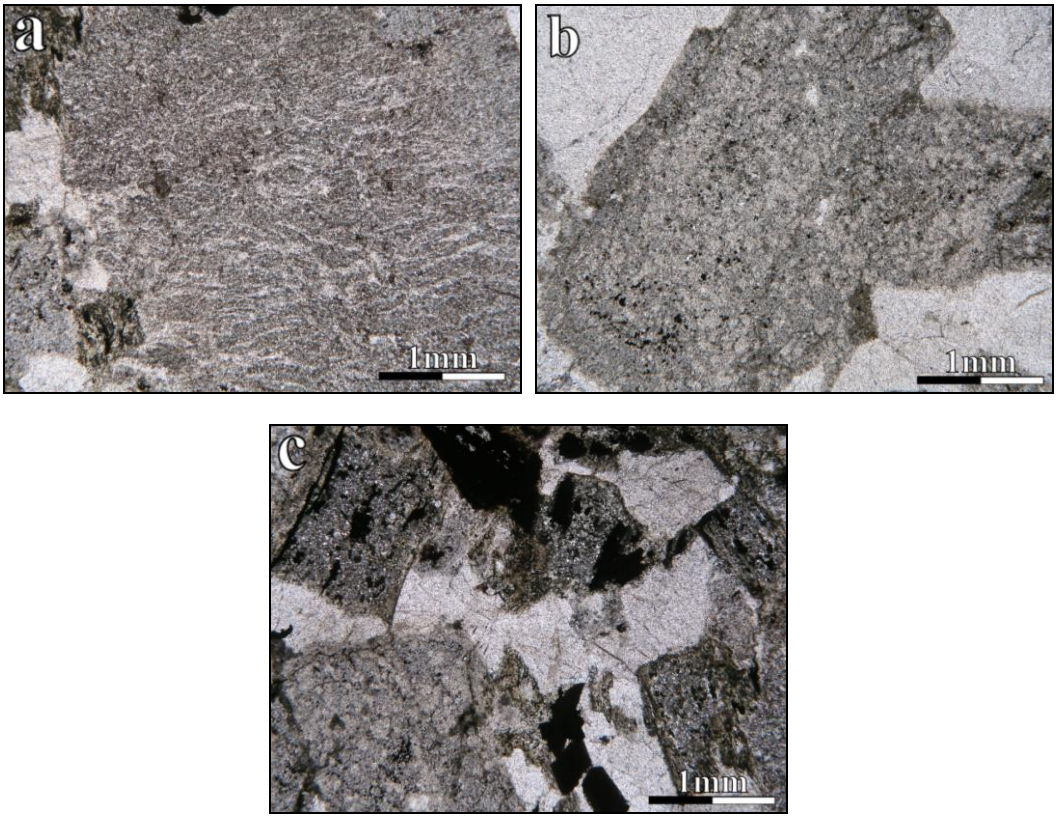


Fig. Ap8 (a-c): Sub-solidus textures in sample No. AZ024 (NM [295 216]) (all XPL): **(a)** Alkali feldspar with homogeneous granular texture. **(b)** Plagioclase feldspar once having an RM2 two fold type zonation (once typified by an equigranular sericitised core) now has an uneven mottled granular nature highly confined to core region. **(c)** Uneven granular appearance of chloritised biotite adjacent to an isolated patch of interstitial quartz.

cleavage planes and quartz forms selective isolated drusy looking mosaics between crystal margins implying that it is secondary (**Fig. Ap8 (c)**).

A2.2 Type 1 diorite component

These show a complex textural assemblage constituting evidence for mafic-felsic magma interaction. The following consistent thin section scale mixing textures are presented in **Fig. Ap9 (a-f)**:

a.) Alkali feldspar with three fold zonation and internal zonal embayment (the most representative type of mineral zonation profile present in all ROMG components, however apart from the example shown here, this is only discernible via CL microscopy)

b.) Complex simple concordant plagioclase zonation with intense mantling phases

c.) Plagioclase feldspar xenocrysts

d.) Corroded rapakivi feldspars

e.) Glomerocrystic amphibole clots

f.) Poly-crystalline quartz ocelli

Petrographic textural heterogeneity chiefly consists of variable mantling phases of subhedral amphibole on alkali feldspar (or *vice-versa*), cuspate orientated swirls of subhedral-euhedral resorbed plagioclases, embayed alkali feldspar, xenocrysts (some rapakivi-type megacrysts/glomeroxenocrysts having corroded uneven internal contacts with each other), ocelli type mantling phases on quartz xenocrysts, clots of glomerophyric hornblende (Castro & Stephens 1992; Sial *et al.* 1998; Janoušek *et al.* 2000), and evenly distributed acicular apatite. Xenocrystic alkali feldspars from adjacent RM2 (some having amphibole inclusion trails restricted to individual zones) are commonly present within diorite and also cross-cut RM2/diorite crenulate interfaces.

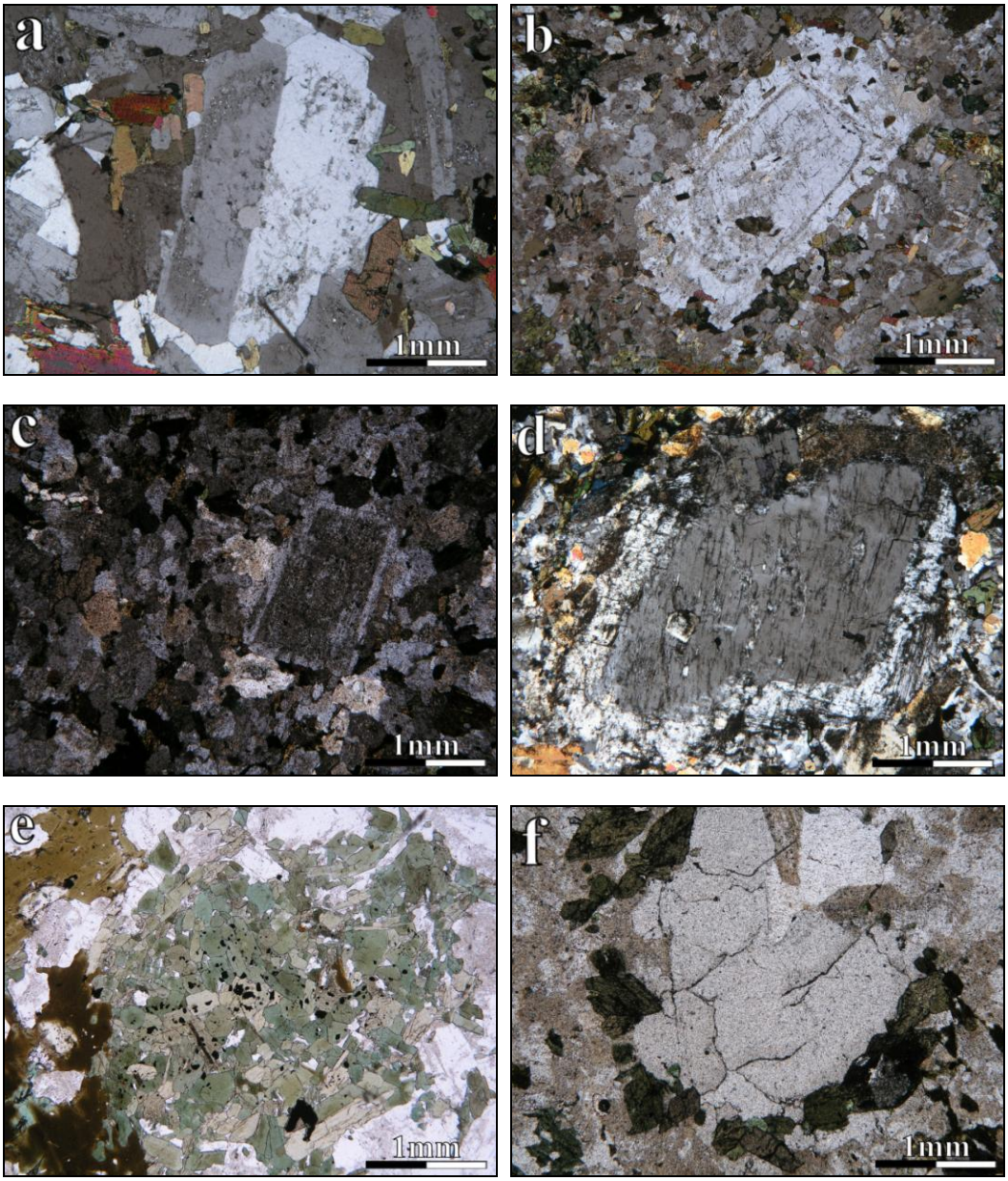


Fig. Ap9 (a-f): Mafic-felsic magma interaction textures in Knockvologan Type 1 diorite component (**a-d** XPL and **e-f** PPL). Textures are as follows: **(a)** Alkali feldspar displaying three-fold zonation with characteristic patchy outer zone that embays the core region (sample No. JR46 (NM [278 140])). **(b)** Isolated plagioclase feldspar xenocryst with simple concordant zoning, and a skeletal core typified by sericitic alteration (sample No. RR0114 (NM [307 202])). Note the thin outer zone region (in the orders of a tenth of a mm) and the predominantly mono-mineralic plagioclase groundmass wrapping around the plagioclase considered. **(c)** Isolated euhedral plagioclase feldspar with tabular sericitised core (sample No. AZD02 (NM [310 208])). **(d)** Anhedral rapakivi feldspar xenocryst with corroded upper margin (same sample as in **(c)**). **(e)** Glomerocrystic hornblende clot partially mantled by tabular biotite (sample No. JR27 (NM [278 140])). (**f**) Polycrystalline quartz ocellus. Lozenge shaped titanite and subhedral hornblende forms the ocellus-mantling phase (sample No. AZD02 (NM [310 208])).

A2.2 Type 2 diorite component

Within Type 2 diorites, there is little textural heterogeneity with respect to Type 1 diorites. However, there are some examples of isolated xenocrystic quartz. One of the main heterogeneous features observed in these diorites is the complex breakdown of clino-pyroxene (augite) to hornblende and quartz within the cores of subhedral crystals giving a skeletal outer rim (**Fig. Ap10**).

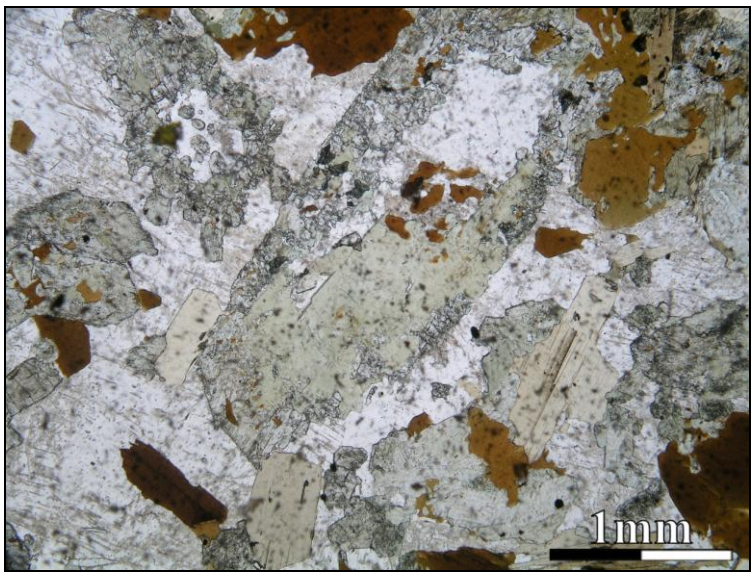


Fig. Ap10: Euhedral clino-pyroxene (augite) replaced by amphibole and quartz in Type 2 Aird Mór diorite (sample No. JR41 (NM [323 177])) (PPL).

A2.2 Mafic magmatic enclaves

Textural heterogeneity observed within Type 1 diorites in the Knockvologan mixing and mingling zone is mirrored by MME that occur in disrupted diorite intrusions, or are adjacent to larger bodies of diorite. In composite MME, such features exist in variable proportions and characterise different MME phases. The only other textures presented here that are not particularly abundant to Type 1 diorites, but occur in MME are shown in **Plate Ap11 (a-c)**:

a.) Glomerocrystic biotite clots

b.) Poly-crystalline quartz with biotite/titanite ocellus phase

c.) Glomerocrystic titanite

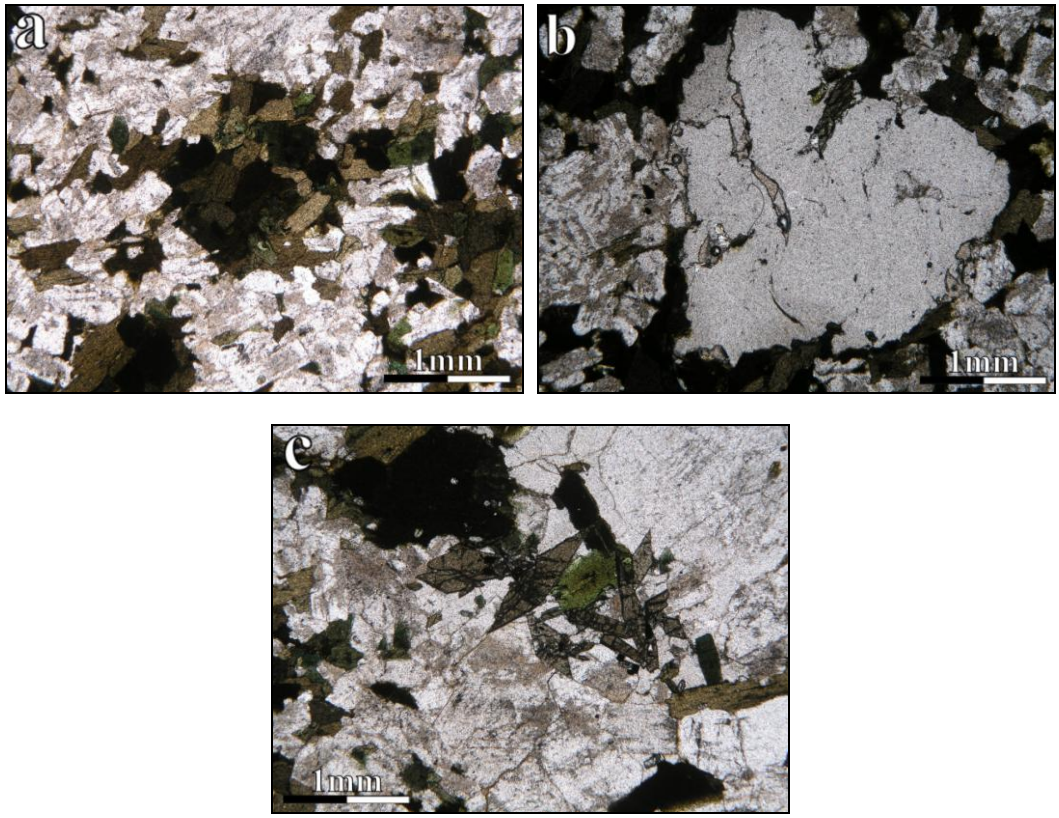


Fig. Ap11 (a-c): Mafic-felsic magma interaction textures in MME from Knockvologan (sample No. AZD040 (NM [292 192])) (all PPL). Textures are as follows: **(a)** Glomerocrystic biotite clots with no mantle. Note groundmass has subhedral plagioclase with or without sericitised cores. **(b)** Isolated poly-crystalline quartz ocellus with biotite and minor titanite as the ocellus phase. **(c)** Isolated glomerocrystic association of euhedral titanite.

A2.2 Hornblende phyric enclaves

Petrographic criteria for mafic-felsic magma interaction (in the most primitive end-members observed in terms of a spectrum of ROMG MME based on field petrology) are observed from **Fig. Ap12**. Magnification of textures a to d are depicted in **Fig. Ap13 (a-d)**. Augites are common anhedral phenocryst phases generally mantled by various phases (**Fig. Ap12 (c)**). Groundmass in these enclaves is typically micro-diorite preserving a hornfelsed flow foliation around xenocrysts (Pugliese & Petford 2001).

Textures interpreted as resulting from Mafic-felsic magma interaction are:

a.) Highly corroded and embayed plagioclase feldspar xenocrysts having plumose resorbtion surfaces and a three-fold type zonation

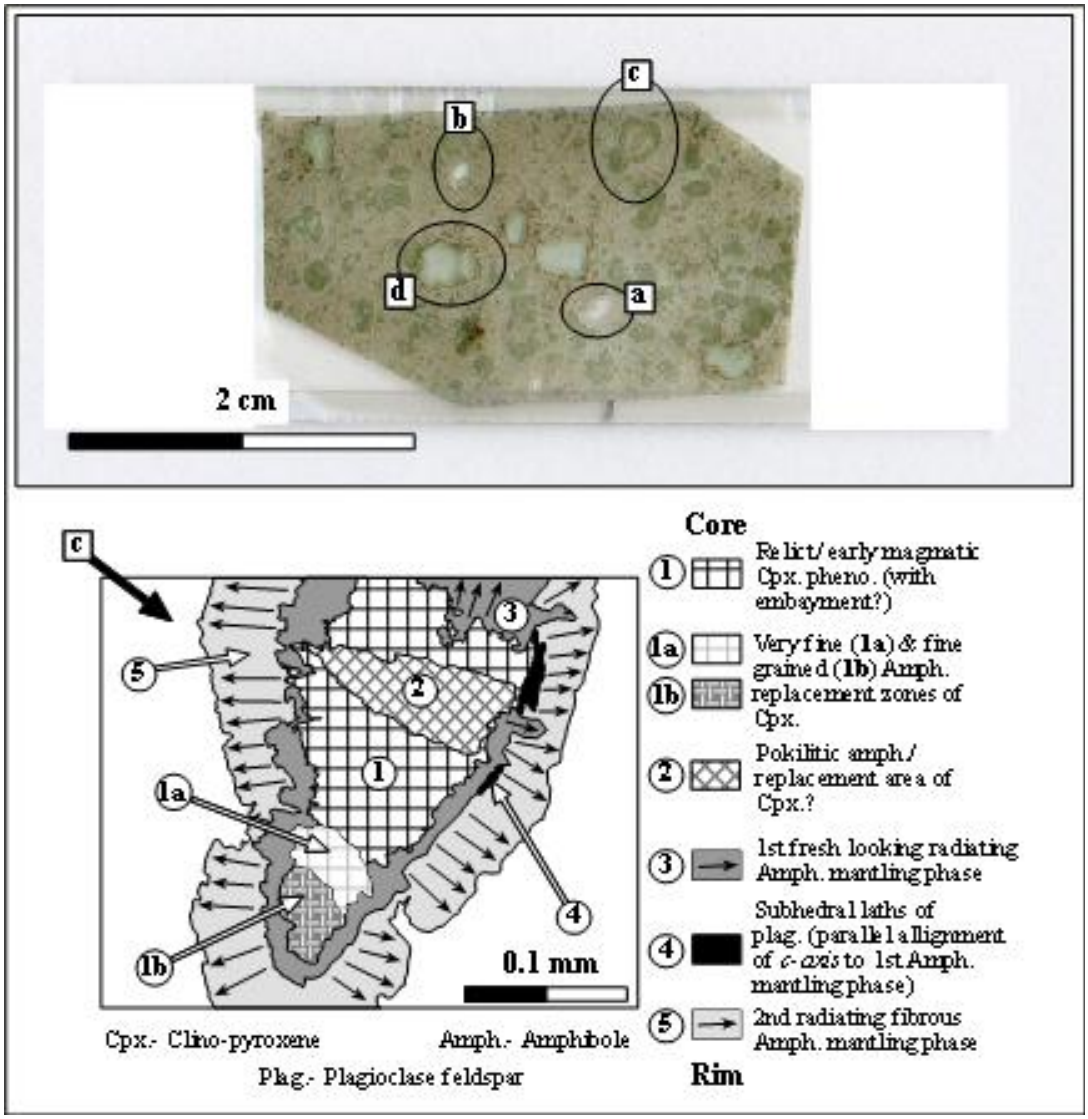


Fig. Ap12: Hybridisation textures from a hornblende phyric MME within host RM2 from Eilean nan Griogag (Sample AZEN01 (NM [307 191])). Letters on the thin section correspond to the photomicrographs in **Fig. Ap13 (a-d)**. The schematic sketch highlights an important relict pyroxene phase mantled by complex array of amphibole phases that is depicted in **Fig. Ap13 (c)**.

b.) Quartz ocelli

c.) Complex poly-phase mantling of amphibole on relict augite

d.) Clots of glomerophyric hornblende with various mantling phases

The most complex texture associated with mafic-felsic magma interaction observed in these MME (and has only been noted in this enclave type) is shown in **Fig. Ap12 (c)**, and an outline diagram depicting this unique texture is presented in accompanying cartoon. As with the Type 2 diorites, there are abundant examples of relict augite crystals replaced by

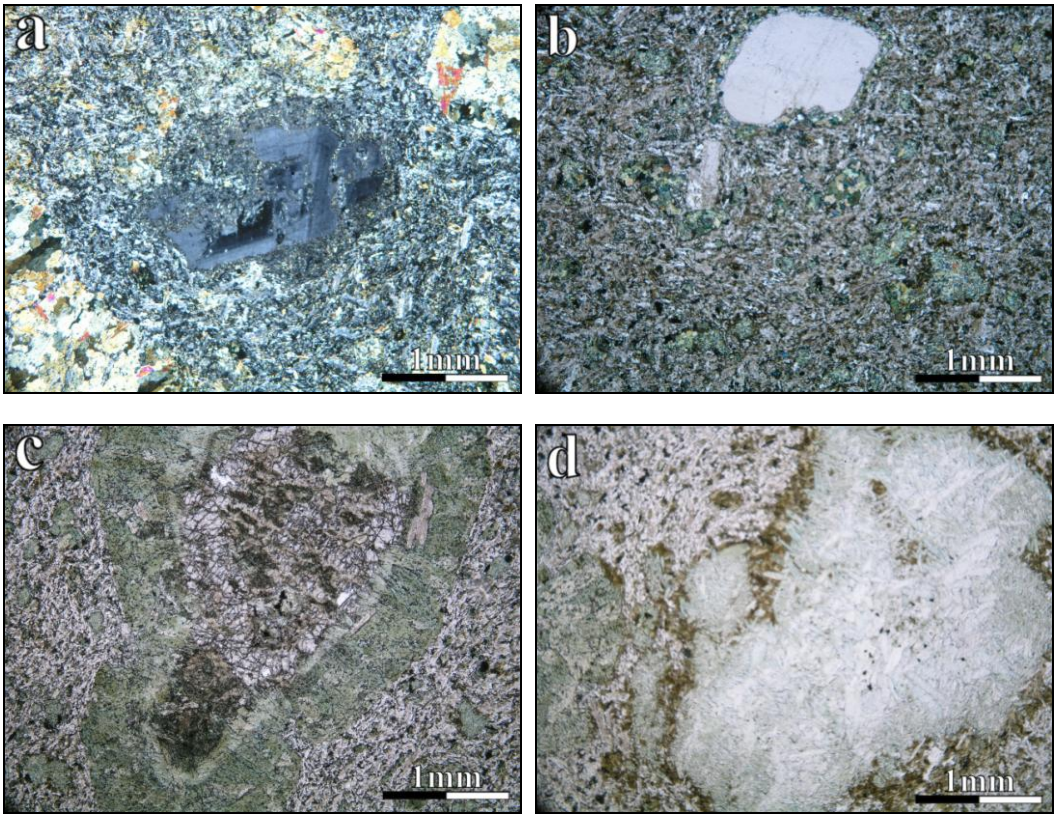


Fig. Ap13 (a-d): Hybridisation textures from a hornblende phyric MME within host RM2 from Eilean nan Griogag (sample No. AZEN01 (NM [307 191])) (a-b XPL and c-d PPL): **(a)** A highly resorbed isolated rare anhedral plagioclase feldspar xenocryst showing deep embayment within core, and a corroded outer rim in the top-right area of the crystal. Such xenocrysts have a characteristic three-fold zonation (refer to text) and an isolated mantling phase of acicular biotite and lath like plagioclase. Surrounding groundmass is lath like plagioclase, subhedral amphibole and biotite, which is sub-parallel/wrapping around the xenocryst, and Fe-Ti oxides. **(b)** Corroded anhedral quartz ocellus with biotite-amphibole (titanite can also be an ocellus phase) making up the thin ocellus surface. Also note embayed alkali feldspar micro-xenocryst (Carlsbad twin discernible) adjacent to the quartz ocellus. **(c)** Replacement of relict/early magmatic clino-pyroxene phenocrysts (augite) by biotite-amphibole aggregates forming anhedral-subhedral glomerophyric amphibole clots. Also note the fibrous nature of at least two amphibole mantling phases with subhedral plagioclase laths aligned perpendicular between this interface. **(d)** Highly irregular glomerophyric amphibole with an acicular biotite ocellus phase. Note internal agglomeration of amphibole has larger elongate radiating crystals in the core and smaller radiating crystals towards the rim.

amphibole, giving a heterogeneous distribution of characteristic green globular structures in these MME. The complexity of these structures arises in the fact that the internal alteration of augite is selectively heterogeneous, and there are at least two fibrous amphibole phases.

A2.2 Type 1 lamprophyres

Type 1 lamprophyres mirror the mixing textures observed in Type 1 diorite and MME (excluding hornblende phyric types) in terms of xenocrystic crystal assemblages and the groundmass is typically heterogeneous and made up of plagioclases with different zonation profiles. Examples of such features are displayed in **Fig. Ap14 (a-c)**, which are taken from the core of a Type 1 sheet at Eilean Eion:

a.) Intense boxy cellular structure in plagioclase xenocrysts

b.) Plagioclase feldspar glomeroxenocrysts, xenocrysts and groundmass with feldspars having contrasting zonation profiles

c.) Quartz ocelli

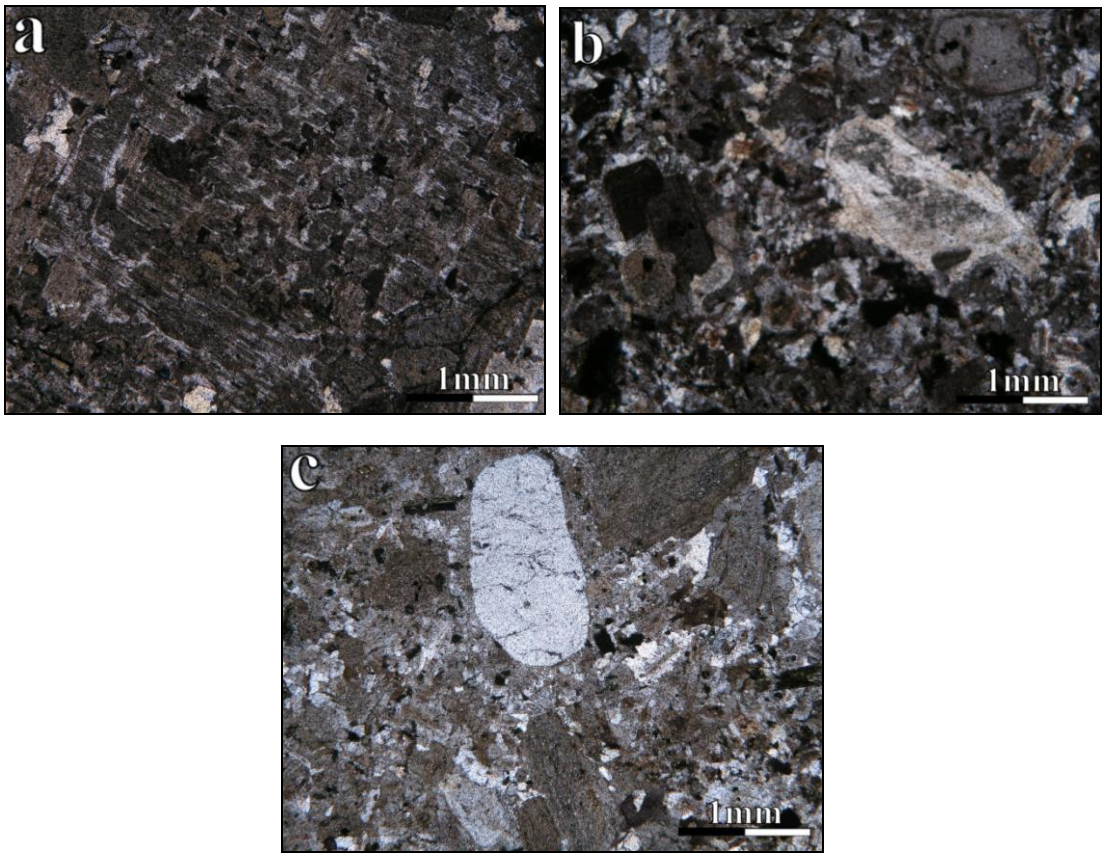


Fig. Ap14 (a-c): Mafic-felsic magma interaction textures in Type 1 lamprophyres (sample No. ZCLS02 (NM [300 241])) (a-b XPL and c PPL): **(a)** Most intense example of a boxy cellular feldspar observed in any ROMG component. **(b)** Isolated plagioclase feldspar xenocrysts (some as glomeroxenocrysts) and a euhedral quartz (top right) with an internal biotite and titanite ocellus phase set within a groundmass predominantly composed of plagioclase with different types of zonation. **(c)** Isolated quartz ocellus with polycrystalline plagioclase forming the mantling phase.

A2.2 Type 2 lamprophyres

Type 2 lamprophyres do not mirror the mixing textures observed in Type 1 lamprophyres in terms of xenocrystic crystal assemblages or groundmass assemblages, as they are homogeneous. However, the main characteristic textural feature already documented to be prevalent throughout such sheets is glomerocrystic hornblende, which in some cases can be mantled by biotite, titanite or opaque oxides.

Appendix Three
MODAL ANALYSIS

Introduction

ROMG modal data generated from field, point count and QXRD techniques used to produce the QAP diagrams in Chapter Three are presented. Standards, procedural blanks and methods utilised at the University of St. Andrews X-Ray laboratory are also provided to show how QXRD fractions have been prepared and analysed.

A3.1 Modal field data.

Number	Facies	Sample	G.R.	Q (%)	A (%)	P (%)	Total	BIOT(%)AV
1	RM1	A	308 252	40	59	1	100	9.5
2	RM1	B	303 247	35	64	1	100	0
3	RM1	C	302 243	35	64	1	100	8.5
4	RM1	D	301 242	5	94	1	100	12.5
5	RM1	E	300 231	35	64	1	100	9
6	RM2	F	301 230	40	58	2	100	0
7	RM2	G	298 229	40	57	3	100	0
8	RM2	H	296 216	40	52	8	100	12.5
9	RM2	I	311 210	45	50	5	100	12.5
10	RM2	J	310 209	45	45	10	100	17.5
11	RM2	K	312 207	27.5	32.5	30	90	22.5
12	RM2	L	309 201	30	40	30	100	27.5
13	RM2	M	310 191	35	20	45	100	37.5
14	RM2	N	310 191	40	30	30	100	25
15	RM2	O	310 191	20	20	60	100	40
16	RM2	P	311 186	35	45	20	100	17.5
17	RM1a	Q	312 186	30	30	40	100	0
18	RM2	R	313 185	30	35	35	100	25
19	RM2	S	316 183	35	35	30	100	17.5
20	RM2	T	318 184	40	40	20	100	17.5
21	RM2	U	319 186	25	50	25	100	17.5
22	RM2	V	322 187	30	45	25	100	15
23	RM2	W	324 182	30	45	25	100	20
24	RM2	X	325 183	30	35	35	100	22.5
25	RM2	Y	323 192	30	45	25	100	20
26	RM2	Z	321 193	20	70	10	100	12.5
27	RM2	AA	322 189	25	65	10	100	17.5
28	RM2	AB	323 178	40	50	10	100	15
29	RM2	AC	325 178	35	60	5	100	22.5
30	RM2	AD	321 179	20	70	10	100	20
31	T1 Diorite	AE	325 179	10	0	90	100	0
32	RM2	AF	338 166	40	55	5	100	17.5
33	T1 Diorite	AG	338 167	10	10	80	100	0
34	T1 Diorite	AH	338 168	5	5	90	100	0
35	RM2	AI	338 169	45	25	30	100	0
36	RM2	AJ	330 167	35	45	20	100	15
37	RM1a	AK	331 167	40	30	30	100	7.5
38	T1 Diorite	AL	328 168	5	5	90	100	0
39	RM2	AM	324 171	20	20	60	100	25
40	T1 Diorite	AN	325 172	5	20	75	100	0
41	RM2	AO	327 170	30	30	40	100	17.5
42	RM2	AP	327 170	30	40	30	100	17.5
43	RM2	AQ	325 167	30	30	40	100	22.5
44	RM2	AR	342 175	10	50	40	100	0
45	T2 Diorite	AS	322 176	5	15	80	100	0
46	Aolite	AT	343 171	15	70	15	100	0
47	RM1a	AU	347 170	30	60	10	100	5
48	RM1a	AV	347 169	30	60	10	100	5
49	RM2	AW	347 170	35	60	5	100	7.5
50	RM2	AX	347 171	40	25	35	100	32.5
51	RM1a	AY	346 170	50	30	20	100	7.5
52	Aplite	AZ	348 169	35	55	10	100	5
53	RM2	AAA	352 172	30	40	30	100	12.5
54	RM2	AAB	357 171	30	50	20	100	17.5
55	RM2	AAC	354 169	35	55	10	100	9
56	RM1a	AAD	357 240	35	35	30	100	0
57	RM1a	AAE	359 225	40	35	25	100	0
58	Aplite	AAF	295 216	35	35	30	100	0
59	RM1a	AAG	361 218	40	30	30	100	0
60	RM1a	AAH	362 222	40	30	30	100	0
61	RM1a	AAI	367 202	25	40	35	100	0
N/a	T1 Lamp.	AAJ	368 178	5	10	85	100	0
62	RM2	AAK	352 212	40	50	10	100	6.5
63	RM1	AAL	351 215	50	45	5	100	0

A3.2 Modal Point Count Data (sampling targets n=500 with stage interval of three used connected to a SWIFT point counter).

No.	G.R.	Q	A	P	Biot.	Musc.	Hbld.	Cpx.	Ti.	Ap.	All.	Fe-Ti.	Zr.	QAP (%)	Q (%)	A (%)	P (%)
RM1a																	
JR2	368 179	44.00	18.60	32.60	4.40	0.40	-	-	-	-	-	-	-	95.20	0.46	0.20	0.34
JR7	364 218	31.40	29.60	32.40	4.60	2.00	-	-	-	-	-	-	-	93.40	0.34	0.32	0.35
RM1																	
AZ005(1)	-	31.60	18.60	41.60	6.00	0.20	-	-	1.40	-	-	0.40	-	91.80	0.34	0.20	0.45
AZ005(2)	-	35.60	7.40	39.00	13.40	-	0.80	-	3.00	-	-	0.80	-	82.00	0.43	0.09	0.48
AZ005(3)	-	48.60	24.80	25.40	1.00	-	-	-	0.20	-	-	-	-	98.80	0.49	0.25	0.26
AZ005(4)	-	49.40	22.20	27.80	0.40	-	-	-	-	-	-	0.20	-	99.40	0.50	0.22	0.28
AZ005(5)	-	31.40	27.60	38.40	2.20	0.20	-	-	-	0.20	-	-	-	97.40	0.32	0.28	0.39
JR1	355 216	17.60	46.80	28.00	7.20	0.40	-	-	-	-	-	-	-	92.40	0.19	0.51	0.30
JR5	356 192	31.60	18.60	41.60	6.00	0.20	-	-	1.40	-	-	0.40	-	91.80	0.34	0.20	0.45
JR9	353 243	14.80	50.00	27.20	6.20	-	-	-	0.80	0.80	-	0.20	-	92.00	0.16	0.54	0.30
JR14	348 249	31.00	36.20	26.40	5.00	-	-	-	0.20	0.20	-	0.80	-	93.60	0.33	0.39	0.28
JR15	364 216	33.60	29.60	29.40	7.20	-	-	-	0.20	-	-	-	-	92.60	0.36	0.32	0.32
JR18	365 187	35.60	7.40	39.00	13.40	-	0.80	-	3.00	-	-	0.80	-	82.00	0.43	0.09	0.48
JR21	326 230	25.00	30.00	37.40	7.00	-	0.60	-	-	-	-	-	-	92.40	0.27	0.32	0.40
JR25	268 140	48.60	24.80	25.40	1.00	-	-	-	0.20	-	-	-	-	98.80	0.49	0.25	0.26
		49.40	22.20	27.80	0.40	-	-	-	-	-	-	0.20	-	99.40	0.50	0.22	0.28
JR12	280 227	31.40	27.60	38.40	2.20	0.20	-	-	-	0.20	-	-	-	97.40	0.32	0.28	0.39
RM2																	
JR19	341 202	35.40	21.80	33.00	9.60	-	-	-	0.20	-	-	-	-	90.20	0.39	0.24	0.37
JR20	349 192	38.00	33.60	17.20	11.20	-	-	-	-	-	-	-	-	88.80	0.43	0.38	0.19
JR3	297 222	56.20	9.60	33.00	0.40	0.50	-	-	-	0.20	0.20	-	-	98.80	0.57	0.10	0.33
JR4	320 194	23.20	22.60	43.20	9.00	-	-	-	0.40	0.20	-	0.40	0.20	89.00	0.26	0.25	0.49
JR6	336 231	20.00	50.40	26.80	2.40	-	-	-	0.40	-	-	-	-	97.20	0.21	0.52	0.28
JR8	332 177	24.60	17.20	43.00	13.00	-	1.00	-	-	0.20	-	1.00	-	84.80	0.29	0.20	0.51
		27.00	16.60	42.60	12.60	-	0.80	-	0.40	-	-	-	-	86.20	0.31	0.19	0.49
JR11	314 212	22.20	5.20	66.20	7.80	-	1.00	-	1.00	0.40	-	0.40	-	93.60	0.24	0.06	0.71
JR16	296 192	27.00	20.80	43.60	7.40	-	0.20	-	0.20	0.40	-	-	0.40	91.40	0.30	0.23	0.48
JR22	328 211	28.00	24.20	37.80	9.00	-	-	-	1.00	-	-	-	-	90.00	0.31	0.27	0.42
JR32	295 155	64.40	16.40	16.00	2.80	-	-	-	0.40	-	-	-	-	96.80	0.67	0.17	0.17
JR33	295 155	28.40	-	52.40	17.40	-	-	-	1.00	-	-	0.80	-	80.80	0.35	0.00	0.65
JR39	298 205	28.20	17.20	48.00	5.80	-	0.40	-	0.40	-	-	-	-	93.40	0.30	0.18	0.51
JR40	323 177	17.20	35.80	38.00	7.60	-	0.20	-	0.80	-	-	0.40	-	91.00	0.19	0.39	0.42
JR45	353 191	54.20	3.00	40.60	-	1.20	-	-	-	-	-	1.00	-	97.80	0.55	0.03	0.42
JR13	302 220	22.20	43.20	30.20	4.00	-	0.20	-	0.40	-	-	-	-	95.60	0.23	0.45	0.32
T1 Diorite																	
JR31	309 189	3.20	-	63.60	22.40	-	9.00	-	1.40	0.40	-	-	-	66.80	0.05	0.00	0.95
T2 Diorite																	
JR24	325 185	1.40	-	41.80	19.20	-	36.40	-	0.20	1.00	-	-	-	43.20	0.03	0.00	0.97
JR41	323 177	2.40	-	20.40	28.60	-	-	44.20	3.80	0.20	-	0.20	-	22.80	0.11	0.00	0.89

A3.3 Modal QXRD/SIROQUANT refined data (contrast corrected weight % <10% with respect to chi-squared fit apart from and converted from UXD format by XCH Version 1).

Sample	Qtz.	error	Or. 1.	error	Mi. (max)	error	Ab. (low)	error	Biot. 2M1	error	Musc.	error	Global X2	Total QAP %	Q %	A %	P %
Syenite																	
AZ007(1)	11.60	**0.27**	13.00	**0.61**	20.50	**0.80**	53.50	**0.84**	1.50	**0.90**	-	-	6.78	98.60	11.76	33.98	54.26
AZ007(2)	12.10	**0.26**	23.80	**0.49**	24.70	**0.51**	38.00	**0.74**	1.40	**0.26**	-	-	9.11	98.60	12.27	49.19	38.54
Aplite																	
AZ023	33.60	**0.40**	14.80	**0.4**	18.00	**0.43**	32.50	**0.66**	1.20	**0.22**	-	-	7.21	98.90	33.97	33.16	32.86
AZ025	35.30	**0.43**	11.20	**0.41**	20.10	**0.44**	32.00	**0.68**	1.50	**0.23**	-	-	6.94	98.60	35.80	31.74	32.45
RM1a																	
AF0201	44.70	**0.64**	15.20	**0.43**	20.10	**0.47**	17.00	**0.80**	2.30	**0.23**	0.80	**0.8**	7.82	97.00	46.08	36.39	17.53
JR2	47.30	**0.75**	7.80	**0.47**	20.50	**0.52**	20.20	**0.86**	3.00	**0.25**	1.20	**0.9**	7.62	95.80	49.37	29.54	21.09
JR7	32.50	**0.53**	14.40	**0.47**	21.60	**0.52**	22.80	**0.84**	5.00	**0.25**	3.50	**0.8**	8.55	91.30	35.60	39.43	24.97
JR17	36.60	**0.60**	15.10	**0.48**	13.90	**0.51**	26.40	**0.84**	5.80	**0.26**	2.10	**0.9**	7.01	92.00	39.78	31.52	28.70
RR0125	34.70	**0.57**	16.70	**0.48**	14.30	**0.50**	25.00	**0.84**	4.80	**0.26**	4.50	**0.9**	7.41	90.70	38.26	34.18	27.56
RR0133	43.90	**0.67**	8.10	**0.44**	24.50	**0.51**	19.60	**0.83**	1.30	**0.24**	2.60	**0.8**	7.04	96.10	45.68	33.92	20.40
D1	24.90	**0.70**	10.20	**0.76**	30.50	**1.02**	23.20	**1.38**	3.50	**0.41**	7.70	**1.3**	11.62	88.80	28.04	45.83	26.13
RM1																	
AF0207(1)	34.40	**0.45**	9.20	**0.67**	18.70	**0.57**	35.20	**0.54**	2.50	**0.42**	-	-	5.53	97.50	35.28	28.62	36.10
AF0207(2)	37.30	**0.62**	11.10	**0.82**	21.40	**0.65**	28.50	**0.77**	0.17	**0.56**	-	-	6.67	98.30	37.95	33.06	28.99
AF0208	37.90	**0.35**	6.00	**0.48**	19.00	**0.40**	35.80	**0.40**	1.30	**0.31**	-	-	6.04	98.70	38.40	25.33	36.27
AF02	32.50	**0.45**	16.30	**0.46**	15.20	**0.49**	30.50	**0.78**	5.60	**0.25**	-	-	8.87	94.50	34.39	33.33	32.28
AZ004	36.30	**0.83**	10.30	**0.75**	24.30	**0.91**	27.10	**1.31**	2.10	**0.41**	-	-	10.81	98.00	37.04	35.31	27.65
AZ005	38.30	**0.58**	13.70	**0.51**	21.30	**0.55**	23.50	**0.93**	3.30	**0.28**	-	-	8.75	96.80	39.57	36.16	24.28
(a)	38.00	**0.53**	12.10	**0.47**	21.80	**0.51**	25.60	**0.84**	2.50	**0.26**	-	-	8.64	97.50	38.97	34.77	26.26
(b)	41.40	**0.59**	10.00	**0.49**	20.60	**0.52**	25.10	**0.86**	2.90	**0.27**	-	-	7.77	97.10	42.64	31.51	25.85
(c)	32.20	**0.47**	13.10	**0.48**	24.30	**0.52**	27.60	**0.83**	2.80	**0.26**	-	-	7.68	97.20	33.13	38.48	28.40
(d)	43.70	**0.53**	11.60	**0.42**	21.20	**0.45**	21.50	**0.77**	2.00	**0.23**	-	-	7.48	98.00	44.59	33.47	21.94
AZ010	35.20	**0.48**	19.10	**0.46**	17.00	**0.48**	26.10	**0.80**	2.60	**0.25**	-	-	9.69	97.40	36.14	37.06	26.80
AZ014	35.90	**0.47**	13.10	**0.43**	18.10	**0.46**	28.60	**0.75**	4.10	**0.24**	-	-	6.84	95.70	37.51	32.60	29.89
AZ015	34.10	**0.44**	11.80	**0.43**	18.20	**0.45**	33.50	**0.70**	2.40	**0.23**	-	-	6.56	97.60	34.94	30.74	34.32
JR09	35.80	**0.46**	16.40	**0.43**	18.10	**0.46**	25.60	**0.76**	4.10	**0.24**	-	-	8.19	95.90	37.33	35.97	26.69
JR12	38.60	**0.43**	14.10	**0.38**	19.90	**0.41**	26.00	**0.67**	1.40	**0.21**	-	-	8.07	98.60	39.15	34.48	26.37
JR14	36.90	**0.50**	12.70	**0.45**	16.80	**0.48**	29.30	**0.78**	4.20	**0.25**	-	-	6.87	95.70	38.56	30.83	30.62
JR15	32.70	**0.45**	10.80	**0.46**	21.60	**0.49**	29.50	**0.78**	5.40	**0.25**	-	-	6.82	94.60	34.57	34.25	31.18
JR18	30.60	**0.46**	16.10	**0.49**	14.60	**0.52**	31.90	**0.81**	6.70	**0.27**	-	-	6.59	93.20	32.83	32.94	34.23
JR21	40.00	**0.51**	12.80	**0.44**	16.90	**0.46**	25.70	**0.77**	4.60	**0.24**	-	-	7.21	95.40	41.93	31.13	26.94
JR25	32.90	**0.42**	16.30	**0.42**	20.60	**0.45**	29.20	**0.72**	0.90	**0.23**	-	-	9.18	99.00	33.23	37.27	29.49
JR47	36.40	**0.46**	13.30	**0.43**	17.80	**0.46**	30.30	**0.72**	2.20	**0.24**	-	-	7.91	97.80	37.22	31.80	30.98
RR0123	32.20	**0.44**	12.60	**0.45**	19.30	**0.49**	29.50	**0.77**	6.50	**0.25**	-	-	6.01	93.60	34.40	34.08	31.52
RR0124	30.90	**0.40**	15.30	**0.42**	17.70	**0.45**	31.20	**0.71**	5.00	**0.23**	-	-	6.97	95.10	32.49	34.70	32.81
AZ055	2.60	**0.64**	17.60	**1.34**	12.90	**1.65**	58.80	**1.94**	8.10	**0.75**	-	-	8.27	91.90	2.83	33.19	63.98
RM2																	
AZ016	29.20	**0.47**	23.20	**0.54**	9.70	**0.56**	30.10	**0.88**	7.80	**0.29**	-	-	6.93	92.20	31.67	35.68	32.65
AZ020	29.80	**0.47**	14.50	**0.51**	1.50	**0.54**	37.10	**0.80**	3.60	**0.28**	-	-	6.73	96.40	30.91	30.60	38.49
AZ026	36.20	**0.44**	13.60	**0.41**	16.60	**0.43**	31.60	**0.68**	2.00	**0.22**	-	-	7.74	98.00	36.94	30.82	32.24
AZ029	32.20	**0.44**	13.90	**0.45**	16.80	**0.48**	33.70	**0.74**	3.40	**0.25**	-	-	7.01	96.60	33.33	31.78	34.89
AZ035	35.90	**0.53**	11.30	**0.49**	13.70	**0.52**	33.40	**0.81**	5.70	**0.27**	-	-	6.11	94.30	38.07	26.51	35.42
JR04	25.30	**0.39**	15.50	**0.48**	19.10	**0.51**	34.20	**0.78**	5.90	**0.26**	-	-	6.83	94.10	26.89	36.77	36.34
JR05	31.40	**0.44**	12.80	**0.46**	15.60	**0.49**	34.10	**0.75**	6.00	**0.25**	-	-	6.82	93.90	33.44	30.24	36.32
JR08	30.30	**0.47**	15.40	**0.5**	10.30	**0.54**	37.10	**0.80**	6.80	**0.28**	-	-	6.37	93.10	32.55	27.60	39.85
JR11	37.80	**0.48**	12.60	**0.43**	15.70	**0.46**	29.10	**0.74**	4.80	**0.24**	-	-	8.03	95.20	39.71	29.73	30.57
JR13	34.50	**0.49**	14.10	**0.47**	16.30	**0.51**	27.40	**0.83**	7.70	**0.27**	-	-	7.39	92.30	37.38	32.94	29.69
JR16	28.40	**0.39**	15.20	**0.45**	22.00	**0.48**	30.70	**0.75**	3.60	**0.24**	-	-	7.86	96.30	29.49	38.63	31.88
JR19	29.60	**0.47**	14.60	**0.51**	14.80	**0.54**	32.30	**0.85**	8.80	**0.29**	-	-	7.19	91.30	32.42	32.20	35.38
JR20	43.20	**0.57**	12.20	**0.45**	18.00	**0.48**	20.90	**0.84**	5.80	**0.25**	-	-	8.52	94.30	45.81	32.03	22.16
JR20b	32.70	**0.49**	16.80	**0.5**	13.30	**0.53**	31.10	**0.83**	6.10	**0.27**	-	-	8.22	93.90	34.82	32.06	33.12
JR22	32.40	**0.44**	13.20	**0.45**	16.10	**0.48**	32.20	**0.75**	6.10	**0.25**	-	-	7.6	93.90	34.50	31.20	34.29
JR3	34.40	**0.45**	13.80	**0.43**	18.60	**0.46**	31.90	**0.72**	1.30	**0.24**	-	-	8.87	98.70	34.85	32.83	32.32
JR33	10.00	**0.34**	25.70	**0.68**	14.90	**0.68**	37.40	**1.01**	12.10	**0.38**	-	-	9.6	88.00	11.36	46.14	42.50
JR36	7.90	**0.34**	24.40	**0.7**	16.10	**0.72**	38.40	**1.06**	13.20	**0.41**	-	-	8.75	86.80	9.10	46.66	44.24
JR39	33.10	**0.49**	17.10	**0.49**	14.30	**0.52**	29.00	**0.83**	6.40	**0.27**	-	-	7.73	93.50	35.40	33.58	31.02
JR45	34.00	**0.48**	17.50	**0.47**	15.50	**0.50**	33.00	**0.77**	0.20	**0.26**	-	-	8.36	1.00	34.00	33.00	33.00
RR105	30.70	**0.42**	17.90	**0.45**	19.70	**0.48**	29.50	**0.77**	2.30	**0.25**	-	-	9.79	97.80	31.39	38.45	30.16
RR108	34.60	**0.45**	11.90	**0.43**	18.20	**0.46**	31.90	**0.72**	3.30	**0.24**	-	-	6.92	96.60	35.82	31.16	33.02
RR115	32.30	**0.45**	12.40	**0.46**	15.00	**0.49**	34.40	**0.74**	5.90	**0.25**	-	-	6.27	94.10	34.33	29.12	36.56
RR129	31.40	**0.49**	12.50	**0.51**	17.60	**0.54**	35.00	**0.83**	3.60	**0.28**	-	-	6.15	96.50	32.54	31.19	36.27
AZ030	30.10	**0.54**	16.70	**0.57**	20.50	**0.69**	27.40	**1.00**	5.30	**0.31**	-	-	9.59	94.70	31.78	39.28	28.93
AZ034	30.60	**0.60**	15.50	**0.62**	18.70	**0.76**	30.30	**1.06**	4.90	**0.34**	-	-	6.82	95.10	32.18	35.96	31.86
AZ036	37.30	**0.57**	13.90	**0.5**	21.50	**0.61**	26.10	**0.89**	1.20	**0.28**	-	-	8.29	98.80	37.75	35.83	26.42
AZ037	41.50	**0.62**	16.40	**0.5**	16.00	**0.60**	25.40	**0.88**	0.80	**0.27**	-	-	8.43	99.30	41.79	32.63	25.58

Sample	Qtz.	error	Or. 1.	error	Mi. (max)	error	Ab. (low)	error	Biot. 2M1	error	Musc.	error	Global X2	Total QAP %	Q %	A %	P %
RM2																	
AZ050	34.00	**0.61**	17.00	**0.59**	14.70	**0.72**	27.80	**1.01**	6.50	**0.32**	-	-	8.56	93.50	36.36	33.90	29.73
AZ053	35.60	**0.59**	16.50	**0.55**	15.50	**0.67**	26.20	**0.96**	6.30	**0.30**	-	-	7.51	93.80	37.95	34.12	27.93
AZ019	25.70	**0.68**	11.90	**0.82**	25.50	**1.00**	32.20	**1.37**	4.80	**0.45**	-	-	11.18	95.30	26.97	39.24	33.79
RR0120	1.46	**0.49**	12.30	**0.82**	33.00	**1.04**	29.30	**1.41**	10.90	**0.49**	-	-	11.7	89.20	16.37	50.78	32.85

Sample	Qtz.	error	Or. 1.	error	Ab. (low)	error	Biot. 2M1	error	Actin.	error	Trem.	error	Global X2	Total QAP %	Q %	A %	P %
T1 D (-Mi.)																	
AZD01	1.80	**0.25**	12.60	**0.74**	37.80	**0.74**	10.40	**0.29**	10.40	**0.61**	-	-	6.85	79.20	2.27	50.00	47.73
AZD02	2.10	**0.25**	18.00	**0.71**	34.50	**0.71**	7.30	**0.27**	11.30	**0.60**	-	-	6.35	81.40	2.58	55.04	42.38
AZD03	1.50	**0.25**	16.80	**0.73**	38.30	**0.76**	8.60	**0.28**	10.80	**0.62**	-	-	8.19	80.70	1.86	50.68	47.46
AZD04	6.60	**0.28**	11.90	**0.72**	35.70	**0.71**	13.60	**0.31**	12.10	**0.63**	-	-	8.5	74.70	8.84	43.37	47.79
JR26a	36.20	**0.49**	14.10	**0.44**	26.90	**0.77**	1.10	**0.24**	-	-	-	-	7.7	98.90	36.60	36.20	27.20
JR26b	41.90	**0.56**	19.70	**0.45**	20.00	**0.84**	0.50	**0.25**	-	-	-	-	8.25	99.50	42.11	37.79	20.10
JR35	50.50	**0.82**	13.90	**0.55**	26.30	**0.96**	9.40	**0.31**	-	-	-	-	8.56	90.70	55.68	15.33	29.00
T1 D (+Mi.)																	
AZD01	2.10	**0.31**	16.10	**0.66**	50.40	**1.09**	10.60	**0.39**	11.70	**0.67**	9.20	**1.09**	6.89	68.60	3.06	23.47	73.47
AZD02	4.80	**0.31**	17.50	**0.67**	46.00	**1.08**	6.80	**0.36**	12.60	**0.67**	12.30	**1.05**	6.78	68.30	7.03	25.62	67.35
AZD03	9.10	**0.27**	0.20	**0.54**	42.30	**0.86**	8.60	**0.30**	13.00	**0.53**	7.00	**0.88**	7.58	71.40	12.75	28.01	59.24
AZD04	9.30	**0.32**	15.90	**0.62**	36.60	**1.02**	14.90	**0.41**	13.40	**0.63**	10.00	**1.00**	8.51	61.80	15.05	25.73	59.22
JR10	2.60	**0.27**	23.80	**0.63**	42.70	**0.95**	9.10	**0.33**	14.40	**0.59**	7.60	**0.97**	8.66	69.10	3.76	34.44	61.79
JR23	1.30	**0.30**	12.40	**0.64**	28.50	**1.12**	10.10	**0.38**	23.70	**0.72**	23.80	**0.98**	8.75	42.20	3.08	29.38	67.54
JR26a	41.90	**0.84**	16.90	**0.61**	34.40	**1.02**	2.10	**0.32**	0.80	**0.65**	4.00	**1.04**	7.99	93.20	44.96	18.13	36.91
JR26b	47.90	**0.92**	23.00	**0.62**	25.90	**1.02**	1.10	**0.31**	0.00	**0.62**	2.00	**1.02**	7.76	96.80	49.48	23.76	26.76
JR27	10.50	**0.30**	18.60	**0.57**	37.50	**0.92**	8.10	**0.31**	14.80	**0.57**	10.40	**0.90**	7.78	66.60	15.77	27.93	56.31
JR29b	5.40	**0.30**	27.10	**0.71**	40.10	**1.04**	7.80	**0.35**	11.80	**0.64**	7.80	**1.05**	8.63	72.60	7.44	37.28	55.23
JR31	3.90	**0.30**	20.50	**0.66**	43.90	**1.04**	11.70	**0.39**	9.20	**0.64**	10.80	**1.03**	8.23	68.30	5.71	30.01	64.28
JR35	48.80	**0.88**	13.50	**0.54**	24.80	**0.97**	8.90	**0.31**	1.00	**0.59**	4.00	**0.94**	8.81	87.10	56.03	15.50	28.47
RR0113	3.50	**0.31**	25.90	**0.75**	40.80	**1.10**	13.40	**0.43**	5.50	**0.69**	11.00	**1.08**	8.27	70.20	4.99	36.89	58.12
RR0119	9.00	**0.36**	29.00	**0.8**	38.60	**1.13**	6.60	**0.37**	10.20	**0.69**	6.60	**1.15**	10.63	76.60	11.75	37.86	50.39
T2 D (-Mi.)																	
JR24	2.60	**0.34**	5.90	**0.72**	19.50	**1.34**	13.90	**0.47**	21.7	**0.78**	36.4	**1.10**	7.38	28.00	9.29	21.07	69.64
JR41	7.60	**0.35**	5.80	**0.69**	11.10	**1.38**	29.00	**0.71**	13.6	**0.71**	32.8	**1.05**	9.55	24.50	31.02	23.67	45.31
MME (-Mi.)																	
JR37	3.80	**0.31**	23.60	**0.71**	37.40	**1.10**	16.00	**0.46**	10.80	**0.67**	8.50	**1.09**	10.08	64.80	5.86	36.42	57.72
JR38	3.50	**0.33**	25.60	**0.77**	32.60	**1.17**	19.90	**0.54**	11.00	**0.70**	7.50	**1.15**	13.55	61.70	5.67	41.49	52.84
RR0118	5.80	**0.31**	19.10	**0.67**	40.60	**1.06**	10.40	**0.38**	13.80	**0.66**	10.20	**1.05**	7.95	65.50	8.85	29.16	61.98
AZEN07	1.80	**0.40**	19.50	**0.88**	42.90	**1.39**	8.60	**0.48**	14.10	**0.87**	13.10	**1.36**	11.89	64.20	2.80	30.37	66.82
AZEN05	8.10	**0.35**	24.40	**0.76**	35.70	**1.16**	10.10	**0.41**	13.70	**0.71**	8.10	**1.16**	8.13	68.20	11.88	35.78	52.35
AZEN04	9.10	**0.38**	27.00	**0.83**	33.40	**1.24**	10.20	**0.43**	12.80	**0.75**	7.50	**1.22**	9.17	69.50	13.09	38.85	48.06
AZEN03	4.50	**0.35**	30.90	**0.9**	35.70	**1.25**	6.60	**0.41**	15.30	**0.77**	7.00	**1.25**	9.06	71.10	6.33	43.46	50.21
AZEN02	15.40	**0.44**	17.00	**0.7**	36.40	**1.15**	9.20	**0.40**	11.60	**0.70**	10.30	**1.13**	7.54	68.80	22.38	24.71	52.91
AZEN01	39.20	**0.95**	14.30	**0.72**	33.90	**1.22**	5.20	**0.39**	0.70	**0.77**	6.70	**1.22**	7.36	87.40	44.85	16.36	38.79

Sample	Mi. (max)	error
T1 D (-Mi.)		
AZD01	27.00	**0.71**
AZD02	26.80	**0.68**
AZD03	24.10	**0.73**
AZD04	20.50	**0.70**
JR26a	21.70	**0.54**
JR26b	17.90	**0.54**
JR35	0.00	**0.75**

A3.4 XRF Summary of Procedural Blanks and Standards.

Prior to any QXRD analysis, common standard laboratory practices were employed to address contamination, use of representative sample proportions (of different ROMG components) and accuracy of method. In order to address these issues (so that a representative amount of known sample could be used for XRD analysis) procedural quartz blanks followed by various powdered mixtures of RM1 sample AZ005 and constant runs of RM1 sample DLC1/AF207 were run via X-Ray Fluorescence (XRF); mainly for trace element analysis so that standards could be generated for the ROMG. All quartz procedural blanks and RM1 samples used for this technique are documented.

Four procedural quartz blanks were run using XRF for trace element data prior to analysis of RM1 samples to enable consistent analytical methods. The data for these analyses are shown in **Appendix A3.5** from blank one to blank four.

Detection limits and calibrations ranges used (in ppm) are also given for each trace element in **Appendix A3.5** and are set variables used throughout this study for all XRF analyses considered later on for RM1 samples. The range of data depicted in **Appendix A3.5** shows consistency and that a lack of variation is apparent throughout all runs for all trace elements analysed. There is low presence and restricted ranges for Cr (1.5 to 2.1 ppm), Ni (1.8 to 1.9 ppm) and Cu (2.9 to 3.2 ppm). Low limits for Ba and Sr are also present (which is acceptable considering many Caledonian granites have been processed in the rock-crushing lab at St Andrews such as the high Ba-Sr granites of the Argyll Suite (Oliver *pers. comm.* 2007)) in the form of <3 ppm for Ba and a constant of 0.6 ppm is present for Sr. Rare Earth Elements (REE) are all <3 ppm and all other trace elements are <1 ppm with exception of W having an average of 1272 ppm for the four runs which is expected due to the 'jaws' of the rock crusher being predominantly made out of this element. Therefore the trace element data depicted for the procedural quartz blanks indicates that nothing is out of the ordinary in terms of contamination and follow up runs for RM1 powders were ran as the next procedure in order to access 'within sample' modal heterogeneity.

It is often difficult to ascertain the extent of heterogeneity (particularly if *sub-solidus* processes have been extensive and are apparent in the field) that exist in a granitoid at various scales, and what the implications of textural heterogeneity can have on whole rock geochemistry. Thus one way to address heterogeneity at the sample scale and to produce a standard for a granitoid complex, so that the correct amount of representative sample may be used for different components is to use one of two methods. The first method involves

running XRF analysis of various powdered permutations of a well-known facies, whilst the other method simply involves running numerous consecutive powders from the same sample. Whilst using the latter method has its disadvantages (as solely relying on one sample being representative to a specific facies is problematic), when both are used in tandem, many inferences can be made on within sample geochemical heterogeneity.

The first method was rigidly applied for the ROMG to test 'within' sample heterogeneity. RM1 sample AZ005 was one of the largest samples (collected from the field type locality for RM1) in the excess of 20 kg. It was used for production of powdered mixtures of RM1 which was done by using four clean fist sized hand specimens (A, B, C and D; roughly 1.5 to 3 kg each), crushing each sample and mixing them respectively (**Appendix A3.6**). Sample AZ005 in **Appendix A3.6** simply reflects the excess material, which was considerably larger than specimens A to D (in the excess of >7.5 kg) crushed and ran as an independent sample used for comparison.

In similar instances to the quartz procedural blank data (**Appendix A3.5**), as a whole the samples from AZ005A to AZ005D show little spread or variation in trace element data, and no apparent abrupt differences are present when compared to the much larger quantity of sample used for sample AZ005. The most obvious trace element pattern is the high presence of Ba and Sr, which is highly characteristic of the RM1 facies of the ROMG, and well within the limits of the high Ba-Sr granites of the Argyll suite (Atherton & Ghani 2002). The greatest apparent difference in terms of standard deviation is also present for Ba (21.08 to one standard deviation), which has a tendency of having high compatibility when considering fractionation of mafic sources and high mobility in terms of aqueous *sub-solidus* processes. Therefore as it is present in such high concentrations and because of these factors, it is always a reasonable geological prediction to expect that Ba or Sr (as both are Group II elements) could show the greatest values and spread of trace element data for samples across the whole of the ROMG or for many other zoned Caledonian granitoids. Most of the transition metal elements in **Appendix A3.7** have constant values of <1.5 (as well as the actinoids and Pb) for one standard deviation with exception of V being 2.87 and Zr being 3.04. Light REE are slightly more varied in terms of one standard deviation with Ce having the greatest value of 5.60. Ti, Mn and Fe that are calculated as a percentage from oxides (see major elements in **Appendix A3.7**) are also constant and minimal.

The second method used to address ROMG heterogeneity involved four consecutive XRF runs of sample DLC1/AF0207. This was done (following quartz procedural blanks and sample AZ005) using this specific sample, as it comes from the most representative part and

type locality of the RM1 facies. Meticulous field, thin section and CL petrography was completed on RM1 samples within and close proximity to Red Bay Quarry prior to choosing this sample as the most representative RM1 standard for testing heterogeneity via XRF; and for use later on when considering feldspar samples for *in situ* elemental and isotopic analysis. Major and trace element data for four XRF runs of sample DLC1/AF0207 is shown in **Appendix A3.6**, with calibration ranges for major element data also depicted. Once more there is similar overlap in terms of consistency of trace element data throughout all the four runs and identical patterns are also observed here within the trace element data for this sample and the other Red Bay Quarry RM1 sample AZ005 (compare both **Appendix A3.5** and **Appendix A3.7**). Unsurprisingly, the largest trace element differences per sample are for Ba (171.75 ppm) and Sr (76.5 ppm). Major element variation from four runs of DLC1/AF0207 shows SiO_2 to be the highest (reflecting the quartz rich nature of this facies of the ROMG) having an average of 72.070%.

As with the trace elements, a prominent consistency for all the major elements is apparent per sample runs one to four (with SiO_2 having the largest value of 0.291 to one standard deviation) and loss on ignition (LOI) data is at a constant at 0.8, which is minimal loss per sample. Thus it can be ascertained from both methods used that there is little overall 'within' sample geochemical heterogeneity for a representative sample(s) of RM1 of the ROMG. It also makes sense that a standard of four fist sized hand specimens were crushed (as opposed to crushing an excess of 5 to 10 kg per sample) for all samples due to the trends shown here, and the powder obtained from such samples were utilised for all XRF/QXRD analysis done in this study. Once all samples needed for QXRD were crushed and XRD sized fractions were produced, all XRD sized fractions obtained were subsequently crushed even further to produce finer powders that could be used within the correct particle size limits for analysis via a diffractometer.

A3.5 Quartz procedural blank trace element data with calibration ranges used for all samples in this study.

µg/g	Blank 1	Blank 2	Blank 3	Blank 4	Average	Limit of detection	Calibration range (ppm)
Ti	-	-	-	-	-	-	-
V	< 1	< 1	< 1	< 1	**1**	3	0.3 -> 2000
Cr	2.0	2.1	1.7	1.5	**1.825**	5.475	0.5 - 24000
Mn	-	-	-	-	-	-	-
Fe	-	-	-	-	-	-	-
Ni	1.9	1.8	1.8	1.9	**1.85**	5.55	0.3 - 13500
Cu	2.9	3.1	2.8	3.2	**3**	9	0.9 - 30000
Zn	< 1	< 1	< 1	< 1	**1**	3	1 - 12000
Ga	<1	<1	<1	<1	**1**	0	1 - 99
Rb	0.8	0.7	0.9	0.8	**0.7925**	2.3775	0.06 - 8600
Sr	0.6	0.6	0.6	0.6	**0.6**	1.8	0.3 - 4600
Y	0.5	0.5	0.5	0.5	**0.5**	1.5	0.5 - 720
Zr	< 1	< 1	< 1	< 1	**1**	3	0.4 - 11000
Nb	1.0	1.0	1.0	1.0	**1**	3	0.05 - 960
Ba	< 3	< 3	< 3	< 3	**3**	9	1 - 120000
La	< 3	< 3	< 3	< 3	**3**	9	1 - 20000
Ce	< 3	< 3	< 3	< 3	**3**	9	1 - 32000
Pr	< 3	< 3	< 3	< 3	**3**	9	328720
Nd	< 3	< 3	< 3	< 3	**3**	9	1 - 8300
Pb	< 1	< 1	< 1	< 1	**1**	3	1 - 9200
Th	< 1	< 1	< 1	< 1	**1**	3	0.1 - 1000
U	< 1	< 1	< 1	< 1	**1**	3	0.2 - 659
Hf	< 3	< 3	< 3	< 3	**3**	9	1.0 - 290
Ta	< 3	< 3	< 3	< 3	**3**	9	1 - 305
W	1222.0	1289.0	1359.0	1218.0	**1272**	3816	1 - 720

A3.6 RM1 sample AZ005 trace element heterogeneity test.

µg/g	AZ005	AZ005 A	AZ005 AB	AZ005 ABCD	AZ005 B	AZ005 C	AZ005 CD	AZ005 D	Average	SD
Ti %	0.15	0.14	0.14	0.15	0.15	0.15	0.15	0.14	**0.15**	0.01
V	22	18	18	20	23	27	21	19	**21**	2.87
Cr	9	8	8	8	8	10	8	9	**8**	0.83
Mn %	0.03	0.02	0.02	0.02	0.02	0.03	0.02	0.03	**0.02**	0.00
Fe %	0.99	0.90	0.94	0.95	0.94	1.03	0.96	0.94	**0.96**	0.04
Ni	< 1.5	< 1.5	< 1.5	< 1.5	< 1.5	< 1.5	< 1.5	< 1.5	**< 1.5**	< 1.5
Cu	2	2	2	2	2	2	3	2	**2**	0.37
Zn	25	24	24	25	25	26	26	25	**25**	0.84
Ga	15	14	15	15	15	16	15	15	**15**	0.47
Rb	86	85	84	83	83	84	83	84	**84**	1.01
Sr	225	229	226	228	225	229	227	221	**226**	2.64
Y	22	19	21	20	20	22	20	20	**20**	1.04
Zr	145	138	143	136	142	143	139	140	**141**	3.04
Nb	11	10	10	10	11	11	10	10	**11**	0.35
Ba	583	550	541	554	556	586	548	522	**555**	21.08
La	45	40	41	38	42	44	42	38	**41**	2.46
Ce	99	88	91	86	91	98	92	82	**91**	5.60
Pr	5	5	7	5	5	6	6	5	**5**	0.79
Nd	41	34	41	39	38	42	35	34	**38**	3.45
Pb	21	20	23	21	21	21	21	20	**21**	0.81
Th	8	9	8	8	8	9	8	8	**8**	0.55
U	< 0.9	< 0.9	< 0.9	< 0.9	< 0.9	< 0.9	< 0.9	< 0.9	**< 0.9**	< 0.9

A3.7 Major element and trace element data for RM1 sample DLC1/AF0207.

%	Sample 1	Sample 2	Sample 3	Sample 4	AV	SD	STDEV/AV %	Calibration range %
Na_2O	4.12	4.2	4.22	3.99	**4.133**	0.104	2.53%	0.05 - 11.20
MgO	0.68	0.71	0.75	0.65	**0.698**	0.043	6.12%	0.01 - 49.50
Al_2O_3	13.49	13.64	13.7	13.69	**13.630**	0.097	0.71%	0.02 - 88.50
SiO_2	72.5	71.9	71.88	72	**72.070**	0.291	0.40%	0.1 - 99.60
P_2O_5	0.1	0.09	0.1	0.1	**0.098**	0.005	5.13%	0.01 - 2.50
SO_3	<0.01	<0.01	<0.01	<0.01	**0.010**	0.000	0.00%	0.05 - 5.00
Cl	0.09	0.06	0.06	0.08	**0.073**	0.015	20.69%	0.05 - 5.00
K_2O	5	4.98	4.99	4.95	**4.980**	0.022	0.43%	0.01 - 15.40
CaO	1.18	1.06	1.12	1.15	**1.128**	0.051	4.54%	0.01 - 65.50
TiO_2	0.32	0.34	0.33	0.3	**0.323**	0.017	5.30%	0.05 - 3.30
MnO	0.06	0.05	0.05	0.05	**0.053**	0.005	9.52%	0.001 - 0.50
Fe_2O_3	2.06	1.92	2	1.98	**1.990**	0.058	2.90%	0.02 - 55.50
LOI	0.8	0.8	0.8	0.8	**0.800**	0.000	0.00%	
µg/g								
V	30	33	33	32	**32.000**	1.414	4.42%	
Cr	10	10	10	11	**10.250**	0.500	4.88%	
Ni	6	7	7	6	**6.500**	0.577	8.88%	
Cu	4	3	4	5	**4.000**	0.816	20.41%	
Zn	35	37	35	38	**36.250**	1.500	4.14%	
Ga	15	16	15	17	**15.750**	0.957	6.08%	
Rb	86	88	87	88	**87.250**	0.957	1.10%	
Sr	305	300	303	302	**302.500**	2.082	0.69%	
Y	16	16	17	16	**16.250**	0.500	3.08%	
Zr	151	154	152	153	**152.500**	1.291	0.85%	
Nb	12	12	12	12	**12.000**	0.000	0.00%	
Ba	715	737	723	728	**725.750**	9.215	1.27%	
La	44	47	46	51	**47.000**	2.944	6.26%	
Ce	91	92	90	95	**92.000**	2.160	2.35%	
Pr	7	6	6	10	**7.250**	1.893	26.11%	
Nd	31	31	31	34	**31.750**	1.500	4.72%	
Hf	4	4	4	2	**3.500**	1.000	28.57%	
Ta	<3	<3	<3	<3	**3.000**	0.000	0.00%	
W	619	615	627	620	**620.250**	4.992	0.80%	
Pb	20	23	20	21	**21.000**	1.414	6.73%	
Th	9	8	9	8	**8.500**	0.577	6.79%	
U	<1	<1	<1	<1	**1.000**	0.000	0.00%	

A3.8 Preparation of granitoid samples for X-Ray analysis at St. Andrews University.

1.) Rock cutting Laboratory safe working practice.

Equipment*:* Small rock saw with diamond-coated blade.

Safety requirements: laboratory coat, safety goggles and ear protection.

Procedure: Fresh pieces of granite are required for XRF/QXRD so that there is no contamination from organic matter or e.g. marker pen. For extremely large samples, (5-10 kg) they need to be broken down further with a sledge hammer (safety goggles required) so that they can fit within the relative limits of the rock saw. Once one is ready to cut a specimen, one should press the start button (green button) to get the blade rolling. The tap must be then turned on and an extremely high flow of water is needed as this in turn cools and aids in the cutting. The specimen is then laid flat and gently fed in (both hands should be either side of the saw adding firm pressure to the specimen when it is fed in). For preparation of stubs for thin section, the process is continued until one is happy with an adequate size of stub. Once finished, the red button should be pressed to end the process and the tap should be turned off.

As the rock saw motor is extremely old, it should be used in hourly intervals and rested for 20 mins per interval. This prevents the motor from overheating. If the motor does severely overheat an automatic shut down system kicks in and turns off the motor. Occasionally, the rubber band might fly off during the cutting; this usually occurs if great stresses are applied or one is not cutting straight. If this occurs, good practice is to change to another rubber band.

As the samples are wet during this stage, they need to dry out before they can go into the jaw crusher, so space them out on paper towels on a table making sure that one labels the paper towels they are drying on. Similarly, for thin section stubs, label the side that you want for sectioning with a paint pen.

2.) Rock crushing & grinding laboratory safe working practice.

With all laboratory work, the lab must be kept clean in order to avoid contamination of equipment and samples. Therefore, all equipment has to be thoroughly cleaned with acetone before starting work and in-between samples. Cleaning procedures are also given below.

Equipment: Fly press, Jaw crusher and Tema disc with Agate grinding set.

***Safety requirements*:** laboratory coat, goggles and face mask (face mask should be changed after 3 days use). Also note that the main extractor fan and the vacuum has to be on at all times whilst working in the lab. **Also, there is to be no hammering in this room.**

Procedure: **Fly press** - Fist size samples are approximately the correct size for putting into the jaw crusher. For larger fresh samples, they can be broken down using the spring loaded fly press. The sample is placed accordingly into the jaws of the press and the main lever is wound up anticlockwise until the sample is sufficiently clamped. The door should then be closed and the 'car jack' motion with the separate long steel lever will break the sample. The same lever is then inserted and should be turned back to the original position as this will release the tension from the springs and put the jaws back to their original setting.

Procedure: **Jaw crusher** - During the jaw crushing stage, it is vital that contamination is cut out. Therefore the first stage involves cleaning. The plastic basin below (where the sample is collected) should be removed and cleaned with acetone and then blasted with the airline. The jaw crusher is opened with the lever on the right hand side. Once fully open, using the brushes provided, one should vigorously scrub the individual jaws and then clean with Acetone (tissue paper should be provided). Again the airline should be used in order to get rid of the remaining acetone. The screwdriver provided is for dislodging any coarse pieces that get stuck down the left hand side corner of the crusher. The lid should also be cleaned. Once clean, it should be closed flush and the gap between the jaws must be set to an 8-9mm gap using the 'portcullis' type lever (The gap must not exceed 1.5cm). The green start button can then be pressed so that the rollers can kick into action. Do not put in a sample straight away and wait for at least 10 seconds so that the machine can get up to speed. The fist-sized samples can then be individually placed into the jaws (one at a time after one is crushed). **Whilst the sample is loaded in, the lid must remain firmly closed during the operation**.

The basin is only removed when the machine has stopped after one has pressed the red stop button. The sample should then be tipped into a large sample bag and labelled appropriately (i.e. no., jaw crush and date).

Procedure: **Tema disc grinder -** Before and in-between each sample, a cleaning process is employed. The Tema comprises of an outer casing, an inner ring and a solid disk. Once the ring and disc are placed inside the casing, 70-80 ml of quartz should be evenly distributed between them (a paint brush can be used as long as it is cleaned per sample and a new one is replaced per 10 samples) and the lid should be placed on top. When clamping the Tema into base, make sure the correct base (agate) is used and the handles on the lid are parallel to the handles on the outside casing. When sitting on the barrel, the clamping device should be correctly in place and the protective lid should be shut down. The green start button can be pressed and the running time for the quartz should be 30 secs. Once the timed process is over (press the red stop button), the quartz can be emptied on glazed paper and thrown away. Again, clean out the Tema disc grinder and the glazed paper in the vacuum using the acetone and airline. The glazed paper should be thrown away and replaced after at least 5 samples.

Once the Tema disc grinder is clean, one should fill it ¾ full with the jaw crush fraction and run it for 1 min, 30 secs. Repeat the process until the jaw crush fraction has gone (if one is going to do mineral separates) and one is left with a large coarse fraction. For **XRF**, the fraction has to be very fine so run a representative scooped sample from the coarse fraction (75-80ml) for 2 mins. Use a 200 ml plastic cup for measurements.

For **QXRD**, the 'mini' Tema disc grinder is used**.** The 'mini' Tema disc grinder should be cleaned in the same manner as the large Tema disc grinder. Approximately 8-10 g (or x 10 spatulas of the XRF powder) is loaded into the 'mini' Tema disc grinder and it should be run for 1 min, 30 secs.

3.) X-Ray laboratory safe working practice

Equipment: Hammer & anvil press or pneumatic air press.

Safety requirements: laboratory coat.

Procedure: **Pressed pellets** (trace element analysis).

1.) Clean the anvils and pellet making equipment with Acetone. Fix the main part of the vessel (piece with the hollow tube) to its base.

2.) Insert an anvil shiny side up into the hollow so it slides down to the bottom (**Please do not drop or dent the anvils, as they are extremely expensive to replace**).

3.) Weigh out approximately 7.000 g of a desired sample into a clean plastic cup using the electronic scale.

4.) Using a wooden lollypop stick, add 4-5 drops of (more Si rich, add 5 drops) of glue solution (this is a binding agent for the pellets) and mix thoroughly until the sample is evenly mixed. Note the sample go darker in colour.

5.) Pour in the sample from the cup into the pellet vessel and shake until the powder is level. Put in the other anvil shiny side down and press it down if need be so that it meets the powder. Then add the long cylindrical piece that fits in the hollow making sure there is a rubber band on the top of it.

6.) Turn the finger light handle on the right hand side of the main unit clockwise to lower the base of the press and insert the vessel when there is an appropriate gap. Remember to turn the finger light handle the opposite way to tighten the press.

7.) Pump the jack handle up and down until **10 - 12 tonnes** of pressure are applied to the sample. The sample must be left for 30 secs - 1 min under such pressure.

8.) One should then release the pressure slowly and gently via the finger light handle. Once the vessel is taken out, it should be turned upside down and the base must be screwed off. The plastic anvil catcher is then placed on top and the vessel is inserted, clamped into the main press.

9.) Pump the jack handle up and down until one hears a drop. The vessel is then taken out and the pellet removed (pinching the anvils is necessary). The pellet is then labelled on its side gently with a black thin tipped permanent marker pen or a pencil.

10.) It is then placed into an oven on top of a paper towel in order to dry out over night. When it is taken out of the oven the following day, it should not be directly placed into a labelled sample bag, as it would be hot enough to melt the bag. Therefore, give the pellet/s sufficient time to cool down before putting it into a labelled sample bag.

* Note, if the old 'hammer & anvil' press is not used anymore, apply a similar procedure when using the singular knob type pressurised press. Take into account that if you turn the knob anti-clockwise (360^0) this releases the pressure and make sure the knob is tight when applying pressure (i.e. when using the air line to press the powder). If there is a slight leak in the airline, then keep applying pressure with the valve so that it is approximately within the limits of 12-14 tonnes-OV-RAM.

Procedures: **Fusion glass discs/beads** (major element analysis) **& Loss on ignition samples**

Equipment: High precision weighing scale, x2 Carbolite ovens, hotplate, 16 platinum crucibles and 32mm platinum mould, ceramic crucibles, extended tongs, x2 spatulas and an onsite Mac with an emissions loss calculation spreadsheet.

Please note platinum crucibles are very expensive (roughly £300 each) so please be careful with them. Do not bend or scratch them. They should be kept ultra-clean and if one is running a large sample size, they should be left in 50% HCl overnight (or 2 hours minimum if one is strapped for time), and then subsequently be cleaned with water under the tap (use the tongs to grab at least two) and put in the oven to dry out.

Prior to fusions, check whether your samples contain pyrite (this sulphide can damage the Pt crucible) or substantial carbonate (one could use a LECO here). If they do, please consult Angus Calder for further instruction.

Safety requirements: laboratory coat, **teflon based safety gloves & headset with visor (when using the oven/s it is mandatory to wear this equipment).**

Procedure: **Fusion glass discs/beads** - All XRF powders should be readily identified, bagged and adequately labelled at this stage. Firstly, **clean crucibles** should be ready and set up in an appropriate labelled rack (maximum of 16) and the two Carbolite ovens should be set up to an according temperature prior to weighing here. One should be at 1100^{o}C (for fusions) and one at roughly 900-1000^{o}C (for loss on ignition calculations). For the Carbolite oven on the left, make sure that allumina briquettes are set up in an opposite angled pair as this makes step 5.) easier (see below). Make sure that an adequate portion of flux is put into a sample bag (please do not take flux directly from the beaker it is stored in as one does not want to contaminate the flux) and suitable standards are chosen. Once this is done, the following steps are taken:

Weighing*:*

1.) Standard/s need to be run so that an idea of error and consistency (human induced and analytical errors) can be measured: for granitoid rocks, the most appropriate choice of standards is **GS-N**, **AC-E** and the USGS silver plume granodiorite **GSP-2** (bottle no 0256). Data for acceptable levels regarding these standards can be checked on the Internet at http://www.geoanalyst.org. If one is working a large sample set (e.g. n=100), construct glass beads for all three standards at the start, middle and end of the sample population.

2.) Firstly, put a clean Pt crucible on the scales (check to see if the crucible is clean as opposed to having a dull sheen of a bubble on its inside which indicates that it is dirty), tear the scale (set to 0.0000) and accurately weigh 4g of Li (meta borate) flux using the sample bag. Record the measurement in the Mac spreadsheet accordingly when the scales have stabilised (remember to shut the door on the scales to keep the draught out). Don't worry if the last digit (fourth d.p.) dances too much (>instrumental error than 0.05 wt.%). Once this is done, tear the scale again and weigh 0.5g of your sample using the large spatula into the crucible (an 8:1 ratio/dilution factor is essentially used). Record the measurement in the Mac spreadsheet. Don't worry again if one is slightly over in the weighing department as some of the sample is lost in the Carbolite oven (volatiles) and a little extra helps to

fill the mould better. Note the flux used here is 80%meta and 20% tetra. With the flux, as it is hydroscopic, keep it in the **desiccator** over night so that it is 'crisp' and dry the following day. Please don't leave bags of flux lying around the lab.

3.) The next procedure requires adding a small proportion of ammonium iodide (0.02g). Using a small spatula provided, this can be easily estimated. The ammonium iodide acts as an oxidant and a lubricant (stops the mix of the sample and flux sticking to the crucible) and it generally 'burns' off in the oven. The flux + sample + ammonium iodide is then evenly mixed using the small spatula making sure the spatula does not touch the edges or base of the crucible. The sample is now ready to go in the oven.

Using the Carbolite oven(s):

4.) **Please note that the oven(s) are extremely hot, so it is again (repetition here) mandatory to use the safety equipment provided**. Using the tongs, the crucible should be gently pinched at the top (try not to dent the crucible) and placed on the right hand briquette in the oven (this is if you are right handed). The handle on the top left of the oven is used to close and open the front. Also, make sure Angus Calder shows you how to hold the tongues properly as this will be important in pouring the molten sample in the mould later on. Leave the sample in the oven for **8-10 minutes**.

5.) After this time period elapses, the sample must be taken out and gently swirled to aid in the mixing of the flux and sample. Tetra borate flux is quite viscous and the sample needs to be a homogeneous mix, so give the sample in the crucible a good swirl (don't be shy to expose the bottom of the crucible). The sample is then placed back in the oven and the Pt mould is placed on the left briquette. Leave the sample and mould in the oven for a further **2-3 minutes**. Remember, whilst you are waiting for your sample to be fused in the oven, one should be going through a conveyor belt process of weighing out the rest of one's samples (steps 1-3) so that they are ready to go in the oven (16 max.). One could also weigh out samples relative to the emissions loss step (16 max) described below.

6.) After a **total of 12-13 minutes** in the oven, the oven door should be opened and the molten sample should be carefully poured into the mould (again, make sure you know how to hold the tongs properly). Try not to spill sample in the oven, as it will eat its way through it. Also, a good idea is to have the mould at an angle (diamond) so that the corner sticks out prominently which makes it easier to get at the edge with the tongs. Take out the crucible and carefully place it on the heat resistant blocks provided. The mould with the molten sample is then taken out and placed on a heat resistant briquette, which has a fitting. Sometimes, the molten sample will not conform to the mould and can be restricted to staying on one side of the mould. If this occurs, give the sample a good swirl and if need be, put the mould with the molten sample back in the oven for a few minutes. Again, when it is taken out, swirl if necessary and place on the fitting.

7.) The sample will cool (you will hear a cracking sound) and after approximately 5 minutes, place the sample (flat glass bead/disc) within the mould on the hotplate (use the 'oil' looking dot in the middle of the glass as an indicator for when it can be placed on the hotplate). After the sample has cooled down sufficiently (just use the palm of your hand for an indication of whether the sample has cooled down enough), gently and carefully label the glass bead/disk (top side), and remove it from the mould finally placing it into a small-labelled sample bag. Repeat this process for all samples in question.

8.) Due to the natural environment, (i.e. living by the sea), there is a problem of incorporation of Na in the sample if it is not adequately looked after (a jump of 0.03-0.3%). Therefore, double bag the samples in question and leave them in the **desiccator**.

9.) Finally, put the Pt crucibles back into the 50% HCl so they can be adequately cleaned.

Loss of ignition:

This is a straightforward process and the following steps are taken:

1.) Porcelain crucibles are used in this process. Don't worry if they look dirty as the previous sample that has been in them has been roasted and this should not affect your analysis. These crucibles can be found in the draw directly below the main weighing scale. Put the crucibles in an appropriate order on the labelled rack provided.

2.) Taking a crucible (you can wipe it with a clean tissue if there is loose material inside it), place it on the scale and tear it. Weigh in approximately 1g of sample. Note down the sample weight in the Mac spreadsheet provided.

3.) Tear the scale whilst the crucible and sample are still on the scale, and lift off the crucible placing it back in the rack provided. Note the negative weight given and again insert this number into the relative area on the Mac spreadsheet. Do this for all samples in question.

4.) Place the sample/s (16 max.) in the 900-1000^{o}C Carbolite oven remembering (writing down) the order you have placed them in. The samples are then left in the oven (1 hour), and are re-weighed in order to calculate the loss of ignition. The relative data is then put into the Mac-spreadsheet so that an automatic calculation is made in Excel for the loss of ignition.

Finally, as in all work, remember to save your data. Therefore, using the apple button (hold it down), press S. This should auto-save your data.

A3.9 SIROQUANT procedure.

1.) Firstly, when the powder for a sample is run through the diffractometer, spectra files are saved as uxd. files (text files), which need to be converted to raw. files (binary read for the system). The uxd. files are converted to raw. files using a program called ConVX. The relative uxd. files must be highlighted in ConVX as Bruker files and subsequently converted into a folder of one's choice as Diffrac-AT RAW output files. This is a simple task and should be done with ease providing the relative software is available.

2.) Prior to using SIROQUANT version 2, every sample must be grouped relative to each facies (in terms of zonation) and a list of minerals present (that would have been observed during detailed petrography) in the plutonic components should be made. For the ROMG, the following minerals were listed and used relative to a specific facies:

Felsic components

- RM1a (equigranular-biotite-muscovite granite) quartzco, ortho1, albite1, mcline, biotite, muscov1
- Syenite - quartzco, ortho1, albite1, mcline, biotite
- Type 1 & 2 aplite sheets - quartzco, ortho1, albite1, mcline, biotite
- RM1 - (equigranular-biotite-granite) quartzco, ortho1, albite1, mcline, biotite
- RM2 - (alkali feldspar-megacrystic granite) quartzco, ortho1, albite1, mcline, biotite
- x1 K-feldsp. From a pegmatite at Eilean Srianach (all feldspar phases calibrated by Angus Calder)

Mafic components *(*Refer to Zaniewski *et al.* 2006); note relict CPX's not added due to thin section observations (refer to Castro & Stephens 1992).

- Knockvologan type diorite - quartzco, ortho1, albite1, actinol, tremol

x4 samples run with the above but with mcline (although none evident in thin section; this was done to observe the nature of refinement/dangers in generating bad data)

- Aird Mór type diorite - quartzco, ortho1, albite1, actinol, tremol
- MME - quartzco, ortho1, albite1, actinol, tremol

3.) In the default structure file, refine structures of specific mineral phases to fit samples (prepare a HKL file e.g. for quartz-quartz.co in a specific folder (consult Angus Calder who will set up relative monochronomater i.e. at 2-theta angle 3 in the relevant section)). An Azmain file was created for such specific mineral phases using the AF/02/01 spectra (RM1 from Red Bay Quarry) to create a standard spectra for all samples considered. This standard allows a reference point so that in the next procedure, a consistent stripped background can be created and applied to samples.

Note that when a spectra is created, indicative peaks occur at certain Angstroms (A^0) which can be defined by the identify phases button when clicked on and off (looks like a painters palette). Relative mineral peaks to observe are as follows; $10A^0$- biot./musc.; $22A^0$- K.feld.; $25A^0$- Plag.; $28A^0$- Qtz.; $30A^0$- K-feld.; $31A^0$- Qtz).

4.) Stripping the background consists of taking out irrelevant points to get a representative spectra/adequate fit relative to a granitoid sample. A stripped background standard is created and should be saved (as table) and in this case was saved as AZBCKD.bkd. When subtracting a trace, one has to take in account the mineral phases present (again refer to petrography). Once the background is fitted (use fit button) and then subtracted (use subtract button), the CSIRO (process) button is pressed, which will work out a fit relative to the original trace. Effectively, the difference in the original pattern to the calculated pattern is the line difference.

5.) The next steps entail pressing the button that looks like a scroll that will bring up a sub-menu. On the sub menu, the automatic pre-scale box is un-ticked (**note: when running samples after calibration here, this box should always remain ticked**). Various stages of refinement include ticking the instrument zero (an adjustment of displacement) and then pressing on OK.

The CSRIO button can then be used to refine shift spectra. Using the button that looks like a scroll, the instrument zero is taken off. At this stage, three things can be refined which makes SIROQUANT a useful program:

A - Unit cell (particularly useful where solid-solution series occurs in mineral group)

B - Orientation (one can set and calibrate different preferred orientations)

C - Width of spectra peaks

6A.) Click on the unit cells X to refine what is required. In the case of microcline, one may refine aspects needed but the auto-pre scale must be on prior to use of CSRIO. The X^2 button (chi-squared) will give the indication of fit. One can always go back into the button that looks like a scroll for refining felspars.

As standards in terms of background and Azmain are set up, and each individual spectra peak is not meticulously calibrated (for A, B & C) with limits of fit <15% with average of 4-6% for X^2, data is generated quickly and is semi-quantitative.

6B.) In the button that looks like a scroll, it is important **to set the dampening factor to 0.2** which should be a set parameter for all runs. This concerns the actual phase shift of the spectra on the x axis which can range from 0.1 to 1, so the dampening factor and width orientation (can not be 0.4 for the unit cell) add a greater flexibility to fitting refined data to the Azmain spectra.

6C.) This concerns the actual widths (in the button that looks lke a scroll, orientation is taken off and the w's are clicked in selected areas to calibrate widths for specific mineral phases) of the peaks for certain mineral phases. Once certain widths are calibrated, the CSIRO can be pressed to get an accurate spectra. The way C can be monitored is to use the biotite peak for each sample. Good semi-quantitative data should be in the limits of of <6% X^2.

7.) Saving data is done by clicking the pie chart button (copy to clipboard), and when asked to clear the contents, press OK. This data can then be pasted into Microsoft Excel. **Note that the errors generated are not actual errors to the % of a mineral phase present, but relative to the ERROR OF FIT, which tend to be 5-10% relative (i.e. weight 1.5-3% either side of the fitted spectra)**.

8.) When starting a new sample, click new sample and then load scan. As the files were converted prieviously using ConVX, the next file to choose is under raw siemens (**it is better to chose a sample of the same facies so that mineral phases do not need to be removed or**

added, which can be done in the edit current task menu). Once this is chosen, one should click on paramaters-background and load the background standard created (this is in the created folder (e.g. AZ) under AZBCKD.bkd). This is then fitted and subtracted and the method for calibrating peaks which do not look relative to the standard are modified using the parameters mentioned above. Then the CSIRO and copying/pasting the data are the final steps.

A3.10 Weighed standards used for SIROQUANT QXRD.

	SIROQUANT			WEIGHED			DIFFERENCE		
SAMPLE	**qtz**	**k-feld**	**plag**	**qtz**	**k-feld**	**plag**	**qtz**	**k-feld**	**plag**
1	34	33	33	33.3	33.3	33.4	-0.7	0.3	0.4
2	8	72	20	10.2	69.7	20.1	2.2	-2.3	0.1
3	19	23	58	20.0	20.0	60.1	0.9	-3.0	2.1
4	45	16	39	49.5	11.5	39.0	4.5	-4.5	0.0
5	72	10	18	69.7	15.3	15.0	-2.3	5.3	-3.0

A3.11 Repeat runs of RM1 sample AZ005 (NM[30401 24008]) for all types of modal analysis.

Field Petrology	**Q**	**A**	**P**
Sample Name	**%**	**%**	**%**
AZ005(1)	40.00	59.00	1.00
AZ005(2)	35.00	64.00	1.00
AZ005(3)	35.00	64.00	1.00
AZ005(4)	5.00	94.00	1.00
AZ005(5)	35.00	64.00	1.00
AVERAGE	30.00	69.00	1.00
2σ	28.28	28.28	0.00

Point Counting	**Q**	**A**	**P**
Sample Name	**%**	**%**	**%**
AZ005(1)	34.42	20.26	45.32
AZ005(2)	43.41	9.02	47.56
AZ005(3)	49.19	25.10	25.71
AZ005(4)	49.70	22.33	27.97
AZ005(5)	32.24	28.34	39.43
AVERAGE	41.79	21.01	37.20
2σ	16.29	14.71	19.89

QXRD	**Q**	**A**	**P**
Sample Name	**%**	**%**	**%**
AZ005	39.57	36.16	24.28
AZ005(a)	38.97	34.77	26.26
AZ005(b)	42.64	31.51	25.85
AZ005(c)	33.13	38.48	28.40
AZ005(d)	44.59	33.47	21.94
AVERAGE	39.78	34.88	25.34
2σ	8.73	5.28	4.81

All Avgs.	37.19	41.63	21.18

A3.12 ROMG averages and data spread (to two standard deviations) for all types of modal analyses. Note for QXRD data +Mi/-Mi refers to calibration with or without microcline as a mineral phase.

Field Petrology (n = 59)

	RM1a	*RM1*	*RM2*	*Type 1 Diorite*	*Type 2 Diorite*
	n = 8	n = 7	n = 38	n = 5	n = 1
Q	33.57	38.57	32.36	7.00	5.00
2σ	12.54	11.13	15.98	5.48	0.00
A	40.00	52.29	43.77	8.00	15.00
2σ	28.28	27.17	27.16	15.17	0.00
P	4.04	9.14	23.59	85.00	80.00
2σ	28.73	25.41	30.33	14.14	0.00

Point Counting (n = 36)

	RM1a	*RM1*	*RM2*	*Type 1 Diorite*	*Type 2 Diorite*
	n = 2	n = 15	n = 16	n = 1	n = 2
Q	26.61	36.63	34.98	4.79	6.88
2σ	17.82	21.60	27.80	0.00	10.30
A	17.08	27.88	22.92	0.00	0.00
2σ	17.19	25.51	29.76	0.00	0.00
P	22.98	35.48	42.10	95.21	93.12
2σ	0.63	16.68	29.31	0.00	10.30

QXRD (n = 88)

	RM1a	*RM1*	*RM2*	*Type 1 Diorite (+Mi)*	*Type 1 Diorite (-Mi)*	*Type 2 Diorite (-Mi)*
	n = 7	n = 24	n = 34	n = 7	n = 14	n = 2
Q	40.40	35.63	32.54	21.42	17.20	20.15
2σ	14.64	15.33	15.08	45.42	36.95	30.74
A	35.83	33.38	34.68	41.20	28.14	22.37
2σ	10.89	5.78	10.73	26.70	13.73	3.68
P	23.77	30.99	32.78	37.38	54.65	57.47
2σ	8.30	15.85	9.79	23.30	28.71	34.42

Appendix Four
CL & MINERAL GEOCHEMISTRY

Introduction

This part of the appendix presents working CL conditions used at the University of St. Andrews and micro-geochemical data for feldspars in Chapter Four, generated at the University of Copenhagen and the Danish Lithosphere Centre, Copenhagen. It provides a working CL manual written by one of my supervisors and modified by myself and breaks down all EPMA and Pb-Pb data in a series of tables. It also summarises all bulk NIST 610 glass standard data measurements as discussed in Chapter Four.

For actual raw data hardcopies generated straight from instruments (EPMA (JEOL Super-probe) and LA-MC-ICP-MS (AXIOM)), these have been scanned and appropriate data tables, conversions and fractionation corrections per feldspar can be found in **Attachments to Appendix (on memory stick labelled AZ ROMG 2017) A7: DLC Electronic Raw Data**.

A4.1 CL Manual (University of St. Andrews)

This guide was originally written by Prof. Adrian Finch (University of St. Andrews) back in 2003 and has been modified. It has been inserted purely in context to this part of the appendix so that the CL working conditions and procedures used in this thesis are understood.

'Technical Specifications of the Machine

A Technocyn 8200 Mk V Luminoscope is fitted with an Alcatel Vacuum Pump. The chamber is mounted on a Nikon Optiphot Microscope which has had the normal stage replaced by the CL chamber. A digital camera is mounted on the third ocular of the microscope.

Layout of the Guide

This guide is in three parts. The first is a SHORT version (summarised to one page) for those students who are familiar with the machine and only require prompts for successful operation. The second part is a LONG version of the operation guide, detailing each step and explaining the responses expected from the equipment. This section is aimed at students using the equipment for the first time. The third part of the guide is a series of instructions to take photographs.

Guide to Using the CL at St Andrews
(SHORT version)

1. *Switch on plugs at Wall (Microscope, Luminoscope and Photo control)*
2. *Turn on Microscope Light*
   Turn on Power switch on luminoscope
3. *Pull out Chamber door on left of CL chamber*
4. *Load samples and push door closed.*
5. *Turn* ***OPERATE*** *switch to "2" and wait for vacuum*
6. *Turn* ***ADJUST kV*** *switch 1 full turn to the left*
7. *Turn* ***OPERATE*** *switch to "3"*
8. *Using* ***ADJUST kV,*** *allow current to settle down to 800 μA*

*9. Keep at optimum conditions with **VACUUM CONTROL** knob*

When one has finished...

*10. Turn **OPERATE** switch to "2", then to "1", chamber vents automatically*

More samples? Go to 3

11. Remove your samples and close chamber door

*12. Switch off **POWER** on luminoscope and plugs at wall*

Guide to Using the CL at St Andrews
(LONG version)

Starting Conditions

These starting conditions are assumed by the following sets of instructions. Some of them are evident when the machine is switched off but others will require the control box to be switched on before you can check.

On the Chamber --

* *CHAMBER DOOR pushed closed.*
* *TOP PLATE (including electron gun) in place.*

On the Luminoscope --

* ***OPERATE*** *switch set to "1".*
* *Green* ***POWER*** *switch off (points to the left).*
* *When* ***POWER*** *is on,* ***ENABLE*** *light on, all others in array are off.*

On the Microscope --

* *Sub-stage lighting off.*
* *Two very useful beer-mats to hand.*

Photographic Control unit --

* *Control knob turned to* ***AUTOMATIC*** *on dial on front.*

Operation

1. *Switch on all plugs at the wall (Microscope, luminoscope and photo control unit.*
2. *Turn rotating sub-stage lighting switch on the microscope anticlockwise to minimum setting.*

   Sub-stage lighting comes on
3. *Turn green power switch on luminoscope clockwise.*

Luminoscope display lights up

4. *Pull left-hand side of CL chamber (loading door).*

   Door slides out revealing samples on a moving carriage

5. *Using the x-y movement controls, move the sample carriage as far to the left as possible to allow loading of samples.*

6. *Load your samples onto the tray (you will look at the right-hand sample first).*

7. *Push chamber door securely closed.*

   Turn the ***VACUUM CONTROL*** *knob a full turn clockwise.*

8. *Turn* ***OPERATE*** *switch on luminoscope to "2".*

   Vacuum pump comes on
   Vacuum pump rhythm starts to change
   Vacuum gauge responds and starts to fall

9. *Wait for vacuum to go down to at least 0.1 Torr.*

Check: ***ENABLE*** *and* ***READY*** *lights are on, all others off.*

When Vacuum is good...

10. *Turn the* ***ADJUST kV*** *knob a full turn anticlockwise.*

    Turn the ***VACUUM CONTROL*** *knob a full turn clockwise.*

11. *Turn luminoscope* ***OPERATE*** *switch to "3".*

    kV ON *light comes on*
    kV gauge responds
    CATHODE CURRENT *(digital display) responds*

12. *If there is a 'click' and an alarm, the* ***kV ON*** *light goes off, the* ***kV TRIP*** *light is on and the kV gauge reads zero, then a safety circuit within the luminoscope has tripped. To restart:-*

    a). *Return* ***OPERATE*** *switch to "2"*
    b). *Turn* ***ADJUST kV*** *knob one full turn anticlockwise*
    c). *Turn* ***VACUUM CONTROL*** *knob one full turn anticlockwise*
    d). *Try again from 10.*

13. *Optimum conditions are 14 kV for feldspars, apatites, carbonates, sodalites and fluorites, 14kV+ for quartz. Don't be frightened to use lower kVs if what you want to see is luminescing, since this minimises damage to the slide.*

The Operation

- *You will probably find at first that you cannot achieve the required kV for a* ***CATHODE CURRENT*** *of 600 μA. The factor that determines which current is stable with which voltage is the state of the vacuum. The skill (!) of CL work is knowing how to juggle* ***ADJUST kV*** *and* ***VACUUM CONTROL*** *to provide the required conditions.*
- *At first as the vacuum slowly increases, the current will drop and so you must slowly increase the kV to compensate. You are now trying to keep the* ***CATHODE CURRENT*** *constant (digital display at 600). Eventually the kV will reach the required values. However, to keep it there, you must now adjust the* ***VACUUM CONTROL*** *knob to keep the* ***vacuum*** *constant. The* ***VACUUM CONTROL*** *knob allows a small amount of air to seep into the chamber, exactly compensating for the amount of air drawn out by the vacuum pump. THIS IS AN ART FORM! Sometimes tiny differences in the* ***VACUUM CONTROL*** *will significantly influence kV and cathode current.*
- *Turn the sub-stage lighting on. To change from PPL to CL views, insert the beer-mats over the sub-stage light source - this provides a simple way of switching between PPL and CL images. (If you set the sub-stage lighting too high then you'll blind yourself going between the images).*
- *Move the sample using the x and y adjusting screws on the end of the position control arm on the chamber. To take photographs, see the separate section on photography.*

When you have finished...

14. *Turn the* ***OPERATE*** *switch to "2".*

    kV ON *light goes out, CATHODE CURRENT goes to zero, kV goes to zero*

15. *Turn the* ***OPERATE*** *switch to "1".*

    Pump goes off, chamber vents automatically

MORE SAMPLES? Go to 4.

Shut Down Procedure

16. Open chamber and remove your samples.

17. Push chamber door securely closed.

18. Switch off ***POWER*** *switch on luminoscope and plugs at the wall.*

A Few Handy Tips

- *Run the CL at the lowest kV at which you are sure that the minerals you want to study are luminescing. Araldite mounting becomes unstable at around 12 kV and at very high kVs can actually luminesce yellow or orange.*
- *Keep the sample on the move as much as possible. This reduces the likelihood of losing the slide or burning the mount. Use fast films (e.g. ASA 1000) to reduce exposure times during photography and move the sample immediately after a photograph is taken.*
- *When working at hard vacuums, don't move the x-y position controls jerkily - this allows gulps of air into the chamber, which ruins the state of the vacuum.*
- *Sometimes when you're starting, the vacuum is very unstable. This is because of adsorbed moisture and gases on the inside of the chamber. Allow a few minutes without the electron beam to let the vacuum settle down.*
- *Occasionally when you start, there is little current for the kV being applied. This is because there are no ions in rarefied atmosphere in the chamber to conduct the current. In you increase the voltage too much; the current suddenly gives (a lighting strike!) and immediately trips the safety control in the luminoscope. If you are having trouble in getting a current to flow, then slowly crank up the voltage but be prepared to immediately wind it down again, once you feel it is about to pass current. With practice, you can stop it tripping the safety switch. Once a chamber has passed a current, there are usually enough ions in the chamber to stop this problem arising again.*
- *Remember - Don't hang about - be swift and efficient.*

Guide to Photography at St Andrews

- *Make sure that the photographic unit is connected to the camera, and that it is switched on.*
- *Find the view that you want to photograph in the normal binocular microscope.*
- *Pull the black handle on the right-hand side of the eye piece to the out position - the view in the binocular microscope darkens.*
- *Check that there is an image in the single eyepiece at the top of the column - check focus in this eyepiece!*
- *For AUTOMATIC exposures, click the photographic unit to* ***AUTO*** *and select the relevant film speed. The light-meter on the top of the column should register an exposure time (the red light is out).*
- *For MANUAL exposures, set the exposure time as required.*
- *Press the* ***EXPOSE*** *button on the photographic unit and the shutter opens (green light comes on)*
- *When you have finished, remove the film from the camera'.*

A4.2 Bulk EPMA feldspar data. Analyses are given in weight percent and were Mikson corrected using Geopro at the Danish lithosphere Centre, Copenhagen. Symbol * refers to dissolution zone. An, Ab and Or are expressed as molar percent.

1.) DLC 1A - AF0207: K-feldspar - Red Bay Quarry (RM1) (traverse 1a2-1a31) n=27

1a2	63.78	0.00	18.15	0.09	0.00	0.00	0.00	0.69	15.62	0.060	0.042	98.42	0.00	6.27	93.73	**3**
1a3	63.24	0.00	18.57	0.16	0.02	0.00	0.06	1.03	15.18	0.213	0.087	98.56	0.62	9.26	90.12	**3**
1a5	63.70	0.07	18.26	0.11	0.00	0.00	0.08	0.63	15.64	0.242	0.064	98.79	0.80	5.75	93.45	2
1a4	63.95	0.07	18.22	0.14	0.00	0.00	0.06	0.80	15.19	0.301	0.065	98.79	0.57	7.38	92.05	2
1a6	63.56	0.03	18.11	0.07	0.07	0.00	0.04	0.36	16.16	0.298	0.063	98.76	0.37	3.27	96.36	2
1a7	63.54	0.03	18.23	0.15	0.00	0.00	0.05	1.01	15.02	0.362	0.095	98.47	0.49	9.20	90.30	2
1a8	63.19	0.02	18.45	0.10	0.08	0.00	0.06	0.85	15.23	0.405	0.053	98.44	0.60	7.81	91.60	2
1a9	63.96	0.08	18.38	0.18	0.01	0.00	0.00	0.39	15.97	0.481	0.146	98.58	0.02	3.56	96.42	2
1a10	63.57	0.03	18.39	0.16	0.00	0.00	0.07	0.80	15.38	0.403	0.079	98.87	0.73	7.27	92.00	2
1a11	63.75	0.02	18.33	0.09	0.00	0.00	0.00	0.58	15.85	0.173	0.063	98.85	0.00	5.25	94.75	2
1a12	63.56	0.02	18.17	0.17	0.00	0.00	0.02	0.72	15.67	0.162	0.091	98.57	0.21	6.50	93.29	2
1a13	64.02	0.02	18.25	0.21	0.03	0.00	0.03	0.69	15.88	0.160	0.000	99.28	0.28	6.15	93.57	2
1a14	63.67	0.03	18.16	0.09	0.09	0.00	0.00	0.62	15.94	0.013	0.056	98.67	0.00	5.60	94.40	**1**
1a15	63.58	0.00	18.34	0.11	0.00	0.00	0.00	0.66	15.94	0.028	0.085	98.73	0.00	5.89	94.11	**1**
1a18	63.16	0.01	18.37	0.07	0.00	0.00	0.02	0.86	15.49	0.000	0.038	98.02	0.15	7.76	92.09	**1**
1a20	63.55	0.00	18.11	0.19	0.00	0.00	0.06	0.44	15.82	0.138	0.027	98.33	0.63	4.06	95.32	**1**
1a21	63.19	0.02	18.60	0.15	0.00	0.00	0.02	1.05	14.80	0.725	0.188	98.74	0.17	9.75	90.08	2
1a30	64.55	0.09	18.21	0.08	0.00	0.00	0.08	1.49	14.42	0.674	0.118	99.70	0.81	13.46	85.73	2
1a22	63.37	0.03	18.81	0.11	0.00	0.00	0.06	1.16	14.69	0.750	0.124	99.11	0.60	10.67	88.73	2
1a24	63.46	0.02	18.38	0.13	0.00	0.00	0.02	1.18	14.79	0.377	0.143	98.49	0.18	10.79	89.02	2
1a23	63.22	0.02	18.56	0.09	0.01	0.00	0.06	0.85	15.21	0.720	0.147	98.89	0.57	7.74	91.69	2
1a25	63.42	0.00	18.27	0.09	0.00	0.00	0.05	0.60	15.71	0.140	0.098	98.37	0.50	5.42	94.08	**3**
1a26	63.68	0.00	18.35	0.12	0.00	0.00	0.02	0.76	15.34	0.067	0.160	98.48	0.17	6.95	92.88	**3**
1a27	63.51	0.00	18.35	0.09	0.00	0.00	0.03	0.79	15.54	0.075	0.056	98.45	0.34	7.15	92.51	**3**
1a28	63.42	0.01	18.18	0.04	0.00	0.00	0.00	0.59	15.98	0.051	0.011	98.28	0.00	5.32	94.68	**3**
1a29	64.27	0.00	18.25	0.05	0.03	0.00	0.00	0.57	16.11	0.092	0.058	99.43	0.01	5.09	94.90	**3**
1a31	64.62	0.00	18.15	0.12	0.00	0.00	0.00	0.69	15.66	0.038	0.077	99.35	0.00	6.26	93.74	**3**

Point	**SiO_2**	**TiO_2**	**Al_2O_3**	**FeO**	**MnO**	**MgO**	**CaO**	**Na_2O**	**K_2O**	**BaO**	**SrO**	**TOTAL**	**An**	**Ab**	**Or**	**Zone**
1.) DLC 1D - AF0207: K-feldspar - Red Bay Quarry (RM1) (traverse 1a143-1a206) n=64																
1a143	65.53	0.00	18.46	0.11	0.02	0.02	0.04	0.97	15.18	0.057	0.051	100.44	0.39	8.77	90.83	**3**
1a144	65.61	0.00	18.33	0.09	0.04	0.00	0.03	0.91	15.28	0.060	0.020	100.36	0.29	8.27	91.44	**3**
1a145	64.78	0.00	18.54	0.03	0.04	0.00	0.05	0.86	15.19	0.062	0.008	99.57	0.53	7.88	91.59	**3**
1a146	65.38	0.00	18.42	0.09	0.00	0.00	0.04	0.98	15.07	0.010	0.004	100.00	0.40	8.99	90.60	**3**
1a147	65.69	0.01	18.51	0.18	0.00	0.00	0.01	0.89	15.32	0.073	0.004	100.69	0.14	8.11	91.75	**3**
1a148	64.26	0.00	18.60	0.14	0.00	0.00	0.01	0.70	15.70	0.086	0.078	99.56	0.07	6.31	93.62	**3**
1a149	65.18	0.02	18.59	0.05	0.00	0.00	0.05	1.10	15.05	0.083	0.082	100.19	0.46	9.94	89.60	**3**
1a150	65.18	0.00	18.36	0.18	0.23	0.00	0.05	1.00	15.10	0.077	0.053	100.22	0.53	9.06	90.41	**3**
1a151	65.39	0.01	18.40	0.12	0.01	0.00	0.04	1.07	15.08	0.112	0.037	100.26	0.41	9.70	89.89	**3**
1a152	65.62	0.05	18.08	0.20	0.01	0.00	0.03	0.68	15.70	0.114	0.041	100.53	0.29	6.19	93.52	**3**
1a153	64.95	0.00	18.80	0.03	0.00	0.00	0.07	0.93	15.12	0.130	0.027	100.05	0.66	8.52	90.82	**3**
1a154	65.10	0.03	18.20	0.00	0.02	0.00	0.06	0.84	15.39	0.101	0.087	99.83	0.58	7.62	91.80	2
1a155	65.35	0.04	18.47	0.12	0.02	0.00	0.04	0.96	15.41	0.115	0.122	100.64	0.36	8.62	91.02	2
1a156	65.42	0.03	18.43	0.08	0.00	0.00	0.03	0.66	15.68	0.180	0.115	100.62	0.31	5.99	93.69	2
1a157	65.10	0.00	18.16	0.04	0.00	0.00	0.04	0.38	16.01	0.281	0.102	100.11	0.39	3.47	96.14	2
1a158	65.30	0.01	18.67	0.11	0.00	0.00	0.03	1.00	15.28	0.122	0.070	100.58	0.31	8.98	90.71	2
1a159	65.30	0.06	18.43	0.11	0.07	0.00	0.02	0.69	15.54	0.182	0.125	100.52	0.17	6.28	93.55	2
1a160	64.59	0.02	18.45	0.14	0.00	0.00	0.00	0.66	15.58	0.258	0.095	99.79	0.02	6.06	93.92	2
1a161	63.71	0.00	18.53	0.14	0.00	0.00	0.02	0.41	15.97	0.107	0.074	98.96	0.18	3.70	96.11	2
1a162	64.48	0.02	18.49	0.06	0.00	0.00	0.02	0.64	15.81	0.008	0.044	99.56	0.20	5.79	94.01	2
1a163	64.79	0.03	18.54	0.04	0.00	0.01	0.00	0.60	15.63	0.238	0.048	99.92	0.00	5.52	94.48	**1**
1a164	64.50	0.02	18.44	0.06	0.00	0.00	0.00	0.66	15.68	0.065	0.073	99.50	0.04	6.04	93.92	**1**
1a165	64.32	0.03	18.43	0.05	0.10	0.00	0.02	0.47	15.99	0.098	0.025	99.52	0.15	4.24	95.61	**1**
1a166	65.39	0.00	18.25	0.06	0.04	0.00	0.03	0.80	15.24	0.000	0.060	99.88	0.32	7.37	92.31	**1**
1a167	65.50	0.03	18.35	0.20	0.00	0.00	0.05	0.93	15.25	0.033	0.008	100.35	0.51	8.45	91.03	**1**
1a168	64.82	0.00	18.59	0.07	0.07	0.00	0.00	1.00	15.05	0.052	0.058	99.71	0.04	9.14	90.82	**1**
1a169	65.20	0.01	18.70	0.09	0.03	0.00	0.04	0.93	15.36	0.127	0.056	100.54	0.38	8.38	91.24	**1**
1a170	65.15	0.00	18.54	0.07	0.01	0.00	0.00	0.89	15.61	0.048	0.067	100.40	0.00	7.98	92.02	**1**
1a171	65.03	0.00	18.50	0.14	0.00	0.00	0.02	0.93	15.51	0.000	0.062	100.20	0.20	8.33	91.47	**1**
1a172	64.59	0.02	18.47	0.03	0.08	0.00	0.00	0.91	15.40	0.036	0.057	99.58	0.00	8.22	91.78	**1**
1a173	65.61	0.00	18.42	0.01	0.05	0.00	0.00	0.39	16.10	0.145	0.021	100.75	0.00	3.55	96.45	**1**
1a174	65.10	0.02	18.68	0.19	0.07	0.00	0.01	0.89	15.49	0.000	0.021	100.47	0.08	8.04	91.88	**1**
1a175	64.48	0.00	18.56	0.07	0.00	0.00	0.01	0.80	15.37	0.067	0.095	99.45	0.12	7.31	92.56	**1**
1a176	65.09	0.00	18.44	0.12	0.00	0.00	0.00	0.64	15.83	0.122	0.052	100.30	0.00	5.75	94.25	**1**
1a177	65.29	0.00	18.49	0.09	0.04	0.00	0.01	0.94	15.44	0.057	0.048	100.40	0.05	8.50	91.45	***1**
1a178	65.54	0.00	18.17	0.15	0.00	0.00	0.01	0.72	15.74	0.000	0.038	100.36	0.07	6.50	93.43	***1**
1a179	65.17	0.00	18.39	0.02	0.00	0.00	0.02	1.15	15.29	0.000	0.044	100.08	0.17	10.23	89.61	***1**
1a180	65.48	0.00	18.40	0.09	0.00	0.00	0.07	0.95	15.25	0.038	0.060	100.34	0.73	8.62	90.65	***1**
1a181	65.36	0.00	18.73	0.10	0.00	0.00	0.06	1.19	14.84	0.047	0.069	100.40	0.55	10.79	88.66	***1**
1a182	65.84	0.02	18.57	0.05	0.00	0.00	0.01	0.66	14.93	0.032	0.071	100.19	0.11	6.28	93.61	***1**
1a183	64.90	0.00	18.21	0.11	0.02	0.00	0.00	0.39	15.82	0.107	0.038	99.59	0.00	3.60	96.40	***1**
1a184	65.78	0.01	18.46	0.07	0.02	0.00	0.03	1.10	15.12	0.059	0.020	100.67	0.30	9.94	89.76	***1**

Point	SiO_2	TiO_2	Al_2O_3	FeO	MnO	MgO	CaO	Na_2O	K_2O	BaO	SrO	TOTAL	An	Ab	Or	Zone
1.) DLC 1D - AF0207: K-feldspar - Red Bay Quarry (RM1) (traverse 1a143-1a206) n=64																
1a185	65.36	0.01	18.55	0.14	0.08	0.00	0.00	0.66	15.60	0.031	0.033	100.46	0.00	6.02	93.98	***1**
1a186	65.74	0.03	18.61	0.09	0.00	0.00	0.02	0.68	15.88	0.014	0.043	101.10	0.19	6.06	93.75	**1**
1a187	64.40	0.04	17.91	0.16	0.00	0.00	0.02	0.46	16.02	0.063	0.075	99.15	0.19	4.20	95.61	**1**
1a188	65.56	0.00	18.19	0.02	0.00	0.00	0.05	0.77	15.57	0.029	0.067	100.25	0.51	6.92	92.57	**1**
1a189	65.10	0.00	18.56	0.09	0.01	0.00	0.04	0.56	15.74	0.039	0.019	100.16	0.40	5.09	94.50	**1**
1a190	65.01	0.00	18.36	0.14	0.00	0.00	0.00	0.58	15.79	0.060	0.032	99.97	0.00	5.28	94.72	**1**
1a191	65.20	0.00	18.23	0.14	0.06	0.00	0.00	0.97	15.31	0.035	0.079	100.03	0.00	8.81	91.19	2
1a192	65.79	0.02	18.50	0.16	0.00	0.00	0.06	1.04	14.93	0.093	0.038	100.62	0.57	9.50	89.93	2
1a193	66.00	0.05	18.67	0.06	0.03	0.00	0.03	0.92	15.05	0.136	0.016	100.95	0.26	8.47	91.26	2
1a194	64.88	0.00	18.81	0.04	0.01	0.00	0.10	1.16	14.85	0.316	0.110	100.28	1.04	10.48	88.48	2
1a195	65.83	0.04	18.30	0.18	0.07	0.00	0.03	0.93	15.00	0.190	0.000	100.63	0.29	8.59	91.13	2
1a196	65.30	0.01	18.75	0.17	0.05	0.00	0.08	1.10	15.28	0.209	0.000	101.04	0.76	9.76	89.48	2
1a197	65.42	0.02	18.54	0.10	0.00	0.00	0.11	1.17	14.99	0.171	0.000	100.63	1.05	10.53	88.42	2
1a198	63.84	0.02	18.82	0.00	0.01	0.00	0.06	1.03	14.78	0.133	0.000	98.73	0.64	9.49	89.86	2
1a199	65.86	0.00	18.54	0.20	0.00	0.00	0.06	1.32	14.62	0.107	0.000	100.77	0.58	11.97	87.45	**3**
1a200	65.35	0.00	18.13	0.07	0.00	0.02	0.08	1.12	14.68	0.141	0.018	99.67	0.78	10.34	88.87	**3**
1a201	65.87	0.00	18.32	0.07	0.02	0.00	0.06	1.39	14.89	0.084	0.000	100.77	0.59	12.34	87.07	**3**
1a202	65.60	0.05	18.07	0.08	0.09	0.00	0.05	1.11	15.07	0.142	0.000	100.32	0.51	9.98	89.51	**3**
1a203	65.66	0.02	18.33	0.08	0.01	0.00	0.08	0.75	15.32	0.069	0.000	100.39	0.83	6.86	92.31	**3**
1a204	65.58	0.00	18.04	0.14	0.00	0.00	0.05	1.27	14.84	0.056	0.002	100.07	0.46	11.45	88.10	**3**
1a205	65.07	0.01	18.17	0.16	0.00	0.01	0.02	0.66	15.74	0.140	0.007	100.02	0.17	5.95	93.88	**3**
1a206	65.54	0.02	18.62	0.08	0.01	0.00	0.07	0.90	15.16	0.021	0.000	100.45	0.71	8.21	91.09	**3**

Point	SiO_2	TiO_2	Al_2O_3	FeO	MnO	MgO	CaO	Na_2O	K_2O	BaO	SrO	TOTAL	An	Ab	Or	Zone
2.) DLC 3A - AF/02/01: K-feldspar - Torr na h'Annaid, Bendoran (RM1a) (traverse 1a529-1a601) n=61																
1a529	63.18	0.04	18.45	0.14	0.01	0.00	0.01	1.17	15.03	0.131	0.028	98.20	0.1	10.6	89.3	**7**
1a530	64.01	0.04	18.46	0.03	0.03	0.00	0.03	1.30	14.61	0.179	0.000	98.69	0.3	11.8	87.8	**7**
1a531	64.36	0.00	18.56	0.05	0.02	0.00	0.01	1.18	14.84	0.052	0.021	99.10	0.1	10.8	89.1	**7**
1a533	63.89	0.00	18.02	0.06	0.03	0.00	0.00	0.84	15.25	0.101	0.064	98.26	0.0	7.7	92.3	**7**
1a534	64.26	0.00	18.41	0.00	0.00	0.00	0.00	0.97	15.21	0.104	0.038	98.99	0.0	8.8	91.2	**7**
1a535	63.88	0.03	18.30	0.10	0.00	0.00	0.01	0.90	15.24	0.090	0.012	98.56	0.1	8.3	91.7	**7**
1a536	64.46	0.02	18.25	0.00	0.06	0.00	0.01	0.98	15.16	0.069	0.034	99.05	0.1	8.9	90.9	**7**
1a537	62.06	0.00	18.07	0.04	0.00	0.01	0.10	0.56	15.64	0.163	0.000	96.64	1.0	5.1	93.9	**7**
1a538	63.91	0.00	18.04	0.00	0.00	0.00	0.00	1.03	15.04	0.323	0.076	98.42	0.0	9.4	90.6	**5**
1a539	63.53	0.05	18.11	0.00	0.00	0.00	0.01	1.50	14.17	0.609	0.108	98.08	0.1	13.8	86.1	**5**
1a540	63.88	0.02	18.01	0.00	0.03	0.00	0.00	1.13	15.07	0.403	0.058	98.61	0.0	10.2	89.8	**5**
1a540	63.92	0.00	17.90	0.05	0.00	0.00	0.00	1.03	15.12	0.428	0.042	98.49	0.0	9.4	90.6	**5**
1a541	63.82	0.06	18.23	0.00	0.00	0.00	0.00	1.27	14.79	0.475	0.094	98.75	0.0	11.5	88.5	**5**
1a542	63.30	0.02	18.06	0.00	0.00	0.00	0.02	0.23	15.81	0.872	0.046	98.36	0.2	2.2	97.6	**5**
1a547	63.75	0.02	18.13	0.12	0.00	0.03	0.00	0.62	15.53	0.403	0.042	98.65	0.0	5.7	94.3	**5**
1a548	64.13	0.03	18.15	0.00	0.02	0.00	0.00	0.70	15.43	0.288	0.079	98.82	0.0	6.4	93.6	**5**
1a549	63.43	0.03	17.98	0.04	0.00	0.00	0.00	0.26	16.00	0.533	0.033	98.31	0.0	2.4	97.6	**5**
1a550	63.97	0.00	18.27	0.00	0.00	0.00	0.01	1.09	15.09	0.257	0.105	98.80	0.1	9.9	90.0	**5**
1a551	64.11	0.01	18.31	0.00	0.00	0.00	0.00	1.03	14.96	0.323	0.056	98.80	0.0	9.5	90.5	**5**
1a552	64.41	0.00	18.22	0.01	0.00	0.00	0.00	1.64	13.98	0.256	0.080	98.60	0.0	15.1	84.9	**5**
1a553	64.34	0.04	18.69	0.02	0.00	0.00	0.00	1.05	14.78	0.249	0.032	99.20	0.0	9.7	90.3	**5**
1a554	63.98	0.00	18.25	0.00	0.00	0.00	0.00	1.18	14.93	0.338	0.034	98.72	0.0	10.7	89.3	**5**
1a555	64.10	0.06	18.51	0.02	0.03	0.00	0.00	0.96	14.79	0.735	0.149	99.36	0.0	9.0	91.0	**5**
1a556	64.36	0.00	18.31	0.00	0.00	0.03	0.00	1.20	14.82	0.432	0.082	99.23	0.0	11.0	89.0	**5**
1a558	64.31	0.01	18.04	0.03	0.00	0.00	0.00	1.56	13.92	0.574	0.113	98.57	0.0	14.5	85.5	4
1a557	64.52	0.04	18.47	0.00	0.00	0.00	0.01	1.28	14.43	0.790	0.115	99.65	0.1	11.9	88.1	4
1a560	63.35	0.05	18.69	0.00	0.00	0.01	0.02	1.31	14.25	0.863	0.072	98.62	0.2	12.2	87.6	4
1a561	64.25	0.01	18.46	0.08	0.01	0.00	0.00	1.41	14.08	0.826	0.104	99.23	0.0	13.2	86.8	**3**
1a562	64.00	0.05	18.55	0.00	0.02	0.00	0.01	1.54	13.98	0.880	0.091	99.12	0.1	14.3	85.6	**3**
1a563	63.68	0.06	18.33	0.03	0.01	0.00	0.03	1.48	13.92	1.008	0.111	98.67	0.3	13.9	85.8	**3**
1a564	64.05	0.07	18.30	0.00	0.00	0.00	0.02	1.50	14.11	1.001	0.097	99.15	0.2	13.9	85.9	**3**
1a565	64.05	0.03	18.42	0.00	0.07	0.00	0.03	1.50	14.02	0.946	0.084	99.15	0.3	13.9	85.7	**3**
1a567	64.17	0.08	18.26	0.00	0.00	0.00	0.03	1.17	14.56	0.718	0.057	99.04	0.3	10.9	88.9	**3**
1a571	63.96	0.01	18.06	0.00	0.01	0.01	0.00	1.59	13.95	0.668	0.069	98.33	0.0	14.8	85.2	**3**
1a568	64.20	0.05	18.47	0.08	0.00	0.01	0.00	0.87	14.94	0.678	0.051	99.36	0.0	8.2	91.8	**3**
1a572	64.15	0.00	18.21	0.00	0.01	0.00	0.00	1.00	14.51	0.714	0.125	98.72	0.0	9.5	90.5	**3**
1a573	63.70	0.00	17.94	0.13	0.05	0.00	0.00	0.89	14.67	0.698	0.081	98.15	0.0	8.4	91.6	**3**
1a569	64.29	0.03	18.72	0.01	0.03	0.00	0.04	1.79	13.79	0.690	0.094	99.48	0.4	16.4	83.2	**3**
1a576	64.32	0.08	18.55	0.02	0.01	0.00	0.02	1.45	14.08	0.942	0.071	99.54	0.2	13.5	86.3	2
1a577	63.97	0.04	18.76	0.00	0.00	0.00	0.01	1.82	13.35	0.996	0.072	99.02	0.1	17.1	82.7	2
1a578	63.67	0.04	18.63	0.00	0.00	0.00	0.01	1.96	13.45	1.089	0.038	98.89	0.1	18.1	81.8	2
1a579	63.85	0.06	18.44	0.07	0.00	0.01	0.04	1.57	13.75	0.990	0.131	98.91	0.4	14.7	84.9	2
1a580	64.22	0.06	18.63	0.00	0.12	0.00	0.00	1.27	14.56	0.733	0.053	99.64	0.0	11.7	88.3	2
1a575	64.35	0.00	18.44	0.00	0.00	0.00	0.00	1.12	14.87	0.282	0.094	99.15	0.0	10.3	89.7	2
1a583	65.31	0.03	18.42	0.16	0.06	0.00	0.00	4.96	9.23	0.136	0.036	98.33	0.0	44.9	55.1	**1**
1a585	64.11	0.00	18.06	0.00	0.00	0.00	0.02	1.24	14.72	0.337	0.060	98.55	0.2	11.3	88.4	**1**
1a586	64.28	0.01	18.03	0.00	0.00	0.00	0.04	1.27	14.45	0.338	0.045	98.46	0.4	11.7	87.8	**1**
1a587	64.47	0.00	18.31	0.07	0.05	0.00	0.00	0.80	15.08	0.354	0.074	99.21	0.0	7.5	92.5	**1**
1a588	64.37	0.02	18.31	0.08	0.00	0.00	0.02	0.74	15.42	0.291	0.048	99.31	0.2	6.8	93.0	**1**
1a589	64.55	0.00	18.32	0.04	0.00	0.00	0.01	0.62	15.52	0.266	0.072	99.40	0.1	5.8	94.2	**1**

Point	SiO_2	TiO_2	Al_2O_3	FeO	MnO	MgO	CaO	Na_2O	K_2O	BaO	SrO	TOTAL	An	Ab	Or	Zone
2.) DLC 3A - AF/02/01: K-feldspar - Torr na h'Annaid, Bendoran (RM1a) (traverse 1a529-1a601) n=61																
1a590	63.83	0.04	18.32	0.00	0.00	0.00	0.00	0.38	15.97	0.333	0.070	98.95	0.0	3.5	96.5	**1**
1a591	65.62	0.02	18.59	0.03	0.02	0.00	0.01	3.66	11.24	0.269	0.078	99.53	0.1	33.1	66.8	**1**
1a592	64.41	0.05	17.99	0.03	0.02	0.00	0.00	0.65	15.29	0.268	0.004	98.71	0.0	6.1	93.9	**1**
1a593	64.50	0.00	18.26	0.00	0.00	0.00	0.00	0.86	14.99	0.355	0.045	99.01	0.0	8.0	92.0	**1**
1a594	64.07	0.05	18.46	0.03	0.00	0.00	0.00	1.17	14.42	0.537	0.034	98.77	0.0	11.0	89.0	**1**
1a595	63.03	0.03	18.42	0.00	0.00	0.00	0.00	0.50	15.47	0.705	0.038	98.19	0.0	4.6	95.4	**1**
1a596	64.43	0.00	18.28	0.01	0.07	0.00	0.00	1.12	14.69	0.221	0.062	98.89	0.0	10.4	89.6	**1**
1a597	64.07	0.02	18.34	0.00	0.00	0.00	0.01	0.95	14.72	0.716	0.200	99.03	0.1	8.9	91.0	**1**
1a599	63.88	0.00	18.36	0.02	0.00	0.00	0.00	1.23	14.84	0.505	0.022	98.85	0.0	11.2	88.8	**1**
1a600	63.69	0.06	18.49	0.00	0.00	0.00	0.00	1.25	14.61	0.529	0.023	98.65	0.0	11.5	88.5	**1**
1a601	64.43	0.00	18.48	0.00	0.06	0.00	0.01	1.26	14.59	0.557	0.032	99.41	0.1	11.6	88.3	**1**

Point	SiO_2	TiO_2	Al_2O_3	FeO	MnO	MgO	CaO	Na_2O	K_2O	BaO	SrO	TOTAL	An	Ab	Or	Zone
3.) DLC 7A - RR0120: K-feldspar (from RM2 juxtaposed to diorite) (traverse 1a73-1a138) n=59																
1a73	64.21	0.02	18.26	0.09	0.03	0.00	0.06	1.00	14.97	0.195	0.109	98.94	0.61	9.20	90.20	4
1a74	63.86	0.00	18.31	0.03	0.03	0.01	0.04	1.03	15.00	0.215	0.112	98.63	0.37	9.44	90.18	4
1a75	64.03	0.02	18.48	0.06	0.00	0.00	0.09	1.02	15.24	0.256	0.067	99.25	0.87	9.13	90.00	4
1a76	64.30	0.01	18.17	0.01	0.00	0.00	0.05	1.08	14.80	0.291	0.079	98.78	0.50	9.90	89.60	4
1a77	63.85	0.00	18.36	0.06	0.01	0.00	0.07	1.41	14.50	0.374	0.111	98.75	0.70	12.79	86.51	4
1a79	63.27	0.02	18.40	0.05	0.00	0.00	0.09	1.07	14.65	0.446	0.120	98.13	0.96	9.91	89.13	4
1a81	63.86	0.02	18.35	0.09	0.00	0.00	0.17	1.16	14.72	0.603	0.161	99.14	1.70	10.55	87.75	4
1a82	64.13	0.00	18.58	0.05	0.00	0.00	0.11	2.23	12.97	0.706	0.154	98.93	1.07	20.52	78.42	4
1a83	63.47	0.00	18.50	0.04	0.00	0.00	0.05	0.92	14.93	0.852	0.072	98.82	0.49	8.49	91.02	4
1a84	64.27	0.03	18.40	0.03	0.00	0.00	0.09	1.44	14.52	0.594	0.126	99.49	0.90	12.98	86.13	4
1a85	64.02	0.00	18.26	0.00	0.00	0.00	0.10	1.66	13.68	0.585	0.091	98.39	0.99	15.41	83.61	**3**
1a86	63.60	0.00	18.20	0.06	0.04	0.01	0.05	0.81	15.30	0.692	0.138	98.90	0.55	7.42	92.03	**3**
1a87	63.47	0.01	18.25	0.10	0.10	0.00	0.11	0.91	14.92	0.791	0.128	98.78	1.08	8.41	90.51	**3**
1a88	63.13	0.00	18.28	0.07	0.01	0.00	0.06	0.61	15.25	0.883	0.155	98.45	0.60	5.70	93.70	**3**
1a89	63.57	0.04	18.30	0.03	0.00	0.00	0.04	0.69	15.24	0.897	0.081	98.87	0.39	6.40	93.21	**3**
1a90	63.18	0.04	18.65	0.12	0.00	0.00	0.06	0.97	14.49	0.985	0.153	98.64	0.65	9.16	90.19	**3**
1a91	63.59	0.07	18.12	0.09	0.01	0.00	0.02	0.68	15.18	1.240	0.053	99.05	0.19	6.39	93.43	**3**
1a92	63.26	0.02	18.46	0.03	0.00	0.00	0.04	0.93	14.87	0.893	0.116	98.60	0.38	8.61	91.01	**3**
1a93	63.58	0.07	18.57	0.08	0.04	0.00	0.15	1.02	14.45	0.893	0.196	99.04	1.50	9.57	88.93	**3**
1a94	63.87	0.00	18.47	0.06	0.04	0.00	0.11	1.05	14.95	0.915	0.221	99.68	1.07	9.51	89.42	**3**
1a95	64.62	0.03	18.21	0.17	0.00	0.00	0.00	0.95	15.22	0.314	0.095	99.60	0.00	8.65	91.35	2
1a96	64.48	0.03	17.94	0.14	0.05	0.00	0.04	1.06	15.05	0.233	0.076	99.09	0.36	9.60	90.04	2
1a97	64.45	0.00	18.38	0.06	0.00	0.00	0.04	1.00	15.21	0.141	0.077	99.35	0.36	9.01	90.63	2
1a98	64.44	0.03	18.29	0.06	0.00	0.00	0.06	0.69	15.51	0.165	0.119	99.37	0.58	6.26	93.15	2
1a100	64.31	0.00	17.96	0.16	0.00	0.01	0.06	1.04	14.97	0.166	0.153	98.83	0.64	9.52	89.85	2
1a101	63.98	0.03	18.27	0.12	0.00	0.00	0.01	0.87	15.09	0.214	0.090	98.68	0.12	8.05	91.82	2
1a102	64.90	0.03	18.04	0.03	0.00	0.00	0.00	1.12	14.72	0.498	0.032	99.37	0.00	10.32	89.68	2
1a103	64.43	0.01	18.26	0.06	0.00	0.00	0.01	0.96	15.21	0.403	0.143	99.50	0.11	8.76	91.13	2
1a104	64.05	0.03	18.02	0.07	0.00	0.00	0.01	0.78	15.05	0.427	0.117	98.55	0.13	7.25	92.62	**1**
1a105	64.00	0.02	18.50	0.00	0.00	0.00	0.03	1.04	14.59	0.453	0.180	98.80	0.27	9.73	90.00	**1**
1a106	64.62	0.00	17.93	0.09	0.00	0.00	0.03	0.87	15.33	0.129	0.101	99.10	0.27	7.94	91.78	**1**
1a107	64.80	0.04	18.08	0.05	0.00	0.00	0.01	0.95	15.17	0.123	0.136	99.36	0.11	8.69	91.20	**1**
1a108	63.88	0.02	17.97	0.11	0.00	0.00	0.00	0.79	15.58	0.174	0.096	98.63	0.00	7.18	92.82	**1**
1a110	64.63	0.02	18.00	0.09	0.01	0.00	0.01	0.71	15.45	0.110	0.045	99.06	0.07	6.53	93.40	**1**
1a113	64.83	0.00	17.96	0.08	0.02	0.00	0.01	0.94	15.32	0.100	0.051	99.31	0.05	8.53	91.42	**1**
1a114	64.50	0.00	18.04	0.02	0.03	0.00	0.02	0.74	15.41	0.089	0.100	98.94	0.23	6.75	93.01	**1**
1a115	63.77	0.02	18.09	0.04	0.00	0.00	0.01	0.95	14.77	0.362	0.102	98.12	0.10	8.89	91.01	**1**
1a116	64.00	0.00	18.06	0.04	0.00	0.00	0.00	0.82	15.24	0.164	0.114	98.44	0.02	7.58	92.40	**1**
1a117	64.31	0.03	18.19	0.17	0.00	0.00	0.01	0.93	15.08	0.114	0.104	98.94	0.10	8.58	91.31	**1**
1a118	65.05	0.02	18.03	0.18	0.04	0.00	0.02	0.98	14.93	0.103	0.164	99.51	0.17	9.07	90.75	**1**
1a119	64.91	0.00	17.96	0.15	0.00	0.00	0.00	0.92	15.57	0.067	0.055	99.64	0.04	8.24	91.72	**1**
1a120	64.56	0.02	18.06	0.06	0.08	0.00	0.00	0.87	15.47	0.154	0.032	99.30	0.00	7.85	92.15	**1**
1a121	64.83	0.02	18.17	0.10	0.00	0.00	0.00	0.67	15.53	0.107	0.035	99.47	0.00	6.16	93.84	**1**
1a122	64.77	0.00	17.79	0.07	0.00	0.00	0.02	0.90	15.59	0.103	0.122	99.37	0.24	8.05	91.71	**1**
1a123	64.72	0.00	17.65	0.04	0.00	0.00	0.00	0.86	15.46	0.191	0.049	98.96	0.00	7.76	92.24	*
1a124	64.58	0.02	18.14	0.09	0.07	0.00	0.05	1.07	15.26	0.206	0.101	99.58	0.47	9.58	89.96	*
1a125	64.58	0.03	18.40	0.12	0.03	0.00	0.00	0.87	15.26	0.201	0.059	99.55	0.00	7.95	92.05	*
1a126	64.76	0.00	17.85	0.06	0.00	0.00	0.04	1.00	14.98	0.140	0.089	98.91	0.43	9.13	90.44	*
1a127	64.75	0.01	17.83	0.17	0.00	0.00	0.03	0.83	15.23	0.030	0.120	98.99	0.25	7.60	92.14	*
1a129	64.60	0.00	17.91	0.13	0.11	0.01	0.04	0.81	15.24	0.024	0.060	98.93	0.37	7.48	92.15	*
1a130	64.49	0.00	17.95	0.07	0.07	0.01	0.01	0.65	15.42	0.076	0.041	98.79	0.09	6.05	93.86	*
1a131	64.39	0.00	18.25	0.06	0.00	0.00	0.05	1.11	15.00	0.090	0.128	99.07	0.45	10.07	89.47	*
1a132	64.69	0.00	18.02	0.12	0.01	0.00	0.05	1.07	15.10	0.062	0.133	99.26	0.47	9.71	89.82	*
1a133	64.75	0.00	18.32	0.12	0.00	0.00	0.06	0.87	15.26	0.098	0.123	99.59	0.55	7.92	91.52	*
1a134	64.27	0.03	18.06	0.07	0.00	0.00	0.04	0.95	15.12	0.093	0.066	98.70	0.39	8.69	90.92	4
1a135	64.54	0.03	17.81	0.06	0.02	0.00	0.02	0.80	15.46	0.136	0.086	98.95	0.21	7.24	92.54	4
1a136	64.32	0.00	17.68	0.05	0.00	0.00	0.03	0.69	15.52	0.058	0.105	98.46	0.27	6.32	93.41	4
1a137	64.16	0.00	18.35	0.06	0.00	0.00	0.04	0.90	15.28	0.110	0.110	99.00	0.39	8.18	91.43	4
1a138	64.13	0.02	17.56	0.13	0.00	0.00	0.04	0.85	15.28	0.189	0.034	98.22	0.42	7.73	91.85	4

Point	SiO_2	TiO_2	Al_2O_3	FeO	MnO	MgO	CaO	Na_2O	K_2O	BaO	SrO	TOTAL	An	Ab	Or	Zone
4.) DLC 10-11B - RR0119: Feldspar micro-pheno. (Phase one double MME) (traverse 1a602-1a630) n=24																
1a602	62.80	0.02	23.08	0.17	0.00	0.00	4.39	8.87	0.21	0.056	0.309	99.90	35.0	64.0	1.0	**3**
1a603	62.33	0.01	22.76	0.17	0.00	0.00	4.49	8.70	0.34	0.073	0.296	99.17	35.8	62.6	1.6	**3**
1a604	63.38	0.02	22.45	0.19	0.00	0.00	3.88	9.18	0.37	0.054	0.284	99.80	31.3	67.0	1.8	**3**
1a605	63.33	0.04	22.39	0.20	0.01	0.00	3.81	9.38	0.26	0.111	0.285	99.81	30.6	68.2	1.2	**3**
1a606	63.37	0.01	22.33	0.09	0.07	0.01	3.80	9.25	0.22	0.070	0.268	99.48	30.9	68.1	1.1	**3**
1a607	62.12	0.03	23.07	0.11	0.03	0.02	4.64	8.93	0.20	0.070	0.262	99.48	36.2	62.9	0.9	2
1a611	63.07	0.00	22.17	0.10	0.00	0.00	3.87	9.24	0.19	0.033	0.240	98.90	31.3	67.8	0.9	2
1a614	62.61	0.06	23.21	0.12	0.09	0.00	4.64	8.81	0.13	0.054	0.293	100.01	36.6	62.8	0.6	**1**
1a615	62.92	0.01	22.81	0.16	0.01	0.00	4.44	8.91	0.15	0.011	0.266	99.69	35.3	64.0	0.7	**1**
1a616	62.39	0.00	23.09	0.13	0.00	0.01	4.68	8.90	0.12	0.030	0.223	99.57	36.6	62.9	0.6	**1**
1a617	62.13	0.00	23.36	0.15	0.07	0.01	4.69	8.66	0.27	0.056	0.287	99.68	37.0	61.7	1.3	**1**
1a618	62.46	0.01	22.95	0.15	0.00	0.00	4.57	8.74	0.31	0.068	0.272	99.53	36.1	62.4	1.5	**1**
1a619	63.23	0.00	22.12	0.20	0.00	0.00	3.57	9.25	0.43	0.046	0.285	99.13	29.2	68.7	2.1	**1**
1a620	62.57	0.03	22.56	0.08	0.00	0.00	4.40	8.79	0.27	0.029	0.298	99.02	35.2	63.6	1.3	**1**
1a621	62.14	0.00	23.11	0.07	0.06	0.00	4.69	8.92	0.17	0.000	0.308	99.45	36.5	62.8	0.8	**1**
1a622	61.85	0.03	22.78	0.10	0.00	0.00	4.84	8.76	0.20	0.073	0.249	98.88	37.6	61.5	0.9	**1**
1a623	63.04	0.00	22.18	0.14	0.00	0.00	3.78	9.23	0.25	0.043	0.300	98.95	30.8	68.0	1.2	**1**
1a624	62.07	0.00	23.20	0.19	0.00	0.00	4.77	8.76	0.22	0.043	0.274	99.52	37.2	61.8	1.0	**1**
1a625	61.04	0.03	23.85	0.19	0.05	0.01	5.42	8.44	0.16	0.028	0.280	99.48	41.2	58.1	0.7	**1**
1a626	61.32	0.02	23.11	0.17	0.00	0.02	5.05	8.51	0.25	0.059	0.283	98.78	39.2	59.7	1.1	2
1a627	60.83	0.00	24.16	0.09	0.04	0.00	5.71	8.15	0.23	0.080	0.298	99.57	43.2	55.8	1.0	2
1a628	60.32	0.03	24.69	0.18	0.00	0.00	6.49	7.94	0.11	0.014	0.264	100.02	47.2	52.3	0.5	2
1a629	62.45	0.01	22.93	0.13	0.01	0.03	4.38	8.95	0.23	0.066	0.254	99.44	34.7	64.2	1.1	**3**
1a630	62.82	0.06	22.89	0.11	0.00	0.01	4.34	8.93	0.24	0.066	0.309	99.78	34.6	64.3	1.2	**3**

Point	SiO_2	TiO_2	Al_2O_3	FeO	MnO	MgO	CaO	Na_2O	K_2O	BaO	SrO	TOTAL	An	Ab	Or	Zone
5.) DLC 8-9F - RR0119: Feldspar xeno. - Knockvologan (Phase two double MME) (traverse 1a37-1a71) n=35																
1a37	62.76	0.06	22.85	0.17	0.00	0.00	4.40	8.80	0.39	0.007	0.254	99.69	34.93	63.21	1.86	4
1a38	62.43	0.01	22.51	0.22	0.02	0.00	4.33	8.91	0.31	0.054	0.272	99.07	34.43	64.09	1.48	4
1a39	62.64	0.01	22.72	0.22	0.00	0.01	4.22	9.00	0.29	0.082	0.268	99.46	33.66	64.95	1.39	4
1a40	62.35	0.00	23.29	0.09	0.07	0.00	4.37	8.80	0.13	0.032	0.266	99.40	35.24	64.15	0.60	4
1a41	62.23	0.02	23.24	0.20	0.06	0.01	4.45	8.96	0.17	0.025	0.257	99.62	35.15	64.04	0.81	4
1a42	62.26	0.00	23.12	0.24	0.10	0.00	4.49	9.08	0.22	0.043	0.267	99.83	34.98	64.00	1.02	4
1a43	62.43	0.01	22.59	0.14	0.01	0.00	4.21	8.99	0.30	0.052	0.185	98.91	33.62	64.95	1.44	4
1a44	61.40	0.03	23.44	0.15	0.00	0.00	5.40	8.22	0.25	0.064	0.222	99.18	41.58	57.26	1.16	4
1a45	62.02	0.02	23.34	0.28	0.00	0.00	5.01	8.40	0.47	0.125	0.188	99.85	38.88	58.96	2.15	**3**
1a46	61.77	0.00	23.45	0.18	0.01	0.02	4.96	8.49	0.46	0.173	0.233	99.75	38.41	59.46	2.13	**3**
1a47	61.50	0.02	23.45	0.22	0.03	0.00	5.20	8.28	0.52	0.070	0.208	99.50	39.99	57.61	2.40	**3**
1a48	60.37	0.00	24.40	0.12	0.00	0.00	6.19	7.82	0.38	0.113	0.217	99.61	45.86	52.45	1.69	**3**
1a49	60.49	0.01	24.19	0.12	0.00	0.00	5.90	7.94	0.41	0.117	0.192	99.37	44.25	53.90	1.85	**3**
1a50	59.99	0.10	24.34	0.13	0.00	0.01	6.01	7.90	0.40	0.104	0.249	99.24	44.85	53.36	1.79	**3**
1a51	61.22	0.00	24.03	0.17	0.00	0.01	5.70	7.99	0.48	0.150	0.261	100.00	43.12	54.70	2.18	**3**
1a52	59.68	0.03	24.76	0.21	0.11	0.02	6.72	7.62	0.37	0.081	0.197	99.79	48.56	49.86	1.58	**3**
1a53	61.02	0.02	23.91	0.20	0.01	0.01	5.41	8.07	0.50	0.099	0.261	99.50	41.59	56.13	2.29	**3**
1a54	60.51	0.00	24.06	0.16	0.00	0.00	5.79	8.08	0.49	0.155	0.224	99.47	43.23	54.60	2.17	**3**
1a55	59.11	0.00	25.08	0.15	0.03	0.01	6.77	7.48	0.29	0.024	0.258	99.21	49.36	49.38	1.26	2
1a56	60.51	0.00	23.54	0.12	0.00	0.01	5.21	8.25	0.38	0.101	0.253	98.37	40.39	57.86	1.76	2
1a57	62.65	0.00	23.03	0.18	0.01	0.02	4.68	8.82	0.27	0.055	0.181	99.89	36.51	62.26	1.23	2
1a58	61.96	0.01	23.24	0.29	0.05	0.00	4.55	8.93	0.25	0.094	0.156	99.53	35.60	63.23	1.17	2
1a59	62.27	0.00	23.41	0.17	0.00	0.00	5.38	8.45	0.40	0.078	0.212	100.37	40.56	57.63	1.81	2
1a60	60.42	0.05	24.11	0.21	0.01	0.00	5.74	8.18	0.33	0.076	0.245	99.37	43.03	55.49	1.48	2
1a61	59.63	0.00	23.98	0.23	0.00	0.02	5.31	8.38	0.29	0.000	0.168	98.01	40.66	58.04	1.30	**1**
1a62	61.88	0.01	23.47	0.14	0.00	0.00	5.27	8.65	0.20	0.014	0.218	99.85	39.89	59.21	0.90	**1**
1a63	62.43	0.02	23.11	0.22	0.00	0.00	4.51	9.04	0.21	0.093	0.170	99.81	35.19	63.82	0.98	**1**
1a64	61.50	0.00	24.03	0.22	0.00	0.00	5.86	8.31	0.19	0.031	0.190	100.32	43.44	55.74	0.82	**1**
1a65	61.93	0.01	23.63	0.12	0.00	0.00	5.23	8.50	0.26	0.058	0.121	99.86	40.01	58.82	1.18	**1**
1a66	61.38	0.03	23.21	0.09	0.00	0.00	5.09	8.76	0.20	0.070	0.182	99.01	38.76	60.31	0.92	**1**
1a67	63.88	0.00	21.92	0.21	0.01	0.00	3.53	9.47	0.26	0.138	0.185	99.59	28.83	69.90	1.27	**1**
1a68	62.55	0.04	23.07	0.16	0.00	0.00	4.16	9.07	0.24	0.080	0.218	99.58	33.27	65.61	1.13	**1**
1a69	62.36	0.01	21.77	0.21	0.00	0.01	4.27	9.19	0.19	0.027	0.201	98.23	33.63	65.47	0.90	**1**
1a70	63.16	0.05	22.60	0.12	0.00	0.00	4.34	9.22	0.14	0.044	0.233	99.90	34.01	65.34	0.65	**1**
1a71	63.06	0.00	22.93	0.09	0.00	0.01	4.29	9.01	0.23	0.051	0.209	99.87	34.11	64.82	1.06	**1**

A4.3 Bulk NIST 610 glass data only. AV relates to absolute values to one or two standard deviations. As for 1 to 4, these are data from; 1 - Willigers *et al.* (2002); 2 - Mathez & Waight (2003); 3 - Baker *et al.* (2004); 4 - Gagnevin *et al.* (2005).

Xtal DLC	$^{205}Tl/^{203}Tl$	$^{206}Pb/^{204}Pb$	±2 SE	$^{207}Pb/^{204}Pb$	±2 SE	$^{208}Pb/^{204}Pb$	±2 SE	$^{207}Pb/^{206}Pb$	±2 SE	$^{208}Pb/^{206}Pb$	±2 SE	$^{206}Pb/^{204}Pb$: ^{201}Pb	$^{206}Pb/^{204}Pb$: ^{200}Pb	^{206}Pb (V)
RM1	1.0192	17.050	0.009	15.512	0.009	36.974	0.015	0.90976	0.00850	2.16862	0.00900	17.045	17.056	1.92
1A	1.0187	17.046	0.010	15.503	0.011	36.959	0.011	0.90957	0.00610	2.16842	0.01020	17.038	17.050	2.20
	1.0183	17.046	0.011	15.504	0.010	36.966	0.016	0.90962	0.00640	2.16848	0.00740	17.037	17.075	2.29
	1.0182	17.048	0.013	15.508	0.012	36.971	0.016	0.90961	0.00620	2.16859	0.00610	17.040	17.048	2.27
1D	1.0168	17.048	0.010	15.509	0.010	36.966	0.016	0.90974	0.00580	2.16851	0.00820	17.040	17.043	2.65
	1.0180	17.048	0.008	15.511	0.009	36.976	0.015	0.90988	0.00960	2.16881	0.00920	17.038	17.043	2.67
	1.0215	17.048	0.016	15.510	0.015	36.965	0.026	0.90976	0.01080	2.16847	0.01370	17.043	17.051	1.22
	1.0214	17.045	0.008	15.509	0.008	36.967	0.013	0.90973	0.00610	2.16869	0.00730	17.038	17.044	1.65
	1.0180	17.046	0.010	15.509	0.012	36.963	0.021	0.90979	0.01010	2.16818	0.01250	17.044	17.049	1.57
	1.0181	17.041	0.012	15.505	0.013	36.950	0.020	0.90975	0.00720	2.16838	0.00960	17.039	17.043	1.68
RM1	1.0179	17.043	0.017	15.510	0.019	36.958	0.025	0.90993	0.00890	2.16825	0.01040	17.040	17.044	1.25
RM1a	1.0166	17.046	0.028	15.508	0.029	36.968	0.031	0.90979	0.00800	2.16878	0.00780	17.038	17.049	2.63
3A	1.0167	17.041	0.033	15.502	0.031	36.955	0.036	0.90979	0.00650	2.16862	0.00590	17.033	17.044	2.64
	1.0179	17.061	0.029	15.522	0.028	37.001	0.031	0.90977	0.00600	2.16887	0.00570	17.052	17.063	2.48
	1.0210	17.047	0.019	15.509	0.018	36.969	0.027	0.90985	0.00740	2.16903	0.01160	17.036	17.062	0.85
	1.0212	17.048	0.022	15.510	0.022	36.978	0.031	0.90975	0.00900	2.16862	0.01310	17.039	17.059	0.84
	1.0211	17.045	0.016	15.506	0.018	36.962	0.021	0.90980	0.00840	2.16882	0.00970	17.035	17.047	1.01
RM1a	1.0206	17.041	0.010	15.504	0.013	36.947	0.018	0.90975	0.00620	2.16825	0.00710	17.037	17.046	2.44
RM2	1.0177	17.050	0.008	15.510	0.007	36.982	0.019	0.90970	0.01030	2.16863	0.01370	17.041	17.047	2.95
7A	1.0181	17.045	0.009	15.506	0.010	36.956	0.013	0.90969	0.00880	2.16832	0.00820	17.037	17.044	2.68
	1.0187	17.045	0.010	15.506	0.010	36.957	0.017	0.90963	0.00840	2.16827	0.01130	17.042	17.047	2.65
	1.0193	17.046	0.016	15.508	0.012	36.962	0.024	0.90978	0.00930	2.16842	0.01090	17.041	17.046	2.07
RM2	1.0192	17.047	0.007	15.508	0.009	36.964	0.012	0.90982	0.00680	2.16845	0.00900	17.039	17.044	2.17
MME1	1.0217	17.054	0.018	15.514	0.023	36.978	0.020	0.90971	0.01010	2.16844	0.01290	17.051	17.066	0.79
10-11B	1.0219	17.032	0.017	15.494	0.019	36.930	0.024	0.90970	0.00780	2.16854	0.01100	17.028	17.043	0.86
MME1	1.0217	17.042	0.017	15.504	0.018	36.955	0.022	0.90984	0.00860	2.16885	0.01090	17.031	17.046	0.88
MME2	1.0181	17.047	0.013	15.507	0.016	36.957	0.019	0.90969	0.00510	2.16805	0.00950	17.045	17.052	1.52
8-9F	1.0182	17.050	0.013	15.514	0.016	36.961	0.027	0.90986	0.01020	2.16847	0.01110	17.046	17.051	1.14
	1.0185	17.040	0.014	15.501	0.016	36.941	0.020	0.90970	0.00790	2.16787	0.01100	17.038	17.041	1.05
	1.0175	17.058	0.013	15.520	0.013	36.995	0.020	0.90994	0.00570	2.16881	0.00910	17.048	17.056	1.83
MME2	1.0194	17.043	0.012	15.505	0.014	36.959	0.019	0.90972	0.00790	2.16868	0.01140	17.036	17.041	1.70
Mean	1.0191	17.046	0.014	15.508	0.015	36.964	0.021	0.90976	0.00787	2.16852	0.00982	17.040	17.050	1.82
AV (1)	0.0016	0.005	0.006	0.005	0.006	0.014	0.006	0.00009	0.00158	0.00025	0.00220	0.005	0.008	0.68
AV (2)	0.0032	0.010	0.013	0.010	0.012	0.028	0.012	0.00017	0.00316	0.00051	0.00440	0.010	0.016	1.36

1	17.041 ± 0.011	15.498 ± 0.011	36.924 ± 0.032	-	-
2	17.038 ± 12	15.492 ± 11	36.919 ± 31	0.9093 ± 1	2.1670 ± 5
3	17.052 ± 2	15.515 ± 2	36.991 ± 5	0.90986 ± 5	2.1694 ± 1
4	17.041 ± 3	15.497 ± 2	36.934 ± 6	0.90949 ± 5	2.1675 ± 1

A4.4 Bulk Pb-Pb feldspar data.

Point	$^{206}Pb/^{204}Pb$	2σ	$^{207}Pb/^{204}Pb$	2σ	$^{208}Pb/^{204}Pb$	2σ	$^{208}Pb/^{206}Pb$	2σ	$^{207}Pb/^{206}Pb$	2σ	Distance (mm)	Zone
1.(a)) DLC 1A - AF0207: K-feldspar - Red Bay Quarry (RM1) (traverse A-B) n=10												
NIST-610	*17.046*	*0.011*	*15.504*	*0.010*	*36.966*	*0.016*	*2.16848*	*0.00740*	*0.90962*	*0.00640*	-	-
rim1	**16.998**	0.011	**15.290**	0.009	**35.858**	0.023	**2.14789**	0.00022	**0.92444**	0.00022	0.00	**3**
2	**16.983**	0.006	**15.293**	0.007	**35.852**	0.012	**2.14929**	0.00017	**0.92520**	0.00018	0.15	**3**
3	**16.971**	0.013	**15.276**	0.012	**35.818**	0.025	**2.14902**	0.00033	**0.92499**	0.00022	0.30	**3** & 2
4	**16.946**	0.016	**15.276**	0.015	**35.794**	0.033	**2.15084**	0.00021	**0.92625**	0.00016	0.45	2 & **1**
5	**16.920**	0.014	**15.258**	0.012	**35.756**	0.029	**2.15178**	0.00034	**0.92646**	0.00018	0.60	**1**
6	**16.904**	0.019	**15.240**	0.017	**35.728**	0.037	**2.15146**	0.00033	**0.92644**	0.00019	0.75	**1**
7	**16.939**	0.011	**15.291**	0.012	**35.821**	0.024	**2.15347**	0.00026	**0.92779**	0.00021	0.90	**1**
8	**16.919**	0.013	**15.255**	0.011	**35.777**	0.027	**2.15311**	0.00021	**0.92668**	0.00024	1.05	**1**
9	**16.934**	0.014	**15.283**	0.013	**35.819**	0.026	**2.15337**	0.00029	**0.92730**	0.00039	1.20	**1**
core10	**16.918**	0.036	**15.280**	0.037	**35.770**	0.061	**2.15406**	0.00044	**0.92936**	0.00081	1.35	**1**
NIST-610	*17.048*	*0.013*	*15.508*	*0.012*	*36.971*	*0.016*	*2.16859*	*0.00610*	*0.90961*	*0.00620*	-	-

Point	$^{206}Pb/^{204}Pb$	2σ	$^{207}Pb/^{204}Pb$	2σ	$^{208}Pb/^{204}Pb$	2σ	$^{208}Pb/^{206}Pb$	2σ	$^{207}Pb/^{206}Pb$	2σ	Distance (mm)	Zone
1.(b)) DLC 1D - AF0207: K-feldspar - Red Bay Quarry (RM1) (traverse C-D) n=13												
NIST-610	*17.048*	*0.008*	*15.511*	*0.009*	*36.976*	*0.015*	*2.16881*	*0.00920*	*0.90988*	*0.00960*	-	-
1	**16.972**	0.021	**15.296**	0.015	**36.537**	0.038	**2.15333**	0.00045	**0.91811**	0.00051	0.00	**3**
3	**16.970**	0.014	**15.317**	0.010	**36.570**	0.029	**2.15432**	0.00035	**0.91919**	0.00034	1.11	2
4	**16.987**	0.011	**15.317**	0.009	**36.580**	0.020	**2.15399**	0.00031	**0.91894**	0.00031	1.49	2 & **1**
5	**16.967**	0.018	**15.297**	0.015	**36.542**	0.036	**2.15376**	0.00022	**0.91890**	0.00017	1.86	**1**
6	**16.968**	0.014	**15.294**	0.011	**36.540**	0.030	**2.15345**	0.00028	**0.91881**	0.00013	2.23	**1**
7	**16.979**	0.013	**15.295**	0.013	**36.541**	0.028	**2.15209**	0.00021	**0.91830**	0.00020	2.60	**1**
8	**16.978**	0.014	**15.285**	0.012	**36.522**	0.032	**2.15087**	0.00022	**0.91760**	0.00020	3.34	**1**
10	**17.020**	0.013	**15.308**	0.012	**36.576**	0.026	**2.14931**	0.00034	**0.91734**	0.00026	4.09	**1**
11	**16.993**	0.018	**15.292**	0.017	**36.544**	0.038	**2.15029**	0.00040	**0.91808**	0.00024	4.46	**1**
12	**16.982**	0.016	**15.290**	0.017	**36.518**	0.038	**2.15052**	0.00055	**0.91870**	0.00033	4.83	**1**
13	**16.955**	0.018	**15.266**	0.016	**36.467**	0.039	**2.15080**	0.00030	**0.91881**	0.00021	5.20	**1**
14	**16.954**	0.021	**15.271**	0.021	**36.468**	0.049	**2.15101**	0.00030	**0.91919**	0.00024	5.57	**1**
15	**16.940**	0.019	**15.252**	0.019	**36.421**	0.039	**2.15003**	0.00034	**0.91936**	0.00026	5.94	**1**
NIST-610	*17.048*	*0.016*	*15.510*	*0.015*	*36.965*	*0.026*	*2.16847*	*0.01370*	*0.90976*	*0.01080*	-	-

Point	$^{206}Pb/^{204}Pb$	2σ	$^{207}Pb/^{204}Pb$	2σ	$^{208}Pb/^{204}Pb$	2σ	$^{208}Pb/^{206}Pb$	2σ	$^{207}Pb/^{206}Pb$	2σ	Distance (mm)	Zone
2.) DLC 3A - AF/02/01: K-feldspar - Torr na h'Annaid, Bendoran (RM1a) (traverse E-F) n=21												
NIST-610	*17.061*	*0.029*	*15.522*	*0.028*	*37.001*	*0.031*	*37.001*	*0.031*	*0.90977*	*0.00600*	-	-
1	**17.241**	0.017	**15.397**	0.014	**36.888**	0.033	**2.13928**	0.00083	**0.90863**	0.00043	0.00	6
2	**17.011**	0.027	**15.374**	0.017	**36.657**	0.046	**2.15526**	0.00125	**0.92001**	0.00070	0.40	6 & **5**
3	**16.904**	0.020	**15.334**	0.017	**36.524**	0.043	**2.16067**	0.00030	**0.92349**	0.00020	0.80	**5**
4	**16.994**	0.032	**15.324**	0.014	**36.528**	0.036	**2.14900**	0.00306	**0.91796**	0.00144	1.20	**5**
5	**16.942**	0.023	**15.326**	0.018	**36.546**	0.047	**2.15670**	0.00092	**0.92110**	0.00065	1.60	**5**
6	**17.153**	0.023	**15.366**	0.017	**36.776**	0.044	**2.14368**	0.00056	**0.91236**	0.00043	2.00	**5** & 4
7	**17.172**	0.048	**15.351**	0.042	**36.741**	0.104	**2.13982**	0.00098	**0.91049**	0.00035	2.40	4
8	**17.194**	0.020	**15.372**	0.020	**36.820**	0.042	**2.14160**	0.00033	**0.91097**	0.00028	2.80	4 & **3**
9	**17.253**	0.018	**15.389**	0.016	**36.871**	0.037	**2.13748**	0.00027	**0.90880**	0.00018	3.20	**3** & 2
core 10	**17.240**	0.027	**15.374**	0.024	**36.847**	0.058	**2.13726**	0.00045	**0.90891**	0.00036	3.60	2 & **1**
core 11	**17.252**	0.021	**15.364**	0.021	**36.803**	0.051	**2.13253**	0.00105	**0.90743**	0.00038	4.00	**1**
12	**17.212**	0.019	**15.353**	0.018	**36.765**	0.044	**2.13556**	0.00192	**0.90893**	0.00094	4.40	PP
poik plag 1	**17.285**	0.163	**15.284**	0.050	**36.598**	0.112	**2.12414**	0.00964	**0.90425**	0.00412	4.80	PP
poik plag 1	**17.166**	0.080	**15.244**	0.039	**36.436**	0.091	**2.12492**	0.00868	**0.90594**	0.00348	5.20	PP & **5**
15	**17.134**	0.113	**15.309**	0.097	**36.655**	0.234	**2.13944**	0.00076	**0.91136**	0.00057	5.60	**5**
16	**16.986**	0.030	**15.340**	0.016	**36.571**	0.044	**2.15264**	0.00193	**0.92085**	0.00122	6.00	**5**
17	**16.858**	0.030	**15.302**	0.026	**36.413**	0.065	**2.16021**	0.00074	**0.92566**	0.00045	6.40	**5**
18	**16.979**	0.032	**15.333**	0.020	**36.568**	0.053	**2.15381**	0.00155	**0.92118**	0.00091	6.80	**5**
19	**16.903**	0.057	**15.299**	0.047	**36.451**	0.116	**2.15608**	0.00128	**0.92329**	0.00081	7.20	**5**
20	**16.916**	0.058	**15.297**	0.040	**36.464**	0.097	**2.15302**	0.00146	**0.92165**	0.00097	7.60	**5** & 6
21	**17.062**	0.044	**15.338**	0.035	**36.623**	0.084	**2.14657**	0.00083	**0.91740**	0.00046	8.00	6
NIST-610	*17.047*	*0.019*	*15.509*	*0.018*	*36.969*	*0.027*	*2.16903*	*0.01160*	*0.90985*	*0.00740*	-	-

Point	$^{206}Pb/^{204}Pb$	2σ	$^{207}Pb/^{204}Pb$	2σ	$^{208}Pb/^{204}Pb$	2σ	$^{208}Pb/^{206}Pb$	2σ	$^{207}Pb/^{206}Pb$	2σ	Distance (mm)	Zone
3.) DLC 7A - RR0120: K-feldspar (from RM2 juxtaposed to diorite) (traverse 1, G-H) n=24												
NIST-610	*17.045*	*0.009*	*15.506*	*0.010*	*36.956*	*0.013*	*2.16832*	*0.00820*	*0.90969*	*0.00880*	-	-
rim 1	**17.231**	0.009	**15.358**	0.008	**36.808**	0.021	**2.13553**	0.00018	**0.90704**	0.00016	0.00	4
2	**17.236**	0.010	**15.356**	0.008	**36.803**	0.021	**2.13519**	0.00020	**0.90680**	0.00021	0.23	**3**
3	**17.233**	0.008	**15.365**	0.008	**36.800**	0.016	**2.13550**	0.00018	**0.90749**	0.00020	0.45	**3**
4	**17.237**	0.010	**15.343**	0.008	**36.765**	0.018	**2.13314**	0.00039	**0.90619**	0.00029	0.68	**3**
5	**17.249**	0.012	**15.321**	0.009	**36.748**	0.023	**2.13093**	0.00026	**0.90458**	0.00029	0.90	**3**
6	**17.258**	0.010	**15.328**	0.009	**36.754**	0.020	**2.12954**	0.00058	**0.90428**	0.00030	1.13	**3** & 2
7	**17.324**	0.018	**15.356**	0.014	**36.817**	0.025	**2.12551**	0.00082	**0.90202**	0.00083	1.36	2
8	**17.306**	0.029	**15.341**	0.010	**36.759**	0.024	**2.12403**	0.00255	**0.90196**	0.00143	1.58	2
10	**17.354**	0.034	**15.348**	0.014	**36.823**	0.037	**2.12194**	0.00228	**0.89997**	0.00118	2.04	**1**
12	**17.280**	0.036	**15.354**	0.009	**36.789**	0.028	**2.12943**	0.00291	**0.90466**	0.00155	2.49	**1**
13	**17.155**	0.015	**15.322**	0.011	**36.688**	0.026	**2.13816**	0.00068	**0.90912**	0.00038	2.71	**1**
14	**17.137**	0.015	**15.335**	0.015	**36.700**	0.030	**2.14154**	0.00031	**0.91128**	0.00018	2.94	**1**
core 15	**17.114**	0.024	**15.278**	0.023	**36.575**	0.051	**2.13721**	0.00090	**0.90901**	0.00043	3.17	**1**
16	**17.075**	0.016	**15.315**	0.013	**36.622**	0.031	**2.14447**	0.00027	**0.91300**	0.00022	3.39	**1**
17	**17.125**	0.019	**15.309**	0.015	**36.634**	0.037	**2.13979**	0.00117	**0.91031**	0.00069	3.62	**1**
18	**17.153**	0.022	**15.307**	0.015	**36.644**	0.035	**2.13632**	0.00117	**0.90856**	0.00063	3.85	**1**
20	**17.206**	0.012	**15.335**	0.011	**36.707**	0.027	**2.13367**	0.00046	**0.90745**	0.00019	4.30	2 & **3**
21	**17.214**	0.017	**15.328**	0.012	**36.714**	0.032	**2.13277**	0.00071	**0.90700**	0.00035	4.52	**3**
22	**17.256**	0.015	**15.330**	0.010	**36.685**	0.023	**2.12619**	0.00097	**0.90470**	0.00044	4.75	**3** & 2
24	**17.263**	0.045	**15.329**	0.011	**36.664**	0.029	**2.12238**	0.00500	**0.90399**	0.00225	5.20	1
25	**17.204**	0.031	**15.314**	0.017	**36.595**	0.039	**2.12641**	0.00217	**0.90658**	0.00106	5.43	1
26	**17.201**	0.019	**15.304**	0.014	**36.594**	0.032	**2.12713**	0.00121	**0.90617**	0.00050	5.65	1 & **3**
27	**17.183**	0.018	**15.336**	0.014	**36.660**	0.031	**2.13341**	0.00160	**0.90883**	0.00075	5.88	**3** & 2
rim 28	**17.115**	0.014	**15.320**	0.013	**36.642**	0.032	**2.14127**	0.00034	**0.91161**	0.00021	6.11	2 & 4
NIST-610	*17.045*	*0.010*	*15.506*	*0.010*	*36.957*	*0.017*	*2.16827*	*0.01130*	*0.90963*	*0.00840*	-	-

Point	$^{206}Pb/^{204}Pb$	2σ	$^{207}Pb/^{204}Pb$	2σ	$^{208}Pb/^{204}Pb$	2σ	$^{208}Pb/^{206}Pb$	2σ	$^{207}Pb/^{206}Pb$	2σ	Distance (mm)	Zone
4.) DLC 10-11B - RR0119: Feldspar micro-pheno. (Phase one double MME) (traverse J-K) n=5												
NIST-610	*17.03182*	*0.02*	*15.49431*	*0.019*	*36.9299*	*0.02*	*2.168538*	*0.011*	*0.909695*	*0.0078*	-	-
1	**16.427**	0.246	**14.991**	0.233	**35.755**	0.542	**2.17654**	0.00130	**0.93271**	0.00096	0.00	3, mainly **2**
2	**16.061**	0.095	**14.776**	0.080	**35.131**	0.192	**2.18492**	0.00126	**0.93851**	0.00071	0.45	**1**
3	**16.264**	0.115	**14.884**	0.089	**35.363**	0.213	**2.17465**	0.00352	**0.93471**	0.00176	0.90	**1**
4	**16.338**	0.137	**14.790**	0.145	**35.390**	0.312	**2.16620**	0.00235	**0.92486**	0.00237	1.35	**1**
5	**16.061**	0.164	**14.575**	0.139	**34.876**	0.353	**2.17321**	0.00248	**0.92937**	0.00073	1.80	2, mainly **3**
NIST-610	*17.042*	*0.017*	*15.504*	*0.018*	*36.955*	*0.022*	*2.16885*	*0.01090*	*0.90984*	*0.00860*	-	-

Point	$^{206}Pb/^{204}Pb$	2σ	$^{207}Pb/^{204}Pb$	2σ	$^{208}Pb/^{204}Pb$	2σ	$^{208}Pb/^{206}Pb$	2σ	$^{207}Pb/^{206}Pb$	2σ	Distance (mm)	Zone
5.) DLC 8-9F - RR0119: Feldspar xeno. - Knockvologan (Phase two double MME) (traverse L-M) n=20 (started 0.48 mm in)												
NIST-610	*17.058*	*0.013*	*15.520*	*0.013*	*36.995*	*0.020*	*2.16881*	*0.00910*	*0.90994*	*0.00570*	-	-
1	**16.599**	0.048	**15.207**	0.046	**36.163**	0.110	**2.17922**	0.00145	**0.93227**	0.00064	0.48	4
2	**16.593**	0.054	**15.147**	0.043	**36.175**	0.141	**2.18046**	0.00398	**0.92961**	0.00095	0.95	4 & **3**
3	**16.610**	0.049	**15.217**	0.030	**36.247**	0.086	**2.18316**	0.00167	**0.93359**	0.00142	1.43	3
4	**16.935**	0.148	**15.226**	0.037	**36.413**	0.133	**2.15092**	0.01094	**0.91802**	0.00583	1.90	**3** & 2
5	**16.551**	0.059	**15.079**	0.056	**35.916**	0.132	**2.17226**	0.00210	**0.92844**	0.00092	2.38	2
6	**16.652**	0.046	**15.179**	0.045	**36.188**	0.089	**2.17182**	0.00108	**0.92772**	0.00058	2.86	2
7	**16.695**	0.050	**15.144**	0.047	**36.158**	0.111	**2.16585**	0.00099	**0.92433**	0.00076	3.33	2
8	**16.801**	0.031	**15.183**	0.033	**36.247**	0.062	**2.15953**	0.00092	**0.92024**	0.00080	3.81	2
9	**16.765**	0.047	**15.174**	0.041	**36.198**	0.098	**2.16161**	0.00115	**0.92255**	0.00075	4.29	2, mainly **1**
10	**16.743**	0.044	**15.209**	0.037	**36.289**	0.087	**2.16655**	0.00106	**0.92473**	0.00077	4.76	**1**
11	**16.753**	0.065	**15.173**	0.046	**36.210**	0.119	**2.16290**	0.00157	**0.92281**	0.00149	5.24	**1**
12	**16.808**	0.065	**15.169**	0.065	**36.234**	0.152	**2.15437**	0.00124	**0.91841**	0.00084	5.71	**1**
13	**16.817**	0.071	**15.075**	0.062	**36.060**	0.144	**2.14722**	0.00188	**0.91447**	0.00094	6.19	**1**
14	**16.764**	0.057	**15.111**	0.054	**36.114**	0.129	**2.15368**	0.00126	**0.91807**	0.00049	6.67	**1**
15	**16.736**	0.065	**15.126**	0.060	**36.098**	0.144	**2.16032**	0.00062	**0.92208**	0.00059	7.14	**1**
16	**16.686**	0.059	**15.077**	0.052	**36.011**	0.130	**2.15827**	0.00070	**0.92042**	0.00040	7.62	**1**
17	**16.722**	0.049	**15.094**	0.045	**36.083**	0.108	**2.15802**	0.00057	**0.91965**	0.00043	8.10	**1**
18	**16.722**	0.074	**15.037**	0.063	**35.937**	0.153	**2.14905**	0.00165	**0.91602**	0.00075	8.57	**1**
19	**16.773**	0.058	**15.088**	0.050	**36.093**	0.115	**2.15159**	0.00156	**0.91681**	0.00069	9.05	**1**
20	**16.761**	0.096	**15.061**	0.076	**36.062**	0.188	**2.15098**	0.00185	**0.91381**	0.00095	9.52	**1**
NIST-610	*17.043*	*0.012*	*15.505*	*0.014*	*36.959*	*0.019*	*2.16868*	*0.01140*	*0.90972*	*0.00790*	-	-

A4.5 Bulk Pb-Pb averages data.

1.) DLC 1A - AF0207: K-feldspar from Red Bay Quarry (RM1) (traverse A-B)											
isotopic avs.	**$^{206}Pb/^{204}Pb$**	2σ	**$^{207}Pb/^{204}Pb$**	2σ	**$^{208}Pb/^{204}Pb$**	2σ	**$^{208}Pb/^{206}Pb$**	2σ	**$^{207}Pb/^{206}Pb$**	2σ	n =
Zone 1	**16.922**	0.018	**15.268**	0.017	**35.779**	0.034	**2.15287**	0.00031	**0.92734**	0.00033	2
Zone 2	**16.958**	0.014	**15.276**	0.014	**35.806**	0.029	**2.14993**	0.00027	**0.92562**	0.00019	2
Zone 3	**16.991**	0.009	**15.292**	0.008	**35.855**	0.018	**2.14859**	0.00020	**0.92482**	0.00020	6

1.) DLC 1A - AF0207: K-feldspar from Red Bay Quarry (RM1) (traverse C-D)											
isotopic avs.	**$^{206}Pb/^{204}Pb$**	2σ	**$^{207}Pb/^{204}Pb$**	2σ	**$^{208}Pb/^{204}Pb$**	2σ	**$^{208}Pb/^{206}Pb$**	2σ	**$^{207}Pb/^{206}Pb$**	2σ	n =
Zone 1	**16.974**	0.016	**15.285**	0.015	**36.514**	0.036	**2.15121**	0.00032	**0.91851**	0.00022	10
Zone 2	**16.978**	0.012	**15.317**	0.010	**36.575**	0.024	**2.15415**	0.00033	**0.91906**	0.00032	2
Zone 3	**16.972**	0.021	**15.296**	0.015	**36.537**	0.038	**2.15333**	0.00045	**0.91811**	0.00051	1

2.) DLC 3A - AF/02/01: K-feldspar - Torr na h'Annaid, Bendoran (RM1a) (traverse E-F)											
isotopic avs.	**$^{206}Pb/^{204}Pb$**	2σ	**$^{207}Pb/^{204}Pb$**	2σ	**$^{208}Pb/^{204}Pb$**	2σ	**$^{208}Pb/^{206}Pb$**	2σ	**$^{207}Pb/^{206}Pb$**	2σ	n =
Zone 1	**17.246**	0.024	**15.369**	0.023	**36.825**	0.055	**2.13490**	0.00075	**0.90817**	0.00037	2
Zone 2	**17.246**	0.023	**15.382**	0.020	**36.859**	0.048	**2.13737**	0.000	**0.90886**	0.000	2
Zone 3	**17.223**	0.019	**15.381**	0.018	**36.845**	0.040	**2.13954**	0.00030	**0.90989**	0.00023	2
Zone 4	**17.172**	0.048	**15.351**	0.042	**36.741**	0.104	**2.13982**	0.00098	**0.91049**	0.00035	1
Zone 5	**16.996**	0.044	**15.321**	0.031	**36.549**	0.076	**2.15045**	0.00187	**0.91874**	0.00098	12
Zone 6	**17.152**	0.031	**15.367**	0.024	**36.755**	0.059	**2.14293**	0.00083	**0.91302**	0.00044	2
poikilitic phase	**17.248**	0.091	**15.318**	0.034	**36.681**	0.078	**2.12985**	0.00578	**0.90659**	0.00253	2

3.) DLC 7A - RR0120: K-feldspar (from RM2 juxtaposed to diorite) (traverse 1, G-H)											
isotopic avs.	**$^{206}Pb/^{204}Pb$**	2σ	**$^{207}Pb/^{204}Pb$**	2σ	**$^{208}Pb/^{204}Pb$**	2σ	**$^{208}Pb/^{206}Pb$**	2σ	**$^{207}Pb/^{206}Pb$**	2σ	n =
Zone 1	**17.231**	0.009	**15.358**	0.008	**36.808**	0.021	**2.13553**	0.00018	**0.90704**	0.00016	1
Zone 2	**17.315**	0.023	**15.349**	0.012	**36.788**	0.024	**2.12477**	0.00169	**0.90199**	0.00113	2
Zone 3	**17.228**	0.013	**15.335**	0.010	**36.723**	0.024	**2.13175**	0.00066	**0.90635**	0.00035	10
Zone 4	**17.186**	0.026	**15.321**	0.014	**36.673**	0.034	**2.13376**	0.00169	**0.90765**	0.00086	10

4.) DLC 10-11B - RR0119: Feldspar micro-pheno. (Phase one double MME) (traverse J-K)											
isotopic avs.	**$^{206}Pb/^{204}Pb$**	2σ	**$^{207}Pb/^{204}Pb$**	2σ	**$^{208}Pb/^{204}Pb$**	2σ	**$^{208}Pb/^{206}Pb$**	2σ	**$^{207}Pb/^{206}Pb$**	2σ	n =
Zone 1	**16.061**	0.164	**14.575**	0.139	**34.876**	0.353	**2.17321**	0.00248	**0.92937**	0.00073	1
Zone 2	**16.427**	0.246	**14.991**	0.233	**35.755**	0.542	**2.17654**	0.00130	**0.93271**	0.00096	1
Zone 2/3	**16.221**	0.116	**14.817**	0.105	**35.295**	0.239	**2.17526**	0.00238	**0.93269**	0.00161	3

5.) DLC 8-9F - RR0119: Feldspar xeno. - Knockvologan (Phase two double MME) (traverse L-M)											
isotopic avs.	**$^{206}Pb/^{204}Pb$**	2σ	**$^{207}Pb/^{204}Pb$**	2σ	**$^{208}Pb/^{204}Pb$**	2σ	**$^{208}Pb/^{206}Pb$**	2σ	**$^{207}Pb/^{206}Pb$**	2σ	n =
Zone 1	**16.754**	0.063	**15.116**	0.054	**36.116**	0.130	**2.15621**	0.00126	**0.91915**	0.00076	12
Zone 2	**16.675**	0.047	**15.146**	0.045	**36.127**	0.098	**2.16736**	0.00128	**0.92518**	0.00077	4
Zone 3	**16.713**	0.083	**15.197**	0.036	**36.278**	0.120	**2.17152**	0.00553	**0.92707**	0.00273	3
Zone 4	**16.599**	0.048	**15.207**	0.046	**36.163**	0.110	**2.17922**	0.00145	**0.93227**	0.00064	1

Appendix Five
ROMG SAMPLE STATIONS

Introduction

A full list and locality maps of samples collected in the field is presented here, including country rock samples that have not been discussed in this study. Specimen numbers, grid reference and what processed state the sample can be found in right from the cutting laboratory, the crushing laboratory and X-Ray laboratory is provided.

A5.1 ROMG sample reference list.

The key utilised in the bulk sample reference list is as follows:

Key

*	Type 1 Caledonian intrusion relative to sample no S71153 of (Rock & Hunter 1987)
TC	Sample donated for St. Andrews undergraduate teaching collection (consult Prof. Adrian Finch)
e.g. 169	Samples not used for Zaniewski PhD
e.g.169	Samples used for Zaniewski PhD (QXRD & XRF)
	Sample in St Andrews under storage space/for J.R. sample set, only the powders are present
√	Adequate/process completed
x	Not adequate/sample not present
-	Not relevant/ usually due to not enough sample present
d	Old data available, but J.R.'s samples have no emissions loss data whereas R.R. data has
	Sample powder not used and in Dr. John Reavy's office

Note all Thin Sections are at UCC

√1Dx1	Thick section at UCC (if in bold, used for CL, EPMA & LA MC ICP MS)
√1Dx2**	Dr. Graham McLeod was donated stub 1A

bohs-**V.S**	< 1kg	bag of hand specimens
- S	1-2 kg	bag of hand specimens
- M	2-5kg	bag of hand specimens
- L	5 kg	bag of hand specimens

Total samples	n=175
Total samples used	n=129
Total samples unused	n=46

Lithologies

RM1

RM1a

RM2

Aplite

Diorite type 1

Diorite type 2

MME

Lamprophyre

Iona Gp.

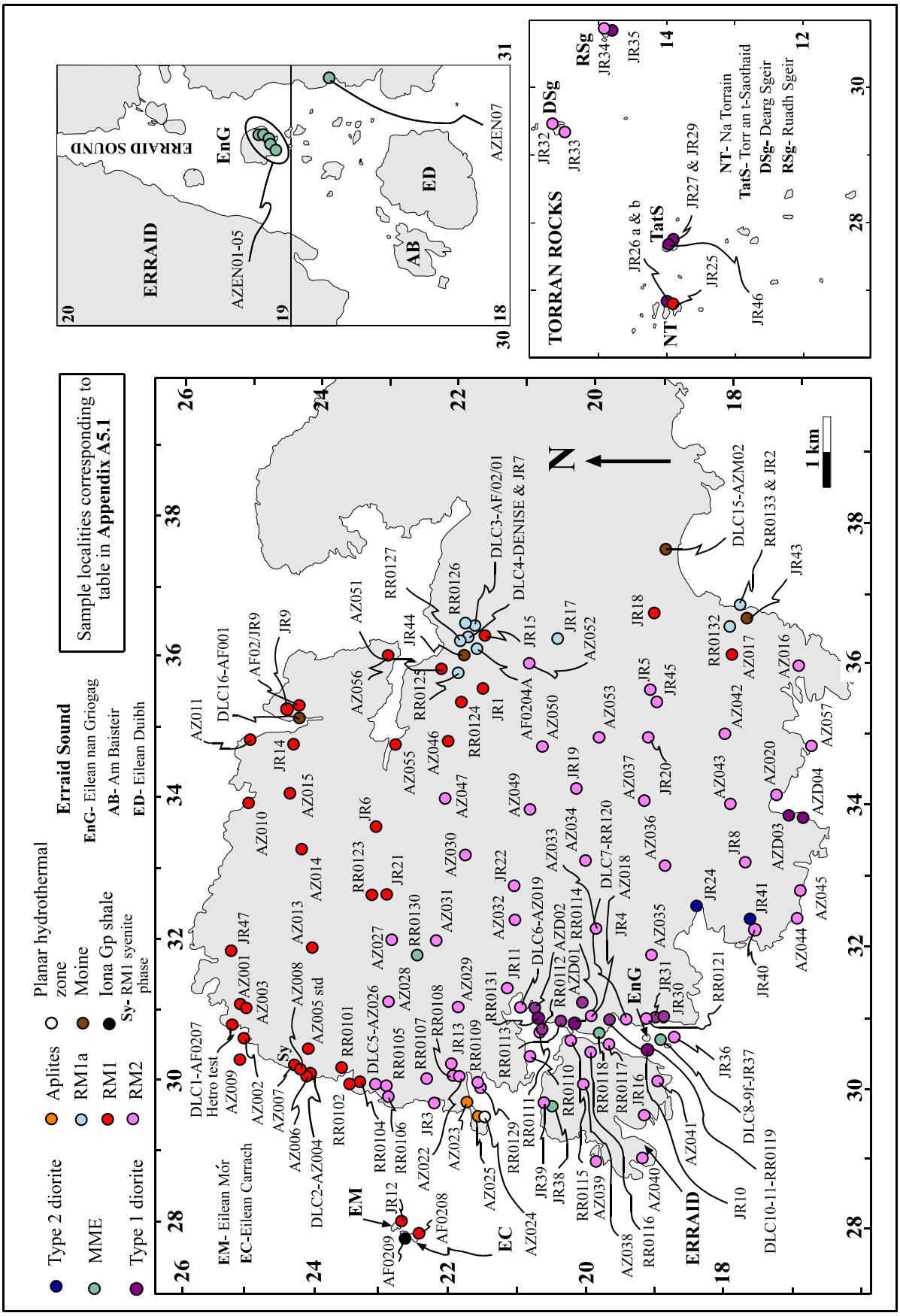
Moine

			CUTTING LAB				**CRUSH. LAB**				**X-RAY LAB**	
n =	Specimen no.	GR & Lithology	S = Specimen St. Andrews (comments)	T/S	Stub for T/S	Bits for Jaw crusher	Disposable **F(1)** Jaw crush	Min sep. **F(2)** Coarse	XRF **F(3)** Fine	QXRD **F(4)** V. Fine	Pressed pellet	Fusion disc/bead
1	RR0101	30112 23497G	x1 Huge, 5 kg+ S	x2	-	-	-	√	√	√ **d**	x2 **d**	broken **d**
2	RR0102	29874 23341G	bohs-**L**./ x1, 2-3kg S	-	√	x	x	x	x	x	x	x
3	DLC12/RR0103*	29874 23341	bohs-V.S., 3-4 pieces	-	√**12Ax2**	√	√	√	√	√	√	√
4	RR0104	29903 23183G	bohs-**M**	x2	-	-	-	√	√	√ **d**	x2 **d**	√ **d**
5	RR0105	29971 22923G	bohs-**M**/x1, 5kg S	-	√	√	√	√	√	√	√	√
6	RR0106	29894 22821G	bohs-**L**/x1, 3-4kg S	-	√	x	x	x	x	x	x	x
7	RR0107	30059 22384G	bohs-**M**	x2	-	-	-	√	√	√ **d**	x2 **d**	√ **d**
8	RR0108	30144 21952G	bohs-**S**/x1, 1-2 kg S	-	√	√	√	√	√	√	√	√ **d**
9	RR0109	30056 21539G	bohs-**S**/x1, 4-5 kg S	-	√	x	x	x	x	x	x	x
10	RR0110	30381 20862G	bohs-**M** S	x2	-	-	-	√	√	√ **d**	x2 **d**	√ **d**
11	RR0111	30885 20663G	bohs-**M**/x1, 5kg+ S	-	√	x	x	x	x	x	x	x
12	RR0112	30873 20638B	bohs-**S**-**VS**/x 3 pieces	-	√	√	x	x	x	x	x	x
13	RR0113	30829 20386B	Small S at UCC	-	√	√	√	√	√	√	√	√
14	RR0114	30786 20234B	x2 bohs-**M**	x2	-	-	-	√	√	√ **d**	x2 **d**	√ **d**
15	RR0115	30696 20235G	bohs-**M**-**L**/x1, 2-4kg S	-	√	√	√	√	√	√	√	√
16	RR0116	30677 20081G	bohs-**S**/x1, 2-3 kg S	-	√	x	x	x	x	x	x	x
17	RR0117	30736 19829G	bohs-**L**/x1, 2-4 kg S	-	√	x	x	x	x	x	x	x
18	RR0118	30739 19820	-	√	√	√	√	√	√	√	√ **d**	√
19	RR0119	30844 29672B *TC*	x2 bohs'-**M**/@ UCC	√	√10-11Bx1	√	√	√	√	√	√	√
20	RR0120-DLC7	30967 19410G *TC*	bohs-**L**/x1, 2kg S	-	√**7Ax1**	√	√	√	√	√	√	√
21	RR0121	30888 19238G	bohs-**L**	√	-	-	-	-	-	-	x **d**	x
22	RR0123	32652 23090G	bohs-**L**	-	√	√	√	√	√	√	√	√
23	RR0124	35326 21913G	bohs-**S**/x1, 2-4kg S	-	√	√	√	√	√	√	√	√
24	RR0125	35763 21971G	bohs-**M**/x1, 1-2 kg S	-	√	√	√	√	√	√	√	√
25	RR0126	36219 21899G *TC*	bohs-**L**	x2	-	-	-	-	√	√ **d**	x2 **d**	√ **d**
26	RR0127	36328 21918G	bohs-**L**	√	-	-	-	-	-	-	-	-
27	RR0129	29975 21553G	bohs-**M**	x	√	√	√	√	√	√	√	√
28	RR0130	31745 22450	x1, 4 kg S	x2	-	-	-	√	√	√ **d**	x2 **d**	√ **d**
29	RR0131	30934 20760B	x1, flat 2-5 kg S	x2	-	-	-	√	√	√ **d**	x2 **d**	broken **d**
30	RR0132	36570 18020G	bohs-**M**	-	-	x	x	x	x	x	x	x
31	RR0133	36750 17840G	bohs-**M**-**L**	-	√	√	√	√	√	√	√	√
32	AF001-DLC 16	3524 2424*TC*	x1 lx-bedded psammite	x 2	√	√	√	√	√	√	√	√
33	AZ-MO2-DLC 15	375 189*TC*	x 1 regional leucosomes	-	√	√	√	√	√	√	√	√
34	AF02	3524 2424G *TC*	bohs-**L**/ x1, 4 kg S	√	√	√	√	√	√	√	√	√
35	AF/02/01-DLC3	3641 2171 *TC*	bohs-**V.S.**	√	√**3Ax2**	√	√	√	√	√	√	√
36	AF0204A	3631 2176	√	√	x	x	x	x	x	x	x	x
37	AF0205	No GR	x2, 4-5kg S	-	-	-	-	-	-	-	-	-
38	AF0206	No GR	bohs-**L**	-	-	-	-	-	-	-	-	-
39	AF0207-DLC1	Red Bay Quarry *TC*	x1, 4kg + S	x4	√**1Dx2**	√	√	√	√	√	√	√
40	AF0208	Eilean Carrach, G	bohs-**M**. Note v. red gr.	-	√	√	√	√	√	√	√	√
41	AF209	No GR	bohs-**M**	√	√	√	√	√	√	√ N/a	√	√
42	EMPA 6-DLC 4	364 218	x	√	√	x	x	√	√	√	√	√
43	JR1	355 216G	bohs-**S.** √ @ UCC	√	-	-	-	-	√ @ UCC	x	x **d**	x **d**
44	JR2	368 179G	bohs-**S.** √ @ UCC	x 2	-	-	-	-	x 2	√	√ **d**	√ **d**
45	JR3	297 222G	x	√	-	-	-	-	√	√	√ **d**	√ **d**
46	JR4	320 194G	√	√	-	-	-	-	√	√	√ **d**	√ **d**
47	JR5	356 192G	bohs-**S.** √ @ UCC	√	-	-	-	-	√	√	√ **d**	√ **d**
48	JR6	336 231G	bohs-**S.** √ @ UCC	√	-	-	-	-	√ @ UCC	x	x	x **d**
49	JR7	364 218G	x	√	-	-	-	-	√	√	√ **d**	√ **d**
50	JR8	332 177G	bohs-**S.** √ @ UCC	√	-	-	-	-	√	√	√ **d**	√ **d**
51	JR9	353 243G	x	√	-	-	-	-	√	√	√ **d**	√ **d**
52	JR10	307 191B	x	√	-	-	-	-	√	√	√ **d**	√ **d**
53	JR11	314 212G	x	√	-	-	-	-	√	√	√ **d**	√ **d**
54	JR12	280 227G	x	√	-	-	-	-	√	√	√ **d**	√ **d**
55	JR13	302 220G	x1 **S.** S √ @ UCC	√	-	-	-	-	√	√	√ **d**	√ **d**
56	JR14	348 243G	bohs-**S.** √ @ UCC	√	-	-	-	-	√	√	√ **d**	√ **d**
57	JR15	364 216G	bohs-**S.** √ @ UCC	√	-	-	-	-	√	√	√ **d**	√ **d**
58	JR16	296 192G	bohs-**S.** √ @ UCC	√	-	-	-	-	√	√	√ **d**	√ **d**
59	JR17	363 205G	x	x	-	-	-	-	√	√	√ **d**	√ **d**
60	JR18	365 187G	x	√	-	-	-	-	√	√	√ **d**	√ **d**
61	JR19	341 202G	x	√	-	-	-	-	√ **d**	√	√ **d**	√ **d**
62	JR20	349 192G	bohs-**S.** √ @ UCC	x 2	-	-	-	-	x2 a/b √ **d**	√	√ **d**	√a / √b **d**
63	JR21	326 230G	x	√	-	-	-	-	√ **d**	√	√ **d**	√ **d**
64	JR22	328 211G	bohs-**S.** √ @ UCC	√	-	-	-	-	√ **d**	√	√ **d**	√ **d**
65	JR23	309 186B	√	√	-	-	-	-	√ **d**	√	√ **d**	√ **d**
66	JR24	325 185B	x	√	-	-	-	-	√ **d**	√	√ **d**	√ **d**
67	JR25	268 140GA	bohs-**S.** √ @ UCC	√	-	-	-	-	√ **d**	√	√ **d**	√ **d**
68	JR26 a & b	268 140GB	x	√	-	-	-	-	x2 a/b √**d**	√	√ **d**	√a / √b **d**
69	JR27	278 140B	x	√	-	-	-	-	√ **d**	√	√ **d**	√ **d**
70	JR28?? Check	278 140GB	S & powders missing	√	-	-	-	-	x	x	√ **d**	√ **d**
71	JR30	309 189GA	Small S at UCC	√	-	-	-	-	√ @ UCC	x	√ **d**	√ **d**

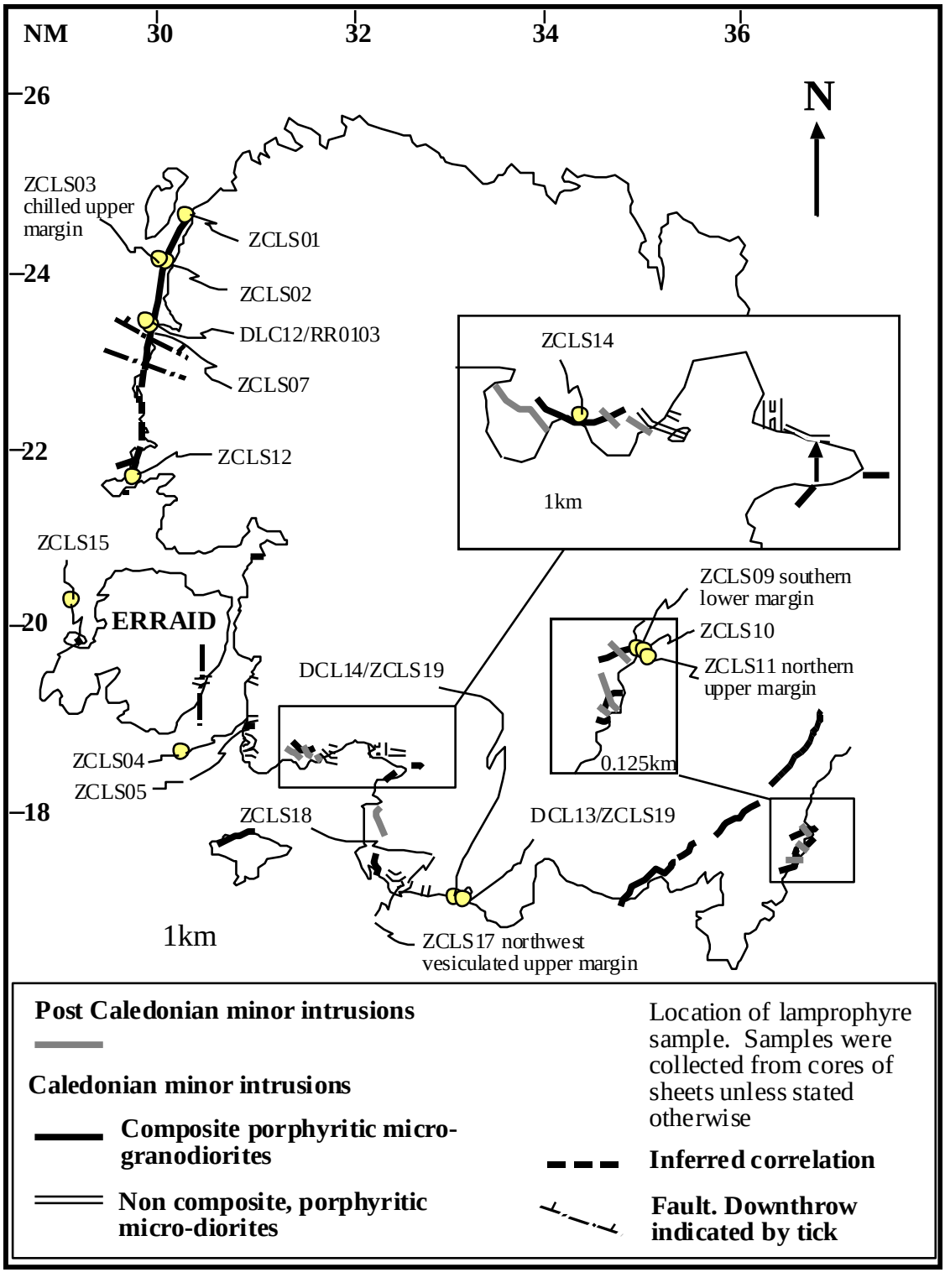
			CUTTING LAB				CRUSH. LAB				X-RAY LAB	
n =	Specimen no.	GR & Lithology	S = Specimen St. Andrews (comments)	T/S	Stub for T/S	Bits for Jaw crusher	Disposable **F(1)** Jaw crush	Min sep. **F(2)** Coarse	XRF **F(3)** Fine	QXRD **F(4)** V. Fine	Pressed pellet	Fusion disc/bead
72	JR31	309 189B	Small S at UCC	√	-	-	-	-	√ **d**	√	√ **d**	√ **d**
73	JR32	295 155G	bohs-**S.** √ @ UCC	√	-	-	-	-	√ @ UCC	x	√ **d**	√ **d**
74	JR33	295 155GA	x	√	-	-	-	-	√ **d**	√	√ **d**	√ **d**
75	JR34	308 148G	x	x	-	-	-	-	√ @ UCC	x	√ **d**	√ **d**
76	JR35	308 148B	x	√	-	-	-	-	√ **d**	√	√ **d**	√ **d**
77	JR36	306 189GA	x	√	-	-	-	-	√ **d**	√	√ **d**	√ **d**
78	JR37-DLC8-9F	306 189GB *TC*	Small stub only for T/S	√	√**8Fx1**	-	-	-	√ **d**	√	√ **d**	√ **d**
79	JR38	298 205B	x	√	-	-	-	-	√ **d**	√	√ **d**	√ **d**
80	JR39	298 205G	√ Small S at UCC	√	-	-	-	-	√ **d**	√	√ **d**	√ **d**
81	JR40	323 177G	bohs-**S.** √ @ UCC	√	-	-	-	-	√ **d**	√	√ **d**	√ **d**
82	JR41	323 177B	Small S at UCC	√	-	-	-	-	√ **d**	√	√ **d**	√ **d**
83	JR42	No GR	x	√	-	-	-	-	√ **d**	√	√ **d**	√ **d**
84	JR43	367 179S	x	√	-	-	-	-	√ **d**	√	√ **d**	√ **d**
85	JR44	361 218S	x	√	-	-	-	-	√ **d**	√	√ **d**	√ **d**
86	JR45	355 191G	x	√	-	-	-	-	√ **d**	√	√ **d**	√
87	JR46	278 140	x	√	-	-	-	-	x	x	x	x
88	JR47	318 252G	?	?	-	-	-	-	√	√	√	√ **d**
89	AZ001	31150 25090G *TC*	-	-	-	-	-	-	-	-	-	-
90	AZ002	30684 24946G	√	-	-	-	-	-	-	-	-	-
91	AZ003	31150 25090G	Largest ROMG S	-	-	-	-	-	-	-	-	-
92	AZ004-DLC2	30013 23997G *TC*	-	-	-	-	-	√	√	√	√	√
93	AZ005	30401 24008G *TC*	bohs-**L**/ x1, 2-3 kg	-	√	√	√	√	√	√	√	√
94	AZ006	30049 24034G	√	-	-	-	-	-	-	-	-	-
95	AZ007	30162 24201G	-	√	√	√	√	√	√	√	√	√
96	AZ008	30154 24234G	√	-	-	-	-	-	-	-	-	-
97	AZ009	33028 25030G	Large S on shelf	-	-	-	-	-	-	-	-	-
98	AZ010	33994 24999G	bohs-**L**/x1-2 kg sample	-	√	√	√	√	√	√	√	√
99	AZ011	34871 24907G	Large S on shelf	-	-	-	-	-	-	-	-	-
100	AZ013	31977 24045G	Large S on shelf	-	-	-	-	-	-	-	-	-
101	AZ014	33260 24172G	bohs-**M**	-	√	√	√	√	√	√	√	√
102	AZ015	34094 24355G	bohs-**M**	-	√	√	√	√	√	√	√	√
103	AZ016	36044 16980G	bohs-**L**	-	√	√	√	√	√	√	√	√
104	AZ017	36184 18054G	Large S on shelf	-	-	-	-	-	-	-	-	-
105	AZ018	30954 20053G	Large S on shelf	-	-	-	-	-	-	-	-	-
106	AZ019-DLC6	31038 20933G	√	-	√	√	√	√	√	√	√	√
107	AZ020	34029 17302G	bohs-**L**/x1, 3-5 kg S	-	√	√	√	√	√	√	√	√
108	AZ022	30140 21980G	Large S on shelf	-	-	-	-	-	-	-	-	-
109	AZ023	29701 21739G	bohs-**S**	√	√	√	√	√	√	√	√	√
110	AZ024	29529 21661G	√	√	-	-	-	-	-	-	-	-
111	AZ025	29581 21575G	bohs-**S**	x 2	√	√	√	√	√	√	√	√
112	AZ026-DLC5	29984 23041G	bohs-**S**	√	√	√	√	x	√	√	√	√
113	AZ027	32018 22887G	Large S on shelf	-	-	-	-	-	-	-	-	-
114	AZ028	31189 22947G	Large S on shelf	-	-	-	-	-	-	-	-	-
115	AZ029	31067 21913G	bohs-**L**	-	√	√	√	√	√	√	√	√
116	AZ030	33124 21804G	√	-	-	-	-	-	-	-	-	-
117	AZ031	31909 22221G	Large S on shelf	-	-	-	-	-	-	-	-	-
118	AZ032	32209 20988G	bohs-**S.** √ @ UCC	-	-	-	-	-	-	-	-	-
119	AZ033	32296 19959G	Large S on shelf	-	-	-	-	-	-	-	-	-
120	AZ034	33203 20045G	Large S on shelf	-								
121	AZ035	31940 19099G	bohs-**L**	-	√	√	√	√	√	√	√	√
122	AZ036	33031 18930G	Large S on shelf	-	-	√	√	√	√	√	√	√
123	AZ037	34016 19221G	√	-	-	√	√	√	√	√	√	√
124	AZ038	30016 20007G	√	-	-	-	-	-	-	-	-	-
125	AZ039	28966 19862G	Large S on shelf	-	-	-	-	-	-	-	-	-
126	AZ040	29223 19211G	bohs-**M**	x2	√	√	√	√	√	√	√	
127	AZ041	30222 19009G *TC*	Large S on shelf	-	-	-	-	-	-	-	-	-
128	AZ042	35077 18068G	Large S on shelf	-	√	√	√	√	√	√	√	√
129	AZ043	34080 18000G	√	-	-	-	-	-	-	-	-	-
130	AZ044	32398 16973G	Large S on shelf	-	-	-	-	-	-	-	-	-
131	AZ045	32894 17008G	Large S on shelf	-	-	-	-	-	-	-	-	-
132	AZ046	350 221	√	-	-	-	-	-	-	-	-	-
133	AZ047	341 221	√	-	√	√	√	√	√	√	√	√
134	AZ049	339 209	√	-	-	-	-	-	-	-	-	-
135	AZ050	348 207	√	-	√	√	√	√	√	√	√	√
136	AZ051	358 221	√	-	-	-	-	-	-	-	-	-
137	AZ052	359 209	√	-	-	-	-	-	-	-	-	-
138	AZ053	350 199	√	-	√	√	√	√	√	√	√	√
139	AZ055	348 229	√	-	√	√	√	√	√	√	√	√
140	AZ056	360 229	√	-	-	-	-	-	-	-	-	-
141	AZ057	349 169	√	-	-	-	-	-	-	-	-	-
142	AZD01	31162 20004	bohs-**S**	-	√	√	√	√	√	√	√	√
143	AZD02	31068 20883	bohs-**V.S**	x2	√	√	√	√	√	√	√	√
144	AZD03	33887 17282	x1, 2 kg S	-	√	√	√	√	√	√	√	√
145	AZD04	33803 16902	bohs-**V.S**	-	√	√	√	√	√	√	√x2	√

			CUTTING LAB				**CRUSH. LAB**				**X-RAY LAB**	
n =	Specimen no.	GR & Lithology	S = Specimen St. Andrews (comments)	T/S	Stubb for T/S	Bits for Jaw crusher	Disposable **F(1)** Jaw crush	Min sep. **F(2)** Coarse	XRF **F(3)** Fine	QXRD **F(4)** V. Fine	Pressed pellet	Fusion disc/bead
146	ZCLS01	30340 24621	√	-	-	-	-	-	-	-	-	-
147	ZCLS02	30078 24124	√	√	√	-	-	-	-	-	-	-
148	ZCLS03	30079 24125	√	-	-	-	-	-	-	-	-	-
149	ZCLS04	30913 18912	√	-	-	-	-	-	-	-	-	-
150	ZCLS05	30949 18821	√	-	-	-	-	-	-	-	-	-
151	ZCLS07	29887 23337	√	-	-	-	-	-	-	-	-	-
152	ZCLS09	36783 17631	√	-	-	-	-	-	-	-	-	-
153	ZCLS10	36781 17637	√	-	-	-	-	-	-	-	-	-
154	ZCLS11	36782 17638	√	-	-	-	-	-	-	-	-	-
155	ZCLS12	29762 21662	*TC*	-	-	-	-	-	-	-	-	-
156	ZCLS14	31569 18482	√	-	-	-	-	-	-	-	-	-
157	ZCLS15	29085 19805	bohs-**V**.**S**, x1, 2-4 kg	-	√	√	√	√	√	√	√	√
158	ZCLS17-MARGIN	32426 16996	bohs-**M**/x1, 2-4 kg S	-	√	√	√	√	√	√	√	√
159	ZCLS18-CORE OF17	32677 16989	bohs-**L**-**M**	-	√	√	√	√	√	√	√	√
160	ZCLS19c - DLC 13	347 168	-	-	-	√	√	√	√	√	√	√
161	ZCLS19c - DLC 14	347 168	-	-	-	√	√	√	√	√	√	√
162	AZ005 A	30401 24008G	√	-	-	√	√	√	√	√	√ **d**	-
163	AZ005 B	30401 24008G	√	-	-	√	√	√	√	√	√ **d**	-
164	AZ005 C	30401 24008G	√	-	-	√	√	√	√	√	√ **d**	-
165	AZ005 D	30401 24008G	√	-	-	√	√	x	√	√	√ **d**	-
166	AZ005 A+B	30401 24008G	√	-	-	√	√	√	√	-	√ **d**	-
167	AZ005 C+D	30401 24008G	√	-	-	√	√	√	√	-	√ **d**	-
168	AZ005 A+B+C+D	30401 24008G	√	-	-	√	√	√	√	-	√ **d**	-
169	JR29 b	278 140 GA	-	-	-	√	√	√	√	√	√	√
170	AZEN01/4/04	30724 19113 *TC*		√								
171	AZEN02/4/04	30725 19108	-	-								
172	AZEN03/4/04	30712 19101	-	-								
173	AZEN04/4/04	30700 19093		-								
174	AZEN05/4/04	30669 19083	-	-								
175	AZEN07/4/04	30945 18825	-	-								

A5.2 Sample stations map.



A5.3 Lamprophyre sample stations map.



Appendix Six
PUBLISHED MATERIAL

Introduction

Re-mapping of the whole intrusion during 2005-2006 field-seasons provided the opportunity to produce a field descriptive examination with emplacement model for the ROMG in the Scottish Journal of Geology. This published article clearly assisted in improving the geological knowledge of the area considered, providing a stimulus for Mcleod *et al*. (2011) to further characterise magma mixing within the ROMG and Petronis *et. al*. (2012) to provide a critique on the emplacement model proposed in Zaniewski *et al.* (2006).

My supervisors are thanked for rigorously keeping me on track to publish an academic paper during my PhD as one of my targets. Prof. Anthony Harris is also thanked for his insights into the Moine Supergroup as per his contribution in Zaniewski *et al.* (2006).

The following paper is thus presented within this part of the appendix:

ZANIEWSKI, A., REAVY, R.J. & HARRIS A.L. 2006. Field relationships and emplacement of the Ross of Mull Granite (ROMG), Argyllshire. *Scottish Journal of Geology* **42**, 179-189.

Field relationships and emplacement of the Caledonian Ross of Mull Granite, Argyllshire

A. Zaniewski[1], R. J. Reavy[1] & A. L. Harris[2]

[1]*Department of Geology, National University of Ireland, Cork, Ireland*
[2]*School of Earth, Ocean and Planetary Sciences, University of Cardiff, Cardiff, CF10 3YE, UK*

Synopsis

The Ross of Mull granite (ROMG) occupies the largest part of the pre-Tertiary inlier of the Ross of Mull peninsula. Previous ideas that the Moine Thrust crops out in the Sound of Iona have now been discounted. Recent models have proposed that: (a) the Sound of Iona Fault and the associated mylonites on Iona are part of a steeply inclined extensional fault throwing down to the ESE, bringing high grade Sgurr Beag or Knoydart Nappe Moine rocks to the same erosion level as the foreland units on Iona; and (b) one of the main Caledonian thrusts must extend to a point no more than 10–15 km from the projected trace of the Great Glen Fault. A hypothetical intersection would occur SW of Mull and it is proposed here that the intersection of these two structures has been the dominant control on the siting of the ROMG. In this model, magmas using this intersection as an ascent site were emplaced eastwards as flattish sheets within an overall east-dipping extensional zone that has high-grade Moine lithologies in its hanging wall. The present erosion level provides a section through a granitoid complex from a roof zone with flattened diorite enclaves and abundant country rock xenoliths to a clearly demonstrable westward-dipping floor; a situation which may be unique in the British Caledonian granitoid complexes.

Introduction

The Ross of Mull and Iona pre-Tertiary inlier is an important area where the relationships between Caledonian rocks and their foreland are well exposed and can be critically examined (Fig. 1).

The significance of this area is its close proximity to what are two of the largest structures in Scotland: the Great Glen Fault which is inferred to run some 20 km offshore to the south of the inlier, and the Moine Thrust or a structure replacing or displacing the Moine Thrust which, it has long been realized, must pass through the Sound of Iona. Its critical structural position in this respect is commented on in this paper, together with a description of the field relationships of the components of the Ross of Mull granite (ROMG: the intrusive igneous rocks that constitute the complex range in composition from diorite through granodiorite to granite; the term ROMG is proposed here as a simple term to cover all these modal varieties). A hypothetical role for the major structures in the channelling and emplacement of the magmas making up the ROMG is discussed.

The ROMG is located at the western end of the Ross of Mull peninsula and occupies an onshore area of the order of 70–80 km^2. However the complex extends offshore to the SW beyond the Torran Rocks (Fig. 2) so the actual total area could be as much as 140km^2 (Highton 2001); the onshore outcrop could represent only about half of the actual areal extent of the ROMG.

The earliest research on the area was published by Cunningham-Craig (1911), one of the classic Highland Geological Survey of Scotland Memoirs. Despite the excellent coastal exposure (which facilitated an extensive industry of granite quarrying), little research was carried out on the granite, its internal variation and contact relations for close to 90 years. Harris & Highton (1999) compiled various unpublished maps from a variety of sources and compiled British Geological Survey Sheet 43S. Other recent relevant research was carried out by Rock & Hunter (1987) on the minor intrusions, and by Petford *et al*. (1996); Pugliese & Petford (2001) who used the diorite component within the ROMG to model melt infiltration and topology within mafic microgranular enclaves (MMEs). Highton (2001) described detailed field locations of small selected areas of specific petrological interest.

This paper stems from detailed remapping of the entire complex which has resulted in reclassification of all the components present. The internal and contact field relations are documented and an emplacement model is proposed within a regional tectonic framework.

The western contact of the granite is with Iona Group (Torridonian?) sediments which were originally unconformable on, but are now mainly in steeply inclined tectonic contact with, Lewisian (late Archaean) gneisses. The latter have been described by Bailey & Anderson (1925) and Fraser (1977). The gneisses, the steeply dipping mylonite zones that occur within both them and along much of their contact with the Iona Group metasediments, and the metasediments themselves, have been thermally metamorphosed by the granite.

To the east, the complex intruded amphibolite-facies Moine Supergroup rocks (Fig. 3), xenoliths of which

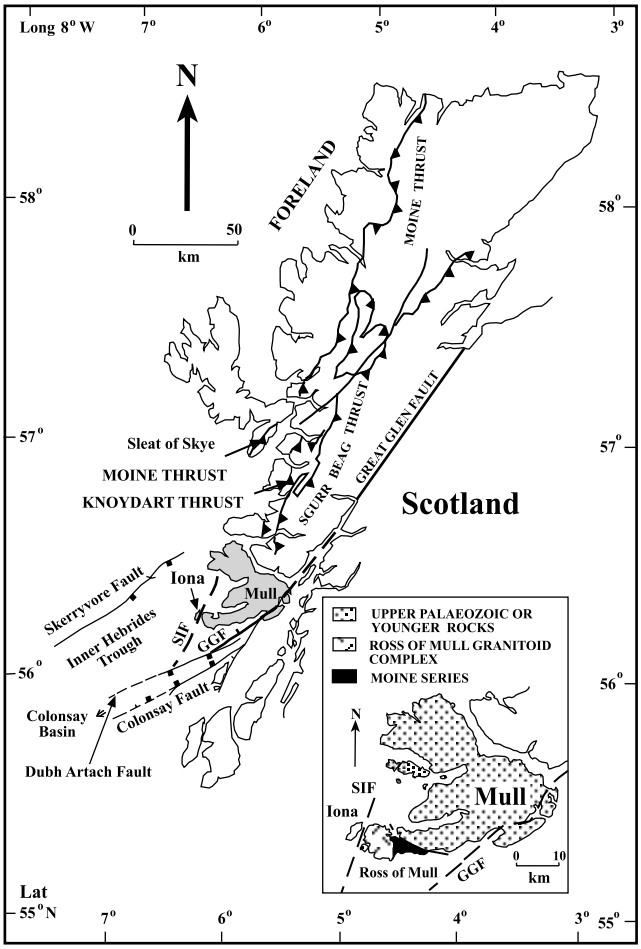


FIG. 1. Major Caledonian faults north of the Great Glen Fault (GGF). SIF, Sound of Iona Fault. Inset: general geological map of Mull and Iona (adapted from Potts *et al.* 1995; Pharaoh *et al.* 1996).

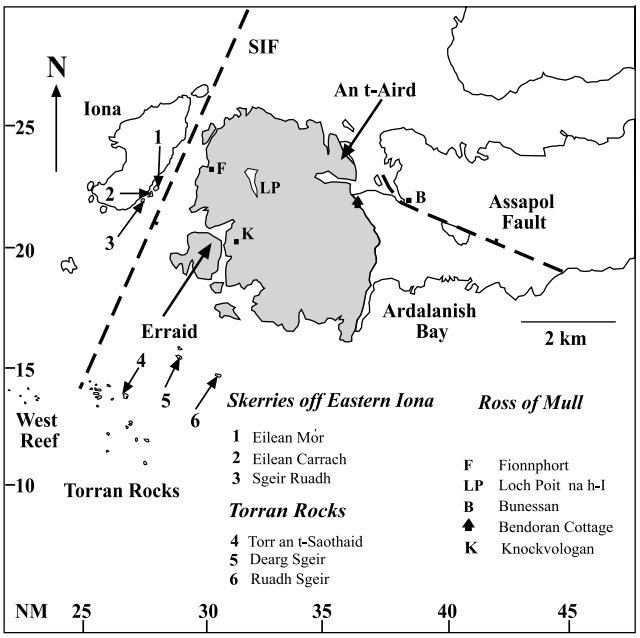
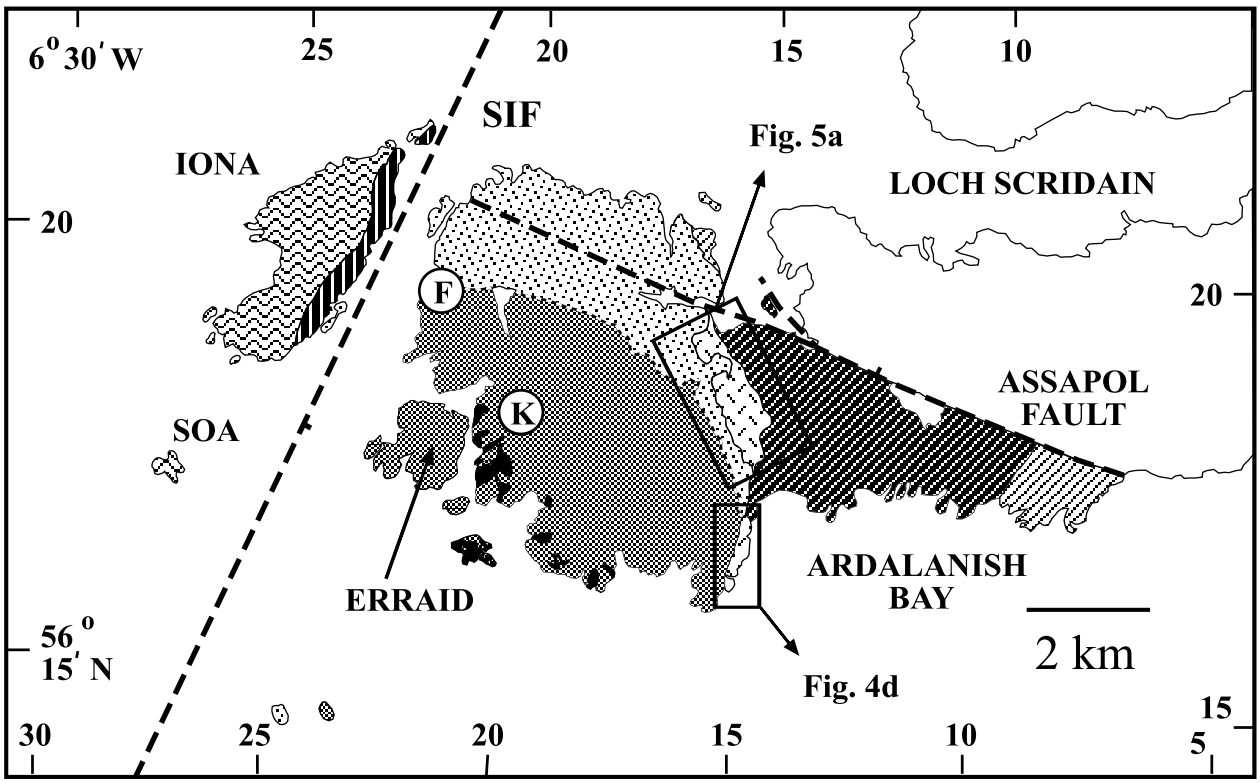


FIG. 2. Generalized map depicting localities on the Ross of Mull, islands adjacent to the western contact of the granite (off Iona) and the series of offshore islands within the centre of the ROMG (Torran Rocks).

persist as far west as the Sound of Iona. The lithostratigraphy, structural and metamorphic history of the Ross of Mull Moines have been described by Holdsworth *et al.* (1987), who established the presence of both the Morar (=Shiaba) and Glenfinnan (=Assapol) Groups. They adduced evidence for polyphase deformation (D1–D3) that culminated in the formation of the upright, kilometre-scale, D3 Assapol Synform that contains the latter group in its core. The synform, which plunges gently SSW, folded rocks that had already suffered at least two phases of isoclinal folding and amphibolite-facies regional metamorphism. Its ESE limb is steep to vertical, while its NW limb dips SE at steep to moderate angles.

The presence of Moine rocks in juxtaposition with Lewisian and its Iona Group cover rocks across the Sound of Iona led to the suggestion (Cunningham-Craig 1911) that the trace of the Moine Thrust must lie in the Sound. The Moine pelitic and semipelitic rocks of suitable composition had developed regional kyanite and/or staurolite (Cunningham-Craig 1911; Holdsworth *et al.* 1987; Wheeler *et al.* 2004) before the ROMG was emplaced. Holdsworth *et al.* (1987) concluded that, here, the regional metamorphic mineral parageneses implied an anomalously high grade for Moine rocks adjacent to the Moine Thrust. To explain this anomaly they drew on the foreland-propagating thrust model proposed by Barr *et al.* (1986). This model invoked Scandian thrust sheets of progressively higher metamorphic grade, the Moine, Knoydart and Sgurr Beag nappes, being emplaced one above the other. Thus the presence of high grade Moine rocks adjacent to the foreland rocks of Iona implies a significant vertical displacement in the Sound of Iona which must have post-dated the thrusting. Subsequently, the nature and possible significance of a major fault in the Sound of Iona, originally separating the Iona Group with its adjacent and older Lewisian Complex from the Moine on the Ross of Mull to the east, were discussed by Potts *et al.* (1995). They concluded that the Sound of Iona Fault (SIF) and the associated mylonites on Iona are related to a steeply inclined extensional fault system. This threw the Moine Nappe down to the ESE and brought higher grade Sgurr Beag or Knoydart Nappe Moine down to the same structural level as the Caledonian foreland on Iona. Because the Iona Group, Moine schists and Iona mylonites are all thermally metamorphosed by the ROMG, the age of this extensional fault system can be constrained to between 425 Ma, the inferred age of the Moine Thrust (Kelley & Powell 1985), and 414 ± 3 Ma (Halliday *et al.* 1979), the age of the complex.

Although undated, the Assapol Synform and its related minor to intermediate-scale folds and crenulation cleavages probably originated during the late Silurian (Scandian) thrusting. The earlier structures and the metamorphic peak may be late Proterozoic (Knoydartian) or early Ordovician (Grampian) in age. The relative age of the cleavage of the Iona Group metasediments and the deformation which gave rise to the Assapol Synform is unknown, but they may have



FORELAND SEQUENCE

Iona Group
Lewisian Complex

MOINE SUPERGROUP

Assapol Group
Shiaba Group

ROCKS OF THE MULL IGNEOUS COMPLEX (PALAEOCENE)

Tertiary lavas cut by dolerite intrusions

ROCKS OF THE CALEDONIAN ROSS OF MULL GRANITE

RM1: Equigranular biotite granite

RM1a: Leucocratic marginal muscovite-biotite granite

RM2: Alkali feldspar-megacrystic granite/granodiorite

Diorite

Symbols

Fault, crossmark on downthrow side

Geological boundaries

(Observed/ inferred)

(Gradational contact between RM1 & RM2)

F Fionnphort

K Knockvologan

FIG. 3. Solid geological map of the western end of the Ross of Mull (revised from Sheet 43S).

been broadly contemporary, albeit formed at very different crustal levels on either side of the present position of the SIF. Cleavage/bedding relationships in the Iona Group metasediments point to a synform to the ESE (Potts *et al.* 1995), which may have been a footwall synform to the Moine Thrust, while the Assapol

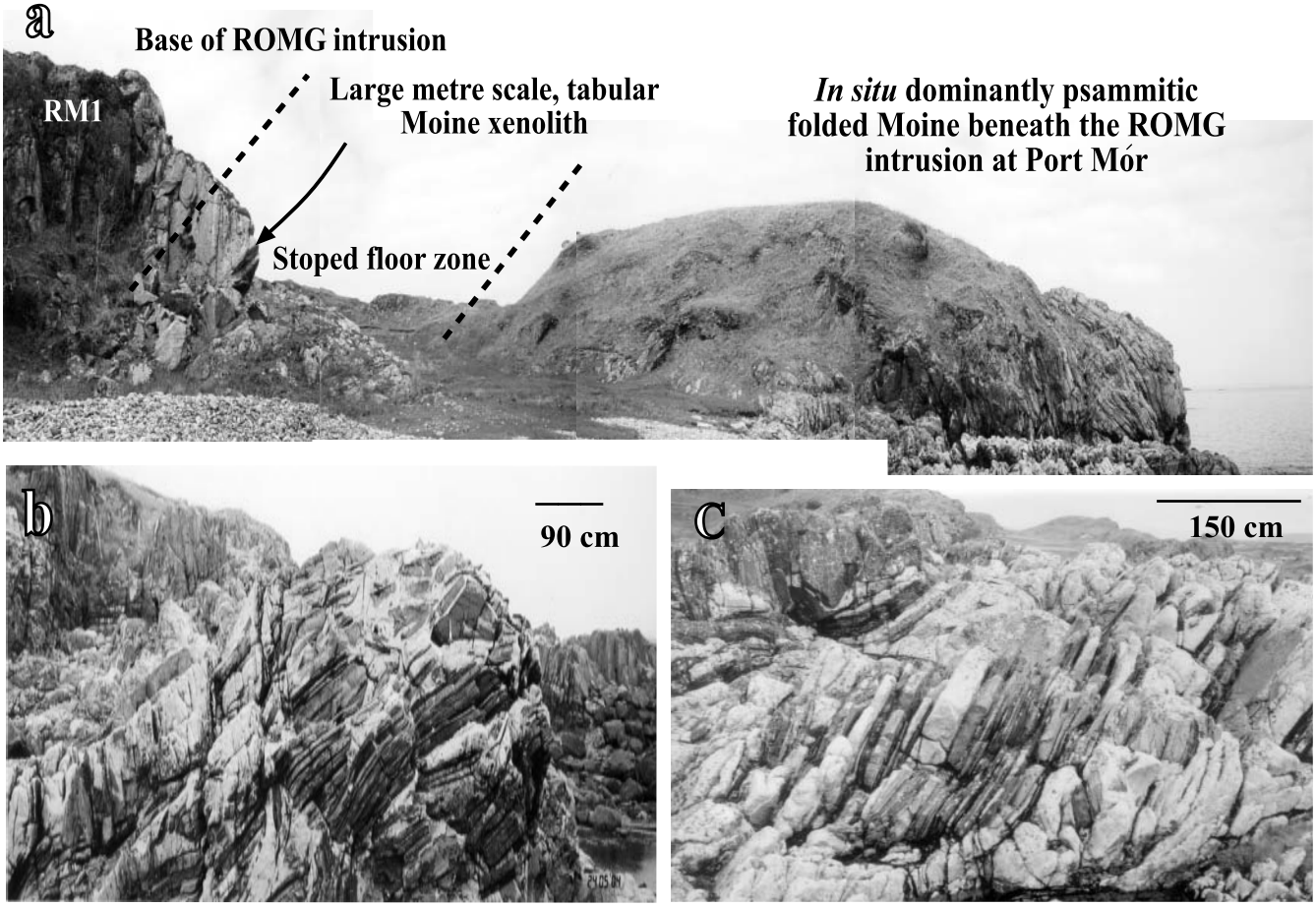


FIG. 4. (a) A west–east 125 m photographic cross-section at A'Bhulaidh [NM 367 181] depicting the base of the intrusion and the floor zone containing extremely tabular psammitic Moine xenoliths (centimetre to metre scale). The Moine floor pendants retain similar geometry to that of the *in situ* country rock. (b) Looking approximately towards 010 from NM 367 175 at a west–east oblique section through the floor zone. Note the consistent approximate north–south strike and WSW dip geometries within the xenoliths (analogous to thrust imbricate type structures in places). These features are consistent with magmas sheeting in from the WSW. (c) General view of granite sheets passively injecting along bedding-parallel schistosity planes in folded psammites at the west side of Ardalanish Bay [NM 366 176]. (d) Simplified geological map of the southern–eastern contact zone at Ardalanish Bay.

Synform is a hanging-wall fold probably formed during hanging-wall shortening late in the Scandian deformation episode.

Because these conclusions preclude the presence, at the present erosion surface, of a low-angle east-dipping (Moine) thrust in the Sound of Iona, the suggestion by Beckinsale & Obradovich (1973) that the magma feeding the ROMG was emplaced from the east, along the pathway provided by the thrust zone, is no longer tenable. It seems inevitable that one or more of the main Caledonian (Scandian) thrusts underlie, or are cut by, the ROMG at depth and must extend in subcrop to the Great Glen Fault zone, while the plane of the SIF carrying the trace(s) of its intersection with the thrust(s), could itself be inferred to intersect the Great Glen Fault zone some 30 km SSW of Iona. The possible implications for magma siting and ascent of this fault configuration will be addressed later.

Field relations: the envelope

The western contact of the granite with the Iona Group metasediments, is exposed on the skerries of Eilean Carrach and Sgeir Ruadh [277 224] (Fig. 2), just off the east coast of Iona, and immediately adjacent to cordierite-bearing, hornfelsed Iona Group sediments (Cunningham-Craig 1911; Potts *et al.* 1995). The eastern contact of the granite with Morar (=Shiaba) and Glenfinnan (=Assapol) Group metasediments can be traced from An-t-Aird [355 235] in the north, past Bendoran Cottage [364 218] to the west side of Ardalanish Bay on the south coast [367 177] (Highton 2001). It is well exposed and displays a range of spectacular structural and metamorphic features which vary with lithology and with the pre-granite deformation and metamorphic history of the Moines in the contact zone. At the west end of Ardalanish Bay [e.g. 376 177] the floor of the intrusion is in well exposed contact with Glenfinnan (=Assapol) Group psammites and an intricate zone, up to 0.5 km wide, of sheeting, wedging and stoping is developed (Fig. 4).

There is a contact zone, gradational from psammites, probably still *in situ* but with abundant granite sheets, to granite packed with orientated tabular psammite xenoliths, to granite with abundant but discrete psammite xenoliths. There is minimal field evidence for

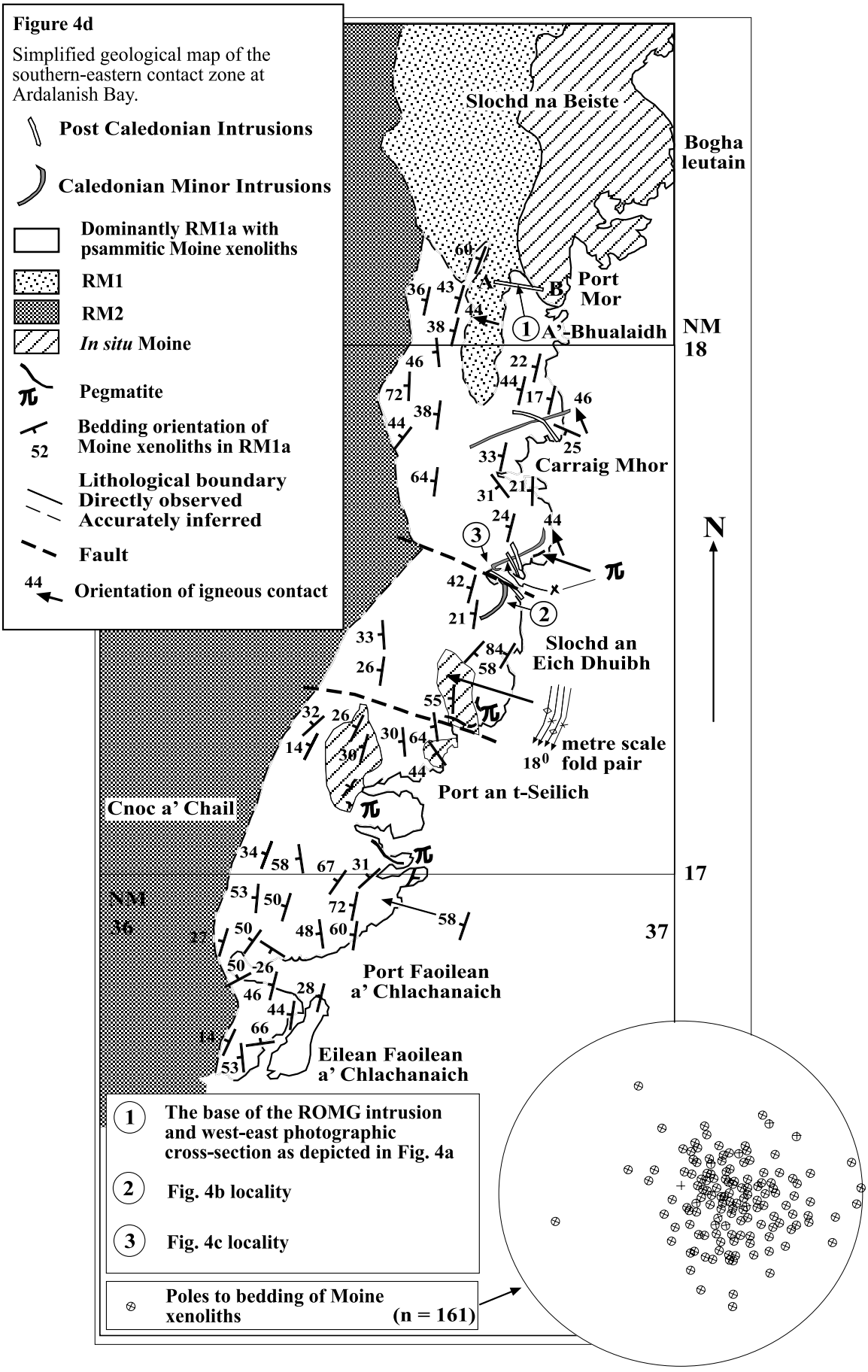


Figure 4d

Simplified geological map of the southern-eastern contact zone at Ardalanish Bay.

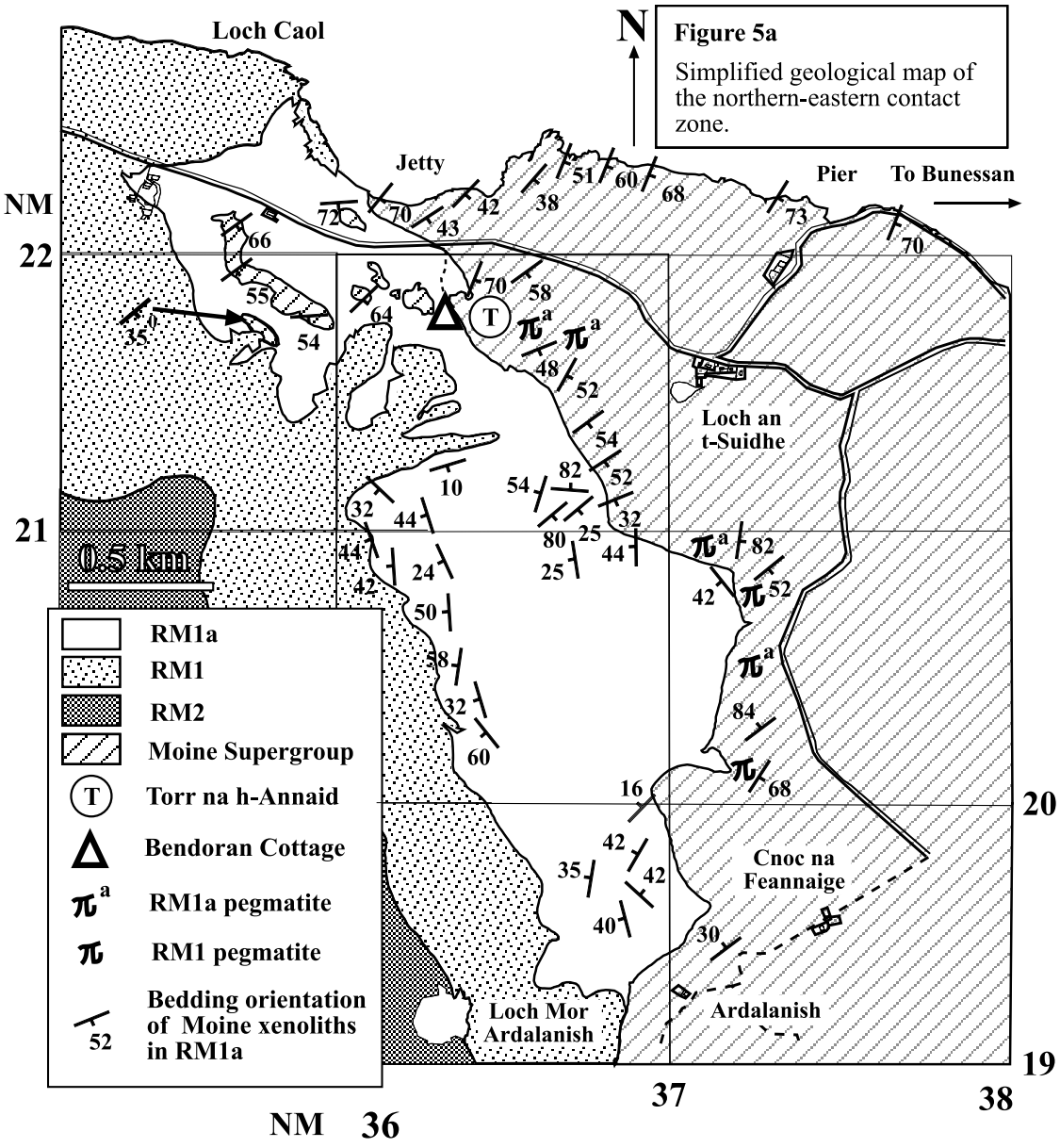




FIG. 5. (a) Simplified geological map of the northeastern contact zone. (b) *In situ* contact migmatites at Torr na h-Annaid [NM 364 218] providing strong evidence for granite envelope interaction; exact location of photo is indicated by circled 'T' in (a).

country-rock *in situ* anatexis in this locality as the Moine lithologies are predominantly psammitic. The granite here is highly heterogeneous; both RM1 and RM1a (see below for classification) are present. As will be detailed below, RM1a is believed to represent a melt of a pelitic Moine protolith.

By contrast, on the north side of the peninsula near Bendoran [364 218] (Fig. 5), the Glenfinnan (=Assapol) Group country rocks are largely pelitic, and there is abundant evidence of granite-induced anatexis of suitable Moine lithologies with the development of contact migmatites. Here the thermal overprint of regional parageneses is best developed, recently extensively studied by Wheeler *et al.* (2004). The contact is marked by a complex migmatitic zone of locally derived granite with stoped blocks, xenoliths and rafts of pelitic hornfels. Bodies of leucocratic granite enclose fragments of refractory garnet–biotite- and Al-silicate-rich restite which commonly carry relict schistosity. The larger pelitic bodies, mapped within the granite near its margin, are probably still attached to the envelope. The orientation of penetrative foliations dipping SSE at moderate angles is consistent between adjacent bodies, and similar to that in country-rock pelites adjacent to the pluton. The white granitoid (RM1a, see below) within this migmatite zone is characterized by white K-feldspar, in contrast to the pink K-feldspar seen in the facies which comprise the bulk of the body. White granitoid is also seen elsewhere in the ROMG but is localized around Moine xenoliths suggesting that the white facies results from local interaction with the envelope rather than being an independent intrusive facies.

Numerous inclusions and blocks of Moine metasediment, completely surrounded at crop by granite, are a conspicuous feature of many parts of the complex. The orientation of tectonic structures and fabrics in the larger bodies is sufficiently coherent to suggest that they are essentially *in situ*, probably being attached to the roof of the intrusion. This conclusion is supported by the ghost preservation of the Morar (=Shiaba)/Glenfinnan (=Assapol) lithostratigraphic boundary by xenoliths in the granite (Holdsworth *et al.* 1987).

Field relations: the ROMG

The complex is heterogeneous and three distinct facies of granitoid and a synplutonic diorite component have been identified (Fig. 3).

Granitoids

The three granitoid facies are: (1) an equigranular biotite granite, here termed RM1 (=G_{RM1} on the British Geological Survey, Ross of Mull (43 S) Sheet; Harris & Highton 1999); (2) a leucocratic, marginal muscovite–biotite granite, RM1a (=G_{RM1a}) which forms a white contact facies up to *c.* 800 m wide along the eastern contact and locally adjacent to pelitic Moine xenoliths; and (3) an alkali feldspar–megacrystic biotite granite/granodiorite RM2 (=to both G_{RM2} and G_{RM3}). G_{RM3} is

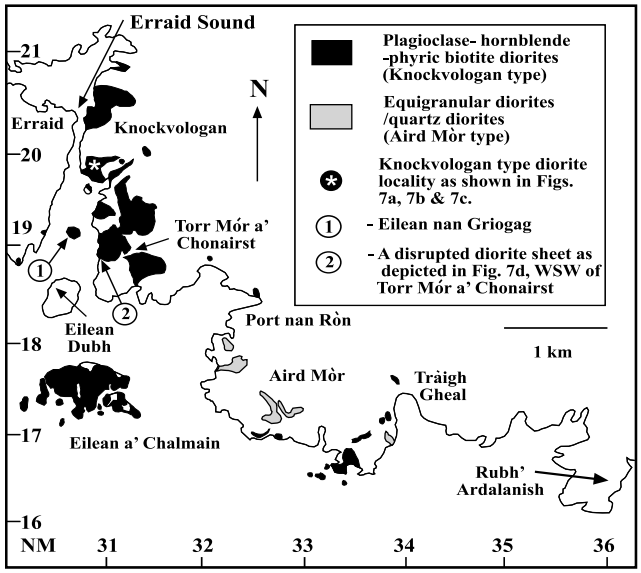


FIG. 6. Solid geological map illustrating the distribution and type of diorite intrusions within the ROMG.

not now recognized as an independent facies; contacts between RM1 and RM2 are gradational over *c.* 1 km and hence the intrusion is here described as 'zoned' rather than 'composite'.

RM1 The outer facies, RM1, is an equigranular, quartz-rich, biotite granite in which plagioclase commonly appears not to be present in hand specimen. Thus field petrography alone would suggest that this facies is modally an alkali feldspar granite; however, thin-section petrography reveals that plagioclase constitutes 20–25% of the felsic minerals, by mode, but is frequently reddened. Sparse hornblende occurs as isolated euhedral crystals; allanite and titanite are usually present in variable amounts (J. Faithfull pers. comm.). Mafic inclusions are rare and pervasive fabrics are absent. This facies is in contact with the country rocks at the western and eastern margins of the complex, although there is the complication of the widespread development of RM1a along much of the eastern contact where pelitic country rocks are involved.

RM1a Thin-section work reveals an equigranular quartz-rich rock (30% on average), with generally equal proportions of plagioclase and perthitic microcline. All the abundant deep red biotite crystals are rich in inclusions of zircon and zoned and non-zoned apatite. Muscovite occurs in clusters with biotite or as isolated crystals. At Bendoran, by contrast with Ardalanish, muscovite is more abundant in hand specimen. This is the only facies lacking titanite.

RM2 RM1 grades into RM2. A north–south traverse, e.g. from Fionnphort [302 232] to Knockvologan [312 190], shows the gradual change in modal mineralogy (Fig. 3). The RM2 facies not only contains more plagioclase and biotite and less quartz than RM1, but also has rare hornblende. The most striking feature of RM2 is the development of megacrystic alkali feldspars which range in size from 8–15 mm.

Thin sections show the megacrystic phase to be orthoclase microperthite. Sericitization of anhedral–

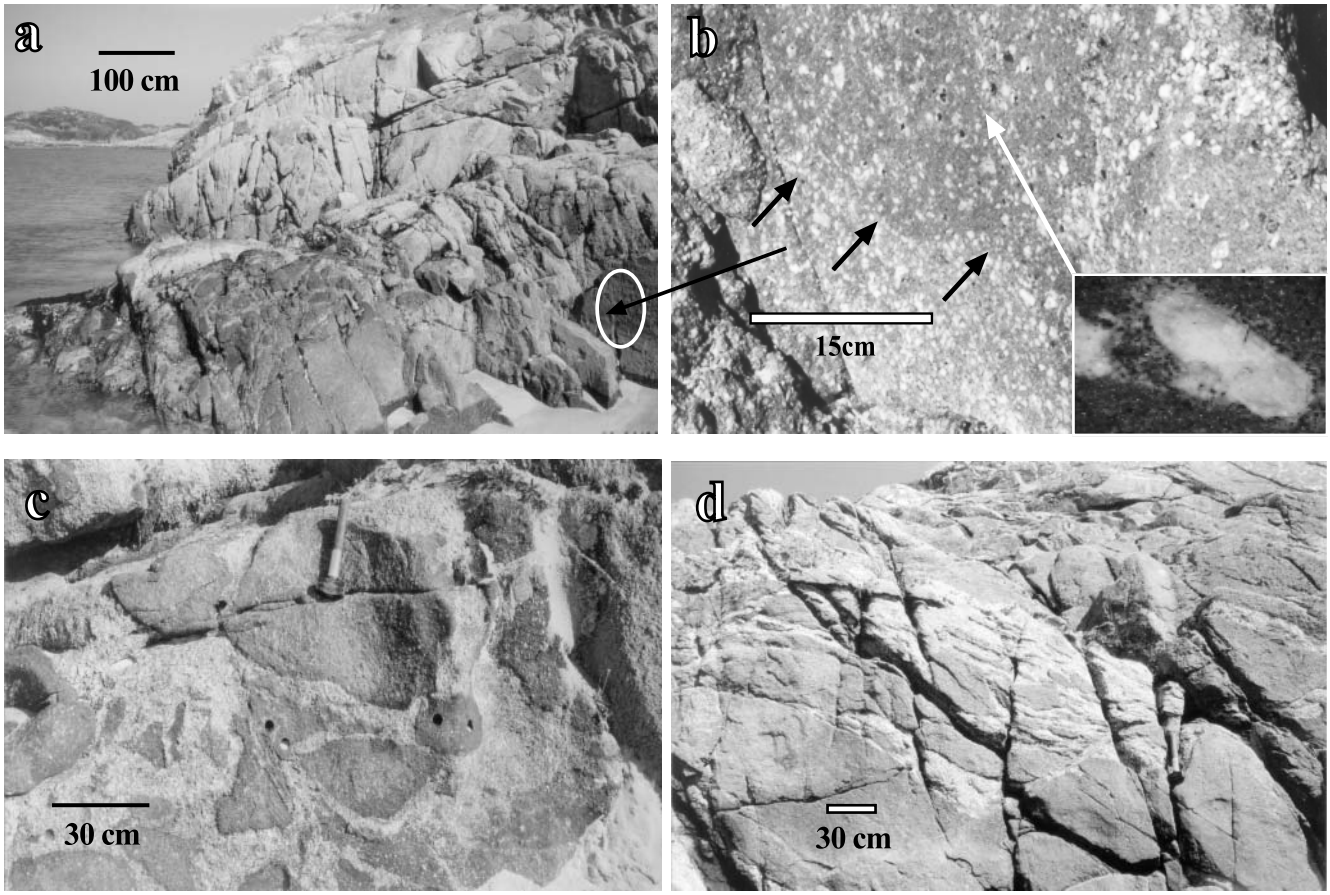


FIG. 7. (a) Typical example of the Knockvologan type facies of diorite and related mafic microgranular enclaves (MMEs) within the Erraid Sound at Knockvologan beach [NM 308 182]. The island due west in the background is Erraid. (b) Further inspection of the intrusion in (a) illustrates the complexity of acid–basic interaction at the microscale (in the form of mixing textures such as rapakivi feldspars with amphibole inclusion trails, quartz ocelli and feldspar mantling hornblende) but also basic–basic interaction exhibited here by double MMEs. The black arrows denote the cuspate mingled interface between the two MMEs which is characterized by high concentrations of alkali feldspar xenocrysts, with some cross-cutting this contact at the perpendicular, indicative of dynamic phenocryst exchange. The feldspar xenocryst inset is 14 mm. (c) Globular MMEs at Knockvologan beach derived from the major diorite body shown in (a). MMEs have differing proportions of xenocrysts but all are porphyritic. (d) Example of a disrupted diorite body with cuspate xenocrystic MMEs WSW of Torr Mor a' Chonairst [NM 309 188] (refer to Fig. 6). The bulk distribution dip 20–30° ESE (main elongation direction in the photo) and a vague internal fabric is defined by an orientation of xenocryts running in the same direction.

subhedral plagioclase cores is very variable; some strongly zoned crystals are very fresh while other adjacent crystals are highly altered, indicative of batch mixing processes (Grogan & Reavy 2002). Biotite is dispersed throughout the rock but also occurs as aggregates, associated with Fe–Ti oxides. Primary hornblende, where present, has been occasionally replaced by biotite. Acicular and anhedral apatite, Fe–Ti oxides and euhedral lozenge-shaped titanite (1–2 mm) are common accessories. Zoned allanites and acicular rutile (restricted to chloritized biotite) are rare and zircon commonly occcurs as inclusions in biotite.

Diorites

In the western and southern parts of its outcrop on the Ross of Mull and offshore on the Torran Rocks, RM2 is injected by a series of diorites (Fig. 6).

This area displays, on excellent coastal exposures, some of the best evidence of acid–basic interaction displayed by any Scottish Caledonian granitoid. The western extent of the zone is quite sharply defined by the tidal inlet of Erraid Sound [307 202], which may contain a fault. South of Knockvologan this facies is well exposed on the coast at the east side of Erraid Sound [e.g. 307 197] and on the tidal islands of Eilean nan Griogag [307 191] and the unnamed skerries to the south [e.g. 307 309]. Brief visits have revealed that the islands of Eilean Dubh [305 185] and Eilean a'Chalmain [307 175] and the Torran rocks of Dearg Sgeir [295 156], Ruadh Sgeir [307 149] and Torr an t-Saothaid [277 146] lie within this zone (Fig. 3). Other components are seen at the east end of Port nan Ròn [325 184] and around Aird Mór [323 177] (Fig. 6). At all these localities, there is abundant evidence that hybrid diorite melts have been emplaced into partially crystallized, cooler, host megacrystic granite, producing great petrological variability. Certain areas, such as the east side of Erraid Sound and Eilean a' Chalmain (Fig. 6), are dominated by diorite and are interpreted as representing sites of injection of discrete diorite pulses; over much of the rest of the area of acid–basic interaction, bodies of diorite pillowed off

such intrusions or became dispersed as MMEs. As this area occurs towards the centre of a reversely zoned intrusion, it is likely that the last major intrusive phase was the injection, interaction and partial disruption and dispersion of a major diorite component before the complete crystallization of at least part of the host granitoid. Although there is evidence of *in situ* mixing at the present level in some cases, the overall impression is that much of the mixing in the diorites had already occurred at deeper levels prior to their emplacement as synplutonic intrusions within the granitoid host.

Although there is obviously a complex spectrum of petrological and textural features present, two main facies of diorite and their associated MMEs have been recognized, representing differing degrees of mixing (Fig. 6): (1) plagioclase–hornblende–phyric biotite diorites which make up the vast proportion of the area of diorite outcrop (Knockvologan type); and (2) equigranular diorites/quartz diorites (Aird Mór type).

The Knockvologan type rocks are petrographically highly heterogeneous at both outcrop (Fig. 7) and thin-section scale. They are coarse- to medium-grained and contain zoned alkali feldspar xenocrysts, quartz ocelli and overgrowth textures (quartz mantled by hornblende, hornblende mantled by alkali feldspar and *vice versa*) constituting abundant evidence for magma mixing. Thin-section petrography shows that the alkali feldspar xenocrysts have perthitic cores and a highly seriticized plagioclase rim (10 mm core with 1 mm rim on average). Resorption surfaces within the crystals are common. The groundmass is a mosaic of zoned plagioclase, hornblende, alkali feldspar and quartz. Titanite is a common accessory phase and acicular apatite, indicative of quenching, occurs throughout.

The Aird Mór type consists of more homogeneous, finer grained diorites than the Knockvologan type. Petrographically, three modes of occurrence of hornblende can be distinguished: (a) as euhedral overgrowths on remnant clinopyroxenes, (b) poikilitically enclosed in plagioclase, and (c) as subhedral to anhedral clusters associated with biotite and Fe–Ti oxides. Alkali feldspar xenocrysts are rare and the groundmass is dominated by plagioclase and quartz.

Mapping of the structural orientation of the Knockvologan diorite bodies and their associated MME swarms show that in many cases gently inclined tabular sheets were emplaced synplutonically into the granitoid and subsequently became disrupted, producing swarms of extremely flattened and sheared enclaves (Fig. 7d).

Field relations: minor intrusions

The last manifestation of Caledonian magmatism was the widespread emplacement of mostly low-angle composite cross-cutting sheets and dykes which generally have a westward component of dip. Their composition and hybrid nature broadly mirror the plutonic components of the ROMG, implying that acid–basic interaction continued to be important throughout the waning stages of magmatism.

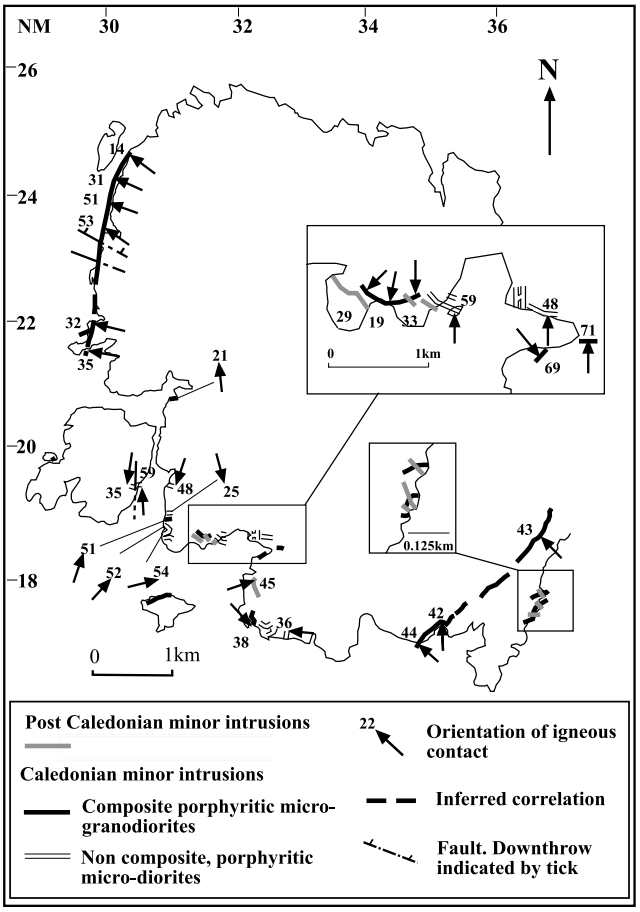


FIG. 8. Map showing the distribution of Caledonian minor intrusions on the Ross of Mull.

The present work, which builds on that of Rock & Hunter (1987), has shown that two main types exist (Fig. 8): (1) composite porphyritic micro-granodiorites; and (2) non-composite, porphyritic micro-diorites. Abundant type 1 sheets form a roughly arcuate swarm, dipping NW at Fionnphort, west at Eilean nam Bò, SW at Aird Mór and NW at Ardalanish; type 2 sheets are much less common and appear to trend randomly (Fig. 8).

Structural controls on siting and emplacement

Recent studies of the tectonics of granitoids in the area (e.g. Jacques & Reavy 1994; Reavy 2001) have emphasized the distinction between siting, ascent and emplacement.

Ascent is the transport of batches of melt through the crust from the site of melt generation to the level of emplacement. This phenomenon will usually be closely controlled by the lithospheric-scale structures responsible for the siting of the initial magmatism. Work in the SW Grampian area by Jacques & Reavy (1994) showed that concentric zoned or composite plutons are sited above the intersections of major crustal lineaments and fault/shear zones.

Emplacement involves the construction of so-called 'plutons' from the batches or pulses of ascended magma. In many cases this is probably by lateral spreading

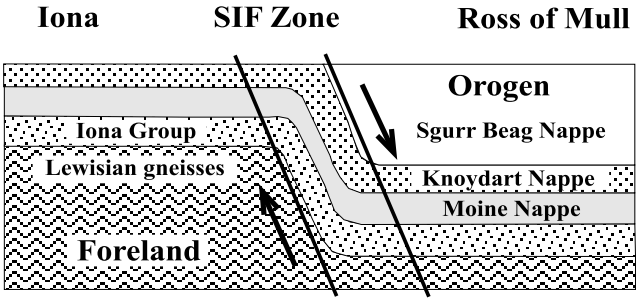


FIG. 9. Regional diagrammatic cross-section across the Sound of Iona fault (SIF) zone (extensional model) (adapted from Potts *et al.* 1995).

whereby flattish sheets were emplaced to form thin tabular and often discoid laccolithic bodies. As the ROMG is reversely zoned and centred offshore to the SW, and assuming that it has similar controls on its siting as other adjacent plutons in SW Argyllshire, we propose that the most likely site of magma ascent must be at the intersection of the SIF and the Dubh Artach Fault (the latter being a Great Glen-related splay) which occurs SW of the Torran Rocks (Pharaoh *et al.* 1996). The SIF has been proposed as a steep extensional, post-thrusting fault throwing down several kilometres to the ESE (Potts *et al.* 1995) and initially bringing Ross of Mull amphibolite-facies Moine rocks into contact with Iona Group rocks and Lewisian gneisses (Fig. 9).

Direct evidence for the thrust relationship is no longer seen because the initial thrust contact has been displaced by the SIF and the ROMG. We propose that steep extensional movements on the SIF may have been linked to more general extensional collapse within the Caledonian orogen, as is consistent with the interpretation of Dewey & Strachan (2003). We envisage that the ROMG was constructed from pulses of magma rising in the conduit provided by the fault intersection described above. Magma passing up this ascent zone was then emplaced northeastward as flattish sheets (Fig. 10) in the late-orogenic extensional environment produced by the collapse of Scandian nappes. Further evidence to support this emplacement style comes from xenolith studies of a Permian dyke just north of Fionnphort (J. Faithfull pers. comm.). The varied suite of crustal xenoliths contained in this dyke strongly suggests that the ROMG is underlain by a variety of crustal lithologies at no great depth below its base (J. Faithfull pers. comm.).

Conclusions

The ROMG is a reversely zoned body centred offshore to the SW of the Ross of Mull. It is proposed that batches of magma ascended along the steep intersection of the extensional SIF and a fault/faults related to the Great Glen Fault system; the complex then formed by

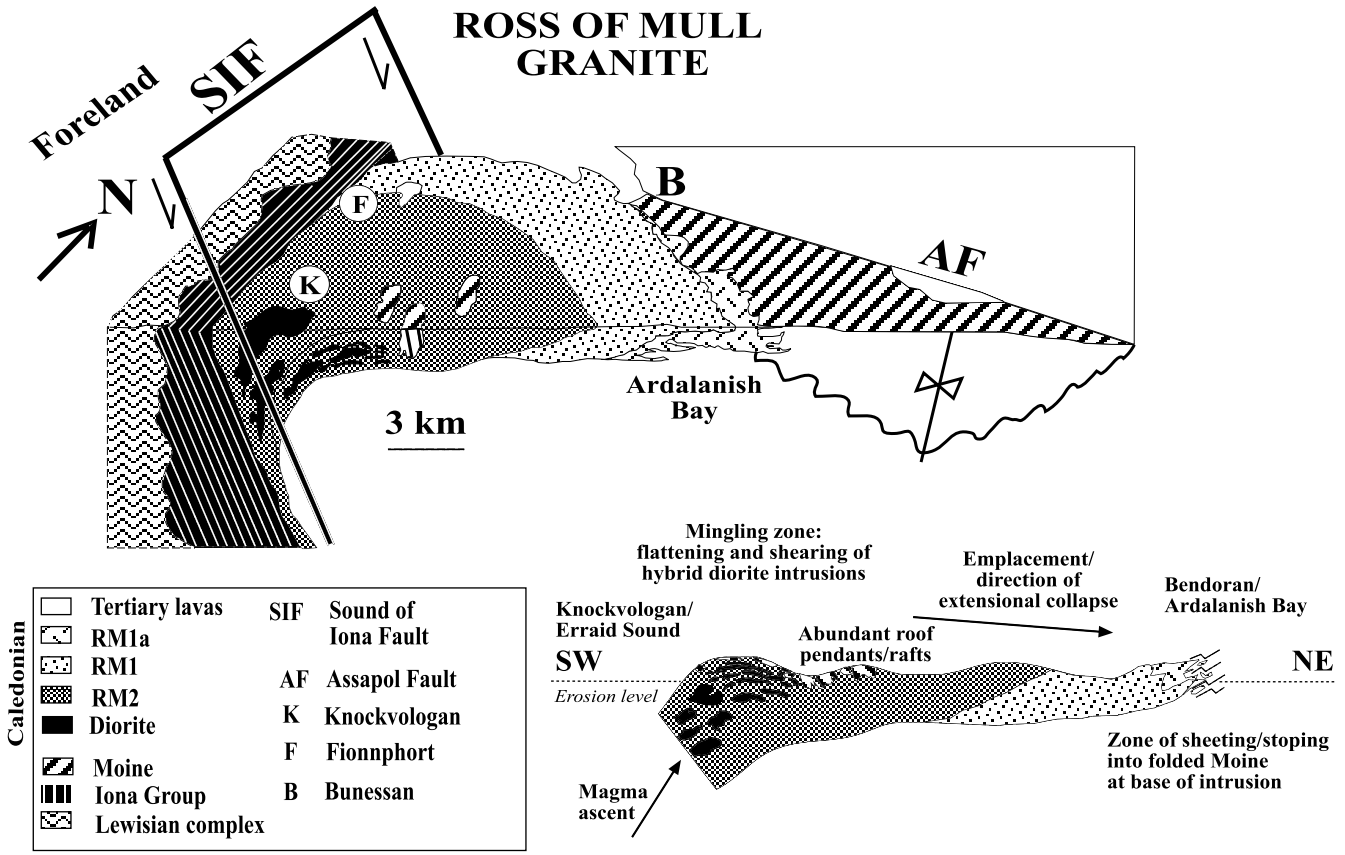


FIG. 10. Block diagram across the Sound of Iona fault (SIF) zone depicting the proposed emplacement geometry of the flattish batches of melt within an extensional regime created by the combined movements of the SIF and eastward-directed collapse within Caledonian thrust nappes. An accompanying simplified cross-section through the sheeted ROMG is also shown, highlighting the key areas and processes from roof to floor.

the northeastward emplacement of gently inclined sheets from the site of ascent; this was facilitated by extensional collapse in the overlying Moine nappes, the early stages of which may have involved the formation of the SIF itself. The later plutonic facies exhibit abundant evidence for acid–basic interaction, implying substantial mantle input. Geochemical data (Zaniewski unpubl. data) imply that the magmas were probably the result of anatexis of deep crust by enriched mantle material during a period of post-orogenic uplift and extension (similar to other Argyll suite plutons (Stephens & Halliday 1984; Tarney & Jones 1994; Atherton & Ghani 2002)). Anatexis of Moine metasediments to produce granitoid melt occurred only locally. Many of the larger Moine blocks apparently enclosed within the granite are roof pendants and the base of the complex is well exposed along its eastern margin. As the horizontal distance across the onshore outcrop (from envisaged floor to roof) is approximately 6 km, it is difficult to envisage that the ROMG can be more than several kilometres thick.

Acknowledgements

A.Z. acknowledges financial support from University College Cork and would like to thank Malcolm Hole and Jeremy Preston for introducing him to Caledonian magmatism; we have benefited greatly from discussions in the field with Adrian Finch, John Faithfull and Brian O'Driscoll. We would like to thank Nigel and Rosie Burgess and John and Eleanor Wagstaff for logistical support on Mull. The manuscript has been greatly improved by a meticulous, detailed and constructive review by John Faithfull (Hunterian Museum, University of Glasgow) and a thorough assessment by Jeremy Preston (HRH Ltd, Aberdeen). We would like to dedicate this paper to the memory of the late Robert Hunter who first introduced R.J.R. and A.L.H. to the complexity of acid–basic magma interaction on Knockvologan beach.

References

ATHERTON, M.P. & GHANI, A.A. 2002. Slab breakoff; a model for Caledonian, late granite syn-collisional magmatism in the orthotectonic (metamorphic) zone of Scotland and Donegal, Ireland. *Lithos,* **62**, 65–85.

BAILEY, E.B. & ANDERSON, E.M. 1925. *The Geology of Staffa, Iona and Western Mull.* Memoir of the Geological Survey, Geological Survey, UK.

BARR, D., HOLDSWORTH, R.E. & ROBERTS, R.M. 1986. Caledonian ductile thrusting in a Precambrian metamorphic complex: the Moine of north-western Scotland. *Geological Society of America, Bulletin,* **97**, 754–764.

BECKINSALE, R.D. & OBRADOVICH, J. 1973. Potassium-argon ages for minerals from the Ross of Mull, Argyllshire. *Scottish Journal of Geology,* **9**, 147–156.

CUNNINGHAM-CRAIG, E.H. 1911. South part of the Ross of Mull and adjacent islands. *In* Cunningham-Craig, E.H., Wright, W.B. & Bailey, E.B. (eds) *The Geology of Colonsay and Oronsay with part of the Ross of Mull.* Memoir of the Geological Survey of Scotland, 75–100.

DEWEY, J.F. & STRACHAN, R.A. 2003. Changing Silurian-Devonian relative plate motion in the Caledonides. Sinstral transpression to sinstral transtension. *Journal of the Geological Society, London,* **160**, 209–218.

FRASER, F.M. 1977. *The Lewisian and Torridonian geology of Iona.* PhD thesis, University of St. Andrews.

GROGAN, S.E. & REAVY, R.J. 2002. Disequilibrium textures in the Leinster granite complex, SE Ireland: evidence for acid-acid magma mixing. *Mineralogical Magazine,* **66**, 929–939.

HALLIDAY, A.N., AFTALION, M., BREEMEN, O.V. & JOCELYN, J. 1979. Petrogenetic significance of Rb-Sr and U-Pb isotopic systems in the 400 Ma old British Isles granitoids and their hosts. *In* Harris, A.L., Holland, C.H. & Leake, B.E. (eds) *The Caledonides of the British Isles Reviewed,* Geological Society, London, 653–661.

HARRIS, A.L. & HIGHTON, A.J. 1999. *Ross of Mull. Sheet 43S. Solid and Drift.* 1:50 000 Provisional Series, British Geological Survey, Keyworth, Nottingham.

HIGHTON, A.J. 2001. Cnoc Mor to Rubh'Ardalanish & Knockvologan to Eilean a'Chalmain. *In* Stevenson, D., Bevins, R.E., Milward, D., Highton, A.J., Parsons, I., Stone, P. & Wadsworth, W.J. (eds) *Caledonian Igneous Rocks of Great Britain,* Joint Nature Conservation Committee, 417–424.

HOLDSWORTH, R.E., HARRIS, A.L. & ROBERTS, A.M. 1987. The stratigraphy, structure and regional significance of Moine rocks of Mull, Argyllshire, W. Scotland. *Geological Journal,* **22**, 83–107.

JACQUES, J.M. & REAVY, R.J. 1994. Caledonian plutonism and major lineaments in the SW Scottish Highlands. *Journal of the Geological Society, London,* **151**, 955–969.

KELLEY, S.P. & POWELL, D. 1985. Relationships between marginal thrusting and movement on major internal shear zones in the north Highland Caledonides, Scotland. *Journal of Structural Geology,* **7**, 43–56.

PETFORD, N., PATERSON, B., MCCAFFREY, K. & PUGLIESE, S. 1996. Melt infiltration and advection in microdioritic enclaves. *European Journal of Mineralogy,* **8**, 405–412.

PHARAOH, T.C., MORRIS, J.H., LONG, C.B. & RYAN, P.D. 1996. *Tectonic Map of Britain, Ireland and adjacent areas.* 1:500 000 series, British Geological Survey, Keyworth, Nottingham.

POTTS, G.J., HUNTER, R.H., HARRIS, A.L. & FRASER, F.M. 1995. Late-orogenic extensional tectonics at the NW margin of the Caledonides in Scotland. *Journal of the Geological Society, London,* **152**, 907–910.

PUGLIESE, S. & PETFORD, N. 2001. Reconstruction and visualisation of melt topology in veined microdioritic enclaves. *Electronic Geosciences,* **6** (2), 1–23.

REAVY, R.J. 2001. Caledonian granites – emplacement. Symposium Edition. *Open University Geological Society Journal,* **22**(2).

ROCK, N.M.S. & HUNTER, R.H. 1987. Late Caledonian dyke-swarms of northern Britain: spatial and temporal intimacy between lamprophyric and granitic magmatism around the Ross of Mull pluton, Inner Hebrides. *Geologische Rundschau,* **76** (3), 805–826.

STEPHENS, W.E. & HALLIDAY, A.N. 1984. Geochemical contrasts between late Caledonian granitoid plutons of northern, central and southern Scotland. *Transactions of the Royal Society of Edinburgh: Earth Sciences,* **75**, 259–273.

TARNEY, J. & JONES, C.E. 1994. Trace element geochemistry of orogenic igneous rocks and crustal growth models. *Journal of the Geological Society, London,* **151**, 855–868.

WHEELER, J., MANGAN, L.S. & PRIOR, D.J. 2004. Disequilibrium in the Ross of Mull contact metamorphic aureole, Scotland; a consequence of polymetamorphism. *Journal of Petrology,* **45** (4), 835–853.

MS. accepted for publication 13 *June* 2006

REFERENCES

ANGUS, N.S. 1962. Ocellar hybrids from the Tyrone Igneous Series, Ireland. *Geological Magazine* **99**, 9-26.

ANDERSON, A.T. 1984. Probable relations between plagioclase zoning and magma dynamics, Fuego Volcano, Guatemala. *American Mineralogist* **69**, 660-676.

ANDERSSON, U.B. & EKLUND, O. 1994. Cellular plagioclase intergrowths as a result of crystal-magma mixing in the Proterozoic Åland rapakivi batholiths, SW Finland. *Contributions to Mineralogy and Petrology* **117**, 124-136.

ATHERTON, M.P. & GHANI, A.A. 2002. Slab breakoff; a model for Caledonian, late granite syn-collisional magmatism in the orthotectonic (metamorphic) zone of Scotland and Donegal, Ireland. *Lithos* **62**, 65-85.

BAKER, J., PEATE, D., WAIGHT, T., & MEYZEN, C. 2004. Pb isotopic analysis of standards and samples using a ^{207}Pb-^{204}Pb double spike and thallium to correct for mass bias with a double-focusing MC-ICP-MS. *Chemical Geology* **211**, 275-303.

BARBARIN, B. 1988. Field evidence for successive mixing and mingling between the Piolard diorite and the Saint-Julien-la-Vêtre Monzogranite (Nord-Forez. Massif Central, France). *Canadian Journal of Earth Science* **25**, 49-59.

BARBARIN, B. 2005. Mafic magmatic enclaves and mafic rocks associated with some granitoids of the central Sierra Nevada Batholith, California: nature, origins, and relations with the hosts. *Lithos* **80**, 155-177.

BAXTER, S. & FEELY, M.M.J. 2002. Magma mixing and mingling textures in granitoids: examples from the Galway granite, Connemara, Ireland. *Mineralogy & Petrology* **76**, 63-74.

BECKINSALE, R.D. & OBRADOVICH, J. 1973. Potassium-argon ages for minerals from the Ross of Mull, Argyllshire. *Scottish Journal of Geology* **9**, 147-156.

BLUNDY, J. & CASHMAN, K. 2008. Petrologic reconstruction of magmatic system variables and processes. *Reviews in Mineralogy and Geochemistry*, **69**, 179-239.

BOWEN, N.L. 1922. The behaviour of inclusions in igneous magmas. *Journal of Geology* **30**, 313-570.

BROOKS, R.J., FINCH, A.A., HOLE, D.E., TOWNSEND., P.D. & WU, Z. 2002. The red to near-infrared luminescence in alkali feldspar. *Contributions to Mineralogy and Petrology* **143**, 484-494.

CASTRO, A. & STEPHENS, W.E. 1992. Amphibole-rich polycrystalline clots in calc-alkaline granitic rocks and their enclaves. *Canadian Mineralogist* **30**, 1093-1112.

COX, R.A., DEMPSTER, T.J., BELL, B.R. & ROGERS, G. 1996. Crystallisation of the Shap Granite: Evidence from zoned K-feldspar megacrysts. *Journal of the Geological Society, London* **153**, 625-635.

CRABTREE, S.M. & LANGE, R.A 2011. Complex phenocryst textures and zoning patterns in andesites and dacites: evidence of degassing-induced rapid crystallisation. *Journal of Petrology* **52**, 3-38.

DALY, J.S. & POLI, G. 1999. Petrogenetic insights from microchemical investigations from magmatic K-Feldspars in the 7 Ma Elba monzo-granite. *Irish Journal of Earth Sciences* **17**, 128.

DAVIDSON, J.P., MORGAN, D.J. & CHARLIER, B.L.A 2007. Isotopic microsampling of magmatic rocks. *Elements* **3**, 253-259.

DEWEY, J.F., DALZIEL, I.W.D., REAVY, R.J. & STRACHAN, R.A. 2015. The Neoproterozoic to Mid-Devonian evolution of Scotland: a review and unresolved issues. *Scottish Journal of Geology* **51**, 5-30.

DICKIN, A.P. 1981. Isotope geochemistry of Tertiary rocks from the Isle of Skye, N.W. Scotland. *Journal of Petrology* **22**, 155-189.

DICKIN, A.P., BROWN, J.L., THOMPSON, R.N. & O'HARA, M.J. 1984. Crustal contamination and the granite problem in the British Tertiary Volcanic Province. *Philosophical Transactions of the Royal Society of London.* Series A, Mathematical and Physical Sciences **310**, Issue 1514, 778-780.

FAITHFULL, J.W. & UPTON, B.G.J. 2006. Xenolithic insights into the deep geology beneath the Ross of Mull. *Scottish Journal of Geology* **42**, 37-41.

FERNANDEZ, A.N. & BARBARIN, B. 1991. Relative rheology of coeval mafic and felsic magmas: nature of resulting interaction processes and shape and mineral fabrics of mafic micro-granular enclaves. *In* Didier, J. & Barbarin, B. (eds.), *Enclaves and granite petrology*. Elsevier, Amsterdam, 263-275 (Developments in Petrology 13).

FINCH, A.A. 2003. Cathodoluminescence at the University of St Andrews. Instruction guide. *Unpublished Manual for Technocyn 8200 Mk V Luminoscope fitted with Alcatel Vacuum Pump*, University of St Andrews.

FINCH, A.A., HOLE, D.E. & TOWNSEND, P.D. 2003. Orientation dependence of luminescence in plagioclase. *Physics and Chemistry of Minerals* **30**, 373-381.

FINCH, A.A. & KLEIN, J. 1999. The causes and petrological significance of cathodoluminescence emissions from alkali feldspars. *Contributions to Mineralogy and Petrology* **135**, 234-243.

GAGNEVIN, D., DALY, J.S., POLI, G. & MORGAN, D. 2005. Microchemical and Sr isotopic investigation of zoned K-feldspar megacrysts: Insights into the petrogenesis of a granitic system and disequilibrium crystal growth. *Journal of Petrology* **46**, 1689-1724.

GAGNEVIN, D., DALY, J.S., WAIGHT, T.E., MORGAN, D. & POLI, G. 2005. Pb isotopic zoning of K-feldspar megacrysts determined by Laser Ablation Multiple-Collector ICP-MS: Insights into granite petrogenesis. *Geochimica et Cosmochimica Acta* **69**, 1899-1915.

GINIBRE, C., WÖRNER, G. & KRONZ, A. 2004. Structure and dynamics of the Laacher See magma chamber (Eifel, Germany) from major and trace element zoning in sanidine: A cathodoluminescence and electron microprobe study. *Journal of Petrology* **45**, 2197-2223.

GINIBRE, C., WÖRNER, G. & KRONZ, A. 2007. Crystal zoning as an archive for magma evolution. *Elements*, **3**, 261-266.

GÖTZE, J., KRBETSCHEK, M.R., HABERMANN, D. & WOLF, D. 2000. High-resolution cathodoluminescence studies of feldspar minerals. *In* Pagel, M., Barbarin, V., Blanc, P. & Ohnenstetter, D. (eds.), *Cathodoluminescence in geosciences*. Springer, Berlin, Heidelberg New York, 245-270.

GROGAN, S.E. & REAVY, R.J. 2002. Disequilibrium textures in the Leinster granite complex, SE Ireland: evidence for acid-acid magma mixing. *Mineralogical Magazine* **60**, 929-939.

GROGAN, S.E. 2004. The petrogenetic evolution of the Leinster Granite Complex, SE Ireland. *Unpublished PhD Thesis*, National University Ireland, University College Cork.

HAGNI, A.M. 2002. Fine particle characterization by reitveld QXRD, CLM and SEM-EDS phase mapping. *Journal of the Minerals, Metals and Materials Society* **54**, 24-26.

HALLIDAY, A.N., AFTALION, M., BREEMEN, O.V. & JOCELYN, J. 1979. Petrogenetic significance of Rb-Sr and U-Pb isotopic systems in the 400 Ma old British Isles granitoids and their hosts. *In* Harris, A.L., Holland, C.H. & Leake, B.E. (eds.), *The Caledonides of the British Isles reviewed*, 653-661. Geological Society of London.

HARRIS, A.L. & HIGHTON, A.J. (Compilers). 1999. British Geological Survey. 1:50 000 (Ross of Mull). Sheet 43S. Solid and Drift. 1:50 000 Provisional Series. Keyworth: British Geological Survey.

HART, S.R. 1984. A large-scale isotopic anomaly in the Southern Hemisphere mantle. *Nature* **309**, 753-757.

HIBBARD, M.J. 1981. The magma mixing origin of mantled feldspars. *Contributions to Mineralogy & Petrology* **76**, 158-170.

HIBBARD, M.J. 1991. Textural anatomy of twelve magma-mixed granitoid systems. *In* Didier J, Barbarin B (eds.), *Enclaves and granite petrology*. Elsevier, Amsterdam, 431-444 (Developments in Petrology 13).

HOLCOMBE, R. 2005. GEOrient V.9.2 Stereographic projections and rose diagram plots software.

HOLDSWORTH, R.E., HARRIS, A.L. & ROBERTS, A.M. 1987. The stratigraphy, structure and regional significance of Moine rocks of Mull, Argyllshire, W. Scotland. *Geological Journal* **22**, 83-107.

JANOUŠEK, V., BOWES, D.R., BRAITHWAITE, J.R. & ROGERS, G. 2000. Micro-structural and mineralogical evidence for limited involvement of magma mixing in the petrogenesis of a Hercynian high-K calc-alkaline intrusion: the Kozárovice granodiorite, Central Bohemian Pluton, Czech Republic. *Transactions of the Royal Society of Edinburgh*: *Earth Sciences* **91**, 15-26.

JACQUES, J.M. & REAVY, R.J. 1994. Caledonian plutonism and major lineaments in the SW Scottish Highlands. *Journal of the Geological Society, London* **151**, 955-969.

KRBETSCHEK, M.R., GÖTZE, J., IRMER, G., RIESER, U. & TRAUTMAN, T. 2002. The red luminescence emission of feldspar and its wavelength dependence on K, Na, Ca – composition. *Mineralogy and Petrology* **76**, 167-177.

LOFGREN, G. 1974. Temperature induced zoning in synthetic plagioclase feldspar. *In* MacKenzie, W.S. & Zussman, J. (eds.), *The feldspars*. Proceedings of a NATO Advanced Study Institute Manchester 11-21 July 1972, *Manchester University Press*. Crane, Russak & Company, New York, 277-292 (Developments in Petrology 13).

LOOMIS, T.P. 1982. Numerical simulations of crystallisation processes of plagioclase in complex melts: the origin of major and oscillatory zoning in plagioclase. *Contributions to Mineralogy and Petrology* **81**, 219-229.

LOVAS, G.A. & BUDA, G. 2004. Efficiency of Rietveld-based XRD quantification of mineral abundance in granitic rocks, a case study. *Acta Mineralogica-Petrographica* **45/1**, 49-53.

MATHEZ, E.A. & WAIGHT, T.E. 2003. Lead isotopic disequilibrium between sulphide and plagioclase in the Bushveld Complex and the chemical composition of large layered intrusions. *Geochimica et Cosmochimica Acta* **67**, 1875-1888.

MCATEER, C.A. 2009. Provenance of Metasedimentary Sequences in the Scottish and Irish Caledonides. *Unpublished PhD Thesis,* National University Ireland, University College Dublin, 79.

MCLEOD, G.W., DEMPSTER, T.D. & FAITHFULL, J.W. 2011. Deciphering magma-mixing processes using zoned titanite from the Ross of Mull Granite, Scotland. *Journal of Petrology* **52**, 55-82.

MUIR, R.J., IRELAND, T.R., BENTLEY, M.R., FITCHES, W.R. & MALTMAN, A.J. 1997. A Caledonian age for the Kiloran Bay appinite intrusion on Colonsay, Inner Hebrides. *Scottish Journal of Geology* **33**, 75-83.

OLIVER, G.H.J., WILDE, S.A. & WAN, Y.S. 2008. Geochronology and geodynamics of Scottish granitoids from the late Neoproterozoic break-up of Rodinia to Palaeozoic collision. *Journal of the Geological Society, London* **165**, 661-674.

PALIVCOWÁ, M., WALDHAUSROVÁ, J. & LEDVINKOVÁ, V. 1995. Ocelli in mafic rocks of granitic complexes. *Krystallinikum* **22**, 149-186.

PEATE, D.W. & HAWKESWORTH, C.J. 2005. U-series disequilibria: insights into mantle melting and the time scales of magma differentiation. *Reviews of Geophysics* **43**, RG1003 1-43.

PEATE, D.W., BARKER, A.K., RIISHUUS, M.S. & ANDREASEN, R. 2008. Temporal variations in crustal assimilation of magma suites in the East Greenland flood basalt province: tracking the evolution of magmatic plumbing systems. *Lithos*, **102**, 179-197.

PEMBROKE, J.W. 1997. The recognition and significance of magma mixing and mingling in granites. *Unpublished PhD Thesis*, Oxford Brookes University.

PETFORD, N., PATERSON, B., MCCAFFREY, K. & PUGLIESE, S. 1996. Melt infiltration and advection in micro-dioritic enclaves. *European Journal of Mineralogy* **8**, 405-412.

PETRONIS, M.S., O'DRISCOLL, B., STEVENSON, C.T.E. & REAVY, R.J. 2012. Controls on emplacement of the Caledonian Ross of Mull Granite, NW Scotland: Anisotropy of magnetic susceptibility and magmatic and regional structures. *Geological Society of America Bulletin* **124**, 906- 927.

PHARAOH, T.C., MORRIS, J.H., LONG, C.B. & RYAN, P.D. (Compilers). 1996. 1:500 000 Tectonic Map of Britain, Ireland and adjacent areas. Keyworth: British Geological Survey.

PITCHER, W.S. 1991. Synplutonic dykes and mafic enclaves. *In* Didier, J. & Barbarin, B. (eds.), *Enclaves and granite petrology*. Elsevier, Amsterdam, 383-392 (Developments in Petrology 13).

POLI, G. & PERUGINI, D. 2002. Stop n. 6(a) Sant'Andrea. *In* Poli, G., Perugini, D., Rocchi, S. & Dini, A. (eds.), *Miocene to recent plutonism and volcanism in the Tuscan Magmatic Province (Central Italy)*. Eurogranites, European Network of Laboratories Granites, Part V, 275-279.

POTTS, G.J., HUNTER, R.H., HARRIS, A.L. & FRASER, F.M. 1995. Late-orogenic extensional tectonics at the NW margin of the Caledonides in Scotland. *Journal of the Geological Society, London* **152**, 907-910.

PUGLIESE, S. & PETFORD, N. 2001. Reconstruction and visualisation of melt topology in veined micro-dioritic enclaves. *Electronic Geosciences* **6**, 1-22.

READ, H.H. 1961. Aspects of Caledonian magmatism in Britain. *Liverpool & Manchester Geological Journal* **2**, 653-683.

REAVY, R.J. 2001. Caledonian granites-emplacement. *Open University Geological Society Journal* **22(2)**, Symposium Edition.

RIETVELD, H.M. 1967. Line profiles of neutron powder-diffraction peaks for structure refinement. *Acta Crystallographica* **22**, 151-152.

RIETVELD, H.M. 1969. A profile refinement method for nuclear and magnetic structures. *Journal of applied Crystallography* **2**, 65-71.

ROCK, N.M.S. & HUNTER, R.H. 1987. Late Caledonian dyke-swarms of northern Britain: spatial and temporal intimacy between lamprophyric and granitic magmatism around the Ross of Mull pluton, Inner Hebrides. *Geologische Rundschau* **76/3,** 805-26.

SANDRIN, A., EDFELT Â., WAIGHT, T.E., BERGGREN, R., ELMING S-A, 2009. Physical properties and petrologic description of rock samples from an IOCG mineralized area in the northern Fennoscandian Shield, Sweden. *Journal of Geochemical Exploration*, **103(2-3)**, 80–96.

SIAL, A.N., FERREIRA, V.P., FALLICK, A.E., JERÓNIMO, M. & CRUZ, M. 1998. Amphibole rich clots in calc-alkaline granitoids in the Borborema province, northeastern Brazil. *Journal of South American Earth Sciences* **11**, 457-471.

SPARKS, R.S.J. & MARSHALL, L.A. 1986. Thermal and mechanical constraints on mixing between mafic and silicic magmas. *Journal of Volcanology & Geothermal Research* **29**, 99-124.

SOPER, N.J. 1986. The Newer Granite problem: a geotectonic review. *Geological Magazine* **123,** 227-236.

STEPHENS, W.E. & HALLIDAY, A.N. 1984. Geochemical contrasts between late Caledonian granitoid plutons of northern, central and southern Scotland. *Transactions of the Royal Society of Edinburgh: Earth Sciences* **75**, 259–273.

STEPHENS, W.E., HOLDEN, P. & HENNEY, P.J. 1991. Microdioritic enclaves within the Scottish Caledonian granitoids and their significance for crustal magmatism. *In* Didier, J. & Barbarin, B. (eds.), *Enclaves and granite petrology*. Elsevier, Amsterdam, 125-134 (Developments in Petrology 13).

STIMAC, J.A. & WARK, D.A. 1992. Plagioclase mantles on sanidine in silicic lavas, Clear Lake, California: Implications for the origin of rapakivi texture. *Geological society of America Bulletin* **104**, 728-744.

STRECKEISEN, A. 1976. To each plutonic rock its proper name. *Earth Science Reviews* **12**, 1-33.

STULL, J. 1979. Mantled feldspars and synneusis. *American Mineralogist* **64**, 524-518.

TYRELL, S., HAUGHTON, P.D.W., DALY, J.S., KOKFELT, T.F. & GAGNEVIN, D. 2006. The use of common Pb isotope composition of detrital K-feldspar grains as a provenance tool and its application to Upper Carboniferous palaeodrainage, Northern England. *Journal of Sedimentary Research*, 76, 324-345.

UBIDE, T., GALÉ, C., LARREA, P., ARRANZ, E., LAGO, M. & TIERZ, P. 2014. The relevance of crystal transfer to magma mixing: a case study in composite dykes from the Central Pyrenees. *Journal of Petrology* **55**, 1535-1559.

VANCE, J.A. 1962. Zoning in igneous plagioclase: normal and oscillatory zoning. *American Journal of Science* **260**, 746-760.

VANCE, J.A. 1965. Zoning in igneous plagioclase: patchy zoning. *Journal of Geology* **73**, 529-536.

VANCE, J.A. 1969. On Synneusis. *Contributions to Mineralogy and Petrology* **24**, 7-29.

WATSON, J. 1984. The ending of the Caledonian orogeny in Scotland. *Journal of the Geological Society, London* **141**, 193-214.

WILLIGERS, B.J.A., BAKER, J.A., KROGSTAD, E.J. & PEATE, D.W. 2002. Precise and accurate *in situ* Pb-Pb dating of apatite, monazite, and sphene by laser ablation multiple-collector ICP-MS. *Geochimica et Cosmochimica Acta* **66**, 1051-1066.

WYLLIE, P.J., COX, K.G. & BIGGAR, G.M. 1962. The habit of apatite in synthetic systems and igneous rocks. *Journal of Petrology* **3**, 238-243.

ZANIEWSKI, A., REAVY, R.J. & HARRIS A.L. 2006. Field relationships and emplacement of the Ross of Mull Granite (ROMG), Argyllshire. *Scottish Journal of Geology* **42**, 179-189.